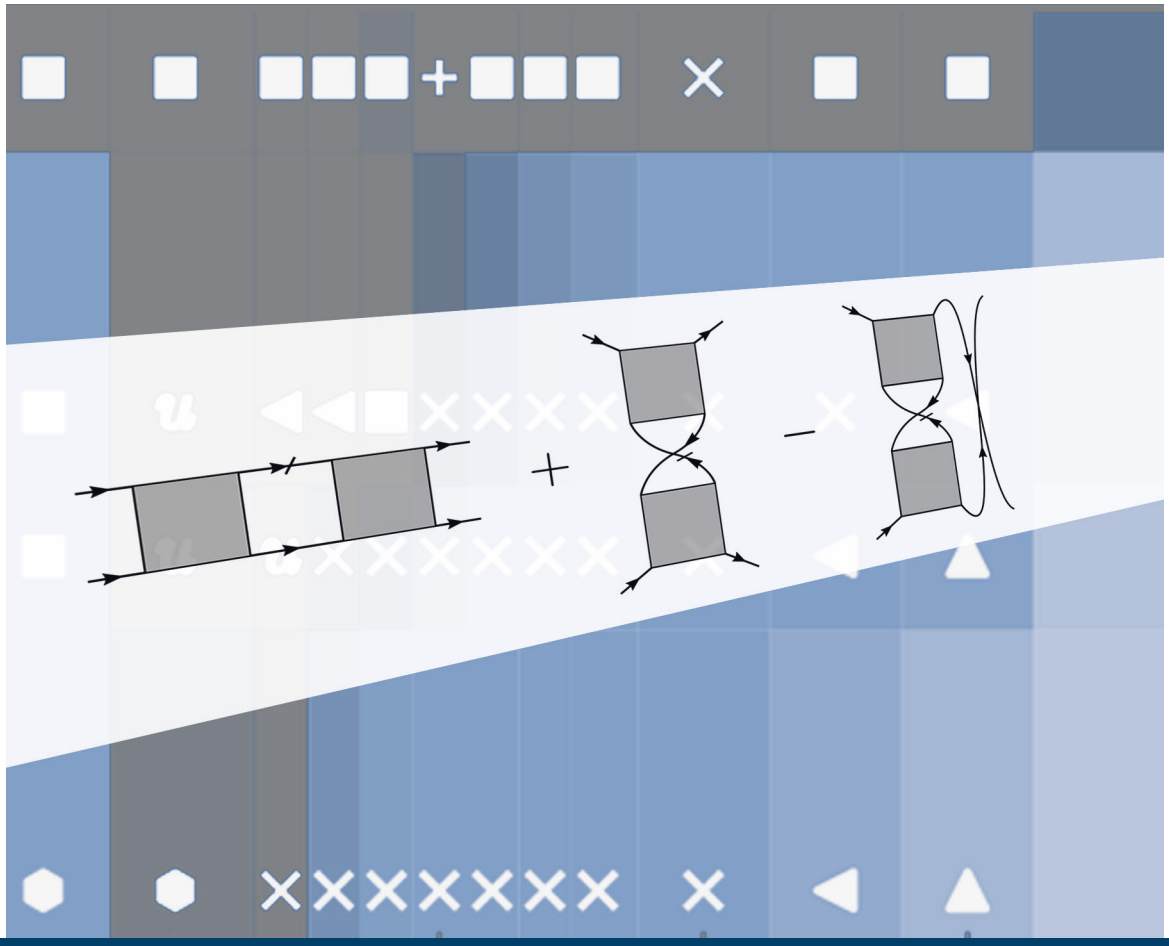

A Unified Framework for Functional Renormalisation Group Calculations and its Application to Three Dimensional Hubbard Models

Jannis Ehrlich

Schlüsseltechnologien / Key Technologies
Band / Volume 248
ISBN 978-3-95806-582-6

Mitglied der Helmholtz-Gemeinschaft

JÜLICH
Forschungszentrum

Schriften des Forschungszentrums Jülich
Reihe Schlüsseltechnologien / Key Technologies Band / Volume 248

Forschungszentrum Jülich GmbH
Peter Grünberg Institut (PGI)
Quanten-Theorie der Materialien (PGI-1/IAS-1)

A Unified Framework for Functional Renormalisation Group Calculations and its Application to Three Dimensional Hubbard Models

Jannis Ehrlich

Schriften des Forschungszentrums Jülich
Reihe Schlüsseltechnologien / Key Technologies Band / Volume 248

ISSN 1866-1807 ISBN 978-3-95806-582-6

Bibliografische Information der Deutschen Nationalbibliothek.
Die Deutsche Nationalbibliothek verzeichnet diese Publikation in der
Deutschen Nationalbibliografie; detaillierte Bibliografische Daten
sind im Internet über http://dnb.d-nb.de abrufbar.

Herausgeber und Vertrieb:	Forschungszentrum Jülich GmbH Zentralbibliothek, Verlag 52425 Jülich Tel.: +49 2461 61-5368 Fax: +49 2461 61-6103 zb-publikation@fz-juelich.de www.fz-juelich.de/zb
Umschlaggestaltung:	Grafische Medien, Forschungszentrum Jülich GmbH
Druck:	Grafische Medien, Forschungszentrum Jülich GmbH
Copyright:	Forschungszentrum Jülich 2021

Schriften des Forschungszentrums Jülich
Reihe Schlüsseltechnologien / Key Technologies, Band / Volume 248

D 82 (Diss. RWTH Aachen University, 2021)

ISSN 1866-1807
ISBN 978-3-95806-582-6

Vollständig frei verfügbar über das Publikationsportal des Forschungszentrums Jülich (JuSER)
unter www.fz-juelich.de/zb/openaccess.

Acknowledgements

This thesis would not have been possible without the support of many people throughout the years of my doctoral studies. First of all I thank Carsten Honerkamp and Stefan Blügel for giving me the opportunity to work on this interesting project, being part of both of their groups, enabling my participation at national and international workshops and conferences and refereeing this thesis. I am especially grateful to Carsten Honerkamp for his supervision, fruitful scientific discussions and his patience with this thesis.

I sincerely appreciated the collaboration with Jacob Beyer, Lennart Klebl and Jonas Hauck with whom I had plenty productive discussions and who helped in improving the quality and generality of the resulting code. I want to gratefully acknowledge the support by Daniel Rohe, who analysed the parallelisation of my code not only once and provided very helpful advice for a significant improvement, so that chapter 4.5 is devoted to him. I am further thankful for the scientific exchange and collaboration on the functional renormalisation group with Cornelia Hille, Agnese Tagliavini, and my former colleagues Julian Lichtenstein, David Sánchez de la Peña, and especially Giulio Schober and Timo Reckling. I further want to thank Mathias Müller and Christoph Friedrich for their support in questions concerning perturbation theory and their numerical implementation.

For the creation of such a pleasant, inspiring atmosphere I am thankful to all the present and former colleagues at the RWTH Aachen, among them Sebastian Larisch, Lukas Weber, Feng Xiong, Mathias Schumacher, Jonas Becker, Patrick Emonts, Christian Eckhardt and Lisa Markhof, and at the Peter Grünberg Institut at the Forschungszentrum Jülich, among them Fabian Lux, Gregor Michalicek, Christian Gerhorst, Stefan Rost, Philipp Rüßmann, Jens Bröder and Rico Friedrich.

Great thanks for proofreading (parts) of the manuscript of this thesis go to Christoph Friedrich, Lennart Klebl, Jonas Hauck and, especially, to Gisela Deitert.

I further gratefully acknowledge the computing time granted by the JARA-HPC Vergabegremium on the supercomputer JURECA [1] at Froschungszentrum Jülich, as well as financial support through the Deutsche Forschungsgesellschaft through the research training group RTG1995.

Finally, but most importantly, I thank my parents for their help and advice through all the years and I thank Anna for her love and being a strong support even when everything seems to cause trouble.

Abstract

In this thesis a general framework for calculations of the two-fermion interaction based on the Functional Renormalisation Group (FRG) approach is developed. It comprises an implementation of the corresponding flow equations in the spinful and in an SU(2)-symmetric version and for each of them both, a pure momentum space parametrisation and a form-factor based parametrisation of the two-fermion interaction are implemented. The form-factor based approach is in terms of the recently developed Truncated Unity Functional Renormalisation Group (TUFRG) [2], for which this thesis provides a generalisation to spinful systems. In addition, I show that the resulting implementation is properly scaling in terms of parallelisation for a large number of multi-core CPUs and with the system size according to the theoretical limitations. As the exploitation of symmetries of the two-fermion interactions facilitates the treatment of larger system sizes due to the focus on independent elements, these symmetries are discussed to some extent within this thesis.

The resulting code is first tested against well-established results for the $t - t'$ Hubbard model on a square lattice, for which also the convergence of the TUFRG approach with an increasing length of form-factors to the results of the full momentum parametrisation is shown. Based on these successful tests the code is used to investigate two different three-dimensional systems by an application of the TUFRG approach:
First, the simple cubic, isotropic Hubbard model is investigated where a transition to an antiferromagnetic ground state is observed at half filling. The critical scale indicating this transition behaves similar to the corresponding Néel temperature obtained by other approaches in dependence of the Hubbard-U parameter in the weak coupling region. When this Hubbard model is successively hole-doped away from half filling within this weak coupling region, the antiferromagnetic ordering first becomes incommensurate before a d-wave superconducting phase emerges. In the case of an even stronger hole doping a dominant antiferromagnetic phase is observed again, which now features planar ordering vectors (i.e. $(\pi, \pi, 0)$) instead of cube diagonal ones (i.e. (π, π, π)).

As a second application, the anisotropic Hubbard model with isotropic hoppings to first and to second nearest neighbours within the xy-plane and with a weak hopping in the z-direction was considered, which was chosen to resemble the planar structure of cuprate or nickelate superconductors. To investigate the influence of the additional hopping on the $t - t'$-diagram known from the two-dimensional case, I focused on systems in which the chemical potential is chosen to fulfil the van-Hove condition of the xy-plane. In this setting an increasing hopping in the z-direction leads to a decrease of the critical scale for the antiferromagnetic and for the d-wave superconducting phase, while the phase boundary between them only changes on a small level with respect to t'. The most striking difference is the appearance of a p-wave superconducting phase and corresponding strong fluctuations at large $-t'$ values in the ferromagnetic phase.

Zusammenfassung

Im Rahmen dieser Dissertation wird ein allgemeines Framework für die Berechnung der effektiven Wechselwirkung zwischen zwei Fermionen auf Basis der Funktionellen Renormierungsgruppe (FRG) entwickelt. Dieses enthält eine Implementierung der entsprechenden Flussgleichungen für den Fall vollständiger Spinabhängigkeit und für den SU(2)-symmetrischen Fall. Für beide Varianten existiert sowohl eine Version, in der die vollständige Impulsabhängigkeit der Wechselwirkung erhalten ist, sowie eine, in der die Wechselwirkung durch Formfaktoren parametrisiert wird. Die auf Formfaktoren basierende Variante entspricht der vor kurzer Zeit vorgestellten Truncated Unity Functional Renormalisation Group (TUFRG) [2], für die in dieser Dissertation eine Verallgemeinerung zu spinabhängigen Systemen entwickelt wurde. Darüberhinaus wird eine gute Skalierung der Implementierung der Flussgleichungen erreicht sowohl in Hinblick auf eine Parallelisierung mit einer hohen Anzahl von multi-Kern CPUs, als auch in Hinblick auf die Systemgröße entsprechend der theoretischen Limitierung. Die Ausnutzung von Symmetrien der Wechselwirkung zwischen zwei Elektronen bewirkt, dass nur die voneinander unabhängigen Elemente dieser Wechselwirkung berechnet werden müssen, wodurch größere Systeme numerisch behandelt werden können. Dementsprechend werden diese Symmetrien ausführlich in dieser Dissertationsschrift behandelt.

Der resultierende Simulationscode wird zunächst gegen die bekannten Ergebnisse des $t-t'$ Hubbard Models auf einem Quadratgitter getestet. Für diesen Fall wird auch gezeigt, dass die TUFRG mit zunehmender Reichweite der Formfaktoren zu dem Ergebnis konvergiert, das aus der Parametrisierung der Wechselwirkung im Impulsraum resultiert. Auf Basis dieser erfolgreichen Tests wird die vorliegende Implementierung genutzt, um zwei verschiedene dreidimensionale Systeme mithilfe der TUFRG zu untersuchen:
Zunächst wird das kubische, isotrope Hubbard Model untersucht, das einen Phasenübergang zu einem antiferromagnetischen Grundzustand bei halber Füllung zeigt. Es wird dabei festgestellt, dass die kritische Skala, die in unserer TUFRG Implementierung diesen Übergang anzeigt, und die Néel Temperatur, die aus anderen numerischen Herangehensweisen resultiert, in gleicher Weise vom Hubbard-U Parameter im Bereich schwacher Wechselwirkung abhängen. Wird das halb gefüllte Hubbard Model in diesem Bereich mit Löchern dotiert, so wird die antiferromagnetische Ordnung zunächst inkommensurat, bevor eine supraleitende Phase mit d-Wellen Ordnung auftritt. Wird das System darüberhinaus mit Löchern dotiert, so tritt wieder eine antiferromagnetische Phase auf, die jetzt planare Ordnungsvektoren (d.h. $(\pi, \pi, 0)$) an Stelle von Würfeldiagonalen (d.h. (π, π, π)) besitzt.

Als zweite Anwendung wird das anisotrope dreidimensionale Hubbard Model mit einem isotropen Hüpfterm zu den nächsten zwei Nachbarn innerhalb der xy-Ebene und einem schwachen Hüpfterm in der z-Richtung betrachtet, um die planare Struktur von Kupfer- oder Nickel-basierten Supraleitern zu reproduzieren. Um den Einfluss des zusätzlichen Hüpfterms auf das $t - t'$ Phasendiagramm des zweidimensionalen Falls zu untersuchen, wurde das chemische Potential so gewählt, dass die van-Hove Bedingung in der xy-Ebene erhalten wird. In dieser Situation führt ein zunehmender Hüpfparameter in z-Richtung zu einer Abnahme der kritischen Skala für die antiferromagnetische und für die d-Wellen supraleitende Phase, während sich die Phasengrenze zwischen beiden in Bezug auf t' kaum verändert wird. Im Weiteren ist der auffälligste Unterschied das Auftreten starker supraleitender Fluktuationen mit p-Wellen Symmetrie in der ferromagnetischen Phase bei großen $-t'$ Werten.

Contents

List of Definitions

List of Theorems and Corollaries

List of Figures

1. Introduction

The discovery of superconductivity in mercury in 1911 [3] raised the vision of physicists to achieve this state of matter at room temperature. A material with this property would revolutionise the energy system by a reduction of energy losses, lead to smaller generators, transformators and engines, and allow for superconducting electronics which enables a significant increase in computation speed [4]. However, in the succeeding research superconductivity in several other materials was observed, which led to an increase in the critical temperature from $\approx$ 4K in mercury, to a maximum of $\approx$ 30K in niobium compounds. The microscopic mechanism of these conventional superconductors was theoretically well explained by the Bardeen-Cooper-Schrieffer (BCS) theory [5], according to which a phonon induces an attractive interaction between electrons close to the Fermi-surface. This results in the formation of so called "Cooper" pairs of two electrons which behave roughly as bosons, which condensate into a macroscopic quantum state and which, thus, becomes energetically favourable below a critical temperature.

However, heavy fermion superconductors [6] and organic superconductors [7], which were discovered in 1979 and in 1980, could not be described by this theory which led to the name "unconventional superconductors". This group was enlarged when the first copper-oxide superconductor (LaSrCuO) was discovered in 1986 [8], which boosted research, resulting in alloys with critical temperatures above 100K. As this is well above the boiling point of liquid nitrogen (77K), the naming "high-temperature superconductor" (HTS) was established. In 2006 the first iron-pnictide superconductor was discovered [9] (LaFePO). The experimental optimisation and a variation of the accompanying elements led to both, the discovery of iron-chalcogenide superconductors and an increase of the critical temperature to $\approx$ 100K (for a monolayer of the iron-chalcogenide FeSe on a $SrTiO_3$ substrate [10, 11]) such that the iron-based superconductors also belong to the group of HTS. Very recently superconductivity was also observed in nickelates [12], for which one can expect a forthcoming increase in critical temperatures, such that they may also belong to the group of HTS. Finally, superconductivity was found in hydrides [13] for temperatures of $\approx$ 200K with a very high pressure of $\approx$ 100GPa, which is, therefore, far away from realistic applications, so that we focus on the copper-, on the nickel- and on the iron-based superconductors.

A feature which appears in the structure of all these HTS is a layer, which consists of the transition metal ion (Cu/Ni/Fe) arranged on a square lattice and which are connected to each other via oxygen atoms in the case of cuprates and nickelates or which are connected by tetrahedrically arranged P-, As-, Se- or Ti-atoms above or below the plane in the case of iron-based superconductors. In both cases, the ions forming the quadratic lattice are providing the superconducting mechanism. In cuprates, a few of these planes can be stacked together by Ca-atoms to form an active block, which alternates with charge reservoir blocks made of alkaline earth oxides. In the iron based case different atoms acting as charge reservoirs can be placed in the hollow left by the tetrahedra. These properties provide a lot of possibilities in terms of material combinations, dopants, number of layers, *etc.* to improve the critical temperature.

As the critical temperatures of these HTS are still well below room temperature, the understanding of the mechanisms that drive superconductivity is important, as these can point out modifications by which the critical temperatures can be increased. While the BCS theory succeeded in this way for the conventional superconductors, it fails in explaining the superconductivity for HTS due to a

shallow reservoir of charge carriers introduced by doping, which, in addition, feature strong Coulomb correlations. As these connect the internal charge and spin degrees of freedom of the charge carriers a description in terms of Landau's quasiparticle picture is insufficient to describe all possible electronic states [14, 15, 16, 17]. These correlation effects lead to a plethora of different many-particle states like spin-density waves (SDW) and their peculiar forms of para-magnetism (PM), anti-ferro-magnetism (AFM) and ferro-magnetism (FM), as well as charge-density waves (CDW) and also superconductivity with all possible different kinds of ordering vectors and spatial behaviour [18, 19]. As charge, spin or pairing fluctuations of the different possible orderings influence each other a variation of the parameters of the system, like, for example, by doping or by an application of pressure, leads to a rich phase diagram in which some phases coexist. In the case of a hole doping of cuprates, for example, an antiferromagnetic phase is next to the superconducting phase which coexists with an incommensurate spin-density wave and a charge-density wave for some parameter region and compete with each other [20, 17]. Similarly, a coexistence of a spin-density wave regime with superconductivity was found for FeSe [21, 22] as well as in the iron-pnictides 122 FeAs [23] in contradiction to the Meissner effect.

A lot of effort has, therefore, been taken by theoretical physicists to understand the correlated electron system and to find out the mechanism of high temperature superconductivity within the last 35 years. As the material-specific properties calculated *ab initio* by the density functional theory (DFT) do not include correlation effects because of the mean-field character of DFT [24, 25], by the GW-approximation include only one of the three pairing channels [26, 27, 28] and are restricted to weak interactions, or by higher level schemes like T-matrix approaches [29] or Parquet equations [30, 31] are limited due to their numerical difficulty, the investigation of HTS is mainly based on models which reduce the full complex system to the physically relevant part. Due to the large amount of thermally reachable free states, the electrons close to the Fermi-surface are those from which the correlation effects originate, so that a model, which is based on these states, is sufficient. The simplest model is the Hubbard model [32, 33, 34], whose two-dimensional version was related to the unconventional superconductivity in La_2CuO_4 by Anderson in 1987 [35, 36]. Since then, especially the two-dimensional Hubbard model has been studied intensively by various methods with the aim to understand the unconventional superconductivity, suggesting that superconductivity is driven by antiferromagnetic correlations. However, as the active layers of the HTS are still embedded in a three-dimensional structure, I will, in this thesis, investigate the influence of this third dimension on the superconducting order observed in the two-dimensional model.

For the solution of models of interacting electrons suitable methods have to be used. While the Quantum Monte Carlo method provides most accurate results, it can not be applied to all systems and to all parameter ranges because of the so-called "sign-problem" [37, 38]. On the one hand, starting from strong interactions the dynamical mean field theory maps the complex lattice problem to an impurity model and asserts a local self-energy, by which it can only resolve local effects [39, 40]. On the other hand perturbative methods start from weak interactions. However, the most commonly used ones are based on the random phase approximation (RPA) [41, 42, 28] and on the Bethe-Salpeter Equation (BSE) [43, 28] and treat only one kind of pairing interactions at a time, so that the full competition between different phases can not be resolved. The corresponding next step in order to combine the calculations of these different interactions is currently under development in terms of the parquet approach [44, 45] and the so called T-matrix approach [29, 46]. Besides of these, different methods have been developed within the last years to efficiently calculate the many-particle interactions, like the dynamical vertex approximation [47], the dual fermion approach [48], TRILEX [49], QUADRILEX [50], a dual parquet scheme [51] and others. However, the Functional Renormalisation Group (FRG),

which is a formally exact theory, provides a natural combination of the different possible many-particle interactions.

Renormalisation Group (RG) methods directly connect the microscopic description of the electron system with an effective macroscopic one by successively including contributions from the interactions between the electrons. Therefore, a scale parameter is introduced, which separates the electronic modes into those, which are already included in an effective interaction, and those, which are not yet included and whose interaction will be described by it. A successive lowering of the scale parameter then leads to a full effective description of the system [52, 53]. The FRG approaches take over the RG idea to generating functionals of many-particle Green's functions or those of vertex functions which become dependent on the scale. An expansion of the generating functionals in terms of the external source fields leads to a hierarchy of coupled differential equations for many-particle Green's functions or interactions. Polchinski [54] therefore provided an expansion in terms of the bare interaction initially for a ϕ^4 theory, which was also adapted for the calculation of fermionic systems [55, 56, 57]. However, a formulation in terms of one-particle irreducible vertex functions, which was first derived for bosonic systems [58], provided a computationally advantageous form, so that it was transferred to fermionic systems by three different groups (Kopietz [59], Salmhofer and Honerkamp [60], and Halboth and Metzner [61]) at the same time. While the provided system of differential equations is formally exact, it consists of an infinite number of equations so that it has to be truncated. It has been shown that a truncation at the two-particle interaction level provides good results, when the Fermi-surface is sufficiently smooth and the interactions are sufficiently small.

As the FRG includes all two-particle channels in an unbiased way, it is suitable for the interaction of correlation effects. Since its development and its first application the FRG has been further improved in accuracy, as a small modification of the propagator can already include effects beyond the two-particle truncation [62, 63]. Furthermore, an extension motivated by the Parquet-equation led to the so-called multi-loop FRG, which aims at improving the FRG accuracy beyond the two-particle truncation [64, 65, 66]. In addition, more efficient parametrisation schemes of the equations [67, 68] led to a new approximative scheme called Truncated Unity Functional Renormalisation Group (TUFRG)[2], due to which a much higher resolution of the interaction becomes reachable and supercomputers can be used efficiently. Thus, the FRG based on Fermi-surface patching has successfully been applied to several two-dimensional models containing up to three bands, like bilayer Hubbard models [69], Graphene [70, 71, 72], the three band Emery model [73], nodal line materials (like ZrSiS) [74], iron-based superconductors [75] or Sr_2RuO_4 [76, 77] to identify their corresponding phase diagrams. The TUFRG approach now allows an investigation of three-dimensional models. In the scope of this thesis I will apply it to the three-dimensional Hubbard model in order to understand the influence of the third dimension on superconductivity in HTS.

All in all, this thesis is structured as follows:
In order to provide a unified theoretical foundation and notation the necessary preliminaries will be introduced in chapter 2, namely the quantum mechanical notation used throughout this thesis (sec. 2.1, 2.2), as well as the path integral formulation in terms of Grassmann fields (sec. 2.3). Additionally, some background information on Group theory in the framework of solid state physics is provided. In chapter 3 the theoretical background of this thesis is layed out. At first, I derive some properties of the many-particle Green's functions which are useful to simplify calculations (sec. 3.1). In a short excursus on the perturbation theory I introduce the diagrammatic representations of fermionic interactions (sec. 3.2). In section 3.3 I provide a connection of the Green's functions to fermionic bilinears and susceptibilities, which are the experimentally accessible properties describing

the correlation effects. The full set of Functional Renormalisation Group equations for systems with or without SU(2)-symmetry is derived in section 3.5. Therein, I explicitly focus on the flow equations for the two-particle interactions, the self-energy and the susceptibilities. Finally, the Truncated Unity formulation for the two-particle interactions with and without SU(2)-symmetry are derived (sec. 3.6).

In chapter 4 the numerical implementation of the full (TU)FRG scheme is discussed by considering all relevant elements and their behaviour under symmetries used to simplify calculations. Therefore, I present momentum and frequency meshes as well as the construction of models (sec. 4.1). As the behaviour of multi-orbital models under point-group symmetries is complicated, I provide a more detailed analysis of it in terms of a natural basis. Based on the point group symmetries, the construction of form-factors is discussed in section 4.2. In the approximation of static interactions or even zero-temperature, the frequency integration or Matsubara summation of Green's functions can be carried out analytically. The corresponding derivations are, therefore, performed for different cut-off schemes frequently used in FRG calculations (sec. 4.3). Finally, this chapter is ended by a discussion of the parallelisation strategy for which corresponding scaling results are presented (sec. 4.5).

Chapter 5 is dedicated to the results obtained by the code presented above for the Hubbard model, which itself is presented at the beginning of the corresponding chapter. In a first step, we investigate the two-dimensional one-band Hubbard model and compare it with results previously obtained by other groups to verify the correctness of our code (sec. 5.2). In section 5.3 the phase diagram of the half-filled, simple-cubic three-dimensional Hubbard model obtained by the TUFRG is compared with the results obtained by other methods, resulting in a good agreement between the methods in the case of weak interactions. As the method provides reasonable results, it is further applied to this model under doping, which results in a rich phase diagram, including d-wave superconductivity. In order to return to our initial question I simulate the transition from two to three dimensions by varying the movement of electrons in the z-direction. Corresponding phase diagrams are discussed in section 5.4 with the van-Hove condition in the two-dimensional planes, showing that superconductivity of p-wave type can occur for specific sets of parameters.

Chapter 6 sums up all the results and provides an outlook for future developments.

2. Preliminaries

The field theoretical description of quantum mechanics established in this chapter, section 2.3, is the basis of the derivation of the FRG equations. To provide the reader a coherent reading, we introduce the general quantum mechanical notation used in this thesis (Sec. 2.1) and the Fock-space or occupation number representation (Sec. 2.2) beforehand. To complete the mathematical background required for this thesis we furthermore provide the reader some basic results from group theory in section 2.4, which are necessary for the discussion of symmetries and for the derivation of form-factors.

Throughout this thesis we use Planck units, i.e. $\hbar = 1$, $k_\mathrm{B} = 1$, and denote the temperature by T, while $\beta := 1/T$ denotes its inverse.

2.1. Quantum Mechanical Notations

The electronic structure of a solid is generated by the electrons, which have to be described quantum mechanically. The corresponding notation of the required mathematical objects and the most prominent operators used throughout this thesis can be found in tables 2.1 and 2.2, respectively.

In general, the state of a quantum mechanical system is described by the state vector $|\varphi\rangle$, whose time evolution is defined by the Schrödinger equation

$$i\frac{\partial}{\partial t}|\varphi\rangle = \hat{H}|\varphi\rangle \tag{2.1}$$

with the Hamiltonian $\hat{H} = \hat{H}_0 + \hat{H}_\mathrm{int}$ describing the physical system, which is split into a one-particle part $\hat{H}_0$ and an interacting part $\hat{H}_\mathrm{int}$. This equation can, formally, be solved by the time-evolution operator

$$\hat{\mathcal{U}}(t) = \exp\left(-i\hat{H}t\right). \tag{2.2}$$

However, there is an ambiguity in assigning the time dependence to the operator $\hat{A}$, to the state $|\varphi\rangle$ or to both. Therefore, three different pictures are commonly used:

3 dim. vector	$\boldsymbol{r} := (r_x, r_y, r_z)$
configuration space	$\mathcal{O} \subset \mathbb{R}^n$
state vector	$\lvert\varphi\rangle \in L^2(\mathcal{O}, \mathbb{C})$
scalar product	$\langle\varphi\lvert\psi\rangle := \int d^3r\, \varphi^*(\boldsymbol{r})\psi(\boldsymbol{r})$
operator	$\hat{A}$
expectation value	$\langle\hat{A}\rangle_\varphi := \langle\varphi\rvert\hat{A}\lvert\varphi\rangle$
commutator	$[\hat{A}, \hat{B}] := \hat{A}\hat{B} - \hat{B}\hat{A}$
anti-commutator	$\{\hat{A}, \hat{B}\} := \hat{A}\hat{B} + \hat{B}\hat{A}$

Table 2.1.: Table of quantum mechanical notations.

unity operator	$\hat{\mathbf{1}}$
position operator	$\hat{r} = (\hat{r}_x, \hat{r}_y, \hat{r}_z)$
momentum operator	$\hat{p} = (\hat{p}_x, \hat{p}_y, \hat{p}_z)$
orbital momentum operator	$\hat{L} = (\hat{L}_x, \hat{L}_y, \hat{L}_z)$
spin operator	$\hat{S}_i = (\hat{S}_x, \hat{S}_y, \hat{S}_z)$
Hamilton operator	$\hat{H}$
particle Number operator	$\hat{N}$
modified Hamiltonian	$\hat{K} = \hat{H} - \mu\hat{N}$

Table 2.2.: Table of basic quantum mechanical operators.

$$\text{Schrödinger Picture} \qquad |\varphi(t)\rangle_{\mathrm{S}} = \hat{U}(t)\,|\varphi\rangle \qquad \hat{A}_{\mathrm{S}} = \hat{A} \tag{2.3}$$

$$\text{Heisenberg Picture} \qquad |\varphi\rangle = |\varphi\rangle \qquad \hat{A}(t) = \hat{U}^{\dagger}(t)\hat{A}\hat{U}(t) \tag{2.4}$$

$$\text{Interaction Picture} \qquad |\varphi(t)\rangle_{\mathrm{I}} = e^{-i\hat{H}_{\mathrm{int}}t}\,|\varphi\rangle \qquad \hat{A}_{\mathrm{I}}(t) = e^{i\hat{H}_0 t}\hat{A}e^{-i\hat{H}_0 t} \quad . \tag{2.5}$$

Regarding the argument of the time-evolution operator, one may consider the system based on an imaginary time $\tau = it$, which is advantageous for systems at finite temperature T. Such an imaginary time picture can be obtained by a Wick rotation of the Hamiltonian, which is a continuation of the Hamiltonian to imaginary times. As this imaginary time τ is real valued, it simplifies a lot of calculations, but also gives rise to other difficulties. We define the imaginary time-evolution operator in analogy to the real time one, given by equation (2.2), as

$$\hat{\mathcal{U}}(\tau) = \exp\left(-\hat{H}\tau\right). \tag{2.6}$$

The distinction between imaginary and real time becomes apparent by the use of t or τ as argument, respectively. The different pictures defined in equations (2.3) to (2.5) can be formulated analogously in imaginary times by the corresponding replacement of $\tau = it$. The Fourier transformation of the real time argument t and the corresponding inverse Fourier transformation

$$|\varphi(\omega)\rangle = \int \mathrm{d}t\, e^{i\omega t}\,|\varphi(t)\rangle \quad \text{and} \quad |\varphi(t)\rangle = \frac{1}{2\pi}\int \mathrm{d}t\, e^{-i\omega t}\,|\varphi(\omega)\rangle \tag{2.7}$$

converts the expression to the frequency domain with arguments ω and correspondingly back to real time. The counterpart for finite temperatures is the Fourier series

$$|\varphi(\tau)\rangle = \frac{1}{\beta}\sum_{\omega_n} e^{-i\omega_n\tau}\,|\varphi(\omega_n)\rangle \quad \text{with coefficients} \quad |\varphi(\omega_n)\rangle = \int_0^{\beta} \mathrm{d}\tau\, e^{i\omega_n\tau}\,|\varphi(\tau)\rangle\,, \tag{2.8}$$

which, for imaginary times, leads to the Matsubara frequencies $\omega_n = \frac{2n+1}{\beta}\pi$ for Fermions and $\nu_n = \frac{2n}{\beta}\pi$ for Bosons, indicated via a subscript n of the variable.

If several operators are applied to a system at different times, they have to be in the correct time order due to the change of state resulting from the measurement process. To ensure this, we define the time-ordering operator which commutes the operators correspondingly.

Definition 1 (Permutation Group and Time-Ordering Operator)

- *The **symmetric group** of m elements S_m is defined as the group of all permutations of the set $\{1,\dots,m\}$.*
- *Let $\{\hat{O}_i(x_i,t_i)\}_{i\mathbb{N},i\leq m}$ be a set of m operators acting on some arguments x_i at time t_i, and let $\mathrm{sgn}(\pi)$ be the sign of the permutation $\pi \in S_m$. Then the **imaginary time-ordering operator** $\mathcal{T}$ is defined as*

$$\mathcal{T}[\hat{O}_1(x_1,\tau_1)\dots\hat{O}_m(x_m,\tau_m)] := \sum_{\pi\in S_m} \mathrm{sgn}(\pi)\Theta(\tau_{\pi(1)}-\tau_{\pi(2)})\dots\Theta(\tau_{\pi(m-1)}-\tau_{\pi(m)}) \\ \hat{O}_{\pi(1)}(x_{\pi(1)},\tau_{\pi(1)})\dots\hat{O}_{\pi(m)}(x_{\pi(m)},\tau_{\pi(m)}) \tag{2.9}$$

The action of the time-ordering operator, therefore, leads to a reordering of all operators, such that for every pair of operators the left one has a later time argument than the right one. That is, the final order is

$$\hat{O}_n(x_n,\tau_n)\dots\hat{O}_0(x_0,\tau_0) \quad \text{with} \quad \tau_n > \tau_{n-1} > \dots \tau_1 > \tau_0. \tag{2.10}$$

An analogous time-ordering operator for imaginary times can be defined straight forwardly.

The general basis of a quantum mechanical system is given by the direct product of the position or the momentum space and the spin space. The position and the momentum space are spanned by their eigenvectors, which are orthonormal and complete according to

$$\begin{aligned} \langle \boldsymbol{r}|\boldsymbol{r}'\rangle &= \delta(\boldsymbol{r}-\boldsymbol{r}') \qquad \text{and} \qquad \int \mathrm{d}\boldsymbol{r}\ |\boldsymbol{r}\rangle\langle\boldsymbol{r}| = \mathbf{1} \\ \langle \boldsymbol{k}|\boldsymbol{k}'\rangle &= \delta(\boldsymbol{k}-\boldsymbol{k}') \qquad \text{and} \qquad \int \mathrm{d}\boldsymbol{k}\ |\boldsymbol{k}\rangle\langle\boldsymbol{k}| = \mathbf{1} \end{aligned} \tag{2.11}$$

and which are related to each other according to

$$\langle \boldsymbol{r}|\boldsymbol{k}\rangle = \frac{1}{(2\pi)^3} e^{i\boldsymbol{k}\boldsymbol{r}}. \tag{2.12}$$

We define the projection of the state vector $|\varphi\rangle$ to the position or the momentum space basis as wave-functions in position or in momentum space, respectively, given by

$$\varphi(\boldsymbol{r}) := \langle \boldsymbol{r}|\varphi\rangle \qquad \text{and} \qquad \varphi(\boldsymbol{k}) := \langle \boldsymbol{k}|\varphi\rangle\,. \tag{2.13}$$

Based on equation (2.12) we obtain

$$\varphi(\boldsymbol{k}) = \int \mathrm{d}\boldsymbol{r}\ \varphi(\boldsymbol{r})\, e^{-i\boldsymbol{k}\boldsymbol{r}} \quad \text{and} \quad \varphi(\boldsymbol{r}) = \frac{1}{(2\pi)^3}\int \mathrm{d}\boldsymbol{k}\ \varphi(\boldsymbol{k})\, e^{i\boldsymbol{k}\boldsymbol{r}}, \tag{2.14}$$

which we define as the Fourier transformation of the wave-functions from position to momentum space and the corresponding inverse Fourier transformations, respectively.

The atoms in a solid are positioned in a periodic arrangement, forming the Bravais lattice. All vectors $\boldsymbol{K}$, for which $e^{i\boldsymbol{K}\boldsymbol{R}} = 1$ holds for all $\boldsymbol{R}$ of the Bravais lattice, form the reciprocal lattice and are, therefore, called reciprocal lattice vectors. The Brillouin zone (BZ) $\mathcal{B}$ is then the part of the momentum space, which is closer to $\boldsymbol{K} = \mathbf{0}$ than to any other $\boldsymbol{K}$, and we denote its volume by $|\mathcal{B}|$. Due to the condition on $\boldsymbol{K}$ the BZ is a square (cube) of side length 2π for a square (cubic) lattice. We define the (inverse) lattice Fourier transformation similar to equation (2.14) as

$$f(\boldsymbol{k}) = \sum_{\boldsymbol{R}} f(\boldsymbol{R})\, e^{-i\boldsymbol{k}\boldsymbol{R}} \qquad \text{and} \qquad f(\boldsymbol{R}) = \frac{1}{|\mathcal{B}|}\int \mathrm{d}\boldsymbol{k}\ f(\boldsymbol{k})\, e^{i\boldsymbol{k}\boldsymbol{R}}, \tag{2.15}$$

with $\boldsymbol{k} \in \mathcal{B}$. In this thesis we treat a perfect crystalline solid state system, such that the periodicity leads to a translational invariance of the Hamilton operator $\hat{H}$. Therefore, the solutions of the Schrödinger equation are common eigenstates of the Hamiltonian $\hat{H}$ and the translation operator $\hat{T}_{\boldsymbol{R}}$. Eigenfunctions of the translation operator are the plane wave-functions according to

$$\hat{T}_{\boldsymbol{R}}\,|\boldsymbol{k}\rangle = e^{-i\boldsymbol{k}\boldsymbol{R}}\,|\boldsymbol{k}\rangle\,, \tag{2.16}$$

where we denote $\boldsymbol{k}$ as Bloch wave-vector. Due to the previous discussions we note that any $\boldsymbol{k}'$ always has the same eigenvalue with respect to the translation vector as the corresponding Bloch wave-vector $\boldsymbol{k} = \boldsymbol{k}' - \boldsymbol{K}$ in the first Brillouin zone. It is, therefore, sufficient to find the eigenfunctions of $\hat{H}$ for every Bloch momentum $\boldsymbol{k}$ separately, leading to the basis of Bloch vectors $|\Psi_{\boldsymbol{k},n,s}\rangle$, where n is the band index. The band structure of the material is then formed by the eigenvalues $\varepsilon_{\boldsymbol{k},n,s}$ as functions of $\boldsymbol{k}$, n and s.

While the Bloch vectors are delocalised due to their construction by plane waves, it is often useful to work with a basis localised at the atomic positions. A direct approach is to take the atomic wave basis $|\varphi\rangle_{o,s}$ with orbital o and spin s for each atom and move it to its position by $\varphi_{o,s,\boldsymbol{R}} = \varphi_{o,s}(\boldsymbol{r} - \boldsymbol{R})$. With

$$\psi_{o,s,\boldsymbol{k}} = \frac{1}{\mathcal{N}} \sum_{\boldsymbol{R}} |\varphi_{o,s,\boldsymbol{R}}\rangle \, e^{i\boldsymbol{k}\boldsymbol{R}} \tag{2.17}$$

we define a Bloch like vector as a basis for the electron system, which is an eigenstate of the translation operator. However, the basis created by this approach is only orthogonal on one site, while orbitals from different sites may overlap. To overcome this problem, we define the Wannier states as

$$|\Phi_{\boldsymbol{R},o,s}\rangle = \frac{1}{|\mathcal{B}|} \sum_{n} \int \mathrm{d}^3k \, U^{\dagger}_{no}(\boldsymbol{k}) \, |\Psi_{\boldsymbol{k},n,s}\rangle \, e^{-i\boldsymbol{k}\boldsymbol{R}}, \tag{2.18}$$

or

$$|\Psi_{\boldsymbol{k},n,s}\rangle = \sum_{o} \sum_{\boldsymbol{R}} U_{no}(\boldsymbol{k}) \, |\Phi_{\boldsymbol{R},o,s}\rangle \, e^{i\boldsymbol{k}\boldsymbol{R}}, \tag{2.19}$$

which form an orthonormal, complete basis for the electronic solid state system. U is a unitary matrix, defining the map from Bloch bands n to Wannier orbitals o. As a shorthand notation for Bloch and Wannier bases we only write the set of quantum numbers, i.e.

$$|\boldsymbol{k}ns\rangle := |\Psi_{\boldsymbol{k},n,s}\rangle \,, \quad \text{and} \quad |\boldsymbol{R}os\rangle := |\Phi_{\boldsymbol{R},o,s}\rangle \,, \tag{2.20}$$

respectively. If, further, the explicit quantum numbers and bases are of no relevance for a statement, we combine them according to

$$|x\rangle := |\boldsymbol{R}os\rangle \qquad \text{and} \qquad |k\rangle := |\boldsymbol{k}ns\rangle \tag{2.21}$$

so that x and k also act as combined variables if used as argument. As we typically work with time arguments for position space functions and with frequency arguments for momentum space functions, we denote the whole collection of arguments by an integer according to $1 = (x, \tau)$ or $1_t = (x, t)$ for imaginary or real times in position space and $1_k = (k, \omega_n)$ or $1_\omega = (k, \omega)$ for Matsubara or for real frequencies in momentum space.

So far, we have established the basic notations for an efficient description of one particle. But as we are interested in many electron effects, we introduce the corresponding space, the Fock space, for their description in the next section.

2.2. The Fock Space

The electronic part of a solid state system consists of $N \in \mathbb{N}$ identical electrons. As the considerations of the previous section 2.1 hold for the basis of each particle, the N-particle Hilbert space $\mathcal{H}_N$ is the tensor product of all the N one-particle Hilbert spaces $\mathcal{H}$ according to

$$\mathcal{H}_N := \bigotimes_{i=1}^{N} \mathcal{H} \quad \text{with the canonical basis} \quad |x_1 \dots x_N\rangle := \bigotimes_{i=1}^{N} |x_i\rangle\,, \tag{2.22}$$

equipped with the scalar product and the completeness relation in the form of

$$\langle x_1, \dots, x_N | x'_1, \dots, x'_N\rangle = \prod_{i=1}^{N} \langle x_i | x'_i\rangle \quad \text{and} \quad \sum_{x_1,\dots,x_N} |x_1, \dots, x_N\rangle \langle x_1, \dots, x_N| = \hat{\mathbf{1}}, \tag{2.23}$$

respectively. The many-particle wave-function $\psi_N(\boldsymbol{r}) := \langle \boldsymbol{r} | x_1, \dots, x_N\rangle$ for fermions, as electrons are, has to be antisymmetric to fulfil the Pauli criterion, that is, an interchange of the particles with arguments x_i and x_j results in a change of sign. The Hilbert space of fermions $\mathcal{F}_N$ is, hence, the space created by antisymmetrising the states of the full N-particle Hilbert space $\mathcal{H}_N$, equipped with the same scalar product and a closure relation with respect to the antisymmetrised basis. The expectation value of an operator $\hat{A}$ acting on a many-particle state is invariant under the antisymmetrisation, as the fermions of the systems we consider are identical and indistinguishable.

In this construction we would have to know the exact state of each particle to construct the antisymmetrised product state $|x_1\rangle \cdots |x_N\rangle$, but as the particles are indistinguishable, we have to sum over all equivalent states in which the particles interchange their states. Thus, it is of more relevance to know if a state is occupied or not, as fermionic states can only be occupied once. Therefore, we label all states of the one-particle basis $\{|x_\lambda\rangle\}_{\lambda\in\mathbb{N}_0}$ by a natural number λ and write their occupation numbers $n_i \in \{0, 1\}$ in the state vector $|n_0 \cdots n_j \cdots\rangle$ which have to fulfil $N = \sum_i n_i$. We define the set of corresponding spaces as Fock space:

Definition 2 (Fock Space)
*Let $\mathcal{F}_N$ be the Hilbert space describing N-particles. Then the **Fock space** $\mathcal{F}$ is defined by*

$$\mathcal{F} := \bigoplus_{N=0}^{\infty} \mathcal{F}_N. \tag{2.24}$$

The operation of adding or removing a state vector to the many-particle Hilbert space is given in this occupation number representation by setting the corresponding occupation number from 0 to 1 or from 1 to 0, respectively. This is, therefore, interpreted as addition or removal of particles from a state, which corresponds to a transition from $\mathcal{F}_N$ to $\mathcal{F}_{N+1}$ and vice versa. The corresponding operators are defined as follows:

Definition 3 (Creation, Annihilation and Number Operators)
Let $|n_1 \cdots n_\alpha \cdots\rangle \in \mathcal{F}$ be an N-particle Fock state. Then the ***fermion creation operator*** *$\hat{c}^\dagger_\alpha$ is defined as*

$$\hat{c}^\dagger_\alpha |n_0 \cdots n_\alpha \cdots\rangle := \begin{cases} +|n_0 \cdots 1 \cdots\rangle & \text{for} \quad n_\alpha = 0 \text{ and } \sum_{i=0}^{\alpha-1} n_i = N_{<\alpha} \text{ even} \\ -|n_0 \cdots 1 \cdots\rangle & \text{for} \quad n_\alpha = 0 \text{ and } \sum_{i=0}^{\alpha-1} n_i = N_{<\alpha} \text{ uneven} \\ 0 & \text{for} \quad n_\alpha = 1 \end{cases} \tag{2.25}$$

and the ***fermion annihilation operator*** *$\hat{c}_\alpha$ is defined as the adjoint operator of the fermion creation one, thus*

$$\hat{c}_\alpha |n_0 \ldots n_\alpha \ldots\rangle := \begin{cases} +|n_0 \cdots 0 \cdots\rangle & \text{for } n_\alpha = 1 \text{ and } \sum_{i=0}^{\alpha-1} n_i = N_{<\alpha} \text{ even} \\ -|n_0 \cdots 0 \cdots\rangle & \text{for } n_\alpha = 1 \text{ and } \sum_{i=0}^{\alpha-1} n_i = N_{<\alpha} \text{ uneven} \\ 0 & \text{for } n_\alpha = 0. \end{cases} \tag{2.26}$$

The ***number operator*** *$\hat{n}_\alpha$ for state α is defined as*

$$\hat{n}_\alpha := \hat{c}^\dagger_\alpha \hat{c}_\alpha \tag{2.27}$$

and the ***total number operator*** *$\hat{N}$ is defined as*

$$\hat{N} := \sum_{i=0}^{N} \hat{n}_i. \tag{2.28}$$

We remark that, according to this definition, the subscript α of the creation, annihilation and number operator refers to the state of the one-particle basis it is acting on. In addition, every state in the Fock space can be described by all the corresponding creation operators acting on the vacuum state $|0\rangle$. To account for the energy required or released by the addition or the removal of a particle, respectively, the chemical potential μ is introduced. The full system with a varying number of particles is, therefore, described by the generalised Hamiltonian $\hat{K} := \hat{H} - \mu\hat{N}$. The following commutation relations, again, directly follow from the definition of the creation and the annihilation operators, which can easily be proved.

Corollary 2.1 (Anticommutation Relations for Creation and Annihilation Operators)
The anticommutation relation of the fermionic creation operators $\hat{c}^\dagger_\alpha$ and the fermionic annihilation operators $\hat{c}_\alpha$ are

$$\{\hat{c}^\dagger_\alpha, \hat{c}^\dagger_\beta\} = 0 \quad , \qquad \{\hat{c}_\alpha, \hat{c}_\beta\} = 0 \qquad \text{and} \qquad \{\hat{c}^\dagger_\alpha, \hat{c}_\beta\} = \delta_{\alpha\beta}. \tag{2.29}$$

The creation and the annihilation operators can be transformed to another basis $|\beta\rangle$ by the closure relation of this new basis. Thus, the operators become

$$\hat{c}^\dagger_\beta = \sum_\alpha \langle\alpha|\beta\rangle\, \hat{c}^\dagger_\alpha \quad , \qquad \hat{c}_\beta = \sum_\alpha \langle\beta|\alpha\rangle\, \hat{c}_\alpha. \tag{2.30}$$

When the new basis is the one of the position space $\{|\boldsymbol{r}\rangle\}$, then the corresponding representation of the wave-function $\phi_\alpha(\boldsymbol{r}) = \langle \boldsymbol{r}|\alpha\rangle$ can be identified. The new operators are called field creation and annihilation operators, which are given by

$$\hat{\psi}^\dagger(\boldsymbol{r}) := \sum_\alpha \phi^*_\alpha(\boldsymbol{r})\hat{c}^\dagger_\alpha \qquad \text{and} \qquad \hat{\psi}(\boldsymbol{r}) := \sum_\alpha \phi_\alpha(\boldsymbol{r})\hat{c}_\alpha, \tag{2.31}$$

respectively.

In the many-particle setting, operators acting on all particles are classified according to the way their action can be decomposed. The operator $\hat{A}$ is called a one-particle operator when its action on an N-particle direct-product state $|x_1, \ldots, x_N\rangle$ can be represented by

$$\hat{A}\,|x_1, \ldots, x_N\rangle = \sum_{i=1}^{N} \hat{A}_i\,|x_1, \ldots, x_N\rangle\,, \tag{2.32}$$

that is by the sum of $\hat{A}_i$ acting on each particle. Such an operator is, for instance, the kinetic energy operator. When the action of the operator $\hat{A}$ on an N-particle state is given by the sum of $\hat{A}_{ij}$ acting on pairs of particles, that is by

$$\hat{A}\,|x_1, \ldots, x_N\rangle = \sum_{1\le i\le j\le N} \hat{A}_{ij}\,|x_1, \ldots, x_N\rangle\,, \tag{2.33}$$

like the Coulomb operator, it is called a two-particle operator. Using the transformations given in equation (2.30), all operators can be transformed to creation and annihilation operators in the Fock basis. For one-particle and for two-particle operators $\hat{T}$ and $\hat{V}$, respectively, this reads as

$$\hat{T} = \sum_{\lambda\mu} \langle\lambda|\,T\,|\mu\rangle\,\hat{c}^\dagger_\lambda \hat{c}_\mu \qquad \text{with} \qquad \langle\lambda|\,T\,|\mu\rangle = \sum_\alpha \langle\lambda|\alpha\rangle\,U_\alpha\,\langle\alpha|\mu\rangle \tag{2.34}$$

$$\hat{V} = \frac{1}{2}\sum_{\lambda\mu\nu\rho} \langle\lambda\mu|\,V\,|\nu\rho\rangle\,\hat{c}^\dagger_\lambda \hat{c}^\dagger_\mu \hat{c}_\nu \hat{c}_\rho \qquad \text{with} \qquad \langle\lambda\mu|\,V\,|\nu\rho\rangle = \sum_{\alpha\beta} \langle\lambda\mu|\alpha\beta\rangle\,V_{\alpha\beta}\,\langle\alpha\beta|\nu\rho\rangle\,. \tag{2.35}$$

As the actions of creation and annihilation operators can directly be performed by changing the corresponding occupation numbers in Fock space, this representation allows more efficient calculations. For example, the action of annihilation operators on an empty state results in 0, so that it is advantageous in the presence of several creation and annihilation operators to let the annihilation operators act first, like in the two-particle operator case. This ordering is defined as normal ordering:

Definition 4 (Normal Ordering)
Multiple creation and annihilation operators are in ***normal order****, when all creation operators are left of the annihilation operators. The notation*

$$:\hat{A}_i\hat{A}_j: \tag{2.36}$$

implies that the operators within the colons have to be commuted until they are in normal order.

To illustrate the normal ordering, we consider the case of two operators, $\hat{A}_i$ and $\hat{A}_j$, which can be creation or annihilation operators. Then, normal ordering implies

$$: \hat{A}_i \hat{A}_j := \begin{cases} \hat{A}_i \hat{A}_j & \text{for } \hat{A}_i = \hat{c}_i^\dagger,\ \hat{A}_j = \hat{c}_j \\ -\hat{A}_j \hat{A}_i & \text{for } \hat{A}_i = \hat{c}_i,\ \hat{A}_j = \hat{c}_j^\dagger. \end{cases} \tag{2.37}$$

While only the lowest N states of a system of non-interacting electrons in its ground state at $T = 0$ are occupied by electrons, at finite temperatures $T \neq 0$ the system has a finite probability to be in an other, excited, many-particle state. The whole system based on the set of possible states is described by the grand canonical partition function.

Definition 5 (Grand Canonical Partition Function)
Let a many-particle system be described by the Hamiltonian $\hat{H}$, the total number operator $\hat{N}$ and the chemical potential μ. Then the ***grand canonical partition function*** *at inverse temperature β is defined by*

$$\mathcal{Z} := Tr\left(e^{-\beta(\hat{H}-\mu\hat{N})}\right), \tag{2.38}$$

and the ***grand canonical potential*** *is defined as*

$$\Omega := -\frac{1}{\beta}\ln(\mathcal{Z}). \tag{2.39}$$

According to the finite possibilities of the system to be in a particular state, we define the thermal average of an operator, in which every state is weighted by its probability.

Definition 6 (Thermal Average)
Let the prerequisites be given as in definition 5, and let $\hat{\mathcal{T}}$ be the time-ordering operator. Then the ***thermal average*** *of an operator $\hat{A}$ is defined as*

$$\langle \hat{A} \rangle := \frac{1}{\mathcal{Z}} Tr\left(e^{-\beta(\hat{H}-\mu\hat{N})}\hat{\mathcal{T}}[\hat{A}]\right). \tag{2.40}$$

While the formulation in the Fock basis is quite comfortable, one still requires the one-particle basis functions, that is, the antisymmetrised eigenstates of the one-particle Hamilton operators. An advantage is, therefore, to formulate the theory in the eigenstates of the annihilation operator as shown in the following.

2.3. Grassmann Fields and Path Integral

The eigenstates of the annihilation operators $\hat{c}$ introduced in the previous section 2.2 are the Fock states $|\psi\rangle \in \mathcal{F}$ for which

$$\hat{c}_i |\psi\rangle = \psi_i |\psi\rangle \tag{2.41}$$

holds. As two fermionic annihilation operators anticommute, their eigenvalues ψ_α have to be anticommuting, too. The Grassmann algebra, in the following defined without mathematical accuracy, provides Grassmann numbers which fulfil this property. The definition further provides rules for the calculation with these Grassmann variables.

Definition 7 (Grassmann Algebra)

- *Variables ψ_i which anticommute, i.e.*

$$\{\psi_i, \psi_j\} = \psi_i\psi_j + \psi_j\psi_i = 0 \quad \textit{for} \quad i \neq j \tag{2.42}$$

  *are called **Grassmann numbers** or **Grassmann variables**. Due to the anticommutation they are nilpotent, that is $\psi_i^2 = 0$.*

- *The algebra generated by a set of N Grassmann variables $\{\psi_i\}_{i\leq N}$ as generators with an addition and an antisymmetric multiplication operation is called **Grassmann algebra**. Its basis is spanned by all unique products of generators, resulting in a dimension of 2^N.*

- *For N being even, the conjugation of a Grassmann variable is denoted by $\bar{\psi}$ and is defined as the complex conjugate $\bar{\psi} := (\psi)^*$ of its value. The conjugate of a product of Grassmann variables is accordingly $\bar{\psi}_n \cdots \bar{\psi}_1 = (\psi_1 \cdots \psi_n)^*$.*

- *The derivative with respect to a Grassmann variable is defined as*

$$\frac{\partial}{\partial\psi_i}\psi_j := \delta_{ij}, \qquad \frac{\partial}{\partial\psi_i}\bar{\psi}_j := 0, \qquad \frac{\partial}{\partial\bar{\psi}_i}\psi_j := 0. \tag{2.43}$$

  The derivatives anticommute with Grassmann variables and among themselves, i.e. $\frac{\partial}{\partial\psi_i}(\bar{\psi}_j\psi_k) = -\bar{\psi}_j\frac{\partial}{\partial\psi_i}\psi_j$.

- *The integration with respect to a Grassmann variable is defined as*

$$\int \mathrm{d}\psi_i\, \psi_j := \delta_{ij}, \qquad \int d\psi_i\, 1 := 0 \qquad \textit{and} \qquad \int d\psi_i \bar{\psi}_j := 0. \tag{2.44}$$

Based on these Grassmann variables, we can define the eigenstates of the annihilation operator.

Definition 8 (Fermionic Coherent State)
Let $c_i^\dagger$ be fermion creation operators with Grassmann numbers ψ_i as eigenvalues, and let $|0\rangle$ be the vacuum state. Then the ***fermionic coherent state*** *is given by*

$$|\psi\rangle = \exp\left(-\sum_i \psi_i c_i^\dagger\right)|0\rangle\,, \tag{2.45}$$

and the ***adjoint fermionic coherent*** *state is given by*

$$\langle\psi| = \langle 0|\exp\left(\sum_i \bar{\psi}_i c_i\right). \tag{2.46}$$

The Grassmann variables $\psi(\boldsymbol{r})$ and $\bar{\psi}(\boldsymbol{r})$, which correspond to the field operators $\hat{\psi}(\boldsymbol{r})$ and $\hat{\psi}^\dagger(\boldsymbol{r})$, respectively, are called **Grassmann fields**. All the results which are obtained for Grassmann variables and their coherent states also hold for Grassmann fields and their coherent states. We collect some properties of the fermionic coherent states in the following corollary.

Corollary 2.2 (Properties of Coherent States)

1. *The fermion creation operator $c_i^\dagger$ acts on a fermionic coherent state like a field derivative, that is $c_i^\dagger|\psi\rangle = -\frac{\partial}{\partial\psi_i}|\psi\rangle$.*
2. *The fermion annihilation operator c_i acts on the adjoint fermionic coherent state like a field derivative, that is $\langle\psi| c_i = \langle\psi|\frac{\partial}{\partial\psi_i}$.*
3. *The coherent states are not normalised to unity, but result in $\langle\psi|\psi'\rangle = \exp\left(\sum_i \bar{\psi}_i\psi_i'\right)$.*
4. *The closure relation is given by*

$$\int\prod_\alpha \mathrm{d}\bar{\psi}_i\,\mathrm{d}\psi_i, \exp\left(-\sum_i \bar{\psi}_i\psi_i\right)|\psi\rangle\langle\psi| = 1. \tag{2.47}$$

5. *For Fock states $|i\rangle$, $|j\rangle$ and for Grassmann states $|\psi\rangle$ we have*

$$\langle i|\psi\rangle\langle\psi|j\rangle = \langle -\psi|j\rangle\langle i|\psi\rangle\,. \tag{2.48}$$

6. *The trace of an operator is given by*

$$Tr(\hat{A}) = \int\prod_i \mathrm{d}\bar{\psi}_i\,\mathrm{d}\psi_i \exp\left(-\sum_i \bar{\psi}_i\psi_i\right)\langle -\psi|\hat{A}|\psi\rangle\,. \tag{2.49}$$

7. *Let $|\varphi\rangle$ be a Fock state. Then the Grassmann coherent state representation of fermions is given by*

$$|\varphi\rangle = \int\prod_i \mathrm{d}\bar{\psi}_i\,\mathrm{d}\psi_i \exp\left(-\sum_i \bar{\psi}_i\psi_i\right)\varphi(\bar{\psi})\,|\psi\rangle \tag{2.50}$$

with $\varphi(\bar{\psi}) = \langle\psi|\varphi\rangle$, the wave-function of the state $|\psi\rangle$ in the coherent state representation.

8. The matrix element of an operator $A(\hat{c}_\alpha^\dagger, \hat{c}_\alpha)$ based on creation and annihilation operators in normal-order in the coherent basis is given by

$$\langle\psi|\, A(\hat{c}_i^\dagger \hat{c}_i)\, |\psi'\rangle = \exp\left(\sum_i \bar{\psi}_i \psi_i'\right) A[\bar{\psi}_i, \psi_i'], \tag{2.51}$$

where $A[\bar{\psi}_i, \psi_i']$ is the normal-ordered operator with $c_i^\dagger$ and c_i being replaced by $\bar{\psi}_i$ and ψ_i, respectively.

PROOF: 1. By exploiting the definition of fermion coherent states (def. 8) and the Grassmann derivative we derive

$$\begin{aligned}
\hat{c}_i^\dagger\, |\psi\rangle &= \hat{c}_i^\dagger (1 - \psi_i \hat{c}_i^\dagger) \prod_{j\neq i} (1 - \psi_j \hat{c}_j^\dagger)\, |0\rangle && (2.52)\\
&= \hat{c}_i^\dagger \prod_{j\neq i} (1 - \psi_j \hat{c}_j^\dagger)\, |0\rangle && (2.53)\\
&= -\frac{\partial}{\partial \psi_i} (1 - \psi_i \hat{c}_i^\dagger) \prod_{j\neq i} (1 - \psi_j \hat{c}_j^\dagger)\, |0\rangle && (2.54)\\
&= -\frac{\partial}{\partial \psi_i}\, |\psi\rangle\,. && (2.55)
\end{aligned}$$

2. The proof is analogous to the previous one.

3. The scalar product of two coherent states results in

$$\begin{aligned}
\langle\psi|\psi'\rangle &= \langle 0| \prod_i (1 + \bar{\psi}_i \hat{c}_i)(1 - \psi_i \hat{c}_i^\dagger)\, |0\rangle && (2.56)\\
&= \prod_i (1 + \bar{\psi}_i \psi_i) && (2.57)\\
&= \exp\left(\sum_i \bar{\psi}_i \psi_i\right) && (2.58)
\end{aligned}$$

which, in general, is unequal to 1.

4. We refer to [78], chapter 1.5. for this proof.

5. Equation (2.48) directly follows from the anticommutation of Grassmann numbers.

6. We start by writing out the trace in terms of occupation number states, insert the closure relation (point 4, eq. 2.47) and the anticommutativity of scalar products (point 5, eq. (2.48)). Thus we obtain for an operator $\hat{A}$

$$\begin{aligned}
\mathrm{Tr}\,(\hat{A}) &= \sum_n \langle n|\, \hat{A}\, |n\rangle && (2.59)\\
&= \int \prod_i \mathrm{d}\bar{\psi}_i\, \mathrm{d}\psi_i e^{-\sum_i \bar{\psi}_i \psi_i} \sum_n \langle n|\psi\rangle\, \langle\psi|\, \hat{A}\, |n\rangle && (2.60)\\
&= \int \prod_i \mathrm{d}\bar{\psi}_i\, \mathrm{d}\psi_i e^{-\sum_i \bar{\psi}_i \psi_i}\, \langle -\psi|\, \hat{A} \sum_n |n\rangle\, \langle n|\psi\rangle && (2.61)\\
&= \int \prod_i \mathrm{d}\bar{\psi}_i\, \mathrm{d}\psi_i e^{-\sum_i \bar{\psi}_i \psi_i}\, \langle -\psi|\, \hat{A}\, |\psi\rangle\,. && (2.62)
\end{aligned}$$

7. Equation (2.50) directly results from the closure relation (point 4, eq. (2.47)) applied to a state $|\psi\rangle$.
8. Writing $\langle\psi|\,\hat{A}(\hat{c}_i^\dagger,\hat{c}_i)\,|\psi'\rangle$, we let $\hat{c}_i^\dagger$ act to the left and $\hat{c}_i$ act to the right coherent state. This directly leads to the result given in equation (2.51). ■

The coherent states provide a new basis for the many-particle system. Therefore, the partition function can be reformulated in terms of these states as in the following corollary.

Corollary 2.3 (Partition Function in Coherent States)
Let ψ_i and $\bar{\psi}_i$ be Grassmann variables, and let $\hat{H}$, $\hat{N}$, μ and β be given as in definition 5. Then the grand canonical partition function $\mathcal{Z}$ in a coherent state representation is given by

$$\mathcal{Z} = \int \prod_i \mathrm{d}\bar{\psi}_i\,\mathrm{d}\psi_i\,\exp\left(-\sum_i \bar{\psi}_i\psi_i\right)\langle -\psi|\,e^{-\beta(\hat{H}-\mu\hat{N})}\,|\psi\rangle\,. \tag{2.63}$$

Proof: Applying the trace in coherent states (eq. (2.49)) to the definition of the partition function in definition 5 directly leads to equation (2.63). ■

As the configuration space of many-particle systems is very large, it is useful to define functional integrals which are integrals over field configurations. We will briefly introduce them and use them for the derivation of the FRG equations later on.

To motivate the formulation of path integrals we consider the time evolution of a system from state $|\psi_i\rangle$ with components $\psi_{\alpha,i}$ at time t_i to a final state $\langle\psi_f|$ with components $\bar{\psi}_{\alpha,f}$ at time t_f. Then a matrix element of the evolution operator (see eq. (2.2)) is given by

$$\mathcal{U}(\psi_f t_f,\psi_i t_i) = \langle\psi_f|\,e^{-iH(t_f-t_i)}\,|\psi_i\rangle\,. \tag{2.64}$$

We divide the time interval between initial and final state into M time steps of equal size $\epsilon = \frac{t_f-t_i}{M}$ and denote all intermediate points by t_k, so that we arrive at the original system for $M\to\infty$, implying $\epsilon\to 0$. At each intermediate time point we insert the closure relation of the Grassmann fields with the corresponding fields $\psi_{\alpha,k}$ and $\bar{\psi}_{\alpha,k}$. When applying the Hamiltonian of the time-evolution operator of the intermediate time slices to the states, the creation and the annihilation operators are in an order which corresponds to the one generated by the series representation of the exponential function. The error arising due to a normal ordering of this exponential is quadratic in the size of the time slice ϵ and will vanish in the limit $M\to\infty$. Thus we obtain

$$\begin{aligned}
&\mathcal{U}(\bar{\psi}_{\alpha,f}t_f,\psi_i t_i) = \langle\psi_f|\,e^{-i\,H[\hat{c}^\dagger,\hat{c}](t_f-t_i)}\,|\psi_i\rangle\\
&= \lim_{M\to\infty}\int\prod_{k=1}^{M-1}\prod_\alpha \mathrm{d}\bar{\psi}_{\alpha,k}\,\mathrm{d}\psi_{\alpha,k}e^{-\sum_{k=1}^{M-1}\sum_\alpha \bar{\psi}_{\alpha,k}\psi_{\alpha,k}}\prod_{k=1}^{M}\langle\psi_k|:e^{-i\,\epsilon H[\hat{c}_\alpha^\dagger,\hat{c}_\alpha]}:+\mathcal{O}(\epsilon^2))\,|\psi_{k-1}\rangle\\
&= \lim_{M\to\infty}\int\prod_{k=1}^{M-1}\prod_\alpha \mathrm{d}\bar{\psi}_{\alpha,k}\,\mathrm{d}\psi_{\alpha,k}e^{-\sum_{k=1}^{M-1}\sum_\alpha \bar{\psi}_{\alpha,k}\psi_{\alpha,k}}e^{\sum_{k=1}^{M}(\sum_\alpha \bar{\psi}_{\alpha,k}\psi_{\alpha,k-1}-i\,\epsilon H[\bar{\psi}_{\alpha,k},\psi_{\alpha,k}])}.
\end{aligned}\tag{2.65}$$

All the integrals in this formula are finite, as there is no metric in the Grassmann algebra. In the limit $M\to\infty$ it makes sense to replace the intermediate states $\psi_{\alpha,k}$ by introducing the Grassmann trajectory $\psi_\alpha(t)$ and to define the time-derivative symbolically as $\frac{\partial}{\partial t}\psi_\alpha(t) := \frac{\psi_{\alpha,k}-\psi_{\alpha,k-1}}{\epsilon}$ and the

Hamiltonian of the Grassmann trajectories as $H(\bar{\psi}_\alpha(t), \psi_\alpha(t)) := H(\bar{\psi}_{\alpha,k}, \psi_{\alpha,k-1})$. Rewriting the exponential then results in

$$\mathcal{U}(\bar{\psi}_{\alpha,f} t_f, \psi_{\alpha,i} t_i) = \int_{\psi_\alpha(t_i)}^{\bar{\psi}_\alpha(t_f)} \mathcal{D}[\bar{\psi}_\alpha(t)\psi_\alpha(t)] \exp\left(\sum_\alpha \bar{\psi}_\alpha(t_f)\psi_\alpha(t_f)\right) \exp\left(i \int_{t_i}^{t_f} \mathrm{d}t \left(\sum_\alpha i\,\bar{\psi}_\alpha(t) \frac{\partial \psi_\alpha(t)}{\partial t} - H[\bar{\psi}_\alpha(t), \psi_\alpha(t)]\right)\right), \quad (2.66)$$

which anticipates the definition of the path integral (cf. def. 9).

This formula is derived for the time-evolution operator and will change when, for example, an operator acts between the initial and the final state. Based on this example, we, therefore, define the path integral mathematically incomplete as the procedure for obtaining such an equation.

Definition 9 (Path Integral)
*The **path integral** is defined as the limit of infinitely many discrete time-step splittings of the evolution from an initial state to a final state. We formally define the notation of a path integral as*

$$\int_{\psi_\alpha(t_i)}^{\bar{\psi}_\alpha(t_f)} \mathcal{D}[\bar{\psi}_\alpha(t), \psi_\alpha(t)] := \lim_{M\to\infty} \int \prod_{k=1}^{M-1} \prod_\alpha \mathrm{d}\bar{\psi}_{\alpha,k}\, \mathrm{d}\psi_{\alpha,k}. \quad (2.67)$$

The representation of the partition function in Grassmann variables (see eq. (2.63)) can be simplified by means of these path integrals according to the following lemma.

Lemma 2.4 (Partition Function in Path Integral Formulation)
Let $\hat{H}$, $\hat{N}$, μ and β be given as in definition 5. Then the partition function $\mathcal{Z}$ in a path integral formulation is given as

$$\mathcal{Z} = \int_{\psi_i(\beta) = -\psi_i(0)} \mathcal{D}[\bar{\psi}(\tau), \psi(\tau)] \exp\left(-\int_0^\beta d\tau \left\{\sum_i \bar{\psi}_i(\tau)\left(\frac{\partial}{\partial\tau} - \mu\right)\psi_i(\tau) + H[\bar{\psi}_i(\tau), \psi_i(\tau)]\right\}\right). \quad (2.68)$$

Proof: The continuation of the time-evolution operator to imaginary times results in $\mathcal{U}(\psi_f \tau_f, \psi_i \tau_i) = \langle \psi_f | \, e^{-H(\tau_f - \tau_i)} \, |\psi_i\rangle$. The partition function in coherent states (cf. eq. (2.63)) can be identified as the sum over diagonal matrix elements of this imaginary time-evolution operator over the time interval $[0, \beta]$. Due to the trace there exist antiperiodic boundary conditions for fermions, such that $\psi_i(\beta) = -\psi_i(0)$. Using the results of the time-evolution operator in equation (2.66), the quadratic term in the exponential cancels with the one in equation (2.63), such that the partition function becomes

$$\mathcal{Z} = \int_{\psi_i(\beta) = -\psi_i(0)} \mathcal{D}[\bar{\psi}(\tau), \psi(\tau)] \; e^{-\int_0^\beta d\tau \left\{\sum_i \bar{\psi}_i(\tau)\left(\frac{\partial}{\partial\tau} - \mu\right)\psi_i(\tau) + H[\bar{\psi}_i(\tau), \psi_i(\tau)]\right\}}, \quad (2.69)$$

which completes the proof. ∎

As the exponential in the partition function is quite lengthy, we simplify the notation by introducing the action as follows:

Definition 10 (Action)
Let $\psi_i(\tau)$, $\bar{\psi}_i(\tau)$ be Grassmann variables, and let $H[\bar{\psi}_i(\tau), \psi_i(\tau)]$ be the Hamiltonian of a system given in the coherent state basis. Then the ***action*** *is defined as*

$$\mathcal{S}[\bar{\psi}_i(\tau), \psi_i(\tau)] := \int_0^\beta d\tau \left\{ \sum_i \bar{\psi}_i(\tau) \left(\frac{\partial}{\partial \tau} - \mu \right) \psi_i(\tau) + H[\bar{\psi}_i(\tau), \psi_i(\tau)] \right\}. \tag{2.70}$$

Based on these mathematical tools we are able to derive the FRG equations. In order to be able to understand the symmetries of a solid and to derive the form-factor basis later on, we deal with the basic theory of finite groups in the following.

2.4. Group Theory

The symmetry of the underlying lattice of a solid state system can be used for important simplifications, as all solid state properties have to transform under the corresponding symmetry operations. In addition, the symmetries will be useful for the derivation of form-factors, which we will choose to be basis functions corresponding to the point group symmetry. The framework for a proper treatment of symmetries is given by the group theory, whose relevant parts will be introduced in this section, based on Dresselhaus [79].

At first, we define the notation of symmetry operations according to Schoenflies.

Definition 11 (Schoenflies Notation for Symmetry Operations)
Consider the three-dimensional lattice of a solid state crystal. The axis with the highest order of rotations is defined as ***principal axis****. The symmetry operations are defined as:*

- *E: identity operation*
- *I: inversion operation, taking $x \mapsto -x,\ y \mapsto -y,\ z \mapsto -z$*
- *C_n: rotation by $2\pi/n$ with $n \in \mathbb{N}$*
- *σ_v: reflection on a vertical plane, i.e. through the principle axis*
- *σ_d: reflection on a diagonal plane, i.e. through the principle axis and bisecting the angle between the two two-fold rotation axes orthogonal to the principal axis*
- *σ_h: reflection on a horizontal plane, i.e. perpendicular to the principle axis*
- *S_n: improper rotation, rotation by $2\pi/n$ with $n \in \mathbb{N}$, followed by a reflection in the plane orthogonal to the rotation axis.*

In the following we introduce the mathematical group and define the point group and the crystallographic point group as well.

Definition 12 (Group)

1. *Let $G = \{a, b, \dots\}$ be a set of elements and let $\circ$ be an operation between two elements $a, b \in G$. Then $(G, \circ)$ is called a* ***group****, if and only if*
   - *for all $a, b \in G$ the element $a \circ b$ also is an element of G,*
   - *the operation $\circ$ is associative, i.e. for $a, b, c \in G$ the equality $a \circ (b \circ c) = (a \circ b) \circ c$ holds,*
   - *there exists a neutral element $e \in G$, such that $a \circ e = e \circ a = a$ holds for all $a \in G$,*
   - *for all $a \in G$ there exists an inverse element $a^{-1} \in G$, such that $a \circ a^{-1} = a^{-1} \circ a = e$,*
2. *If the set G is finite, the group is called finite.*
3. *A* ***point group*** *is a finite group consisting of elements which are symmetry operations, which can be denoted by definition 11, and whose operation $\circ$ is their successive action.*
4. *A* ***crystallographic point group*** *is a point group which contains only (improper) rotations with $n \in \{1, 2, 3, 4, 6\}$.*

The restriction of n fixes the total number of possible crystallographic point groups to 32, while there are infinitely many point groups. This restriction is based on the observation made in the crystallography that no other structures have been obtained. However, quasi-crystals may have point groups with, for example, $n = 5$.

Next we consider the multiplication of a group element with itself.

Theorem 2.5 (n-Repetitiveness of a Finite Group)
Let $(G, \circ)$ be a finite group. Then there exists an $n \in \mathbb{N}$, such that $a^n := \underbrace{a \circ a \circ \dots \circ a}_{n \text{ times}} = e$ holds for any $a \in G$.

Proof: Let y be a repetition, such that $y = x^p = x^q$ with $p > q$. We can write $p = q + n$ such that

$$y = x^p = x^{q+n} = x^q \circ x^n \tag{2.71}$$

but, by construction, it is also $y = x^q$. Therefore, it follows that $x^n = e$. ■

To assign a size to a group, we define its order and, based on the previous theorem, the order of a group element.

Definition 13 (Order of Group and Elements)
Let $(G, \circ)$ be a group. Then

- *the* ***order of the group*** *is defined as the number of elements in the group,*
- *the* ***order of an element*** *$a \in G$ is the smallest n for which $a^n = e$ holds.*

In a next step we relate elements to each other according to the following definition.

Definition 14 (Conjugate Elements and Class)

1. *Let $(G, \circ)$ be a group and let $a, b \in G$. Then a and b are called **conjugate**, if and only if $b = x \circ a \circ x^{-1}$ for all $x \in G$.*
2. *The set of all conjugate elements of G is called a **class**.*

These conjugate elements obtain some relations to each other, as the following theorem shows.

Theorem 2.6 (Same Order of Class Elements)
Let $(G, \circ)$ be a group.

1. *Let $a, b, c \in G$ and let b be conjugate to a and let c be conjugate to b. Then c is conjugate to a, too.*
2. *Let $a_1, a_2, \ldots, a_m \in G$ be a class. Then all the elements $a_1, a_2, \ldots, a_m$ of the class have the same order.*

Proof: 1. According to the definition of the conjugation we can write

$$b = x \circ a \circ x^{-1} \qquad \text{and} \qquad c = y \circ b \circ y^{-1} \tag{2.72}$$

with $x, y \in G$. By substitution we obtain

$$c = y \circ x \circ a \circ x^{-1} y^{-1} = (y \circ x) \circ a \circ (y \circ x)^{-1}, \tag{2.73}$$

thus, c is conjugate to a as $y \circ x \in G$.

2. Without loss of generality assume a_1 to have the order n, i.e. $a_1^n = e$. As all a_j are in the same class, they are conjugated to a_1 according to $a_j = x \circ a_1 \circ x^{-1}$ for any $x \in G$. Then,

$$a_j^n = \underbrace{(x \circ a_1 \circ x^{-1}) \circ (x \circ a_1 \circ x^{-1}) \circ \cdots \circ (x \circ a_1 \circ x^{-1})}_{n \text{ times}}. \tag{2.74}$$

Due to the commutativity $x \circ x^{-1} = e$, leading to $a_j^n = x \circ a_1^n \circ x^{-1} = x \circ e \circ x^{-1} = e$, so that a_j has the same order n as a_1 has. ■

So far, we have dealt with one group and its elements. However, it is interesting to relate two different groups to each other, as it might be easier to deal with one of them instead of the other.

Definition 15 (Isomorph, Homomorph)
Let $(G, \circ)$ and $(F, \cdot)$ be two groups.

- *If the groups have the same order and there exists a bijective map between their elements, then $(G, \circ)$ and $(F, \cdot)$ are called **isomorphic**.*
- *If $(G, \circ)$ has order n and $(F, \cdot)$ has order $m > n$ and there exists a surjective map $M : G \to F$, then $(G, \circ)$ and $(F, \cdot)$ are called **homomorphic**.*

Based on the isomorphic relation between two groups, we can relate the abstract groups to groups based on matrices, which can be dealt with more easily.

Definition 16 (Representation)
*Let $\mathcal{G} = (G, \circ)$ be an abstract group. Let R be a set of n-dimensional square matrices and let "$\cdot$" be the matrix-product operation so that $\mathcal{R} = (R, \cdot)$ is a group, called **substitution group**. If $\mathcal{R}$ is homomorphic or isomorphic to $\mathcal{G}$, $\mathcal{R}$ is called a **representation** of $\mathcal{G}$ and a matrix $R(a)$ is assigned to each element a of $\mathcal{G}$, such that $R(a \circ b) = R(a) \cdot R(b)$ holds for all $a, b \in \mathcal{G}$.*

The representation of a group in terms of square matrices is helpful in several ways. At first the quantum mechanical wave-function will transform under the symmetry operation similar to the transformation of its matrix under the application of the symmetry matrix. Secondly, quantum mechanical operators are typically written in matrix form, so that a symmetry operation in matrix form can be applied to it more easily.

However, a representation is not unique, as a similarity transformation $UR(a)U^{-1}$ with an invertible square matrix U generates a new set of matrices, which is also a good representation. Additionally, another representation can be obtained by combining two representations to a larger matrix, for example, as

$$\begin{pmatrix} R(a) & 0 \\ 0 & R'(a) \end{pmatrix}. \tag{2.75}$$

This matrix is reducible, as all group elements are in the same block form. But, a similarity transformation of this latter matrix can mix up all the elements, such that the block form is lost. However, the matrix remains reducible. Based on these observations we define some more terms to classify representations.

Definition 17 (Properties of Representations)
Let $\mathcal{R} = (R, \cdot)$ be a representation of a group $\mathcal{G}$ based on a set R of n-dimensional square matrices and the matrix-product operation denoted by "$\cdot$".

1. *Then $\mathcal{R}$ is called n-**dimensional**.*
2. *Let $\tilde{\mathcal{R}} = (\tilde{R}, \cdot)$ be another representation of $\mathcal{G}$. Then $\mathcal{R}$ and $\tilde{\mathcal{R}}$ are called **equivalent**, if there exists a regular n-dimensional square matrix U, such that the equality*

   $$N(a) = U \cdot M(a) \cdot U^{-1} \tag{2.76}$$

   holds for all $a \in \mathcal{G}$ and for the corresponding matrices $M(a) \in \mathcal{R},\ N(a) \in \tilde{\mathcal{R}}$.
3. *The representation $\mathcal{R}$ is called **reducible**, if it is equivalent to a representation in which all matrices have a common block structure, i.e.*

   $$M(a) = \begin{pmatrix} M_1(a) & 0 \\ 0 & M_2(a) \end{pmatrix}. \tag{2.77}$$

   *Otherwise it is called **irreducible**.*

To understand the reducibility in more detail, assume a reducible representation Γ_r of a group G which is irreducible in the group G'. This relation indicates that some interaction breaks up a degenerate energy level in G' into non- or less degenerate ones in group G. Due to group theory we know which symmetry is related to this degeneracy and in how many levels it will split up.

As we have already stated, every representation has an arbitrariness with respect to a unitarity transformation. Therefore, it is useful to work with the trace of a representation, which is called character, as it does not change under these transformations.

Definition 18 (Characters)
Let $\mathcal{G} = (G, \circ)$ be a group and let $\mathcal{R} = (R, \cdot)$ be a corresponding representation. Let $a \in G$ be a group element and let $R(a)$ be its representing matrix. Then the ***character*** *of a is defined as $\chi(a) = Tr(R(a))$.*

As the trace is independent under similarity transformations, the character is also independent. For the character, the following theorem provides some very helpful relations.

Theorem 2.7 (Properties of Irreducible Representations)
Let $\mathcal{G} = (G, \circ)$ be a group with N elements, let there be n_c classes $C_{q \leq n_c}$ with n_q elements each, and let there be n_{irrep} inequivalent irreducible representations given by $\mathcal{R}_i = (R, \cdot)$, $i \leq n_{irrep}\}$. Then

1. *the dimension n_i of a representation $\mathcal{R}_i$ is equivalent to the character of the identity map, i.e. $n_i = \chi_i(e)$,*
2. *the characters χ_i of $\mathcal{R}_i$ are the same for all elements of the same class,*
3. *the number n_c of classes and the number of inequivalent irreducible representations n_{irrep} (i.e. different $\mathcal{R}_i$ of $\mathcal{G}$) are equivalent,*
4. *the characters χ_i of a class C_q and those of a class $C_{q'}$ are orthogonal to each other, i.e.*

$$\sum_{i=1}^{n_{irrep}} \chi_i(C_q)\chi_i(C_{q'}) = \delta_{qq'} N/n_q, \tag{2.78}$$

5. *the characters χ_i of a representation $\mathcal{R}_i$ and the characters χ_j of a representation $\mathcal{R}_j$ are orthogonal to each other, i.e.*

$$\sum_{q=1}^{n_c} h_q \chi_i(C_q)\chi_j(C_q) = \delta_{ij} N. \tag{2.79}$$

Proof: For the proofs of these statements we refer to [79], as they are lengthy and out of the scope of this thesis. ■

Based on this theorem it is possible to write down all the characters of a class in an $n_c \times n_{\text{irrep}}$ square table, called character table. The orthogonality relations simplify the calculations needed to fill those

tables. Considering the orthogonality, one can regard the representation Γ_i creating an h-dimensional vector space

$$V_{\mu,\nu}^{(\Gamma_i)} = [R_{\mu\nu}^{\Gamma_i}(a_1), R_{\mu\nu}^{\Gamma_i}(a_2), \ldots, R_{\mu\nu}^{\Gamma_i}(a_h)], \tag{2.80}$$

in which particular vectors are labelled by the indices Γ_i, μ, ν. All distinct vectors in this space are orthogonal, leading to the observation that two representations are orthogonal, if at least one of the three indices differs.

Finally, we define the projection operator to an irreducible representation, which will be very useful for the derivation of the form-factor basis.

Definition 19 (Projection Operator)
Let $\mathcal{G}$ be a group with irreducible representations $\mathcal{R}_i$ with character χ_i. Then the ***projection operator***

$$\mathcal{P}(\mathcal{R}_i) = \sum_{g\in\mathcal{G}} \chi_i^*(g) g \tag{2.81}$$

projects out the contribution which transforms in $\mathcal{R}_i$.

With the mathematical background at this stage, we are in a position to focus on the physical problem of correlated electrons.

3. Theory

Condensed matter systems consist of atomic nuclei in a periodic arrangement and of electrons. The nuclei of charge $Z_l e$ (with e being the fundamental electronic charge and Z_l the nuclear charge number) are located at positions $\boldsymbol{R}_l$ and generate a periodic potential affecting the electrons. As the atomic nuclei are significantly heavier than the electrons, calculations of the electronic system for static nuclei result in small errors only. Therefore, the full condensed matter problem is separated into an atomic and an electronic one by applying the Born-Oppenheimer approximation. As pointed out in the introduction, the focus of this thesis is on the effects of electronic correlations, so that we consider only the electronic problem whose corresponding Hamiltonian

$$\hat{H} = \underbrace{\sum_{i=1}^{N} \left[\frac{\hat{\boldsymbol{p}}_i^2}{2m} + V(\hat{\boldsymbol{r}}_i) \right]}_{=:\hat{H}_0} + \underbrace{\sum_{i=1}^{N} \sum_{j=i+1}^{N} \frac{e^2}{|\hat{\boldsymbol{r}}_i - \hat{\boldsymbol{r}}_j|}}_{=:\hat{H}_\mathrm{I}} \tag{3.1}$$

describes the N electrons of a condensed matter system in the periodic potential

$$V(\hat{\boldsymbol{r}}) = -\sum_l \frac{Z_l e^2}{|\boldsymbol{R}_l - \hat{\boldsymbol{r}}|} \tag{3.2}$$

of the atomic nuclei. The non-interacting part $\hat{H}_0$ of the Hamiltonian is a one-particle operator which sums up the kinetic and the potential energy of each electron. The interacting part $\hat{H}_\mathrm{I}$ is a two-particle operator, which describes the Coulomb-interaction between two electrons of the system. The evaluation of this term is the crucial part for the description of the electronic system, as the duality of representations makes an analytical solution impossible and as the large number of electrons makes a numerical exact solution impossible, so that additional approximations to the full solid state electron system are necessary[1].

For many materials, like for example semi-conductors, the electronic system can well be described by the behaviour of one electron in the effective potential of all the other electrons. In this case the properties of the electronic system can be represented by one-particle expectation values. Many other materials, like the HTS we are interested in, are not well described by such an effective one-particle picture. In those cases, the expectation value of two one-particle operators differs from the product of their expectation values, so that the electron-electron interaction has to be treated more accurately. We define the correlation function which provides an objective measure to differentiate these types of materials.

[1] In many cases, the Hamiltonian of the full electronic part is simplified to a model one, which can be discussed more easily. To simplify the notation, all the following derivations and definitions are always with respect to the Hamiltonian $\hat{H}$, describing the system, its Fock basis or coherent states.

Definition 20 (Correlation Function and Correlated Electrons)
Let $\hat{A}$ and $\hat{B}$ be operators acting at (imaginary) space-time 1 and 2, respectively. Then their ***correlation function*** *is given by*

$$\chi_{\hat{A}\hat{B}}(1,2) := \left\langle \hat{A}(1)\hat{B}(2) \right\rangle . \tag{3.3}$$

Let $\hat{A}$ and $\hat{B}$ be one-particle electron operators. Then the electrons are ***uncorrelated****, if*

$$\chi_{\hat{A}\hat{B}}(1,2) \simeq \left\langle \hat{A}(1) \right\rangle \left\langle \hat{B}(2) \right\rangle , \tag{3.4}$$

otherwise they are ***correlated****.*

The simplest correlation functions are those in which $\hat{A}$ and $\hat{B}$ are fermion annihilation and creation operators, like in $\chi(1_t, 2_t) = \langle c^\dagger_{1_t} c_{2_t} \rangle$. Physically, this is the probability of finding an electron at space-time 1_t, when one is added at space-time 2_t. This correlation function is the one-particle Green's function and will be discussed later on, as most one-particle expectation values can be derived from it. In the limit $2_t \to 1_t^+$, for instance, it becomes the expectation value of the particle number.

Increasing the order of complexity, we let the operator product $\hat{A}\hat{B}$ consist of two electron creation and two electron annihilation operators, such that the correlation function describes the correlations between two electrons. The definition of the term **correlated electrons** according to equation (3.4) is based on these operators. Physically, this equations states that electrons are correlated, when the correlation function of the product of both one-particle operators is significantly different to the product of the mean field expectation values of each operator. To obtain an operator product as required, $\hat{A}$ and $\hat{B}$ are chosen as fermion-bilinears as given in the following definition.

Definition 21 (Fermion-Bilinears)
Let $c^\dagger_s(i)$ and $c_s(i)$ be the creation and the annihilation operators of a particle with spin s in a solid at site and orbital index i and let $\boldsymbol{\sigma}$ be a Pauli matrix. Then we define:

1. ***Charge-Density operator:*** $\hat{\rho}(1) = \sum_s \hat{c}^\dagger_s(1)\hat{c}_s(1)$.
2. ***Spin operators:*** $\hat{S}^i(1) = \frac{1}{2}\sum_{s,s'} \hat{c}^\dagger_s(1)\sigma^i_{ss'}\hat{c}_{s'}(1)$*, where σ^i corresponds to the Pauli matrices with $i \in \{0, x, y, z\}$.*
3. ***Pairing operator:*** $\hat{p}(1,2) = \hat{c}_{s_1}(1)\hat{c}_{s_2}(2)$.

One can directly see that charge- and spin-density operators are one-particle operators, thus

$$\chi_{\mathrm{cd}}(1,2) := \chi_{\rho\rho}(1,2) \quad = \langle \hat{\rho}(1)\hat{\rho}(2) \rangle \qquad \text{and} \tag{3.5}$$

$$\chi^{ij}_{\mathrm{sd}}(1,2) := \chi_{S^i S^j}(1,2) \; = \langle \hat{S}^i(1)\hat{S}^j(2) \rangle \tag{3.6}$$

are the charge- and the spin-density susceptibility, respectively. Contrary, the pairing operator generates particle pairs only with its adjoint counterpart, so that

$$\chi_{\mathrm{pd}}(1,2) := \chi_{pp^\dagger}(1,2) = \langle \hat{p}(1,2)\hat{p}^\dagger(1,2) \rangle \tag{3.7}$$

is the pairing susceptibility. When these susceptibilities become non-zero they indicate charge-density-waves, spin-density-waves or pairing (superconducting) order, respectively. Frequently, the fermion-bilinears are defined including a form-factor $f_n(x, y)$, whose spatial spread represents some typical behaviour of the bilinears or susceptibilities under lattice symmetries, which is discussed in some more detail in section 3.3.

As all three correlation functions consist of two creation and two annihilation operators they can be obtained from a generalised correlation function (cf. def. 22) by taking the corresponding limits.

Definition 22 (Generalised Correlation Function)
Let the system be in thermal equilibrium and let $1, \ldots, 4$ *be space- and (imaginary) time-coordinates. Then the* ***generalised correlation function*** *is defined as the connected part of the expectation value of two creation and two annihilation operators, i.e.*

$$\begin{aligned}\chi(12,34) &:= \left\langle \hat{\mathcal{T}}[\hat{c}(1)\hat{c}(2)\hat{c}^\dagger(3)\hat{c}^\dagger(4)] \right\rangle_c \\ &= \langle \hat{\mathcal{T}}[\hat{c}(1)\hat{c}(2)\hat{c}^\dagger(3)\hat{c}^\dagger(4)]\rangle - \left\langle \hat{c}(1)\hat{c}^\dagger(4)\right\rangle \left\langle \hat{c}(2)\hat{c}^\dagger(3)\right\rangle + \left\langle \hat{c}(1)\hat{c}^\dagger(3)\right\rangle \left\langle \hat{c}(2)\hat{c}^\dagger(4)\right\rangle . \quad (3.8)\end{aligned}$$

The restriction to the thermal equilibrium ensures that the particle number is conserved, as the trace is zero in all other cases. The denotion of "connected" will be clarified by definition 29 later on in this section. In the case of the limits $4 \to 1^-$ and $3 \to 2^-$ this generalised correlation function becomes the charge-density correlation function after changing the order of operators. With the limits $2 \to 1^-$ and $4 \to 3^-$ one directly obtains the pairing correlation function. A similar combination of exchanging the order of operators and taking limits to equal space-time coordinates leads to the spin-density susceptibility.

A special kind of correlation functions, called response functions, is accessible by experiments. They give the response of a physical observable to an external effect perturbing the equilibrium state of the system. This can be the addition or the removal of particles or a perturbing field. For the latter case we consider, exemplarily, the expectation value of an operator $\hat{A}(1_t)$ under the perturbation of the form $\varphi(2_t)\, s\hat{B}(2_t)$, which is switched on at time t_0. With the time-evolution operator $\mathcal{U}_S(t, t_0) = e^{-i\int_{t_0}^{t} dt' \hat{H} + \varphi(2_t)\hat{B}(2_t)}$ the expectation value of the operator $\hat{A}$ in the Heisenberg picture becomes

$$\delta \left\langle \hat{A}_H(1_t) \right\rangle_{\text{pert}} = \left\langle \hat{U}_S^\dagger(t_1, t_0)\hat{A}(1_t)\hat{U}_S(t_1, t_0) \right\rangle \quad (3.9)$$

$$= \left\langle \hat{A}_H(1_t) \right\rangle + i\int_{t_0}^{t} dt' \varphi(2_t) \left\langle \left[\hat{B}_H(2_t), \hat{A}_H(1_t)\right] \right\rangle + \mathcal{O}(\varphi^2) \quad (3.10)$$

in a perturbation expansion in φ. The coefficients on the right hand side are called response functions whose first order or linear term

$$\chi_{\hat{A}\hat{B}}(1_t, 2_t) := \frac{\partial \left\langle \hat{A}_H(1_t) \right\rangle}{\partial \varphi(2_t)} = -i\theta(t_1 - t_2) \left\langle \left[\hat{A}_H(1_t), \hat{B}_H(2_t)\right] \right\rangle \quad (3.11)$$

is also called susceptibility. This is, therefore, determined by the derivative of an expectation value with respect to a perturbation. Thus, it can be regarded as the second derivative of the grand canonical potential (cf. def. 5) with respect to some perturbation, as expectation values of operators are the

first derivative. Extending this procedure to non-local operators and to non-local perturbations, like magnetisation and magnetic fields, the resulting susceptibilities depend on four arguments. Writing the effects in terms of field operators, the expression takes the same form as the generalised correlation function. Thus the generalised correlation function also contains the experimentally accessible susceptibilities.

The calculation of the generalised correlation function is difficult, as the grand canonical partition function, the grand canonical potential and the wave-function of the stationary Schrödinger equation of the many-electron problem cannot be calculated for generic interacting electron systems. In the following, we will, therefore, discuss a general form of correlation functions, which our approach to solve the problem is based on.

3.1. Green's Functions

As all operators can be expressed by creation and annihilation operators in the occupation number representation, we generalise the previous correlation function to an arbitrary number of operators.

Definition 23 (n-particle Green's Function)
Let $n \in \mathbb{N}$, and let $\langle \cdots \rangle$ denote the expectation value with respect to $\hat{K} = \hat{H}_0 + \hat{H}_I - \mu\hat{N}$ and $\langle \cdots \rangle_0$ the expectation value with respect to the non-interacting Hamiltonian $\hat{K}_0 = \hat{H}_0 - \mu\hat{N}$, and let $\mathcal{T}$ be the time-ordering operator.

- *Let $\hat{c}^\dagger(i_t)$ and $\hat{c}(i_t)$ be the creation and the annihilation operators of states $x_i = (\boldsymbol{r}_i, o_i, s_i)$ in the Heisenberg picture at real times $t_i \in \mathbb{R}$ with $i_t = (x_i, t_i)$. Then*
  - *the n-**particle** (or $2n$-point) **real time Green's function** is defined as*

$$G^{(2n)}(1_t, \ldots, 2n_t) := (-i)^n \left\langle \hat{\mathcal{T}} \left[\hat{c}(1_t) \cdots \hat{c}(n_t) \hat{c}^\dagger(2n_t) \cdots \hat{c}^\dagger(n+1_t) \right] \right\rangle \quad \textit{and} \tag{3.12}$$

  - *the **free** or **non-interacting** n-**particle real time Green's function** is defined as*

$$G_0^{(2n)}(1_t, \ldots, 2n_t) := (-i)^n \left\langle \hat{\mathcal{T}} \left[\hat{c}(1_t) \cdots \hat{c}(n_t) \hat{c}^\dagger(2n_t) \cdots \hat{c}^\dagger(n+1_t) \right] \right\rangle_0 . \tag{3.13}$$

- *Let $\hat{c}^\dagger(i)$ and $\hat{c}(i)$ be the creation and the annihilation operators of states $x_i = (\boldsymbol{r}_i, o_i, s_i)$ in the Heisenberg picture for imaginary times $\tau_1, \ldots, \tau_{2n} \in [0, \hbar\beta]$ with $i = (x_i, \tau_i)$. Then*
  - *the n-**particle** (or $2n$-point) **imaginary time Green's function** is defined as*

$$G^{(2n)}(1, \ldots, 2n) := \left\langle \hat{\mathcal{T}} \left[\hat{c}(1) \cdots \hat{c}(n) \hat{c}^\dagger(2n) \cdots \hat{c}^\dagger(n+1) \right] \right\rangle \qquad \textit{and} \tag{3.14}$$

  - *the **free** or **non-interacting** n-**particle** (or $2n$-point) **imaginary time Green's function** is defined as*

$$G_0^{(2n)}(1, \ldots, 2n) := \left\langle \hat{\mathcal{T}} \left[\hat{c}(1) \cdots \hat{c}(n) \hat{c}^\dagger(2n) \cdots \hat{c}^\dagger(n+1) \right] \right\rangle_0 . \tag{3.15}$$

These Green's functions are the basic elements of a lot of approaches to many-particle physics and, hence, are discussed extensively in basic literature ([78, 80, 28, 81, 82]), which this section is based on.

In definition 23 the basis on which the operators act was chosen as the conventional position space basis. As discussed in section 2.1 a translational invariant basis is advantageous to describe solids, especially for working with lattice models. Therefore, we will typically work with **lattice Green's functions**, which are defined with respect to Wannier functions (see eq. 2.18). The basis transformation is straight forward and results in a replacement of the position space argument by the corresponding lattice vector argument in our notation. Therefore, we now denote $x := (\boldsymbol{R}os)$ and $1 := (x\tau)$, as already introduced in equation (2.21) and the following paragraph in the preliminaries. Throughout this thesis we assume in all theorems and definitions in which Green's functions appear, that these are well defined according to this definition without mentioning all prerequisites.

All the properties which will be discussed for the interacting Green's function in this and in the following section also hold for the free Green's function due to the similarity of their definitions. Based on our notation, we will derive these properties for the lattice imaginary time Green's function, although most of the properties also hold for position-space and for real time Green's functions and differences will be mentioned in short remarks. As the one-particle Green's function has an extraordinary significance, which will become evident in section 3.2, the superscript is neglected and we write $G(1,2) := G^{(2)}(1,2)$.

A comparison of the definitions of the two-particle Green's function $G^{(4)}$ and the generalised susceptibility χ (cf. def. 22) shows that these only differ by the restriction of χ to connected expectation values. They are thus related by subtraction of the uncorrelated part from $G^{(4)}$ according to

$$\chi(1,2;3,4) = G^4(1,2;3,4) - G^2(1;4)G^2(2;3) + G^2(1;3)G^2(2;4), \tag{3.16}$$

which we will derive in detail in the section about diagrammatic representations (see sec. 3.2.2). Although we formally defined different Green's functions for real and for imaginary time, both are equivalent under the identification $t = i\tau$ and can be converted into each other. The restriction of the imaginary time Green's function to the interval $[0, \beta]$ is required to ensure convergence for the trace in an infinite basis. To illustrate this, let $\{|i\rangle\}$ be a complete orthonormal basis built up from the eigenstates of the modified Hamiltonian $\hat{K} = \hat{H} - \mu\hat{N}$ with eigenvalues E_i. For the expansion of the trace in this basis set we assume, without loss of generality, $\tau_1 > \tau_2 > \ldots > \tau_n > \tau_{2n} > \ldots > \tau_{n+1}$ and write the Green's function as

$$G^{(2n)}(1,\ldots,2n) = \frac{1}{\mathcal{Z}} \sum_n e^{-(\beta+\tau_{n+1}-\tau_1)E_n} \langle i|\, \hat{c}_1 e^{-\tau_1 \hat{K}} \ldots e^{\tau_{n+1}\hat{K}} \hat{c}^\dagger_{n+1} \,|i\rangle\,. \tag{3.17}$$

For an infinitely large system, the number of eigenstates is infinite and its spectrum is unbounded, i.e. the eigenenergies E_i can become infinitely large. Only under the requisition $\beta + \tau_{n+1} - \tau_1 > 0$ the exponential factor can ensure a convergence of the sum. The choice of τ_{n+1} and τ_1 as smallest and largest imaginary time, respectively, enforces all other imaginary times to be in an interval of size β.

3.1.1. Properties of the n-particle Green's Function

Based on the general definition of the Green's functions, we will analyse the n-particle Green's functions in this subsection and will focus on imaginary time arguments, as we have to deal with systems at finite temperatures to obtain critical temperatures indicating phase transitions. The corresponding Green's function is antiperiodic due to the cyclic property of the trace, which is also called Kubo-Martin-Schwinger boundary condition [83].

Theorem 3.1 (Kubo-Martin-Schwinger Boundary Condition)
Let G^{2n} be the n-particle Green's function. Then the Green's functions G^{2n} at time $\tau_i = 0$ and $\tau_i = \beta$ for any $i \in \{1,\ldots,2n\}$ are related by

$$G^{2n}(x_1\tau_1,\ldots,x_i\tau_i = 0,\ldots,x_{2n}\tau_{2n}) = -G^{2n}(x_1\tau_1,\ldots,x_i\tau_i = \beta,\ldots,x_{2n}\tau_{2n}). \tag{3.18}$$

PROOF: First, we consider a special case and let $\tau_{n+1} = 0$. Then

$$\begin{aligned} G^{2n}(x_1\tau_1, \ldots, x_{n+1}\underbrace{\tau_{n+1}}_{=0}, \ldots, x_{2n}\tau_{2n}) &= \left\langle \hat{\mathcal{T}}\left[\hat{c}_{x_1}(\tau_1)\cdots\hat{c}^\dagger_{x_{n+1}}(0)\right]\right\rangle \\ &= \left\langle \left\{\hat{\mathcal{T}}\left[\hat{c}_{x_1}(\tau_1)\cdots\hat{c}^\dagger_{x_{n+2}}(\tau_{n+2})\right]\right\}\hat{c}^\dagger_{x_{n+1}}(0)\right\rangle \\ &\overset{\text{def. 6}}{=} \frac{1}{\mathcal{Z}}\mathrm{Tr}\left(\hat{c}^\dagger_{x_{n+1}}(0)\, e^{-\beta\hat{K}}\, \hat{\mathcal{T}}\left[\hat{c}_{x_1}(\tau_1)\cdots\hat{c}^\dagger_{x_{n+2}}(\tau_{n+2})\right]\right) \\ &= \frac{1}{\mathcal{Z}}\mathrm{Tr}\left(e^{-\beta\hat{K}}\, \hat{c}^\dagger_{x_{n+1}}(\beta)\, \hat{\mathcal{T}}\left[\hat{c}_{x_1}(\tau_1)\cdots\hat{c}^\dagger_{x_{n+2}}(\tau_{n+2})\right]\right) \\ &= -\left\langle \hat{\mathcal{T}}\left[\hat{c}_{x_1}(\tau_1)\cdots\hat{c}^\dagger_{x_{n+2}}(\tau_{n+2})\hat{c}^\dagger_{x_{n+1}}(\beta)\right]\right\rangle \\ &= -G^{2n}(x_1\tau_1, \ldots, x_{n+1}\beta, \ldots, x_{2n}\tau_{2n}). \end{aligned} \tag{3.19}$$

In this derivation we used the cyclicity of the trace in the third line and the definition of a time-dependent operator in the Heisenberg representation in the fourth line, and the commutation with $2n-1$ operators generates the "-" in the second last line. The validity of this relation for the last n operators is obtained by their anticommutativity relation, while an analogous calculation is used to obtain the result for the first n arguments. ■

Based on this boundary condition theorem, the imaginary time n-particle Green's function can be continued to an antiperiodic function for all $\tau_i \in \mathbb{R}$. That is, we can define for $\tau_i^0 \in [0, \beta]$ and for $m \in \mathbb{Z}$ a time $\tau_i^m = \tau_i^0 + m\beta$ outside the window $[0, \beta]$ such that

$$G^{2n}(x_1\tau_1, \ldots, x_i\tau_i = \tau_i^0, \ldots, x_{2n}\tau_{2n}) = (-1)^m G^{2n}(x_1\tau_1, \ldots, x_i\tau_i = \tau_i^m, \ldots, x_{2n}\tau_{2n}) \tag{3.20}$$

defines the continuation of the imaginary time Green's function to any $\tau_i \in \mathbb{R}$. However, as this antiperiodically continued imaginary time Green's function is not antiperiodic for all $\tau \in \mathbb{R}$, it cannot be represented by the right hand side of the original Green's function in equation (3.14).

Due to the definition of the Green's function additional symmetries hold, summarised in the following theorem.

Theorem 3.2 (Intrinsic Symmetries of the n-particle Green's Function)
Let $G^{2n}(1, ..., 2n)$ be the n-particle (imaginary or real time) Green's function. Then the following symmetries hold:

1. ***Crossing Symmetry**: The Green's function is antisymmetric in permutations of the first n as well as the last n arguments, i.e.*

$$\begin{aligned} &G^{2n}(1, ..., i, ..., j, ..., n; n+1, ..., 2n) = -G^{2n}(1, ..., j, ..., i, ..., n; n+1, ...2n) \text{ and} \\ &G^{2n}(1, ..., n; n+1, ..., i, ..., j, ..., 2n) = -G^{2n}(1, ..., n; n+1, ..., j, ..., i, ...2n) \end{aligned} \tag{3.21}$$

   for any index pair $i, j \in [0, n]$ or $i, j \in [n+1, 2n]$, respectively.

2. ***Complex Conjugation**: Under complex conjugation the imaginary time Green's function shows the symmetry*

$$\left(G^{2n}\right)^*(x_1\tau_1, \ldots, x_{2n}\tau_{2n}) = G^{2n}(x_{2n}(-\tau_{2n}), \ldots, x_1(-\tau_1)). \tag{3.22}$$

PROOF: 1. Consider the definition of the real or the imaginary time Green's function. If two creation or annihilation operators next to each other change their order in the time-ordered product, their anticommutativity directly leads to a sign change. When other operators are in between them, additional commutations of both operators with these sandwiched ones are necessary. As this always requires two commutations, the resulting factor is one, such that the total sign change is still the result of their commutation with each other.

2. Consider the definition of the imaginary time Green's function with operators in the Heisenberg picture and assume without loss of generality $\tau_1 > \tau_2 > \ldots > \tau_n > \tau_2 n > \ldots > \tau_{n+1}$. Under complex conjugation the time evolution exponents are real valued such that we obtain

$$\begin{aligned}\left(G^{2n}\right)^*(x_1,\tau_1,\ldots,x_{2n}\tau_{2n}) &= \left\langle \hat{\mathcal{T}}\left[e^{\tau_1\hat{K}}\hat{c}_{x_1}e^{-\tau_1\hat{K}}\cdots e^{\tau_{n+1}\hat{K}}\hat{c}^\dagger_{x_{n+1}}e^{-\tau_{n+1}\hat{K}}\right]\right\rangle^* \\ &= \left\langle \hat{\mathcal{T}}\left[e^{-\tau_{n+1}\hat{K}}\hat{c}_{x_{n+1}}e^{\tau_{n+1}\hat{K}}\cdots e^{-\tau_1\hat{K}}\hat{c}^\dagger_{x_1}e^{\tau_1\hat{K}}\right]\right\rangle \\ &= \left\langle \hat{\mathcal{T}}\left[\hat{c}_{x_{n+1}}(-\tau_{n+1})\cdots\hat{c}_{x_{2n}}(-\tau_{2n})\hat{c}^\dagger_{x_n}(-\tau_n)\cdots\hat{c}^\dagger_{x_1}(-\tau_1)\right]\right\rangle \\ &= G^{2n}(x_{2n}(-\tau_{2n}),\ldots,x_1(-\tau_1)),\end{aligned} \tag{3.23}$$

where we used the crossing symmetry to arrange both, the creation and the annihilation operators, in the correct form in the last step. ■

Considering the real time Green's function under complex conjugation, the exponents of the time-evolution operators are complex and thus obtain a sign change under complex conjugation. Therefore, following the proof of the imaginary time Green's function, the time arguments keep their sign under complex conjugation. Although these "symmetries" are no real symmetries in a physical sense, they are very helpful to facilitate calculations. The behaviour of the Green's functions under physical symmetries is investigated in the following subsection.

3.1.2. Behaviour of Green's Functions under Symmetries

We first consider a general symmetry operation of the system in order to simplify the derivation of the behaviour under specific symmetries later on.

Theorem 3.3 (The *n*-particle Green's Function under Symmetries)
Let $\hat{\mathcal{U}}$ represent a similarity transformation which commutes with the modified Hamiltonian $\hat{K} = \hat{H} - \mu\hat{N}$ of the system, i.e. $[\hat{\mathcal{U}}, \hat{K}] = 0$. Then the n-particle Green's functions do not change under the transformation $\hat{\mathcal{U}}$, i.e.

$$\tilde{G}^{(2n)}(1,\ldots,2n) = G^{(2n)}(1,\ldots,2n), \tag{3.24}$$

with $\tilde{G}^{(2n)}$ being the transformed Green's function.

PROOF: This proof corresponds to the one of Rohringer [82]. The creation and the annihilation operators change under the symmetry transformation according to

$$\hat{\tilde{c}}^\dagger_i = \hat{\mathcal{U}}^{-1}\hat{c}^\dagger_i\hat{\mathcal{U}} \qquad \text{and} \qquad \hat{\tilde{c}}_i = \hat{\mathcal{U}}^{-1}\hat{c}_i\hat{\mathcal{U}}, \tag{3.25}$$

so that the transformed n-particle Green's function becomes

$$\tilde{G}^{(2n)}(1,\ldots,2n) := \left\langle \hat{\mathcal{T}} \left[\hat{\tilde{c}}_1(\tau_1) \cdots \hat{\tilde{c}}_n(\tau_n) \hat{\tilde{c}}^\dagger_{2n}(\tau_{2n}) \cdots \hat{\tilde{c}}^\dagger_{n+1}(\tau_{n+1}) \right] \right\rangle . \tag{3.26}$$

For the time evolution of annihilation operators terms of the form

$$\begin{aligned} \hat{\tilde{c}}_i(\tau_i)\hat{\tilde{c}}_j(\tau_j) &= e^{\tau_i \hat{K}}\, \hat{\tilde{c}}_i\, e^{-\tau_i \hat{K}}\, e^{\tau_j \hat{K}}\, \hat{\tilde{c}}_j\, e^{-\tau_j \hat{K}} \\ &= e^{\tau_i \hat{K}}\, \hat{\mathcal{U}}^{-1}\, \hat{c}_i \hat{\mathcal{U}}\, e^{-\tau_i \hat{K}}\, e^{\tau_j \hat{K}}\, \hat{\mathcal{U}}^{-1}\, \hat{c}_j \hat{\mathcal{U}}\, e^{-\tau_j \hat{K}} \\ &= e^{\tau_i \hat{K}}\, \hat{\mathcal{U}}^{-1}\, \hat{c}_i \hat{\mathcal{U}}\, e^{-\tau_i \hat{K}}\, \hat{\mathcal{U}}^{-1} \hat{\mathcal{U}}\, e^{\tau_j \hat{K}}\, \hat{\mathcal{U}}^{-1}\, \hat{c}_j \hat{\mathcal{U}}\, e^{-\tau_j \hat{K}} \\ &= e^{\tau_i \hat{K}}\, \hat{\mathcal{U}}^{-1}\, \hat{c}_i\, e^{-\tau_i \hat{\tilde{K}}}\, e^{\tau_j \hat{\tilde{K}}}\, \hat{c}_j \hat{\mathcal{U}}\, e^{-\tau_j \hat{K}} \end{aligned} \tag{3.27}$$

arise with $\hat{\tilde{K}} = \hat{\mathcal{U}} \hat{K} \hat{\mathcal{U}}^{-1}$. This result is obtained for the creation operators, too, and, due to the cyclicity of the trace, also for the left- and the rightmost terms. In a symbolic notation we thus get

$$G^{(2n)}[\hat{\tilde{c}}^\dagger, \hat{\tilde{c}}, \hat{K}] = G^{(2n)}[\hat{c}^\dagger, \hat{c}, \hat{\tilde{K}}], \tag{3.28}$$

which means that either the operators $\hat{\tilde{c}}$ and $\hat{\tilde{c}}^\dagger$ or the Hamiltonian $\hat{K}$ can be transformed, resulting in the same Green's function. According to the prerequisites $\hat{\mathcal{U}}$ commutates with the Hamiltonian resulting in $\hat{\tilde{K}} = \hat{K}$. Thus the Green's functions in the original and in the transformed system coincide. ■

A physical interpretation of this theorem can be obtained from equation (3.28). The left hand side is the Green's function, in which creation and annihilation operators are transformed under an active transformation $\hat{\mathcal{U}}$ and are expressed in terms of the old reference system. On the right hand side the reference system is transformed, which is achieved by transforming the Hamiltonian with the corresponding passive (or inverse) transformation. Thus, according to the equation, the active and the passive transformation have to coincide.

We apply this general theorem to some specific symmetries of the system. To simplify the notation, we will only write out the necessary dependencies which are subject to the symmetry operation in the following corollary.

Corollary 3.4 (The n-particle Green's Function under Symmetries of the System) *Let $G^{(2n)}(1,\ldots,2n)$ be the n-particle imaginary time Green's function of a system described by the modified Hamiltonian $\hat{K} = \hat{h} - \mu \hat{N}$.*

1. ***Time Translation**: Let $\hat{K}$ be invariant under time translations. Then the Green's function in imaginary time is invariant under translations in time $a \in \mathbb{R}$, i.e.*

$$G^{2n}(\tau_1,\ldots,\tau_{2n}) = G^{2n}(\tau_1 + a,\ldots,\tau_{2n} + a). \tag{3.29}$$

2. ***Spatial Translation**: Let $\hat{K}$ be invariant under a spatial translation $\boldsymbol{r}' \in \mathbb{R}^3$. Then the Green's function is also invariant under this translation, i.e.*

$$G^{2n}(\boldsymbol{r}_1,\ldots,\boldsymbol{r}_{2n}) = G^{2n}(\boldsymbol{r}_1 + \boldsymbol{r}',\ldots,\boldsymbol{r}_{2n} + \boldsymbol{r}'). \tag{3.30}$$

3. ***SU(2) Spin-Symmetry***: *Let $\hat{K}$ be SU(2)-symmetric (spin-symmetric). Then the Green's function conserves the total spin, i.e. the sum of the spins of the creation operators equals the sum of the one of the annihilation operators:*

$$\sum_{i=1}^{n} s_i = \sum_{i=n+1}^{2n} s_i, \tag{3.31}$$

and it is symmetric with respect to a global spin flip, i.e.

$$G^{(2n)}(s_1, \ldots, s_{2n}) = G^{(2n)}(-s_1, \ldots, -s_{2n}). \tag{3.32}$$

4. ***Point Group Symmetry***: *Let $\hat{K}$ be symmetric with respect to a point group Γ, and let $\hat{R} \in \Gamma$ be a symmetry operation of the point group. Then the Green's function is symmetric in the sense of*

$$G^{(2n)}(\hat{R}(\boldsymbol{r}_1), \ldots, \hat{R}(\boldsymbol{r}_{2n})) = G^{(2n)}(\boldsymbol{r}_1, \ldots, \boldsymbol{r}_{2n}). \tag{3.33}$$

5. ***Time and Space Reversal Symmetry***: *Let $\hat{K}$ be a purely real function of the creation and the annihilation operators, then the n-particle Green's function is also purely real.*

6. ***Electron-Hole Symmetry***: *Let $\hat{K}$ be electron-hole symmetric, i.e. $\hat{K}$ does not change under exchanging creation and annihilation operators up to a constant. Then the Green's function is electron-hole symmetric in the sense of*

$$G^{(2n)}(1, \ldots, 2n) = (-1)^n G^{(2n)}(2n, \ldots, 1). \tag{3.34}$$

Proof: 1. **Time Translation Symmetry**:

We define the time translation operator by $\hat{\mathcal{T}}_\tau := e^{-\hat{K}\tau}$, which commutes with the modified Hamiltonian $\hat{K}$, as the latter is time-independent. The creation and the annihilation operators become

$$\begin{aligned} \hat{\tilde{c}}^\dagger_{x_i}(\tau_i) &= e^{\hat{K}\tau}\, \hat{c}^\dagger_{x_i}(\tau_i)\, e^{-\hat{K}\tau} = \hat{c}^\dagger_{x_i}(\tau_i + \tau) \qquad \text{and} \\ \hat{\tilde{c}}'_{x_i}(\tau_i) &= e^{\hat{K}\tau}\, \hat{c}_{x_i}(\tau_i)\, e^{-\hat{K}\tau} = \hat{c}_{x_i}(\tau_i + \tau), \end{aligned} \tag{3.35}$$

which corresponds to a time evolution in the Heisenberg picture with $\tau_i + \tau$. As this holds for all operators, we obtain for the choice of $\tau = a$

$$\tilde{G}^{(2n)}(\tau_1, \ldots, \tau_{2n}) = G^{(2n)}(\tau_1 + a, \ldots, \tau_{2n} + a). \tag{3.36}$$

Due to the commutativity of the time translation operator and $\hat{K}$, we can apply theorem 3.3 to obtain the assertion by

$$G^{(2n)}(\tau_1 + a, \ldots, \tau_{2n} + a) = G^{(2n)}(\tau_1, \ldots, \tau_{2n}). \tag{3.37}$$

A corresponding result for the real time Green's function can be obtained by performing the same lines of the proof.

2. **Space Translation Symmetry**:
   The lattice translation operator $\hat{\mathcal{T}}_{\boldsymbol{r}'}$ is defined via its action on the creation and the annihilation operators

$$\hat{\tilde{c}}^\dagger_{\boldsymbol{r}} = \hat{\mathcal{T}}^{-1}_{\boldsymbol{r}'}\, \hat{c}^\dagger_{\boldsymbol{r}}\, \hat{\mathcal{T}}_{\boldsymbol{r}'} = \hat{c}^\dagger_{\boldsymbol{r}+\boldsymbol{r}'} \qquad \text{and} \qquad \hat{\tilde{c}}_{\boldsymbol{r}} = \hat{\mathcal{T}}^{-1}_{\boldsymbol{r}'}\, \hat{c}_{\boldsymbol{r}}\, \hat{\mathcal{T}}_{\boldsymbol{r}'} = \hat{c}_{\boldsymbol{r}+\boldsymbol{r}'}, \tag{3.38}$$

   which moves their spatial argument by a vector $\boldsymbol{r}'$. As the Hamiltonian itself is invariant under lattice transformations, it commutes with this translation operator. Therefore, the transformed Green's function

$$\begin{aligned}\tilde{G}^{(2n)}(\boldsymbol{r}_1,\dots,\boldsymbol{r}_{2n}) &= \left\langle \hat{\mathcal{T}}\left[\hat{\mathcal{T}}^{-1}_{\boldsymbol{r}'}\, \hat{c}^\dagger_{\boldsymbol{r}_1}\, \hat{\mathcal{T}}_{\boldsymbol{r}'}\, \hat{\mathcal{T}}^{-1}_{\boldsymbol{r}'}\, \hat{c}^\dagger_{\boldsymbol{r}_2}\, \hat{\mathcal{T}}_{\boldsymbol{r}'} \cdots \hat{\mathcal{T}}^{-1}_{\boldsymbol{r}'}\, \hat{c}_{\boldsymbol{r}_{n+1}}\, \hat{\mathcal{T}}_{\boldsymbol{r}'}\right]\right\rangle \\ &= \left\langle \hat{\mathcal{T}}\left[\hat{c}^\dagger_{\boldsymbol{r}_1+\boldsymbol{r}'}\hat{c}^\dagger_{\boldsymbol{r}_2+\boldsymbol{r}'} \cdots \hat{c}_{\boldsymbol{r}_{n+1}+\boldsymbol{r}'}\right]\right\rangle \\ &= G^{(2n)}(\boldsymbol{r}_1+\boldsymbol{r}',\dots,\boldsymbol{r}_{2n}+\boldsymbol{r}')\end{aligned} \tag{3.39}$$

   is equal to the original Green's function $G^{(2n)}(\boldsymbol{r}_1,\dots,\boldsymbol{r}_{2n})$ according to theorem 3.3.

3. **SU(2) Spin Symmetry**:
   The SU(2)-group is generated by the spin operators in three dimensions $\hat{S}_x$, $\hat{S}_y$ and $\hat{S}_z$, which are defined in definition 21.2. By definition, a system is SU(2)-symmetric, if the Hamiltonian commutes with all these generators, i.e.

$$[\hat{H}, \hat{S}_i] = 0 \quad \text{for all } i \in \{x, y, z\}. \tag{3.40}$$

   To show the conservation of the total spin, we consider the spin component in z-direction. As $\hat{S}_z$ is hermitian, the whole Hilbert space can be divided into two orthogonal subsets corresponding to the eigenvalues. Based on the eigenvectors $|S_z, \alpha\rangle$ of this space, which correspond to the eigenvalues of $\hat{S}_z$, the n-particle Green's function can be rewritten as

$$\begin{aligned}&G^{(2n)}_{s_1,\dots,s_{2n}}(1,\dots,2n) \\ &\qquad = \frac{1}{\mathcal{Z}} \sum_{S_z} \sum_{\alpha} \langle S_z, \alpha |\, e^{-\beta \hat{K}}\, e^{\tau_1 \hat{K}}\, \hat{c}^\dagger_{s_1}\, e^{-\tau_1 \hat{K}} \cdots e^{\tau_n \hat{K}}\, \hat{c}^\dagger_{s_n}\, e^{-\tau_n \hat{K}}\, |S_z, \alpha\rangle\,,\end{aligned} \tag{3.41}$$

   with explicitly written traces. The operators of the form $e^{\gamma \hat{K}}$, $\gamma \in \mathbb{C}$ do not change the value of S_z, as $[\hat{S}_z, \hat{K}] = 0$, but they can change the state from α to α'. If we write $s = \frac{1}{2}$ for spin up and $s = -\frac{1}{2}$ for spin down, the commutation relations of $\hat{S}_z$ with the creation and the annihilation operators become

$$[\hat{S}_z, \hat{c}^\dagger_s] = s\, \hat{c}^\dagger_s \qquad \text{and} \qquad [\hat{S}_z, \hat{c}_s] = -s\, \hat{c}_s. \tag{3.42}$$

   From these commutators the effect of the creation and the annihilation operators on basis states $|S_z \alpha\rangle$ directly follows as

$$\hat{c}^\dagger_s\, |S_z, \alpha\rangle = |S_z + s, \alpha'\rangle \qquad \text{and} \qquad \hat{c}_s\, |S_z, \alpha\rangle = |S_z - s, \alpha'\rangle\,. \tag{3.43}$$

Evaluating the expectation value of the Green's function in the $|S_z, \alpha\rangle$-space results in

$$\begin{aligned}\langle S_z, \alpha| e^{-\beta\hat{K}} e^{\tau_1 \hat{K}} \hat{c}^\dagger_{s_1} e^{-\tau_1 \hat{K}} \cdots e^{\tau_n \hat{K}} \hat{c}^\dagger_{s_n} e^{-\tau_n \hat{K}} |S_z, \alpha\rangle \\ = \langle S_z, \alpha | S_z + s_1 + \cdots + s_n - s_{2n} - \cdots - s_{n+1}, \alpha' \rangle \\ = c_{S_z,\alpha\alpha'} \delta_{s_1+\cdots+s_n-s_{2n}-\cdots-s_{n+1},0},\end{aligned} \tag{3.44}$$

where $c_{S_z,\alpha\alpha'}$ is a constant depending on S_z, α and α'. The δ-expression resulting from this evaluation implies $s_1 + \ldots + s_n = s_{2n} + \ldots - s_{n+1}$ and thus the conservation of the total spin. From this we deduce the spin product

$$\prod_{i=1}^{2n} (2s) = +1. \tag{3.45}$$

Next, we consider a general rotation of a spin-state by an angle ϕ. We define the spin rotation operator by

$$\hat{\mathcal{D}}(\boldsymbol{n}, \phi) = e^{-i\phi \boldsymbol{n} \cdot \hat{\boldsymbol{S}}}, \tag{3.46}$$

where $\boldsymbol{n}$ is a unit vector in three dimensions and $\phi \in [0, 2\pi)$. To simplify the derivation we introduce Pauli spinors

$$\hat{\boldsymbol{c}} = \begin{pmatrix} \hat{c}_\uparrow \\ \hat{c}_\downarrow \end{pmatrix} \qquad \text{and} \qquad \hat{\boldsymbol{c}}^\dagger = \begin{pmatrix} \hat{c}^\dagger_\uparrow \\ \hat{c}^\dagger_\downarrow \end{pmatrix} \tag{3.47}$$

which contain both spin components. The transformation according to the general treatment results in

$$\hat{\tilde{\boldsymbol{c}}}^\dagger(\boldsymbol{n}, \phi) = e^{i\phi \boldsymbol{n} \cdot \hat{\boldsymbol{S}}} \hat{\boldsymbol{c}}^\dagger e^{-i\phi \boldsymbol{n} \cdot \hat{\boldsymbol{S}}} \qquad \text{and} \qquad \hat{\tilde{\boldsymbol{c}}}(\boldsymbol{n}, \phi) = e^{i\phi \boldsymbol{n} \cdot \hat{\boldsymbol{S}}} \hat{\boldsymbol{c}} e^{-i\phi \boldsymbol{n} \cdot \hat{\boldsymbol{S}}}. \tag{3.48}$$

To simplify these operators, we take their derivatives with respect to ϕ, use the commutator of $\hat{S}_i$ and $c^{(\dagger)}$ and obtain the differential equation

$$\begin{aligned}\frac{d}{d\phi} \hat{\tilde{\boldsymbol{c}}}^{(\dagger)}(\boldsymbol{n}, \phi) &= i e^{i\phi \boldsymbol{n} \hat{\boldsymbol{S}}} [\boldsymbol{n} \cdot \hat{\boldsymbol{S}}, \hat{\boldsymbol{c}}^{(\dagger)}] e^{-i\phi \boldsymbol{n} \cdot \hat{\boldsymbol{S}}} \\ &= \pm \frac{1}{2} i \boldsymbol{n} \cdot \boldsymbol{\sigma}^{(T)} \hat{\boldsymbol{c}}'^{(\dagger)}(\boldsymbol{n}, \phi)\end{aligned} \tag{3.49}$$

with the initial value $\hat{\tilde{\boldsymbol{c}}}^{(\dagger)}(\boldsymbol{n}, 0) = \hat{\boldsymbol{c}}^{(\dagger)}$. The solution of this initial value problem is

$$\hat{\tilde{\boldsymbol{c}}}^{(\dagger)}(\boldsymbol{n}, \phi) = e^{\pm i \frac{\phi}{2} \boldsymbol{n} \boldsymbol{\sigma}^{(T)}} \hat{\boldsymbol{c}}^{(\dagger)} = \left[\cos\left(\frac{\phi}{2}\right) 1 \pm \sin\left(\frac{\phi}{2}\right) \boldsymbol{n} \cdot \boldsymbol{\sigma}^{(T)} \right] \hat{\boldsymbol{c}}^{(\dagger)} \tag{3.50}$$

and can now be used in the Green's function. As the Hamiltonian commutes with the spin rotation operator $\hat{\mathcal{D}}$, theorem 3.3 implies

$$\tilde{G}^{(2n)}(s_1, \ldots, s_{2n}) = \left\langle \hat{\mathcal{T}} \left[\hat{\tilde{c}}^\dagger_{s_1} \hat{\tilde{c}}^\dagger_{s_2} \ldots \hat{\tilde{c}}_{s_{n+1}} \right] \right\rangle = G^{(2n)}(s_1, \ldots, s_{2n}), \tag{3.51}$$

which is a general relation for any combination of $\boldsymbol{n}$ and ϕ. A spin-flip process is obtained by a rotation of $\phi = \pi$ around the y-axis, $\boldsymbol{n} = (0, 1, 0)^T$, such that

$$\begin{pmatrix} \hat{\tilde{c}}_{\uparrow}^{(\dagger)} \\ \hat{\tilde{c}}_{\downarrow}^{(\dagger)} \end{pmatrix} = \begin{pmatrix} 0 & -1 \\ 1 & 0 \end{pmatrix} \begin{pmatrix} \hat{c}_{\uparrow}^{(\dagger)} \\ \hat{c}_{\downarrow}^{(\dagger)} \end{pmatrix}, \tag{3.52}$$

resulting in $\hat{\tilde{c}}_{\uparrow}^{(\dagger)} = -\hat{c}_{\downarrow}^{(\dagger)}$ and $\hat{\tilde{c}}_{\downarrow}^{(\dagger)} = \hat{c}_{\uparrow}^{(\dagger)}$. Inserting this into the Green's function, writing $\uparrow = -\downarrow$ and vice versa results, under consideration of the spin product, in

$$\tilde{G}^{(2n)}(s_1, \ldots, s_{2n}) = G^{(2n)}(-s_1, \ldots, -s_{2n}) \tag{3.53}$$

as a special case of equation (3.51).

4. **Point Group Symmetry**:
   As $\hat{R}$ is a symmetry operation of the point group of the lattice, we define the corresponding symmetry transformation by

$$\hat{\tilde{c}}^{\dagger}(\boldsymbol{r}) = \hat{R}^{-1}\, \hat{c}^{\dagger}(\boldsymbol{r})\, \hat{R} = \hat{c}^{\dagger}(\hat{R}(\boldsymbol{r})) \qquad \text{and} \qquad \hat{\tilde{c}}(\boldsymbol{r}) = \hat{R}^{-1}\, \hat{c}(\boldsymbol{r})\, \hat{R} = \hat{c}(\hat{R}(\boldsymbol{r})). \tag{3.54}$$

   According to the general result of symmetry operations, we directly derive

$$\begin{aligned} \tilde{G}^{(2n)}(\boldsymbol{r}_1, \ldots, \boldsymbol{r}_{2n}) &= \langle \hat{R}^{-1} \hat{c}^{\dagger}(\boldsymbol{r}_1) \hat{R} \ldots \hat{R}^{-1} \hat{c}(\boldsymbol{r}_{n+1}) \hat{R} \rangle \\ &= \langle \hat{c}^{\dagger}(\hat{R}(\boldsymbol{r}_1)) \ldots \hat{c}(\hat{R}(\boldsymbol{r}_{n+1})) \rangle \\ &= G^{(2n)}(\hat{R}(\boldsymbol{r}_1), \ldots, \hat{R}(\boldsymbol{r}_{2n})) \\ &= G^{(2n)}(\boldsymbol{r}_1, \ldots, \boldsymbol{r}_{2n}), \end{aligned} \tag{3.55}$$

   which generates, due to the commutativity of $\hat{K}$ and $\hat{R}$, the requested relation according to theorem 3.3.

5. **Time and Space Reversal Symmetry**:
   As this symmetry is not considered any further in this thesis, we refer the interested reader to the proof in [82].

6. **Electron-Hole Symmetry**:
   As this symmetry is not considered any further in this thesis, we again refer the interested reader to the proof in [82]. ■

The solid state Hamiltonian (3.1) is invariant under translations by a lattice vector and under time translations so that theorem 3.4 describes the behaviour of the Green's function of a solid under those symmetries. When a time argument of the Green's function is chosen as the time translation, like, for instance, $a = -\tau_{2n}$, the Green's function depends on $2n - 1$ time differences. Therefore, a Fourier transformation reduces the dependencies to $2n - 1$ frequency arguments. When the Green's function is defined for lattice sites $\boldsymbol{R}_i$, then a similar treatment for the spatial arguments leads to a dependence on $2n - 1$ lattice vector differences or on $n - 1$ momentum dependencies. We exploit this reduction of arguments by considering the corresponding momentum and frequency Green's functions.

3.1.3. Momentum and Frequency Green's Functions

We perform the transformation of the system to frequency and momentum space in order to exploit the translation symmetries mentioned in theorem 3.4. As the system is periodic on the lattice and in imaginary time, we can evolve it in the corresponding Fourier series as defined by equations (2.15) and (2.8). Contrary we need a Fourier transformation for the position space and the real time arguments of the Green's function according to equations (2.14) and (2.7), as they are non-periodic. In the following definition we focus on the Fourier transformation of the lattice Green's function and imaginary time one, as they will be needed further on. However, the Fourier transformation of the position space and the real time Green's functions can be defined in exact analogies.

Definition 24 (Fourier Transformation of Green's Functions)

- *Let $G^{(2n)}(\boldsymbol{R}_1, \ldots, \boldsymbol{R}_{2n})$ be the n-particle lattice Green's function with lattice vectors $\boldsymbol{R}_i$. Let $\boldsymbol{k}_i$ be in the first Brillouin zone $\mathcal{B}$ for all $i \in \{0, \ldots, 2n\}$, which has size $|\mathcal{B}|$. Then the lattice Fourier transformation is given by the series*

$$G^{(2n)}(\boldsymbol{k}_1, \ldots, \boldsymbol{k}_{2n}) \coloneqq \sum_{\boldsymbol{R}_1} \cdots \sum_{\boldsymbol{R}_{2n}} e^{-i\boldsymbol{k}_1 \cdot \boldsymbol{R}_1} \ \ldots \ e^{-i\boldsymbol{k}_n \cdot \boldsymbol{R}_n} \, e^{i\boldsymbol{k}_{2n} \cdot \boldsymbol{R}_{2n}} \ \ldots e^{i\boldsymbol{k}_{n+1} \cdot \boldsymbol{R}_{n+1}} \, G^{(2n)}(\boldsymbol{R}_1, \ldots, \boldsymbol{R}_{2n}) \quad (3.56)$$

with the Fourier coefficients

$$G^{(2n)}(\boldsymbol{R}_1, \ldots, \boldsymbol{R}_{2n}) = \frac{1}{|\mathcal{B}|^{2n}} \int_{\mathcal{B}} \mathrm{d}\boldsymbol{k}_1 \ \cdots \int_{\mathcal{B}} \mathrm{d}\boldsymbol{k}_{2n} \, G^{(2n)}(\boldsymbol{k}_1, \ldots, \boldsymbol{k}_{2n}) \, e^{i\boldsymbol{k}_1 \cdot \boldsymbol{R}_1} \ \ldots e^{i\boldsymbol{k}_n \cdot \boldsymbol{R}_n} \, e^{-i\boldsymbol{k}_{2n} \cdot \boldsymbol{R}_{2n}} \ \ldots e^{-i\boldsymbol{k}_{n+1} \cdot \boldsymbol{R}_{n+1}}. \quad (3.57)$$

- *Let $G^{(2n)}(\tau_1, \ldots, \tau_{2n})$ be the imaginary time n-particle Green's function, and let $\omega_i \in \left\{ \frac{(2l+1)\pi}{\beta} \middle| \, l \in \mathbb{N} \right\}$ be Matsubara frequencies $\forall \, i \in \{0, \ldots, 2n\}$. Then its Fourier series is given by*

$$G^{(2n)}(\tau_1, \ldots, \tau_{2n}) = \frac{1}{\beta^{2n}} \sum_{\omega_1, \ldots, \omega_{2n}} G^{(2n)}(\omega_1, \ldots, \omega_{2n}) \, e^{-i\omega_1 \tau_1} \ \ldots \ e^{-i\omega_n \tau_n} \, e^{i\omega_{2n} \tau_{2n}} \ \ldots e^{i\omega_{n+1} \tau_{n+1}} \quad (3.58)$$

with the Fourier coefficients

$$G^{(2n)}(\omega_1, \ldots, \omega_{2n}) \coloneqq \int_0^\beta \mathrm{d}\tau_1 \ldots \int_0^\beta \mathrm{d}\tau_{2n} \, e^{i\omega_1 \tau_1} \ \ldots \ e^{i\omega_n \tau_n} \, e^{-i\omega_{2n} \tau_{2n}} \ \ldots \ e^{-i\omega_{n+1} \tau_{n+1}} \, G^{(2n)}(\tau_1, \ldots, \tau_{2n}). \quad (3.59)$$

Corollary 3.5 (Momentum Space Invariance of the Green's Function)
The momentum space Green's function is invariant under a shift by a reciprocal lattice vector $\boldsymbol{K}$, that is

$$G^{2n}(\boldsymbol{k}_1 + \boldsymbol{K}, \ldots, \boldsymbol{k}_{2n} + \boldsymbol{K}) = G^{2n}(\boldsymbol{k}_1, \ldots, \boldsymbol{k}_{2n}). \tag{3.60}$$

PROOF: Based on the defining equation (3.56) the exponentials become, according to the shift, $\exp(i(\boldsymbol{k}_i + K) \cdot R)$. As $\exp(i\boldsymbol{K} \cdot R) = 1$ only the original momentum variables remain, thus yielding the assertion. ■

Theorem 3.6 (Momentum and Energy Conservation)
Let $\hat{K}$ be invariant under translations by lattice vectors $\boldsymbol{R}$ and under imaginary time translations by β. Let further $G^{(2n)}(x_1\tau_1, \ldots, x_{2n}\tau_{2n})$ be the n-particle lattice Green's function. Then the Green's function only depends on $(n-1)$ time and lattice-vector differences, and the Fourier transformation is given by

$$\begin{aligned} G^{(2n)}(k_1\omega_1, \ldots, k_{2n}\omega_{2n}) = {} & |\mathcal{B}|\, \beta\, \tilde{G}^{(2n)}(k_1\omega_1, \ldots, k_{2n-1}\omega_{2n-1}, o_{2n}s_{2n}) \\ & \sum_{\boldsymbol{K}} \delta(\boldsymbol{K} + \boldsymbol{k}_1 + \ldots + \boldsymbol{k}_n, \boldsymbol{k}_{n+1} + \ldots + \boldsymbol{k}_{2n})\, \delta(\omega_1 + \ldots + \omega_n, \omega_{n+1} + \ldots + \omega_{2n}), \end{aligned} \tag{3.61}$$

with the sum being over all reciprocal lattice vectors $\boldsymbol{K}$.

PROOF: Theorem 3.4 allows us to shift all spatial arguments of the Green's function. For the lattice Green's function we therefore move one argument to the origin without loss of generality, we choose $\boldsymbol{R}_{2n}$, and the Fourier transformation of equation (3.56) becomes

$$\begin{aligned} G^{(2n)}(\boldsymbol{k}_1, \ldots, \boldsymbol{k}_{2n}) = {} & \sum_{\boldsymbol{R}_1} \cdots \sum_{\boldsymbol{R}_{2n}} \\ & e^{-i\boldsymbol{k}_1 \cdot \boldsymbol{R}_1} \ \ldots\ e^{-i\boldsymbol{k}_n \cdot \boldsymbol{R}_n}\, e^{i\boldsymbol{k}_{2n} \cdot \boldsymbol{R}_{2n}}\ \ldots e^{i\boldsymbol{k}_{n+1} \cdot \boldsymbol{R}_{n+1}}\, G^{(2n)}(\boldsymbol{R}_1 - \boldsymbol{R}_{2n}, \ldots, \boldsymbol{R}_{2n-1} - \boldsymbol{R}_{2n}, \boldsymbol{0}). \end{aligned} \tag{3.62}$$

As the sums over lattice vectors $\boldsymbol{R}_i$ contain all the possible corresponding vectors, we can simply shift all but $\boldsymbol{R}_{2n}$ by $\boldsymbol{R}_{2n}$ and write $\tilde{\boldsymbol{R}}_i := \boldsymbol{R}_i - \boldsymbol{R}_{2n}$. The Fourier transformation thus becomes

$$\begin{aligned} G^{(2n)}(\boldsymbol{k}_1, \ldots, \boldsymbol{k}_{2n}) = {} & \sum_{\tilde{\boldsymbol{R}}_1} \cdots \sum_{\tilde{\boldsymbol{R}}_{2n-1}} \sum_{\boldsymbol{R}_{2n}} e^{-i\boldsymbol{k}_1 \cdot (\tilde{\boldsymbol{R}}_1 + \boldsymbol{R}_{2n})}\ \ldots\ e^{-i\boldsymbol{k}_n \cdot (\tilde{\boldsymbol{R}}_n + \boldsymbol{R}_{2n})} \\ & e^{i\boldsymbol{k}_{2n} \cdot \boldsymbol{R}_{2n}}\ \ldots e^{i\boldsymbol{k}_{n+1} \cdot (\tilde{\boldsymbol{R}}_{n+1} + \boldsymbol{R}_{2n})}\, G^{(2n)}(\tilde{\boldsymbol{R}}_1, \ldots, \tilde{\boldsymbol{R}}_{2n-1}, \boldsymbol{0}). \end{aligned} \tag{3.63}$$

Reordering all the exponential terms according to the corresponding lattice vectors $\boldsymbol{R}$ results in the term $\sum_{\boldsymbol{R}_{2n}} e^{i(\boldsymbol{k}_1 + \cdots + \boldsymbol{k}_n - \boldsymbol{k}_{2n} - \cdots - \boldsymbol{k}_{n+1}) \cdot \boldsymbol{R}_{2n}}$, which can be evaluated independent of the Green's function and results in $|\mathcal{B}|\delta(\boldsymbol{K} + \boldsymbol{k}_1 + \cdots + \boldsymbol{k}_n - \boldsymbol{k}_{2n} - \cdots - \boldsymbol{k}_{2n+1})$. In this expression the reciprocal lattice vector $\boldsymbol{K}$ is required, as all $\boldsymbol{k}_i$ are in the first Brillouin zone, while this does not necessarily hold for their sum. The Fourier transformation for the remaining $2n-1$ arguments can be performed as before. As the argument $\boldsymbol{R}_{2n} = \boldsymbol{0}$ is constant and not transformed, we leave it out in the Fourier transformed Green's function.

For the temporal Fourier transformation we proceed in analogous steps compared to the spatial case. Therefore, due to the symmetry under a shift of times, all temporal arguments of the Green's function are moved by $a = -\tau_{2n}$ such that the imaginary times Green's function depends on $n-1$ time differences. The time differences are then substituted by $\tilde{\tau}_i = \tau_i - \tau_{2n}$ for all arguments except for τ_{2n}. The transformation of the limits of the integral results in $[-\tau_{2n}, \beta - \tau_{2n}]$ which is outside of $[0, \beta)$. However, due to the antiperiodicity of the Green's function (cf. eq. (3.20)) any integral over an interval of length β, as we have got it here, is equivalent to an integration over $[0, \beta)$ so that we can directly perform the Fourier transformation of the $2n-1$ elements $\tilde{\tau}_i$. The evaluation of the remaining integral $\int_0^\beta \mathrm{d}\tau_{2n}\ e^{i(\omega_1 + \ldots + \omega_n - \omega_{n+1} - \ldots - \omega_{2n})\tau_{2n}}$ in the Fourier transformation then results in $\beta, \delta(\omega_1 + \ldots + \omega_n, \omega_{n+1} + \ldots + \omega_{2n})$, completing the proof. ■

The δ-distributions in theorem 3.6 correspond to the conservation of momenta up to a reciprocal lattice vector $\boldsymbol{K}$ and to the conservation of energy. That is, the combined energy of all created particles has to equal the combined one of all annihilated particles in the corresponding expectation value of the Green's function. The same holds for the momenta up to $\boldsymbol{K}$, as all $\boldsymbol{k}_i$ have to be in the first Brillouin zone, which does not hold for their sum. This theorem allows a significant simplification of calculations, as the number of independent momenta and that of the frequencies is reduced by one. However, the number of independent orbitals or bands and spins is not reduced.

3.1.4. Time Evolution of Green's Functions

As the Green's functions are time dependent, their time evolution is of particular interest and will be used in the derivation of the perturbation theory (see section 3.2). For means of simplicity, we focus on the non-interacting Green's function in position space and write the time evolution theorem in terms of position space and field operators, although it can analogously be derived in other representations.

Theorem 3.7 (Time-Evolution of Free Green's Functions)
Let $G_0^{(2n)}$ be the free imaginary time Green's function in position space so that $i = (\boldsymbol{r}_i, o_i, s_i, \tau_i)$. Then the free one-particle Green's function G_0 satisfies the equation of motion

$$\beta \left(\frac{\partial}{\partial \tau_1} - \frac{\nabla_{\boldsymbol{r}}^2}{2m} + V_{ext}(\boldsymbol{r}) - \mu \right) G_0(1,2) = \delta(1,2). \tag{3.64}$$

For $n \geq 2$ the time evolution of the n-particle Green's function is given by

$$\begin{aligned} &\beta \left(\frac{\partial}{\partial \tau_1} - \frac{\nabla_{\boldsymbol{r}}^2}{2m} + V_{ext}(\boldsymbol{r}) - \mu \right) G_0^{(2n)}(1, \ldots, 2n) \\ &\qquad = \sum_{\ell=n+1}^{2n} (-1)^{\ell-n-1} \delta(1,\ell) G_0^{(2n-2)}(2, \ldots, n, n+1, \ldots, \not{\ell}, \ldots, 2n) \end{aligned} \tag{3.65}$$

with $\not{\ell}$ denoting that the index ℓ is left out.

Proof: This proof is along the lines of the proof of thm. 4.7 in [81]. The free one-particle Green's function in terms of field operators in the interaction picture (2.5) is

$$G_0(1,2) = \theta(\tau_1 - \tau_2) \left\langle \hat{\psi}_{\mathrm{I}}(x_1\tau_1) \hat{\psi}_{\mathrm{I}}^\dagger(x_2\tau_2) \right\rangle_0 - \theta(\tau_2 - \tau_1) \left\langle \hat{\psi}_{\mathrm{I}}^\dagger(x_2\tau_2) \hat{\psi}_{\mathrm{I}}(x_1\tau_1) \right\rangle_0 \tag{3.66}$$

after having evaluated the time-ordering operator. Here the subscript of the brackets accounts for taking the expectation value with respect to the non-interacting Hamiltonian in position space, i.e.

$$\hat{K}_0 = \hat{H}_0 - \mu\hat{N} = \int \mathrm{d}\boldsymbol{r}'\, \hat{\psi}^\dagger(\boldsymbol{r}') \left(-\frac{\nabla^2_{\boldsymbol{r}'}}{2m} + V_{\mathrm{ext}}(\boldsymbol{r}') - \mu \right) \hat{\psi}(\boldsymbol{r}'). \tag{3.67}$$

The τ_1-derivative of G_0 results in

$$\begin{aligned} \partial_{\tau_1} G_0(x_1\tau_1, 2\tau_2) = {} & \delta(\tau_1 - \tau_2) \left\langle \hat{\psi}_{\mathrm{I}}(x_1\tau_1)\hat{\psi}^\dagger_{\mathrm{I}}(x_2\tau_2) \right\rangle_0 + \theta(\tau_1 - \tau_2) \left\langle \partial_{\tau_1}\hat{\psi}_{\mathrm{I}}(x_1\tau_1)\hat{\psi}^\dagger_{\mathrm{I}}(x_2\tau_2) \right\rangle_0 \\ & + \delta(\tau_2 - \tau_1) \left\langle \hat{\psi}^\dagger_{\mathrm{I}}(x_2\tau_2)\hat{\psi}_{\mathrm{I}}(x_1\tau_1) \right\rangle_0 - \theta(\tau_2 - \tau_1) \left\langle \hat{\psi}^\dagger_{\mathrm{I}}(x_2\tau_2)\partial_{\tau_1}\hat{\psi}_{\mathrm{I}}(x_1\tau_1) \right\rangle_0, \end{aligned} \tag{3.68}$$

where we used the distributional identity $\partial_{\tau_1}\theta(\tau_1 - \tau_2) = \delta(\tau_1 - \tau_2)$. Due to the anticommutation rules for creation and annihilation field operators (cf. eq. (2.1)) the terms with δ functions can be combined, and their evaluation results in $\delta(\boldsymbol{r}_1 - \boldsymbol{r}_2)\delta_{o_1,o_2}\delta_{s_1,s_2} =: \delta(x_1, x_2)$. Both remaining terms can be combined using the time-ordering operator again, resulting in

$$\partial_\tau G(1\tau_1, 2\tau_2) = \delta(x_1, x_2)\delta(\tau_1 - \tau_2) + \left\langle \hat{\mathcal{T}}[\partial_{\tau_1}\hat{\psi}_{\mathrm{I}}(x_1\tau_1)\hat{\psi}^\dagger_{\mathrm{I}}(x_2\tau_2)] \right\rangle_0. \tag{3.69}$$

Hence, the remaining problem of this first part of the proof is to obtain the evolution equation for the creation operator. Due to the interaction picture (cf. eq. (2.5)) the time-derivative results in

$$\partial_{\tau_1}\hat{\psi}_{\mathrm{I}}(x_1\tau_1) = -e^{\hat{K}_0\tau_1}[\hat{\psi}_{\mathrm{I}}(x_1), \hat{K}_0]e^{-\hat{K}_0\tau_1}. \tag{3.70}$$

As the non-interacting part of $\hat{K}_0$ consists of terms of the form $\hat{\psi}(x_i)\hat{\psi}^\dagger(x_i)$, the commutator becomes

$$[\hat{\psi}_{\mathrm{I}}(x_1), \hat{\psi}^\dagger_{\mathrm{I}}(x_2)\hat{\psi}_{\mathrm{I}}(x_2)] = [\hat{\psi}_{\mathrm{I}}(x_1), \hat{\psi}^\dagger_{\mathrm{I}}(x_2)]\hat{\psi}_{\mathrm{I}}(x_2) = \delta(x_1, x_2)\hat{\psi}_{\mathrm{I}}(x_2) = \delta(x_1, x_2)\hat{\psi}_{\mathrm{I}}(x_1), \tag{3.71}$$

which leads to the following equation of motion

$$\partial_{\tau_1}\hat{\psi}_{\mathrm{I}}(x_1\tau_1) = \left(\frac{\nabla^2_{\boldsymbol{r}_1}}{2m} - V_{\mathrm{ext}}(\boldsymbol{r}_1) + \mu \right) \hat{\psi}_{\mathrm{I}}(x_1\tau_1) \tag{3.72}$$

for the field operator $\hat{\psi}_{\mathrm{I}}$. The insertion into equation (3.69) leads to the assertion in equation (3.64).

For the general case of a non-interacting n-particle Green's function in the interaction picture

$$\begin{aligned} G_0^{(2n)}(1, \ldots, 2n) &= \left\langle \hat{\mathcal{T}} \left[\hat{\psi}_{\mathrm{I}}(x_1\tau_1) \cdots \hat{\psi}_{\mathrm{I}}(x_n\tau_n)\hat{\psi}^\dagger_{\mathrm{I}}(x_{2n}\tau_{2n}) \cdots \hat{\psi}^\dagger_{\mathrm{I}}(x_{n+1}\tau_{n+1}) \right] \right\rangle_0 \\ &= (-1)^{\frac{n(n-1)}{2}} \left\langle \hat{\mathcal{T}} \left[\hat{\psi}_{\mathrm{I}}(x_1\tau_1) \cdots \hat{\psi}_{\mathrm{I}}(x_n\tau_n)\hat{\psi}^\dagger_{\mathrm{I}}(x_{n+1}\tau_{n+1}) \cdots \hat{\psi}^\dagger_{\mathrm{I}}(x_{2n}\tau_{2n}) \right] \right\rangle_0 \end{aligned} \tag{3.73}$$

the arguments are reordered according to their index numbering. Like in the one-particle Green's function, the evaluation of the time-ordering operator is crucial for the equation of motion, as it leads to Heaviside functions. This becomes challenging, as all combinations of times are principally possible.

Based on the symmetry group S_m, the n-particle Green's function can, according to definition 1, be rewritten as

$$\begin{aligned} G_0^{(2n)}(1, \ldots, 2n) = (-1)^{\frac{n(n-1)}{2}} & \sum_{\pi \in S_{2n}} \\ & \mathrm{sgn}(\pi)\theta_\tau(\pi_1 - \pi_2) \cdots \theta_\tau(\pi_{2n-1} - \pi_{2n}) \left\langle \hat{\psi}^{(\dagger)}_{\mathrm{I}}(\pi_1) \ldots \hat{\psi}^{(\dagger)}_{\mathrm{I}}(\pi_{2n}) \right\rangle_0 \end{aligned} \tag{3.74}$$

with the abbreviation $\pi_i := \pi(i)$. Here, the time argument is included in the argument i and the notation

$$\hat{\psi}_{\mathrm{I}}^{(\dagger)}(i) = \begin{cases} \hat{\psi}_{\mathrm{I}}(i) & \text{for } 1 \leq i \leq n \\ \hat{\psi}_{\mathrm{I}}^{\dagger}(i) & \text{for } n+1 \leq i \leq 2n \end{cases} \tag{3.75}$$

simplifies the general expression for all possible time orderings. As the derivative only acts on τ_1 we fix this argument and write out all the corresponding terms, i.e. those, in which $\pi_i = 1$. All the other arguments τ_i with $i \neq 1$ can still be permuted in any possible way, such that the remaining part is rewritten as a sum over all permutations σ of the reduced set S_{2n-1}:

$$\begin{aligned} G_0^{(2n)}(1,\ldots,2n) = (-1)^{\frac{n(n-1)}{2}} \sum_{\sigma \in S_{2n-1}} \operatorname{sgn}(\sigma) \\ \Big(& \theta_\tau(1-\sigma_2)\theta_\tau(\sigma_2-\sigma_3)\cdots\theta_\tau(\sigma_{2n-1}-\sigma_{2n}) \left\langle \hat{\psi}_{\mathrm{I}}(1)\hat{\psi}_{\mathrm{I}}^{(\dagger)}(\sigma_2)\cdots\hat{\psi}_{\mathrm{I}}^{(\dagger)}(\sigma_{2n}) \right\rangle_0 \\ & - \theta_\tau(\sigma_2-1)\theta_\tau(\sigma_2-\sigma_3)\cdots\theta_\tau(\sigma_{2n-1}-\sigma_{2n}) \left\langle \hat{\psi}_{\mathrm{I}}^{(\dagger)}(\sigma_2)\hat{\psi}_{\mathrm{I}}(1)\cdots\hat{\psi}_{\mathrm{I}}^{(\dagger)}(\sigma_{2n}) \right\rangle_0 \\ & + \cdots \\ & + \theta_\tau(\sigma_2-\sigma_3)\cdots\theta_\tau(\sigma_{2n-1}-1)\theta_\tau(1-\sigma_{2n}) \left\langle \hat{\psi}_{\mathrm{I}}^{(\dagger)}(\sigma_2)\cdots\hat{\psi}_{\mathrm{I}}(1)\hat{\psi}_{\mathrm{I}}^{(\dagger)}(\sigma_{2n}) \right\rangle_0 \\ & - \theta_\tau(\sigma_2-\sigma_3)\cdots\theta_\tau(\sigma_{2n-1}-\sigma_{2n})\theta_\tau(\sigma_{2n}-1) \left\langle \hat{\psi}_{\mathrm{I}}^{(\dagger)}(\sigma_2)\hat{\psi}_{\mathrm{I}}(1)\cdots\hat{\psi}_{\mathrm{I}}^{(\dagger)}(\sigma_{2n})\hat{\psi}_{\mathrm{I}}(1) \right\rangle_0 \Big). \end{aligned} \tag{3.76}$$

The τ_1-derivative acting on this equation results in δ-distributions due to the Heaviside functions and in time-derivatives of the field operator $\hat{\psi}(1)$ like in the case of the one-particle Green's function. The time-derivative of the operator is obtained by combining equation (3.72) with the time-ordering operator and results in

$$(-1)^{\frac{n(n-1)}{2}} \left\langle \hat{\mathcal{T}} \left[\partial_{\tau_1} \hat{\psi}_{\mathrm{I}}(1)\cdots\hat{\psi}_{\mathrm{I}}(n)\hat{\psi}_{\mathrm{I}}^{\dagger}(n+1)\cdots\hat{\psi}_{\mathrm{I}}^{\dagger}(2n) \right] \right\rangle_0 \tag{3.77}$$

$$= \left(\frac{\nabla_{\boldsymbol{r}_1}^2}{2m} - V_{\mathrm{ext}}(\boldsymbol{r}_1) + \mu \right) G_0^{(2n)}(1,\ldots,2n). \tag{3.78}$$

In order to evaluate the action of the τ_1-derivative on the Heaviside functions, we start by considering only the first two summands in equation (3.76). The resulting δ-distributions can be combined as follows

$$\delta_\tau(1-\sigma_2)\cdots\left\langle \hat{\psi}_{\mathrm{I}}(1)\hat{\psi}_{\mathrm{I}}^{(\dagger)}(\sigma_2)\cdots \right\rangle + \delta_\tau(\sigma_2-1)\cdots\left\langle \hat{\psi}_{\mathrm{I}}(2)\hat{\psi}_{\mathrm{I}}^{(\dagger)}(\sigma_1)\cdots \right\rangle_0 \tag{3.79}$$

$$= \delta_\tau(1-\sigma_2)\cdots\left\langle \left\{ \hat{\psi}_{\mathrm{I}}(1), \hat{\psi}_{\mathrm{I}}^{(\dagger)}(\sigma_2) \right\}\cdots \right\rangle_0. \tag{3.80}$$

According to theorem 2.1 the anticommutator is zero for $\sigma_2 \leq n$ and $\delta_x(1-\sigma_2)$ for $n+1 \leq \sigma_2 \leq 2n$, so that the temporal and the quantum number δ-distributions can be combined. For these first two terms the sum over all permutations $\sigma \in S_{2n-1}$ can, therefore, be restricted by enforcing $\ell := \sigma(2) \in \{n+1,\ldots,2n\}$ which leads to

$$\sum_{\ell+1}^{2n} \delta(1,\ell) \sum_{\substack{\sigma \in S_{2n-1} \\ \sigma_2 = \ell}} \operatorname{sgn}(\sigma)\theta_\tau(1-\sigma_3)\cdots\theta_\tau(\sigma_{2n-1}-\sigma_{2n}) \left\langle \hat{\psi}_{\mathrm{I}}^{(\dagger)}(\sigma_3)\cdots\hat{\psi}_{\mathrm{I}}^{(\dagger)}(\sigma_{2n}) \right\rangle_0. \tag{3.81}$$

In order to obtain a form which can be identified as a Green's function, this expression has to be reformulated as a sum over all permutations of the reduced set

$$\{2,3,\ldots,n,\ldots,\not{\ell},\ldots,2n\} := \{2,3,\ldots,n,\ldots,\ell-1,\ell+1,\ldots,2n\} \tag{3.82}$$

instead of the constraint $\sigma(2)=\ell$. Each permutation $\sigma \in S_{2n-1}$ is, therefore, decomposed into

$$\sigma = \sigma' \circ \sigma^{\ell}, \tag{3.83}$$

where $\sigma' \in S_{n-2}$ and σ^{ℓ} is a cyclic permutation of all variables up to ℓ, making ℓ the first one, while all arguments behind ℓ are left unchanged, i.e.

$$(\sigma^{\ell}(2),\ldots,\sigma^{\ell}(2n)) = (\ell,2,\ldots,\not{\ell},\ldots,2n). \tag{3.84}$$

Due to the decomposition order the total permutation can be rewritten as

$$(\sigma'_l,\sigma'_2,\ldots,\sigma'_{l-1},\sigma'_{l+1},\ldots,\sigma'_{2n}) = (\sigma_2,\ldots,\sigma_{2n}) \tag{3.85}$$

with $\sigma' \in S_{2n-1}$. We note that the sign function then becomes

$$\operatorname{sgn}(\sigma) = \operatorname{sgn}(\sigma')\operatorname{sgn}(\sigma_l) = \operatorname{sgn}(\sigma')\,(-1)^{\ell} \tag{3.86}$$

so that the sum over all permutations in equation (3.81) can be rewritten as one over $\sigma' \in S_{2n-1}$ with the constraint $\sigma'(\ell)=\ell$. As ℓ is unchanged under this constraint, only $2n-2$ elements are permuted so that the sum can be replaced by a sum over all permutations $\pi \in S_{2n-2}$ of the reduced set given in equation (3.82). Equation (3.81) now results in

$$\sum_{\ell+1}^{2n}\delta(1,\ell)(-1)^{\ell}\sum_{\pi\in S_{2n-2}}\operatorname{sgn}(\pi)\theta_\tau(1-\pi_2)\cdots\theta_\tau(\pi_{l-1}-\pi_{l+1})\cdots\theta_\tau(\pi_{2n-1}-\pi_{2n}) \left\langle\hat{\psi}_{\mathrm{I}}^{(\dagger)}(\pi_2)\cdots\hat{\psi}_{\mathrm{I}}^{(\dagger)}(\pi_{l-1})\hat{\psi}_{\mathrm{I}}^{(\dagger)}(\pi_{l+1})\cdots\hat{\psi}_{\mathrm{I}}^{(\dagger)}(\pi_{2n})\right\rangle_0, \tag{3.87}$$

which is the result of the τ_1-derivative on the Heaviside functions for the first two summands in equation (3.76). All other terms can be treated analogously, resulting in

$$\begin{aligned}\beta\left(\frac{\partial}{\partial\tau_1}-\frac{\nabla^2_{\boldsymbol{x}_1}}{2m}\nabla^2_{\boldsymbol{x}_1}+V_{\mathrm{ext}}(\boldsymbol{x}_1)-\mu\right)G_0^{(2n)}(1,\ldots,2n) &= (-1)^{\frac{n(n-1)}{2}}\sum_{\ell=n+1}^{2n}\delta(1,\ell)(-1)^{\ell}\\ &\sum_{\pi\in S_{2n-2}}\operatorname{sgn}(\pi)\,(\theta_\tau(1-\pi_2)\cdots\theta_\tau(\pi_{l-1}-\pi_{l+1})\cdots\theta_\tau(\pi_{2n-1}-\pi_{2n})\\ &+\theta_\tau(\pi_2-1)\theta_\tau(1-\pi_3)\cdots\theta_\tau(\pi_{l-1}-\pi_{l+1})\cdots\theta_\tau(\pi_{2n-1}-\pi_{2n})\\ &+\cdots+\theta_\tau(\pi_2-\pi_3)\cdots\theta_\tau(\pi_{l-1}-\pi_{l+1})\cdots\theta_\tau(\pi_{2n}-1))\\ &\langle\hat{\psi}_{\mathrm{I}}^{(\dagger)}(\pi_2)\cdots\hat{\psi}_{\mathrm{I}}^{(\dagger)}(\pi_{l-1})\hat{\psi}_{\mathrm{I}}^{(\dagger)}(\pi_{l+1})\cdots\hat{\psi}_{\mathrm{I}}^{(\dagger)}(\pi_{2n})\rangle_0,\end{aligned} \tag{3.88}$$

where the index 1 appears at all possible positions in the product of Heaviside functions. Therefore, the explicitly written sum of products of Heaviside functions (second to fourth line) can be rewritten as

$$\theta_\tau(\pi_2-\pi_3)\cdots\theta_\tau(\pi_{\ell-1}-\pi_{\ell+1})\cdots\theta_\tau(\pi_{2n-1}-\pi_{2n}), \tag{3.89}$$

which matches the Heaviside function product of a $(n-1)$-particle Green's function. Indeed, after reordering the field operators, which results in an additional factor $(-1)^{\frac{(n-1)(n-2)}{2}}$, the expression matches the definition of such an $(n-1)$-particle Green's function

$$\begin{aligned}\sum_{\pi\in S_{2n-2}} \operatorname{sgn}(\pi)\theta_\tau(\pi_2-\pi_3)\cdots\theta_\tau(\pi_{\ell-1}-\pi_{\ell+1})\cdots\theta_\tau(\pi_{2n-1}-\pi_{2n}) \\ \left\langle \hat{\psi}_{\mathrm{I}}^{(\dagger)}(\pi_2)\cdots\hat{\psi}_{\mathrm{I}}^{(\dagger)}(\pi_{\ell-1})\hat{\psi}_{\mathrm{I}}^{(\dagger)}(\pi_{\ell+1})\cdots\hat{\psi}_{\mathrm{I}}^{(\dagger)}(\pi_{2n})\right\rangle_0 \\ = (-1)^{\frac{(n-1)(n-2)}{2}} G_0^{(2n-2)}(2,\ldots,n,n+1,\ldots,\not{\ell},\ldots,2n).\end{aligned} \tag{3.90}$$

Substituting the corresponding part in equation (3.88) finally yields the assertion. ■

By equation (3.65), the time evolution of the free n-particle Green's function can directly be related to the non-interacting $(n-1)$-particle Green's function. The resulting hierarchy of Green's functions can, in principle, be solved when the free one-particle Green's function is known. However, as correlation effects are relevant for HTS, the time evolution of the interacting Green's function is of more interest. Let us consider a system with an interaction of the type $\hat{V} = V_{ijkl}\hat{c}_i^\dagger\hat{c}_j^\dagger\hat{c}_l\hat{c}_k$. Then the commutator $[\hat{c},\hat{V}]$, appearing in the time-derivative of the operators in equation (3.70), generates an expression with one annihilation and two creation operators. This increases the number of operators in the expectation value by two, so that each n-particle Green's function additionally depends on the $(n+1)$-particle Green's function. This unbounded hierarchical problem requires intelligent approaches like the perturbation theory (see section 3.2) to obtain results for interacting systems. A different approach is the FRG, which takes a different path, but also starts with the non-interacting Green's function (see section 3.5). Before we proceed in these directions, we note some observations based on theorem 3.7.

According to equation (3.64), G is, indeed, a Green's function in the mathematical sense. Thus, we define the inverse Green's function as follows.

Definition 25 (Inverse one-particle Green's Function)
Let G be given as in theorem 3.7. Then the integral kernel Q defined by

$$\int \mathrm{d}x' \, \frac{1}{\beta}\int_0^\beta \mathrm{d}\tau' \; Q(x,\tau;x',\tau')G(x',\tau') := \beta\left(\frac{\partial}{\partial\tau} - \frac{\nabla_{\boldsymbol{r}}^2}{2m} + V_{ext}(x) - \mu\right)G(x,\tau) \tag{3.91}$$

*is called the **inverse one-particle Green's function** and we define $G_0^1(1,2) := Q(1,2)$.*

Based on this definition, we can reformulate the equation of motion in a dense way.

Corollary 3.8 (Reformulation of the Equation of Motion)
Let G_0^{-1} be the integral kernel as defined in equation (3.91). Then the equation of motion of the one-particle Green's function can equivalently be written as

$$\int \mathrm{d}3 \, G_0^1(1,3)\, G_0(3,2) = \delta(1,2), \tag{3.92}$$

and the time evolution of the n-particle Green's function for $n \geq 2$ can equivalently be written as

$$\int \mathrm{d}1' \, G_0^1(1,1') \, G_0^{(2n)}(1',\ldots,2n) = \sum_{\ell+1}^{2n} (-1)^{\ell-n-1} \delta(1,\ell) \, G_0^{(2n-2)}(2,\ldots,n,n+1,\ldots,\not{\ell},\ldots,2n). \quad (3.93)$$

Proof: These reformulations directly follow from the definition of the integral kernel (cf. def. 25) in combination with theorem 3.7. ■

Although the results in theorem 3.7 were explicitly derived for a specific choice of time arguments and in the position space representation, they can be transferred to the other Green's functions we are dealing with, as we point out in the following remark.

Remark 3.9

1. *Similar time evolution equations can be derived for the other temporal arguments of the Green's function, in which the time-derivative changes signs for the last n arguments.*
2. *Although these equations were explicitly derived for field operators, they also hold in the general occupation number representation. Then the differential part has to be transformed to the corresponding basis, so that transformation terms appear in a form like, for instance, $\langle\alpha|\,\hat{T}\,|\alpha'\rangle$ for the kinetic energy.*
3. *According to definition 25 and item 2 we will, most of the time, work with the inverse Green's function instead of the explicit spatial differential operators, to account for all cases independent of the specific choice of basis.*
4. *A similar derivation for the real time Green's function leads to corresponding results.*

Based on these observations we are in a position to find an explicit analytical expression for the one-particle Green's function.

Theorem 3.10 (Non-Interacting Single-Particle Green's Functions)
Let ε_i be the one-particle energies of the non-interacting time-invariant Hamiltonian $\hat{K}_0$ such that $\sum_i^n \varepsilon_i = E_n$, $n \in \mathbb{N}_0$, are the energy eigenvalues of the n-particle system. Then the free single-particle Green's function for Matsubara frequencies ω_n is represented in the eigenbasis of $\hat{K}_0$ by

$$G_0(x_1,x_2;\omega_n) = \frac{\delta_{1,2}}{i\omega_n - \varepsilon_1}, \quad (3.94)$$

and its real frequency Green's function is represented in the eigenbasis of $\hat{K}_0$ by

$$G_0(x_1,x_2;\omega) = \frac{\delta_{1,2}}{\omega - \varepsilon_2 + i\eta} + \frac{\delta_{1,2}}{\omega - \varepsilon_2 - i\eta}. \quad (3.95)$$

PROOF: As the Hamiltonian $\hat{K}_0$ is time-invariant, the imaginary time Green's function only depends on the time difference $\tau_1 - \tau_2$ (cf. thm. 3.4.1 and thm. 3.6). As $\tau_1, \tau_2 \in [0, \beta]$ the new relative time is within the interval $[-\beta, \beta]$. As the imaginary time Green's function is antiperiodic according to theorem 3.1 we can write $G(x_1, x_2; \tau_1 - \beta) = -G(x_1, x_2; \tau_1)$ so that the temporal Fourier transformation becomes

$$\begin{aligned} G_0(x_1, x_2; \omega_n) &= \frac{1}{2} \int_{-\beta}^{\beta} \mathrm{d}\tau \, G_0(x_1, x_2; \tau) \, e^{i\omega_n \tau} \\ &= \frac{1}{2} \int_{0}^{\beta} \mathrm{d}\tau \, G_0(x_1, x_2; \tau) \, e^{i\omega_n \tau} + \frac{1}{2} \int_{0}^{\beta} \mathrm{d}\tau \, G_0(x_1, x_2; \tau - \beta) \, e^{i\omega_n (\tau - \beta)} \\ &= \frac{1}{2} \int_{0}^{\beta} \mathrm{d}\tau \, G_0(x_1, x_2; \tau) \, e^{i\omega_n \tau} - \frac{1}{2} \int_{0}^{\beta} \mathrm{d}\tau \, G_0(x_1, x_2; \tau) \, (-1) e^{i\omega_n \tau} \\ &= \int_{0}^{\beta} \mathrm{d}\tau \, G_0(x_1, x_2; \tau) \, e^{i\omega_n \tau}. \end{aligned} \tag{3.96}$$

Thus, the time argument of the Green's function is restricted to $\tau \in [0, \beta]$, which is equal to setting $\tau_2 = 0$. The time ordered Green's function in the basis ϕ_i is given as

$$\begin{aligned} G_0(x_1, x_2; \tau_1 = \tau, \tau_2 = 0) &= -\left\langle \hat{\mathcal{T}} \left[\hat{c}_1(\tau) \hat{c}_2^\dagger(0) \right] \right\rangle \\ &= -\frac{1}{\mathcal{Z}} \sum_i \langle \phi_i | \, e^{-\beta \hat{K}_0} e^{\hat{K}_0 \tau} \hat{c}_{x_1} e^{-\hat{K}_0 \tau} \hat{c}_{x_2}^\dagger \, | \phi_i \rangle \, . \end{aligned} \tag{3.97}$$

As we consider the eigenbasis of the Hamiltonian $\hat{K}_0$ for which the creation and the annihilation operators raise or lower the occupation number of the state they act on, the action of $\hat{K}_0$ on the state $\hat{c}_2^\dagger |\psi_i\rangle$ results in $E_i + \varepsilon_2$, because the creation operator adds a particle with energy ε_2 to the system. As only terms with equal initial and final states are contributing, the operator $\hat{c}$ has to delete a particle in the state in which $\hat{c}_2^\dagger$ has created one. Hence we obtain

$$\begin{aligned} G_0(x_1, x_2; \tau_1 = \tau, \tau_2 = 0) &= -\frac{1}{\mathcal{Z}} \sum_i e^{-\beta E_i} e^{(E_i - E_i - \varepsilon_2)\tau} \, \langle \psi_i | \, \hat{c}_{x_1} \hat{c}_{x_2}^\dagger \, | \psi_i \rangle \\ &= -\frac{1}{\mathcal{Z}} \sum_i e^{-\beta E_i} e^{-\varepsilon_2 \tau} \, \langle \psi_i | \, 1 - \hat{n} \, | \psi_i \rangle \, \delta_{1,2} \\ &= -e^{-\varepsilon_2 \tau} (1 - n_F(\varepsilon_2)) \delta_{1,2}, \end{aligned} \tag{3.98}$$

by an application of the anticommutation relation (thm. 2.1) and the number operator. Using this Green's function in the Fourier transformation (3.96), we finally obtain the desired result in

$$\begin{aligned} G_0(x_1, x_2; \omega_n) &= -\int_0^{\beta} \mathrm{d}\tau \, e^{(i\omega_n - \varepsilon_2)\tau} (1 - n_F(\varepsilon_2)) \delta_{1,2} \\ &= -\frac{\delta_{1,2}}{i\omega_n - \varepsilon_2} \underbrace{(1 - n_F(\varepsilon_2)) \left(e^{(i\omega_n - \varepsilon_2)\beta} - 1 \right)}_{=-1} \quad = \frac{\delta_{1,2}}{i\omega_n - \varepsilon_2}. \end{aligned} \tag{3.99}$$

The real time Green's function does not exhibit a periodicity so that the time-integral spans over the whole real axis. Thus both time orderings have to be treated separately. As the Hamiltonian is time-independent, the discussion of equation 3.98 can be done analogously for both terms, resulting in

$$G_0(x_1 t_1 = t, x_2 t_2 = 0) = i \, \theta(t) \, e^{-i\varepsilon_2(t)} \, (1 - n_F(\varepsilon_2)) \, \delta_{1,2} - i \, \theta(-t) \, e^{-i\varepsilon_2 t} \, n_F(\varepsilon_2) \, \delta_{1,2}. \tag{3.100}$$

As $t \in \mathbb{R}$ the terms with the Fermi-function for t in the first part cancel with those for $-t$ in the second one, resulting in

$$G_0(x_1 t_1 = t, x_2 t_2 = 0) = i\,\theta(t)\,e^{-i\varepsilon_2(t)}\,\delta_{1,2} - i\,\theta(-t)\,e^{-i\varepsilon_2 t}\,\delta_{1,2}. \tag{3.101}$$

In order to make the Fourier transformation

$$G_0(x_1 t_1 = t, x_2 t_2 = 0) = i\int_0^\infty \mathrm{d}t\;\, e^{i(\omega-\varepsilon_2)t}\,\delta_{1,2} - i\int_{-\infty}^0 \mathrm{d}t\, e^{i(\omega-\varepsilon_2)t}\,\delta_{1,2} \tag{3.102}$$

convergent, we add an infinitesimal convergence factor by setting $\omega \to \omega \pm i\eta$ with "+" for the first and "-" for the second term and with $\eta = 0^+$, i.e. an infinitely small positive number. From this we obtain

$$G_0(x_1, x_2; \omega) = \frac{\delta_{1,2}}{\omega - \varepsilon_2 + i\eta} - \frac{\delta_{1,2}}{\omega - \varepsilon_2 - i\eta}, \tag{3.103}$$

which proves equation 3.95. ■

We remark that this property is obtained when the creation and the annihilation operators act on the eigenbasis of the Hamiltonian. When the Green's function in another basis set is subject of the calculation, the change of the basis for creation and annihilation operators, as given by equation (2.30), has to be inserted. Therefore, the result derived here can be transferred to any other basis by the application of the corresponding transformation matrices.

These analytic formulas for the non-interacting Green's functions provide a starting point for the calculation of interacting Green's functions, which can be built based on them. Such an approach is provided by the perturbation theory.

3.2. Perturbation Theory

As discussed in the previous section, the interacting Green's function cannot be calculated based on its time evolution. As the many-body wave-function is unknown a direct evaluation is also not possible. We will, therefore, develop a perturbation expansion in the interaction V for the grand canonical potential and for the n-particle Green's function.

3.2.1. Perturbation Expansion

The corresponding perturbation series are given by the Gell-Mann-Low theorem, whose original form is based on the quantum mechanical states. Here we provide it in a formulation for expectation values, as this is more suitable for our purposes.

Theorem 3.11 (Gell-Mann-Low Theorem)
Let $\hat{V}$ be an interaction operator in the interaction picture (cf. eq. (2.5)). Then the grand canonical partition function can be represented by a formal power series according to

$$\mathcal{Z} = \sum_{k=0}^{\infty} \frac{(-1)^k}{k!} \int_0^\beta \mathrm{d}\lambda_1 \cdots \int_0^\beta \mathrm{d}\lambda_k \; Tr(e^{-\beta \hat{K}_0} \mathcal{T}\left[\hat{V}_I(\lambda_1) \cdots \hat{V}_I(\lambda_k)\right]), \tag{3.104}$$

and the interacting temperature n-particle Green's functions are represented by the Gell-Mann-Low formula

$$G^{2n}(1,\ldots,2n) = \sum_{k=0}^{\infty} \frac{(-1)^k}{k!} \int_0^\beta \mathrm{d}\lambda_1 \cdots \int_0^\beta \mathrm{d}\lambda_k \left\langle \hat{\mathcal{T}}\left[\hat{V}_I(\lambda_1) \cdots \hat{V}_I(\lambda_k)\, \hat{c}_1(\tau_1) \cdots \hat{c}_n(\tau_n)\, \hat{c}^\dagger_{2n}(\tau_{2n}) \cdots \hat{c}^\dagger_{n+1}(\tau_{n+1})\right]\right\rangle_0, \tag{3.105}$$

with thermal averages taken with respect to the free modified Hamiltonian $\hat{K}$.

Proof: This proof is a generalisation of the one of theorem 4.6 in the dissertation thesis of Giulio Schober [81] and the corresponding one in chapter 7 in the book of Fetter and Walecka [80]. The change of an operator $\hat{O}$ from the interaction picture to the Heisenberg picture is given by

$$\hat{O}(\tau) = e^{\hat{K}\tau}\, e^{-\hat{K}_0\tau}\, \hat{O}_{\,1}(\tau) e^{\hat{K}_0\tau}\, e^{-\hat{K}\tau}, \tag{3.106}$$

which motivates the definition of a time-evolution operator in the form of

$$\hat{\mathcal{U}}(\tau,\tau') := e^{\hat{K}_0\tau} e^{-\hat{K}(\tau-\tau')} e^{-\hat{K}_0\tau'} \tag{3.107}$$

for τ, $\tau' \in \mathbb{R}$. The change between both pictures can then be rewritten as

$$\hat{O}(\tau) = \hat{\mathcal{U}}(0,\tau)\, \hat{O}_1(\tau)\, \hat{\mathcal{U}}(\tau,0). \tag{3.108}$$

The time-evolution operator satisfies the group property

$$\hat{\mathcal{U}}(\tau,\tau')\, \hat{\mathcal{U}}(\tau',\tau'') = \hat{\mathcal{U}}(\tau,\tau''), \tag{3.109}$$

is not unitary and fulfils the equation of motion according to

$$\begin{aligned}\frac{\partial}{\partial\tau}\hat{\mathcal{U}}(\tau,\tau') &= e^{\hat{K}_0\tau}\,\hat{K}_0\,e^{-\hat{K}(\tau-\tau')}\,e^{-\hat{K}_0\tau'} - e^{\hat{K}_0\tau}\,\hat{K}\,e^{-\hat{K}(\tau-\tau')}\,e^{-\hat{K}_0\tau'}\\ &= e^{\hat{K}_0\tau}\,(\hat{K}_0-\hat{K})\,e^{-\hat{K}_0\tau}\,\hat{\mathcal{U}}(\tau,\tau')\\ &= -\hat{V}_{\mathrm{I}}(\tau)\,\hat{\mathcal{U}}(\tau,\tau').\end{aligned} \tag{3.110}$$

For the initial condition $\hat{\mathcal{U}}(\tau_0,\tau_0)=\hat{\mathbf{1}}$, which holds at initial time τ_0, the equation of motion has a unique solution $\hat{\mathcal{U}}(\tau,\tau_0)$ for $\tau>\tau_0$ according to the Picard-Lindelöf theorem. An explicit representation of the solution $\hat{\mathcal{U}}(\tau,\tau_0)$ is obtained by a successive integration of the equation of motion

$$\begin{aligned}\hat{\mathcal{U}}(\tau_1,\tau_0) &= \hat{\mathcal{U}}(\tau_0,\tau_0)+\sum_{k=1}^{\infty}(-1)^k\int_{\tau_0}^{\tau_1}\mathrm{d}\lambda_1\int_{\tau_0}^{\lambda_1}\mathrm{d}\lambda_2\cdots\int_{\tau_0}^{\lambda_{k-1}}\mathrm{d}\lambda_k\,\hat{V}_{\mathrm{I}}(\lambda_1)\cdots\hat{V}_{\mathrm{I}}(\lambda_k)\\ &:= \sum_{k=0}^{\infty}(-1)^k\int_{\tau_0}^{\tau_1}\mathrm{d}\lambda_1\int_{\tau_0}^{\lambda_1}\mathrm{d}\lambda_2\cdots\int_{\tau_0}^{\lambda_{k-1}}\mathrm{d}\lambda_k\,\hat{V}_{\mathrm{I}}(\lambda_1)\cdots\hat{V}_{\mathrm{I}}(\lambda_k)\\ &= \sum_{k=0}^{\infty}\frac{(-1)^k}{k!}\int_{\tau_0}^{\tau_1}\mathrm{d}\lambda_1\cdots\int_{\tau_0}^{\tau_1}\mathrm{d}\lambda_k\,\hat{\mathcal{T}}[\hat{V}_{\mathrm{I}}(\lambda_1)\cdots\hat{V}_{\mathrm{I}}(\lambda_k)]\end{aligned} \tag{3.111}$$

with $\lambda_i\in[\tau_0,\tau_1]$, and with the time-ordering operator in the last line symmetrising the expression.

The definition of the time-evolution operator in equation (3.107) leads to

$$e^{-\hat{K}\tau} = e^{-\hat{K}_0\tau}\,\hat{\mathcal{U}}(\tau,0), \tag{3.112}$$

so that the partition function can be rewritten as

$$\mathcal{Z} = \mathrm{Tr}\,(e^{-\beta\hat{K}}) = \mathrm{Tr}\,(e^{-\beta\hat{K}_0}\,\hat{\mathcal{U}}(\beta,0)). \tag{3.113}$$

The insertion of the explicit form of $\hat{\mathcal{U}}$ as provided by equation (3.111) then leads to the desired result.

Turning to the n-particle Green's function we assume descending times $\tau_1>\ldots>\tau_n>\tau_{n+1}>\ldots>\tau_{2n}$ such that

$$G^{(2n)}(1,\ldots,2n) = (-1)^{\frac{n(n-1)}{2}}\frac{1}{\mathcal{Z}}\mathrm{Tr}\left(e^{-\beta\hat{K}}\hat{c}_{x_1}(\tau_1)\cdots\hat{c}^{\dagger}_{x_{2n}}(\tau_{2n})\right), \tag{3.114}$$

in which the prefactor results from commuting the last n operators to correct time ordering. By applying equation (3.112) and by transferring the operators to the interaction picture (cf. eq. (3.108)) this Green's function becomes

$$\begin{aligned}&G^{(2n)}(1,\ldots,2n)\\ &= (-1)^{\frac{n(n-1)}{2}}\frac{1}{\mathcal{Z}}\mathrm{Tr}\left(e^{-\beta\hat{K}_0}\hat{\mathcal{U}}(\beta,0)\hat{\mathcal{U}}(0,\tau_1)\hat{c}_{\mathrm{I},x_1}(\tau_1)\hat{\mathcal{U}}(\tau_1,0)\cdots\hat{\mathcal{U}}(0,\tau_{2n})\hat{c}^{\dagger}_{\mathrm{I},x_{2n}}(\tau_{2n})\hat{\mathcal{U}}(\tau_{2n},0)\right)\\ &= (-1)^{\frac{n(n-1)}{2}}\frac{1}{\mathcal{Z}}\mathrm{Tr}\left(e^{-\beta\hat{K}_0}\hat{\mathcal{U}}(\beta,\tau_1)\hat{c}_{\mathrm{I},x_1}(\tau_1)\hat{\mathcal{U}}(\tau_1,\tau_2)\cdots\hat{\mathcal{U}}(\tau_{2n-1},\tau_{2n})\hat{c}^{\dagger}_{\mathrm{I},x_{2n}}(\tau_{2n})\hat{\mathcal{U}}(\tau_{2n},0)\right).\end{aligned} \tag{3.115}$$

All the operators in the expansion of the time-evolution operator $\hat{\mathcal{U}}(\tau_1,\tau_2)$ in equation (3.111) are within the time interval $[\tau_1,\tau_2]$ and in correct time order. Thus its insertion into this equation for the Green's function will maintain the correct time order, and the time-ordering operator $\hat{\mathcal{T}}$ can be introduced without any further changes. All time-evolution operators $\hat{\mathcal{U}}$ can be moved to the left

and can be combined due to their group property (cf. eq. (3.109)), which results in the time ordered expression

$$G^{(2n)}(1,\ldots,2n) = (-1)^{\frac{n(n-1)}{2}} \frac{1}{\mathcal{Z}} \mathrm{Tr}\left(e^{-\beta \hat{K}_0}\, \hat{\mathcal{T}}\left[\hat{\mathcal{U}}(\beta,0)\, \hat{c}_{\mathrm{I}x_1}(\tau_1)\cdots \hat{c}^\dagger_{\mathrm{I}x_{2n}}(\tau_{2n})\right]\right). \tag{3.116}$$

After re-establishing the original order of operators, the Gell-Mann-Low formula

$$G^{(2n)}(1,\ldots,2n) = \frac{1}{\mathcal{Z}} \mathrm{Tr}\left(e^{-\beta \hat{K}_0}\, \hat{\mathcal{T}}\left[\hat{\mathcal{U}}(\beta,0)\, \hat{c}_{\mathrm{I}x_1}(\tau_1)\ldots \hat{c}^\dagger_{\mathrm{I}x_{n+1}}(\tau_{n+1})\right]\right) \tag{3.117}$$

is obtained by using $\mathcal{U}$ from equation (3.111). For any time-order different to the one assumed in this calculation, the proof can be performed analogously, leading to the same result. ■

Physically, the Gell-Mann-Low theorem means that an initial state is adiabatically connected to a final state of the system. For instance, if the system is in the non-interacting ground state at $\tau = 0$ and the interaction is slowly switched on such that it can not leave this ground state, the system evolves to the fully interacting state at the first τ_i. Conversely, if the interaction is slowly switched off after the last time τ_f, it connects the fully interacting state with the ground state at $\tau = \beta$. These relations are more apparent in the original form of the theorem for real times (cf. ref. [80, 84]) where the system evolves from the ground state at $t \to -\infty$ to the fully interacting system at $t = 0$ and back to the ground state at $t \to \infty$.

The Gell-Mann-Low theorem provides an expansion of the Green's functions and of the grand canonical partition function in terms of interactions. To illustrate this, we consider an interaction V of m particles which conserves the particle number. Each occurrence of this interaction adds m creation and m annihilation operators to the expectation value. Therefore, when k interactions of m particles are inserted, the resulting expectation value on the right hand side corresponds to the Green's function $G_0^{(2n+k\cdot 2m)}$, where $k \cdot 2m$ legs are connected with interactions. That is, every interacting n-particle Green's function is related to an $2n+k\cdot 2m$-particle non-interacting Green's function. The latter could be determined by the time evolution of Green's functions (cf. thm. 3.7), such that we arrive at a consistent set of equations for the interacting system. However, Wick's theorem provides a useful simplification to avoid the hierarchies resulting from this approach by combining pairs of creation and annihilation operators to single-particle Green's functions.

Theorem 3.12 (Wick Theorem for non-interacting n-particle Green's Functions)
The non-interacting n-particle Green's function $G_0^{(2n)}(1,\ldots,2n)$ factorises into products of non-interacting one-particle Green's functions G_0, i.e.

$$\begin{aligned} G_0^{(2n)}(1,\cdots,2n) &= \sum_{\pi\in S_n} \mathrm{sgn}(\pi)\, G_0(1;\pi_{n+1})\cdots G_0(n;\pi_{2n}) \\ &= \det\left([G_0(i,n+j)]_{i,j=1,\ldots,n}\right), \end{aligned} \tag{3.118}$$

where the second line is a reformulation in terms of a determinant.

PROOF: The proof directly follows from the equation of motion of the n-particle Green's function (see thm. 3.7). The reformulated equation of motion (3.93) is multiplied with $G(2',1)$, and an integral over the new internal variable 1 is performed. With the equivalence

$$\int \mathrm{d}1 \int \mathrm{d}1'\, G_0(2';1)\, G_0^{-1}(1;1')\, G_0^{(2n)}(1',2,\ldots,2n) = \int \mathrm{d}1'\, \delta(2',1')\, G_0^{(2n)}(1',2,\ldots,2n) = G_0^{(2n)}(2',2,\ldots,2n), \quad (3.119)$$

the left hand side can be reformulated. A straight forward evaluation of the right hand side results in

$$G_0^{(2n)}(2',2,\ldots,2n) = \sum_{k=1}^{n} (-1)^{1+k}\, G_0(2';n+k)\, G_0^{(2n-2)}(2,\ldots,n;n+1,\ldots,\cancel{n+k},\ldots,2n). \quad (3.120)$$

The theorem can now be proved by induction in n. For $n = 1$ the equation (3.118) trivially holds. Assuming that it is also fulfilled for $(n-1)$, that is, it holds for $G^{(2n-2)}$, equation (3.120) becomes

$$\begin{aligned} G_0^{(2n)}(2',2,\ldots,2n) &= \sum_{k=1}^{n} (-1)^{1+k}\, G_0^{(2)}(2';1+k) \sum_{\pi\in S_{n-1}} \mathrm{sgn}(\pi) \\ &\quad G_0(2;\pi_{n+1}) \cdots G_0(k+1;\pi_{n+k})\, G_0(k+2;\pi_{n+k+2}) \ldots G_0(n;\pi_{2n}) \\ &= \sum_{\pi\in S_n} \mathrm{sgn}(\pi) G_0(1;\pi_{n+1}) \cdots G_0(n;\pi_{2n}), \end{aligned} \quad (3.121)$$

showing that the assertion also holds for n. Writing the right hand side of this expression in a matrix form with respect to the arguments, this expression results in the determinant of this matrix. ■

When a creation and an annihilation operator are combined to form a Green's function in the sense of the Wick Theorem, they are said to be **contracted**.

An application of the Wick theorem (thm. 3.12) to the right hand side of the Gell-Mann-Low theorem (thm. 3.11) generates all possible contractions of creation and annihilation operators. To illustrate this and to introduce some terms, which will be properly defined in section 3.2.2, we assume a two-particle interaction like the Coulomb interaction. This corresponds to an interaction order of $m = 2$ according to the considerations made before providing the Wick theorem. As all variables introduced by applying the Wick theorem only appear as integral variables they will be labelled as combined integer index with a tilde (e.g. $\tilde{1}$). We refer to them as **internal arguments** and to those which also appear on the left hand side as **external arguments**. The Green's function of equation (3.105) thus becomes

$$\begin{aligned} G^{(2n)}(1,\ldots,2n) &= \frac{1}{\mathcal{Z}} \sum_{k=0}^{\infty} \frac{(-\beta)^k}{k!2^k} \left(\prod_{i=1}^{k} \int \mathrm{d}\tilde{1}_i \cdots \int \mathrm{d}\tilde{4}_i\, V_\circ(\tilde{1}_i,\tilde{2}_i;\tilde{3}_i,\tilde{4}_i) \right) \\ &\quad \times G_0^{(2n+4k)}(1,\ldots,n,\tilde{1}_1,\tilde{2}_1,\ldots,\tilde{1}_k,\tilde{2}_k;n+1,\ldots,2n,\tilde{3}_1,\tilde{4}_1,\ldots,,\tilde{1}_k,\tilde{2}_k) \\ &= \frac{1}{\mathcal{Z}} \sum_{k=0}^{\infty} \frac{(-\beta)^k}{k!2^k} \sum_{\pi\in S_{2n+4k}} \left(\prod_{i=1}^{k} \int \mathrm{d}\tilde{1}_i \cdots \int \mathrm{d}\tilde{4}_i\, V_\circ(\tilde{1}_i,\tilde{2}_i;\tilde{3}_i,\tilde{4}_i) \right) \\ &\quad \times \mathrm{sgn}(\pi) G_0(1;\pi_{n+1}) \cdots G_0(n;\pi_{2n})\, G_0(\tilde{3}_1;\pi_{\tilde{1}_1})\, G_0(\tilde{4}_1;\pi_{\tilde{2}_1}) \cdots G_0(\tilde{3}_k;\pi_{\tilde{1}_k})\, G_0(\tilde{4}_k;\pi_{\tilde{2}_k}), \end{aligned} \quad (3.122)$$

where π permutes the last $n+2k$ arguments creating all possible combinations of the first $n+2k$ arguments with the last $n+2k$ arguments. All these possibilities can basically be split into three

categories: First, there are terms in which a Green's function connects two external arguments, which, therefore, describes a particle not interacting with any other particle. Second, several Green's functions can connect only internal arguments, thus forming a so called **bubble**. Third, several Green's functions connect external points with internal ones, thus referring to interactions between particles. As the partition function can be seen as a Green's function without external legs, it only consists of terms of the second kind, which, therefore, are called **vacuum bubbles**, i.e.

$$\mathcal{Z} = \sum_{k=0}^{\infty} \frac{1}{2^k k!} \sum_{\pi \in S_{2k}} (-\beta)^k \left(\prod_{i=1}^{k} \int \mathrm{d}\tilde{1}_i \cdots \int \mathrm{d}\tilde{4}_i \, V_\circ(\tilde{1}_i, \tilde{2}_i; \tilde{3}_i, \tilde{4}_i) \right) \times \operatorname{sgn}(\pi) \, G_0(\tilde{3}_1; \pi_{\tilde{1}_1}) \, G_0(\tilde{4}_1; \pi_{\tilde{2}_1}) \cdots G_0(\tilde{3}_k; \pi_{\tilde{1}_k}) \, G_0(\tilde{4}_k; \pi_{\tilde{2}_k}). \quad (3.123)$$

As the terms arising due to the combination of perturbation expansion and Wick theorem always have a similar structure, the introduction of diagrams is useful, which on the one hand visualise the physical processes taking place and on the other hand simplify the calculations.

3.2.2. Diagrams

The numerous terms arising from the perturbation expansion in combination with the Wick theorem always consist of Green's interactions, whose internal arguments are connected to each other or to external arguments by single-particle Green's functions. Their systematic visualisation is achieved by the generalised Feynman diagrams, which are defined in the following according to reference [81].

Definition 26 (External and Internal Arguments)

Let $1, \ldots, 2n$ and $\tilde{1}, \ldots, \widetilde{2m}$ denote the arguments of a contribution to the perturbation expansion and Wick contraction of the n-particle Green's function. Then

1. *the arguments $1, \ldots, n$ are denoted as **external ingoing arguments**, and the arguments $n+1, \ldots, 2n$ are denoted as **external outgoing arguments**.*
2. *the arguments $\tilde{1}, \ldots, \tilde{m}$ are called **internal ingoing arguments** and the arguments $\widetilde{m+1}, \ldots, \widetilde{2m}$ are called **internal outgoing arguments** for all m-particle interactions in the perturbation expansion.*

Definition 27 (Generalised Feynman Diagrams)

Let $G^{(2n)}(1, \ldots, 2n)$ be an n-particle Green's function given by a perturbation series with the m-particle interaction $V_\circ(\widetilde{1}, \ldots, \widetilde{2m})$ provided by the Gell-Mann-Low formula (3.105) on which the contractions due to the Wick theorem are performed. Then we define the diagrammatic elements as follows:

1. *All external arguments are represented as points at which exactly one Green's function starts (external ingoing) or ends (external outgoing), and they are called **external slots**.*

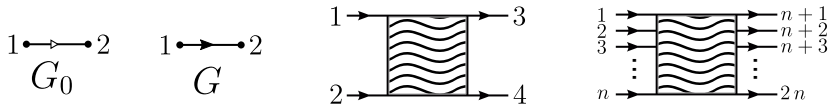

Figure 3.1.: The basic diagrammatic elements defined in definition 27 (from left to right): The bare propagator, the interacting Green's function, the two-particle interaction and a general n-particle interaction.

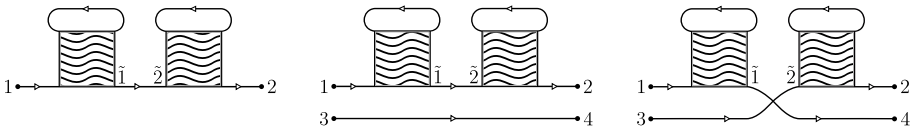

Figure 3.2.: Graphical representation of the operation of cutting a propagator line of the left diagram: An unconnected line is inserted (middle) and a permutation of the slots of the line which is supposed to be cut with the new external arguments is performed (right).

2. *The interaction is represented by a filled rectangle which has m* ***internal ingoing slots*** *for $\tilde{1}, \ldots, \tilde{m}$ and m* ***internal outgoing slots*** *for $\widetilde{m+1}, \ldots, \widetilde{2m}$. The bare slots are marked by short unconnected in- or outpointing arrows, respectively.*

3. *Each non-interacting one-particle Green's function $G_0(a, b)$ is represented by an open arrow connecting an outgoing slot a with an ingoing slot b, called* ***propagator****.*

4. *Each full one-particle Green's function $G(a, b)$ is represented by a filled arrow connecting an outgoing slot a with an ingoing slot b, called* ***full propagator****.*

A diagram obtained by these rules is called a ***Generalised Feynman Diagram****.*

The basic diagrammatic elements are illustrated in figure 3.1. We remark that due to the Wick theorem there is no need to define a diagram for an n-particle Green's function. These diagrammatic elements and their corresponding rules allow us to draw all possible contributions to the n-particle Green's function based on the perturbation expansion. The operation of cutting a propagator, which is diagrammatically illustrated in figure 3.2, is helpful to classify these diagrams. Physically, we consider a propagator $G_0(\tilde{1}, \tilde{2})$ which connects two internal slots $\tilde{1}$ and $\tilde{2}$. Cutting this propagator then results in

$$G_0(\tilde{1}; \tilde{2}) \mapsto (-1) G_0(\tilde{1}; \tilde{2}')\, G_0(\tilde{1}'; \tilde{2}). \tag{3.124}$$

This operation can be viewed as adding a propagator $G_0(\tilde{1}'; \tilde{2}')$ to the full Feynman diagram and then permuting one of the indices with one of $G_0(\tilde{1}; \tilde{2})$, resulting in the minus sign.

We define the following nomenclature taken from [81] for the classification of diagrams, illustrated in figure 3.3.

Definition 28 (Classification of Generalised Feynman Diagrams)
Let $\mathcal{F}$ be a Generalised Feynman diagram constructed in accordance with definition 27. Then

1. *(a subset of) the Feynman diagram $\mathcal{F}$ is called a* ***bubble diagram*** *if it has no connection to an external slot;*
2. *the Feynman diagram $\mathcal{F}$ is called* ***bubble-free*** *if every interaction vertex is connected (by a series of Green's functions) to at least one external slot;*
3. *the Feynman diagram $\mathcal{F}$ is called* ***connected*** *if it has at least one interaction vertex and if every interaction vertex is connected (by a series of Green's functions) to all external slots.*

In the following, let $\mathcal{F}$ be a connected Feynman diagram with $2n$ external slots. Then

4. *a propagator is called* ***internal*** *if it connects two internal slots, and it is called* ***external*** *if it connects an external with an internal slot;*
5. *an internal propagator is called* ***non-essential*** *if the diagram remains connected after cutting the propagator and it is called* ***essential*** *otherwise;*
6. *an essential propagator is called an* ***extremity propagator*** *if the diagram is separated into two parts, of which one has exactly two external slots. Otherwise it is called a* ***torso propagator****;*
7. *the diagram is called* ***one-line-reducible*** *(or* ***one-particle-reducible****) if it has at least one essential line, and it is called* ***one-line-irreducible*** *(or* ***one-particle-irreducible****) otherwise;*
8. *the diagram is called* ***amputable*** *if it has at least one extremity line, and it is called* ***non-amputable*** *or* ***fully amputated*** *otherwise;*
9. *the diagram is called n-**line irreducible** (or n-**particle irreducible**) if it remains connected after cutting n internal lines simultaneously, and it is called n-**line reducible** (or n-**particle reducible**) otherwise.*

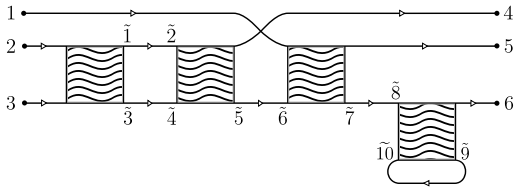

Figure 3.3.: Diagrammatic representation of the terms defined in Def. 28. The lines connecting the graph with the labels $1, \ldots, 6$ are external lines, while all the others are internal ones. The lines connecting the two interactions in the left ($\tilde{1}-\tilde{2}, \tilde{3}-\tilde{4}$) and the line connecting the rightmost interaction with itself ($\tilde{9}-\widetilde{10}$) are non-essential, as the graph remains connected upon cutting those lines, while the other two internal lines ($\tilde{5}-\tilde{6}, \tilde{7}-\tilde{8}$) are essential, so that the graph is one-particle irreducible. The graph is also amputable, as the line $\tilde{7}-\tilde{8}$ is an extremity propagator, as after cutting, the part of the rightmost interaction has exactly two external lines, while the line $\tilde{5}-\tilde{6}$ is a torso-propagator. Considering only the part of the diagram containing the two interactions to the left, one obtains a two-particle reducible diagram, as it separates after the simultaneous splittings of the two propagators $\tilde{1}-\tilde{2}$ and $\tilde{3}-\tilde{4}$.

According to the rules above two classes of sub-diagrams can be identified which appear multiple times in the displayed and in higher order Green's functions. It is sufficient to calculate only one of them exemplarily, as topologically equal diagrams always result in the same value. First, every contributing connected diagram can be accompanied by an infinite series of bubble diagrams. As the partition function in the denominator also consists of an infinite series of bubble diagrams (cf. eq. (3.123)), these contributions will cancel according to the cancellation theorem 3.13, which we will introduce next. Second, any unconnected, bubble-free diagram consists of at least two connected diagrams with lower order in n. To exclude these diagrams, we will deal with connected Green's functions, which we will introduce in definition 29 below, in which those contributions are subtracted.

Theorem 3.13 (Cancellation Theorem)
Let $G^{(2n)}$ be the n-particle Green's function and let $V_\circ$ be an m-particle interaction. Then $G^{(2n)}$ is represented by the sum over all bubble-free Feynman graphs with $2n$ external slots and k interaction vertices, i.e.

$$\begin{aligned} G^{(2n)}(1,\dots,2n) = \sum_{k=0}^{\infty} \frac{(-\beta)^k}{k!2^k} \sum_{\substack{\pi\in S_{2n+m\cdot k}\\ \pi \text{ bubble-free}}} \Bigg(\prod_{i=1}^{k} \int \mathrm{d}\widetilde{1}_i \cdots \int \mathrm{d}\widetilde{2m}_i \\ \times V_\circ(\widetilde{1}_i,\dots \widetilde{m}_i; \widetilde{m+1}_i,\dots,\widetilde{2m}_i)\Bigg) \operatorname{sgn}(\pi)\, G_0(1;\pi_{n+1})\cdots G_0(n;\pi_{2n}) \\ \times G_0(\widetilde{m+1}_1;\pi_{\widetilde{1}_1})\cdots G_0(\widetilde{2m}_1;\pi_{\widetilde{m}_1})\cdots G_0(\widetilde{m+1}_k;\pi_{\widetilde{1}_k})\cdots G_0(\widetilde{2m}_k;\pi_{\widetilde{m}_k}). \end{aligned} \tag{3.125}$$

Proof: We abbreviate the expression behind the sum over the permutations in equation (3.122) by

$$\begin{aligned} \mathrm{Val}[n,k,\pi] := (-\beta)^k \left(\prod_{i=1}^{k} \int \mathrm{d}\widetilde{1}_i \cdots \int \mathrm{d}\widetilde{2m}_i\, V_\circ(\widetilde{1}_i,\dots \widetilde{m}_i; \widetilde{m+1}_i,\dots \widetilde{2m}_i)\right) \operatorname{sgn}(\pi) G_0(1;\pi_{n+1})\cdots \\ \cdots G_0(n;\pi_{2n})\, G_0(\widetilde{m+1}_1;\pi_{\widetilde{1}_1})\cdots G_0(\widetilde{2m}_1;\pi_{\widetilde{m}_1})\cdots G_0(\widetilde{m+1}_k;\pi_{\widetilde{1}_k})\cdots G_0(\widetilde{2m}_k;\pi_{\widetilde{m}_k}), \end{aligned} \tag{3.126}$$

where the indices refer to the information characterising a contribution, that is $2n$ external legs, k interactions and the permutation π.

Every Feynman graph resulting from a permutation $\pi \in S_{2n+m\cdot k}$ can be uniquely decomposed into $\pi = \pi' \circ \sigma$, that is into a bubble-free graph $\pi' \in S_{2n+m\cdot l}$ and a pure vacuum bubble graph $\sigma \in S_{m\cdot(k-l)}$ with $l \in \{0,\dots,k\}$. The sign of such a decomposition is $\operatorname{sgn}(\pi) = \operatorname{sgn}(\pi')\operatorname{sgn}(\sigma)$ and the contribution becomes

$$\mathrm{Val}\,[n,k,\pi] = \mathrm{Val}\,[n,l,\pi']\ \mathrm{Val}\,[0,k-l,\sigma]. \tag{3.127}$$

When these terms are inserted into the sum over the permutations, several of them produce the same contribution, as it is irrelevant which l interactions are connected to the external slots and which $k-l$ interactions appear only inside the bubble terms. Therefore, the sum in equation (3.126) can be rewritten as

$$\sum_{\pi\in S_{n+2k}} \mathrm{Val}\,[n,k,\pi] = \sum_{l=0}^{k} \frac{k!}{l!(k-l)!} \sum_{\substack{\pi'\in S_{n+2l}\\ \pi' \text{bubble free}}} \mathrm{Val}\,[n,l,\pi'] \sum_{\sigma\in S_{2(k-l)}} \mathrm{Val}\,[0,k-l,\sigma], \tag{3.128}$$

where the stochastic factor counts all the possibilities to arrange those k vertices into a bubble-free and into a bubble part. The Green's function can now be rewritten as

$$\begin{aligned} &G^{(2n)}(1,\dots,2n) \\ &\qquad = \frac{1}{\mathcal{Z}} \sum_{k=0}^{\infty} \sum_{l=0}^{k} \frac{1}{l!\, 2^l} \sum_{\substack{\pi' \in S_{n+2l} \\ \pi' \text{bubble free}}} \mathrm{Val}[n,l,\pi'] \, \frac{k!}{l!(k-l)!} \sum_{\sigma \in S_{2(k-l)}} \mathrm{Val}[0,k-l,\sigma], \end{aligned} \tag{3.129}$$

where the summation can be rewritten according to

$$\sum_{k=0}^{\infty} \sum_{l=0}^{k} f(l) g(k-l) = \sum_{l=0}^{\infty} \sum_{l'=0}^{\infty} f(l) g(l') = \sum_{l=0}^{\infty} f(l) \sum_{l'=0}^{\infty} g(l'). \tag{3.130}$$

Hence, the desired result is obtained by

$$\begin{aligned} G^{(2n)}(1,\dots,2n) &= \frac{1}{\mathcal{Z}} \sum_{l=0}^{\infty} \frac{1}{l! 2^l} \sum_{\substack{\pi' \in S_{n+2l} \\ \pi' \text{bubble free}}} \mathrm{Val}[n,l,\pi'] \sum_{l'=0}^{\infty} \frac{1}{l'!} \sum_{\sigma \in S_{2l'}} \mathrm{Val}[0,l',\sigma] \\ &= \sum_{l=0}^{\infty} \frac{1}{l! 2^l} \sum_{\substack{\pi' \in S_{n+2l} \\ \pi' \text{bubble free}}} \mathrm{Val}[n,l,\pi'], \end{aligned} \tag{3.131}$$

where we identified the sum over vacuum bubbles by the partition function as given in equation (3.123). As this cancels the prefactor $\mathcal{Z}^{-1}$, the expansion of $\mathrm{Val}[n,l,\pi']$ equals the assertion. ■

This theorem provides a proper expansion of the n-particle Green's function in terms of interactions, as the expansion of the partition function in the denominator, which could give rise to unbounded terms, was cancelled. Moving to the second part of reoccurring diagrams, we first observe that the one-particle Green's function only consists of connected Feynman diagrams. For Green's functions with $n \geq 2$, however, the expression still contains non-connected Feynman diagrams, as discussed before. These non-connected diagrams can be regarded as different combinations of connected diagrams for $k \in \{1,\dots,n-1\}$ particles. As these have already been calculated according to their contribution to Green's functions of lower order, the only relevant new contributions are the connected terms.

Definition 29 (Connected n-particle Green's Function)
*Let $Val\,[n,k,\pi]$ be defined for an n-particle Green's function $G^{(2n)}$ like in equation (3.126). Then the **connected n-particle Green's function** $G_{\mathrm{c}}^{(2n)}$ is given by the sum over all connected diagrams with n external ingoing and n external outgoing points, i.e.*

$$G_c^{(2n)}(1,\dots,2n) := \sum_{k=0}^{\infty} \frac{1}{k! 2^k} \sum_{\substack{\pi \in S_{n+2k} \\ \pi \ connected}} Val\,[n,k,\pi]. \tag{3.132}$$

The sum over all connected diagrams is obtained by subtracting all combinations of non-connected diagrams which are contained in the sum of all permutations. As the non-connected diagrams can be identified as connected Green's functions of lower order, this is equivalent to

$$G_{\mathrm{c}}^{(2n)}(1,\ldots,2n) = G^{(2n)}(1,\ldots,2n) - \sum_{\sigma\in S_{2n}} \mathrm{sgn}(\sigma) \prod_{k=1}^{n-1} \sum_{i_k=0}^{n \bmod(k)} (G_{\mathrm{c}}^{(2k)})^{i_k} \Bigg|_{\sum_{k=1}^{n-1} k i_k = n} . \tag{3.133}$$

In this equation

(a) the sum over permutations permutes all external arguments, which, for the sake of shortness, are not written in the product part,

(b) the product and the sum in the subtracted part create all possible combinations of Green's functions of lower order, where

(c) the sums are restricted by modulo operations, as a Green's function of order k can only appear $n \times \mod(k)$ times to fit the requirement of $2n$ external legs. However, the combination of Green's functions can still result in terms with more external legs than the left hand side has, such that

(d) the restriction $\sum_{k=1}^{n-1} k i_k = n$ is required, stating that only those diagrams contribute in which exactly $2n$ external legs are obtained.

In order to illustrate this formula, we exemplarily consider the two- and the three-particle Green's functions as simplest cases. The subtracted part of the two-particle Green's function has the form $G\,G$, on which the permutations yield the connected Green's function as

$$G_{\mathrm{c}}^{(4)}(1,2;3,4) = G^{(4)}(1,2;3,4) - G(1;3)G(2;4) + G(1;4)G(2;3). \tag{3.134}$$

The subtracted part of the three-particle Green's function has terms of two kinds, $G^{(4)}G$ and $G\,G\,G$. By permutations we obtain 24 different possibilities to arrange the external legs for the first case and six different possibilities for the second case. The high number of 24 for the first case arises as there are six different possibilities for the external legs to connect to the two-particle Green's function and four different possibilities to arrange them at the incoming and at the outgoing legs of it. As the latter are related by the symmetry of the Green's function, as discussed in section 3.1.1, it is sufficient to calculate the value of the diagram only once and then exploit the symmetry relations.

3.2.3. Diagrammatic Groups

Despite all the previous simplifications for the connected diagrams, the right hand side of their interaction expansion still contains an infinite sum over all interactions. As two-particle interactions, like the Coulomb interaction denoted by $V_\circ$ and diagrammatically depicted by a wave line, are the most important ones for interacting electrons, we restrict ourselves to these in the following. The interaction expansion of the single-particle Green's function in terms of these two-particle interactions is diagrammatically displayed in figure 3.4. As some groups of sub-diagrams appear repeatedly we combine them to the self-energy and to effective interactions as follows.

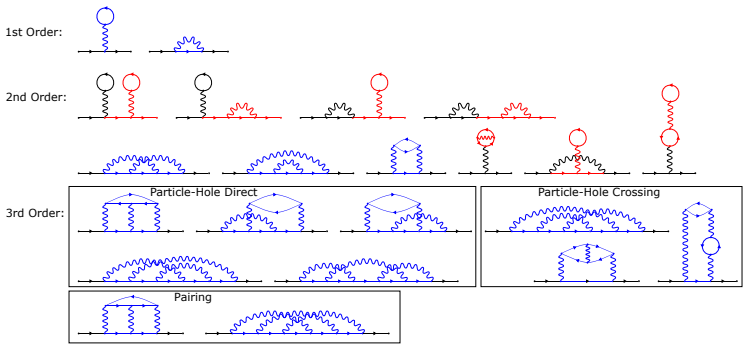

Figure 3.4.: Feynman Diagrams of the zeroth, first, second and (incomplete) third order interaction expansion corresponding to the Gell-Mann and Low theorem and to the Wick theorem for the one-particle Green's function. Here, the bare interaction $V_\circ$ is represented by an undirected wave line. The contributions to the self-energy of this expansion (see def. 30) are in blue. Those parts of the diagram which can be replaced by a full Green's function (see text) are red. The third-order diagrams are grouped corresponding to the channels they belong to. Remark that this diagrammatic representation does not account for correct prefactors and signs.

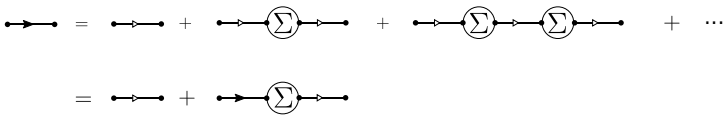

Figure 3.5.: The diagrammatic representation of the Dyson equation.

Definition 30 (Diagrammatic Groups)
Let $\mathcal{F}$ be the Feynman diagram of the n-particle Green's function $G^{(2n)}$ of a system with a two-particle interaction. Then we define:

- ***Self-Energy**: The sum of all one-particle irreducible sub-diagrams of $\mathcal{F}$ with one internal incoming and one internal outgoing slot defines the self-energy Σ. The self-energy is diagrammatically represented by a circle labelled with Σ with corresponding two slots.*
- ***Effective Interaction**: All one-particle irreducible diagrammatic blocks with two internal incoming and two internal outgoing slots define the effective interaction $\gamma^{(4)}$. It is diagrammatically represented by a filled square with two incoming slots on its left side and two outgoing slots on its right side.*

The first contributions to the self-energy and to the effective interaction are diagrammatically displayed in figure 3.4. As the expansion of the interacting one-particle Green's function consists of

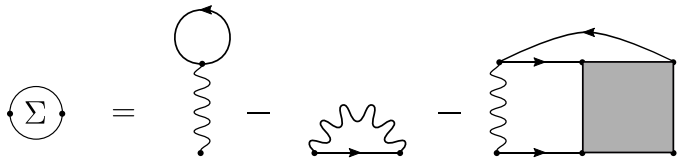

Figure 3.6.: Diagrammatic representation of the Schwinger-Dyson equation for the calculation of the self-energy.

all the sub-diagrams contained in the self-energy connected by a non-interacting one-particle Green's function, its formula can be rewritten as

$$\begin{aligned} G(1;2) &= G_0(1;2) + G_0(1;\tilde{1})\Sigma(\tilde{1};\tilde{2})G_0(\tilde{2};2) + G_0(1;\tilde{1})\Sigma(\tilde{1};\tilde{2})G_0(\tilde{2};\tilde{3})\Sigma(\tilde{3};\tilde{4})G_0(\tilde{4};2) + \dots \\ &= G_0(1;2) + G_0(1;\tilde{1})\Sigma(\tilde{1};\tilde{2})G(\tilde{2};1) \\ &= \left[G_0^{-1}(1;2) - \Sigma(1;2)\right]^{-1}, \end{aligned} \tag{3.135}$$

which is the Dyson equation for the Green's function[2], whose Feynman diagram is depicted in figure 3.5. Here, we implicitly assumed an integration over internal arguments. In a first approximation only the first-order contributions are considered, so that the self-energy becomes $\Sigma(1;2) = V_\circ(1,\tilde{1})G(\tilde{1};\tilde{1}^+)\delta(1,2) + V_\circ(1;2)G(1;2)$, which are the well known Hartree and Fock contributions [85, 86]. To become more accurate we investigate the diagrams contributing to the self-energy and identify sub-diagrams which appear in the self-energy itself and are connected to the rest of the diagram by two propagators (sub-diagrams in blue in fig. 3.4). Such sub-diagrams will appear at each internal line in the infinite expansion so that we can convolute those contributions to the self-energy. In this way the diagram is simplified by replacing the self-energy block and its connecting free Green's functions by one full Green's function.

In the diagrams contributing to the self-energy we can identify contributions of the effective interaction. At first, it seems reasonable to connect the effective interaction with itself to obtain the self-energy. However, this approach will lead to an overcounting of diagrams such that it is given by the Schwinger-Dyson equation

$$\begin{aligned} \Sigma(1;2) = -V_\circ(1;\tilde{1})G(1;\tilde{2})G(\tilde{1};\tilde{3})\gamma^{(4)}(\tilde{3},\tilde{2};\tilde{4},2)G(\tilde{4};\tilde{1}) \\ + V_\circ(1;\tilde{1})G(1;1^+)\delta(1,2) - G(1;2)V_\circ(1;2), \end{aligned} \tag{3.136}$$

in which we explicitly account for the Hartree and Fock terms and which is diagrammatically shown in figure 3.6.

By the introduction of diagrammatic groups we shifted the difficulty of the calculation of an infinite amount of diagrams to the calculation of the effective interaction. When we investigate the structure of the diagrams it consists of, we observe that it contains, on the one hand, the bare two-particle interaction, which is, in this discussion, the Coulomb interaction $V_\circ$, but which can in general be non-local and non-instantaneous, and, on the other hand, it contains complicated diagrams including several interactions. Within the latter ones there often is at least a sub-diagram in which two interactions are connected to each other by two propagators so that this sub-diagram can be convoluted to

[2]The first line is motivated by the classification of diagrams, however, the convergence of this series is not guaranteed. The formally exact form of the Dyson equation is, therefore, provided by the third line, as will be derived in chapter 3.4, corollary 3.16.

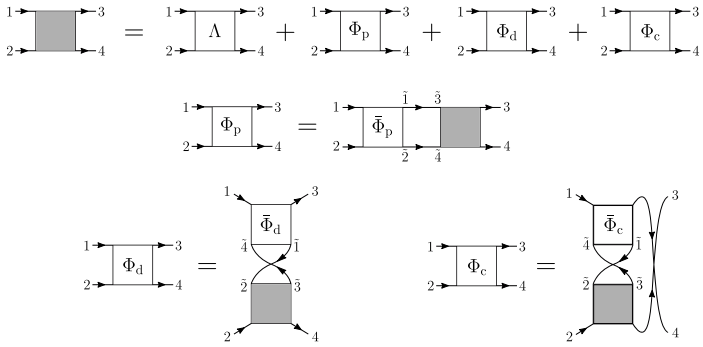

Figure 3.7.: Diagrammatic representation of the vertex decomposition according to the parquet scheme and to the corresponding Bethe-Salpeter equations.

a two-particle reducible effective interaction. If this procedure is repeated as often as possible, large parts of the diagrams can directly be obtained when the two-particle reducible effective interaction is known. The full effective interaction then contains all contributions which are two-particle reducible and those which are not. As there are three different ways of defining the two-particle reducibility, three different channels can be identified, corresponding to pairing and to two different particle-hole channels. This decomposition leads to the Parquet approach, which is defined as follows.

Definition 31 (Parquet Theory)
Consider the generalised Feynman diagrams of the effective interaction $\gamma^{(4)}(1,2;3,4)$ *of a system with a two-particle interaction* $V_\circ$*, and let* $1,\,2$ *denote ingoing and* $3,\,4$ *outgoing slots. Then the full interaction* $\gamma^{(4)}$ *is decomposed as*

$$\gamma^{(4)}(1,2;3,4) = \Lambda(1,2;3,4) + \Phi^p(1,2;3,4) + \Phi^d(1,2;3,4) + \Phi^c(1,2;3,4), \tag{3.137}$$

in which the contributions are defined as

1. ***Fully Irreducible*** Λ*: All the diagrams which cannot be separated into two parts by cutting two full propagator lines, i.e. two-particle irreducible diagrams;*
2. ***Pairing Channel*** Φ^p*: Cutting two propagators separates the labels* $1,2$ *from the labels* $3,4$*;*
3. ***Direct Particle-Hole Channel*** Φ^d*: Cutting two propagators separates the labels* $1,3$ *from the labels* $2,4$*, and;*
4. ***Crossing Particle-Hole Channel*** Φ^c*: Cutting two propagators separates the labels* $1,4$ *from the labels* $2,3$*;*

and they are diagrammatically represented by squares with corresponding labels and two ingoing and two outgoing slots.

The contributions which are not reducible in a channel r *are called the* ***irreducible part in channel*** r *and are defined as* $\bar{\Phi}^r := \gamma^{(4)} - \Phi^r$*.*

The set of ***Parquet equations***

$$\gamma^{(4)} = \Phi^r + \bar{\Phi}^r \tag{3.138}$$

in combination with the set of ***Bethe-Salpeter equations*** *(BSE)*

$$\gamma^{(4)} = \bar{\Phi}^r + \bar{\Phi}^r (GG)^r \gamma^{(4)}, \tag{3.139}$$

for $r \in \{p,\ d,\ c\}$ *is called the* ***Parquet approach****. The approximation* $\Lambda = V_\circ$ *in the Parquet approach is called* ***Parquet approximation****.*

A contribution which is reducible in one channel (i.e. it belongs to Φ^{r}) is irreducible in the other ones (i.e. it belongs to $\bar{\Phi}_{\mathrm{r}'\neq\mathrm{r}}$) so that the decomposition of the contributions into the different channels is unique. Therefore the Parquet approach, which is represented in form of diagrams in figure 3.7, provides a full self-consistent set of equations to obtain the full two-particle interaction $\gamma^{(4)}$. The BSE (cf. eq. (3.139)) generates all the contributions of the corresponding channel, that is all the contributions which are two-particle reducible in this channel. As a connection of two full vertices $\gamma^{(4)}$ would lead to a double-counting of ladder-type diagrams, the full vertex $\gamma^{(4)}$ is connected to the irreducible part $\bar{\Phi}^{\mathrm{r}}$ of this channel. But as the irreducible part of channel r $\bar{\Phi}^{\mathrm{r}}$ is obtained by all the contributions from channels $\mathrm{r}' \neq \mathrm{r}$, the BSEs of the other channels are required to be solved beforehand. This can still be resolved by a self-consistency condition including all the contributions. However, due to the corresponding iterative character the contributions from the previous iteration have to be removed to avoid a double-counting. This problem can be solved by reformulating the equation based on $\Phi^{\mathrm{r}} = \gamma^{(4)} - \bar{\Phi}^{\mathrm{r}}$ into

$$\Phi^{\mathrm{r}} = \bar{\Phi}^{\mathrm{r}} (GG)^{\mathrm{r}} \gamma^{(4)}, \tag{3.140}$$

so that only the reducible parts are calculated for each channel. Due to the Parquet equation (cf. eq. (3.137)), the full interaction consists of all these contributions, such that this set of three BSEs constitutes a simpler self-consistent approach, which avoids double-counting right from the beginning. At the same time, the self-energy and this two-particle effective interaction form another self-consistent set of equations, as the full propagators in the BSE (3.140) includes the self-energy. The connected two-particle Green's function now is obtained by adding full propagators to the four legs of the two-particle interaction. As the discussion of the diagrams is based on two-particle interactions, all the Green's functions of higher order will be based on combinations of two-particle effective interactions and full propagators.

This Parquet approach was proposed by De Dominicis and Martin in 1964 [30, 31] and was applied to the Kondo model by Abrikosov [87]. Although this set of equations remains numerically difficult it was used for some basic investigations especially of the Hubbard model [88, 89, 90]. However, due to the complexity, additional approximations are very common and have to be chosen appropriately for the physical problem. Taking the initial interaction from a dynamical mean field theory calculation leads to the DΓA approach developed by Rohringer [82, 91]. A replacement of all the interactions by the bare interaction leads to the fluctuating exchange (FLEX) method [92, 93, 94], which contains all the channel contributions in a ladder form.

A different approach based on one-particle properties is provided by the Hedin equations [26], which are defined in definition 32 and are depicted in figure 3.8.

Definition 32 (Hedin Equations)
Let $V_\circ$ be a local interaction between two particles, i.e. $V_\circ(1^+, 2)$. Let $\tilde{G}_0$ be the non-interacting Green's function with respect to the one-particle Hamiltonian including the Hartree potential $H_0(1) + V_\circ(1,2)G(2;2^+)$, and let Σ_{xc} be the self-energy excluding the Hartree contribution. Then the set of equations

$$G(1;2) = G_0(1;2) + G_0(1;\tilde{1})\Sigma_{xc}(\tilde{1};\tilde{2})G(\tilde{2};2), \tag{3.141}$$

$$\Sigma_{xc}(1;2) = iG(1;\tilde{1})W(1^+;\tilde{2})\tilde{\Gamma}(\tilde{1};2;\tilde{2}), \tag{3.142}$$

$$W(1;2) = V_\circ(1;2) + V_\circ(1;\tilde{1})P(\tilde{1};\tilde{2})W(\tilde{2};2), \tag{3.143}$$

$$P(1;2) = -iG(1;\tilde{1})G(\tilde{2};1)\tilde{\Gamma}(\tilde{1};\tilde{2};2), \tag{3.144}$$

$$\tilde{\Gamma}(1;2;3) = \delta(1;2)\delta(1;3) + \frac{\delta\Sigma_{xc}(1;2)}{\delta G(\tilde{1};\tilde{2})}G(\tilde{1};\tilde{3})G(\tilde{4};\tilde{2})\tilde{\Gamma}(\tilde{3};\tilde{4};3) \tag{3.145}$$

*is called **Hedin Equations** in imaginary time. W is called **screened interaction** and P is called **polarisability**.*

This set of equations is focusing on the screening of the bare Coulomb interaction by electron-hole pairs, which plays an important role in solids and, therefore, treats those explicitly in terms of the polarisability (cf. eq. (3.144)) and the screened interaction (cf. eq. (3.143)). This, however, corresponds to the direct electron-hole channel of the Parquet approach, in which the dependence of the Coulomb interaction on only two spatial coordinates and its instantanity is exploited. All the other channels, the non-local and the non-instantaneous interactions are generated by the three-point interaction $\tilde{\Gamma}$.

The Hedin equations are usually derived by the Schwinger functional derivative technique, and the Feynman diagrams we presented here are only used to illustrate and classify the corresponding results. In the analytical derivation a time-dependent test-potential φ is introduced and set to zero after the calculation. Its effect on the Green's function and the effective potential gives rise to the set of Hedin equations [26, 95]. Obviously, the set of Hedin equations has to be treated self-consistently, which is, in general, not possible, as the functional derivative of the self-energy in the equation for the three-point vertex can not be treated in an exact way, neither analytically nor numerically.

The simplest approximation is $\tilde{\Gamma}(1;2;3) = \delta(1;2)\delta(1;3)$. When inserted into the self-energy equation it becomes $\Sigma(1;2) = G(1;2)W(1^+;2)$, from which the name GW**-approximation** is derived. In this approximation the polarisability becomes

$$P(1;2) = G(1;2)G(2;1), \tag{3.146}$$

so that the screened interaction is a pure screening of the full interaction by electron-hole terms. An approximation of this form for the interaction is called **random-phase approximation**, which is always present in the GW-approximation. The calculation of band structures based on this approach is, by now, a standard in solid state theory and is implemented in several codes for *ab initio* calculations [96, 97]. In contrast to the density functional theory (DFT) [24, 25], the resulting band structures are physically meaningful and do not result from an effective one-particle problem. Calculations based

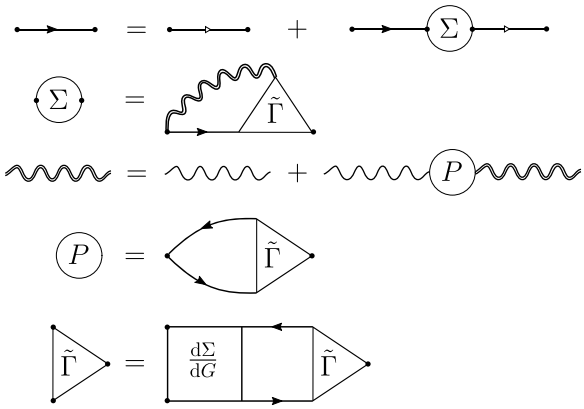

Figure 3.8.: Diagrammatic representation of the full set of Hedin equations. Due to the locality in space and time, the bare (effective) interaction is collapsed to a (double) wave line.

on the GW-approximation therefore provide significantly better results for the electronic structure of materials compared to the Kohn-Sham bands obtained by DFT. However, in the case of strongly correlated materials there is still a significant difference between experimentally measured properties and the GW-based results. This can be achieved by iterating the self-consistent set of Hedin equations to generate an expansion of the self-energy in terms of the screened interaction [26, 98]. The GW-approximation therefore accounts for the first order. The second order expression requires the first order three-point interaction. The insertion of the first order Σ into the functional derivative results in $W + G\frac{\delta W}{\delta G}$ of which only the first one contributes to the first order, as the second term generates a second order contribution in W. The third order contribution to Σ then consists of the $G\frac{\delta W}{\delta G}$ part of the derivative of the first order Σ combined with the zeroth order Γ, the W part of the first order Σ combined with first order Γ and the derivative of the second order Σ combined with the zeroth order Γ. As the expansion becomes more involved in the following orders, this can best be represented by diagrams (cf. app. of [26]).

For an efficient calculation different contributions appearing in the expansions are typically combined to an effective four point interaction called T-matrix [29, 99]. Due to the different contributions a T-matrix can be defined for each channel which can be calculated independently by a BSE. Therefore, it can be seen as an intermediate method between the GW-approximation and the Parquet approach. These additional contributions to the self-energy become important for physical effects close to completely filled or to completely empty bands, so that current research aims at adding them to *ab initio* calculations in the context of the GW-approximation. With this insight it has been shown that magnons have an effect on the band-structure of iron, cobalt and nickel [100, 46].

The presented perturbation expansion in terms of interactions is, due to its character, limited to weak interactions. However, with the different approximations it provides one possibility of calculating the full interacting Green's function as well as the partition function of the system. As the physical observables of correlations are the susceptibilities, we regard their relation in the following.

3.3. Fermionic Bilinears and Susceptibilities

As the fermionic bilinears and the susceptibilities set up by them are rarely discussed in literature we discuss their theoretical background at this point and repeat the corresponding definitions for the sake of completeness. The susceptibilities we are interested in are based on the fermionic bilinears of the charge, the spin and the pairing operators as provided by definition 21. Here, we generalise the corresponding definitions to non-local density- and spin-operators and to a generalised pairing operator as

$$\hat{\rho}_n(1,2) = \sum_s \hat{c}_s^\dagger(1)\hat{c}_s(2)\, f_n(1,2), \tag{3.147}$$

$$\hat{S}_n^i(1,2) = \frac{1}{2}\sum_{s,s'} \hat{c}_s^\dagger(1)\sigma_{ss'}^i\hat{c}_{s'}(2)\, f_n(1,2) \quad \text{and} \tag{3.148}$$

$$\hat{p}_n(1,2) = \hat{c}_{s_1}(1)\hat{c}_{s_2}(2)\, f_n(1,2). \tag{3.149}$$

The form-factor f_n allows all possible combinations of the corresponding creation and annihilation operators and can, therefore, be used for a spatial characterisation of the operator. To obtain susceptibilities of these generalised operators in analogy to those in equations (3.5)-(3.7) we have to combine the operators with their adjoint, as the expectation value will otherwise be zero. Thus, the charge-density χ_{cd}, the spin-density χ_{sd} or the pairing susceptibility χ_{p} are given by

$$\chi_{\mathrm{cd},nn'}(1,2) := \langle\hat{\rho}_n(1,2)\hat{\rho}_{n'}^\dagger(1,2)\rangle, \tag{3.150}$$

$$\chi_{\mathrm{sd},nn'}^{ij}(1,2) := \langle\hat{S}_n^i(1,2)(\hat{S}_{n'}^j)^\dagger(1,2)\rangle \quad \text{and} \tag{3.151}$$

$$\chi_{\mathrm{p},nn'}(1,2) := \langle\hat{p}_n(1,2)\hat{p}_{n'}^\dagger(1,2)\rangle, \tag{3.152}$$

respectively. A special case of the spin-density susceptibility is the magnetic-density susceptibility χ_{md} (cf. [66]) given by

$$\chi_{\mathrm{md},nn'}(1,2) := \chi_{\mathrm{sd},nn'}^{zz}(1,2) = \langle\hat{S}_n^z(1,2)(\hat{S}_{n'}^z)^\dagger(1,2)\rangle. \tag{3.153}$$

Due to the translational symmetry of the lattice it is useful to transform the bilinears to momentum space, resulting in

$$\hat{\rho}_n(q) = \frac{1}{\beta|\mathcal{B}|}\sum_s \int \mathrm{d}k\; \hat{c}_s(k)\hat{c}_s^\dagger(k+q) f_n(k,q), \tag{3.154}$$

$$\hat{S}_n^i(q) = \frac{1}{\beta|\mathcal{B}|}\frac{1}{2}\sum_{ss'} \int \mathrm{d}k\; \hat{c}_s(k)\sigma_{ss'}^i\hat{c}_{s'}^\dagger(k+q) f_n(k,q) \quad \text{and} \tag{3.155}$$

$$\hat{p}_{n,ss'}(q) = \frac{1}{\beta|\mathcal{B}|}\int \mathrm{d}k\; \hat{c}_s^\dagger(k)\hat{c}_{s'}^\dagger(q-k) f_n(k,q). \tag{3.156}$$

For convenience we only choose form-factors which are static and which solely depend on the fermionic momentum, that is $f_n(\boldsymbol{k},\boldsymbol{q}) = f_n(\boldsymbol{k})$, as they already provide a full set of basis functions (cf. sec. 3.6). When we consider the susceptibilities in momentum space, the transfer-momentum $\boldsymbol{q}$ has to be equal in both bilinears according to the same argument as in lattice space. Therefore the susceptibilities are momentum conserving. Moreover, $\boldsymbol{q}$ is a bosonic momentum, as it results from the difference between two fermionic momenta. A similar consideration focusing on the translational symmetry with respect to time leads to the dependence on a bosonic frequency ν, so that the sus-

ceptibilities depend on the generalised bosonic momentum $q = (\nu, \boldsymbol{q})$. As four fermionic creation and annihilation operators appear in all the different susceptibilities and as the total spin s_b of a susceptibility is the sum of them it is bosonic. Hence the susceptibilities behave as bosonic objects.

The generalised form of the one-particle operators also introduces a dependence on two form-factor indices. As those form-factors describe the spatial character of the particle pairs, they allow us to categorise, for example, instabilities in terms of an s- or a d-wave character (cf. sec. 4.2).

The explicit form of the density or of the magnetic susceptibility in terms of creation and annihilation operators reveals that both of them are different linear combinations of the same terms consisting of two creation and of two annihilation operators, *i.e.*

$$\begin{aligned}\chi_{\mathrm{cd/md},nn'} = a\, f_n(1,2)\, f_n^*(1,2)\, \Big(&\Big\langle \hat{c}_\uparrow^\dagger(1)\, \hat{c}_\uparrow(1)\, \hat{c}_\uparrow^\dagger(2)\, \hat{c}_\uparrow(2) \Big\rangle + \Big\langle \hat{c}_\downarrow^\dagger(1)\, \hat{c}_\downarrow(1)\, \hat{c}_\downarrow^\dagger(2)\, \hat{c}_\downarrow(2) \Big\rangle \\ &\pm \Big\langle \hat{c}_\uparrow^\dagger(1)\, \hat{c}_\downarrow(1)\, \hat{c}_\downarrow^\dagger(2)\, \hat{c}_\uparrow(2) \Big\rangle \pm \Big\langle \hat{c}_\downarrow^\dagger(1)\, \hat{c}_\downarrow(1)\, \hat{c}_\uparrow^\dagger(2)\, \hat{c}_\uparrow(2) \Big\rangle \Big)\,, \end{aligned} \tag{3.157}$$

with a constant a, where the upper line corresponds to χ_{cd} and the lower one to χ_{md}. Therefore, when the four different two-particle expectation values required for the charge susceptibility χ_{cd} (cf. eq. (3.150)) and for the magnetic susceptibility χ_{md} (cf. eq. (3.153)) are directly calculated they can be combined to either of the two susceptibilities. Due to this similarity and as χ_{md} is the z-spin-density wave, we use the extended spin-vector. That is, it includes the identity matrix as zeroth component such that $\hat{S}^0 = \hat{\rho}$, which leads to $\chi_{\mathrm{cd}} = \chi_{\mathrm{sd}}^{00}$. Treating the x- and the y-spin-density waves in the same way as $\chi_{\mathrm{cd/md}}$ in equation (3.157) one observes that χ_{sd}^{xx} and χ_{sd}^{yy} are different linear combinations of the same terms, too. A corresponding treatment of the other possible combinations of the spin operators $\hat{S}^{i\in\{0,x,y,z\}}$ leads to similar combinations, each consisting of four different terms, which differ by prefactor signs after changing between x- and y- or between 0- and z- spin components. As all the different terms in the susceptibilities are different linear combinations of the expectation values of creation and annihilation operator pairs, we combine them in a matrix:

$$\begin{pmatrix} \langle \hat{c}_\uparrow^\dagger \hat{c}_\downarrow \hat{c}_\downarrow^\dagger \hat{c}_\uparrow \rangle & \langle \hat{c}_\uparrow^\dagger \hat{c}_\downarrow \hat{c}_\uparrow^\dagger \hat{c}_\downarrow \rangle & \langle \hat{c}_\uparrow^\dagger \hat{c}_\downarrow \hat{c}_\downarrow^\dagger \hat{c}_\downarrow \rangle & \langle \hat{c}_\uparrow^\dagger \hat{c}_\downarrow \hat{c}_\uparrow^\dagger \hat{c}_\uparrow \rangle \\ \langle \hat{c}_\downarrow^\dagger \hat{c}_\uparrow \hat{c}_\downarrow^\dagger \hat{c}_\uparrow \rangle & \langle \hat{c}_\downarrow^\dagger \hat{c}_\uparrow \hat{c}_\uparrow^\dagger \hat{c}_\downarrow \rangle & \langle \hat{c}_\downarrow^\dagger \hat{c}_\uparrow \hat{c}_\downarrow^\dagger \hat{c}_\downarrow \rangle & \langle \hat{c}_\downarrow^\dagger \hat{c}_\uparrow \hat{c}_\uparrow^\dagger \hat{c}_\uparrow \rangle \\ \langle \hat{c}_\downarrow^\dagger \hat{c}_\downarrow \hat{c}_\downarrow^\dagger \hat{c}_\uparrow \rangle & \langle \hat{c}_\downarrow^\dagger \hat{c}_\downarrow \hat{c}_\uparrow^\dagger \hat{c}_\downarrow \rangle & \langle \hat{c}_\downarrow^\dagger \hat{c}_\downarrow \hat{c}_\downarrow^\dagger \hat{c}_\downarrow \rangle & \langle \hat{c}_\downarrow^\dagger \hat{c}_\downarrow \hat{c}_\uparrow^\dagger \hat{c}_\uparrow \rangle \\ \langle \hat{c}_\uparrow^\dagger \hat{c}_\uparrow \hat{c}_\downarrow^\dagger \hat{c}_\uparrow \rangle & \langle \hat{c}_\uparrow^\dagger \hat{c}_\uparrow \hat{c}_\uparrow^\dagger \hat{c}_\downarrow \rangle & \langle \hat{c}_\uparrow^\dagger \hat{c}_\uparrow \hat{c}_\downarrow^\dagger \hat{c}_\downarrow \rangle & \langle \hat{c}_\uparrow^\dagger \hat{c}_\uparrow \hat{c}_\uparrow^\dagger \hat{c}_\uparrow \rangle \end{pmatrix}, \tag{3.158}$$

in which we omitted, for the sake of brevity, the form-factors $f_n(k) f_{n'}^*(k')$ and the arguments which have the form $\hat{c}^\dagger(k)\hat{c}(k+q)\hat{c}^\dagger(k')\hat{c}(k'+q)$ in all the terms. According to the previous discussion, this matrix splits into four 2×2-blocks where the expectation values of $\hat{\boldsymbol{S}}^x$ and of $\hat{\boldsymbol{S}}^y$ are obtained from linear combinations of the upper left one, while the lower right one can be combined to form those of $\hat{\boldsymbol{S}}^0$ and $\hat{\boldsymbol{S}}^z$. The lower left and the upper right part of it contain the combinations of both pairs.

A further analysis of the contributing terms reveals that the matrix elements can equally be reformulated in terms of the generalised spin-density operators

$$\begin{aligned} \hat{n}_{\uparrow,n}(1,2) &:= f_n(1,2)\, \hat{c}_\uparrow^\dagger(1)\hat{c}_\uparrow(2) \qquad \text{and} \\ \hat{n}_{\downarrow,n}(1,2) &:= f_n(1,2)\, \hat{c}_\downarrow^\dagger(1)\hat{c}_\downarrow(2) \end{aligned} \tag{3.159}$$

and the operators

$$\begin{aligned} \hat{S}_n^+(1,2) &:= f_n(1,2) \left(\hat{S}^x(1,2) + i\hat{S}^y(1,2) \right) = f_n(1,2) \left(\hat{c}_\uparrow^\dagger(1)\hat{c}_\downarrow(1) \right) \qquad \text{and} \\ \hat{S}_n^-(1,2) &:= f_n(1,2) \left(\hat{S}^x(1,2) - i\hat{S}^y(1,2) \right) = f_n(1,2) \left(\hat{c}_\downarrow^\dagger(1)\hat{c}_\uparrow(1) \right) . \end{aligned} \tag{3.160}$$

That is, the lines of the matrix (3.158) correspond to $\hat{S}^+$, $\hat{S}^-$, $\hat{n}_\downarrow$ and $\hat{n}_\uparrow$ and the elements reflect the expectation values of their combinations.

In a spin-symmetric system the creation and the annihilation operators corresponding to the same argument need to have the same spin if their contribution shall not vanish, as it is preserved by the Hamiltonian. Therefore, only the lower right 2×2-block of the matrix (3.158) is non-zero and, therefore, only the magnetic- and the charge-density susceptibilities do not vanish.

The pairing susceptibility, as defined above, depends on both pairs of spins of the inserted pairing bilinears so that all spin combinations are possible. In analogy to the charge- and the spin-density case presented above, we combine all the possible contributions in a matrix:

$$\begin{pmatrix} \langle \hat{c}_\uparrow \hat{c}_\downarrow \hat{c}^\dagger_\downarrow \hat{c}^\dagger_\uparrow \rangle & \langle \hat{c}_\uparrow \hat{c}_\downarrow \hat{c}^\dagger_\uparrow \hat{c}^\dagger_\downarrow \rangle & \langle \hat{c}_\uparrow \hat{c}_\downarrow \hat{c}^\dagger_\downarrow \hat{c}^\dagger_\downarrow \rangle & \langle \hat{c}_\uparrow \hat{c}_\downarrow \hat{c}^\dagger_\uparrow \hat{c}^\dagger_\uparrow \rangle \\ \langle \hat{c}_\downarrow \hat{c}_\uparrow \hat{c}^\dagger_\downarrow \hat{c}^\dagger_\uparrow \rangle & \langle \hat{c}_\downarrow \hat{c}_\uparrow \hat{c}^\dagger_\uparrow \hat{c}^\dagger_\downarrow \rangle & \langle \hat{c}_\downarrow \hat{c}_\uparrow \hat{c}^\dagger_\downarrow \hat{c}^\dagger_\downarrow \rangle & \langle \hat{c}_\downarrow \hat{c}_\uparrow \hat{c}^\dagger_\uparrow \hat{c}^\dagger_\uparrow \rangle \\ \langle \hat{c}_\downarrow \hat{c}_\downarrow \hat{c}^\dagger_\downarrow \hat{c}^\dagger_\uparrow \rangle & \langle \hat{c}_\downarrow \hat{c}_\downarrow \hat{c}^\dagger_\uparrow \hat{c}^\dagger_\downarrow \rangle & \langle \hat{c}_\downarrow \hat{c}_\downarrow \hat{c}^\dagger_\downarrow \hat{c}^\dagger_\downarrow \rangle & \langle \hat{c}_\downarrow \hat{c}_\downarrow \hat{c}^\dagger_\uparrow \hat{c}^\dagger_\uparrow \rangle \\ \langle \hat{c}_\uparrow \hat{c}_\uparrow \hat{c}^\dagger_\downarrow \hat{c}^\dagger_\uparrow \rangle & \langle \hat{c}_\uparrow \hat{c}_\uparrow \hat{c}^\dagger_\uparrow \hat{c}^\dagger_\downarrow \rangle & \langle \hat{c}_\uparrow \hat{c}_\uparrow \hat{c}^\dagger_\downarrow \hat{c}^\dagger_\downarrow \rangle & \langle \hat{c}_\uparrow \hat{c}_\uparrow \hat{c}^\dagger_\uparrow \hat{c}^\dagger_\uparrow \rangle \end{pmatrix}, \tag{3.161}$$

with the argument structure $\hat{c}(k)\hat{c}(q-k)\hat{c}^\dagger(k')\hat{c}^\dagger(q-k')$ for all the terms. In this matrix representation we observe a similar block structure and spin combination structure as in the spin-density case. When we consider the lower right 2×2-block of elements, which is built from pairing operators with equal spins, that is $\hat{p}_{ss}$, we observe that the spin is conserved on the diagonal ones while it is flipped on the other ones. Therefore, in the case of an SU(2)-symmetry, only the diagonal ones will be non-zero. We also can identify the diagonal elements to belong to a triplet pairing with a total spin $s_b = 1$ and a total magnetic momentum $m_b = \pm 1$. The upper left 2×2-block is based on the pairing operators with opposite spins, that is $\hat{p}_{s\bar{s}}$ with $\bar{s} = -s$. Therefore, the sum over these elements results in the triplet pairing susceptibility with the total magnetic moment $m_b = 0$. To obtain singlet pairing, that is with the total spin $s_b = 0$ and the total magnetic moment $m_b = 0$, we need to subtract the second line from the first one. The upper right and the lower left block, again, are combinations of the singlet- and the triplet-pairing operators. Like in an SU(2)-symmetric system non-vanishing terms have to have the same number of creation operators and of annihilation operators for each spin direction, as the Hamiltonian preserves the spin. Thus, only the upper left block and the diagonal part of the lower right block are non-zero, so that it is sufficient to consider the singlet and the triplet pairings.

As the different susceptibilities depend on a characteristic combination of fermion operators, we denote those consisting of a creation and of an annihilation operator as electron-hole (eh) fermion-bilinear, those consisting of two annihilation operators as hole-hole (hh) fermion-bilinear and those consisting of two creation operators as electron-electron (ee) fermion-bilinear. Both, hh and ee fermion-bilinears obviously belong to the class of pairing bilinears.

To investigate the question whether the system approaches an ordered state, we have to observe if the corresponding static susceptibility shows a divergence. In the case of a charge-density wave state the static susceptibility resulting from the sum of the four elements of the lower right block of the spin-susceptibility matrix diverges. The $\boldsymbol{q}$-vector corresponding to the divergence defines the wave-vector of the density-wave, while the form-factors $f_n(q, p)$ define their symmetry in momentum space. This symmetry can exemplarily be shown for the two-dimensional case on a square lattice: The susceptibility is said to have the character of an s-wave, when a rotation in the plane is not changing its value. It is said to have a $d_{x^2-y^2}$-wave character, when the values differ by the factor of -1 under a rotation of $\pi/2$. Similar considerations hold for the magnetic susceptibility, which consists of the same sub-matrix, but with alternating signs according to equal or unequal spin polarisations. This susceptibility indicates an (anti-)ferromagnetic ordering, spin-density-waves and nematic states

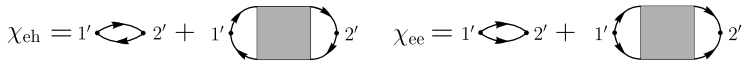

Figure 3.9.: Diagrammatic representation of the electron-hole (left) and electron-electron (right) susceptibility.

resulting from Pomeranchuk instabilities. Similarly, the system is in a spin-singlet or in a spin-triplet pairing state when, according to the pairing matrix, the sum of the corresponding pairing susceptibilities with total spin $s_b = 0$ or $s_b = \pm 1$ shows a divergence.

All the elements of both susceptibility matrices above can be obtained from the generalised susceptibility, so that the two-particle Green's function can be used to calculate them. As the two-particle Green's function depends on four arguments, while the susceptibilities discussed here only depend on two of them, the correct limits have to be taken, as discussed subsequent to definition 22. Diagrammatically this corresponds to connecting the two legs of the two-particle Green's function with each other. When we employ the results from the perturbation theory at this point, we obtain the susceptibilities as

$$\chi_{\mathrm{eh}}(1';2') = G(1;2)G(2^-;1^-)+ \tag{3.162}$$

$$\int \mathrm{d}\tilde{1} \cdots \int \mathrm{d}\tilde{4}\, G(1;\tilde{1})\, G(2;\tilde{2})\, \gamma^{(4)}(\tilde{1},\tilde{2};\tilde{3},\tilde{4})\, G(\tilde{3};1^-)\, G(\tilde{3},2^-) \quad \text{and} \tag{3.163}$$

$$\chi_{\mathrm{ee}}(1';2') = f_n(1;2;1')G(1;2)G(1^-;2^-)+ \tag{3.164}$$

$$\int \mathrm{d}\tilde{1} \cdots \int \mathrm{d}\tilde{4}\, G(1;\tilde{1})\, G(1^-;\tilde{2})\, \gamma^{(4)}(\tilde{1},\tilde{2};\tilde{3},\tilde{4})\, G(\tilde{3};2^-)\, G(\tilde{3},2^-). \tag{3.165}$$

Thus, the susceptibilities consist of a loop of two propagators plus a two-particle interaction that has two pairs of propagators connected to each other. In the case of (spin-) density-susceptibilities the incoming legs of the interaction are pairwise connected to the outgoing legs, while for pairing susceptibilities both incoming and both outgoing legs are connected to each other as illustrated in figure 3.9. In the SU(2)-symmetric case, both connected pairs differ by the same bosonic spin s_b, while in the general case the susceptibility can have different bosonic spins for the two propagator pairs.

The contributions of the propagator loop only contain one-particle contributions and usually diverge at $T = 0$ (or at $\Lambda = 0$ in the FRG case, cf. sec. 3.5), while the second one contains the effects of particles interacting with each other, as it includes the two-particle interactions $\gamma^{(4)}$. Therefore, the second term is the relevant part to observe real phase transitions at finite T caused by correlation effects. The FRG thus aims at a direct calculation of this two-particle interaction. The FRG also allows a direct calculation of the susceptibilities, such that we define the generating functionals for both, for fermionic interactions and for susceptibilities based on fermionic bilinears in the following.

3.4. Generating Functionals

In the preceding section we observed that the two-particle interaction is a relevant term for the occurrence of phases based on many-particle effects. For the FRG equations, the field theory is employed, which basically replaces the creation and the annihilation operators by the corresponding Grassmann variables in the expectation values. Thus the definitions and the derivations of the previous sections can be performed analogously. We remark, however, that no time-ordering operator appears in the field-theoretical definition of Green's functions, as the functional integral always represents time-ordered products.

It is well known that expectation values of observables like particle number, magnetisation or entropy can be obtained as derivatives of the grand canonical partition function. For the particle number operator $\hat{N}$, for example,

$$\langle \hat{N} \rangle = \frac{1}{\beta} \frac{\partial \ln \mathcal{Z}}{\partial \mu} \tag{3.166}$$

holds, so that the grand canonical partition function can be viewed as the generating functional of the particle expectation value. The aim of this section is to generalise this observation and find similar generating functionals for the Green's functions, its connected sibling or the effective action by corresponding derivatives. These generating functionals will provide a simple generic form for further calculations. For all the following derivations and definitions we let $\bar{\psi},\ \psi$ be Grassmann fields and let $\mathcal{S}[\bar{\psi}, \psi] = (\bar{\psi}, G_0^{-1}\psi) + V[\bar{\psi}, \psi]$ be the action as defined in definition 10. Based on these prerequisites we define as follows:

Definition 33 (Generating Functional for Green's Functions)
The functional

$$\mathcal{G}[\eta, \bar{\eta}] := \frac{1}{\mathcal{Z}} \int \mathcal{D}[\psi, \bar{\psi}] \, \exp\left(-\mathcal{S}[\bar{\psi}, \psi]\right) \, \exp\left((\bar{\eta}, \psi) + (\bar{\psi}, \eta)\right) \tag{3.167}$$

is called the ***generating functional for Green's functions*** *and the fields $\bar{\eta}, \eta$ are called* ***source fields****.*

Theorem 3.14 (Generation of n-particle Imaginary Time Green's Functions)
The generating functional $\mathcal{G}$ as defined in definition 33 generates all imaginary time n-particle Green's functions.

Proof: The differentiation of $\mathcal{G}$ by the source fields η and $\bar{\eta}$ results in

$$\begin{aligned} \frac{\delta \mathcal{G}[\bar{\eta}, \eta]}{\delta \eta(1)} &= -\frac{1}{\mathcal{Z}} \int \mathcal{D}[\bar{\psi}, \psi] \, e^{-\mathcal{S}[\bar{\psi}, \psi]} \, \bar{\psi}(1) \, e^{(\bar{\eta}, \psi) + (\bar{\psi}, \eta)} = -\left\langle \bar{\psi}(1) \right\rangle |_{\bar{\eta}=\eta=0} \quad \text{and} \\ \frac{\delta \mathcal{G}[\bar{\eta}, \eta]}{\delta \bar{\eta}(1)} &= \frac{1}{\mathcal{Z}} \int \mathcal{D}[\bar{\psi}, \psi] \, e^{-\mathcal{S}[\bar{\psi}, \psi]} \, \psi(1) \, e^{(\bar{\eta}, \psi) + (\bar{\psi}, \eta)} = \left\langle \psi(1) \right\rangle |_{\bar{\eta}=\eta=0} , \end{aligned} \tag{3.168}$$

respectively. Here, the thermal average, as discussed at the end of section 2.3, is identified for vanishing source fields. The corresponding expectation values will be zero, as Grassmann fields only give non-zero expectation values in pairs. To obtain those pairs the same number of η and $\bar{\eta}$ derivatives have

to be performed on the generating functional $\mathcal{G}$. Generalising this result and taking care of the minus sign resulting from the derivatives with respect to some η we obtain

$$G^{(2n)}(1,\ldots,2n) = (-1)^n \left.\frac{\delta^{2n}\mathcal{G}[\bar{\eta},\eta]}{\delta\bar{\eta}(1)\cdots\delta\bar{\eta}(n)\delta\eta(2n)\cdots\delta\eta(n+1)}\right|_{\bar{\eta}=\eta=0}, \tag{3.169}$$

where the source fields are set to zero at the end, so that only the real fermionic fields remain. Identifying the field expectation value with the definition of the Green's function (def. 23) completes the proof. ■

As mentioned in the discussion of Feynman diagrams, it is advantageous to consider only connected Green's functions (see def. 29), as, otherwise, some contributions are calculated several times. The corresponding generating functional is easily obtained from the general Green's function one.

Definition 34 (Generating Functional for Connected Green's Functions)
Let $\mathcal{G}$ be the generating functional for Green's functions as given in definition 33. Then the functional

$$\mathcal{W}[\bar{\eta},\eta] := -\ln\left(\frac{\mathcal{G}[\bar{\eta},\eta]}{\mathcal{Z}}\right) = -\ln\int\mathcal{D}[\bar{\psi},\psi]\,\exp\left(-\mathcal{S}[\bar{\psi},\psi]\right)\,\cdot\,\exp\left((\bar{\eta},\psi)+(\bar{\psi},\eta)\right) \tag{3.170}$$

is called ***generating functional for connected Green's functions****.*

In this definition the term $1/\mathcal{Z}$ removes the grand canonical partition function from the definition of $\mathcal{G}$ so that only the functional integral remains.

Theorem 3.15 (Generation of n-particle Connected Green's Functions)
The generating functional $\mathcal{W}$ as given in definition 34 generates all connected imaginary time n-particle Green's functions.

Proof: We will not give a full proof of this theorem, but we will exemplarily show that it holds for one- and for two-particle connected Green's functions. By differentiation with respect to the source fields $\bar{\eta}$ and η we obtain

$$\begin{aligned}
&-\frac{\delta^2}{\delta\bar{\eta}_1\delta\eta_2}\left[\ln\left\langle e^{(\bar{\eta},\psi)+(\bar{\psi},\eta)}\right\rangle\right]\Big|_{\eta=\bar{\eta}=0}\\
&=-\frac{\delta}{\delta\bar{\eta}_1}\left[\left\langle e^{(\bar{\eta},\psi)+(\bar{\psi},\eta)}\right\rangle^{-1}\left\langle\bar{\psi}_2 e^{(\bar{\eta},\psi)+(\bar{\psi},\eta)}\right\rangle\right]\Big|_{\eta=\bar{\eta}=0}\\
&=\left[\frac{\left\langle\psi_1 e^{(\bar{\eta},\psi)+(\bar{\psi},\eta)}\right\rangle\left\langle\bar{\psi}_2 e^{(\bar{\eta},\psi)+(\bar{\psi},\eta)}\right\rangle}{\left\langle e^{(\bar{\eta},\psi)+(\bar{\psi},\eta)}\right\rangle^2}\right]\Big|_{\eta=\bar{\eta}=0} - \frac{\left\langle\psi_1\bar{\psi}_2 e^{(\bar{\eta},\psi)+(\bar{\psi},\eta)}\right\rangle}{\left\langle e^{(\bar{\eta},\psi)+(\bar{\psi},\eta)}\right\rangle}\\
&=G_{\mathrm{c}}(1;2).
\end{aligned} \tag{3.171}$$

As we consider fermions, all the terms with an unequal number of creation and annihilation field operators vanish, and, therefore, only the second term in the second last line is non-zero. This term is identified as the one-particle Green's function, which equals the one-particle connected Green's function as discussed in the section on Feynman diagrams (cf. section 3.2.2).

For the more interesting two-particle case, we derive

$$
\begin{aligned}
&-\frac{\delta^4}{\delta\bar{\eta}_1\delta\bar{\eta}_2\delta\eta_4\delta\eta_3}\left[\ln\left\langle e^{(\bar{\eta},\psi)+(\bar{\psi},\eta)}\right\rangle\right]\Big|_{\eta=\bar{\eta}=0}\\
&=\frac{\delta^2}{\delta\bar{\eta}_1\delta\bar{\eta}_2}\left[\frac{\left\langle\bar{\psi}_4 e^{(\bar{\eta},\psi)+(\bar{\psi},\eta)}\right\rangle\left\langle\bar{\psi}_3 e^{(\bar{\eta},\psi)+(\bar{\psi},\eta)}\right\rangle}{\left\langle e^{(\bar{\eta},\psi)+(\bar{\psi},\eta)}\right\rangle^2}+\frac{\left\langle\bar{\psi}_4\bar{\psi}_3 e^{(\bar{\eta},\psi)+(\bar{\psi},\eta)}\right\rangle}{\left\langle e^{(\bar{\eta},\psi)+(\bar{\psi},\eta)}\right\rangle}\right]\Bigg|_{\eta=\bar{\eta}=0}\\
&=\left[\frac{\left\langle\psi_1\psi_2\bar{\psi}_4\bar{\psi}_3 e^{(\bar{\eta},\psi)+(\bar{\psi},\eta)}\right\rangle}{\left\langle e^{(\bar{\eta},\psi)+(\bar{\psi},\eta)}\right\rangle}\right.\\
&\quad\left.-\frac{\left\langle\psi_2\bar{\psi}_3 e^{(\bar{\eta},\psi)+(\bar{\psi},\eta)}\right\rangle\left\langle\psi_1\bar{\psi}_4 e^{(\bar{\eta},\psi)+(\bar{\psi},\eta)}\right\rangle-\left\langle\psi_1\bar{\psi}_3 e^{(\bar{\eta},\psi)+(\bar{\psi},\eta)}\right\rangle\left\langle\psi_2\bar{\psi}_4 e^{(\bar{\eta},\psi)+(\bar{\psi},\eta)}\right\rangle}{\left\langle e^{-(\bar{\eta},\psi)+(\bar{\psi},\eta)}\right\rangle^2}\right]\Bigg|_{\eta=\bar{\eta}=0}\\
&=G^{(4)}(1,2;4,3)-G(1;4)G(2;3)+G(2;4)G(1;3)\\
&=G_{\mathrm{c}}^{(4)}(1,2;4,3).
\end{aligned}
\tag{3.172}
$$

From the second to the third line, again, the vanishing of terms with an unequal number of creation and annihilation operators has been considered. The observation that the second last line equals the connected two-particle Green's function given in equation (3.134), completes this part of the proof. For Green's functions of higher order corresponding derivatives of higher order have to be calculated with respect to the commutation rules for Grassmann fields. ■

In section 3.3 we discussed that the effective interaction is the relevant part leading to phase transitions. For a definition of a generating functional for these terms, we have to take into account that the expectation values of the creation and the annihilation operators are non-zero when the source terms of $\mathcal{W}$ are present. These expectation values define new average fields by

$$
\phi_i(\bar{\eta},\eta) := \langle\psi_i\rangle_{\bar{\eta},\eta} = -\frac{\delta}{\delta\bar{\eta}_i}\mathcal{W}[\bar{\eta},\eta] \qquad \text{and} \qquad \bar{\phi}_i(\bar{\eta},\eta) := \langle\bar{\psi}_i\rangle_{\bar{\eta},\bar{\eta}} = \frac{\delta}{\delta\eta_i}\mathcal{W}[\bar{\eta},\eta]. \tag{3.173}
$$

An inversion of these relations leads to an expression for the source fields in terms of these new fields, that is $\eta(\bar{\phi},\phi)$ and $\bar{\eta}(\bar{\phi},\phi)$. The generating functional for the effective action can now be defined based on the Legendre transformation of $\mathcal{W}[\bar{\eta},\eta]$ with respect to the new average fields ϕ and $\bar{\phi}$.

Definition 35 (Generating Functional for the Effective Action)
Let $\mathcal{W}[\bar{\eta},\eta]$ be the generating functional for connected Green's functions and let ϕ and $\bar{\phi}$ be the average fields of the field variables ψ and $\bar{\psi}$, respectively, generated by $\mathcal{W}$ in the presence of sources η and $\bar{\eta}$ according to equation (3.173). *Then the* ***generating functional for the effective action*** *Γ is defined by the Legendre transformation of $\mathcal{W}$ with respect to the average fields, i.e.*

$$
\Gamma[\bar{\phi},\phi] := \mathcal{W}[\bar{\eta}(\bar{\phi},\phi),\eta(\bar{\phi},\phi)] + \left(\bar{\phi},\eta\right) + (\bar{\eta},\phi)\,. \tag{3.174}
$$

In analogy to the Green's functions the one-particle irreducible n-particle vertex functions are defined based on this generating functional.

Definition 36 (One-particle Irreducible n-particle Vertex Functions)
Let Γ, ϕ and $\bar{\phi}$ be as defined in definition 35. Then the ***one-particle irreducible*** *n-**particle vertex functions*** *are defined as*

$$\gamma^{2n}(1,\dots,2n) := \frac{\delta^{2n}\Gamma[\bar{\phi},\phi]}{\delta\bar{\phi}_1\cdots\delta\bar{\phi}_n\delta\phi_{2n}\cdots\delta\phi_{n+1}}\bigg|_{\phi=\bar{\phi}=0}. \tag{3.175}$$

Before we derive some properties and relations between both generating functionals we define the matrices of the derivatives of second order as helpful quantities.

Definition 37 (Matrices of the Second Order Derivatives)
Let η and $\bar{\eta}$ be source fields of $\mathcal{G}$ and let ϕ and $\bar{\phi}$ be the average fields of ψ and $\bar{\psi}$ as provided by definition 35. Then the second order derivatives are provided by the operators

$$\boldsymbol{\delta}^2_\eta(1,2) := \begin{pmatrix} -\delta_{\bar{\eta}_1}\delta_{\eta_2} & \delta_{\bar{\eta}_1}\delta_{\bar{\eta}_2} \\ \delta_{\eta_1}\delta_{\eta_2} & -\delta_{\eta_1}\delta_{\bar{\eta}_2} \end{pmatrix} \quad \text{and} \quad \boldsymbol{\delta}^2_\phi(1,2) := \begin{pmatrix} \delta_{\bar{\phi}_1}\delta_{\phi_2} & \delta_{\bar{\phi}_1}\delta_{\bar{\phi}_2} \\ \delta_{\phi_1}\delta_{\phi_2} & \delta_{\phi_1}\delta_{\bar{\phi}_2} \end{pmatrix}. \tag{3.176}$$

Based on these helpful operators and the two definitions above (def. 35 and def. 36) the following corollary is directly obtained.

Corollary 3.16 (Properties of the Generating Functional for Effective Action)
Let ϕ, $\bar{\phi}$, η, $\bar{\eta}$ and Γ be as given in definition 35. Then the following holds:

1. *The effective potential satisfies the reciprocity relations*

$$\begin{aligned} &\frac{\delta}{\delta\bar{\phi}}\Gamma[\bar{\phi},\phi] = \eta \quad \textit{and} \\ &\frac{\delta}{\delta\phi}\Gamma[\bar{\phi},\phi] = -\bar{\eta}. \end{aligned} \tag{3.177}$$

2. *The Legendre transformation of Γ is the generating functional $\mathcal{W}$.*
3. *In the absence of sources the effective action is stationary.*
4. *The matrices of the derivatives of second order of Γ and $\mathcal{W}$ are reciprocal to each other, i.e. $\boldsymbol{\delta}^2_{\bar{\phi}}\Gamma = (\boldsymbol{\delta}^2_\eta\mathcal{W})^{-1}$. This particularly implies $\boldsymbol{G} = (\boldsymbol{\gamma}^{(2)})^{-1}$*
5. *The self-energy Σ can be written as $\Sigma = G^{-1} - \gamma^{(2)}$.*
6. *The expansion of the generating functional Γ in Grassmann fields is given by*

$$\Gamma[\bar{\phi},\phi] = \sum_{n=0}^{\infty}\frac{(-1)^n}{(n!)^2}\gamma^{(2n)}(1,\dots,2n)\bar{\phi}_1\cdots\bar{\phi}_n\phi_{2n}\cdots\phi_{n+1}. \tag{3.178}$$

7. *The n-particle interactions $\gamma^{(2n)}$ are one-particle irreducible and for $n \geq 2$ given by*

$$\gamma^{(2n)} = (1)^n \sum_{k}^{\infty} \frac{1}{k! 2^k} \sum_{\substack{\pi \in \mathcal{S}_{n+2k} \\ \pi \text{ one-line-irreducible}}} Val_{amp}\,[n, k, \pi], \tag{3.179}$$

with Val_{amp} being the amputated Feynman diagrams defined by equation 3.126.

8. *The n-particle connected Green's functions $G^{(2n)}$ for $n \geq 2$ are related to the one-particle irreducible interactions $\gamma^{(2n)}$ by*

$$\begin{aligned} &G_c^{(2n)}(1, \ldots, 2n) \\ &\quad = (-1)^n G(1, \tilde{1}) \cdots G(n, \tilde{n})\, G(2n, \tilde{2n}) \cdots G(n+1, \widetilde{n+1}) \gamma^{(2n)}(\tilde{1}, \ldots, \tilde{2n}) + \mathcal{R} \end{aligned} \tag{3.180}$$

with $\mathcal{R}$ being the remainder which consists of all the tree diagrams built up by at least two interactions $\gamma^{(2m)}$ of order $m \leq n$ connected by propagators and which contains at least one torso line.

Proof: 1. By performing the differentiation, applying the chain rule and inserting the definition of the fields ϕ and $\bar{\phi}$, one directly obtains

$$\begin{aligned} \frac{\delta}{\delta \bar{\phi}_i} \Gamma[\bar{\phi}_i, \phi_i] &= \left(\frac{\delta \mathcal{W}}{\delta \eta_j}, \frac{\delta \eta_j}{\delta \bar{\phi}_i} \right) + \left(\frac{\delta \bar{\eta}_j}{\delta \bar{\phi}_i}, \frac{\delta \mathcal{W}}{\delta \bar{\eta}_j} \right) + \left(\frac{\delta \bar{\phi}_j}{\delta \bar{\phi}_i}, \eta_j \right) - \left(\bar{\phi}_j, \frac{\delta \eta_j}{\delta \bar{\phi}_i} \right) + \left(\frac{\delta \bar{\eta}_j}{\delta \bar{\phi}_i}, \phi_j \right) \\ &= \left(\bar{\phi}_j, \frac{\delta \eta_j}{\delta \bar{\phi}_i} \right) - \left(\frac{\delta \bar{\eta}_j}{\delta \bar{\phi}_i}, \phi_j \right) + \eta_i - \left(\bar{\phi}_j, \frac{\delta \eta_j}{\delta \bar{\phi}_i} \right) + \left(\frac{\delta \bar{\eta}_j}{\delta \bar{\phi}_i}, \phi_j \right) \\ &= \eta_i, \end{aligned} \tag{3.181}$$

which is the desired result. Remark that we implicitly assumed a summation over the indices appearing twice. An analogous calculation for the field ϕ results in the companion equation.

2. Due to the definition of Γ and to the reciprocity relations of the fields as provided by corollary 3.16.1, $\mathcal{W}$ is the Legendre transformation of Γ according to

$$\mathcal{W}[\bar{\eta}, \eta] = \Gamma[\bar{\phi}(\bar{\eta}, \eta), \phi(\bar{\eta}, \eta)] - (\bar{\eta}, \phi) - \left(\bar{\phi}, \eta\right). \tag{3.182}$$

3. In the absence of sources, the reciprocity relations in corollary 3.16.1 are equal to zero. Therefore, the generating functional does not change with respect to fields and thus is stationary in this case.

4. The calculation of the derivatives of the average fields and the use of the chain rule result in

$$\begin{aligned} \delta(3,1) = \frac{\delta \phi_3}{\delta \phi_1} &= \frac{\delta}{\delta \phi_1} \left[-\frac{\delta \mathcal{W}}{\delta \bar{\eta}_3} \right] = -\left(\frac{\delta^2 \mathcal{W}}{\delta \bar{\eta}_3 \delta \eta_2}, \frac{\delta^2 \Gamma}{\delta \bar{\phi}_2 \delta \phi_1} \right) + \left(\frac{\delta^2 \mathcal{W}}{\delta \bar{\eta}_3 \delta \bar{\eta}_2}, \frac{\delta^2 \Gamma}{\delta \phi_2 \delta \phi_1} \right) \\ \delta(3,1) = \frac{\delta \bar{\phi}_3}{\delta \bar{\phi}_1} &= \frac{\delta}{\delta \bar{\phi}_1} \left[\frac{\delta \mathcal{W}}{\delta \eta_3} \right] = \left(\frac{\delta^2 \mathcal{W}}{\delta \eta_3 \delta \eta_2}, \frac{\delta^2 \Gamma}{\delta \bar{\phi}_2 \delta \bar{\phi}_1} \right) - \left(\frac{\delta^2 \mathcal{W}}{\delta \eta_3 \delta \bar{\eta}_2}, \frac{\delta^2 \Gamma}{\delta \phi_2 \delta \bar{\phi}_1} \right) \\ 0 = \frac{\delta \phi_3}{\delta \bar{\phi}_1} &= \frac{\delta}{\delta \bar{\phi}_1} \left[-\frac{\delta \mathcal{W}}{\delta \bar{\eta}_3} \right] = -\left(\frac{\delta^2 \mathcal{W}}{\delta \bar{\eta}_3 \delta \eta_2}, \frac{\delta^2 \Gamma}{\delta \bar{\phi}_2 \delta \bar{\phi}_1} \right) + \left(\frac{\delta^2 \mathcal{W}}{\delta \bar{\eta}_3 \delta \bar{\eta}_2}, \frac{\delta^2 \Gamma}{\delta \phi_2 \delta \bar{\phi}_1} \right) \\ 0 = \frac{\delta \bar{\phi}_3}{\delta \phi_1} &= \frac{\delta}{\delta \phi_1} \left[\frac{\delta \mathcal{W}}{\delta \eta_3} \right] = \left(\frac{\delta^2 \mathcal{W}}{\delta \eta_3 \delta \eta_2}, \frac{\delta^2 \Gamma}{\delta \bar{\phi}_2 \delta \phi_1} \right) - \left(\frac{\delta^2 \mathcal{W}}{\delta \eta_3 \delta \bar{\eta}_2}, \frac{\delta^2 \Gamma}{\delta \phi_2 \delta \phi_1} \right). \end{aligned} \tag{3.183}$$

Rewritten in matrix form, we obtain

$$\begin{aligned}\begin{pmatrix}\delta_{3,1} & 0\\ 0 & \delta_{3,1}\end{pmatrix} &= \int \mathrm{d}2 \begin{pmatrix} -\frac{\delta^2\mathcal{W}}{\delta\bar{\eta}_3\delta\eta_2} & \frac{\delta^2\mathcal{W}}{\delta\bar{\eta}_3\delta\bar{\eta}_2} \\ \frac{\delta^2\mathcal{W}}{\delta\eta_3\delta\eta_2} & -\frac{\delta^2\mathcal{W}}{\delta\eta_3\delta\bar{\eta}_2}\end{pmatrix} \begin{pmatrix} \frac{\delta^2\Gamma}{\delta\bar{\phi}_2\delta\phi_1} & \frac{\delta^2\Gamma}{\delta\bar{\phi}_2\delta\bar{\phi}_1} \\ \frac{\delta^2\Gamma}{\delta\phi_2\delta\phi_1} & \frac{\delta^2\Gamma}{\delta\phi_2\delta\bar{\phi}_1}\end{pmatrix} \\ &=: \int \mathrm{d}2\, \boldsymbol{\delta}_\eta^2\mathcal{W}\, \boldsymbol{\delta}_\phi^2\Gamma(2;1),\end{aligned} \tag{3.184}$$

and it can directly be observed that the matrix of the derivatives of second order for Γ is the inverse of the matrix of the second order derivatives of $\mathcal{W}$, in short-hand notation

$$\boldsymbol{\delta}_\phi^2\Gamma = (\boldsymbol{\delta}_\eta^2\mathcal{W})^{-1}. \tag{3.185}$$

When the fields vanish we directly obtain

$$\boldsymbol{\gamma}^{(2)} = \boldsymbol{\delta}_\phi^2\Gamma\big|_{\phi=\bar{\phi}=0} = (\boldsymbol{\delta}_\eta^2\mathcal{W})^{-1}\big|_{\eta=\bar{\eta}=0} = \boldsymbol{G}^{-1}. \tag{3.186}$$

5. According to part 4 of this corollary the one-particle effective interaction is the inverse of the Green's function. As the full one-particle Green's function fulfils the Dyson equation (eq. (3.135)), it can be replaced by $\gamma^{(2)}$ and rearranged, so that it results in

$$\Sigma = G_0^{-1} - \gamma^{(2)}. \tag{3.187}$$

As G_0^{-1} corresponds to the non-interacting system, the self-energy corresponds to the difference between the interacting and the non-interacting system. Therefore, this relation is frequently used to define the self-energy.

6. The expansion of $\Gamma[\bar{\phi},\phi]$ in Grassmann fields ϕ and $\bar{\phi}$ is

$$\begin{aligned}\Gamma[\bar{\phi},\phi] = &\sum_{n=0}^{\infty} \frac{(-1)^n}{(n!)^2} \\ &\times \int \mathrm{d}1 \cdots \int \mathrm{d}2n\ \frac{\delta^{2n}\Gamma[\bar{\phi},\phi]}{\delta\bar{\phi}_1\cdots\delta\bar{\phi}_n\delta\phi_{2n}\cdots\delta\phi_{n+1}}\bigg|_{\bar{\phi}=\phi=0} \bar{\phi}_1\cdots\bar{\phi}_n\phi_{2n}\cdots\phi_{n+1}\end{aligned} \tag{3.188}$$

where $\gamma^{(2n)}$ can directly be identified as expansion coefficients.

7. A proof of the one-particle irreducibility and the expansion in Feynman diagrams based on the FRG method can be found in Schober [81], theorem 5.17. An alternative approach to this theorem in terms of a diagrammatic expansion is provided by Negele and Orland [78], though, it is not a rigorous general proof.

8. To obtain the expansions for the n-particle Green's function, similar calculations as performed for corollary 3.16.4 are necessary with $2n-1$ field derivatives acting on ϕ_i. The result of the action of a first field derivative has already been obtained in equation (3.183). Additional field derivatives can directly act either on Γ, or on $\mathcal{W}$, which then result in additional terms of the form $\frac{\delta^m\Gamma}{\delta\phi_1\cdots\delta\phi_m}$. Due to the chain rule the derivative of $\mathcal{W}$ is connected to all the terms of the derivatives of Γ. As we consider fermions, only those terms with an equal number of Grassmann and conjugated Grassmann fields contribute, and the derivatives can be rewritten in terms of n-particle Green's functions and n-particle interactions. Due to the product rule the sum of all the possible terms arising from the differentiation has to vanish.

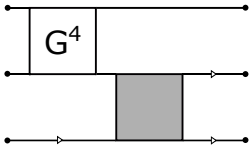

Figure 3.10.: Graphical representation of a term contributing to the three-particle Green's function. As the two-particle interactions are connected via a torso line, the contribution is one-particle irreducible.

In the case that all the derivatives first act on $\mathcal{W}$, we obtain the n-particle Green's function with $\gamma^{(2)}$ at all but one of its legs. If we, therefore, add G as the inverse to $\gamma^{(2)}$ to all the corresponding legs, we obtain the pure n-particle Green's function which has to sum up to zero with all the other terms. In the other extreme case, in which all the additional derivatives act on Γ, we obtain $\gamma^{(2n)}$ connected to a one-particle Green's function. Due to the addition of G all of its legs become connected to such a Green's function, thus leading to the first term of equation (3.180).

In all the other terms the derivative leads to a Green's function connected to at least two, but less than $n-1$ interactions. Therefore, only terms of G^{2n-2} appear in there, such that we can recursively consider these cases. Starting for the two-particle case, the restriction to fermions only allows two different terms, resulting in

$$G^4(1,2;3,4) = G(1,\tilde{1})\, G(2,\tilde{2})\, \gamma^{(2n)}(\tilde{1},\tilde{2};\tilde{3},\tilde{4})\, G(\tilde{3},3)\, G(\tilde{4},4). \tag{3.189}$$

Considering the three-particle case, one can observe besides the extreme terms containing G^6 or $\gamma^{(6)}$, a third term arises from the differentiation, namely

$$G^4(1,2;4,\tilde{1})\, \gamma^{(4)}(\tilde{1},\tilde{2};\tilde{3},\tilde{4})\, G(3,\tilde{2})\, G(\tilde{3},5)\, G(\tilde{4},6). \tag{3.190}$$

In this term, we can insert the expression for the two-particle Green's function, resulting in two two-particle interactions $\gamma^{(4)}$ connected to each other by one one-particle Green's function. In a diagrammatic representation this connection line corresponds to a torso-line, as the diagram splits into two parts when it is cut. A diagrammatic representation of this argument is shown in figure 3.10. The procedure just presented has to be continued for Green's functions of higher order, resulting in the fact that the residue of equation (3.180) always contains a torso-line. ■

Based on these functionals, the calculation of susceptibilities, which was the motivation of our discussion, is still not directly possible. However, according to the discussion in section 3.3, the susceptibilities can be obtained by calculating the effective actions and by adding closed Green's function loops to them. In the same section we also discussed that susceptibilities behave as bosons. By adding source terms of the fermion bilinears to the generating functional we are, therefore, able to derive an explicit expression for them.

Definition 38 (Generating Functional for the Effective Action and for Susceptibilities) *Let ψ, $\bar{\psi}$ be Grassmann fields, η, $\bar{\eta}$ fermionic source fields, B a boson-like field based on a fermionic bilinear, and let J be the corresponding source field. Furthermore, let*

$$\mathcal{S}[\psi, \bar{\psi}, J] = -(\psi, G_0^{-1}\psi) + V[\bar{\psi}, \psi] + (J, B) \tag{3.191}$$

be the effective action of the system. Then

$$\mathcal{W}[\bar{\eta}, \eta, J] = -\ln \int \mathcal{D}[\psi, \bar{\psi}]\ e^{-\mathcal{S}[\bar{\psi}, \psi, J]}\ e^{(\bar{\eta}, \psi) + (\bar{\psi}, \eta)} \tag{3.192}$$

*is the **generating functional for connected fermionic Green's functions and for the susceptibilities** and its Legendre transformation*

$$\Gamma[\bar{\phi}, \phi, J] = \mathcal{W}[\bar{\eta}(\bar{\phi}, \phi), \eta(\bar{\phi}, \phi), J] + \left(\bar{\phi}, \eta\right) + (\bar{\eta}, \phi) \tag{3.193}$$

*is the **generating functional for the effective action and for the susceptibilities**.*

Any derivative of $\mathcal{W}$ with respect to the source fields J leads to the corresponding fermion bilinear appearing in the the expectation value. Therefore, for any fermion bilinear we are interested in, we add the corresponding source term. Although the fermion bilinears are treated as bosons, they are defined by a fixed combination of fermion creation and annihilation operators. As only expectation values with an equal number of them are non-zero, the non-local charge- and spin-density bilinears appear with an equal number of fermionic creation and annihilation operators, while two additional creation (annihilation) operators appear for each (adjoint) pairing operator. As the fermion bilinears are characterised by a form-factor (see section 3.3), a form-factor index appears for each fermion bilinear in the expectation value.

In analogy to the n-fermion interactions or vertices as derivatives of the $\Gamma[\bar{\phi}, \phi]$ functional, the Legendre transformation allows us to define corresponding n-fermion and m-boson vertices as follows:

Definition 39 (One-particle Irreducible n-Fermion, m-Boson Interactions) *Let Γ be as defined in definition 38. Let n_i and n_j be the number of incoming and outgoing slots, respectively, and $2n = n_i + n_j$. Then the **one-particle irreducible** n-**fermion** m-**boson interactions** (or **vertices**) are*

$$\gamma_\eta^{(2n,m)}(1, \ldots, n_i; n_i{+}1, \ldots, 2n; 1', \ldots, m') := \left.\frac{\delta^{(2n+m)}\Gamma[\bar{\phi}, \phi, J]}{\delta\bar{\phi}_1 \cdots \delta\bar{\phi}_{n_i}\delta\phi_{2n} \cdots \delta\phi_{n_i+1}J_{1'} \cdots J_{m'}}\right|_{\phi=\bar{\phi}=J=0} \tag{3.194}$$

with η denoting the type of present fermion-bilinear fields.

When the fermion bilinear field is replaced by a purely bosonic one, this interaction would require $n_i = n_j$. In our case however, the interaction is only non-zero if the total number of Grassmann and adjoint Grassmann fields of the fermion bilinear and of fermions adds up to zero, that is if

$n_i - n_j = \sum_{i=0}^{m} \sigma(B_{m_i})$ with $\sigma(B_{m_i}) = -2, 0, 2$ for $B \propto p^\dagger$, $B \propto \bar{\psi}\psi$ and $B \propto p$, respectively. Therefore, $n_i + n_j$ will always be an even number such that we define their sum as $2n$.

For the rest of this thesis we will maintain the argument structure of the n-fermion m-boson interaction as incoming fermions, outgoing fermions and bosons when bosons or fermion bilinears are present. When there is no argument in one of the fermionic parts, we will place a "$\cdot$" in the corresponding place to clarify the correspondence of the arguments to the fields, while we will drop the bosonic arguments and the bosonic index η when they are absent.

As the fermionic part of this generating functional equals the one in definition 35, the results given in corollary 3.16 still hold. The field expansion in corollary 3.16.6, however, now also has to include the bosonic fields and thus becomes

$$\begin{aligned}\Gamma[\bar{\phi}, \phi, J] = &\sum_{m,n_i,n_j=0}^{\infty} \frac{(-1)^{n_j}}{m! n_i! n_j!} \int \mathrm{d}1 \cdots \int \mathrm{d}2n \int \mathrm{d}1' \cdots \int \mathrm{d}m' \\ &\times \gamma_\eta^{(2n,m)}(1, \ldots, n_i; n_i+1, \ldots, n; 1', \ldots, m')\ \bar{\phi}_1 \cdots \bar{\phi}_{n_i} \phi_{2n} \cdots \phi_{n_i+1} J_{1'} \cdots J_{m'} \quad (3.195) \\ &:= \sum_{m,n=0}^{\infty} \mathcal{A}^{(2n,m)\Lambda}[\bar{\phi}, \phi, J].\end{aligned}$$

Obviously, solely derivatives with respect to the generating Grassmann fields generate the effective one-particle irreducible interactions $\gamma^{(2n,0)}$ like before. Each derivative with respect to the source fields J, however, leads to a bosonic field or a fermion bilinear. Therefore, two derivatives with respect to the generator of an electron-hole bilinear like ρ or S^i lead to corresponding susceptibilities of electron-hole type $\gamma_{\mathrm{eh}}^{(0,2)} = \chi_{\mathrm{eh}}$. Two derivatives with respect to the generators of a pairing bilinear p and its adjoint bilinear $\bar{p}$ lead to the pairing susceptibility $\gamma_{\mathrm{ee}}^{(0,2)} = \chi_{\mathrm{ee}}$. A combination of one derivative with respect to the source terms J and one with respect to two Grassmann fields results in vertices $\gamma^{(2,1)}$ representing the interaction between a fermion-bilinear and a pair of fermions. Those interactions will be called fermion-boson interaction in the following, which also includes the case of fermion-bilinears due to their boson-like behaviour. If the fermion-bilinear present in such an interaction is of electron-hole type, it has to couple to a Grassmann field and an adjoint one and we denote it by $\gamma_{\mathrm{eh}}^{(2,1)}$. If the fermion-bilinear is of hole-hole type, the interaction has to couple to two adjoint Grassmann fields, resulting in the hole-hole fermion-boson interaction $\gamma_{\mathrm{hh}}^{(2,1)}$, while the adjoint case of electron-electron fermion-bilinears leads to the electron-electron fermion-boson interaction $\gamma_{\mathrm{ee}}^{(2,1)}$. Those fermion-boson interactions will be needed in the flow equations in order to generate the full interacting susceptibilities.

As the following derivation of the FRG equations is based on the n-fermion m-boson vertices $\gamma^{(2n,m)}$ we consider their symmetries, too.

Corollary 3.17 (Properties of Effective Fermion-Boson Interactions)
Let $\gamma^{(n,m)}$ be the n-fermion m-bilinear interaction according to definition 39. Then it obeys the following symmetry relations:

1. *For the fermionic part the **crossing symmetries** hold*

$$\begin{aligned}&\gamma^{(n,m)}(1, \ldots, i, \ldots, j, \ldots, n_i; n_i+1, \ldots, 2n; 1', \ldots, m') \\ &\qquad = -\gamma^{(n,m)}(1, \ldots, j, \ldots, i, \ldots, n_i; n_i+1, \ldots, 2n; 1', \ldots, m'), \ \textit{and} \quad (3.196)\end{aligned}$$

$$\gamma^{(n,m)}(1,\dots,n_i;n_i+1,i,\dots,j,\dots,\dots,2n;1',\dots,m') = -\gamma^{(n,m)}(1,\dots,n_i;n_i+1,\dots,j,\dots,i,\dots,2n;1',\dots,m'), \tag{3.197}$$

while the bosonic (bilinear) part is invariant under the exchange of particles so that

$$\gamma^{(n,m)}(1,\dots,2n;1',\dots,i,\dots,j,\dots m') = \gamma^{(n,m)}(1,\dots,2n;1',\dots,j',\dots,i',\dots,m'). \tag{3.198}$$

2. *The* ***complex conjugation*** *inverts the order of fermionic and bosonic arguments and changes the times of the fermionic arguments, i.e.*

$$\left(\gamma^{(2n,m)}(x_1\tau_1,\dots,x_{2n}\tau_{2n};x_{1'}\tau_{1'},\dots,x_{m'}\tau_{m'})\right)^* = \gamma^{(2n,m)}(x_{2n}(-\tau_{2n}),\dots,x_1(-\tau_1);x_{m'}(-\tau_{m'}),\dots,x_{1'}(-\tau_{1'})), \tag{3.199}$$

which, in the frequency domain, results in

$$\left(\gamma^{(2n,m)}(x_1\omega_1,\dots,x_{2n}\omega_{2n};x_{1'}\nu_{1'},\dots,x_{m'}\nu_{m'})\right)^* = \gamma^{(2n,m)}(x_{2n}(-\omega_{2n}),\dots,x_1(-\omega_1);x_{m'}(-\nu_{m'}),\dots,x_{1'}(-\nu_{1'})). \tag{3.200}$$

3. *Let $\hat{H}$ be invariant under a translation $a\in\mathbb{R}$ in time. Then $\gamma^{(2n,m)}$ also is invariant under time translations, i.e.*

$$\gamma^{(2n,m)}(\tau_1,\dots,\tau_{2n};\tau_{1'},\dots,\tau_{m'}) = \gamma^{(2n,m)}(\tau_1+a,\dots,\tau_{2n}+a;\tau_{1'}+a,\dots,\tau_{m'}+a). \tag{3.201}$$

4. *Let $\hat{H}$ be invariant under a translation $\boldsymbol{r}'\in\mathbb{R}^3$ in space. Then $\gamma^{(2n,m)}$ also is invariant under spatial translations, i.e.*

$$\gamma^{(2n,m)}(\boldsymbol{r}_1,\dots,\boldsymbol{r}_{2n};\boldsymbol{r}_{1'},\dots,\boldsymbol{r}_{m'}) = \gamma^{(2n,m)}(\boldsymbol{r}_1+\boldsymbol{r}',\dots,\boldsymbol{r}_{2n}+\boldsymbol{r}';\boldsymbol{r}_{1'}+\boldsymbol{r}',\dots,\boldsymbol{r}_{m'}+\boldsymbol{r}'). \tag{3.202}$$

5. *Let $\hat{H}$ be SU(2)-symmetric. Then $\gamma^{(2n,m)}$ conserves the total spin, i.e.*

$$\sum_{i=1}^{2n} s_i = \sum_{i=0}^{m} s_i', \tag{3.203}$$

and is symmetric under a global spin-flip, i.e.

$$\gamma^{(2n,m)}(s_1,\dots,s_{2n};s_{1'},\dots,s_{m'}) = \gamma^{(2n,m)}(-s_1,\dots,-s_{2n};-s_{1'},\dots,-s_{m'}). \tag{3.204}$$

6. *Let $\hat{H}$ be symmetric under a point-group Γ and let $\hat{R}\in\Gamma$ be a symmetry operation of the point group. Then $\gamma^{(2n,m)}$ is symmetric under the point group operation $\hat{R}$ according to*

$$\gamma^{(2n,m)}(\boldsymbol{r}_1,\dots,\boldsymbol{r}_{2n};\boldsymbol{r}_{1'},\dots,\boldsymbol{r}_{m'}) = \gamma^{(2n,m)}(\hat{R}(\boldsymbol{r}_1),\dots,\hat{R}(\boldsymbol{r}_{2n});\hat{R}(\boldsymbol{r}_{1'}),\dots,\hat{R}(\boldsymbol{r}_{m'})). \tag{3.205}$$

7. The Fourier transformation of $\gamma^{(2n,m)}(1,\ldots,2n;1',\ldots,m')$ *is given by*

$$\begin{aligned}
&\gamma^{(2n,m)}(k_1\omega_1,\ldots,k_{2n}\omega_{2n};k_{1'}\omega_{1'},\ldots,k_{m'},\omega_{m'})\\
&= \frac{1}{(2\pi)^{d(2n+m)}\beta^{2n+m}}\int \mathrm{d}\boldsymbol{r}_1\ \cdots \int \mathrm{d}\boldsymbol{r}_{2n}\int_0^\beta \mathrm{d}\tau_1\ \cdots \int_0^\beta \mathrm{d}\tau_{2n}\\
&e^{-i(\boldsymbol{k}_1\cdot\boldsymbol{r}_1+\omega_1\tau_1)}\ \ldots\ e^{-i(\boldsymbol{k}_n\cdot\boldsymbol{r}_n+\omega_n\tau_n)}\,e^{i(\boldsymbol{k}_{2n}\cdot\boldsymbol{r}_{2n}+\omega_{2n}\tau_{2n})}\ \ldots e^{i(\boldsymbol{k}_{n+1}\cdot\boldsymbol{r}_{n+1}+\omega_{n+1}\tau_{n+1})}\\
&\qquad e^{-i(\boldsymbol{k}_{1'}\cdot\boldsymbol{r}_{1'}+\omega_{1'}\tau_{1'})}\,e^{-i(\boldsymbol{k}_{m'}\cdot\boldsymbol{r}_{m'}+\omega_{m'}\tau_{m'})}\gamma^{(2n,m)}(1,\ldots,2n;1',\ldots,m'). \quad (3.206)
\end{aligned}$$

PROOF: 1. This directly follows from the anticommutivity of Grassmann fields and from the commutivity of the corresponding fermionic bilinears and bosons.

2. For the fermionic part, the proof is along the same line with the one of theorem 3.2. For the bosonic part, the same considerations combined with the observation that $B^*(\tau) = B(-\tau)$ lead to the desired result. The result in the frequency domain is directly obtained by the insertion of the imaginary time relation into the Fourier transformation.
3. This proof is along the same line with the one of corollary 3.4.1.
4. This proof is along the same line with the one of corollary 3.4.2.
5. This relation is proved along the same lines with the one of corollary 3.4.3. Every fermion bilinear adds terms of $\pm s_{1'} \pm s_{2'}$ to the spin summation in equation (3.44), where "+" refers to a creation and "−" to an annihilation operator. As the total number of incoming momenta again has to equal the total number of outgoing momenta, the bosonic spin is maintained within the interaction, leading to the desired result.
6. This proof is along the same line with the one of corollary 3.4.4.
7. This relation directly follows from applying the Fourier transformation to the generating functional. ■

3.5. Functional Renormalisation Group

The main principle of the renormalisation approach is based on the idea of Wilson [52, 53]. The underlying concept is to split the whole energy range into windows of a finite energy range and then, successively, consider interactions within these. In more detail, all high energetic modes above a first cut-off whose interactions are described by a model Hamiltonian are summed up to construct an effective Hamiltonian. This is then used for an energy window between the first and a second cut-off, where, again, all corresponding modes are integrated out to obtain another effective action. Repeating this procedure down to zero energy leads to the total effective interaction between particles of the particular model and thus to the correct partition function of the system. Mathematically, this approach is based on the splitting of the covariance and the measure with respect to the scale parameter, thus providing a semi-group property. However, such an iterative, analytical treatment is only possible for a few models like the Ising model [101, 59].

To cast the renormalisation procedure into a generally applicable and numerically treatable mathematical form, the limit of infinitesimally sized energy windows is taken, so that a real non-negative cut-off parameter Λ defines this window. Thus, ordinary differential equations for the effective one-particle irreducible n-fermion m-boson[3] interactions (including susceptibilities) can be derived, which are called flow equations. The solution to these differential equations is then a flow through the phase space from the non-interacting system to the full interacting system. This approach is called functional renormalisation group (FRG), as it casts the semi-group approach of the Wilson renormalisation group into a functional form. There exist different approaches to this method, like, for example, the one by Polchinski [54] or the one by Wetterich [58, 102]. The formulation for interacting fermions based on the formulation of Wetterich was derived by Salmhofer and Honerkamp [60, 103], as well as [59] at basically the same time. While Metzner *et al.* provide an extensive review on this method in [104], our derivation is rather based on the derivations by Schober [81].

In order to restrict the energy to a finite window in the formalism, we take the common choice of modifying the free Green's function by a cut-off. We remark that alternatives to this choice exist, like, for example, a regularisation of the two-particle interaction (cf. e.g. [105]). Our choice leads to the following definition:

Definition 40 (Cut-Off and Regularised Free Green's Function)
Let G_0 be the free one-particle Green's function of a system. Then we call $\Lambda \in [0, \infty)$ the ***cut-off parameter***, ***flow parameter*** *or* ***scale parameter****, if G_0 is regularised by Λ such that*

$$G_0^\Lambda = \begin{cases} 0 & \text{for } \Lambda = \Lambda_0 \\ G_0 & \text{for } \Lambda \to \Lambda_f. \end{cases} \tag{3.207}$$

G_0^Λ is then called the ***regularised free Green's function*** *and $Q^\Lambda := (G_0^\Lambda)^{-1}$ is called the* ***inverse operator*** *or the* ***covariant****.*

According to this definition, the regularised free Green's function vanishes when all modes of the system are cut away, and it becomes the original free Green's function when all modes are included,

[3] For reasons of brevity we refer to interactions of fermions and fermion-bilinears also as fermion-boson interactions, as the latter show a boson-like behaviour.

that is when the full system is restored. These conditions leave space for different choices of the implementation of the cut-off. One possibility [106] is to add a regulator R^Λ with $R^{\Lambda_0} = \infty$ and $R^{\Lambda_f} = 0$ to the inverse propagator $Q = G_0^{-1}$ so that

$$Q^\Lambda(1;2) = Q(1;2) + R^\Lambda(1;2) \tag{3.208}$$

fulfils the conditions. Alternatively, one can multiply the free Green's function with a cut-off function C^Λ with $C^{\Lambda_0} = 0$ and $C^{\Lambda_f} = 1$ so that

$$G_0^\Lambda(1;2) = C^\Lambda(1;2)G_0(1;2). \tag{3.209}$$

A further discussion on the actual choice of cut-off functions can be found in chapter 4.3 with some focus on numerical details.

When the regularised free Green's function is inserted into the generating functionals $\mathcal{G}$, $\mathcal{W}$ or Γ, all of these and all of their derivatives become regularised and depend on the flow parameter Λ. That is, the average fields ϕ and $\bar{\phi}$ needed for the Legendre transformation from $\mathcal{W}$ to Γ, all connected Green's functions, and all one-particle irreducible n-fermion m-boson vertices $\gamma^{(2n,m)}$ depend on the scale parameter Λ, which is indicated by the superscript Λ [4]. Flow equations for $\gamma^{(2n,m)\Lambda}$ are obtained by the comparison of fields, when the field expansion of Γ is introduced into its Λ-derivative, as we will derive in the subsequent section.

3.5.1. Functional Flow Equations

As Γ is the Legendre transformation of the generating functional of connected Green's functions $\mathcal{W}^\Lambda$ we first derive the flow equation for $\mathcal{W}^\Lambda$.

Theorem 3.18 (Flow Equation for the Generating Functional of Connected Green's Functions)
Let G_0^Λ be the regularised free Green's function and let $\mathcal{W}^\Lambda[\eta, \bar{\eta}, J]$ be the generating functional of connected Green's functions given by definition 34. Then its flow equation is given by

$$\frac{\mathrm{d}}{\mathrm{d}\Lambda}\mathcal{W}^\Lambda[\eta,\bar{\eta},J] = \left(\frac{\delta\mathcal{W}^\Lambda}{\delta\eta}, \left[\frac{\delta Q^\Lambda}{\delta\Lambda}\right]\frac{\delta\mathcal{W}^\Lambda}{\delta\bar{\eta}}\right) + Tr\left(\left[\frac{\delta Q^\Lambda}{\delta\Lambda}\right]\frac{\delta^2\mathcal{W}^\Lambda}{\delta\bar{\eta}\delta\eta}\right). \tag{3.210}$$

Proof: By rewriting the derivative of the generating functional as

$$\frac{\mathrm{d}}{\mathrm{d}\Lambda}\mathcal{W}^\Lambda[\eta,\bar{\eta},J] = -e^{\mathcal{W}^\Lambda}\frac{\mathrm{d}}{\mathrm{d}\Lambda}e^{-\mathcal{W}^\Lambda} \tag{3.211}$$

its explicit expression can be written without the logarithm. The evaluation of the derivative results in

$$\begin{aligned}\frac{\mathrm{d}}{\mathrm{d}\Lambda}\mathcal{W}^\Lambda &= -e^{\mathcal{W}^\Lambda}\int\mathcal{D}[\bar{\psi},\psi]\ (\bar{\psi},\dot{Q}^\Lambda\psi)\ e^{-\mathcal{S}[\bar{\psi},\psi,J]}\ e^{(\bar{\eta},\psi)+(\bar{\psi},\eta)} \\ &= -e^{\mathcal{W}^\Lambda}(-\delta_\eta,\dot{Q}^\Lambda\delta_{\bar{\eta}})\underbrace{\int\mathcal{D}[\bar{\psi},\psi]\ e^{-\mathcal{S}[\psi,\bar{\psi},J]}\ e^{(\bar{\eta},\psi)+(\bar{\psi},\eta)}}_{e^{-\mathcal{W}^\Lambda}},\end{aligned} \tag{3.212}$$

[4] Most derivations of the FRG equations shift the Λ-dependence to the source fields η and $\bar{\eta}$, so that ϕ and $\bar{\phi}$ remain Λ independent. Although both choices result in the same flow equations, our choice appears more natural.

where the Grassmann fields are rewritten with source term derivatives. The first derivative of the scalar product gives rise to a term of the form $(\delta_{\bar\eta}\mathcal{W}^\Lambda)e^{-\mathcal{W}^\Lambda}$. The second derivative then leads to a similar term with $\delta_\eta\mathcal{W}^\Lambda$ and to a second derivative of $\mathcal{W}^\Lambda$. The latter term only is non-zero when both derivatives correspond to fields with the same quantum numbers, as fermionic fields can only appear in pairs, and can, therefore, be written in terms of a trace. This leads to

$$\frac{\mathrm{d}}{\mathrm{d}\Lambda}\mathcal{W}^\Lambda = e^{\mathcal{W}^\Lambda}e^{-\mathcal{W}^\Lambda}\left(\frac{\delta\mathcal{W}^\Lambda}{\delta\eta},\dot{Q}^\Lambda\frac{\delta\mathcal{W}^\Lambda}{\delta\bar\eta}\right) + \mathrm{Tr}\left(\dot{Q}^\Lambda\frac{\delta^2\mathcal{W}^\Lambda}{\delta\eta\delta\bar\eta}\right), \tag{3.213}$$

which is the desired result. ∎

In the next step, we use the Legendre transformation to obtain the flow equation for $\Gamma^\Lambda[\phi^\Lambda,\bar\phi^\Lambda,J]$.

Theorem 3.19 (Flow Equation for the One-particle-irreducible Vertex Generating Functional)
Let Q^Λ be the inverse, regularised free propagator, let ϕ^Λ and $\bar\phi^\Lambda$ be average fields as defined in equation (3.173), let $\boldsymbol{Q}^\Lambda = (\boldsymbol{G}_0^\Lambda)^{-1}$ and $\boldsymbol{G}^\Lambda$ be given by

$$\boldsymbol{Q}^\Lambda =: \begin{pmatrix} Q^\Lambda & 0 \\ 0 & -Q^{\Lambda t}\end{pmatrix} \qquad \text{and} \qquad \boldsymbol{G}^\Lambda =: \begin{pmatrix} G^\Lambda & 0 \\ 0 & -G^{\Lambda t}\end{pmatrix} = (\boldsymbol{\delta}^2_\phi\Gamma^\Lambda)^{-1}\big\|_{\phi=\bar\phi=J=0} \tag{3.214}$$

with $Q^{\Lambda t}(1;2) = Q^\Lambda(2;1)$ and $G^{\Lambda t}(1;2) = G^\Lambda(2;1)$. Let furthermore $\tilde{\boldsymbol{\Sigma}}^\Lambda[\phi^\Lambda,\bar\phi^\Lambda,J] := (\boldsymbol{G}^\Lambda)^{-1} - \boldsymbol{\delta}^2_\phi\Gamma^\Lambda[\phi^\Lambda,\bar\phi^\Lambda,J]$ be the field independent part of the interaction.

Then the flow equation for the generating functional of one-particle irreducible interactions is given by the Wetterich equation [58]

$$\begin{aligned}\frac{\mathrm{d}}{\mathrm{d}\Lambda}\Gamma^\Lambda[\phi^\Lambda,\bar\phi^\Lambda,J] + \left(\frac{\delta\Gamma}{\delta\phi^\Lambda},\frac{\partial\phi^\Lambda}{\partial\Lambda}\right) + \left(\frac{\delta\Gamma}{\delta\bar\phi^\Lambda},\frac{\partial\bar\phi^\Lambda}{\partial\Lambda}\right)& \\ = -\left(\bar\phi^\Lambda,\dot{Q}^\Lambda\phi^\Lambda\right) - \frac{1}{2}Tr\left(\dot{\boldsymbol{Q}}^\Lambda(\boldsymbol{\delta}^2_\phi\Gamma^\Lambda[\phi^\Lambda,\bar\phi^\Lambda,J])^{-1}\right),&\end{aligned} \tag{3.215}$$

or, equivalently, by

$$\begin{aligned}\frac{\mathrm{d}}{\mathrm{d}\Lambda}\Gamma^\Lambda[\phi^\Lambda,\bar\phi^\Lambda,J] + \left(\frac{\delta\Gamma}{\delta\phi^\Lambda},\frac{\partial\phi^\Lambda}{\partial\Lambda}\right) + \left(\frac{\delta\Gamma}{\delta\bar\phi^\Lambda},\frac{\partial\bar\phi^\Lambda}{\partial\Lambda}\right) = -\left(\bar\phi^\Lambda,\dot{Q}^\Lambda\phi^\Lambda\right) - Tr\left(\dot{Q}^\Lambda G^\Lambda\right)& \\ + \frac{1}{2}Tr\left(-\boldsymbol{G}^\Lambda\dot{\boldsymbol{Q}}^\Lambda\boldsymbol{G}^\Lambda\left(\tilde{\boldsymbol{\Sigma}}^\Lambda[\bar\phi^\Lambda,\phi^\Lambda,J] + \tilde{\boldsymbol{\Sigma}}^\Lambda[\bar\phi^\Lambda,\phi^\Lambda,J]\boldsymbol{G}^\Lambda\tilde{\boldsymbol{\Sigma}}^\Lambda[\bar\phi^\Lambda,\phi^\Lambda,J] + \dots\right)\right).&\end{aligned} \tag{3.216}$$

Proof: As $\mathcal{W}^\Lambda$ depends on the flow parameter, so do the ϕ^Λ- and the $\bar\phi^\Lambda$-fields, as they are determined by the relation $\phi^\Lambda = -\partial_{\bar\eta}\mathcal{W}^\Lambda$ and $\bar\phi^\Lambda = \partial_\eta\mathcal{W}^\Lambda$. Then, with the definition of Γ^Λ, we obtain

$$\frac{\mathrm{d}}{\mathrm{d}\Lambda}\Gamma^\Lambda[\bar\phi^\Lambda,\phi^\Lambda,J] = \frac{\mathrm{d}}{\mathrm{d}\Lambda}\mathcal{W}^\Lambda[\eta(\bar\phi^\Lambda,\phi^\Lambda),\bar\eta(\bar\phi^\Lambda,\phi^\Lambda),J] + \left(\frac{\mathrm{d}}{\mathrm{d}\Lambda}\bar\phi^\Lambda,\eta\right) + \left(\bar\eta,\frac{\mathrm{d}}{\mathrm{d}\Lambda}\phi^\Lambda\right). \tag{3.217}$$

The left hand side of equation (3.215) is obtained by identifying η and $\bar\eta$ in the last two terms of the right hand side as derivatives of Γ due to the reciprocity relation (cf. thm. 3.16.1) and by shifting them to the left hand side. Only the flow equation of $\mathcal{W}^\Lambda$ is left on the right hand side, which itself is given by theorem 3.18. Due to the definition in equation (3.173) ϕ^Λ and $\bar\phi^\Lambda$ replace the first derivatives of $\mathcal{W}$ with respect to source fields. To express the second field derivative of $\mathcal{W}$, which appears in the trace of Γ, we will use the reciprocity relation (see thm. 3.16.4). Therefore, this term has to be cast into a

corresponding matrix form on which the trace acts additionally. As field derivatives anticommute, we get $\delta_{\bar{\eta}}\delta_{\eta} = -\delta_{\eta}\delta_{\bar{\eta}}$, so that

$$\begin{aligned} Q^{\Lambda}(x_1,x_2)\delta_{\bar{\eta}_2}\delta_{\eta_1}\mathcal{W}^{\Lambda} &= \frac{1}{2}\left(Q^{\Lambda}(x_1,x_2)\delta_{\bar{\eta}_2}\delta_{\eta_1}\mathcal{W}^{\Lambda} - Q^{\Lambda}(x_2,x_1)\delta_{\eta_2}\delta_{\bar{\eta}_1}\mathcal{W}^{\Lambda}\right) \\ &= -\frac{1}{2}\mathrm{Tr}\left(\begin{pmatrix} Q^{\Lambda}(x_1,x_2) & 0 \\ 0 & -Q^{\Lambda}(x_2,x_1)\end{pmatrix}\begin{pmatrix} -\delta_{\bar{\eta}_2}\delta_{\eta_1} & \delta_{\bar{\eta}_2}\delta_{\bar{\eta}_1} \\ \delta_{\eta_2}\delta_{\eta_1} & -\delta_{\eta_2}\delta_{\bar{\eta}_1}\end{pmatrix}\mathcal{W}^{\Lambda}\right) \\ &= -\frac{1}{2}\mathrm{Tr}\left(\boldsymbol{Q}^{\Lambda}\boldsymbol{\delta}_{\eta}^2\mathcal{W}^{\Lambda}\right), \end{aligned} \tag{3.218}$$

where the integration variables of the second term were exchanged in the intermediate step, and the off-diagonal elements do not contribute due to the trace. With the reciprocity relation (see thm. 3.16.4) $\boldsymbol{\delta}_{\eta}^2\mathcal{W}^{\Lambda}$ can be replaced by $(\boldsymbol{\delta}_{\phi}^2\Gamma^{\Lambda})^{-1}$, resulting in the expression (3.215).

To prove equation (3.216) the definition[5] of $\tilde{\boldsymbol{\Sigma}}^{\Lambda}$ is rearranged to

$$\boldsymbol{\delta}_{\phi}^2\Gamma^{\Lambda}[\phi^{\Lambda},\bar{\phi}^{\Lambda},J] = (\boldsymbol{G}^{\Lambda})^{-1} - \tilde{\boldsymbol{\Sigma}}^{\Lambda}[\phi^{\Lambda},\bar{\phi}^{\Lambda},J], \tag{3.219}$$

and its inverse is expanded according to

$$\begin{aligned} \left(\boldsymbol{\delta}_{\phi}^2\Gamma^{\Lambda}\right)^{-1} &= \left(1 - \boldsymbol{G}^{\Lambda}\tilde{\boldsymbol{\Sigma}}^{\Lambda}\right)^{-1}\boldsymbol{G}^{\Lambda} \\ &= \sum_{n=0}^{\infty}\left(\boldsymbol{G}^{\Lambda}\tilde{\boldsymbol{\Sigma}}^{\Lambda}\right)^{n}\boldsymbol{G}^{\Lambda}. \end{aligned} \tag{3.220}$$

We note that, although this series is mathematically exact, it only converges if $|G\tilde{\Sigma}| < 1$.[6]

By inserting this into expression (3.215), the term of order zero of the sum $-\frac{1}{2}\mathrm{Tr}\left(\dot{\boldsymbol{Q}}^{\Lambda}\boldsymbol{G}^{\Lambda}\right)$ is separated and becomes, due to the definition of the given matrices, $-\mathrm{Tr}\left(\dot{Q}^{\Lambda}G^{\Lambda}\right)$. By exploiting the cyclic property of the trace, all the other terms in the trace then directly lead to the expression in equation (3.216). ∎

For a deeper understanding of $\tilde{\boldsymbol{\Sigma}}$, we regard the second derivative of the fermionic field expansion of Γ. Obviously, the constant terms with $n = 0$ vanish and those with $n = 1$ become constant in fermionic fields. Without bosons, this constant coefficient is the inverse Green's function according to $\boldsymbol{\gamma}^{(2,0)^{\Lambda}}\Big|_{\bar{\phi}^{\Lambda}=\phi^{\Lambda}=0} = (\boldsymbol{G}^{\Lambda})^{-1}\big|_{\bar{\phi}^{\Lambda}=\phi^{\Lambda}=0} = \mathrm{diag}(G^{\Lambda},-(G^{\Lambda})^{\mathrm{t}})^{-1}$. Due to its significance, which we pointed out in chapter 3.1, this term was separated and all field-dependent parts were moved to $-\tilde{\boldsymbol{\Sigma}}^{\Lambda}$. Its field expansion, therefore, has no terms for $n = 0$ and for $n = 1$, $m = 0$, while the other terms are two-dimensional matrices of the second field derivatives of the expansion of Γ.

As the obtained flow equations are for the generating functionals, a numerical implementation is not possible. By an expansion in terms of fields we can obtain the corresponding flow equations for either the n-particle Green's functions or for the many-particle interaction functions.

[5] $\tilde{\Sigma}$ can alternatively be defined with a global $-$-sign, resulting in an alternating sign in the expansion of eq. 3.216. This, however, is fixed by the $-$-sign appearing in the field expansion of $\tilde{\Sigma}$ compared to the alternative choice, cf. thm. 3.21.

[6] In weakly interacting systems Σ is typically small, ensuring a convergence of this series.

3.5.2. Vertex Flow Equations

Before we introduce the expansion of Γ^Λ in equation (3.216) in terms of fields we define some objects which will simplify the notation later on.

Definition 41 (Single-Scale Propagator and Dual Propagator)
Let $\boldsymbol{G}^\Lambda$ and $\boldsymbol{Q}^\Lambda$ be defined as in theorem 3.19, equation (3.214)*. Then the **single-scale propagator** is defined as*

$$S^\Lambda(1;2) := -\int \mathrm{d}\tilde{1} \int \mathrm{d}\tilde{2}\, G^\Lambda(1;\tilde{1})\, \dot{Q}^\Lambda(\tilde{1};\tilde{2})\, G^\Lambda(\tilde{2};2) \tag{3.221}$$

with the corresponding matrix form

$$\boldsymbol{S}^\Lambda := -\boldsymbol{G}^\Lambda\, \dot{\boldsymbol{Q}}^\Lambda\, \boldsymbol{G}^\Lambda = \mathrm{diag}(S^\Lambda, -(S^\Lambda)^t). \tag{3.222}$$

*The **dual propagator** is defined as*

$$L^\Lambda(1,2;3,4) := G^\Lambda(1;3)\, S^\Lambda(2;4) + S^\Lambda(1;3)\, G^\Lambda(2;4). \tag{3.223}$$

The diagonal form of $\boldsymbol{S}^\Lambda$ directly follows from the diagonal form of $\boldsymbol{G}^\Lambda$ and $\boldsymbol{Q}^\Lambda$. L^Λ is also symmetric under simultaneous exchanges of both, incoming and outgoing arguments, that is $L^\Lambda(x_1,x_2;x_3,x_4) = L^\Lambda(x_2,x_1;x_4,x_3)$. For numerical calculations it can be advantageous to use another, equivalent form of the single-scale propagator:

Corollary 3.20 (Alternative Form of the Single-Scale Propagator)
The single scale propagator can equally be written as

$$S^\Lambda(1;2) = \left.\frac{\mathrm{d}G^\Lambda(1;2)}{\mathrm{d}\Lambda}\right|_{\Sigma^\Lambda \mathit{fixed}}. \tag{3.224}$$

Proof: We start by differentiating $G^\Lambda (G^\Lambda)^{-1} = 1$ resulting in

$$\frac{\mathrm{d}(G^\Lambda)}{\mathrm{d}\Lambda} = -G^\Lambda \frac{\mathrm{d}(G^\Lambda)^{-1}}{\mathrm{d}\Lambda} G^\Lambda = -G^\Lambda \frac{\mathrm{d}(G_0^\Lambda)^{-1}}{\mathrm{d}\Lambda} G^\Lambda + G^\Lambda \frac{\mathrm{d}\Sigma^\Lambda}{\mathrm{d}\Lambda} G^\Lambda = S^\Lambda + G^\Lambda \frac{\mathrm{d}\Sigma^\Lambda}{\mathrm{d}\Lambda} G^\Lambda, \tag{3.225}$$

where we used the Λ-derivative of the Dyson equation (3.135) for the reformulation in terms of the inverse free Green's function G_0^Λ. When the self-energy Σ^Λ is fixed, the Λ-derivative of Σ^Λ vanishes, which leads to the requested expression. ∎

Turning back to equation (3.216), an expansion of Γ^Λ in terms of fields yields flow equations for the many-particle interactions $\gamma^{(2n,m)}$. As $\tilde{\boldsymbol{\Sigma}}$ is defined as $\tilde{\boldsymbol{\Sigma}}^\Lambda[\phi^\Lambda, \bar{\phi}^\Lambda, J] := (\boldsymbol{G}^\Lambda)^{-1} - \boldsymbol{\delta}^2_\phi \Gamma^\Lambda[\phi^\Lambda, \bar{\phi}^\Lambda, J]$ the field expansion of Γ^Λ also induces a field expansion of $\tilde{\boldsymbol{\Sigma}}^\Lambda$. A flow equation for each n-fermion m-boson interaction is then obtained by comparing the appearing fields on both sides of the equation, as the interactions are only the corresponding expansion coefficients. Based on the structure of the equation, the field derivatives on the right hand side remove fields of the vertices and instead connect internal propagators to the free slot. Therefore, the first contribution to an n-fermion interaction always is an

$(n+1)$-fermion interaction connected to itself by a single-scale propagator. This introduces an infinite hierarchical dependence on interactions of higher order. The other terms which are generated by the series are all combinations of n or less fermion interactions, coming along with $(2n-2)$ fermionic and m bosonic fields, which form a connected Feynman graph. That is, every fermion interaction is connected to one or to two others either by one single-scale propagator and by one Green's function or by two Green's functions. Accordingly, the total number of external bosonic lines to the interactions has to equal the requested one on the left hand side, although the bosons can reside on different interaction vertices. The set of flow equations we will consider is derived in the following theorem.

Theorem 3.21 (Flow Equations for Interactions)
Let Γ^Λ be the scale-dependent, one-particle irreducible generating functional (cf. def. 38) obeying the flow equation in theorem 3.19 and let its expansion be given by equation (3.195)*. Then the flow equations of lowest order are given as follows:*

0) For the grand canonical potential as

$$\beta \frac{d}{d\Lambda}\Omega^\Lambda = \int \mathrm{d}\tilde{1} \int \mathrm{d}\tilde{2}\, \dot{Q}^\Lambda(\tilde{1};\tilde{2})\, G^\Lambda(\tilde{2};\tilde{1}). \tag{3.226}$$

1) For the self-energy as

$$\frac{d}{d\Lambda}\Sigma^\Lambda(1;2) = \int \mathrm{d}\tilde{1} \int \mathrm{d}\tilde{2}\, S^\Lambda(\tilde{1};\tilde{2})\, \gamma^{(4,0)\Lambda}(1,\tilde{2};2,\tilde{1}). \tag{3.227}$$

2) For the two-fermion interaction as

$$\begin{aligned}\dot{\gamma}^{(4,0)\Lambda}(1,2;3,4) = &- \int \mathrm{d}\tilde{1} \int \mathrm{d}\tilde{2}\, S^\Lambda(\tilde{1};\tilde{2})\, \gamma^{(6,0)\Lambda}(\tilde{2},1,2;\tilde{1},3,4) \\ &+ \mathcal{T}^{\mathrm{P},\Lambda}(1,2;3,4) + \mathcal{T}^{\mathrm{D},\Lambda}(1,2;3,4) + \mathcal{T}^{\mathrm{C},\Lambda}(1,2;3,4),\end{aligned} \tag{3.228}$$

with

$$\begin{aligned}\mathcal{T}^{\mathrm{P},\Lambda}(1,2;3,4) &= \frac{1}{2}\int \mathrm{d}\tilde{1} \cdots \int \mathrm{d}\tilde{4}\, L(\tilde{1},\tilde{2};\tilde{3},\tilde{4})\, \gamma^{(4,0)\Lambda}(1,2;\tilde{1},\tilde{2})\, \gamma^{(4,0)\Lambda}(\tilde{3},\tilde{4};3,4) \\ \mathcal{T}^{\mathrm{D},\Lambda}(1,2;3,4) &= \int \mathrm{d}\tilde{1} \cdots \int \mathrm{d}\tilde{4}\, L(\tilde{1},\tilde{2};\tilde{3},\tilde{4})\, \gamma^{(4,0)\Lambda}(1,\tilde{3};3,\tilde{2})\, \gamma^{(4,0)\Lambda}(\tilde{4},2;\tilde{1},4) \\ \mathcal{T}^{\mathrm{C},\Lambda}(1,2;3,4) &= -\int \mathrm{d}\tilde{1} \cdots \int \mathrm{d}\tilde{4}\, L(\tilde{1},\tilde{2};\tilde{3},\tilde{4})\, \gamma^{(4,0)\Lambda}(1,\tilde{3};4,\tilde{2})\, \gamma^{(4,0)\Lambda}(\tilde{4},2;\tilde{1},3).\end{aligned} \tag{3.229}$$

3a) For the electron-hole fermion-boson interactions as

$$\begin{aligned}\dot{\gamma}^{(2,1)\Lambda}_{\mathrm{eh},n}(1;2;1') = &\int \mathrm{d}\tilde{1} \int \mathrm{d}\tilde{2}\, S(\tilde{1};\tilde{2})\gamma^{(4,1)\Lambda}_{\mathrm{eh},n}(1,\tilde{2};2,\tilde{1};1') \\ &+ \frac{1}{2}\, L^\Lambda(\tilde{1},\tilde{2};\tilde{3},\tilde{4})\, \gamma^{(2,1)\Lambda}_{\mathrm{eh},n}(\tilde{3};\tilde{2};1')\, \gamma^{(4,0)\Lambda}(1,\tilde{4};2,\tilde{1}).\end{aligned} \tag{3.230}$$

3b) For the electron-electron fermion-boson interactions as

$$\dot{\gamma}^{(2,1)\Lambda}_{\mathrm{ee},n}(\cdot;1,2;1') = \frac{1}{2}\int \mathrm{d}\tilde{1}\cdots\int \mathrm{d}\tilde{4}\, L^{\Lambda}(\tilde{1},\tilde{2};\tilde{3},\tilde{4})\,\gamma^{(2,1)\Lambda}_{\mathrm{ee},n}(\cdot;\tilde{1},\tilde{2};1')\,\gamma^{(4,0)\Lambda}(\tilde{3},\tilde{4};1,2). \quad (3.231)$$

4a) For the electron-hole susceptibilities as

$$\dot{\chi}^{\Lambda}_{\mathrm{eh},nn'}(1',2') = \int \mathrm{d}\tilde{1}\int \mathrm{d}\tilde{2}\, S(\tilde{1};\tilde{2})\,\gamma^{(2,2)\Lambda}_{\mathrm{eh},nn'}(\tilde{2};\tilde{1};1',2') + \int \mathrm{d}\tilde{1}\cdots\int \mathrm{d}\tilde{4}\, L^{\Lambda}(\tilde{1},\tilde{2};\tilde{3},\tilde{4})\,\gamma^{(2,1)\Lambda}_{\mathrm{eh},n}(\tilde{3};\tilde{2};1')\,\gamma^{(2,1)\Lambda}_{\mathrm{eh},n'}(\tilde{4};\tilde{1};2'). \quad (3.232)$$

4b) For the electron-electron susceptibilities as

$$\dot{\chi}^{\Lambda}_{\mathrm{ee},nn'}(1',2') = \int \mathrm{d}\tilde{1}\int \mathrm{d}\tilde{2}\, S(\tilde{1};\tilde{2})\,\gamma^{(2,2)\Lambda}_{\mathrm{ee},nn'}(\tilde{2};\tilde{1};1',2') + \int \mathrm{d}\tilde{1}\cdots\int \mathrm{d}\tilde{4}\, L^{\Lambda}(\tilde{1},\tilde{2};\tilde{3},\tilde{4})\gamma^{(2,1)\Lambda}_{\mathrm{ee},n}(\cdot;\tilde{1},\tilde{2};1')\,\gamma^{(2,1)\Lambda}_{\mathrm{hh},n}(\tilde{3},\tilde{4};\cdot;2'). \quad (3.233)$$

Proof: [7]The derivations of these flow equations are based on the insertion of the field expansion of Γ (see eq. (3.195)) and on the induced expansion of $\tilde{\mathbf{\Sigma}}$ into equation (3.216). In this proof we implicitly assume an integration or sum over all doubly appearing arguments, to shorten the notation to the relevant part. In this proof we first discuss terms cancelling each other in the flow equation, then consider the action of derivatives on terms of the expansion in general and finally derive the explicit flow equations.

At first, we show that the left hand side of equation (3.216) can be rewritten as

$$\frac{\partial\gamma^{(2n,m)}}{\partial\Lambda}\bar{\phi}_1\ldots\bar{\phi}_{n_i}\phi_{2n}\ldots\phi_{n_i+1}J_{1'}\ldots J_{m'}. \quad (3.234)$$

As the presence of bosonic fields will not change the relation, we only treat the coefficient $\mathcal{A}^{(2n,0)\Lambda}$ explicitly, while a generalisation to an arbitrary m is straight forward. Further, we regard, in this proof, the case of an equal number of ϕ and $\bar{\phi}$ fields and write n instead of n_i to simplify the notation. Considering now the first term of the left hand side of equation (3.216), the scale derivative of the field expansion of Γ can act on the $\gamma^{(2n,m)}$ coefficients, as well as on the fields ϕ^{Λ} or $\bar{\phi}^{\Lambda}$. The derivative then yields

$$\frac{\mathrm{d}}{\mathrm{d}\Lambda}\mathcal{A}^{(2n,0)\Lambda} = \Big[\dot{\gamma}^{(2n,0)\Lambda}(1,\ldots,2n;)\bar{\phi}^{\Lambda}_1\cdots\bar{\phi}^{\Lambda}_n\phi^{\Lambda}_{2n}\cdots\phi^{\Lambda}_{n+1} + \gamma^{(2n,0)\Lambda}(1,\ldots,2n;)\left\{\dot{\bar{\phi}}_i\frac{\delta}{\delta\bar{\phi}_i}\bar{\phi}^{\Lambda}_1\cdots\bar{\phi}^{\Lambda}_n\phi^{\Lambda}_{2n}\cdots\phi^{\Lambda}_{n+1} + \dot{\phi}^{\Lambda}_i\frac{\delta}{\delta\phi^{\Lambda}_i}\bar{\phi}^{\Lambda}_1\cdots\bar{\phi}^{\Lambda}_n\phi^{\Lambda}_{2n}\ldots\phi^{\Lambda}_{n+1}\right\}\Big]. \quad (3.235)$$

Here we can see that the Λ derivative of a field $\phi^{\Lambda}(i)$ can be introduced by inserting $\dot{\phi}^{\Lambda}_i\delta_{\phi^{\Lambda}_i}$ in front of it. Moving these two fields to the front of the whole term does not yield a sign. According to this, the corresponding terms can be written as $(\dot{\bar{\phi}}^{\Lambda}, \frac{\delta\Gamma}{\delta\bar{\phi}^{\Lambda}}) + (\dot{\phi}^{\Lambda}, \frac{\delta\Gamma}{\delta\phi^{\Lambda}})$. Due to the anticommutativity of

[7]We remark that the negative sign of $\tilde{\mathbf{\Sigma}}$ resulting in "$-\mathcal{A}$" is essential for fixing the signs.

the Grassmann fields, this exactly cancels the other terms on the left hand side of equation (3.216), leading to

$$\sum_{m,n=0}^{\infty} \frac{(-1)^n}{m!(n!)^2} \hat{\gamma}^{(2n,m)}(1,\dots,2n;1',\dots m')\bar{\phi}_1^\Lambda \cdots \bar{\phi}_n^\Lambda \phi_{2n}^\Lambda \cdots \phi_{n+1}^\Lambda J_{1'} \dots J_{m'}. \quad (3.236)$$

Before we move on and compare the terms of different order, we determine the field expansion of $\tilde{\mathbf{\Sigma}}$. Therefore we calculate the action of the different second order derivatives on the terms $\mathcal{A}^{2n,m}$. We start with

$$\delta_{\bar{\phi}_\alpha}\delta_{\phi_\beta}\mathcal{A}^{2n,m} = \delta_{\bar{\phi}_\alpha}\delta_{\phi_\beta}\frac{(-1)^{n_j}}{m!n_i!n_j!}\gamma^{(2n,m)\Lambda}(1,\dots,n_i;n+1,\dots,2n;1',\dots,m') \\ \bar{\phi}_1 \cdots \bar{\phi}_{n_i}\phi_{2n}\cdots\phi_{n_i+1}J_{1'}\cdots J_{m'} \quad (3.237)$$

which is 0 for n_i, $n_j = 0$. To let δ_{ϕ_β} act on the corresponding fields, it first has to commute through n_i adjoint fields, resulting in a factor of $(-1)^{n_i}$. As $n_i + n_j$ is even, the sign vanishes. Due to the product rule this derivative acts on all ϕ fields, resulting in n_j additive terms with alternating signs because of the additional commutation. The resulting Kronecker-δ's in each term then contract the argument of the field on which the derivative acted and the argument of the derivative β. With the integrals the Kronecker-δ's can be evaluated such that the argument of the corresponding field in $\gamma^{(2n,m)\Lambda}$ is replaced by β. As $\gamma^{(2n,m)\Lambda}$ is antisymmetric with respect to the arguments, we can move the argument to the same place and rename the other ones, such that all terms become equal, resulting in a factor n_j. Similarly the action of $\delta_{\bar{\phi}_\alpha}$ results in n_i equal terms. Thus we obtain in total

$$\delta_{\bar{\phi}_\alpha}\delta_{\phi_\beta}\mathcal{A}^{2n,m} = \frac{1}{m!(n_i-1)!(n_j-1)!}\gamma^{(2n,m)\Lambda}(\alpha,2,\dots,n_i;n+1,\dots,2n-1,\beta;1',\dots,m') \\ \bar{\phi}_2 \cdots \bar{\phi}_{n_i}\phi_{2n-1}\cdots\phi_{n_i+1}J_{1'}\cdots J_{m'}. \quad (3.238)$$

As the field derivatives anticommute, we have, with

$$\delta_{\phi_\alpha}\delta_{\bar{\phi}_\beta}\mathcal{A}^{2n,m} = -\delta_{\bar{\phi}_\beta}\delta_{\phi_\alpha}\mathcal{A}^{2n,m}, \quad (3.239)$$

the same result as provided by equation (3.238) up to a global factor of -1 and an exchange of α and β. The derivative $\delta_{\bar{\phi}_\alpha}\delta_{\bar{\phi}_\beta}\mathcal{A}^{2n,m}$ vanishes for $n_i \leq 1$. Otherwise, the evaluation of the derivative $\delta_{\bar{\phi}_\beta}$ results, like before, in n_i equivalent terms. In a similar way, the action of the other derivative on the remaining $n_i - 1$ adjoint Grassmann fields results in $n_i - 1$ equivalent terms. Thus the full derivative is provided by

$$\delta_{\bar{\phi}_\alpha}\delta_{\bar{\phi}_\beta}\mathcal{A}^{2n,m} = \frac{(-1)^{n_j}}{m!(n_i-2)!n_j!}\gamma^{(2n,m)\Lambda}(\beta,\alpha,3,\dots,n_i;n+1,\dots,2n,;1',\dots,m') \\ \bar{\phi}_3 \cdots \bar{\phi}_{n_i}\phi_{2n}\cdots\phi_{n_i+1}J_{1'}\cdots J_{m'}. \quad (3.240)$$

Similarly, the derivative $\delta_{\phi_\alpha}\delta_{\phi_\beta}\mathcal{A}^{2n,m}$ can be evaluated, after both derivatives have been commuted through the $\bar{\phi}$ fields resulting in a factor $(-1)^{2n_i} = 1$. Thus the derivative results in

$$\delta_{\phi_\alpha}\delta_{\phi_\beta}\mathcal{A}^{2n,m} = \frac{(-1)^{n_j}}{m!n_i!(n_j-2)!}\gamma^{(2n,m)\Lambda}(1,\dots,n_i;n+1,\dots,2n-2,\alpha,\beta;1',\dots,m') \\ \bar{\phi}_1 \cdots \bar{\phi}_{n_i}\phi_{2n-2}\cdots\phi_{n_i+1}J_{1'}\cdots J_{m'}. \quad (3.241)$$

When we consider the expansion of $\tilde{\boldsymbol{\Sigma}}^\Lambda = \boldsymbol{G}^{-1} - \boldsymbol{\delta}^2_\phi \Gamma^\Lambda$ based on these results now, we observe that $\boldsymbol{G}^{-1}$ cancels the contribution of $\gamma^{(2,0)\Lambda}(\alpha;\beta)$. The expansion of $\tilde{\Sigma}$ is, therefore, based on all $\mathcal{A}^{2n,m}$ where at least two fields of each type appear.

Next, let us consider the first term of the series, that is $\frac{1}{2}\mathrm{Tr}\,(\boldsymbol{S}^\Lambda \tilde{\Sigma}^\Lambda)$. Due to the diagonal structure of $\boldsymbol{S}^\Lambda$ and the trace only terms with $n_i = n_j$ contribute. Evaluating the corresponding term results in

$$\begin{aligned}\frac{1}{2}\Big(&S^\Lambda(1;2)\gamma^{(2n,m)\Lambda}(\tilde{1},\dots,n_i;n_i+1,\dots,2n-1,\tilde{2};1',\dots m') \\ &-S^\Lambda(2;1)\gamma^{(2n,m)\Lambda}(\tilde{2},\dots,n_i;n_i+1,\dots,2n-1,\tilde{1};1',\dots m')\Big) \\ &= S^\Lambda(1;2)\gamma^{2n,m}(\tilde{1},\dots,n_i;n_i+1,\dots,2n-1,\tilde{2};1',\dots m')\end{aligned} \tag{3.242}$$

by exchanging the variables of $\gamma^{(2n,m)}$. We remark that the corresponding fields of the vertex are not written here, for the sake of brevity.

The terms of second order in the series are provided by

$$\begin{aligned}&\frac{1}{2}\mathrm{Tr}\left(\boldsymbol{S}^\Lambda\,\boldsymbol{\delta}^2_\phi m A^{2n,m}\,\boldsymbol{G}\,\boldsymbol{\delta}^2_\phi m A^{2n',m'}\right) \\ &= \frac{1}{2}\mathrm{Tr}\,\Big(S^\Lambda\delta_{\bar{\phi}}\delta_\phi\mathcal{A}^{2n,m}G^\Lambda\delta_{\bar{\phi}}\delta_\phi\mathcal{A}^{2n',m'} + S^{t\Lambda}\delta_\phi\delta_{\bar{\phi}}\mathcal{A}^{2n,m}G^{t\Lambda}\delta_\phi\delta_{\bar{\phi}}\mathcal{A}^{2n',m'} \\ &\qquad - S^\Lambda\delta_{\bar{\phi}}\delta_{\bar{\phi}}\mathcal{A}^{2n,m}G^{t\Lambda}\delta_\phi\delta_\phi\mathcal{A}^{2n',m'} - S^{t\Lambda}\delta_\phi\delta\mathcal{A}^{2n,m}G^\Lambda\delta_{\bar{\phi}}\delta_{\bar{\phi}}\mathcal{A}^{2n,m}\Big).\end{aligned} \tag{3.243}$$

The first two terms of these contributions are only non-zero if each of the two interactions has the same number of free incoming and outgoing legs. In contrast, the third and fourth term also contribute if the number of fields differs, that is $n_i \neq n_j$. When the trace is evaluated, we obtain for the first two terms

$$\begin{aligned}\frac{1}{2}\Big(&S^\Lambda(\tilde{1};\tilde{3})\delta_{\bar{\phi}_{\tilde{3}}}\delta_{\phi_{\tilde{2}}}\mathcal{A}^{2n,m}G^\Lambda(\tilde{2};\tilde{4})\delta_{\bar{\phi}_{\tilde{4}}}\delta_{\phi_{\tilde{2}}}\mathcal{A}^{2n',m'} \\ &+ S^\Lambda(\tilde{3};\tilde{1})\delta_{\phi_{\tilde{3}}}\delta_{\bar{\phi}_{\tilde{2}}}\mathcal{A}^{2n,m}G^\Lambda(\tilde{4};\tilde{2})\delta_{\phi_{\tilde{4}}}\delta_{\bar{\psi}_{\tilde{1}}}\mathcal{A}^{2n',m'}\Big).\end{aligned} \tag{3.244}$$

As we will make a comparison of coefficients to obtain the flow equations, we observe that for any choice of $\mathcal{A}^{2n,m}$ and $\mathcal{A}^{2n',m'}$ there is a corresponding one in which both contributions exchange roles. In this case the S^Λ and G^Λ are exchanged in the second term compared to the first one. Therefore, a relabelling of the corresponding internal indices allows us to rewrite the expression as

$$\frac{1}{2}L^\Lambda(\tilde{1},\tilde{2};\tilde{3},\tilde{4})\delta_{\bar{\phi}_{\tilde{3}}}\delta_{\phi_{\tilde{2}}}\mathcal{A}^{2n,m}\delta_{\bar{\phi}_{\tilde{4}}}\delta_{\phi_{\tilde{2}}}\mathcal{A}^{2n',m'}. \tag{3.245}$$

Similarly the last two terms of equation (3.243)

$$\begin{aligned}-\frac{1}{2}\Big(&S^\Lambda(\tilde{1};\tilde{3})\delta_{\bar{\phi}_{\tilde{4}}}\delta_{\bar{\phi}_{\tilde{3}}}\mathcal{A}^{2n,m}G^\Lambda(4;2)\delta_{\phi_{\tilde{2}}}\delta_{\phi_{\tilde{1}}}\mathcal{A}^{2n',m'} \\ &+ S^\Lambda(\tilde{3};\tilde{1})\delta_{\phi_{\tilde{1}}}\delta_{\phi_{\tilde{2}}}\mathcal{A}^{2n,m}G^\Lambda(\tilde{1};\tilde{4})\delta_{\bar{\phi}_{\tilde{3}}}\delta_{\bar{\phi}_{\tilde{1}}}\mathcal{A}^{2n,m}\Big)\end{aligned} \tag{3.246}$$

can be cast into

$$-\frac{1}{2}L^\Lambda(\tilde{1},\tilde{2};\tilde{3},\tilde{4})\delta_{\bar{\phi}_{\tilde{2}}}\delta_{\bar{\phi}_{\tilde{3}}}\mathcal{A}^{2n,m}\delta_{\phi_{\tilde{4}}}\delta_{\phi_{\tilde{1}}}\mathcal{A}^{2n',m'}. \tag{3.247}$$

Based on these general results we can insert the different terms of the expansion and perform a comparison of coefficients to obtain the corresponding flow equations. We start with the term of order zero, that is the one which is constant in fields.

0) The lowest order of the expansion on the left hand side of equation (3.236) is $n_i = n_j = m = 0$, that is, it is constant in fields. By identifying the corresponding term on the right hand side of equation (3.216) as $\mathrm{Tr}\,(\dot{Q}G)$ the flow equation for the grand canonical potential is directly obtained as

$$\dot{\gamma}^{(0,0)\Lambda} = \beta\dot{\Omega}^{\Lambda} = -\mathrm{Tr}\,(\dot{Q}^{\Lambda}G^{\Lambda}) = \dot{Q}^{\Lambda}(\tilde{1};\tilde{2})\,G^{\Lambda}(\tilde{2};\tilde{1}). \tag{3.248}$$

1) The next order of the field expansion is $n_i = n_j = 1$ and $m = 0$, that is, it is of first order in fermionic fields, which will lead to the flow equation for the self-energy (cf. eq. (3.227)). The terms on the right hand side which, contain one of both types of the Grassmann fields, are $(\bar{\phi}^{\Lambda}, \dot{Q}\phi^{\Lambda})$ and according to equations (3.242) and (3.238) one of the form $S^{\Lambda}\gamma^{(4,0)\Lambda}$. This results in

$$-\dot{\gamma}^{(2,0)\Lambda}(1;2)\,\bar{\phi}_1^{\Lambda}\,\phi_2^{\Lambda} = -\dot{Q}^{\Lambda}(1;2)\,\bar{\phi}_1^{\Lambda}\,\phi_2^{\Lambda} - S^{\Lambda}(\tilde{1};\tilde{2})\gamma^{(4,0)\Lambda}(\tilde{2},1;2,\tilde{1})\bar{\phi}_1^{\Lambda}\,\phi_2^{\Lambda}. \tag{3.249}$$

By rearranging the terms, by identifying $\Sigma = Q - \gamma^{(2,0)}$ and by using the antisymmetry in arguments of $\gamma^{(4,0)\Lambda}$ we obtain the required flow equation of the self-energy

$$\dot{\Sigma}^{\Lambda}(1;2) = \dot{Q}^{\Lambda} - \dot{\gamma}^{(2,0)\Lambda} = S^{\Lambda}(\tilde{1};\tilde{2})\gamma^{(4,0)\Lambda}(1,\tilde{2};2,\tilde{1}). \tag{3.250}$$

Due to this and to the field independent flow equation we have taken care of all the terms outside the trace on the right hand side. Thus, there are only terms originating from the trace which contribute to the flow equations of higher order.

2) Next, we consider terms of second order in Grassmann fields (i.e. $n_i = n_j = 2$, $m = 0$) which is, for the left hand side of equation (3.236)

$$\frac{1}{4}\dot{\gamma}^{(4,0)\Lambda}(1,2;3,4)\,\bar{\phi}_1\,\bar{\phi}_2\,\phi_4\,\phi_3. \tag{3.251}$$

As this is an equal number of both types of Grassmann fields the first term of the trace on the right hand side contributes as $-1/4 S^{\Lambda}(\tilde{1};\tilde{2})\gamma^{(6,0)\Lambda}(\tilde{2},1,2;\tilde{1},3,4)$. Also all the terms in equation (3.243) contribute, as they all have two Grassmann fields of both types if $\gamma^{(4,0)\Lambda}$ is inserted into both places. Evaluating the first two terms we obtain, according to equation (3.245),

$$\frac{1}{2}\,L^{\Lambda}(\tilde{1},\tilde{2};\tilde{3},\tilde{4})\,\gamma^{(4,0)\Lambda}(\tilde{3},1;3,\tilde{2})\,\gamma^{(4,0)\Lambda}(\tilde{4},2;4,\tilde{1}). \tag{3.252}$$

As we consider fermionic interactions which have to be antisymmetric, this term on the right hand side has to be antisymmetric, too. As there are two incoming indices and two outgoing indices, the antisymmetrisation operator $\hat{\mathcal{A}}$ applied to both interactions results in

$$\begin{aligned}&\hat{\mathcal{A}}\left(\gamma^{(4,0)\Lambda}(\tilde{3},1;3,\tilde{2})\,\gamma^{(4,0)\Lambda}(\tilde{4},2;4,\tilde{1})\right)\\&=\frac{1}{(2!)^2}\Big(\gamma^{(4,0)\Lambda}(\tilde{3},1;3,\tilde{2})\,\gamma^{(4,0)\Lambda}(\tilde{4},2;4,\tilde{1})-\gamma^{(4,0)\Lambda}(\tilde{3},2;3,\tilde{2})\,\gamma^{(4,0)\Lambda}(\tilde{4},1;4,\tilde{1})\\&\qquad-\gamma^{(4,0)\Lambda}(\tilde{3},1;4,\tilde{2})\,\gamma^{(4,0)\Lambda}(\tilde{4},2;3,\tilde{1})+\gamma^{(4,0)\Lambda}(\tilde{3},2;4,\tilde{2})\,\gamma^{(4,0)\Lambda}(\tilde{4},1;3,\tilde{1})\Big).\end{aligned}\tag{3.253}$$

The first and the last, as well as the second and the third line can be combined, as they equal each other pairwise by relabelling the internal indices. When the antisymmetry of the interaction under exchange of its arguments is exploited, this finally results in

$$\begin{aligned}&\frac{1}{4}L^{\Lambda}(\tilde{1},\tilde{2};\tilde{3},\tilde{4})\Big(\gamma^{(4,0)\Lambda}(1,\tilde{3};3,\tilde{2})\,\gamma^{(4,0)\Lambda}(\tilde{4},2;\tilde{1},4)\\&\qquad-\gamma^{(4,0)\Lambda}(\tilde{3},2;\tilde{2},3)\,\gamma^{(4,0)\Lambda}(1,\tilde{4};4,\tilde{1})\Big).\end{aligned}\tag{3.254}$$

The first term constitutes the direct electron-hole contribution $\mathcal{T}^{\mathrm{D},\Lambda}$ and the second one the crossing electron-hole contribution $\mathcal{T}^{\mathrm{C},\Lambda}$ up to a prefactor of $1/4$. Finally, we consider the last two terms originating from equation (3.243), which can be considered according to equation (3.247) and results in

$$-\frac{1}{2}L^{\Lambda}(\tilde{1},\tilde{2};\tilde{3},\tilde{4})\;\frac{1}{2}\gamma^{(4,0)\Lambda}(1,2;\tilde{1},\tilde{2})\;\frac{1}{2}\gamma^{(4,0)\Lambda}(\tilde{3},\tilde{4};3,4)\tag{3.255}$$

This contribution is already antisymmetric, as all the terms obtained from the antisymmetry operator can be converted to the same form due to the antisymmetry of the interaction. This is exploited to change the sign, such that we can directly identify it as the pairing contribution $\mathcal{T}^{\mathrm{P},\Lambda}$ up to a prefactor of $1/4$. By combining all the results the prefactors of $1/4$ cancel out, and the flow equation for the two-fermion interaction equals the assertion in equation (3.228).

3) The next terms of the expansion to be considered are the interactions $\gamma^{(2,1)\Lambda}$. As the same boson or fermion bilinear field has to appear in the expansion on both sides, the bosonic terms appearing on the right hand side have to be of the same kind. First, we regard the fermion-boson interaction of electron-hole type, which is based on $n_i = n_j = 1$ and $m = 1$, that is

$$-\dot{\gamma}^{(2,1)\Lambda}_{\mathrm{eh},n}(1;2;1')\;\bar{\phi}_1\,\phi_2 J_{\mathrm{eh},n}(1').\tag{3.256}$$

As an equal number of Grassmann and adjoint Grassmann fields is present, the first term of the series on the right hand side contributes as $-S^{\Lambda}(\tilde{1};\tilde{2})\gamma^{(4,1)\Lambda}_{\mathrm{eh},n}(1,\tilde{2};2,\tilde{1};1')$. A second contribution originates from the term containing the interactions $\gamma^{(2,1)}_{\mathrm{eh},n}$ and $\gamma^{(4,0)}$. As they can appear in both positions in equation (3.243) the corresponding terms can be evaluated via equation (3.245). Combining all the contributions we obtain

$$\begin{aligned}\dot{\gamma}^{(2,1)\Lambda}_{\mathrm{eh},n}(1;2;1')&=S(\tilde{1};\tilde{2})\gamma^{(4,1)\Lambda}_{\mathrm{eh},n}(1,\tilde{2};2,\tilde{1};1')\\&\quad+\frac{1}{2}\,L^{\Lambda}(\tilde{1},\tilde{2};\tilde{3},\tilde{4})\,\gamma^{(2,1)\Lambda}_{\mathrm{eh},n}(\tilde{3};\tilde{2};1')\,\gamma^{(4,0)\Lambda}(1,\tilde{4};2,\tilde{1}),\end{aligned}\tag{3.257}$$

in which we exploited the antisymmetry of $\gamma^{(4,0)\Lambda}$ to change the sign of the second contribution.

Second, we consider the term

$$\frac{1}{2}\dot{\gamma}^{(2,1)\Lambda}_{\mathrm{ee},n}(\cdot;1,2;1')\,\phi_2\,\phi_1 J_{\mathrm{ee},n}(1') \tag{3.258}$$

based on $n_i = 0$, $n_j = 2$ and $m = 1$. As this term requires only two Grassmann fields and no adjoint ones, the second order terms of the geometric series is the first one to contribute. In fact only the last two terms of equation (3.243) contribute with the interactions $\gamma^{(2,1)\Lambda}_{\mathrm{ee},n}$ and $\gamma^{(4,0)\Lambda}$ in either position. According to equation (3.247) we thus obtain

$$\dot{\gamma}^{(2,1)\Lambda}_{\mathrm{ee},n}(\cdot;1,2;1') = \frac{1}{2}\,L^{\Lambda}(\tilde{1},\tilde{2};\tilde{3},\tilde{4})\,\gamma^{(2,1)\Lambda}_{\mathrm{ee},n}(\cdot;\tilde{1},\tilde{2};1')\,\gamma^{(4,0)\Lambda}(\tilde{3},\tilde{4};1,2). \tag{3.259}$$

Similarly, a flow equation for $\gamma^{(2,1)\Lambda}_{\mathrm{hh},n}$ can be obtained as

$$\dot{\gamma}^{(2,1)\Lambda}_{\mathrm{hh},n}(1,2;\cdot;1') = \frac{1}{2}\,L^{\Lambda}(\tilde{1},\tilde{2};\tilde{3},\tilde{4})\,\gamma^{(2,1)\Lambda}_{\mathrm{hh},n}(\tilde{3},\tilde{4};\cdot;1')\,\gamma^{(4,0)\Lambda}(1,2;\tilde{1},\tilde{2}). \tag{3.260}$$

4) Finally, we derive the flow equations for the susceptibilities $\chi^{\Lambda}_{\mathrm{ee},n} = \gamma^{(0,2)\Lambda}_{\mathrm{ee},n}$ and $\chi^{\Lambda}_{\mathrm{eh},n} = \gamma^{(0,2)\Lambda}_{\mathrm{eh},n}$. The fermion bilinears on the right hand side of equation (3.216) have to correspond to those which the susceptibilities are based on. As there are no Grassmann fields present on the left hand side, the first term of the series results in $1/2 S^{\Lambda}(\tilde{1};\tilde{2})\,\gamma^{(2,2)\Lambda}_{\eta}(\tilde{2};\tilde{1};1',2')$ for both cases with η denoting the channel we consider. The second order term on the right hand side can contain two interactions in which as many fermions are created as are destroyed such that none of them remains. The electron-hole susceptibility is based on two electron-hole bilinears, such that a combination of two electron-hole fermion-boson interactions $\gamma^{(2,1)\Lambda}_{\mathrm{eh},n}$ creates the correct number of bosonic fields. As both of them contain an equal number of both Grassmann field types, only the first part of equation (3.243) contributes and equation (3.245) provides the corresponding contribution. The full flow equation, therefore, results in

$$\begin{aligned}\dot{\chi}^{\Lambda}_{\mathrm{eh},nn'}(1',2') = {} & S(\tilde{1};\tilde{2})\,\gamma^{(2,2)\Lambda}_{\mathrm{eh},nn'}(\tilde{2};\tilde{1};1',2') \\ & + L^{\Lambda}(\tilde{1},\tilde{2};\tilde{3},\tilde{4})\gamma^{(2,1)\Lambda}_{\mathrm{eh},n}(\tilde{3};\tilde{2};1')\,\gamma^{(2,1)\Lambda}_{\mathrm{eh},n'}(\tilde{4};\tilde{1};2').\end{aligned} \tag{3.261}$$

The electron-electron susceptibility is based on a pairing and on an adjoint pairing fermion-bilinear so that a combination of the corresponding electron-electron and of the hole-hole fermion-boson interactions creates the required bosonic fields in the second order term. Both of the required fermion-boson interactions come with either two Grassmann or with two adjoint Grassmann fields, so that only the last two terms of equation (3.243) contribute. These terms can be combined as in equation (3.247) such that the full flow equation for the pairing susceptibility is

$$\begin{aligned}\dot{\chi}^{\Lambda}_{\mathrm{ee},nn'}(1',2') = {} & S(\tilde{1};\tilde{2})\,\gamma^{(2,2)\Lambda}_{\mathrm{ee},nn'}(\tilde{2};\tilde{1};1',2') \\ & + L^{\Lambda}(\tilde{1},\tilde{2};\tilde{3},\tilde{4})\gamma^{(2,1)\Lambda}_{\mathrm{ee},n}(\cdot;\tilde{1},\tilde{2};1')\,\gamma^{(2,1)\Lambda}_{\mathrm{hh},n'}(\tilde{3},\tilde{4};\cdot;2').\end{aligned} \tag{3.262}$$

With these flow equations the proof is completed and παντα ρει [107]. ■

Remark 3.22
As obtained by theorem 3.21, the two last contributions to the two-particle interaction are related by

$$\mathcal{T}^{\mathrm{D},\Lambda}(1,2;3,4) = -\mathcal{T}^{\mathrm{C},\Lambda}(1,2;4,3). \tag{3.263}$$

A diagrammatic representation of the flow equations in theorem 3.21 can be found in figure 3.11, which also visualises the physical significance of the different contributions. Two distinct classes of diagrams can be distinguished here: First, in the flow equations of interactions with the same number of incoming and of outgoing slots a diagram appears in which an interaction with one additional pair of incoming and outgoing slots is connected to itself by a single-scale propagator. By those diagrams, higher order interactions are included in the interactions of lower order, which constitutes a hierarchy of interactions. The second type of diagrams are those in which two interactions are connected with each other by a pairing or by an electron-hole propagator. These dual propagators consist of a single-scale propagator and a full Green's function (cf. def. 41) for either of the two particles, although only one of both possibilities is displayed in the diagrams. Therefore these contributions correspond to pairs of particles interacting twice with each other. For higher orders than those displayed here, diagrams with a closed loop consisting of several interactions connected by (single-scale) propagators can appear. We note that despite our analytical derivation a purely diagrammatical one is also possible, see for example the PhD-thesis by Jakobs [108].

For the self-energy only one diagram of the first type appears, so that it contains the rescaling of the single-particle properties due to the interactions with all the other particles at higher energy scales. The flow equation of the two-particle interaction consists of one diagram of the first type and thus contains all effective three-particle interactions. In addition there are three two-particle reducible contributions. Due to the three possible ways of two-particle reducibility they can be identified as the pairing, the direct and the crossing electron-hole contributions. The electron-hole type diagrams differ by an exchange of external variables, which diagrammatically results in crossed external legs. Therefore, the effective interaction at a scale Λ contains all the possible interactions of a pair of particles with energies larger than Λ, as two full interactions are connected to each other.

The flow equations contributing to the fermion-boson vertices are given by the corresponding vertex connected to a two-fermion interaction by a dual propagator. Thus, they include all the terms in which their outgoing/incoming particles interact with each other. In the electron-hole case, there is an additional contribution of a one-boson two-fermion vertex connected to itself, again representing all two-particle irreducible contributions. Finally the susceptibilities or two-boson interactions consist of two fermion-boson interactions connected by pairing or by electron-hole propagators. Thus they represent the creation of a particle pair or of an electron-hole pair from a bosonic field and create a bosonic field by their annihilation, which we have already seen before for the susceptibilities in section 3.3, where the form-factors could be interpreted as fermion-boson interactions.

Solving the set of flow equations corresponds to a simultaneous integration in the range $\Lambda_0 \to \infty \searrow 0$ of all of them. The initial conditions are chosen corresponding to the assumption of a free system at the initial scale Λ_0. That is, the self-energy is assumed to vanish and the two-fermion interaction is set to a model dependent interaction. When the flow equation of the susceptibilities is integrated over the range in the absence of interactions, the integrated susceptibilities have to equal the free part as

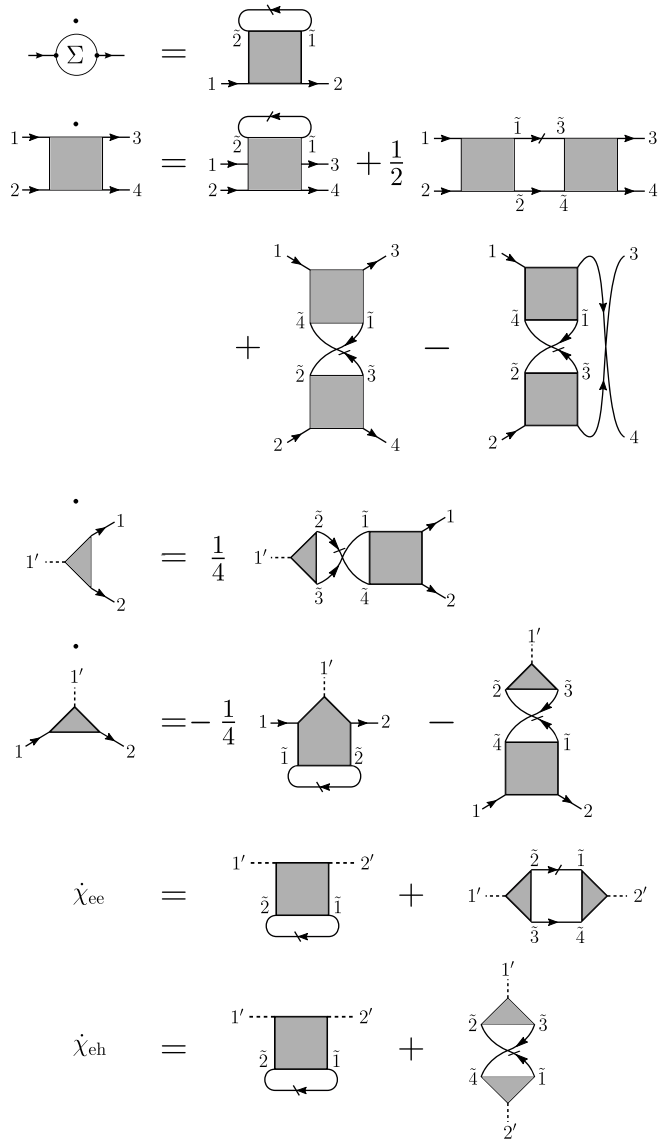

Figure 3.11.: Diagrammatic representation of the flow equations as provided by theorem 3.21

described in equation (3.162). Therefore the initial fermion-boson interaction $\gamma_\eta^{(2,1)\Lambda}$ has to be chosen as the form-factor of the fermion bilinear it corresponds to. These form-factors obtain a different non-local structure due to their flow-equations, which then leads to the corresponding interacting susceptibilities. We remark that there are also approaches in which the flow starts with an effective action obtained by other methods like DMFT [109] which already include some modes, so that the initial scale has to be adapted as well as the initial conditions.

When we focus on the flow-equation of the two-fermion interaction with its four contributions, we observe that it maintains its decomposition upon this integration.

Corollary 3.23 (Decomposition of the Two-Fermion Interaction)
Let $\gamma^{(4,0)\Lambda}$ be given as in theorem 3.21 and let it obey the flow equation provided by 3.228. Then for any $\Lambda \in [0,\infty)$, $\gamma^{(4,0)\Lambda}$ can be decomposed according to

$$\gamma^{(4,0)\Lambda} = \gamma^{(4,0)\Lambda_0} + \int_{\Lambda_0}^{\Lambda} \mathrm{d}\Lambda'\, \gamma^{(6,0)\Lambda'} S^{\Lambda'} + \Phi^{\mathrm{P},\Lambda} + \Phi^{\mathrm{D},\Lambda} + \Phi^{\mathrm{C},\Lambda} \tag{3.264}$$

with

$$\Phi^{\mathrm{P},\Lambda} := \int_{\Lambda_0}^{\Lambda} \mathrm{d}\Lambda'\, \mathcal{T}^{\mathrm{P},\Lambda'}, \qquad \Phi^{\mathrm{D},\Lambda} := \int_{\Lambda_0}^{\Lambda} \mathrm{d}\Lambda'\, \mathcal{T}^{\mathrm{D},\Lambda'} \quad \textit{and } \Phi^{\mathrm{C},\Lambda} := \int_{\Lambda_0}^{\Lambda} \mathrm{d}\Lambda'\, \mathcal{T}^{\mathrm{C},\Lambda'}. \tag{3.265}$$

Proof: The assertion directly follows from the linearity of the integration. ∎

As these given flow equations are only of lowest order of an infinite hierarchy of diagrams, this set of equations has to be truncated. In this thesis we employ the common approximation and only consider contributions of an order $2n+m < 5$, which is neglecting the interactions of higher order, that is $\gamma^{(6,0)\Lambda}$, $\gamma^{(4,1)\Lambda}$ and $\gamma^{(2,2)\Lambda}$ in theorem 3.21.

However, the replacement of S by $\dot{G}$, called Katanin substitution (see thm. 3.24) as proposed in [62], introduces diagrams in which a tadpole diagram $\gamma^{(4,0)\Lambda} S^\Lambda$ is on the replaced internal line, so that it includes contributions of the vertex of higher order $2(n+1)$. Hence, if we consider diagrams up to a fixed power $n_{\max}$ of V there is an unresolved ambiguity of choosing either S^Λ or $\dot{G}^\Lambda$ [63].

In the following theorem (based on section 2.2 in [63]) we explicitly show for the $\gamma^{(4,0)\Lambda}$-interaction that it contains contributions originating from $\gamma^{(6,0)\Lambda}$, which can then be generalised to any order of $n_{\max}$ straight forwardly. To simplify the notation we do not write all the dependencies explicitly, but keep the notation in form of traces, which is an intermediate step between theorems 3.19 and 3.21, where the contributing terms due to the expansion have already been identified. In this form the flow equation for the two-particle interaction reads

$$\dot{\gamma}^{(4,0)\Lambda} = -\frac{1}{2}\mathrm{Tr}\left(S^\Lambda \gamma^{(6,0)\Lambda}\right) + \frac{1}{2}\mathrm{Tr}\left(S^\Lambda \gamma^{(4,0)\Lambda} G^\Lambda \gamma^{(4,0)\Lambda}\right). \tag{3.266}$$

The flow equation for the three-particle interaction [63] becomes, in this form,

$$\begin{aligned}\dot{\gamma}^{(6,0)\Lambda} = &-\frac{1}{2}\mathrm{Tr}\left(S^\Lambda \gamma^{(8,0)\Lambda}\right) + \frac{1}{2}\mathrm{Tr}\left(S^\Lambda \gamma^{(6,0)\Lambda} G^\Lambda \gamma^{(4,0)\Lambda}\right) \\ &- \frac{1}{2}\mathrm{Tr}\left(S^\Lambda \gamma^{(4,0)\Lambda} G^\Lambda \gamma^{(4,0)\Lambda} G^\Lambda \gamma^{(4,0)\Lambda}\right).\end{aligned} \tag{3.267}$$

Theorem 3.24 (Katanin Substitution)
Let $\gamma^{(2n,0)\Lambda} = 0$ for all $n \geq 4$. Consider the flow equation for $\gamma^{(4,0)\Lambda}$ for the initial conditions $\gamma^{(6,0)\Lambda_0} = 0$ and $G^{\Lambda_0} = 0$. Then the flow equation (3.228) holds in the approximation to third order in $\gamma^{(4,0)\Lambda}$ with the replacement

$$L^{\Lambda}(1,2;3,4) = \frac{1}{2}\frac{\mathrm{d}}{\mathrm{d}\Lambda} G^{\Lambda}(1;3)\, G^{\Lambda}(2;4) \tag{3.268}$$

and with

$$\frac{1}{2}\frac{\mathrm{d}}{\mathrm{d}\Lambda}\, Tr\left(G^{\Lambda}\,\gamma^{(4,0)\Lambda}\,G^{\Lambda}\,\gamma^{(4,0)\Lambda}\,G^{\Lambda}\,G^{\Lambda}\,\gamma^{(4,0)\Lambda}\right) \tag{3.269}$$

replacing the $\gamma^{(6,0)\Lambda}$ term.

Proof: In equation (3.225) we derived

$$\dot{G}^{\Lambda} = S^{\Lambda} + G^{\Lambda}\dot{\Sigma}^{\Lambda}G^{\Lambda}, \tag{3.270}$$

that is the replacement leads to an error of $\dot{\Sigma}^{\Lambda}$. According to its flow equation (3.227) this is of first order in $\gamma^{(4,0)\Lambda}$. Based on this we consider the flow equation (3.267) of the three-particle interaction $\gamma^{(6,0)\Lambda}$ of which the $\gamma^{(8,0)\Lambda}$ contribution vanishes according to the approximation. While the term in which three $\gamma^{(4,0)\Lambda}$ are connected with each other contribute right from the beginning, the contributions with $\gamma^{(6,0)\Lambda}$ being connected to $\gamma^{(4,0)\Lambda}$ only arise during the flow due to the initial condition for $\gamma^{(6,0)\Lambda}$. Therefore, these contributions are of fourth order in $\gamma^{(4,0)\Lambda}$ and the flow equation becomes

$$\dot{\gamma}^{(6,0)\Lambda} = -\frac{1}{2}\mathrm{Tr}\left(S^{\Lambda}\gamma^{(4,0)\Lambda}G^{\Lambda}\gamma^{(4,0)\Lambda}G^{\Lambda}\gamma^{(4,0)\Lambda}\right) + \mathcal{O}((\gamma^{(4,0)\Lambda})^4). \tag{3.271}$$

Replacing S^{Λ} by $\dot{G}^{\Lambda}$ in this expression leads to another term of fourth order in $\gamma^{(4,0)\Lambda}$ due to equation (3.270). As Λ-derivatives of $\gamma^{(4,0)\Lambda}$ also lead to terms of fourth order, we can write the differential equation as

$$\dot{\gamma}^{(6,0)\Lambda} = -\frac{1}{6}\frac{\mathrm{d}}{\mathrm{d}\Lambda}\mathrm{Tr}\left(G^{\Lambda}\,\gamma^{(4,0)\Lambda}\,G^{\Lambda}\,\gamma^{(4,0)\Lambda}\,G^{\Lambda}\,\gamma^{(4,0)\Lambda}\right) + \mathcal{O}((\gamma^{(4,0)\Lambda})^4). \tag{3.272}$$

This equation can be integrated according to the initial conditions when the terms of fourth order are neglected, which results in

$$\gamma^{(6,0)\Lambda} = -\frac{1}{6}\mathrm{Tr}\left(G^{\Lambda}\,\gamma^{(4,0)\Lambda}\,G^{\Lambda}\,\gamma^{(4,0)\Lambda}\,G^{\Lambda}\,\gamma^{(4,0)\Lambda}\right). \tag{3.273}$$

This corresponds to a diagram in which every vertex has two external slots and two internal ones. When equation (3.273) is inserted into the flow equation of $\gamma^{(4,0)\Lambda}$, the single-scale propagator can connect two slots of the same vertex or two from different ones. In both cases there are three equivalent possibilities due to the cyclicity of the trace. When a two-particle vertex is connected to itself, terms of the form $\gamma^{(4,0)\Lambda}S^{\Lambda}$ appear, which can be identified as the flow equation of the self-energy Σ^{Λ}. Combining these terms with the ones of second order and using equation (3.270) yields

$$\mathrm{Tr}\left(S^{\Lambda}\gamma^{(4,0)\Lambda}G^{\Lambda}\gamma^{(4,0)\Lambda}\right) + \mathrm{Tr}\left(G^{\Lambda}\dot{\Sigma}^{\Lambda}G^{\Lambda}\gamma^{(4,0)\Lambda}G^{\Lambda}\gamma^{(4,0)\Lambda}\right) = \mathrm{Tr}\left(\dot{G}^{\Lambda}\gamma^{(4,0)\Lambda}G^{\Lambda}\gamma^{(4,0)\Lambda}\right). \tag{3.274}$$

The remaining terms of third order in $\gamma^{(4,0)\Lambda}$ are those in which the vertices are connected to each other by S^Λ. By replacing this S^Λ by $\dot{G}^\Lambda$ we again obtain an error of fourth order in $\gamma^{(4,0)\Lambda}$. When the derivative is written in front of the trace we also obtain derivatives of $\gamma^{(4,0)\Lambda}$, which also introduce terms of fourth order. In total, this leads to

$$\frac{1}{2}\frac{\mathrm{d}}{\mathrm{d}\Lambda}\left(G^\Lambda\gamma^{(4,0)\Lambda}G^\Lambda\gamma^{(4,0)\Lambda}G^\Lambda G^\Lambda\gamma^{(4,0)\Lambda}\right)+\mathcal{O}((\gamma^{(4,0)\Lambda})^4). \tag{3.275}$$

As we consider the weak coupled regime, the desired expression is obtained by neglecting the term of fourth order. ■

In the proof of theorem 3.24 we neglected contributions of fourth order in $\gamma^{(4,0)\Lambda}$ and inserted the two-particle self-energy Σ which is reasonable for our investigations. This scheme was, however, originally introduced to fulfil Ward identities up to a higher order in a truncated flow equation [62]. In the corresponding paper it is shown that the frequency or momentum Ward identities are fulfilled for a momentum or frequency cut-off, respectively, for one order higher in $\gamma^{(4,0)\Lambda}$ than the truncation to second or third order. In addition, the substitution of S^Λ by $\dot{G}^\Lambda$ leads to an additional improvement of the Ward identities, as the non-overlapping diagrams, which are those where a vertex is connected to itself, are absent. Additionally, it is shown that the Ward identities are exactly fulfilled in the ladder approximation.

The so-called multi-loop FRG [64, 66] can be regarded as an extension of the results obtained by this proof. As it originally results from the Parquet equation, we will compare it to the FRG equations in the following section.

3.5.3. Comparison of the Perturbation Theory and the Functional Renormalisation Group

The flow equations provided in theorem 3.21 and the Parquet equations defined in definition 31 exhibit some similarities, which become apparent in the diagrammatic representation. However, while the Parquet equations provide a self-consistent set of equations to calculate the two-particle interaction, the FRG equations are differential equations for it. Only when the flow equation (3.228) is integrated over the full range of the scale parameter from $\Lambda_0 \to \infty$ to 0, the full two-particle interaction is obtained, which is, according to corollary 3.23,

$$\gamma^{(4,0)\Lambda=0}=\gamma^{(4,0)\Lambda_0}-\int_{\Lambda_0}^{0}\mathrm{d}\Lambda\,\gamma^{(6,0)\Lambda}S^\Lambda+\int_{\Lambda_0}^{0}\mathrm{d}\Lambda\,\mathcal{T}^{\mathrm{P},\Lambda}+\int_{\Lambda_0}^{0}\mathrm{d}\Lambda\,\mathcal{T}^{\mathrm{D},\Lambda}+\int_{\Lambda_0}^{0}\mathrm{d}\Lambda\,\mathcal{T}^{\mathrm{C},\Lambda}. \tag{3.276}$$

The resulting $\gamma^{(4,0)\Lambda=0}$ is the same object as the two-particle interaction in the Parquet approach. From the direct comparison of equations (3.276) and (3.137) one would assume that the different contributions $\int\mathcal{T}_\mathrm{r}$ to the FRG flow equation equal Φ_r of the Parquet equation. This is, however, not the case, as we will argue in the following[8]. The simplest way to arrive at this point is to assume a scale dependence for the Parquet objects and calculate the derivatives. We assume that the two-particle irreducible contribution Λ_irr is scale independent while all the other contributions Φ_r depend on the scale Λ. The derivative, therefore, results in $\dot{\gamma}^{(4,0)\Lambda}=\sum_\mathrm{r}\Phi_\mathrm{r}^\Lambda$. In the BSE for each contribution the derivative results in derivations of each object, that is $\gamma^{(4,0)\Lambda}$, $\bar{\Phi}_\mathrm{r}^\Lambda$ and either of the two Green's functions (see fig. 3.7). The expression in which the derivative acts on the Green's functions is the

[8] I want to emphasize that the following analysis was performed at the beginning of the work on my PhD thesis and remained unpublished. However, a similar comparison was published by Kugler *et al.*[64] shortly afterwards.

one most similar to the FRG one. However, this Parquet dual propagator contains the derivative of either Green's function while the FRG dual propagator consists of a single-scale propagator and a full Green's function. If we replace the single-scale propagator by the Katanin substitution (cf. thm. 3.24) this difference is removed. However, the second striking difference, namely that a full vertex is connected to a channel-irreducible interaction, remains untouched by this. In order to make this equation equal to the FRG one we require the channel reducible part interaction $\bar{\Phi}_\mathrm{r}$ to become the full interaction. To obtain this we consider the contribution in which the derivative acts on the full interaction. In this way the derivative $\dot{\Phi}_\mathrm{r}^\Lambda$ is itself inserted into the equation, by which we obtain a term of the form $\gamma^{(4,0)\Lambda}\dot{G}^\Lambda G^\Lambda \left(\bar{\Phi}_\mathrm{r}^\Lambda G^\Lambda G^\Lambda \bar{\Phi}_\mathrm{r}^\Lambda\right)$. The last part of the expression in brackets is two-particle reducible in the channel r which we consider and, therefore, creates the lowest order contribution to Φ_r^Λ. An other contribution resulting from the insertion of $\dot{\Phi}_\mathrm{r}^\Lambda$ is one in which the derivative acts on the full interaction again. This allows us to iteratively insert $\dot{\Phi}_\mathrm{r}^\Lambda$ into the equation and obtain all orders of reducible diagrams in channel r, which can be combined to obtain the full FRG flow equation.

Although we identified an equivalence between one part of the scale-derivative Parquet equation and the FRG equation, other contributions appear, too, which, in the FRG case, have to be contributed by $\gamma^{(6,0)\Lambda}$. In order to replace the derivation of the full interaction and the channel-irreducible interaction the scale derivative BSEs of the other channels have to be inserted. As derivatives acting on full and on channel irreducible interactions appear again, this procedure has to be repeated infinitely often, until all derivatives only act on Green's functions (see figure 3.12 for an illustration of this process). A diagrammatical comparison shows that corresponding loop terms are, indeed, present in the contributions from the six-point interaction. Nonetheless, the FRG equations typically are truncated by neglecting the three-particle interaction due to their numerical complexity. Therefore a recent attempt to make both approaches provide equal results is the addition of contributions arising from the scale-derivative of the Parquet equations to the FRG flow equations for the two-particle interaction. As the successive insertion of derivatives increases the number of dual-propagator loops, the contributions can be classified by their total number of loops in addition to the two-particle reducibility. The scale derivative of a Green's function appears in only one loop, so that an inductive structure with the classic FRG equations at lowest order allows an efficient calculation for all orders. This so called multi-loop FRG (mFRG) has recently been developed, discussed and applied in [64, 65, 110, 66] and reveals a good convergence of the mFRG interaction towards the Parquet interaction with an increasing loop-number.

Next, we consider the self-energy provided by the perturbation theory (Schwinger-Dyson Equation, see eq. 3.136) and compare it to the FRG one (see eq. 3.227). If we proceed in the same way as before and make the objects of the perturbation theory scale-dependent and consider the derivative of the self-energy, we obtain contributions of the form $V_\circ \dot{G}$ from the Hartree and Fock terms. The term including the two-fermion interaction now splits up into four contributions, as every Green's function and the vertex are subject to the scale-derivative. When we take the derivative of the Green's function, we obtain terms of the form $V_\circ^\Lambda G^\Lambda G^\Lambda \gamma^{(4,0)\Lambda}$, of which one is particle-particle and two are particle-hole reducible. Therefore these contributions, as well as the Hartree and Fock terms, are contained in $\gamma^{(4,0),\Lambda}\dot{G}^\Lambda$. As $\dot{G}^\Lambda = S^\Lambda + G^\Lambda \dot{\Sigma}^\Lambda G^\Lambda$ (cf. eq. (3.225)) this already provides the FRG flow equation (3.227) as well as an additional contribution $\gamma^{(4,0)\Lambda} G^\Lambda \dot{\Sigma}^\Lambda G^\Lambda$. The derivative of the full interaction itself requires a successive insertion of its own flow equation similar to the previous case for the interactions. This insertion always leads to a term reducible in one of the channels according to the combination of two interactions in the SDE. However, in an actual numerical calculation one may simply insert the derivative of the interaction calculated in the same step. Thus, from an analytical

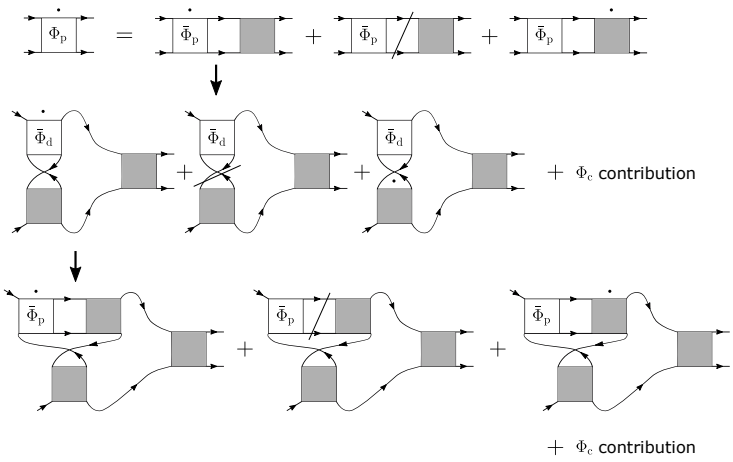

Figure 3.12.: Schematic representation of the procedure to obtain the derivative of the Parquet equation for the pairing channel. As the derivative also acts on the interactions, they have to be replaced by the derivative of its constituents, here we illustrate the insertion of the direct particle-hole contribution. In the inserted channel the derivative of the two-particle interactions has to be replaced again, here illustrated by an insertion of the pairing channel. This procedure continues until only the derivative of the dual propagator remains, thus resulting in an infinite hierarchy of equations.

point of view, the self-energies based on FRG and the scale-derivative of the SDE differ by two terms, which is similarly obtained by an actual diagrammatical expansion of the interaction in [65].

Finally, let us take a look at the susceptibilities. In both cases they are characterised by an ingoing boson which generates a pair of fermions, which annihilates into a boson again. In the FRG case this creation and annihilation takes place in fermion-boson interactions which may have a momentum and spin structure. Two of those interactions are then connected by a single-scale propagator and by a Green's function to form the susceptibility. On the contrary, in the perturbation theory this fermion-boson interaction is point-like, that is structureless, and the susceptibility consists of two contributions. At first there is a bubble, where two Green's functions connect the two fermion-boson points. Second, there is a contribution where these fermion-boson points are connected via two pairs of Green's functions to a full two-fermion interaction. In order to compare both cases, we reformulate the susceptibility of the perturbation theory by introducing extended fermion-boson interactions, which combine the point-like interaction as such and this very interaction connected to the two-fermion interaction, such that the susceptibility can be rewritten in terms of two fermion-boson interactions of this kind connected by a pair of Green's functions, which is a formulation that allows a further comparison between the FRG and the perturbation theory.

If the objects in the perturbation theory formulation are assumed to be scale-dependent and if we keep the higher order interactions fixed for the corresponding Λ, the newly obtained flow equation for susceptibilities directly equals the one of the FRG, when the derivative of the Green's function is replaced by the single-scale operator according to corollary 3.20. The derivative applied to the equation of the fermion-boson interaction only affects the Green's functions because we keep $\gamma^{(4,0)\Lambda}$ fixed, and because the point-like fermion-boson interaction is scale-independent. Again, due to corollary 3.20, we can replace the Green's function with the scale-derivative by the single-scale propagator. Then, only

the point-like interaction has to be replaced by the extended fermion-boson interaction to make this perturbation theory based flow-equation equal to the FRG one. This corresponds to the insertion of a dual propagator and a two-fermion interaction between the point-like interaction and the single-scale propagator Green's function pair.

Taking all these arguments into consideration shows that all the contributions of the FRG equations in our truncation to $2n + 2m < 5$ are contained in the perturbation theory. However, by a scale-dependent treatment of the perturbation theory, additional terms arise. Those terms can partially be included in the truncated FRG equations by calculating multi-loop corrections [66].

3.5.4. SU(2)-Symmetric Flow Equations

Although we employ the $2n + 2m < 5$-vertex truncation and although we don't use the multi-loop extension, the FRG equations are still highly involved. In fact, each integration step of the differential equation of the two-particle interaction requires to perform four integrations (respective sums) over all degrees of freedom. As many systems exhibit an SU(2)-symmetry, the calculation can be simplified by exploiting the resulting symmetries according to theorem 3.4.3 (see also [60]). The spin is, therefore, treated explicitly and is extracted from the general label i in this section. According to the conservation of the total spin the one-particle Green's functions, the self-energy, the single-scale propagator and the electron-hole fermion-boson vertex are diagonal in spin space, that is, for example, $G_{s_1;s_2}(1;2) = G(1;2)\delta_{s_1,s_2}$, while the electron-electron fermion-boson interactions become $\gamma^{(2,1)\Lambda}_{\mathrm{ee};s_1,s_2}(1;2;1') = \gamma^{(2,1)\Lambda}_{\mathrm{ee}}(1;2;1')\delta_{s_1,-s_2}$. The full two-particle interaction can now be written as

$$\gamma^{(4,0)\Lambda}_{s_1,s_2;s_3,s_4}(1,2;3,4) = -V^{\Lambda}(1,2;3,4)\delta_{s_1,s_3}\delta_{s_2,s_4} + \bar{V}^{\Lambda}(1,2;3,4)\delta_{s_1,s_4}\delta_{s_2,s_3}, \tag{3.277}$$

with V^{Λ} and $\bar{V}^{\Lambda}$ being spin-independent interactions. The flow equations of these SU(2)-symmetric, spin-independent objects are given by the following theorem.

Theorem 3.25 (SU(2)-Symmetric Flow Equations)
Let the system under consideration be SU(2)-symmetric, let the flow equation for the n-fermion and m-boson interactions $\gamma^{(2n,m)\Lambda}$ in the $2n + 2m < 5$-vertex truncation be given by theorem 3.21 and let $i = (\boldsymbol{r}_i, o_i, \tau_i)$. Let, furthermore, V^{Λ} be the spin-independent two-fermion interaction corresponding to $\gamma^{(4,0)\Lambda}$. Then the full two-particle vertex is given by

$$\gamma^{(4,0)\Lambda}_{s_1,s_2;s_3,s_4}(1,2;3,4) = -V^{\Lambda}(1,2;3,4)\delta_{s_1,s_3}\delta_{s_2,s_4} + V^{\Lambda}(1,2;4,3)\delta_{s_1,s_4}\delta_{s_2,s_3}, \tag{3.278}$$

and the flow equations are given as follows:

1) For the self-energy as

$$\Sigma^{\Lambda}(1,2) = \int \mathrm{d}\tilde{1} \int \mathrm{d}\tilde{2}\, S^{\Lambda}(\tilde{1};\tilde{2})\left(-2V^{\Lambda}(1,\tilde{2};2,\tilde{1}) + V^{\Lambda}(1,\tilde{2};\tilde{1},2)\right). \tag{3.279}$$

2) For the two-particle interaction as

$$\dot{V}^{\Lambda}(1,2;3,4) = \bar{\mathcal{T}}^{\mathrm{P},\Lambda}(1,2;3,4) + \bar{\mathcal{T}}^{\mathrm{D},\Lambda}(1,2;3,4) + \bar{\mathcal{T}}^{\mathrm{C},\Lambda}(1,2;3,4), \tag{3.280}$$

with

$$\begin{aligned}
\bar{\mathcal{T}}^{\mathrm{P},\Lambda}(1,2;3,4) &= -\int \mathrm{d}\tilde{1}\,\cdots\int \mathrm{d}\tilde{4}\, L(\tilde{1},\tilde{2};\tilde{3},\tilde{4})\, V^{\Lambda}(1,2;\tilde{1},\tilde{2})\, V^{\Lambda}(\tilde{3},\tilde{4};3,4),\\
\bar{\mathcal{T}}^{\mathrm{D},\Lambda}(1,2;3,4) &= \int \mathrm{d}\tilde{1}\,\cdots\int \mathrm{d}\tilde{4}\, L(\tilde{1},\tilde{2};\tilde{3},\tilde{4})\,\big(-2V^{\Lambda}(1,\tilde{3};3,\tilde{2})\, V^{\Lambda}(\tilde{4},2;\tilde{1},4)\\
&\qquad + V^{\Lambda}(1,\tilde{3};3,\tilde{2})\, V^{\Lambda}(\tilde{4},2;4,\tilde{1}) + V^{\Lambda}(1,\tilde{3};\tilde{2},3)\, V^{\Lambda}(\tilde{4},2;\tilde{1},4)\big)\,.\\
\bar{\mathcal{T}}^{\mathrm{C},\Lambda}(1,2;3,4) &= \int \mathrm{d}\tilde{1}\,\cdots\int \mathrm{d}\tilde{4}\, L(\tilde{1},\tilde{2};\tilde{3},\tilde{4})\, V^{\Lambda}(1,\tilde{3};\tilde{2},4)\, V^{\Lambda}(\tilde{4},2;3,\tilde{1}).
\end{aligned} \tag{3.281}$$

3a) For the electron-hole fermion-boson interaction as

$$\begin{aligned}
\dot{\bar{\gamma}}^{(2,1)\Lambda}_{\mathrm{eh},n}(1;2;1'_s) = \int \mathrm{d}\tilde{1}\,\cdots\int \mathrm{d}\tilde{4}\, L(\tilde{1},\tilde{2};\tilde{3},\tilde{4})\, \bar{\gamma}^{(2,1)\Lambda}_{\mathrm{eh},n}(\tilde{3};\tilde{2};1'_s)\\
\big(2V^{\Lambda}(1,\tilde{4};2,\tilde{1})\delta_{s'_1,0} - V^{\Lambda}(1,\tilde{4};\tilde{1},2)\big)\,.
\end{aligned} \tag{3.282}$$

3b) For the electron-electron fermion-boson interaction as

$$\begin{aligned}
&\dot{\bar{\gamma}}^{(2,1)\Lambda}_{\mathrm{ee},n}(\ ;1,2;1'_s)\\
&\qquad = -\frac{1}{2}\int \mathrm{d}\tilde{1}\,\cdots\int \mathrm{d}\tilde{4}\, L(\tilde{1},\tilde{2};\tilde{3},\tilde{4})\, \bar{\gamma}^{(2,1)\Lambda}_{\mathrm{ee},n}(\ ;\tilde{1},\tilde{2};1'_s)\, V^{\Lambda}(\tilde{3},\tilde{4};1,2).
\end{aligned} \tag{3.283}$$

4) And for the susceptibilities as

$$\begin{aligned}
&\bar{\chi}^{\Lambda}_{\mathrm{eh},nn'}(1',2',s_b)\\
&\qquad = \int \mathrm{d}\tilde{1}\,\cdots\int \mathrm{d}\tilde{4}\, L^{\Lambda}(\tilde{1},\tilde{2};\tilde{3},\tilde{4})\, \bar{\gamma}^{(2,1)\Lambda}_{\mathrm{eh},n}(\tilde{3};\tilde{2};1'_{s_b})\bar{\gamma}^{(2,1)\Lambda}_{\mathrm{eh},n}(\tilde{4};\tilde{1};2'_{s_b})(1+\delta_{s_b}),
\end{aligned} \tag{3.284}$$

$$\begin{aligned}
&\bar{\chi}^{\Lambda}_{\mathrm{ee},nn'}(1',2',s_b)\\
&\quad = \int \mathrm{d}\tilde{1}\,\cdots\int \mathrm{d}\tilde{4}\, L^{\Lambda}(\tilde{1},\tilde{2};\tilde{3},\tilde{4})\, \bar{\gamma}^{(2,1)\Lambda}_{\mathrm{ee},n}(\cdot;\tilde{1},\tilde{2};1'_{s_b})\bar{\gamma}^{(2,1)\Lambda}_{\mathrm{hh},n}(\tilde{3},\tilde{4};\cdot;2'_{s_b})(1+\delta_{s_b}).
\end{aligned} \tag{3.285}$$

Proof: Due to the conservation of the total spin the interaction can be decomposed into

$$\begin{aligned}
\gamma^{(4,0)\Lambda}_{s_1,s_2;s_3,s_4}(1,2;3,4) &= -V^{\Lambda}(1,2;3,4)\delta_{s_1,s_3}\delta_{s_2,s_4} + \bar{V}^{\Lambda}(1,2;3,4)\delta_{s_1,s_4}\delta_{s_2,s_3}\\
= -\gamma^{(4,0)\Lambda}_{s_1,s_2;s_4,s_3}(1,2;4,3) &= V^{\Lambda}(1,2;4,3)\delta_{s_1,s_4}\delta_{s_2,s_3} - \bar{V}^{\Lambda}(1,2;4,3)\delta_{s_1,s_3}\delta_{s_2,s_4},
\end{aligned} \tag{3.286}$$

where the second line results from the anticommutativity of the arguments (cf. thm. 3.17.1). By comparing these lines we get

$$\bar{V}^{\Lambda}(1,2;3,4) = V^{\Lambda}(1,2;4,3) = V^{\Lambda}(2,1;3,4), \tag{3.287}$$

so that the full decomposed vertex is given by equation (3.278).

Next, we consider the different flow equations of theorem 3.21:

1) Due to the SU(2)-symmetry the self-energy Σ^Λ and the single-scale propagator S^Λ are diagonal in spin-space. An insertion of the above decomposition into the flow equation of the self-energy (cf. eq. (3.227)) and an evaluation of the spin-sums then directly results in

$$\dot{\Sigma}^\Lambda(1,2) = \int \mathrm{d}\tilde{1} \int \mathrm{d}\tilde{2}\, S^\Lambda(\tilde{1};\tilde{2}) \left(-2V^\Lambda(1,\tilde{2};2,\tilde{1}) + V^\Lambda(1,\tilde{2};\tilde{1},2)\right). \tag{3.288}$$

By the evaluation of the spin-sum $s_1 = s_2$ also holds on the right hand side of the equation, as expected. The resulting spin-δs were, therefore, left out.

2) When the decomposition of the two-particle interaction is inserted into the left hand side of its flow equation (3.228) two different terms are obtained. As V^Λ is spin-independent and as both terms in equation (3.278) are related by symmetry, it is sufficient to consider the flow for only one combination of spins. Without loss of generality we choose to derive the flow equation for the spin combination given by $\delta_{s_1 s_3}\delta_{s_2 s_4}$ and note that exactly the same set of terms would arise for the other choice. As the Green's functions and the single-scale propagators are diagonal in spins, the particle-particle propagator is given by

$$L^\Lambda_{s_1,s_2,s_3,s_4}(1,2;3,4) = L^\Lambda(1,2;3,4)\delta_{s_1 s_3}\delta_{s_2 s_4}. \tag{3.289}$$

Now consider the pairing contribution to the two-particle interaction. An insertion of the decomposition (cf. eq. (3.278)) leads to four terms for which we can evaluate the internal spin-sum. We observe that due to this evaluation the term which originates from the first part of the decomposition at each interaction and the terms originating from the second part of the decomposition at each corresponding place obtain the same external argument and spin structure so that both are. Similarly, the other two terms become equal with an external argument and spin structure where arguments 3 and 4 changed corresponding to the first case. In combination, the prefactor thus vanishes and the pairing channel becomes

$$\begin{aligned}\mathcal{T}^{\mathrm{P},\Lambda}_{s_1,s_2,s_3,s_4}(1,2;3,4) = &\int \mathrm{d}\tilde{1} \cdots \int \mathrm{d}\tilde{4}\, L(\tilde{1},\tilde{2};\tilde{3},\tilde{4}) \\ &\left(V^\Lambda(1,2;\tilde{1},\tilde{2})\, V^\Lambda(\tilde{3},\tilde{4};3,4)\delta_{s_1 s_3}\delta_{s_2 s_4} - V^\Lambda(1,2;\tilde{1},\tilde{2})\, V^\Lambda(\tilde{3},\tilde{4};4,3)\delta_{s_1 s_4}\delta_{s_2 s_3}\right)\end{aligned} \tag{3.290}$$

for SU(2)-symmetric vertices. In the direct electron-hole channel no combinations of vertices are equivalent, so that we obtain

$$\begin{aligned}\mathcal{T}^{\mathrm{D},\Lambda}_{s_1,s_2,s_3,s_4}(1,2;3,4) = \int \mathrm{d}\tilde{1} \cdots \int \mathrm{d}\tilde{4}\, L(\tilde{1},\tilde{2};\tilde{3},\tilde{4}) \big(&2V^\Lambda(1,\tilde{3};3,\tilde{2})V^\Lambda(\tilde{4},2;\tilde{1},4)\delta_{s_1 s_3}\delta_{s_2 s_4} \\ &- V^\Lambda(1,\tilde{3};3,\tilde{2})V^\Lambda(\tilde{4},2;4,\tilde{1})\delta_{s_1 s_3}\delta_{s_2 s_4} - V^\Lambda(1,\tilde{3};\tilde{2},3)V^\Lambda(\tilde{4},2;\tilde{1},4)\delta_{s_1 s_3}\delta_{s_2 s_4} \\ &+ V^\Lambda(1,\tilde{3};\tilde{2},3)V^\Lambda(\tilde{4},2;4,\tilde{1})\delta_{s_1 s_4}\delta_{s_2 s_3}\big),\end{aligned} \tag{3.291}$$

in which the factor 2 in front of the first term of the right hand side results from the spin summation of the inner loop. According to remark 3.22, the same result except for a global minus sign is obtained for the crossing channel by exchanging the arguments 3 and 4. All the terms on the right hand side have contributions from both possible spin-combinations in equation (3.278), which also appear on the left hand side. As it is sufficient to calculate V^Λ only for one spin-combination, we compare the coefficients for the choice of $\delta_{s_1 s_3}\delta_{s_2 s_4}$ and denote the corresponding terms as $\bar{\mathcal{T}}^\Lambda$ for each channel. Thus $\bar{\mathcal{T}}^{\mathrm{P},\Lambda}$ and $\bar{\mathcal{T}}^{\mathrm{C},\Lambda}$ each consist of one contribution, while $\bar{\mathcal{T}}^{\mathrm{D},\Lambda}$ consists of three contributions. We note that by this term, all spin

combinations are possible, thus allowing a fermion-boson interaction for singlet- and one for triplet-pairings.

3a) For this proof we consider the flow equation for the fermion-boson interactions. In the same way as for the purely fermionic interactions in theorem 3.4 it can be shown that the total spin has to be zero and is invariant under a global spin flip if the system is SU(2)-symmetric. Therefore, the electron-electron interaction gains a factor $\delta_{s_1+s_2,s_b}$, while the corresponding factor for the electron-hole interaction is $\delta_{s_1-s_2,s_b}$. Thus, as fermions have the spin $s = \pm\frac{1}{2}$, the possible bosonic spins are $s_b \in \{-1, 0, 1\}$. To obtain $s_b = \pm 1$ both electrons must have equal spins in the electron-electron case, while they must have opposite spins in the electron-hole case. For the bosonic spin $s_b = 0$ this relation holds vice versa, that is equal spins in the electron-hole case and opposite spin directions in the electron-electron case. Because of this consideration it is obvious that the bosonic spin is sufficient to characterise the spin in both cases of $\gamma^{(2,1)\Lambda}$. Due to the invariance under a global spin-flip, the cases for $s_b = +1$ and for $s_b = -1$ are equal, so that we can restrict our investigation to $s_b \in \{0, +1\}$.

When the spin decomposition is introduced into the flow equation of the electron-hole fermion-boson vertex, we have to consider the different possible spin combinations explicitly, as an internal spin loop comes into place. The fermion-boson interaction on the right hand side comes in with $\delta_{\tilde{s}_2-\tilde{2}_3,s_b}$, the dual propagator requires $\delta_{\bar{s}_1\bar{s}_3}$ and $\delta_{\bar{s}_2\bar{s}_4}$, while the first term of equation (3.278) introduces $\delta_{\bar{s}_4,\bar{s}_1}\delta_{s_1,s_2}$. This term can, therefore, only contribute if all internal spins are in the same direction, which only is the case for $s_b = 0$. In this case it gains a factor of 2 by the internal spin-sum. The second term of equation (3.278) always contributes and can be evaluated straight forwardly, such that the full flow equation becomes

$$\dot{\tilde{\gamma}}^{(2,1)\Lambda}_{\mathrm{eh},n}(1;2;1') = \frac{1}{2}\int \mathrm{d}\tilde{1}\ \cdots \int \mathrm{d}\tilde{4}\ L(\tilde{1},\tilde{2};\tilde{3},\tilde{4})\ \gamma^{(2,1)\Lambda}_{\mathrm{eh},n}(\tilde{2};\tilde{3};1') \\ \left(2V^{\Lambda}(1,\tilde{4};2,\tilde{1})\delta_{s_{1'},0} - V^{\Lambda}(1,\tilde{4};\tilde{1},2)\right). \quad (3.292)$$

3b) An insertion of the spin decomposed two-particle vertex (see eq. (3.278)) into the electron-electron case results in two terms, and for each of them the evaluation of the spin-sums results in a spin-combination given by $\delta_{s_1+s_2,s_b}$. By using the antisymmetry of the electron-electron vertex under the exchange of fermion arguments and the symmetry of V^{Λ} under the exchange of both arguments, both terms become equal, resulting in

$$\dot{\tilde{\gamma}}^{(2,1)\Lambda}_{\mathrm{ee},n}(\cdot;1,2;1') = -\int \mathrm{d}\tilde{1}\ldots\int \mathrm{d}\tilde{4}\ L(\tilde{1},\tilde{2};\tilde{3},\tilde{4})\ \gamma^{(2,1)\Lambda}_{\mathrm{ee},n}(\cdot;\tilde{1},\tilde{2};1')\ V^{\Lambda}(\tilde{3},\tilde{4};1,2). \quad (3.293)$$

4) Taking into account the flow equations of the susceptibilities, namely equation (3.233) or equation (3.232), the same considerations as used above lead to the observation that the incoming and the outgoing bosons must have the same spin and that it is sufficient to consider $s_b \in \{0, 1\}$. After performing two internal spin-sums we obtain terms of the form $\delta_{\bar{s}_1+\bar{s}_4,s_1'}\delta_{\bar{s}_1+\bar{s}_4,s_2'}$ in the pairing case and terms of the form $\delta_{\bar{s}_1-\bar{s}_4,s_1'}\delta_{\bar{s}_1-\bar{s}_4,s_2'}$ in the electron-hole case. For an evaluation of the remaining sums the different possible bosonic spin-states have to be considered, due to the limited fermionic states. There are, in both cases, two different spin configurations to obtain the $s_1' = s_2' = 0$ case, such that a factor of 2 arises. Contrariwise, only one possibility exists to obtain the $s_1' = s_2' = \pm 1$ state. Thus the assertions for these cases are obtained. ■

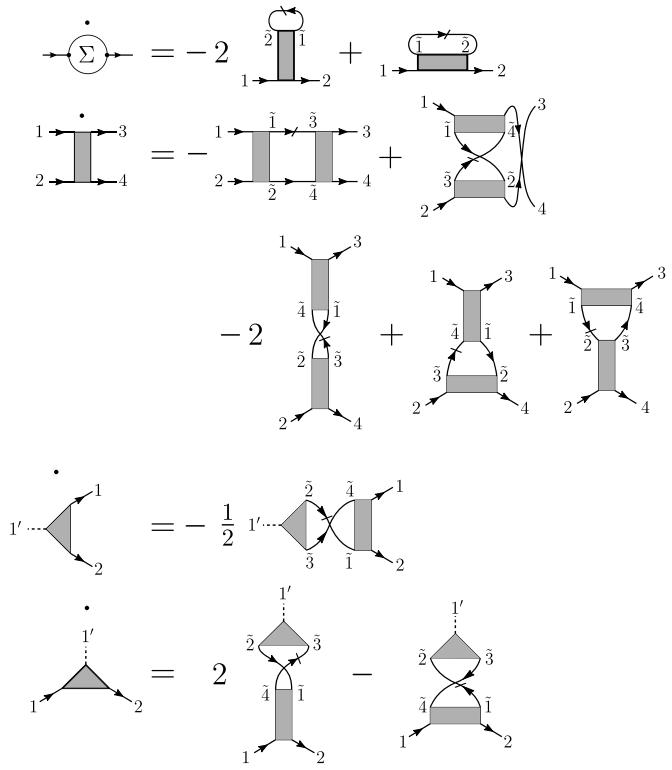

Figure 3.13.: Diagrammatic representation of the SU(2)-symmetric flow equations as provided by theorem 3.25.

These flow equations are diagrammatically depicted in figure 3.13. The rectangular box now represents the SU(2)-symmetric vertex in which the spin is conserved along the short lines. The flow equations, in general, look similar to those of the spinful case in which the former vertex is replaced by the SU(2)-symmetric one. The main difference is that the contribution of the direct electron-hole channel to the effective two-particle interaction now consists of three different diagrams. In contrast tu the spinful interaction previously discussed in corollary 3.17, the SU(2)-symmetric vertex itself is less symmetric.

Corollary 3.26 (Symmetries of the SU(2)-Symmetric Vertex)
Let V^{Λ} be the SU(2)-symmetric interaction as defined in equation (3.278) *based on $\gamma^{(4),\Lambda}$. Then V exhibits the crossing symmetry*

$$V(1,2;3,4) = V(2,1;4,3) \tag{3.294}$$

and the complex conjugation

$$V(1,2;3,4) = V^*(4,3;2,1) \tag{3.295}$$

PROOF: This directly follows from insertion of (3.278) into corollary 3.17. ■

We note that the other symmetries stated in corollary 3.17 hold in the same way for V as they hold for $\gamma^{(4),\Lambda}$. Similar to the spinful case the two-fermion interaction decomposes according to the following corollary.

Corollary 3.27 (Decomposition of the SU(2)-Symmetric Two-Fermion Interaction) *Let V^Λ be given as in theorem 3.25, and let it obey the flow equation provided by equation* (3.280). *Then, for any $\Lambda \in [0,\infty)$, V^Λ can be decomposed according to*

$$V^\Lambda = V^{\Lambda_0} + \bar{\Phi}^{\mathrm{P},\Lambda} + \bar{\Phi}^{\mathrm{D},\Lambda} + \bar{\Phi}^{\mathrm{C},\Lambda} \tag{3.296}$$

with

$$\bar{\Phi}^{\mathrm{P},\Lambda} := \int_{\Lambda_0}^{\Lambda} \mathrm{d}\Lambda'\, \bar{\mathcal{T}}^{\mathrm{P},\Lambda'}, \qquad \bar{\Phi}^{\mathrm{D},\Lambda} := \int_{\Lambda_0}^{\Lambda} \mathrm{d}\Lambda'\, \bar{\mathcal{T}}^{\mathrm{D},\Lambda'} \quad \textit{and} \quad \bar{\Phi}^{\mathrm{C},\Lambda} := \int_{\Lambda_0}^{\Lambda} \mathrm{d}\Lambda'\, \bar{\mathcal{T}}^{\mathrm{C},\Lambda}. \tag{3.297}$$

In order to further simplify the computation, we next consider the translational symmetry in time and space and use the corresponding Fourier transformations.

3.5.5. Flow Equations in Frequency and in Momentum Space

Up to this point all the flow equations have been derived in lattice space and in (imaginary) time. Therefore, all the interactions depend on $2n+m$ generalised quantum numbers, and the integration over two-particle propagator loops includes four integrals/sums of the generalised quantum index $i = (\boldsymbol{r}_i, o_i, s_i, \tau_i)$. As we consider a time-invariant solid state system with a periodic lattice, a transformation to momentum and to frequency space reduces the number of the corresponding independent arguments and the number of integrals, due to the conservation of energy and momentum according to theorem 3.17 and 3.6. Therefore we exploit the notation of the interactions with a reduced number of generalised momentum arguments while all the spin and orbital indices have to be maintained. When we denote the fermionic arguments by $k = (\boldsymbol{k}, \omega)$, the bosonic arguments by $q = (\boldsymbol{q}, \nu)$ and when we use $o = (o, s)$ as a combined spin and orbital index the conservation of energy and momentum leads to the notation

$$\gamma^{(4,0)\Lambda}_{o_1 o_2, o_3 o_4}(k_1, k_2; k_3)\beta\delta_{k_1+k_2, k_3+k_4} = \gamma^{(4,0)\Lambda}_{o_1 o_2, o_3 o_4}(k_1, k_2; k_3, k_4) \tag{3.298}$$

$$\gamma^{(2,1)\Lambda}_{\mathrm{eh},n;o_1,o_2}(k_1; \cdot; q)\beta\delta_{k_1-k_2,q} = \gamma^{(2,1)\Lambda}_{\mathrm{eh},n;o_1,o_2}(k_1; k_2; q) \tag{3.299}$$

$$\gamma^{(2,1)\Lambda}_{\mathrm{ee},n;o_1 o_2}(\cdot; k_1; q)\beta\delta_{k_1+k_2,q} = \gamma^{(2,1)\Lambda}_{\mathrm{ee},n;o_1 o_2}(\cdot; k_1, k_2; q) \quad \text{and} \tag{3.300}$$

$$\gamma^{(0,2)\Lambda}_{\eta,nn'}(q_1)\beta\delta_{q_1,q_2} = \gamma^{(0,2)\Lambda}_{\eta,nn'}(q_1, q_2), \tag{3.301}$$

which can analogously be obtained for the SU(2)-symmetric case.

In order to arrive at flow equations in frequency in and momentum space we simplify the notation by the following definitions.

Definition 42 (Generalised Momentum and Position Space Notation)
Let $k = (\boldsymbol{k}, \omega_n)$ and let $x = (\boldsymbol{R}, \tau)$ be the generalised momentum and position space arguments. Then their product is defined as

$$xk := \boldsymbol{R}\boldsymbol{k} - \tau\omega_n. \tag{3.302}$$

The integral in the generalised momentum space is defined as

$$\int \mathrm{d}k := \int \mathrm{d}\frac{\boldsymbol{k}}{|\mathcal{B}|} \sum_{\omega_n}. \tag{3.303}$$

The integral in the generalised position space is defined as

$$\int \mathrm{d}x := \sum_{\boldsymbol{R}} \int \mathrm{d}\tau\,. \tag{3.304}$$

The δ-distribution in the generalised momentum space is defined as

$$\delta_{k_1,k_2} := |\mathcal{B}|\delta_{\boldsymbol{k}_1,\boldsymbol{k}_2}\delta_{\omega_1,\omega_2}. \tag{3.305}$$

We remark that the number of orbital and spin arguments (in the absence of an SU(2)-symmetry) can not be reduced in such a way. As the lattice symmetry allows us to represent the interaction with a reduced number of arguments, we define the corresponding interaction as follows:

Theorem 3.28 (Frequency and Momentum Space Flow Equations)
Let the system under consideration be time-independent and periodic on a lattice. Let $o_i = (o_i, s_i)$ be a combined spin-orbital index, let $k_i = (\boldsymbol{k}_i, \omega_i)$ be a generalised fermionic momentum and let $q_i = (\boldsymbol{q}_i, \nu_i)$ be the generalised bosonic momentum. Let the flow equations for the n-fermion and m-boson interactions $\gamma^{(2n,m)\Lambda}$ in the $2n + 2m < 5$-vertex truncation be as given in theorem 3.21. Then the flow equations for the corresponding interactions in frequency and in momentum space are given as follows:

1) For the self-energy as

$$\dot{\Sigma}^{\Lambda}_{o_1;o_2}(k) = \frac{1}{\beta}\int \mathrm{d}k' \sum_{\tilde{o}_1,\tilde{o}_2} S^{\Lambda}(k')_{\tilde{o}_1;\tilde{o}_2}\, \gamma^{(4,0)\Lambda}_{o_1,\tilde{o}_2;o_2,\tilde{o}_1}(k,k';k). \tag{3.306}$$

2) For the two-fermion interaction as

$$\dot{\gamma}^{(4,0)\Lambda}_{o_1o_2,o_3o_4}(k_1,k_2;k_3) = \mathcal{T}^{\mathrm{P},\Lambda}_{o_1o_2,o_3o_4}(k_1,k_2;k_3) + \mathcal{T}^{\mathrm{C},\Lambda}_{o_1o_2,o_3o_4}(k_1,k_2;k_3) + \mathcal{T}^{\mathrm{D},\Lambda}_{o_1o_2,o_3o_4}(k_1,k_2;k_3), \tag{3.307}$$

with

$$\mathcal{T}^{\mathrm{P},\Lambda}_{o_1o_2,o_3o_4}(k_1,k_2;k_3) = \frac{1}{\beta}\int \mathrm{d}k \int \mathrm{d}k' \sum_{\tilde{o}_1\ldots\tilde{o}_4} \frac{1}{2}\, L_{\tilde{o}_1\tilde{o}_2,\tilde{o}_3\tilde{o}_4}(k,k') \gamma^{(4,0)\Lambda}_{o_1o_2,\tilde{o}_1\tilde{o}_2}(k_1,k_2;k)\, \gamma^{(4,0)\Lambda}_{\tilde{o}_3\tilde{o}_4,o_3o_4}(k,k';k_3)\, \delta_{k',k_1+k_2-k},$$

$$\begin{aligned}\mathcal{T}^{\mathrm{D},\Lambda}_{o_1o_2,o_3o_4}(k_1,k_2;k_3) &= \frac{1}{\beta}\int \mathrm{d}k \int \mathrm{d}k' \sum_{\tilde{o}_1\dots\tilde{o}_4} L_{\tilde{o}_1\tilde{o}_2,\tilde{o}_3\tilde{o}_4}(k,k') \\ &\qquad \gamma^{(4,0)\Lambda}_{o_1\tilde{o}_3,o_3\tilde{o}_2}(k_1,k;k_3)\,\gamma^{(4,0)\Lambda}_{\tilde{o}_3o_2,\tilde{o}_1o_4}(k',k_2;k)\,\delta_{k',k+k_3-k_1} \\ \mathcal{T}^{\mathrm{C},\Lambda}_{o_1o_2,o_3o_4}(k_1,k_2;k_3) &= -\frac{1}{\beta}\int \mathrm{d}k \int \mathrm{d}k' \sum_{\tilde{o}_1\dots\tilde{o}_4} L_{\tilde{o}_1\tilde{o}_2,\tilde{o}_3\tilde{o}_4}(k,k') \\ &\qquad \gamma^{(4,0)\Lambda}_{o_1\tilde{o}_3,o_4\tilde{o}_2}(k_1,k;k_4)\,\gamma^{(4,0)\Lambda}_{\tilde{o}_4o_2,\tilde{o}_1o_3}(k',k_2;k)\,\delta_{k',k+k_4-k_1},\end{aligned} \tag{3.308}$$

in which we wrote $k_4 = k_1 + k_2 - k_3$ for the sake of brevity.

3) For the fermion-boson interactions as

$$\begin{aligned}\dot{\gamma}^{(2,1)\Lambda}_{\mathrm{eh},n;o_1,o_2}(k_1;\cdot;q) &= \frac{1}{2}\frac{1}{\beta}\int \mathrm{d}k \sum_{\tilde{o}_1\dots\tilde{o}_4} L_{\tilde{o}_1\tilde{o}_2;\tilde{o}_3\tilde{o}_4}(k,k+q) \\ &\qquad \gamma^{(2,1)\Lambda}_{\mathrm{eh},n;\tilde{o}_2;\tilde{o}_3}(k+q;\cdot;q)\,\gamma^{(4,0)\Lambda}_{o_1\tilde{o}_4;o_2\tilde{o}_1}(k_1,k+q;k_2),\end{aligned} \tag{3.309}$$

$$\begin{aligned}\gamma^{(2,1)\Lambda}_{\mathrm{ee},n;\cdot,o_1o_2}(\cdot;k_1;q) &= \frac{1}{2}\frac{1}{\beta}\int \mathrm{d}k \sum_{\tilde{o}_1\dots\tilde{o}_4} L^{\Lambda}_{\tilde{o}_1\tilde{o}_2,\tilde{o}_3\tilde{o}_4}(k,q-k) \\ &\qquad \gamma^{(2,1)\Lambda}_{\mathrm{ee},n;\cdot,\tilde{o}_1\tilde{o}_2}(\cdot;k;q)\,\gamma^{(4,0)\Lambda}_{\tilde{o}_3\tilde{o}_4,o_1o_2}(k,q-k;k_1).\end{aligned} \tag{3.310}$$

4) For the susceptibilities as

$$\begin{aligned}\dot{\gamma}^{(0,2)\Lambda}_{eh,nn'}(q) &= \frac{1}{\beta}\int \mathrm{d}k \sum_{\tilde{o}_1\dots\tilde{o}_4} L^{\Lambda}_{\tilde{o}_1\tilde{o}_2,\tilde{o}_3\tilde{o}_4}(k,k-q) \\ &\qquad \gamma^{(2,1)\Lambda}_{eh,n;\tilde{o}_3,\tilde{o}_2}(k;\cdot;q)\,\gamma^{(2,1)\Lambda}_{eh,n';\tilde{o}_4\tilde{o}_1}(k-q;\cdot;q),\end{aligned} \tag{3.311}$$

$$\begin{aligned}\dot{\gamma}^{(0,2)\Lambda}_{ee,nn'}(q) &= \frac{1}{\beta}\int \mathrm{d}k \sum_{\tilde{o}_1\dots\tilde{o}_4} L^{\Lambda}_{\tilde{o}_1\tilde{o}_2,\tilde{o}_3\tilde{o}_4}(k,q-k) \\ &\qquad \gamma^{(2,1)\Lambda}_{ee,n;\cdot,\tilde{o}_1\tilde{o}_2}(\cdot;k;q)\,\gamma^{(2,1)\Lambda}_{hh,n';\tilde{o}_3\tilde{o}_4,\cdot}(k;\cdot;-q).\end{aligned} \tag{3.312}$$

Proof: In order to arrive at the formulation of the flow equations in frequency and in momentum space a Fourier transformation has to be performed for all the arguments in the equations of theorem 3.21. The resulting momentum space objects fulfil the relations given by theorem 3.6, that is, the one-particle Green's function is diagonal in frequency and in momentum space, and the two-fermion interaction depends on three independent frequencies and momenta, while the fourth is fixed by the conservation of energy and momentum. Similar relations hold for the fermion-boson interactions, so that the difference between the two fermionic, generalised momenta is the bosonic one.

Before we perform the transformations explicitly, we note the following helpful relation

$$\int \mathrm{d}x\, e^{i(k_1-k_2)x} = \int_0^\beta \mathrm{d}\tau \sum_{\boldsymbol{R}} e^{i(\boldsymbol{k}_1-\boldsymbol{k}_2)\boldsymbol{R}-i(\omega_1-\omega_2)\tau} = \beta|\mathcal{B}|\delta_{\omega_1,\omega_2}\delta_{\boldsymbol{k}_1,\boldsymbol{k}_2} = \beta\delta_{k_1,k_2}, \tag{3.313}$$

as the corresponding terms will appear frequently.

1) The Fourier transformation of the flow equation of the self-energy (see eq. (3.227)) is given by

$$\begin{aligned}\dot{\Sigma}_{o_1,o_2}(k_1)\beta\delta_{k_1,k_2} &= \dot{\Sigma}_{o_1,o_2}(k_1;k_2)\\ &= \int \mathrm{d}x_1 \int \mathrm{d}x_2\, e^{-ik_1x_1}\, e^{ik_2x_2}\, \dot{\Sigma}_{o_1,o_2}(x_1;x_2)\\ &= \sum_{\tilde{o}_1,\tilde{o}_2} \int \mathrm{d}x_1 \int \mathrm{d}x_2\, e^{-ik_1x_1} e^{ik_2x_2}\\ &\quad \cdot \int \mathrm{d}\tilde{x}_1 \int \mathrm{d}\tilde{x}_2\, S_{\tilde{o}_1,\tilde{o}_2}(\tilde{x}_1;\tilde{x}_2)\, \gamma^{(4,0)\Lambda}_{o_1,\tilde{o}_2;o_2,\tilde{o}_1}(x_1,\tilde{x}_2;x_2,\tilde{x}_1),\end{aligned} \tag{3.314}$$

which includes the conservation of energy and momentum (cf. thm. 3.6). To obtain the full expression in momentum space, S^Λ and $\gamma^{(4,0)\Lambda}$ given in position space have to be replaced by their Fourier transformed counterparts, that is

$$\begin{aligned}S^\Lambda(\tilde{x}_1;\tilde{x}_2) &= \frac{1}{\beta^2} \int \mathrm{d}k_1' \int \mathrm{d}k_2'\, e^{ik_1'\tilde{x}_1}\, e^{-ik_2'\tilde{x}_2}\, S^\Lambda_{\tilde{o}_1;\tilde{o}_2}(k_1';k_2') \quad \text{and}\\ \gamma^{(4,0)\Lambda}_{o_1,\tilde{o}_2;o_2,\tilde{o}_1}(x_1,\tilde{x}_2;x_2,\tilde{x}_1) &= \frac{1}{\beta^4} \int \mathrm{d}k_1'' \cdots \int \mathrm{d}k_4''\, e^{ik_1''x_1} e^{ik_2''\tilde{x}_2} e^{-ik_3''x_2} e^{-ik_4''\tilde{x}_1}\\ &\qquad \gamma^{(4,0)\Lambda}_{o_1,\tilde{o}_2;o_2,\tilde{o}_1}(k_1'',k_2'';k_3'',k_4'').\end{aligned} \tag{3.315}$$

Due to the translational invariance in time and space, the momentum space objects can be replaced by $\beta\delta_{k_1',k_2'} S^\Lambda_{\tilde{o}_1;\tilde{o}_2}(k_1)$ and $\beta\delta_{k_1''+k_2'',k_3''+k_4''}\gamma^{(4,0)\Lambda}_{o_1,\tilde{o}_2;o_2,\tilde{o}_1}(k_1'',k_2'';k_3'')$. When, after the insertion of these Fourier transformations, all the terms containing the same x-index are combined and the corresponding integrals are evaluated, we obtain

$$\begin{aligned}&\int \mathrm{d}x_1 \int \mathrm{d}x_2 \int \mathrm{d}\tilde{x}_1 \int \mathrm{d}\tilde{x}_2\, e^{-i(k_1-k_1'')x_1}\, e^{i(k_2-k_3'')x_2}\, e^{i(k_1'-k_4'')\tilde{x}_1}\, e^{-i(k_2'-k_2'')\tilde{x}_2}\\ &\qquad = \beta^4 \delta_{k_1,k_1''}\, \delta_{k_2,k_3''}\, \delta_{k_1',k_4''}\, \delta_{k_2',k_2''}\end{aligned} \tag{3.316}$$

for these terms. Due to this, all but one of the momentum space integrals can easily be evaluated, resulting in

$$\dot{\Sigma}_{o_1,o_2}(k_1)\delta_{k_1,k_2} = \frac{1}{\beta} \sum_{\tilde{o}_1,\tilde{o}_2} \int \mathrm{d}k_2'\, S^\Lambda_{\tilde{o}_1;\tilde{o}_2}(k_2')\gamma^{(4,0)\Lambda}_{o_1,\tilde{o}_2;o_2,\tilde{o}_1}(k_1,k_2';k_1)\, \delta_{k_1,k_2}, \tag{3.317}$$

which equals the assertion. To simplify the procedure in the following, we observe that the internal arguments which are connected by the propagator obtain the same momentum, while the external arguments obtain the same momentum dependence as required by the expression on the left hand side.

2) We proceed analogously for the two-particle interaction and leave out the orbital indices, as we have seen that these are not affected by the Fourier transformations. In a first step, the transformation to momentum space yields

$$\begin{aligned}\dot{\gamma}^{(4,0)\Lambda}(k_1,k_2;k_3)\beta\delta_{k_1+k_2,k_3+k_4} &= \dot{\gamma}^{(4,0)\Lambda}(k_1,k_2;k_3,k_4)\\ &= \frac{1}{\beta^4} \int \mathrm{d}x_1 \cdots \int \mathrm{d}x_4\, e^{-ik_1x_1} e^{-ik_2x_2} e^{ik_3x_3} e^{ik_4x_4} \dot{\gamma}^{(4,0)\Lambda}(x_1,x_2;x_3,x_4),\end{aligned} \tag{3.318}$$

where the right hand side of the flow equation has to be inserted. We will treat all the three terms of the right hand side separately, starting with the pairing channel. The Fourier transformation of the two-propagator term results in

$$\begin{aligned} L^{\Lambda}(\tilde{x}_1,\tilde{x}_2;\tilde{x}_3,\tilde{x}_4) &= \frac{1}{\beta^4}\int \mathrm{d}k_1' \,\cdots\int \mathrm{d}k_4'\, e^{ik_1'\tilde{x}_1}e^{ik_2'\tilde{x}_2}e^{-ik_3'\tilde{x}_3}e^{-ik_4'\tilde{x}_4}L^{\Lambda}(k_1',k_2';k_3',k_4') \\ &= \frac{1}{\beta^2}\int \mathrm{d}k_1' \,\cdots\int \mathrm{d}k_4'\, e^{ik_1'\tilde{x}_1}e^{ik_2'\tilde{x}_2}e^{-ik_3'\tilde{x}_3}e^{-ik_4'\tilde{x}_4}L^{\Lambda}(k_1',k_2')\delta_{k_1',k_3'}\delta_{k_2',k_4'}, \end{aligned} \tag{3.319}$$

while the transformation of the interactions is analogous to the one in the self-energy case with a change to the correct arguments. When the terms corresponding to either of the eight position space arguments are combined, each of them again results in a term of the form $\beta\delta_{k_i,k_j}$, as expected. Therefore, we can replace the pairs of position space arguments which are connected by L^{Λ} with the same momentum argument. This procedure corresponds to the evaluation of all but two momentum space integrals, resulting in

$$\begin{aligned} \mathcal{T}^{\mathrm{P},\Lambda}(k_1,k_2;k_3,k_4) = \int \mathrm{d}k_1' \int \mathrm{d}k_2'\, \delta_{k_1+k_2,k_1'+k_2'}\, \delta_{k_1'+k_2',k_3+k_4} \\ L^{\Lambda}(k_1',k_2')\,\gamma^{(4,0)\Lambda}(k_1,k_2;k_1')\,\gamma^{(4,0)\Lambda}(k_1',k_2';k_3). \end{aligned} \tag{3.320}$$

Due to the combination of arguments, we can rewrite the second δ-distribution as $\delta_{k_1+k_2,k_3+k_4}$, such that the reduced argument form corresponding to the translational invariance can be used on the left hand side and the term equals the assertion. At this point we kept up both momentum integrals to simplify the notation, as otherwise k_2' has to be replaced by $k_1+k_2-k_1'$ whenever it appears in L^{Λ} and $\gamma^{(4,0)\Lambda}$. In the electron-hole channels the same steps have to be performed, but the combinations of the lattice space arguments are different so that different exponential terms are combined. When the momentum space integrals are evaluated for the direct ph-term, we obtain

$$\begin{aligned} \mathcal{T}^{\mathrm{D},\Lambda}(k_1,k_2;k_3,k_4) = \int \mathrm{d}k_1' \int \mathrm{d}k_2'\, \delta_{k_1+k_2',k_3+k_1'}\, \delta_{k_1'+k_2,k_2'+k_4} \\ L^{\Lambda}(k_1',k_2')\,\gamma^{(4,0)\Lambda}(k_1,k_1';k_3)\,\gamma^{(4,0)\Lambda}(k_2',k_2;k_1'). \end{aligned} \tag{3.321}$$

Playing around with the arguments of the δ-distribution, we can turn them into the required form of $\delta_{k_1+k_2,k_3+k_4}\delta_{k_1'-k_2',k_1-k_3}$. As the crossing electron-hole term is related to the direct one by simply changing the last two arguments, we can directly read off its Fourier transformation as

$$\begin{aligned} \mathcal{T}^{\mathrm{C},\Lambda}(k_1,k_2;k_3,k_4) = \int \mathrm{d}k_1' \int \mathrm{d}k_2'\, \delta_{k_1+k_2',k_4+k_1'}\, \delta_{k_1'+k_2,k_2'+k_3} \\ L^{\Lambda}(k_1',k_2')\,\gamma^{(4,0)\Lambda}(k_1,k_1';k_4)\,\gamma^{(4,0)\Lambda}(k_2',k_2;k_1'), \end{aligned} \tag{3.322}$$

for which the δ-distributions can be reformulated to $\delta_{k_1+k_2,k_3+k_4}\delta_{k_1'-k_2',k_1-k_4}$, as required.

3) The Fourier transformation of the fermion-boson vertices is along the same lines. The transformation rules for the bosonic arguments are similar to the fermionic case with the generalised bosonic momentum $q=(\boldsymbol{q},\nu)$ replacing the fermionic one. From this it follows that the conservation of momentum and energy for the fermion-boson vertex becomes $\gamma_{\mathrm{eh},n}^{(2,1)\Lambda}(k_1;k_2;q) = \gamma_{\mathrm{eh},n}^{(2,1)\Lambda}(k_1;\cdot;q)\,\beta\,\delta_{k_2-k_1,q}$ in the electron-hole case and a corresponding expression with $\delta_{k_1+k_2,q}$

in the electron-electron case. When we evaluate the expression by the same procedure as above, the flow equation becomes

$$\dot{\gamma}^{(2,1)\Lambda}_{\mathrm{eh},n}(k_1;k_2;q) = \int \mathrm{d}k_1' \int \mathrm{d}k_2' \; L^{\Lambda}(k_1',k_2')\,\gamma^{(2,1)\Lambda}_{\mathrm{eh},n}(k_2';\cdot;q)\,\gamma^{(4,0)\Lambda}(k_1,k_2';k_2) \\ \delta_{k_2'-k_1',q}\,\delta_{k_2'-k_1',k_2-k_1}. \quad (3.323)$$

An evaluation of the k_2'-integral allows us to write the second δ-distribution in terms of the external arguments $q, k_1 - k_2$, thus enabling the expression with reduced arguments. A similar treatment of the electron-electron case leads to

$$\dot{\gamma}^{(2,1)\Lambda}_{\mathrm{ee},n}(\cdot;k_1,k_2;q) = \int \mathrm{d}k_1' \int \mathrm{d}k_2'\, L^{\Lambda}(k_1',k_2')\,\gamma^{(2,1)\Lambda}_{\mathrm{ee},n}(\cdot;k_1';q)\,\gamma^{(4,0)\Lambda}(k_1',k_2';k_1) \\ \delta_{k_1'+k_2',q}\,\delta_{k_1+k_2,k_1'+k_2'}, \quad (3.324)$$

which, with the same arguments as in the electron-hole case, equals the assertion.

4) For the corresponding equations for the susceptibilities, we proceed in the same way and first obtain the conservation of energy and momentum as

$$\dot{\gamma}^{(0,2)\Lambda}_{\mathrm{ee/eh}}(\cdot;\cdot;q_1)\,\beta\,\delta_{q_1,-q_2} = \dot{\gamma}^{(0,2)\Lambda}_{\mathrm{ee/eh}}(\cdot;\cdot;q_1,q_2) \quad (3.325)$$

for both susceptibilities, which we consider next. In the pairing case, the momentum space transformation of the elements in the flow equation then results in

$$\dot{\gamma}^{(0,2)\Lambda}_{\mathrm{ee},nn'}(\cdot;\cdot;q_1,-q_2) = \int \mathrm{d}k_1' \int \mathrm{d}k_2'\,\gamma^{(2,1)\Lambda}_{\mathrm{ee},n}(\cdot;k_1';q_1)\,L^{\Lambda}(k_1',k_2')\,\gamma^{(2,1)\Lambda}_{\mathrm{hh},n'}(k_1';\cdot;q_2) \\ \delta_{k_1'+k_2',q_1}\delta_{k_1'+k_2',-q_2}, \quad (3.326)$$

which can be combined to $\delta_{k_1'+k_2',q_1}\delta_{q_1,-q_2}$ and thus equals the assertion. A similar treatment of the electron-hole susceptibility results in

$$\dot{\gamma}^{(2,0)\Lambda}_{\mathrm{eh},nn'}(\cdot;\cdot;q_1)\beta\delta_{q_1,-q_2} = \int \mathrm{d}k_1' \int \mathrm{d}k_2'\,\gamma^{(2,1)\Lambda}_{\mathrm{eh},n}(k_1';\cdot;q_1)\,L^{\Lambda}(k_1',k_2')\,\gamma^{(2,1)\Lambda}_{\mathrm{eh},n'}(k_2';\cdot;q_2) \\ \delta_{k_1'-k_2',q_1}\,\delta_{-k_1'+k_2',q_2}, \quad (3.327)$$

which completes the proof. ■

In the same way we transform the SU(2)-symmetric flow equation to momentum and to frequency space.

Theorem 3.29 (SU(2)-Symmetric Flow Equation in Momentum and in Frequency Space)

Let the system under consideration be SU(2)-invariant, time-independent and periodic. Let o_i be an orbital index, let $k_i = (\boldsymbol{k}_i, \omega_i)$ be the generalised fermion momentum and $q_i = (\boldsymbol{q}_i, \nu_i)$ be the generalised bosonic momentum. Let the flow equations for the n-fermion and m-boson interactions $\gamma^{(2n,m)\Lambda}$ in the $2n+2m<5$-vertex truncation be given as in theorem 3.25. Then the flow equations for the corresponding interactions in momentum and in frequency space are given as follows:

1. For the self-energy as

$$\dot{\Sigma}^{\Lambda}_{o_1,o_2}(k) = \frac{1}{\beta}\int \mathrm{d}k'\, S^{\Lambda}_{\bar{o}_1,\bar{o}_2}(k')\left(-2V^{\Lambda}_{o_1\bar{o}_2,o_2\bar{o}_1}(k,k';k) + V^{\Lambda}_{o_1\bar{o}_2,\bar{o}_1o_2}(k,k';k')\right). \tag{3.328}$$

2. For the two-particle interaction as

$$V^{\Lambda}_{o_1o_2,o_3o_4}(k_1,k_2;k_3) = \bar{\mathcal{T}}^{\mathrm{P},\Lambda}_{o_1o_2,o_3o_4}(k_1,k_2;k_3) + \bar{\mathcal{T}}^{\mathrm{C},\Lambda}_{o_1o_2,o_3o_4}(k_1,k_2;k_3) + \bar{\mathcal{T}}^{\mathrm{D},\Lambda}_{o_1o_2,o_3o_4}(k_1,k_2;k_3), \tag{3.329}$$

with

$$\begin{aligned}
\bar{\mathcal{T}}^{\mathrm{P},\Lambda}_{o_1o_2,o_3o_4}(k_1,k_2;k_3) &= -\frac{1}{\beta}\int \mathrm{d}k \int \mathrm{d}k' \sum_{\bar{o}_1\dots\bar{o}_4} L_{\bar{o}_1\bar{o}_2,\bar{o}_3\bar{o}_4}(k,k') \\
&\qquad V^{\Lambda}_{o_1o_2,\bar{o}_1\bar{o}_2}(k_1,k_2;k)\, V^{\Lambda}_{\bar{o}_3\bar{o}_4,o_3o_4}(k,k';k_3)\delta_{k',k_1+k_2-k}, \\
\bar{\mathcal{T}}^{\mathrm{D},\Lambda}_{o_1o_2,o_3o_4}(k_1,k_2;k_3) &= \frac{1}{\beta}\int \mathrm{d}k \int \mathrm{d}k' \sum_{\bar{o}_1\dots\bar{o}_4} L_{\bar{o}_1\bar{o}_2,\bar{o}_3\bar{o}_4}(k,k')\, \delta_{k',k+k_3-k_1} \\
&\qquad \big(-2V^{\Lambda}_{o_1\bar{o}_3,o_3\bar{o}_2}(k_1,k;k_3)\, V^{\Lambda}_{\bar{o}_4o_2,\bar{o}_1o_4}(k',k_2;k) \\
&\qquad\quad + V^{\Lambda}_{o_1\bar{o}_3,o_3\bar{o}_2}(k_1,k;k_3)\, V^{\Lambda}_{\bar{o}_4o_2,o_4\bar{o}_1}(k',k_2;k_4) \\
&\qquad\quad + V^{\Lambda}_{o_1\bar{o}_3,\bar{o}_2o_3}(k_1,k;k')\, V^{\Lambda}_{\bar{o}_4o_2,\bar{o}_1o_4}(k',k_2;k)\big), \\
\bar{\mathcal{T}}^{\mathrm{C},\Lambda}_{o_1o_2,o_3o_4}(k_1,k_2;k_3) &= \frac{1}{\beta}\int \mathrm{d}k \int \mathrm{d}k' \sum_{\bar{o}_1\dots\bar{o}_4} L_{\bar{o}_1\bar{o}_3,\bar{o}_2\bar{o}_4}(k,k') \\
&\qquad V^{\Lambda}_{o_1\bar{o}_3,\bar{o}_2o_4}(k_1,k;k')\, V^{\Lambda}_{\bar{o}_4o_2,o_3\bar{o}_1}(k',k_2;k_3)\, \delta_{k',k+k_4-k_1},
\end{aligned} \tag{3.330}$$

in which we wrote $k_4 = k_1 + k_2 - k_3$ for the sake of brevity.

3. For the fermion-boson vertices as

$$\begin{aligned}
\dot{\gamma}^{(2,1)\Lambda}_{eh\ n;o_1,o_2}(k_1;\cdot;q) &= \sum_{\bar{o}_1\dots\bar{o}_4}\int \mathrm{d}k\, L_{\bar{o}_1\bar{o}3;\bar{o}_2\bar{o}_4}(k,k+q)\, \gamma^{(2,1)\Lambda}_{eh\ ,n;\bar{o}_2;\bar{o}_3}(k;\cdot;q) \\
&\qquad \left(2V^{\Lambda}_{o_1\bar{o}_4;o_2\bar{o}_1}(k_1,k+q;k_2) - V^{\Lambda}_{o_1\bar{o}_4;\bar{o}_1o_2}(k_1,k+q;k)\right), \qquad (3.331) \\
\gamma^{(2,1)\Lambda}_{ee,n;o_1o_2}(\cdot;k_1;q) &= -\frac{1}{2}\int \mathrm{d}k \sum_{\bar{o}_1\dots\bar{o}_4} L^{\Lambda}_{\bar{o}_2\bar{o}_3,\bar{o}_1\bar{o}_4}(k,q-k) \\
&\qquad \gamma^{(2,1)\Lambda}_{ee,n;\bar{o}_2\bar{o}_3}(k;q)\, V^{\Lambda}_{\bar{o}_4\bar{o}_1,o_1o_2}(q-k,k;k_1). \qquad (3.332)
\end{aligned}$$

4. For the susceptibilities the flow equations are the same as in the non SU(2)-symmetric case (cf. thm. 3.28) with the additional factors $1+\delta_{s_b}$ accounting for doubly occurring terms like in theorem 3.25.

Proof: The proof is along the same lines with the one for the spinful version in theorem 3.28. However, the lattice space and the time arguments are exchanged in some terms of the SU(2)-symmetric flow equations in comparison to this previous case, which leads to a corresponding exchange of momentum arguments. With respect to this let us regard the two terms of the self-energy. While the first term has exactly the same order of arguments as the one in the spinful case, the third and the fourth argument of the second term switch places, so that its Fourier transformed vertex is $V^{\Lambda}_{o_1o'_1;o_2o'_2}(k,k';k',k)$. Observing the contribution of the direct electron-hole to the two-fermion interaction under this aspect,

we can find that all three terms differ by an exchange of arguments in lattice space and, therefore, in momentum space, too. However, the main momentum transfer for all three contributions remains the same as in the spinful case, that is $k_1 - k_3$. ■

An analysis of the structure of the two-particle interaction flow equations in the generalised momentum arguments reveals that each channel shows a characteristic dependence on one specific generalised transfer momentum. This transfer is bosonic, as it results from a combination of two incoming fermionic momenta, so that each contribution can be parametrised by one bosonic and by two fermionic generalised momenta as defined in table 3.1. For the generalised bosonic momentum transfer we introduce the Mandelstam variables (cf. table 3.1) with the same notation as used for two-particle interactions considered in high energy physics. The corresponding contributions to the flow equation of the two-fermion interaction, therefore, become

$$\begin{aligned}\tilde{\mathcal{T}}^{\mathrm{P}}(s, k_s, k_s') &= \mathcal{T}^{\mathrm{P}}(k_1, k_2; k_3)\\ \tilde{\mathcal{T}}^{\mathrm{D}}(u, k_u, k_u') &= \mathcal{T}^{\mathrm{D}}(k_1, k_2; k_3)\\ \tilde{\mathcal{T}}^{\mathrm{C}}(t, k_t, k_t') &= \mathcal{T}^{\mathrm{C}}(k_1, k_2; k_3),\end{aligned} \tag{3.333}$$

and the analogous holds for the SU(2)-symmetric case. The conservation of momentum of the two-fermion interaction can be described equivalently in either of the channels, as $\delta_{k_1+k_2,k_3,k_4} = \delta_{k_1-k_3,k_4-k_2} = \delta_{k_1-k_4,k_3-k_2}$. Therefore, it is correctly described by either of the channel specific variables, so that

$$\begin{aligned}\gamma^{(4,0)\Lambda}(k_1, k_2; k_3) &= \tilde{\gamma}^{(4,0)\Lambda,\mathrm{P}}(s; k_s, k_s')\\ &= \tilde{\gamma}^{(4,0)\Lambda,\mathrm{D}}(u; k_u, k_u')\\ &= \tilde{\gamma}^{(4,0)\Lambda,\mathrm{C}}(t; k_t, k_t'),\end{aligned} \tag{3.334}$$

and analogously for the SU(2)-symmetric interaction. In the channel contributions $\mathcal{T}^{\mathrm{P}}$, $\mathcal{T}^{\mathrm{D}}$ and $\mathcal{T}^{\mathrm{C}}$ to the flow equation we observe that the two-fermion interaction appears in the channel specific variables. The same holds for the contributions to the flow equation of the SU(2)-symmetric interaction V^{Λ} with the exception of $\tilde{\mathcal{T}^{\mathrm{D}}}$ in which both, $V^{\Lambda,\mathrm{D}}$ and $V^{\Lambda,\mathrm{C}}$, appear.

The fermion-boson interactions are naturally characterised by one fermionic and by one bosonic argument due to the conservation of energy and momentum such that both fermionic momenta differ by or add up to the bosonic one. This naturally introduces a parametrisation of the two-particle interaction appearing in their flow equations by the same fermionic and bosonic momenta, as well as the internal fermionic momentum. Hence the two-fermion interaction is required in the pairing channel parametrisation for the electron-electron fermion-boson vertex, while this is, for the electron-hole case, a parametrisation corresponding to the direct channel. In the SU(2)-symmetric case the same observation holds, but with a combination of one interaction in the direct and one in the crossing channel parametrisation for the electron-hole fermion-boson interaction.

P	$s := k_1 + k_2 = k_3 + k_4$	$k_s := k_1$	$k_s' := k_3$
D	$u := k_1 - k_3 = k_4 - k_2$	$k_u := k_1$	$k_u' := k_4$
C	$t := k_1 - k_4 = k_3 - k_2$	$k_t := k_1$	$k_t' := k_3$

Table 3.1.: Mandelstam variables for the channel-specific momentum transfer.

The parametrisation just introduced for the two-particle interaction is also motivated by an analysis of the momentum structure (without frequency) of typical ordering in the ground state. As discussed in the section about susceptibilities (cf. sec. 3.3), the significant contribution for correlation effects originates from the two-particle vertex. Because of the closed electron-hole or the particle-particle propagator loops their incoming and outgoing fermions must exactly differ by the incoming bosonic momentum. Thus the vertex must have exactly the same momentum structure in the case of charge- or spin-density waves with the same bosonic transfer momentum. Analysing the vertex at the phase transition shows that the dependence on the transfer momentum, which indicates the reached phase, is strong, while the dependence on the two fermionic ones is weak.

Therefore, this mixed fermionic-bosonic parametrisation is more natural and frequently used [103, 67]. However, the different channels for the two-particle interaction require inequivalent fermion-bosonic arguments which have to be transformed to the full fermionic parametrisation according to the right hand side of table 3.1. In the following section we will derive a numerically advantageous form for the calculation of the two-particle interaction which exploits this parametrisation.

3.6. Truncated Unity Functional Renormalisation Group

Based on the observations in the previous section, a form-factor based flow equation is developed in this section, called Truncated Unity FRG (TUFRG), which follows the approach by Lichtenstein and de la Peña [2], which was generalised by me in collaboration with others in reference [111]. This approach provides a computationally beneficial parametrisation of the two-particle interaction for calculations, which was applied to the two-dimensional Hubbard model on square [2] and on hexagonal lattices [72, 112]. Additionally, a corresponding parametrisation of the Parquet equations was developed in collaboration with me [113]. Although the fermionic-bosonic parametrisation just introduced holds for generalised momenta, only the momentum $\boldsymbol{k}$ is explicitly treated in this part, as an advantageous parametrisation is easily derived from the underlying lattice [75]. On the contrary, a similarly efficient parametrisation of the frequency domain is not yet available and is still subject of current research [114, 115, 116, 117, 118], so that the frequency dependence remains unaffected in this part.

To derive the TUFRG flow equations we first introduce the form-factor basis and projections between this basis and the momentum space. Based on the decomposition of the two-particle interaction we then derive the flow equations for three chantices of which each one corresponds to one channel of the original flow equations. As this parametrisation is for the interaction alone, no flow equations for fermion-boson interactions or susceptibilities are considered here.

3.6.1. Form-Factors, Projections and Chantices

The full two-particle interaction exhibits the features of an emerging phase when the corresponding phase boundary is reached. That is a strong dependence on the bosonic momentum, characterising the emerging phase, and a weak dependence on the two fermionic arguments, which coincides with the natural parametrisation of the channel leading to the phase. Therefore, it is reasonable to project the fermionic arguments to a basis of slowly varying form-factors, which is defined in the following. Beforehand, we remark that all momentum space integrals in this section implicitly cover the whole Brillouin zone $\mathcal{B}$ and contain the scaling factor $1/|\mathcal{B}|$, that is $\int \mathrm{d}\boldsymbol{k} := \int_{\mathcal{B}} \frac{\mathrm{d}\boldsymbol{k}}{|\mathcal{B}|}$.

Definition 43 (Form-Factor Basis)

1. *Let $\{f_i(\boldsymbol{R})\}_{i\in\mathbb{N}}$ with $f_i : \mathbb{R}^3 \to \mathbb{C}$ be an orthonormal set of functions based on linear combinations of the functions $\delta_{\boldsymbol{R}}$ which reference the Bravais lattice vectors $\boldsymbol{R}$. Then the set is called a **form-factor basis** which fulfils the completeness and the orthonormality relations, i.e.*

$$\sum_n f_n(\boldsymbol{R})\, f_n^*(\boldsymbol{R}') = \delta(\boldsymbol{R}-\boldsymbol{R}') \qquad \text{and} \qquad \sum_{\boldsymbol{R}} f_m(\boldsymbol{R})\, f_n^*(\boldsymbol{R}) = \delta_{m,n}. \tag{3.335}$$

2. *Let $\{f_i(\boldsymbol{k})\}_{i\in\mathbb{N}}$ be the Fourier transformation of the set $\{f_i(\boldsymbol{R})\}_{i\in\mathbb{N}}$, as defined in 1. Then the set $\{f_i(\boldsymbol{k})\}_{i\in\mathbb{N}}$ is called the **momentum space form-factor basis** which also fulfils the completeness and the orthonormality relations, i.e.*

$$\sum_n f_n(\boldsymbol{k})\, f_n^*(\boldsymbol{k}') = |\mathcal{B}|\delta(\boldsymbol{k}-\boldsymbol{k}') \qquad \text{and} \qquad \int_{\mathcal{B}} d\boldsymbol{k}\, f_m(\boldsymbol{k})\, f_n^*(\boldsymbol{k}) = \delta_{m,n}. \tag{3.336}$$

Here, the lattice space and the momentum space form-factors are related by the Fourier transformation, that is

$$f_n(\boldsymbol{R}) = \int \mathrm{d}\boldsymbol{k}\, e^{-i\boldsymbol{k}\boldsymbol{R}} f_n(\boldsymbol{k}) \qquad \text{and} \qquad f_n(\boldsymbol{k}) = \sum_{\boldsymbol{R}} e^{i\boldsymbol{k}\boldsymbol{R}} f_n(\boldsymbol{R}). \tag{3.337}$$

According to the aforementioned convention, the Fourier normalisation factor is absorbed in the momentum space integral.

The exact choice of form-factors is intentionally left open in the definition. One natural choice is the direct use of Bravais lattice vectors, which are also referred to as bond vectors, as argument $\delta_{\boldsymbol{R}}$. As this set has to be truncated for numerical calculations, it is useful to work with a low number of form-factors, but simultaneously reach a high accuracy. In order to achieve this we choose a set of basis functions which is symmetric under the point group symmetry of the lattice leading to linear combinations of the Bravais vectors with the same lengths. It is assumed that even less form-factors are sufficient to achieve the same accuracy by this approach. Additionally, the momentum space representation after symmetrisation has a simple form consisting of linear combinations of sine and cosine functions, which can be equal to the typical form of the form-factors appearing in the susceptibilities. More details about the derivation and the implementation of the form-factor basis can be found in chapter 4.2.

This definition leaves a freedom of choice for the real form-factor basis. The obvious choice is a direct usage of the Bravais lattice vectors, while exploiting the point group symmetry of the solid state system leads to a symmetrised set of basis functions. As those fit to the system under investigation, the number of necessary form-factors is expected to be reduced. In addition, their momentum space representation in the symmetrised form has a simple form consisting of linear combinations of sine and cosine functions. In order to be able to use the form-factor basis for the two-particle vertex and the contributions to its flow equation a corresponding projection between the two basis sets is required. But as the bosonic momenta, which are supposed to be kept up, are different combinations of the original fermionic momenta for each of the three channels (cf. table 3.1), it is necessary to define the projection operations separately for all three channels.

Definition 44 (Projection between Form-Factor Basis and Full Momentum Basis)
Let $\boldsymbol{v} \in \{\boldsymbol{s}, \boldsymbol{u}, \boldsymbol{t}\}$ be a Mandelstam variable of the P, D or C channel, respectively, and let $\boldsymbol{k}_v$ and $\boldsymbol{k}'_v$ be the corresponding weak dependencies according to table 3.1. Let X be a two-particle object (e.g. $\bar{\gamma}^{(4,0),\Lambda}$, $\bar{V}^{\Lambda}$, $\bar{\mathcal{T}}^{\mathrm{P},\Lambda}$, ...) in the natural parametrisation of a channel, i.e. $X(\boldsymbol{v}, \boldsymbol{k}_v, \boldsymbol{k}'_v)$, and let $\{f_j\}_{j\in\mathbb{N}}$ be a form-factor basis as defined in definition 43. Then

1. *the projections of X to a channel v in the form-factor space is defined by*

$$\hat{\mathbb{P}}_i[X]_{mn}(\boldsymbol{v}) := \int \mathrm{d}\boldsymbol{k}_v \int \mathrm{d}\boldsymbol{k}'_v\, f_m(\boldsymbol{k}_v)\, f_n^*(\boldsymbol{k}'_v)\, X(\boldsymbol{v}, \boldsymbol{k}_v; \boldsymbol{k}'_v); \tag{3.338}$$

2. *the back-projection of an object in the form-factor space to the natural parametrisation of this channel is defined as*

$$X(\boldsymbol{v}, \boldsymbol{k}_v, \boldsymbol{k}'_v) = \sum_{m,n} \left(\hat{\mathbb{P}}_v[X]_{mn}(\boldsymbol{v})\right)\, f_m^*(\boldsymbol{k}_v)\, f_n(\boldsymbol{k}'_v). \tag{3.339}$$

To illustrate the projections just defined, let us consider the projection of the full two-particle interaction to the pairing channel. In order to apply the projection, first the interaction has to be parametrised in the momenta of the pairing channel, which is $\gamma^{(4,0)}(\boldsymbol{k}_s, \boldsymbol{s}-\boldsymbol{k}_s; \boldsymbol{k}'_s)$. In a second step, the projection can be performed, resulting in

$$\hat{\mathbb{P}}[\gamma^{(4,0)}]_{mn}(\boldsymbol{s}) = \int \mathrm{d}\boldsymbol{k}_s \int \mathrm{d}\boldsymbol{k}'_s \, f_m(\boldsymbol{k}_s)\, f_n^*(\boldsymbol{k}'_s)\, \gamma^{(4,0)}(\boldsymbol{k}_s, \boldsymbol{s}-\boldsymbol{k}_s; \boldsymbol{k}'_s). \tag{3.340}$$

Hence the notation of the left hand side requires both steps. Similarly, the projection to the other channels first requires a re-parametrisation in the natural coordinates of the channel, before the actual projection can be performed. If one inserts this projected object into the back-projection, one obtains, due to the completeness-relation of form-factors, the original interaction in the natural parametrisation of the channel it was in. For the case that the projection is applied to the vertices $\gamma^{(4,0)\Lambda}$ and V^Λ and, due to their decomposition, to their channel contributions Φ^v and $\bar{\Phi}^v$, respectively, we define the resulting objects as follows:

Definition 45 (Projected Vertex and Chantices)

1. *Let $\gamma^{(4,0)\Lambda}$ be the full two-particle interaction in the $2n < 5$ approximation, which decomposes according to corollary 3.23 as*

$$\gamma^{(4,0)\Lambda} = \gamma^{(4,0)\Lambda_0} + \Phi^{\mathrm{P},\Lambda} + \Phi^{\mathrm{D},\Lambda} + \Phi^{\mathrm{C},\Lambda}. \tag{3.341}$$

*Then the **vertex projected to channel** $v \in \{P, D, C\}$ is defined as*

$$\gamma_{mn}^{(4,0)v,\Lambda}(\boldsymbol{v}) := \mathbb{P}_v[\gamma^{(4,0)\Lambda}]_{mn}(\boldsymbol{v}), \tag{3.342}$$

*and the pairing, direct electron-hole and crossing electron-hole **chantices** are defined, respectively, as*

$$\begin{aligned} P_{mn}^\Lambda(\boldsymbol{s}) &:= \hat{\mathbb{P}}_P[\Phi^{\mathrm{P},\Lambda}]_{mn}(\boldsymbol{s}), \quad D_{mn}^\Lambda(\boldsymbol{u}) := \hat{\mathbb{P}}_D[\Phi^{\mathrm{D},\Lambda}]_{mn}(\boldsymbol{u}) \quad \textit{and} \\ C_{mn}^\Lambda(\boldsymbol{t}) &:= \hat{\mathbb{P}}_C[\Phi^{\mathrm{C},\Lambda}]_{mn}(\boldsymbol{t}). \end{aligned} \tag{3.343}$$

2. *Let V^Λ be the SU(2)-invariant two-particle interaction, which decomposes according to corollary 3.27 as*

$$V^\Lambda = V^{\Lambda_0} + \bar{\Phi}^{\mathrm{P},\Lambda} + \bar{\Phi}^{\mathrm{D},\Lambda} + \bar{\Phi}^{\mathrm{C},\Lambda}. \tag{3.344}$$

Then the vertex projected to channel $v \in \{P, D, C\}$ is defined as

$$V_{mn}^{v,\Lambda}(\boldsymbol{v}) := \mathbb{P}_v[V^\Lambda]_{mn}(\boldsymbol{v}), \tag{3.345}$$

*and the SU(2)-symmetric pairing, direct electron-hole and crossing electron-hole **chantices** are defined as*

$$\begin{aligned} \bar{P}_{mn}^\Lambda(\boldsymbol{s}) &:= \hat{\mathbb{P}}_P[\bar{\Phi}^{\mathrm{P},\Lambda}]_{mn}(\boldsymbol{s}) \quad \bar{D}_{mn}^\Lambda(\boldsymbol{u}) := \hat{\mathbb{P}}_D[\bar{\Phi}^{\mathrm{D},\Lambda}]_{mn}(\boldsymbol{u}) \quad \textit{and} \\ \bar{C}_{mn}^\Lambda(\boldsymbol{t}) &:= \hat{\mathbb{P}}_C[\bar{\Phi}^{\mathrm{C},\Lambda}]_{mn}(\boldsymbol{t}). \end{aligned} \tag{3.346}$$

As the definition of the chantices[9] is based on the splitting of the full vertex (cf. eq. (3.264)), the flow equation of the vertex directly provides a flow equation for each chantex. That is, the flow equation of the chantex is the contribution of the channel it is based on to the full flow equation, projected to the form-factor space. In detail, the explicit flow equations of the chantices are given by

$$\dot{P}^{\Lambda}_{mn}(\boldsymbol{s}) = \int \mathrm{d}\boldsymbol{k}_s \int \mathrm{d}\boldsymbol{k}'_s \, f_m(\boldsymbol{k}_s)\, f^*_n(\boldsymbol{k}'_s)\, \mathcal{T}^{\mathrm{P},\Lambda}(\boldsymbol{k}_s, \boldsymbol{s}-\boldsymbol{k}_s; \boldsymbol{k}'_s) \tag{3.347}$$

$$\dot{D}^{\Lambda}_{mn}(\boldsymbol{u}) = \int \mathrm{d}\boldsymbol{k}_u \int \mathrm{d}\boldsymbol{k}'_u \, f_m(\boldsymbol{k}_u)\, f^*_n(\boldsymbol{k}'_u)\, \mathcal{T}^{\mathrm{D},\Lambda}(\boldsymbol{k}_u, \boldsymbol{k}'_u-\boldsymbol{u}; \boldsymbol{k}_u-\boldsymbol{u}) \tag{3.348}$$

$$\dot{C}^{\Lambda}_{mn}(\boldsymbol{t}) = \int \mathrm{d}\boldsymbol{k}_t \int \mathrm{d}\boldsymbol{k}'_t \, f_m(\boldsymbol{k}_t)\, f^*_n(\boldsymbol{k}'_t)\, \mathcal{T}^{\mathrm{C},\Lambda}(\boldsymbol{k}_t, \boldsymbol{k}'_t-\boldsymbol{t}; \boldsymbol{k}'_t). \tag{3.349}$$

When these flow equations are calculated, the full vertex is required in each integration step, as it appears in the contributions $\mathcal{T}$. Therefore the back-projections of the chantices to the full vertex are required, which becomes

$$\begin{aligned}
\Phi^{\mathrm{P},\Lambda}(\boldsymbol{k}_1, \boldsymbol{k}_2; \boldsymbol{k}_3) &= \sum_{m,n} P^{\Lambda}_{mn}(\boldsymbol{k}_1+\boldsymbol{k}_2)\, f^*_m(\boldsymbol{k}_1)\, f_n(\boldsymbol{k}_3) \\
\Phi^{\mathrm{D},\Lambda}(\boldsymbol{k}_1, \boldsymbol{k}_2; \boldsymbol{k}_3) &= \sum_{m,n} D^{\Lambda}_{mn}(\boldsymbol{k}_1-\boldsymbol{k}_3)\, f^*_m(\boldsymbol{k}_1)\, f_n(\boldsymbol{k}_1+\boldsymbol{k}_2-\boldsymbol{k}_3) \\
\Phi^{\mathrm{C},\Lambda}(\boldsymbol{k}_1, \boldsymbol{k}_2; \boldsymbol{k}_3) &= \sum_{m,n} C^{\Lambda}_{mn}(\boldsymbol{k}_3-\boldsymbol{k}_2)\, f^*_m(\boldsymbol{k}_1)\, f_n(\boldsymbol{k}_3)
\end{aligned} \tag{3.350}$$

by the back-substitution to full fermionic momenta. Before we further consider the flow equations, we consider the symmetries of the objects in the form-factor space.

Corollary 3.30 (Symmetries of the Projections)
Let X be either the two-particle interaction without spin-symmetry (i.e. $\gamma^{(4,0)\Lambda}$) or the two-particle interaction with spin-symmetry (i.e. V^{Λ}). Let P^{Λ}, C^{Λ} and D^{Λ} or $\bar{P}^{\Lambda}, \bar{C}^{\Lambda}$ and $\bar{D}^{\Lambda}$ denote the corresponding chantices according to definition 45. Then the following symmetry relations hold:

1. *Let $\boldsymbol{K}$ be a reciprocal lattice vector. If X is invariant under a shift of $\boldsymbol{K}$ in every argument in the momentum space, then P, C and D are invariant under a shift of $\boldsymbol{K}$, too.*
2. *Let $\mathbb{P}_v$ be the projection to channel $v \in \{P,C,D\}$. Then the vertex X projected to the form-factor space is symmetric according to*

$$\mathbb{P}_P[X]_{mn;o_1o_2,o_3o_4}(\boldsymbol{s}) = \left(\mathbb{P}_P[X]_{nm;o_3o_4,o_1o_2}(\boldsymbol{s})\right)^*, \tag{3.351}$$

$$\mathbb{P}_D[X]_{mn;o_1o_2,o_3o_4}(\boldsymbol{u}) = \left(\mathbb{P}_D[X]_{nm;o_4o_3,o_2o_1}(\boldsymbol{u})\right)^* \qquad \textit{and} \tag{3.352}$$

$$\mathbb{P}_C[X]_{mn;o_1o_2,o_3o_4}(\boldsymbol{t}) = \left(\mathbb{P}_C[X]_{nm;o_3o_4,o_1o_2}(\boldsymbol{t})\right)^*. \tag{3.353}$$

3. *The chantices are symmetric according to*

$$P^{\Lambda}_{mn;o_1o_2,o_3o_4}(\boldsymbol{s}) = \left(P^{\Lambda}_{nm;o_3o_4,o_1o_2}(\boldsymbol{s})\right)^* \tag{3.354}$$

$$D^{\Lambda}_{mn;o_1o_2,o_3o_4}(\boldsymbol{u}) = \left(D^{\Lambda}_{nm;o_4o_3,o_2o_1}(\boldsymbol{u})\right)^* \tag{3.355}$$

$$C^{\Lambda}_{mn;o_1o_2,o_3o_4}(\boldsymbol{t}) = \left(C^{\Lambda}_{nm;o_3o_4,o_1o_2}(\boldsymbol{t})\right)^* \tag{3.356}$$

and similarly for the SU(2)-symmetric cases $\bar{P}^{\Lambda}$, $\bar{D}^{\Lambda}$ and $\bar{C}^{\Lambda}$.

[9] This corresponds to **chan**nel ver**tices** and has no relation to spirituality.

4. *The direct and the crossing channel are symmetric according to* $D_{mn;o_1o_2,o_3o_4}(\boldsymbol{u}) = -C_{mn;o_1o_2,o_4o_3}(\boldsymbol{u})$ *in the spinful case.*

5. *The chantices are symmetric with respect to the lattice symmetry according to*

$$P^{\Lambda}_{mn}(\boldsymbol{s}) = P^{\Lambda}_{\hat{R}^{-1}(m)\hat{R}^{-1}(n)}(\hat{R}(\boldsymbol{s})), \tag{3.357}$$

where $\hat{R}^{-1}(m)$ *denotes* $f_m(\hat{R}^{-1}(\boldsymbol{k}))$*. This analogously holds for the other channels.*

Proof: [10]

1. At this point, we only consider the pairing channel, as the proof is analogous for the other channels, so that we have to show $P^{\Lambda}_{mn}(\boldsymbol{s}) = P^{\Lambda}_{mn}(\boldsymbol{s}+\boldsymbol{K})$. The projection of a general four-fermion object X under the considered shift

$$\begin{aligned}\mathbb{P}^{\mathrm{P}}[X]_{mn}(\boldsymbol{s}+\boldsymbol{K}) &= \int \mathrm{d}\boldsymbol{k}_s \int \mathrm{d}\boldsymbol{k}'_s\, f_m(\boldsymbol{k}_s)\, f^*_n(\boldsymbol{k}'_s)\, X(\boldsymbol{k}_s, \boldsymbol{s}+\boldsymbol{K}-\boldsymbol{k}_s; \boldsymbol{k}'_s) \\ &= \int \mathrm{d}\boldsymbol{k}_s \int \mathrm{d}\boldsymbol{k}'_s\, f_m(\boldsymbol{k}_s)\, f^*_n(\boldsymbol{k}'_s)\, X(\boldsymbol{k}_s, \boldsymbol{s}-\boldsymbol{k}_s; \boldsymbol{k}'_s) \\ &= \mathbb{P}^{\mathrm{P}}[X]_{mn}(\boldsymbol{s})\end{aligned} \tag{3.358}$$

reveals a corresponding invariance due to the one of X. The required invariance of the chantex P results from this relation, if $X = \Phi^{\mathrm{P},\Lambda}$ is invariant in each argument. As $\Phi^{\mathrm{P},\Lambda}$ is obtained by an integration of $\mathcal{T}^{\mathrm{P},\Lambda}$ over the full range of the scale, it is sufficient to consider the latter one. In the expression for $\mathcal{T}^{\mathrm{P},\Lambda}$ the initial translation by $\boldsymbol{K}$ causes a shift of one incoming momentum of the first and of one outgoing momentum of the second vertex by the same $\boldsymbol{K}$. As the vertex is periodic with respect to each argument according to corollary 3.5, this is equal to the vertices without the shift. Therefore, $\mathcal{T}$ is invariant under a shift of $\boldsymbol{K}$ and with the first part of this proof this translates to $P^{\Lambda}_{mn}(\boldsymbol{s})$.

2. Due to the definition of the projection operator (see def. 44), the vertex has to be symmetric with respect to an exchange of arguments. Because of the complex conjugation symmetry (see cor. 3.17.2) the two-particle interaction in the three different parametrisations becomes

$$\gamma^{(4,0)\Lambda}_{o_1o_2,o_3o_4}(\boldsymbol{k}_u, \boldsymbol{k}'_u - \boldsymbol{u}; \boldsymbol{k}_u - \boldsymbol{u}, \boldsymbol{k}'_u) = \left(\gamma^{(4,0)\Lambda}_{o_4o_3,o_2o_1}(\boldsymbol{k}'_u, \boldsymbol{k}_u - \boldsymbol{u}; \boldsymbol{k}'_u - \boldsymbol{u}, \boldsymbol{k}_u)\right)^* \tag{3.359}$$

and, in combination with the crossing symmetry, we get

$$\begin{aligned}\gamma^{(4,0)\Lambda}_{o_1o_2,o_3o_4}(\boldsymbol{k}_s, \boldsymbol{s}-\boldsymbol{k}_s; \boldsymbol{k}'_s, \boldsymbol{s}-\boldsymbol{k}'_s) &= \gamma^{(4,0)\Lambda}_{o_2o_1,o_4o_3}(\boldsymbol{s}-\boldsymbol{k}_s, \boldsymbol{k}_s; \boldsymbol{s}-\boldsymbol{k}'_s, \boldsymbol{k}'_s) \\ &= \left(\gamma^{(4,0)\Lambda}_{o_3o_4,o_1o_2}(\boldsymbol{k}'_s, \boldsymbol{s}-\boldsymbol{k}'_s; \boldsymbol{k}_s, \boldsymbol{s}-\boldsymbol{k}_s)\right)^* \quad \text{and} \qquad (3.360) \\ \gamma^{(4,0)\Lambda}_{o_1o_2,o_3o_4}(\boldsymbol{k}_t, \boldsymbol{k}'_t - \boldsymbol{t}; \boldsymbol{k}'_t, \boldsymbol{k}_t - \boldsymbol{t}) &= \gamma^{(4,0)\Lambda}_{o_2o_1,o_4o_3}(\boldsymbol{k}'_t - \boldsymbol{t}, \boldsymbol{k}_t; \boldsymbol{k}_t - \boldsymbol{t}, \boldsymbol{k}'_t) \\ &= \left(\gamma^{(4,0)\Lambda}_{o_3o_4,o_1o_2}(\boldsymbol{k}'_t, \boldsymbol{k}_t - \boldsymbol{t}; \boldsymbol{k}_t, \boldsymbol{k}'_t - \boldsymbol{t})\right)^*, \qquad (3.361)\end{aligned}$$

that is a symmetry under an exchange of $\boldsymbol{k}_v$ and $\boldsymbol{k}'_v$. An insertion of the left and of the right hand side of these equations in the definitions of the projections (see def. 44) now reveals the

[10] Although the vertices in momentum space only have three independent arguments, all of them are denoted here to help the reader follow the corresponding steps.

symmetries with respect to the form-factors. As all of the symmetries applied here are also present in the SU(2)-symmetric case (cf. cor. 3.26) the corresponding proof is in direct analogy.

3. For any $\upsilon \in \{\mathrm{P}, \mathrm{D}, \mathrm{C}\}$, all the contributions $\mathcal{T}^{\upsilon,\Lambda}$ to the flow equation show the same behaviour under the complex conjugation and under the crossing symmetry as the full vertex. Therefore, the same considerations as presented in point 2 above lead to the corresponding result.

4. In the non SU(2)-symmetric case we get $\mathcal{T}^{\mathrm{D},\Lambda}(x_1, x_2; x_3, x_4) = -\mathcal{T}^{\mathrm{C},\Lambda}(x_1, x_2; x_4, x_3)$ (see rem. 3.22), which also holds after a Fourier transformation. Employing this in the projection operator directly results in the requested relation.

5. Again, we treat this exemplarily for the projection of an object X to the pairing channel, as the projections to the other channels are analogous. The full vertex is symmetric under the point group operation $\hat{R}$ according to

$$\gamma^{(4,0)\Lambda}(\boldsymbol{k}_1, \boldsymbol{k}_2; \boldsymbol{k}_3, \boldsymbol{k}_4) = \gamma^{(4,0)\Lambda}(\hat{R}(\boldsymbol{k}_1), \hat{R}(\boldsymbol{k}_2); \hat{R}(\boldsymbol{k}_3), \hat{R}(\boldsymbol{k}_4)). \tag{3.362}$$

Projecting this to the pairing channel leads to

$$\begin{aligned}
\mathbb{P}_{\mathrm{P}}[X]_{mn}(\boldsymbol{s}) &= \int \mathrm{d}\boldsymbol{k}_s \int \mathrm{d}\boldsymbol{k}'_s \, f_m(\boldsymbol{k}_s)\, f_n^*(\boldsymbol{k}'_s)\, X(\boldsymbol{k}_s, \boldsymbol{s} - \boldsymbol{k}_s; \boldsymbol{k}'_s) \\
&= \int \mathrm{d}\boldsymbol{k}_s \int \mathrm{d}\boldsymbol{k}'_s \, f_m(\boldsymbol{k}_s)\, f_n^*(\boldsymbol{k}'_s)\, X^{\Lambda}(\hat{R}(\boldsymbol{k}_s), \hat{R}(\boldsymbol{s} - \boldsymbol{k}_s); \hat{R}(\boldsymbol{k}'_s)) \\
&= \int \mathrm{d}\boldsymbol{k}_s \int \mathrm{d}\boldsymbol{k}'_s \, f_m(\hat{R}^{-1}(\boldsymbol{k}_s))\, f_n^*(\hat{R}^{-1}(\boldsymbol{k}'_s))\, X(\tilde{\boldsymbol{k}}_s, \hat{\boldsymbol{s}} - \tilde{\boldsymbol{k}}_s; \tilde{\boldsymbol{k}}'_s) \\
&= \mathbb{P}_{\mathrm{P}}[X]_{\hat{R}^{-1}(m)\hat{R}^{-1}(n)}(\hat{R}(\boldsymbol{s})),
\end{aligned} \tag{3.363}$$

where we changed the integration variables from $\boldsymbol{k}_s$ to $\tilde{\boldsymbol{k}}_s := \hat{R}(\boldsymbol{k}_s)$ and analogously for $\boldsymbol{k}'_s$, which leads to the inverse symmetry operation for the argument of the form-factors. We left out orbital indices, which have their own map with respect to point group symmetries. ■

In comparison to our parametrisation there exists a symmetrised one (cf. Lichtenstein [2]) which preserves more symmetries than our approach does. However, as momenta of the form $(\boldsymbol{k}_1 - \boldsymbol{k}_2)/2$ appear, the momentum integrations also have to cover the second Brillouin zone and the invariance under translations by reciprocal lattice vectors is lost. Although symmetry considerations can translate all the properties back to the first Brillouin zone, we keep the simpler form with a reduced number of symmetries. However, exploiting those already facilitates the calculation of the flow equation for the chantices.

3.6.2. Chantex Flow Equations

The equations (3.347)-(3.349) provide the flow equations for the three chantices. However, as the largest object of the calculations is the full two-particle vertex, it is advantageous to keep only its form-factor-based version as it will be significantly smaller. It is, therefore, useful to project the dual propagators to the form-factor basis, too, so that all the elements only depend on the main momentum and on the form-factor indices.

Definition 46 (Projected Propagators)
Let L^Λ be the dual propagator as provided in definition 41. The projections to the form-factor basis in the pairing and in the electron-hole channel lead to ***projected propagators*** *which are defined as*

$$L^{p,\Lambda}_{ij}(\boldsymbol{s}) := \int \mathrm{d}\boldsymbol{k}\, f_i(\boldsymbol{k})\, f^*_j(\boldsymbol{k})\, L^\Lambda(\boldsymbol{k}, \boldsymbol{s}-\boldsymbol{k}) \quad \textit{and} \tag{3.364}$$

$$L^{eh,\Lambda}_{ij}(\boldsymbol{u}) := \int \mathrm{d}\boldsymbol{k}\, f_i(\boldsymbol{k})\, f^*_j(\boldsymbol{k})\, L^\Lambda(\boldsymbol{k}, \boldsymbol{k}-\boldsymbol{u}), \tag{3.365}$$

respectively.

This definition seems unfavourable, as the propagators then obtain one additional dependency. Nevertheless, this form is numerically advantageous, as all the objects which appear in the flow equations for the chantices are provided in the form-factor basis, depending on the same one bosonic transfer momentum. The right hand side of the flow equation therefore becomes a product of three matrices in the form-factor space for each channel, which can easily be calculated by standard algorithms.

Corollary 3.31 (Flow Equations for Chantices in the Form-Factor Space)
Let P^Λ, C^Λ and D^Λ be the chantices of the pairing, the crossed electron-hole and the direct electron-hole channel as defined in definition 45. Let furthermore $\gamma^{(4,0)v,\Lambda}$ be the full vertex projected to channel $v \in \{P,C,D\}$, and let L^Λ be the projected propagator as given by definition 46. Then the flow equation for the three chantices are given by

$$\dot{P}^\Lambda_{mn}(\boldsymbol{s}; o_1o_2; o_3o_4) = \frac{1}{2}\sum_{ij}\sum_{o'_1\ldots o'_4} \gamma^{(4,0)P,\Lambda}_{mi}(\boldsymbol{s}; o_1o_2, o'_1o'_2) \\ L^{p,\Lambda}_{ij}(\boldsymbol{s}; o'_1o'_2, o'_3o'_4)\, \gamma^{(4,0)P,\Lambda}_{jn}(\boldsymbol{s}; o'_3o'_4, o_3o_4), \tag{3.366}$$

$$\dot{D}^\Lambda_{mn}(\boldsymbol{u}; o_1o_2; o_3o_4) = \sum_{ij}\sum_{o'_1\ldots o'_4} \gamma^{(4,0)D,\Lambda}_{mi}(\boldsymbol{u}; o_1o'_4, o_3o'_1) \\ L^{eh,\Lambda}_{ij}(\boldsymbol{u}; o'_1o'_3, o'_2o'_4)\, \gamma^{(4,0)D,\Lambda}_{jn}(\boldsymbol{u}; o'_2o_2, o'_1o_3), \tag{3.367}$$

$$\dot{C}^\Lambda_{mn}(\boldsymbol{t}; o_1o_2; o_3o_4) = -\sum_{ij}\sum_{o'_1\ldots o'_4} \gamma^{(4,0)C,\Lambda}_{mi}(\boldsymbol{t}; o_1o'_4, o_4o'_1) \\ L^{eh,\Lambda}_{ij}(\boldsymbol{t}; o'_1o'_3, o'_2o'_4)\, \gamma^{(4,0)C,\Lambda}_{jn}(\boldsymbol{t}; o'_2o_2, o'_3o_3). \tag{3.368}$$

Let the system be SU(2)-symmetric and let $\bar{P}^\Lambda, \bar{C}^\Lambda$ and $\bar{D}^\Lambda$ be the chantices of the pairing, the crossed electron-hole and the direct electron-hole channel as defined in definition 45. Let furthermore $V^{v,\Lambda}$ be the full vertex projected to channel $v \in \{P,C,D\}$ and let L^Λ be the propagator as given by definition 46. Then the flow equations of the three chantices are given as

$$\dot{\bar{P}}^\Lambda_{mn}(\boldsymbol{s}; o_1o_2; o_3o_4) = \sum_{ij}\sum_{o'_1\ldots o'_4} V^{P,\Lambda}_{mi}(\boldsymbol{s}; o_1o_2, o'_1o'_2) \\ L^{p,\Lambda}_{ij}(\boldsymbol{s}; o'_1o'_2, o'_3o'_4)\, V^{P,\Lambda}_{jn}(\boldsymbol{s}, ; o'_3o'_4, o_3o_4), \tag{3.369}$$

$$\begin{aligned}\dot{\tilde{D}}^{\Lambda}_{mn}(\boldsymbol{u};o_1o_2;o_3o_4) = &\sum_{ij}\sum_{o_1'\ldots o_4'} L^{eh,\Lambda}_{ij}(\boldsymbol{u};o_1'o_3',o_2'o_4')\\ &\Big(2V^{D,\Lambda}_{mi}(\boldsymbol{u};o_1o_4',o_3o_1')\,V^{D,\Lambda}_{jn}(\boldsymbol{u};o_2'o_2,o_3'o_4)\\ &-V^{D,\Lambda}_{mi}(\boldsymbol{u};o_1o_4',o_3o_1')\,V^{C,\Lambda}_{jn}(\boldsymbol{u};o_2'o_2,o_4o_3')\\ &-V^{C,\Lambda}_{mi}(\boldsymbol{u};o_1o_4',o_1'o_3)\,V^{D,\Lambda}_{jn}(\boldsymbol{u};o_2'o_2,o_3'o_4)\Big),\end{aligned} \tag{3.370}$$

$$\begin{aligned}\dot{\tilde{C}}^{\Lambda}_{mn}(\boldsymbol{t};o_1o_2;o_3o_4) = -\sum_{ij}\sum_{o_1'\ldots o_4'} &V^{C,\Lambda}_{mi}(\boldsymbol{t};o_1o_4',o_4o_1')\\ &L^{eh,\Lambda}_{ij}(\boldsymbol{u};o_1'o_3',o_2'o_4')\,V^{C,\Lambda}_{jn}(\boldsymbol{u};o_2'o_2,o_3'o_3).\end{aligned} \tag{3.371}$$

Proof: For the chantex of the pairing channel in its corresponding parametrisation the projection leads to

$$\begin{aligned}\dot{P}_{mn}(\boldsymbol{s}) = \mathbb{P}[\mathcal{T}^{\mathrm{P},\Lambda}]_{mn}(\boldsymbol{s}) = \frac{1}{2}\int \mathrm{d}\boldsymbol{k}\int \mathrm{d}\boldsymbol{k}_s\int \mathrm{d}\boldsymbol{k}_s'\\ \gamma^{(4,0)\Lambda}(\boldsymbol{k}_s,\boldsymbol{s}-\boldsymbol{k}_s;\boldsymbol{k},\boldsymbol{s}-\boldsymbol{k})\,L^{\mathrm{p},\Lambda}(\boldsymbol{k},\boldsymbol{s}-\boldsymbol{k})\,\gamma^{(4,0)\Lambda}(\boldsymbol{k},\boldsymbol{s}-\boldsymbol{k};\boldsymbol{k}_s',\boldsymbol{s}-\boldsymbol{k}_s')\,f_m(\boldsymbol{k}_s)\,f_n^*(\boldsymbol{k}_s'),\end{aligned} \tag{3.372}$$

where the orbital indices are left out to simplify the notation, as they are of no relevance here. The insertion of unities corresponding to the completeness of the form-factor basis as given by equation (3.336) leads to

$$\begin{aligned}\dot{P}_{mn}(\boldsymbol{s}) &= \frac{1}{2}\int \mathrm{d}\boldsymbol{k}\int \mathrm{d}\boldsymbol{k}'\int \mathrm{d}\boldsymbol{k}''\int \mathrm{d}\boldsymbol{k}_s\int \mathrm{d}\boldsymbol{k}_s'\,\gamma^{(4,0)\Lambda}(\boldsymbol{k}_s,\boldsymbol{s}-\boldsymbol{k}_s;\boldsymbol{k},\boldsymbol{s}-\boldsymbol{k})\\ &\quad\delta(\boldsymbol{k}-\boldsymbol{k}')\,L^{\mathrm{p},\Lambda}(\boldsymbol{k}',\boldsymbol{s}-\boldsymbol{k}')\,\delta(\boldsymbol{k}'-\boldsymbol{k}'')\,\gamma^{(4,0)\Lambda}(\boldsymbol{k}'',\boldsymbol{s}-\boldsymbol{k}'';\boldsymbol{k}_s',\boldsymbol{s}-\boldsymbol{k}_s')\,f_m(\boldsymbol{k}_s)\,f_n^*(\boldsymbol{k}_s')\\ &= \frac{1}{2}\int \mathrm{d}\boldsymbol{k}\int \mathrm{d}\boldsymbol{k}'\int \mathrm{d}\boldsymbol{k}''\int \mathrm{d}\boldsymbol{k}_s\int \mathrm{d}\boldsymbol{k}_s'\sum_{i,j} f_m(\boldsymbol{k}_s)\,\gamma^{(4,0)\Lambda}(\boldsymbol{k}_s,\boldsymbol{s}-\boldsymbol{k}_s;\boldsymbol{k},\boldsymbol{s}-\boldsymbol{k})\,f_i^*(\boldsymbol{k})\\ &\quad f_i(\boldsymbol{k}')\,L^{\mathrm{p},\Lambda}(\boldsymbol{k}',\boldsymbol{s}-\boldsymbol{k}')\,f_j^*(\boldsymbol{k}')\,f_j(\boldsymbol{k}'')\,\gamma^{(4,0)\Lambda}(\boldsymbol{k}'',\boldsymbol{s}-\boldsymbol{k}'';\boldsymbol{k}_s',\boldsymbol{s}-\boldsymbol{k}_s')\,f_n^*(\boldsymbol{k}_s'),\end{aligned} \tag{3.373}$$

where the projection of $\gamma^{(4,0)\Lambda}$ and of L^{Λ} to the form-factor space can be identified according to equations (3.347) and (3.364), which then provides the desired expression.

The procedure is analogous for the derivation of the other two channels in the non-SU(2)-symmetric case as explicitly shown in appendix A.1.1. The derivation of the three channels in the SU(2)-symmetric case is analogous, too. However, as the SU(2)-symmetric D-channel has a peculiar momentum structure in its arguments, its derivation is shown explicitly here, while we refer to appendix A.1.2 for the other channels. Performing the same steps as before for the D-channel we get

$$\begin{aligned}\dot{\tilde{D}}_{mn}(\boldsymbol{u}) &= \mathbb{P}_{\mathrm{D}}[\bar{\mathcal{T}}^{\mathrm{D},\Lambda}]_{mn}(\boldsymbol{u})\\ &= \int \mathrm{d}\boldsymbol{k}\int \mathrm{d}\boldsymbol{k}'\int \mathrm{d}\boldsymbol{k}''\int \mathrm{d}\boldsymbol{k}_u\int \mathrm{d}\boldsymbol{k}_u'\sum_{i,j} f_i(\boldsymbol{k}')\,L^{\mathrm{eh},\Lambda}(\boldsymbol{k},\boldsymbol{k}-\boldsymbol{u})\,f_j^*(\boldsymbol{k}')\end{aligned} \tag{3.374}$$

$$
\begin{aligned}
\times \quad & \big(2 f_m(\boldsymbol{k}_u)\, V^\Lambda(\boldsymbol{k}_u, \boldsymbol{k}-\boldsymbol{u}; \boldsymbol{k}_u-\boldsymbol{u}, \boldsymbol{k})\, f_i^*(\boldsymbol{k})\, f_j(\boldsymbol{k}'')\, V^\Lambda(\boldsymbol{k}, \boldsymbol{k}'_u-\boldsymbol{u}; \boldsymbol{k}-\boldsymbol{u}, \boldsymbol{k}'_u)\, f_n^*(\boldsymbol{k}'_u) \\
& - f_m(\boldsymbol{k}_u)\, V^\Lambda(\boldsymbol{k}_u, \boldsymbol{k}-\boldsymbol{u}; \boldsymbol{k}_u-\boldsymbol{u}, \boldsymbol{k})\, f_i^*(\boldsymbol{k})\, f_j(\boldsymbol{k}'')\, V^\Lambda(\boldsymbol{k}, \boldsymbol{k}'_u-\boldsymbol{u}; \boldsymbol{k}'_u, \boldsymbol{k}-\boldsymbol{u})\, f_n^*(\boldsymbol{k}'_u) \\
& - f_m(\boldsymbol{k}_u)\, V^\Lambda(\boldsymbol{k}_u, \boldsymbol{k}-\boldsymbol{u}; \boldsymbol{k}, \boldsymbol{k}_u-\boldsymbol{u},)\, f_i^*(\boldsymbol{k})\, f_j(\boldsymbol{k}'')\, V^\Lambda(\boldsymbol{k}, \boldsymbol{k}'_u-\boldsymbol{u}; \boldsymbol{k}-\boldsymbol{u}, \boldsymbol{k}'_u)\, f_n^*(\boldsymbol{k}'_u)\big)\,,
\end{aligned}
$$

where the second vertex of the second term and the first vertex of the third term do not have their arguments in the parametrisation of the D-channel, but in the one of the C-channel. As V^Λ can not exchange the two incoming or the two outgoing legs alone, this problem can not be healed by exploiting symmetries of the vertex, as is done in the non SU(2)-symmetric case. Instead, the placement of the arguments corresponds to a projection of the vertex to the crossing channel at the main momentum $\boldsymbol{u}$. Therefore, the corresponding vertices are identified as projections of the vertex to the crossing channel, and thus the assertion is obtained. ■

In the just derived flow equations, the projection of the full vertex to the three different channels appear. However, it is convenient and memory-efficient to directly project the propagators to the other channels instead of recovering the full vertex in each integration step. While this projection is directly obtained from applying the back-projection of a channel and the back-projection to the other one an analogous formulation in position space can be advantageous for some choices of form-factors. Therefore the following theorem gives the corresponding channel-to-channel projection rules. The projection of the full vertex to the three different channels is a fundamental part of the flow equations of the chantices. When the projections provided by definition 44 are directly applied, two steps are necessary: First, the full vertex has to be recovered and then it has to be projected to each channel again. As this intermediate step requires a large amount of memory and as it is, therefore, numerically demanding, it is advantageous to project the chantices directly from one channel to the other. In the momentum space, this projection is directly obtained by combining the back-projection of a channel and the projection to another one. This transformation requires two momentum space integrals for each bosonic momentum which cannot be simplified due to the involved momentum structure. As the form-factors are linear combinations of Kronecker-δs with respect to bond vectors in the lattice space, the transformation to this basis is advantageous. The arising combinatorial problem corresponding to the different non-vanishing combinations of form-factors can be calculated in advance of the calculation, such that at run-time only the Fourier transformation of the chantex to the lattice space is required. The expressions for these direct projections are provided by the following corollary:

Corollary 3.32 (Channel-to-Channel Projections)
Let $\hat{\mathbb{P}}_v$ be the projection operator to a channel $v \in \{P, D, C\}$ in a form-factor basis $\{f_n\}_n$, and let P, C, D be chantices according to definition 45. Neglecting the orbital and the frequency dependency, which is unaffected by the projection, the projections between the channels can be given as follows:

1. Projection of the D-channel to the P-channel:

$$
\begin{aligned}
\hat{\mathbb{P}}_P[D]_{mn}(\boldsymbol{s}) &= \int \mathrm{d}\boldsymbol{k}_s \int \mathrm{d}\boldsymbol{k}'_s\, f_m(\boldsymbol{k}_s)\, f_n^*(\boldsymbol{k}'_s) \sum_{ij} f_i^*(\boldsymbol{k}_s)\, f_j(\boldsymbol{s}-\boldsymbol{k}'_s)\, D_{ij}^\Lambda(\boldsymbol{k}_s-\boldsymbol{k}'_s) \qquad (3.375) \\
&= \sum_{ij} \sum_{\boldsymbol{R}_1, \boldsymbol{R}_2, \boldsymbol{R}_3} f_m(\boldsymbol{R}_1-\boldsymbol{R}_3)\, f_n^*(\boldsymbol{R}_2-\boldsymbol{R}_3)\, f_i^*(\boldsymbol{R}_1)\, f_j(\boldsymbol{R}_2)\, e^{-i\boldsymbol{s}\cdot\boldsymbol{R}_2}\, D_{ij}(\boldsymbol{R}_3).
\end{aligned}
$$

2. Projection of the C-channel to the P-channel:

$$\hat{\mathbb{P}}_P[C]_{mn}(\boldsymbol{s}) = \int \mathrm{d}\boldsymbol{k}_s \int \mathrm{d}\boldsymbol{k}'_s\, f_m(\boldsymbol{k}_s)\, f_n^*(\boldsymbol{k}'_s) \sum_{ij} f_i^*(\boldsymbol{k}_s)\, f_j(\boldsymbol{k}'_s)\, C_{ij}^{\Lambda}(\boldsymbol{k}_s+\boldsymbol{k}'_s-\boldsymbol{s}) \tag{3.376}$$
$$= \sum_{ij} \sum_{\boldsymbol{R}_1,\boldsymbol{R}_2,\boldsymbol{R}_3} f_m(\boldsymbol{R}_1-\boldsymbol{R}_3)\, f_n^*(\boldsymbol{R}_2+\boldsymbol{R}_3)\, f_i^*(\boldsymbol{R}_1)\, f_j(\boldsymbol{R}_2)\, e^{i\boldsymbol{s}\cdot\boldsymbol{R}_3}\, C_{ij}(\boldsymbol{R}_3).$$

3. Projection of the P-channel to the D-channel:

$$\hat{\mathbb{P}}_D[P]_{mn}(\boldsymbol{u}) = \int \mathrm{d}\boldsymbol{k}_u \int \mathrm{d}\boldsymbol{k}'_u\, f_m(\boldsymbol{k}_u)\, f_n^*(\boldsymbol{k}'_u) \sum_{ij} f_i^*(\boldsymbol{k}_u)\, f_j(\boldsymbol{k}_u-\boldsymbol{u})\, P_{ij}^{\Lambda}(\boldsymbol{k}_u+\boldsymbol{k}'_u-\boldsymbol{u}) \tag{3.377}$$
$$= \sum_{ij} \sum_{\boldsymbol{R}_1,\boldsymbol{R}_2,\boldsymbol{R}_3} f_m(\boldsymbol{R}_1-\boldsymbol{R}_2-\boldsymbol{R}_3)\, f_n^*(\boldsymbol{R}_3)\, f_i^*(\boldsymbol{R}_1)\, f_j(\boldsymbol{R}_2)\, e^{i\boldsymbol{u}\cdot(\boldsymbol{R}_2+\boldsymbol{R}_3)}\, P_{ij}(\boldsymbol{R}_3).$$

4. Projection of the C-channel to the D-channel:

$$\hat{\mathbb{P}}_D[C]_{mn}(\boldsymbol{u}) = \int \mathrm{d}\boldsymbol{k}_u \int \mathrm{d}\boldsymbol{k}'_u\, f_m(\boldsymbol{k}_u)\, f_n^*(\boldsymbol{k}'_u) \sum_{ij} f_i^*(\boldsymbol{k}_u)\, f_j(\boldsymbol{k}_u-\boldsymbol{u})\, C_{ij}^{\Lambda}(\boldsymbol{k}_u-\boldsymbol{k}'_u) \tag{3.378}$$
$$= \sum_{ij} \sum_{\boldsymbol{R}_1,\boldsymbol{R}_2,\boldsymbol{R}_3} f_m(\boldsymbol{R}_1-\boldsymbol{R}_2-\boldsymbol{R}_3)\, f_n^*(-\boldsymbol{R}_3)\, f_i^*(\boldsymbol{R}_1)\, f_j(\boldsymbol{R}_2)\, e^{i\boldsymbol{u}\cdot\boldsymbol{R}_2}\, C_{ij}(\boldsymbol{R}_3).$$

5. Projection of the P-channel to the C-channel:

$$\hat{\mathbb{P}}_C[P]_{mn}(\boldsymbol{t}) = \int \mathrm{d}\boldsymbol{k}_t \int \mathrm{d}\boldsymbol{k}'_t\, f_m(\boldsymbol{k}_t)\, f_n^*(\boldsymbol{k}'_t) \sum_{ij} f_i^*(\boldsymbol{k}_t)\, f_j(\boldsymbol{k}'_t)\, P_{ij}^{\Lambda}(\boldsymbol{k}_t+\boldsymbol{k}'_t\boldsymbol{t}) \tag{3.379}$$
$$= \sum_{ij} \sum_{\boldsymbol{R}_1,\boldsymbol{R}_2,\boldsymbol{R}_3} f_m(\boldsymbol{R}_1-\boldsymbol{R}_3)\, f_n^*(\boldsymbol{R}_2+\boldsymbol{R}_3)\, f_i^*(\boldsymbol{R}_1)\, f_j(\boldsymbol{R}_2)\, e^{i\boldsymbol{t}\cdot\boldsymbol{R}_3}\, P_{ij}(\boldsymbol{R}_3).$$

6. Projection of the D-channel to the C-channel:

$$\hat{\mathbb{P}}_C[D]_{mn}(\boldsymbol{t}) = \int \mathrm{d}\boldsymbol{k}_t \int \mathrm{d}\boldsymbol{k}'_t\, f_m(\boldsymbol{k}_t)\, f_n^*(\boldsymbol{k}'_t) \sum_{ij} f_i^*(\boldsymbol{k}_t)\, f_j(\boldsymbol{k}_t-\boldsymbol{t})\, D_{ij}^{\Lambda}(\boldsymbol{k}_t\boldsymbol{k}'_t) \tag{3.380}$$
$$= \sum_{ij} \sum_{\boldsymbol{R}_1,\boldsymbol{R}_2,\boldsymbol{R}_3} f_m(\boldsymbol{R}_1-\boldsymbol{R}_2-\boldsymbol{R}_3)\, f_n^*(-\boldsymbol{R}_3)\, f_i^*(\boldsymbol{R}_1)\, f_j(\boldsymbol{R}_2)\, e^{i\boldsymbol{t}\cdot\boldsymbol{R}_2}\, D_{ij}(\boldsymbol{R}_3).$$

7. These equations can analogously be used to describe the projections between the SU(2)-symmetric chantices, that is between $\bar{P}$, $\bar{D}$ and $\bar{C}$.

Proof: We exemplarily prove the projection of the D-channel chantex to the P-channel and refer to appendix A.2 for the other proofs. In order to project the D-channel to the P-channel, the arguments of Φ^{D} have to be expressed in the coordinates of the P-channel, i.e. $\Phi^{\mathrm{D}}(\boldsymbol{k}_s-\boldsymbol{k}'_s, \boldsymbol{k}_s, \boldsymbol{s}-\boldsymbol{k}_s)$. In the back-projection (see eq. (3.339)) the coordinates $\boldsymbol{u}$, $\boldsymbol{k}_u$ and $\boldsymbol{k}'_u$ also have to be expressed in terms of the P-channel ones, leading to

$$\hat{\mathbb{P}}_{\mathrm{P}}[D]_{mn}(\boldsymbol{s}) = \int \mathrm{d}\boldsymbol{k}_s \int \mathrm{d}\boldsymbol{k}'_s\, f_m(\boldsymbol{k}_s)\, f_n^*(\boldsymbol{k}'_s) \sum_{i,j} f_i^*(\boldsymbol{k}_s)\, f_j(\boldsymbol{s}-\boldsymbol{k}'_s)\, D_{ij}(\boldsymbol{k}_s-\boldsymbol{k}'_s), \tag{3.381}$$

which equals the first line of the assertion (cf. eq. (3.375)). A Fourier transformation of the part behind the sum into the position space leads to

$$\sum_{i,j} \sum_{\boldsymbol{R}_1,\boldsymbol{R}_2,\boldsymbol{R}_3} e^{i\boldsymbol{k}_s\cdot\boldsymbol{R}_1}\, f_i^*(\boldsymbol{R}_1)\, e^{-i(\boldsymbol{s}-\boldsymbol{k}'_s)\cdot\boldsymbol{R}_2}\, f_j(\boldsymbol{R}_2) e^{-i(\boldsymbol{k}_s-\boldsymbol{k}'_s)\cdot\boldsymbol{R}_3}\, D_{ij}(\boldsymbol{R}_3). \tag{3.382}$$

Resorting the exponentials according to the appearance of $\boldsymbol{k}_s$ and $\boldsymbol{k}'_s$, and assigning them to the remaining first part of the expression results in

$$\int \mathrm{d}\boldsymbol{k}_s \int \mathrm{d}\boldsymbol{k}'_s\, f_m(\boldsymbol{k}_s)\, e^{i\boldsymbol{k}_s\cdot(\boldsymbol{R}_1-\boldsymbol{R}_3)}\, f_n^*(\boldsymbol{k}'_s)\, e^{-i\boldsymbol{k}'_s\cdot(-\boldsymbol{R}_2-\boldsymbol{R}_3)}\, e^{-i\boldsymbol{s}\cdot\boldsymbol{R}_2}, \tag{3.383}$$

where the integral over the form-factor multiplied with an exponential with the same argument can be identified as the Fourier transformation of the corresponding position space form-factor, resulting in

$$\hat{\mathbb{P}}_{\mathrm{P}}[D]_{mn}(\boldsymbol{s}) = \sum_{i,j} \sum_{\boldsymbol{R}_1,\boldsymbol{R}_2,\boldsymbol{R}_3} f_m(\boldsymbol{R}_1-\boldsymbol{R}_3)\, f_n^*(-\boldsymbol{R}_2-\boldsymbol{R}_3)\, f_i^*(\boldsymbol{R}_1)\, f_j(\boldsymbol{R}_2)\, e^{-i\boldsymbol{s}\cdot\boldsymbol{R}_2} D_{ij}(\boldsymbol{R}_3), \tag{3.384}$$

which is our second assertion in equation (3.375). ∎

Based on the flow equations given in corollary 3.31 and the projections in corollary 3.32 the TUFRG flow equations for the two-particle interaction can now be performed. The Fourier transformation of the chantex based on the lattice space expression can be combined with the combinatorial prefactor arising from the four form-factors, thus resulting in a square matrix with the size of the number of momenta which describes the full projection.

If the calculation of the flow equation for susceptibilities is additionally requested, the full vertex has to be recovered, as it appears in the flow equation of the fermion-boson vertices. However, if a projection of the fermion-boson interaction to the form-factor space is introduced, it might be possible to directly evaluate its flow equation as a matrix-vector product in the form-factor space. On the other hand, if the susceptibility is calculated in a post-processing way it becomes, by the insertion of unities,

$$\chi^{\mathrm{ee}}_{mn}(\boldsymbol{s}) = \sum_{ij} L^{\mathrm{pp},\Lambda}_{mi}(\boldsymbol{s})\, \gamma^{(4,0)\mathrm{P},\Lambda}_{ij}(\boldsymbol{s})\, L^{\mathrm{pp},\Lambda}_{jn}(\boldsymbol{s}), \tag{3.385}$$

which is also easy to evaluate.

Before we discuss the numerical implementation of the full flow equations, we shortly compare the TUFRG to other, similar approaches which the TUFRG is based on.

3.6.3. Similar Form-Factor Approaches to the Functional Renormalisation Group

Preceding to the Truncated Unity approach presented here, two other parametrisations of the FRG equations based on form-factors were developed. In the "**Exchange Parametrisation**" proposed by Husemann *et al.* [67], the full vertex was decomposed into contributions representing the three physical channels, that is the superconducting channel $\tilde{\Phi}_{\mathrm{SC}}$, the magnetic channel $\tilde{\Phi}_{\mathrm{M}}$ and the forward scattering channel $\tilde{\Phi}_{\mathrm{K}}$. This decomposition is defined by

$$\begin{aligned}
\tilde{\Phi}_{\mathrm{SC}}(\boldsymbol{s},\boldsymbol{k}_s,\boldsymbol{k}'_s) &:= \Phi^{\mathrm{P}}(\boldsymbol{k}_s, \boldsymbol{s}-\boldsymbol{k}_s; \boldsymbol{k}'_s) \\
\tilde{\Phi}_{\mathrm{M}}(\boldsymbol{t},\boldsymbol{k}_t,\boldsymbol{k}'_t) &:= \Phi^{\mathrm{C}}(\boldsymbol{k}_t, \boldsymbol{k}'_t-\boldsymbol{t}; \boldsymbol{k}'_t) \\
\tilde{\Phi}_{\mathrm{K}}(\boldsymbol{u},\boldsymbol{k}_u,\boldsymbol{k}'_u) &:= -2\Phi^{\mathrm{D}}(\boldsymbol{k}_u, \boldsymbol{u}-\boldsymbol{k}'_u; \boldsymbol{u}-\boldsymbol{k}_u) + \Phi^{\mathrm{C}}(\boldsymbol{k}_u, \boldsymbol{u}-\boldsymbol{k}'_u; \boldsymbol{k}'_u).
\end{aligned} \tag{3.386}$$

Thus, the superconducting and the magnetic channels are equal to the P- and the C-channel defined in this thesis, while the forward scattering channel is a linear combination of the D- and the C-channel of the TUFRG approach. In the exchange parametrisation, the interactions of these channels are decomposed into a bosonic propagator and two fermion-boson vertices. The latter ones are then parametrised by a momentum-dependent form-factor and by a fermion-boson vertex which only depends on frequencies and the bosonic momentum argument [114]. A proper formulation of this decomposition generates Λ-dependencies on all the introduced quantities. Hence, flow-equations for all the objects of each channel, that is the bosonic propagator and the fermion-boson vertices, have to be solved, while the form-factors are typically approximated to be scale-independent. On the contrary, the TUFRG uses a projection to a fixed form-factor basis, thus not introducing any additional flow equations.

As the introduction of form-factors results from an expansion of the vertices, it is not straight forward to introduce an additional set. Therefore, the dual propagator can not be projected to the corresponding form-factor basis, and thus the main dependence remains the momentum index. For numerical calculations, this leads to an ambiguity concerning the order of the elements with respect to their argument, which is always disadvantageous for parallelised approaches.

In the "**singular mode**" FRG (SMFRG) proposed by Wang *et al.* [68] the full vertex is projected to the three different channels as given by definition 44. That is, three different versions of the same object are treated, and for each one a separate flow equation has to be calculated. In this approach the dual propagators are also projected to the form-factor basis, such that the flow equations are a matrix product in the form-factor space like in the TUFRG case, which is numerically advantageous compared to the exchange parametrisation. In total, this SMFRG approach requires three numerical steps: First, the calculation of the projected electron-hole and of the particle-particle propagator. Second, the calculation of the vertex projected to channel X V^{X} by projecting the previous change of all the channels Y δV^{Y} to it. Third, the calculation of the new change of the full vertex projected to each channel. This approach has been successfully applied to different model systems like graphene [68], the Kagome lattice at van-Hove filling [119], superconducting FeSe systems [120, 121] and doping effects in LaOCrAs [122].

The steps of the SMFRG are analogous to the ones in the TUFRG, but it is based on the chantices instead of the projected full vertex. This basic element of the SMFRG, however, leads to a difficulty when the exchange propagator is of interest like, for example, for a stability analysis. In addition, reconstructing the full vertex to, for example, calculate the flow of self-energies or fermion-boson vertices, even poses ambiguities. When the back-projection of a projected vertex is considered, only sharp momentum structures of this particular channel are reconstituted, while those of the other channels are smeared out. Therefore, this back-projection should be combined with the decomposition of the full vertex (see cor. (3.23)), which additionally requires the inversion of a large matrix to filter out the contributions of the other channels. On the contrary, the full vertex can easily be recovered in the TUFRG approach, as each chantex directly corresponds to one contribution to the decomposition of the full vertex. Thus, the back-projection directly results in the full vertex and at the same time the chantices represent the exchange propagators.

4. Numerical Implementation

A numerical calculation of the flow equations in theorems 3.28 or 3.29 is a challenging task. At this point we exemplarily consider the two-particle interaction $\gamma^{(4,0)\Lambda}$ or V^{Λ}, respectively, which are the most important objects in our calculation and, at the same time, the most costly objects in terms of memory as well as numerical operations, as they scale with $n_{\mathrm{k}}^3 \cdot n_{\omega}^3 \cdot n_{\mathrm{o}}^4$, with n_{k} being the number of momenta, n_{ω} the number of frequencies and n_{o} the number of orbitals[1] of the system under investigation. The scaling becomes $n_{\mathrm{k}} \cdot n_{\mathrm{ff}}^2 \cdot n_{\omega}^3 \cdot n_{\mathrm{o}}^4$, with n_{ff} representing the number of form-factors in the case of the TUFRG vertex flow equations (cf. thm. 3.31).

In this chapter we now present our numerical approach to overcome these difficulties. At first, we provide some information on the general scheme of the FRG calculation (section 4.1) and the calculation of form-factors (section 4.2). As the calculation of the particle-particle propagators is a numerically expensive task, we provide some additional approximations in combination with their analytical results, simplifying the numerical calculation in section 4.3. For further simplifications, we exploit both, the symmetries of the vertex itself (cf. cor. 3.17.1, 3.17.2) and the symmetries of the lattice (cf. thm. 3.17 and 6) in the way described in section 4.4. Finally, in section 4.5 the parallelisation scheme of the code is described, which employs vectorisation and shared and distributed memory parallelisation.

4.1. Numerical Setup

Our implementation of the FRG flow equations is written in object oriented C++ and its basic structure is displayed in figure 4.1. In order to perform the corresponding calculations, a momentum mesh and a frequency mesh are required, as well as form-factors in the case of truncated unities (cf. sec. 4.2). Based on these objects the initial interaction $\gamma^{(4,0)\Lambda_0}$ (or V^{Λ_0}) is set up according to a provided model. Typically, the fermion-boson interactions and the susceptibilities at the initial scale are set to zero, but they could also be initialised in agreement with the provided model. From this setup the FRG flow loop is started. For each integration step at Λ_i the right hand side of the flow equation has to be calculated. So first, the electron-hole and the particle-particle propagators are calculated, which require the momentum and the frequency mesh and, in the case of the TUFRG also the form-factors. For a TUFRG calculation the second step is the projection from one channel to the others, so that the projection of the full vertex projected to one channel is obtained. Then, the product of the vertex, dual propagator and vertex with the correct combination of momenta, frequencies and orbitals can be calculated. The following integration step for the interactions can then either be performed by the crudest approach, that is $V^{\Lambda_{i+1}} = V^{\Lambda_i} + \mathrm{d}V^{\Lambda_i} \cdot \mathrm{d}\Lambda$, or by integration schemes of higher order for which we use the *odeint* library [123]. If neither the vertex diverges nor the final scale for Λ is reached (typically $\Lambda_f = 0$) a new Λ_{i+1} is determined and a new flow step is performed. Otherwise, the flow is stopped, and the final vertex is analysed.

In the following subsections we present some properties of the momentum mesh, the frequency mesh, the model and implications derived from the choice of the band or the orbital basis.

[1] In the spinful case the spin index is treated as part of the orbital index so that the number of orbitals is doubled.

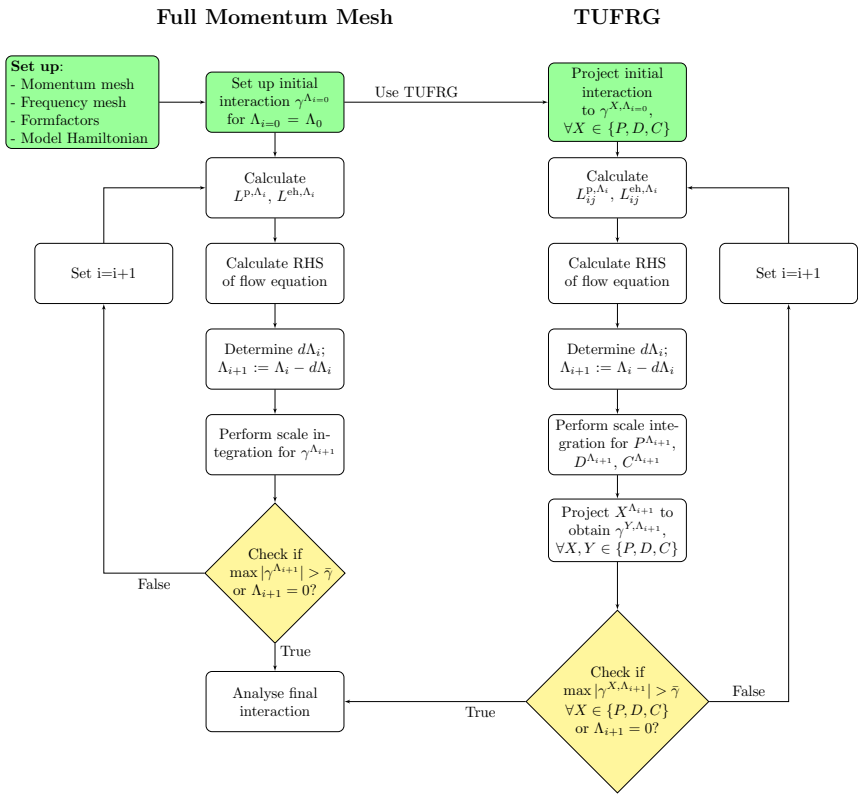

Figure 4.1.: The basic scheme of the code developed within this thesis for the FRG with the vertex in a pure momentum representation (left) and in the TUFRG parametrisation. To simplify the representation we use the abbreviation $\gamma := \gamma^{(4,0)}$ for the two-fermion interaction and $\bar{\gamma} := \gamma_{\max}$ for the threshold which is used to determine the divergence of the flow. The SU(2)-symmetric version of the code follows the same scheme with γ replaced by its SU(2)-symmetric counterpart.

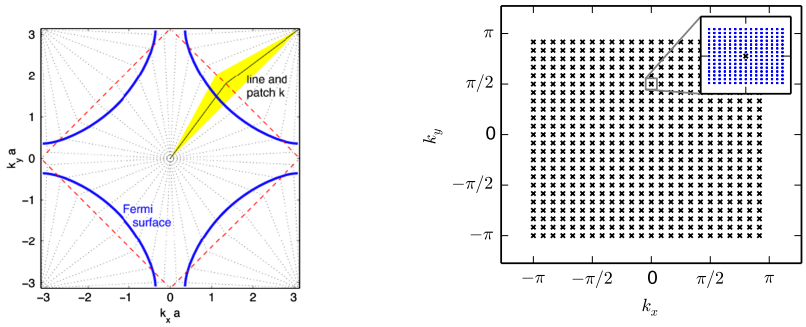

Figure 4.2.: Left: Representation of the N-patch FRG discretisation taken from Metzner [104]. The Brillouin zone is divided into N patches. All interactions depending on a momentum in the patch are represented by the corresponding momentum located at the Fermi-surface, as the dominant interactions are expected close to the Fermi-surface.
Right: Regular two-dimensional lattice of 25×25 points used in the presented code with the inset displaying the refinement of 15×15 points, which is used for the evaluation of the dual propagator.

4.1.1. Momentum Mesh

The momentum mesh can be restricted to the interval $[0, 2\pi)$ for each dimension as the vertex is 2π-periodic in each argument, although the basis vectors of the momentum mesh are not necessarily orthogonal. Therefore, all the additions of momenta have to be back-folded into this momentum space. Due to this it is sufficient for the bosonic argument to be located in this very momentum space, when the mixed fermionic-bosonic notation is used.

As the low energy momenta which are close to the Fermi-surface are the most relevant ones for driving phase transitions, the first FRG approaches used an N-patch scheme [124]. This means that N momentum points are defined on the Fermi-surface on which the vertices are represented, and the whole Brillouin zone is divided into N patches, each belonging to exactly one momentum point (cf. fig. 4.2). Thus, two momenta normally do not exactly add up to another momentum point so that the resulting point is projected to the point on the Fermi-surface of the patch it results in, thus destroying momentum conservation. This approach was improved by adding further shells of momenta, but, nevertheless, it did not heal the problem of destroyed momentum conservation. In order to maintain this, we choose a uniform momentum grid (as first done in [125]) which has to be sufficiently small spaced, so that the Fermi-surface has a proper resolution. Furthermore, a proper resolution is even more important for the dual propagator term L, as it has a strong momentum dependence, because some combinations lead to divergences. Therefore, each momentum of the vertex grid is resolved into a set of fine momenta for the dual propagator calculation. The contribution of the dual propagators to the corresponding vertex elements is then calculated as the average over those fine points. In our approach the refinement is chosen to be uniform for each coarse momentum. However, a different refinement can be implemented for the particle-particle propagator and for the electron-hole propagator, where only the points which exhibit sharp features are treated more accurately, as it has been done by Lichtenstein and de la Peña [2, 126, 112].

4.1.2. Frequency Mesh

For the frequency mesh there does not exist such a restriction. Formally, infinitely many Matsubara frequencies with a spacing of $\frac{2\pi}{\beta}$ have to be taken into consideration. A proper choice of truncation, therefore, mainly depends on the inverse temperature β. An appropriate frequency interval $[-\omega_n, \ldots, \omega_n]$ has to be chosen such that at least Matsubara sums of the propagators for the temperature converge with respect to ω_n. As the addition of frequencies can lead to frequencies outside of the chosen interval, the interval for bosonic frequencies has to be at least twice the size of the fermionic one. However, this separated treatment of fermionic and bosonic frequencies opens the possibility of different approximations for both of them. When the addition of vertices is outside the frequency box, the required vertex element is chosen as the one with the largest frequency in this argument. That is, when the addition of frequencies is outside the interval, the closest one in the interval is chosen, which destroys the energy conservation.

Contrary to this, Wentzell, Hille and Tagliavini [115, 66] use a mixed fermionic-bosonic frequency mesh. In their approach the exact flow inside the full frequency interval is accompanied by a flow of three different objects representing the asymptotic behaviour of the vertex for large frequencies. These three asymptotic limits are achieved by a) sending one fermionic frequency to infinity while maintaining the dependence on the bosonic and on one fermionic frequency; b) by sending both fermionic frequencies to infinity while maintaining the bosonic one; and c) by sending all frequency arguments to infinity.

Alternatively, each channel may only conserve its full bosonic frequency-dependence. When the projection between the channels is required, one may only use the zero-frequency part of the other channel or the zero-frequency of the current channel expressed by the other one [117, 118].

A description of the frequency-dependence in terms of Lorentz curves has been suggested by Husemann [114]. However, these functions do not provide a natural basis of the frequency domain. Therefore an analogous expansion in frequencies similar to the TUFRG one is not available so far. A corresponding frequency-dependence of the interaction is, therefore, not yet implemented in the code presented here.

4.1.3. Model and Basis

Our code is capable of calculating the FRG flow for different types of models which have to be provided by the user through a specific C++ class. Typically, a model is an approximation to the full many-body problem of the solid state Hamiltonian given by equation (3.1), which makes computations of the physically most relevant part feasible. As most effects occur close to the Fermi-surface, usually only those orbitals are considered, which create the bands close to it, while the effects of all the other electrons are included by effective or screened interactions. We will describe the approximation exemplarily for the Hubbard model in chapter 5.

A generic model Hamiltonian in the Wannier basis $|\boldsymbol{R}, o\rangle$ (cf. eq. (2.18)) has the form of

$$\hat{H} = \hat{H}_0 + \hat{H}_{\text{int}} \tag{4.1}$$

with the one-particle part

$$\hat{H}_0 = \sum_{\boldsymbol{R},\boldsymbol{R}'} \sum_{o,o'} \hat{c}^\dagger_{\boldsymbol{R}o} \mathcal{H}_0(\boldsymbol{R}o, \boldsymbol{R}'o')\, \hat{c}_{\boldsymbol{R}'o'} \tag{4.2}$$

and the interacting part

$$\hat{H}_{\text{int}} = \sum_{\boldsymbol{R}_1,\ldots,\boldsymbol{R}_4} \sum_{o_1,\ldots,o_4} \mathcal{V}(\boldsymbol{R}_1 o_1, \ldots, \boldsymbol{R}_4 o_4)\, \hat{c}^\dagger_{\boldsymbol{R}_1 o_1}\, \hat{c}^\dagger_{\boldsymbol{R}_2 o_2}\, \hat{c}_{\boldsymbol{R}_4 o_4}\, \hat{c}_{\boldsymbol{R}_3 o_3}. \tag{4.3}$$

Here, $\mathcal{H}_0(\boldsymbol{R}o\,\boldsymbol{R}'o')$ is the expectation value of the one-particle Hamiltonian in Wannier orbitals providing the kinetic energy, and $\mathcal{V}$ is the interaction between two particles. A generalisation to interactions between $2n$-orbitals is straightforward. In our case the orbital index o also contains the spin quantum number when required. A transformation of the operators to reciprocal space leads to a representation of the Hamiltonians in Bloch states $|\boldsymbol{k}, o\rangle$, which can be used in our framework. Then, the one-particle part is given by

$$\hat{H}_0 = \sum_{o,o'} \int \mathrm{d}\boldsymbol{k}\, \hat{c}^\dagger_{\boldsymbol{k}o}\, \mathcal{H}_0(\boldsymbol{k}, o, o')\, \hat{c}_{\boldsymbol{k}o'} \tag{4.4}$$

and the interacting part is given by

$$\hat{H}_{\text{int}} = \int \mathrm{d}\boldsymbol{k}_1 \cdots \int \mathrm{d}\boldsymbol{k}_4 \sum_{o_1,\ldots,o_4} \mathcal{V}(\boldsymbol{k}_1 o_1, \ldots, R_4 o_4)\, \hat{c}^\dagger_{\boldsymbol{k}_1 o_1}\, \hat{c}^\dagger_{\boldsymbol{k}_2 o_2}\, \hat{c}_{\boldsymbol{k}_4 o_4}\, \hat{c}_{\boldsymbol{k}_3 o_3}. \tag{4.5}$$

However, it is advantageous to work in the band space, as the one-particle Hamiltonian is diagonal here. The basis, in this case, has the additional advantage that the one-particle Green's function can easily be set up. This is achieved by the basis transformation

$$|\boldsymbol{k}, n\rangle = \sum_o U_{no}(\boldsymbol{k})\ |\boldsymbol{k}, o\rangle \tag{4.6}$$

with the unitary matrix $\boldsymbol{U}(\boldsymbol{k})$, which diagonalises the one-particle Hamiltonian according to

$$\mathcal{B}_0(\boldsymbol{k}, n) = \sum_{o,o'} U^*_{no}\, \mathcal{H}_0(\boldsymbol{k}, o, o')\, U_{no'}(\boldsymbol{k}), \tag{4.7}$$

such that the operator can be written as

$$\hat{H}_0 = \sum_n \int \mathrm{d}\boldsymbol{k}\, \hat{c}^\dagger_{\boldsymbol{k}n}\, \mathcal{B}_0(\boldsymbol{k}, n)\, \hat{c}_{\boldsymbol{k}n}. \tag{4.8}$$

The Bloch states $|\boldsymbol{k}, n\rangle$ as the corresponding eigenstates of $\mathcal{H}_0(\boldsymbol{k}, n)$ are only defined up to a phase φ, which we will discuss later in this section.

The transformation of the interacting part of the Hamiltonian takes the form

$$\begin{aligned}\hat{H}_{\text{int}} = \int \mathrm{d}\boldsymbol{k}_1 \cdots \int \mathrm{d}\boldsymbol{k}_4 \sum_{n_1,\ldots,n_4} & \gamma^{(4,0)}(\boldsymbol{k}_1 n_1, \cdots, \boldsymbol{k}_4 n_4) \\ & \times U^*_{n_1 o_1}(\boldsymbol{k}_1)\, U^*_{n_2 o_2}(\boldsymbol{k}_2)\, U_{n_4 o_4}(\boldsymbol{k}_4)\, U_{n_3 o_3}(\boldsymbol{k}_3)\, \hat{c}^\dagger_{\boldsymbol{k}_1 n_1}\, \hat{c}^\dagger_{\boldsymbol{k}_2 n_2}\, \hat{c}_{\boldsymbol{k}_4 n_4}\, \hat{c}_{\boldsymbol{k}_3 n_3}.\end{aligned} \tag{4.9}$$

In our numerical approach, the model can be provided either in a band setting (i.e. by eq. (4.8) and eq. (4.9)) or in an orbital setting (i.e. by eq. (4.4) and eq. (4.5)). In the latter case, the one-particle Hamiltonian is numerically diagonalised by using the Eigen library [127] to enable the construction of one-particle Green's functions in the band basis. As the transformation matrices $U(\boldsymbol{k})$ are thus

obtained, it is possible to perform the flow either in orbital or in momentum space. In the former case, the one-particle Green's function is obtained by calculating

$$G^{\Lambda}_{o_1 o_2}(\boldsymbol{k}\omega) = \sum_n U^*_{no_1}(\boldsymbol{k})\, G^{\Lambda}_n(\boldsymbol{k},\omega)\, U_{no_2}(\boldsymbol{k}) \tag{4.10}$$

for every set of quantum numbers, which increases the numerical work. Contrary, due to the diagonality of the Green's functions, a reduction of numerical demands is expected for a calculation in the band basis. Therefore, two of the internal orbital sums can be evaluated analytically so that the band indices at the propagator lines have to be equal to those at the vertex. In this case, however, the vertex has to be transformed to the band basis according to equation (4.9). A momentum-independent interaction can become momentum-dependent by the transformation matrices, which is called the *orbital makeup*. This orbital makeup can have a significant impact on the results of the corresponding calculations, like, for example, the phase diagram [75]. At the end of the calculation, however, the interaction between different orbitals is usually analysed such that a back-transformation to the corresponding basis has to be performed.

Turning back to the free phase $\phi_n(\boldsymbol{k})$ of the eigenstates in the band basis, a transformation of the form $|\boldsymbol{k}, n\rangle \to e^{i\phi_n(\boldsymbol{k})}\,|\boldsymbol{k}, n\rangle$ leaves the one-particle part invariant due to its cancellation. An analogous transformation can also be defined for the orbital states. As this transformation by a phase leads to a convolution in position space, it has a strong influence on the localisation of Wannier orbitals. Therefore, it can be used to find the maximally localised Wannier functions (MLWF), when these are calculated based on bands, like, for example, Kohn-Sham bands from density functional theory (DFT) calculations [128, 129](cf. also the code Wannier90 [130]). In the following, however, we will use this phase to construct a so called "natural basis", which ensures the point group symmetry of the two-particle interactions. The corresponding discussion is based on Maier [131, 132] (sec. 2.2.2).

In the multi-orbital Wannier basis the point group transformations can be represented by orbital-dependent matrices $\mathbf{M} := M_{oo'}(\boldsymbol{k})$, which combine the three-dimensional matrices corresponding to the mesh and the transformation map of the orbitals. The latter is necessary, because a symmetry operation could map a p_x-orbital to a p_y- or to a p_z-orbital including a phase factor or, in the case of a lattice with more than one kind of atom in the unit cell, it could map an orbital of atom A to an orbital of atom B. As the Hamiltonian describing the system should be symmetric with respect to this point group, the following theorem provides a sufficient condition to exploit it for a reduction of the calculations.

Theorem 4.1 (Point Group Symmetry of the Hamiltonian in Wannier Basis)
Let $|\boldsymbol{k}o\rangle$ be the Wannier basis in momentum space and $\mathcal{H}_0(\boldsymbol{k}, o_1 o_2)$ the corresponding Hamiltonian. Let further $\mathbf{M}(\boldsymbol{k})$ be a unitary matrix representing a point group element of Γ transforming momentum and orbital arguments so that $|\boldsymbol{k}o\rangle \to \left|\hat{R}(\boldsymbol{k})o'\right\rangle = \mathbf{M}(\boldsymbol{k})\,|\boldsymbol{k}o\rangle$. Then the Hamiltonian is symmetric under the point group if and only if

$$\mathcal{H}_0(\hat{R}(\boldsymbol{k})) = \mathbf{M}(\boldsymbol{k})\, \mathcal{H}_0(\boldsymbol{k})\, \mathbf{M}^{\dagger}(\boldsymbol{k}) \tag{4.11}$$

holds for the one-particle Hamiltonian, and

$$\mathcal{V}\left(\hat{R}(\boldsymbol{k}_1)o_1, \hat{R}(\boldsymbol{k}_2)o_2, \hat{R}(\boldsymbol{k}_3)o_3, \hat{R}(\boldsymbol{k}_4)o_4\right) = \sum_{o_1',\ldots,o_4'} M_{o_1o_1'}(\boldsymbol{k}_1)\, M_{o_2o_2'}(\boldsymbol{k}_2)\, M^{\dagger}_{o_4o_4'}(\boldsymbol{k}_4)\, M^{\dagger}_{o_3o_3'}(\boldsymbol{k}_3)\, \mathcal{V}(\boldsymbol{k}_1o_1', \boldsymbol{k}_2o_2', \boldsymbol{k}_3o_3', \boldsymbol{k}_4o_4') \quad (4.12)$$

holds for the interacting Hamiltonian.

PROOF: We consider the Hamiltonian $\hat{H}_0$ and write the creation and the annihilation operators as vectors in orbitals as $\hat{\boldsymbol{c}}_{\boldsymbol{k}}$ and $\hat{\boldsymbol{c}}^{\dagger}_{\boldsymbol{k}}$, respectively, and the Hamilton matrix as $\mathcal{H}$ such that

$$\hat{H}_0 = \int \mathrm{d}\boldsymbol{k}\, \hat{\boldsymbol{c}}^{\dagger}_{\boldsymbol{k}}\, \mathcal{H}(\boldsymbol{k})\, \hat{\boldsymbol{c}}_{\boldsymbol{k}}. \quad (4.13)$$

In the following we will only consider the part under the integral on the right hand side of this equation. By the transformation $\hat{\boldsymbol{c}}_{\boldsymbol{k}} \to \hat{\boldsymbol{c}}'_{\hat{R}(\boldsymbol{k})} = \mathbf{M}(\boldsymbol{k})\hat{\boldsymbol{c}}_{\boldsymbol{k}}$ it becomes

$$(\hat{\boldsymbol{c}}')^{\dagger}_{\hat{R}(\boldsymbol{k})}\, \mathcal{H}(\hat{R}(\boldsymbol{k}))\, \hat{\boldsymbol{c}}'_{\hat{R}(\boldsymbol{k})} = \hat{\boldsymbol{c}}^{\dagger}_{\boldsymbol{k}}\, \boldsymbol{M}^{\dagger}(\boldsymbol{k})\, \mathcal{H}(\hat{R}(\boldsymbol{k}))\, \boldsymbol{M}(\boldsymbol{k})\, \hat{\boldsymbol{c}}_{\boldsymbol{k}}, \quad (4.14)$$

which equals the non-transformed Hamiltonian if equation (4.11) holds.

Transforming the operators for the interacting part in the same way leads to equation (4.12). ■

When this Wannier basis in momentum space is transformed by a phase, that is by $|\boldsymbol{k}o\rangle \to e^{i\varpi_o(\boldsymbol{k})}\,|\boldsymbol{k}o\rangle$, it results in an equivalent basis, and the transformation matrices $\mathbf{M}(\boldsymbol{k})$ have to change their form according to

$$M_{o_1o_2}(\boldsymbol{k}) \to e^{i\varphi_{o_1}(\hat{R}(\boldsymbol{k}))}\, M_{o_1o_2}(\boldsymbol{k})\, e^{-i\varphi_{o_2}(\boldsymbol{k})}. \quad (4.15)$$

Thus, the precise form of the matrices $\mathbf{M}$ depends on the phase φ, such that a momentum-independent matrix $M_{o_1o_2}$ gains a momentum-dependence. Moreover, the multi-orbital model is invariant under a point group symmetry, irrespective of the phase φ.

Concerning the band basis, we would like to obtain a similar relation for its behaviour under point group symmetries. As the eigenvalues of the band Hamilton matrix $\mathcal{B}$ are invariant to unitary matrices, which is the case for the transformation matrices $\mathbf{M}(\boldsymbol{k})$ in theorem 4.1, $\mathcal{B}$ can be cast into a form such that $\mathcal{B}(\hat{R}(\boldsymbol{k})) = \mathcal{B}(\boldsymbol{k})$ holds. However, the fulfilment of the requirements on the interacting part becomes more intricate. This requires the transformation matrices to fulfil an additional condition, as given by the following theorem.

Theorem 4.2 (Point Group Symmetry of the Hamiltonian in Band Basis)
Let $|\boldsymbol{k}o\rangle$, $\mathcal{H}_0(\boldsymbol{k}, o_1o_2)$ and $\mathbf{M}(\boldsymbol{k})$ be as in theorem 4.1. Let further $\mathbf{U}(\boldsymbol{k})$ be a unitary transformation matrix diagonalising $\mathcal{H}_0(\boldsymbol{k}, o_1o_2)$ to $\mathcal{B}(\boldsymbol{k}, n)$ in the corresponding band basis $|\boldsymbol{k}n\rangle = \sum_o U_{no}(\boldsymbol{k})\,|\boldsymbol{k}o\rangle$. If the transformation matrices additionally fulfil the condition

$$\boldsymbol{U}(\hat{R}(\boldsymbol{k})) = \boldsymbol{U}(\boldsymbol{k})\, \mathbf{M}^{\dagger}(\boldsymbol{k}), \quad (4.16)$$

then the one-particle and the interacting Hamiltonian in the band basis are symmetric under point group symmetries at the same time.

PROOF: For the one-particle Hamilton matrix we use

$$\mathcal{B}(\boldsymbol{k}) = \boldsymbol{U}(\boldsymbol{k})\,\mathcal{H}_0(\boldsymbol{k})\,U^\dagger(\boldsymbol{k}) \tag{4.17}$$

in combination with equation (4.11), which leads to

$$\begin{aligned}\mathcal{B}(\hat{R}(\boldsymbol{k})) &= \boldsymbol{U}(\hat{R}(\boldsymbol{k}))\,\mathcal{H}(\hat{R}(\boldsymbol{k}))\,\boldsymbol{U}^\dagger(\hat{R}(\boldsymbol{k})) \\ &= \boldsymbol{U}(\hat{R}(\boldsymbol{k}))\,\mathbf{M}(\boldsymbol{k})\,\mathcal{H}(\boldsymbol{k})\,\mathbf{M}^\dagger(\boldsymbol{k})\,\boldsymbol{U}^\dagger(\hat{R}(\boldsymbol{k})) \\ &= \boldsymbol{U}(\hat{R}(\boldsymbol{k}))\,\mathbf{M}(\boldsymbol{k})\,\boldsymbol{U}^\dagger(\boldsymbol{k})\,\mathcal{B}(\boldsymbol{k})\,\boldsymbol{U}(\boldsymbol{k})\,\mathbf{M}^\dagger(\boldsymbol{k})\,\boldsymbol{U}^\dagger(\hat{R}(\boldsymbol{k})).\end{aligned} \tag{4.18}$$

When we insert $\boldsymbol{U}(\hat{R}(\boldsymbol{k}))$ according to equation (4.16) the unitary matrices cancel each other, so that we obtain $\mathcal{B}(\hat{R}(\boldsymbol{k})) = \mathcal{B}(\boldsymbol{k})$.

Considering the many-particle interaction the transformation leads to

$$\begin{aligned}&\mathcal{V}_{n_1n_2,n_3n_4}(\hat{R}(\boldsymbol{k}_1)\hat{R}(\boldsymbol{k}_2),\hat{R}(\boldsymbol{k}_3)\hat{R}(\boldsymbol{k}_4)) \\ &= U_{n_1o_1}(\hat{R}(\boldsymbol{k}_1))U_{n_2o_2}(\hat{R}(\boldsymbol{k}_2))\mathcal{V}_{o_1o_2,o_3o_4}(\hat{R}(\boldsymbol{k}_1)\hat{R}(\boldsymbol{k}_2),\hat{R}(\boldsymbol{k}_3)\hat{R}(\boldsymbol{k}_4))U^*_{o_4n_4}(\hat{R}(\boldsymbol{k}_4))U^*_{o_3n_3}(\hat{R}(\boldsymbol{k}_3)) \\ &= U_{n_1o_1}(\hat{R}(\boldsymbol{k}_1))\,M_{o_1o_1'}(\boldsymbol{k}_1)\,U_{n_2o_2}(\hat{R}(\boldsymbol{k}_2))\,M_{o_2o_2'}(\boldsymbol{k}_2) \\ &\qquad\qquad \mathcal{V}_{o_1'o_2',o_3'o_4'}(\boldsymbol{k}_1\boldsymbol{k}_2;\boldsymbol{k}_3\boldsymbol{k}_4)\,M^*_{o_4o_4'}(\boldsymbol{k}_4)\,U^*_{o_4n_4}(\hat{R}(\boldsymbol{k}_4))\,M^*_{o_3o_3'}(\boldsymbol{k}_3)\,U^*_{o_3n_3}(\hat{R}(\boldsymbol{k}_3)),\end{aligned} \tag{4.19}$$

where the sum over indices appearing twice is implicitly assumed. Implying condition (4.16) makes the matrices $\mathbf{M}$ vanish due to their unitarity, so that this expression becomes

$$\begin{aligned}&\mathcal{V}_{n_1n_2,n_3n_4}(\hat{R}(\boldsymbol{k}_1)\hat{R}(\boldsymbol{k}_2),\hat{R}(\boldsymbol{k}_3)\hat{R}(\boldsymbol{k}_4)) \\ &\qquad = U_{n_1o_1}(\boldsymbol{k}_1)\,U_{n_2o_2}(\boldsymbol{k}_2)\,\mathcal{V}_{o_1'o_2',o_3'o_4'}(\boldsymbol{k}_1\boldsymbol{k}_2;\boldsymbol{k}_3\boldsymbol{k}_4)\,U^*_{o_4n_4}(\boldsymbol{k}_4)\,U^*_{o_3n_3}(\boldsymbol{k}_3) \\ &\qquad = \mathcal{V}_{n_1n_2,n_3n_4}(\boldsymbol{k}_1\boldsymbol{k}_2;\boldsymbol{k}_3\boldsymbol{k}_4).\end{aligned} \tag{4.20}$$

This equation shows the invariance of the interaction under the corresponding transformation. ■

Theorem 4.2 imposes an additional condition on the diagonalising matrices $\boldsymbol{U}(\boldsymbol{k})$, which has to be fulfilled for a point group symmetric Hamiltonian. It corresponds to the requirement that $\mathcal{H}_0(\hat{R}(\boldsymbol{k}))$ and $\mathcal{H}_0(\boldsymbol{k})$ have to be diagonalised by the same $\boldsymbol{U}(\hat{R}(\boldsymbol{k}))M(\boldsymbol{k})$, which is unique for a $\boldsymbol{U}(\boldsymbol{k})$ due to the group properties. A band basis in which the Hamilton matrix is point group symmetric is called *natural basis*. Such a natural basis is a basis for which the transformation matrices additionally fulfil the condition provided by equation (4.16).

The natural basis, however, is still invariant with respect to a basis transformation $e^{i\varphi_n(\boldsymbol{k})}$ with $\varphi_n(\hat{R}(\boldsymbol{k})) = \varphi_n(\boldsymbol{k})$. This leads to new basis states and, as discussed before, to a change of the transformation matrices $\mathbf{M}(\boldsymbol{k})$ such that condition (4.16) has to be formulated with respect to the transformed matrix.

This undefined phase factor $\phi(\boldsymbol{k})$ might, however, cause some difficulties in the corresponding calculations, as it can have a significant effect on the transformation between lattice and band space as this phase factor is undefined in numerical calculations. Therefore, the transformation matrices have to be smoothed so that all of them correspond to the same smooth phase factor $\phi(\boldsymbol{k})$. However, when only one band is considered, as in the Hubbard model in chapter 5, the transformation to a band basis trivially results in a natural basis.

4.2. Form-Factors

In order to determine the form-factors we consider bond shells, that is, the set of all Bravais lattice vectors with the same length. The number of form-factors corresponding to a shell has to equal the number of its constituting Bravais lattice vectors. In principle, these vectors themselves already form a sufficient set of form-factors. However, form-factors corresponding to the lattice symmetry are assumed to provide better results for the same number of form-factors. The derivation of the corresponding symmetrised form-factors is, therefore, based on the results of group theory, presented in section 2.4 for the 32 crystallographic point groups. When a projection is applied to a trial bond vector of the shell for every irreducible representation according to theorem 19, a linear combination of bond vectors is obtained which requires the character table of the point group. This result is the corresponding symmetrised form-factor, unless it is the null-vector. Therefore, the code contains a generic algorithm to derive the set of form-factors (based on Platt [75], appendix 6.3.3), which is described in the following:

1. For a given shell j, find all Bravais lattice vectors $\boldsymbol{R}_j$ with respect to the origin, which can be obtained by applying the symmetry operations of the group.
2. For each irreducible representation $\mathcal{R}_i$:
   a) take a trial vector $\tilde{\boldsymbol{R}}$ of this shell and
   b) apply the projection operator $\mathcal{P}(\mathcal{R}_i) = \sum_{g\in\mathcal{G}} \chi_i^*(g)g$ to it.
   c) If the result is a (non-zero) linear combination of $\boldsymbol{R}_j$ vectors of this shell, take it as m-th form-factor $f_m^{(j)}$ of this shell; otherwise this reducible representation does not contribute to the form-factor basis.
   d) If this representation is of higher dimension, i.e. $n(\mathrm{E}) > 1$, and if the projection of this representation does not reach all the vectors of this shell, repeat the previous three steps (a-c) with linear independent trial vectors of this shell, until all vectors are reached. If this leads to more than one contribution, diagonalise the coefficient-vectors by the Gram-Schmidt procedure.
3. Normalise the coefficients so that $\sum_{\boldsymbol{R}} f_m^{(j)*}(\boldsymbol{R})\, f_m^{(j)}(\boldsymbol{R}) = 1$ with $\boldsymbol{R}$ denoting all Bravais lattice vectors.
4. Finally, take $R_j = \delta_{\mathbf{0},\boldsymbol{R}_j}$ and perform the Fourier transformation of the form-factors into momentum space.

In order to exemplify this procedure, we consider the point group of a two-dimensional square lattice, which is labelled $\mathrm{C_{4v}}$ in Schoenflies notation, and has the character table displayed in table 4.1. The symmetry operations that map the lattice on itself are a rotation by $\pi/2$ forming the group C2, and rotations by $\pi/4$ and by $-\pi/4$ which form the group $\mathrm{C_4}$. In addition, there are the two classes of

$\mathrm{C_{4v}}$	E	$\mathrm{C_2}$	$2\mathrm{C_4}$	$2\sigma_v$	$2\sigma_d$
$\mathrm{A_1}$	1	1	1	1	1
$\mathrm{A_2}$	1	1	1	-1	-1
$\mathrm{B_1}$	1	1	-1	1	-1
$\mathrm{B_2}$	1	1	-1	-1	1
$\mathrm{E_1}$	2	-2	0	0	0

Table 4.1.: Character table for the crystallographic point group $\mathrm{C_{4v}}$.

Lattice Space Representation				
Irrep	shell 1	shell 2	shell 3	shell 4
A_1	$\frac{1}{4}(\boldsymbol{R}_x+\boldsymbol{R}_{-x}+\boldsymbol{R}_y+\boldsymbol{R}_{-y})$	$\frac{1}{4}(\boldsymbol{R}_{+x+y}+\boldsymbol{R}_{-x+y}+\boldsymbol{R}_{-x-y}+\boldsymbol{R}_{+x-y})$	$\frac{1}{4}(\boldsymbol{R}_{2x}+\boldsymbol{R}_{-2x}+\boldsymbol{R}_{2y}+\boldsymbol{R}_{-2y})$	$\frac{1}{\sqrt{8}}(\boldsymbol{R}_{+2x+y}+\boldsymbol{R}_{-2x-y}+\boldsymbol{R}_{-x+2y}+\boldsymbol{R}_{+x-2y}+\boldsymbol{R}_{-2x+y}+\boldsymbol{R}_{+2x-y}+\boldsymbol{R}_{+x+2y}+\boldsymbol{R}_{-x-2y})$
A_2	0	0	0	$\frac{1}{\sqrt{8}}(\boldsymbol{R}_{+2x+y}+\boldsymbol{R}_{-2x-y}+\boldsymbol{R}_{-x+2y}+\boldsymbol{R}_{+x-2y}-\boldsymbol{R}_{-2x+y}-\boldsymbol{R}_{+2x-y}-\boldsymbol{R}_{+x+2y}-\boldsymbol{R}_{-x-2y})$
B_1	$\frac{1}{4}(\boldsymbol{R}_x+\boldsymbol{R}_{-x}-\boldsymbol{R}_y-\boldsymbol{R}_{-y})$	0	$\frac{1}{4}(\boldsymbol{R}_{2x}+\boldsymbol{R}_{-2x}-\boldsymbol{R}_{2y}-\boldsymbol{R}_{-2y})$	$\frac{1}{\sqrt{8}}(\boldsymbol{R}_{+2x+y}+\boldsymbol{R}_{-2x-y}-\boldsymbol{R}_{-x+2y}-\boldsymbol{R}_{+x-2y}+\boldsymbol{R}_{-2x+y}+\boldsymbol{R}_{+2x-y}-\boldsymbol{R}_{+x+2y}-\boldsymbol{R}_{-x-2y})$
B_2	0	$\frac{1}{4}(\boldsymbol{R}_{+x+y}+\boldsymbol{R}_{-x+y}-\boldsymbol{R}_{-x-y}-\boldsymbol{R}_{+x-y})$	0	$\frac{1}{\sqrt{8}}(\boldsymbol{R}_{+2x+y}+\boldsymbol{R}_{-2x-y}-\boldsymbol{R}_{-x+2y}-\boldsymbol{R}_{+x-2y}-\boldsymbol{R}_{-2x+y}-\boldsymbol{R}_{+2x-y}+\boldsymbol{R}_{+x+2y}+\boldsymbol{R}_{-x-2y})$
$E_1^{(1)}$	$\frac{1}{2}(\boldsymbol{R}_x-\boldsymbol{R}_{-x})$	$\frac{1}{2}(\boldsymbol{R}_{+x+y}-\boldsymbol{R}_{-x-y})$	$\frac{1}{2}(\boldsymbol{R}_{2x}-\boldsymbol{R}_{-2x})$	$\frac{1}{\sqrt{2}}(\boldsymbol{-R}_{+2x+y}-\boldsymbol{R}_{-2x-y})$
$E_1^{(2)}$	$\frac{1}{2}(\boldsymbol{R}_y-\boldsymbol{R}_{-y})$	$\frac{1}{2}(\boldsymbol{R}_{+x-y}-\boldsymbol{R}_{+x-y})$	$\frac{1}{2}(\boldsymbol{R}_{2y}-\boldsymbol{R}_{-2y})$	$\frac{1}{\sqrt{2}}(\boldsymbol{-R}_{+x+2y}-\boldsymbol{R}_{-x-2y})$
$E_1^{(3)}$	-	-	-	$\frac{1}{\sqrt{2}}(\boldsymbol{-R}_{-x+2y}-\boldsymbol{R}_{+x-2y})$
$E_1^{(4)}$	-	-	-	$\frac{1}{\sqrt{2}}(\boldsymbol{-R}_{+2x-y}-\boldsymbol{R}_{-2x+y})$
Momentum Space Representation				
A_1	$\frac{1}{2\pi}(\cos(k_x)+\cos(k_y))$	$\frac{1}{2\pi}\cos(k_x)\cos(k_y)$	$\frac{1}{2\pi}(\cos(2k_x)+\cos(2k_y))$	$\frac{1}{\sqrt{2}\pi}(\cos(2k_x)\cos(k_y)+\cos(k_x)\cos(2k_y))$
A_2	0	0	0	$\frac{1}{\sqrt{2}\pi}(\sin(2k_x)\sin(k_y)-\sin(k_x)\sin(2k_y))$
B_1	$\frac{1}{2\pi}(\cos(k_x)-\cos(k_y))$	0	$\frac{1}{2\pi}(\cos(2k_x)-\cos(2k_y))$	$\frac{1}{\sqrt{2}\pi}(\cos(2k_x)\cos(k_y)-\cos(k_x)\cos(2k_y))$
B_2	0	$\frac{1}{2\pi}\sin(k_x)\sin(k_y)$	0	$\frac{1}{\sqrt{2}\pi}(\sin(2k_x)\sin(k_y)+\sin(k_x)\sin(2k_y))$
$E_1^{(1)}$	$\frac{i}{\sqrt{2}\pi}\sin(k_x)$	$\frac{i}{\sqrt{2}\pi}\sin(k_x+k_y)$	$\frac{i}{\sqrt{2}\pi}\sin(2k_x)$	$\frac{i}{\sqrt{2}\pi}\sin(2k_x+k_y)$
$E_1^{(2)}$	$\frac{i}{\sqrt{2}\pi}\sin(k_y)$	$\frac{i}{\sqrt{2}\pi}\sin(-k_x+k_y)$	$\frac{i}{\sqrt{2}\pi}\sin(2k_y)$	$\frac{i}{\sqrt{2}\pi}\sin(k_x+2k_y)$
$E_1^{(3)}$	-	-	-	$\frac{i}{\sqrt{2}\pi}\sin(-k_x+2k_y)$
$E_1^{(4)}$	-	-	-	$\frac{i}{\sqrt{2}\pi}\sin(2k_x-k_y)$

Table 4.2.: Lattice and momentum shell form-factors of the point group C_{4v} up to the fourth shell. The given vectors are provided by $\boldsymbol{R}_{\pm nx}=\pm n\boldsymbol{a}_x$, $\boldsymbol{R}_{\pm ny}=\pm n\boldsymbol{a}_y$ and $\boldsymbol{R}_{\pm x\pm y}=\pm\boldsymbol{a}_x\pm\boldsymbol{a}_y$. The trial vectors are chosen as $\boldsymbol{R}_{+x}$, $\boldsymbol{R}_{+x+y}$, $\boldsymbol{R}_{2x}$ and $\boldsymbol{R}_{2x+y}=2\boldsymbol{a}_x+\boldsymbol{a}_y$ for the first, second, third and fourth shell, respectively, for all representations except of $E_1^{(2)}$-$E_1^{(4)}$. For $E_1^{(2)}$ the trial vectors are chosen as $\boldsymbol{R}_y$, $\boldsymbol{R}_{+x-y}$ and $\boldsymbol{R}_{2y}$ for the first, second and third shell. For the fourth shell more representations are required, so that we used the additional trial vectors $\boldsymbol{R}_{2x+y}=2\boldsymbol{a}_x-\boldsymbol{a}_y$ and $\boldsymbol{R}_{x+2y}=\pm\boldsymbol{a}_x+2\boldsymbol{a}_y$. The momentum space form-factors are obtained by a Fourier transformation of the lattice space ones.

reflections, each consisting of two operations. Class σ_v is created by the reflection planes along the x- or the y-axis, class σ_d is formed by the planes bisecting the angle between the x- and the y-axis. As representation of the group C_{4v} we can, therefore, use the group which consists of the corresponding matrices .

The zeroth shell only consists of the on-site vector $\boldsymbol{R} = \mathbf{0}$, leading to the form-factor $f_0(\boldsymbol{R}) := \delta_{\mathbf{0},\boldsymbol{R}}$ with the constant momentum space representation $\frac{1}{(2\pi)^d}$, with d denoting the dimension. The first shell is formed by the vectors $\boldsymbol{R} \in \{\boldsymbol{R}_{\pm x}, \boldsymbol{R}_{\pm y}\}$, with $\boldsymbol{R}_x = a\boldsymbol{e}_x$, $\boldsymbol{R}_y = a\boldsymbol{e}_y$, $\boldsymbol{R}_{-x} = -a\boldsymbol{e}_x$ and $\boldsymbol{R}_{-y} = -a\boldsymbol{e}_y$ being the corresponding lattice vectors in positive and negative x- and y-direction with the lattice spacing a. The projection of the first irreducible representation A_1 acting on the trial vector $\boldsymbol{R}_{+x}$ results in

$$\begin{aligned}\mathcal{P}(\mathrm{A_1})\boldsymbol{R}_{+x} &= \chi^*_{\mathrm{A_1}}(\mathrm{E})\boldsymbol{R}_{+x} + \chi^*_{\mathrm{A_1}}(\mathrm{C_2})\boldsymbol{R}_{-x} + \chi^*_{\mathrm{A_1}}(\mathrm{C_4})\boldsymbol{R}_{+y} + \chi^*_{\mathrm{A_1}}(\mathrm{C_4^{-1}})\boldsymbol{R}_{-y} \\ &\quad + \chi^*_{\mathrm{A_1}}(\sigma^1_{\mathrm{v}})\boldsymbol{R}_{+x} + \chi^*_{\mathrm{A_1}}(\sigma^2_{\mathrm{v}})\boldsymbol{R}_{-x} + \chi^*_{\mathrm{A_1}}(\sigma^1_{\mathrm{d}})\boldsymbol{R}_{+y} + \chi^*_{\mathrm{A_1}}(\sigma^2_{\mathrm{d}})\boldsymbol{R}_{-y} \\ &= 2\boldsymbol{R}_{+x} + 2\boldsymbol{R}_{-x} + 2\boldsymbol{R}_{+y} + 2\boldsymbol{R}_{-y}.\end{aligned} \tag{4.21}$$

This form-factor is normalised by a division by 8, as each term yields non-zero only if $\boldsymbol{R} = \boldsymbol{R}_{\pm x}$ or $\boldsymbol{R} = \boldsymbol{R}_{\pm y}$. The real space form-factors resulting from this procedure applied to all the irreducible representations of the point group C_{4v} are summarised in table 4.2 for the first three shells of neighbours. However, as the irreducible representation E_1 is the only one with a dimension of $n = 2$, we additionally regard it in more detail. For the trial vector $\boldsymbol{R}_{+x}$ the projection results in

$$\mathcal{P}(\mathrm{E_1})\boldsymbol{R}_{+x} = 2\boldsymbol{R}_{+x} - 2\boldsymbol{R}_{-x}, \tag{4.22}$$

and hence does not reach all the vectors of this shell. Taking the trial vector $\boldsymbol{R}_{+y}$, which has not yet been reached, this projection results in

$$\mathcal{P}(\mathrm{E_1})\boldsymbol{R}_{+y} = 2\boldsymbol{R}_{+y} - 2\boldsymbol{R}_{-y}, \tag{4.23}$$

so that now all lattice vectors have been reached, resulting in the two contributions corresponding to the representation displayed in table 4.2. Applying the Fourier transformation to these lattice space form-factors in the upper part of table 4.2 leads to their momentum space representation as displayed in the lower part of table 4.2, which are smooth functions, as they are linear combinations of sine and cosine functions.

For the fourth shell there exist eight neighbour vectors of the same length, but we only have five irreducible representations. As there are no zero-entries in the character table for the one-dimensional representations, it can reach all of their corresponding vectors leading to four form-factors. Concerning the four missing form-factors we observe that the E_1-representation does only reach two bond vectors at a time. Hence, a repetition of the projection operation to the E_1-representation with four different trial vectors is required to reach all of them. Thus, we finally obtain the total number of eight form-factors for the fourth shell, which are also shown in position and in momentum space in table 4.2. A simple test directly shows the orthogonality of all form-factors obtained so far.

In the case of the O_h-symmetry, the E_g-representation results in two non-orthogonal coefficient-vectors for the form-factors, corresponding to the momentum space representations $2\cos(k_z) - \cos(k_x) - \cos(k_y)$ and $2\cos(kx) - \cos(k_y) - \cos(k_z)$. By applying the Gram-Schmidt orthonormalisation procedure the second expression becomes $\cos(k_x) - \cos(k_y)$. We provide the resulting momentum space

form-factors of the O_h-point group for the nearest neighbour and for the second nearest neighbour shells in the section on the 3D-Hubbard model (table 5.2 in section 5.3).

For a later discussion we define the following naming convention for some of the form-factors:

Definition 47 (Form-Factor Denomination)

1. *The form-factor* $f = \frac{1}{(2\pi)^d}$ *is called* ***on-site*** *or* ***s-wave form-factor****.*
2. *The form-factor* $f = \frac{1}{(2\pi)^2}(\cos(k_x) + \cos(k_y))$ *in two dimensions, and analogously* $f = \frac{1}{(2\pi)^3}(\cos(k_x) + \cos(k_y) + \cos(k_z))$ *in three dimensions, is called* ***extended s-wave form-factor****.*
3. *The form-factor* $f = \frac{1}{(2\pi)^d}(\cos(k_x) - \cos(k_y))$ *is called* $d_{x^2-y^2}$***-wave form-factor****.*
4. *The form-factor* $f = \frac{1}{(2\pi)^d}(2\cos(k_z) - \cos(k_x) - \cos(k_y))$ *is called* $d_{z^2-x^2-y^2}$*- or* $d_{z^2-r^2}$***-wave form-factor****.*
5. *The form-factor* $f = \frac{1}{(2\pi)^d}\sin(k_i)$ *with* $i \in x, y, z$ *is called* p_i***-wave form-factor****.*

4.3. Implementation of Green's Functions

Based on the implementation of the basic elements, the momentum mesh, the frequency mesh, the model and the form-factors described in the previous sections, we are now at a point at which the Green's functions and the electron-hole and the particle-particle propagators can be calculated. We only consider their representation in band basis, as the transformation to the orbital basis has already been discussed in section 4.1.3. We start this section by defining some of the most frequently used cut-off functions, which are all multiplicative according to equation (3.209) and whose explicit form is important for the functions mentioned above.

Definition 48 (Definition of Cut-Offs)
Let C^Λ *be a cut-off function which regularises* G_0 *such that* $G_0^\Lambda = C^\Lambda G_0$ *fulfils the requirements of definition 40. Then* C^Λ *is called a*

- *sharp momentum shell cut-off if and only if* $C^\Lambda(\boldsymbol{k}) = \theta(|\varepsilon_{\boldsymbol{k}}| - \Lambda)$*,*
- *smooth momentum shell cut-off if and only if* $C^\Lambda(\boldsymbol{k})$ *is a smooth function of the momentum,*
- *sharp frequency cut-off if and only if* $C^\Lambda(\omega) = \theta(|\omega| - \Lambda)$*,*
- *smooth frequency cut-off if and only if* $C^\Lambda(\omega)$ *is a smooth function of the frequency,*
- *ω-frequency cut-off [67] if and only if* $C^\Lambda(\omega) = \frac{\omega^2}{\omega^2+\Lambda^2}$*,*
- *mixed cut-off if and only if* $C^\Lambda(\boldsymbol{k}, \omega)$ *depends on both, momenta* $\boldsymbol{k}$ *and frequencies* ω*,*
- *interaction cut-off [125] if and only if* $C^\Lambda = \Lambda$*, and*
- *temperature cut-off [124] if and only if* $C^{\Lambda=T} \doteq T^{1/2}$*, with temperature* T *as flow parameter.*

The basic idea of these cut-off functions is to regulate the low energy part, in which the typical infrared divergences occur. Although the type of cut-off varies according to this definition, the physical properties of the system remains the same independent of the specific choice, as a first basic discussion [125] pointed out. However, small differences in the critical scale might appear which vanish when the multiloop FRG is applied [66].

Before some of the different cut-off schemes are discussed in more detail, we present some derived forms of the full Green's function and the single-scale propagator, simplifying the implementation later on.

Corollary 4.3 (Full Green's Function and Single-Scale Propagator with Cut-Off)
Let the free Green's function be defined by a multiplicative cut-off function (cf. eq. (3.209)*). Then the full Green's function takes the explicit form*

$$G^{\Lambda} = \frac{C^{\Lambda}}{i\omega - \varepsilon - C^{\Lambda}\Sigma^{\Lambda}}, \tag{4.24}$$

and the single-scale propagator takes the explicit form

$$S^{\Lambda} = \frac{(i\omega - \varepsilon)\partial_{\Lambda} C^{\Lambda}}{[i\omega - \varepsilon - C^{\Lambda}\Sigma^{\Lambda}]^2}. \tag{4.25}$$

Proof: Based on the Dyson-equation (3.135) and on the explicit form of the free Green's function (cf. thm. 3.10) we obtain the desired result from

$$(G^{\Lambda})^{-1} = \frac{i\omega - \varepsilon}{C^{\Lambda}} - \Sigma^{\Lambda} \tag{4.26}$$

by inversion. With theorem 3.20 the single-scale propagator then becomes

$$S^{\Lambda} = \frac{\mathrm{d}}{\mathrm{d}\Lambda} G^{\Lambda}\bigg|_{\Sigma \text{ fixed}} = \frac{\partial_{\Lambda} C^{\Lambda}}{i\omega - \varepsilon - C^{\Lambda}\Sigma^{\Lambda}} + \frac{C^{\Lambda}\partial_{\Lambda}(C^{\Lambda}\Sigma^{\Lambda})}{[i\omega - \varepsilon - C^{\Lambda}\Sigma^{\Lambda}]^2} = \frac{(i\omega - \varepsilon)\partial_{\Lambda} C^{\Lambda}}{[i\omega - \varepsilon - C^{\Lambda}\Sigma^{\Lambda}]^2}, \tag{4.27}$$

which is, again, the desired result. ■

This corollary shows that the difference between the cut-off schemes stems from their explicit form and their derivatives. In the following we, therefore, discuss those cut-off schemes in more detail which are relevant for this thesis, that is the sharp frequency cut-off (cf. sec. 4.3.1), the ω-frequency cut-off (cf. sec. 4.3.2) and the interaction cut-off (cf. sec. 4.3.3). For these cut-offs we, furthermore, provide results in three steps of approximations. First, in the *static vertex approximation* we assume a frequency-independent vertex. We assume the most important interactions to happen at zero frequency transfer and with the lowest fermionic frequency, such that we approximate the full vertex by the corresponding one. In the flow equation of this static vertex the internal arguments are thus related to each other due to the conservation of energy, so that the remaining Matsubara sum can be calculated independently. In the case of the self-energy the internal frequency only appears in the single-scale propagator, so that the corresponding Matsubara sum can be evaluated independently, too. However, this will not lead to a frequency structure of the self-energy, when the calculation initially started with a frequency-independent self-energy. We will often use this approximation, as it was shown for the two-dimensional Hubbard model that the inclusion of higher frequencies changes the results only slightly [67]. However, this approximation allows an analytical evaluation of the Matsubara sum, as only the

propagators remain frequency-dependent, so that a significant numerical advantage can be achieved. Second, to target the ground state phase we additionally go to the zero-temperature limit, where the Matsubara sums become integrals. Third, in addition to the previous approximations, we neglect self-energy effects, which enables simplified analytical evaluations of the propagator loops. In section 4.3.4 we finally provide some short comments on momentum-shell cut-offs and on temperature cut-offs.

4.3.1. The Sharp Frequency Cut-Off

In the case of the sharp frequency cut-off $C^\Lambda = \theta(|\omega| - \Lambda)$, the flow parameter runs from $\Lambda_0 \to \infty$ down to $\searrow 0$. Although Matsubara frequencies are not continuous, we work with the formal Λ-derivative which, in this case, is only given in the sense of a distribution, as $\mathrm{d}_\Lambda C^\Lambda = -\delta(|\omega| - \Lambda)$. As the Matsubara frequencies have a finite spacing, the resulting expression is only well defined in the limit $T \to 0$, where the Matsubara sum converges according to $\frac{1}{\beta}\sum_{\omega_n} \to \frac{1}{2\pi}\int \mathrm{d}\omega$. The expressions of this cut-off result in products of Heaviside functions with a Dirac-delta distribution, which can be solved with the help of the Morris Lemma [133].

Theorem 4.4 (Morris Lemma)
Let δ_α be a function which converges to the Dirac-δ distribution for $\alpha \to 0$, and let θ_α be a function that converges to the Heaviside function in the same limit. Let further $f(x, \theta(x))$ be a sufficiently smooth function in both arguments. Then

$$\delta_\alpha(x) f(x, \theta(x)) \xrightarrow{\alpha \to 0} \delta(x) \int_0^1 du f(0, u). \tag{4.28}$$

Proof: For a proof of this theorem we refer to [133]. ∎

Based on this lemma the single-scale propagator can be reformulated as

$$\begin{aligned} S^\Lambda(\boldsymbol{k}, \omega) &= -\lim_{\alpha \to 0} \delta_\alpha(|\omega| - \Lambda) \frac{i\omega - \varepsilon_{\boldsymbol{k}}}{[i\omega - \varepsilon_{\boldsymbol{k}} - \theta(|\omega| - \Lambda)\Sigma^\Lambda(\boldsymbol{k}, \omega)]^2} \\ &= -\delta(|\omega| - \Lambda) \int_0^1 \mathrm{d}u \frac{i\omega - \varepsilon_{\boldsymbol{k}}}{[i\omega - \varepsilon_{\boldsymbol{k}} - u\Sigma^\Lambda(\boldsymbol{k}, \omega)]^2} \\ &= -\frac{\delta(|\omega| - \Lambda)}{i\omega - \varepsilon_{\boldsymbol{k}} - \Sigma^\Lambda(\boldsymbol{k}, \omega)}, \end{aligned} \tag{4.29}$$

while the Green's function becomes

$$G^\Lambda(\boldsymbol{k}, \omega) = \frac{\theta(|\omega| - \Lambda)}{i\omega - \varepsilon_{\boldsymbol{k}} - \theta(|\omega| - \Lambda)\Sigma^\Lambda(\boldsymbol{k}, \omega)}. \tag{4.30}$$

The frequency integral in the flow equation of the self-energy becomes an integral over the single-scale propagator, which is evaluated according to

$$-\frac{1}{2\pi}\int \mathrm{d}\omega \, \frac{\delta(|\omega| - \Lambda)}{i\omega - \varepsilon_{\boldsymbol{k}} - \Sigma^\Lambda(\boldsymbol{k}, \omega)} = \frac{1}{2\pi} \frac{\varepsilon_{\boldsymbol{k}} + \Sigma^\Lambda(\boldsymbol{k}, \Lambda) + \varepsilon_{\boldsymbol{k}} + \Sigma^\Lambda(\boldsymbol{k}, -\Lambda)}{(i\Lambda - \varepsilon_{\boldsymbol{k}} - \Sigma^\Lambda(\boldsymbol{k}, \Lambda))(-i\Lambda - \varepsilon_{\boldsymbol{k}} - \Sigma^\Lambda(\boldsymbol{k}, -\Lambda))}. \tag{4.31}$$

As the reformulation in equation (4.29) only holds when no other Heaviside or Dirac functions are present, the propagators are given as

$$L^{\Lambda}(\boldsymbol{k}\omega, \boldsymbol{s}\nu) = -\frac{1}{2\pi} \frac{\theta(|\omega| - \Lambda)}{i\omega - \varepsilon_{\boldsymbol{k}} - \theta(|\omega| - \Lambda)\Sigma^{\Lambda}(\boldsymbol{k}, \omega)} \cdot \frac{(i\omega' - \varepsilon_{\boldsymbol{k}'})\delta(|\omega'| - \Lambda)}{[i\omega' - \varepsilon_{\boldsymbol{k}'} - \theta(|\omega'| - \Lambda)\Sigma^{\Lambda}(\boldsymbol{k}', \omega')]^2} - (\omega, \boldsymbol{k}) \leftrightarrow (\omega', \boldsymbol{k}'), \quad (4.32)$$

with $\omega' = \omega + \nu$ and $\boldsymbol{k}' = \boldsymbol{k} + \boldsymbol{s}$ for the electron-hole propagator and $\omega' = -\omega + \nu$ and $\boldsymbol{k}' = -\boldsymbol{k} + \boldsymbol{s}$ for the particle-particle propagator. These expressions can, principally, be reformulated due to the Morris lemma (thm. 4.4), resulting in very lengthy expressions, which we do not present here[2]. In the static vertex approximation $\nu = 0$ the frequency integral can be solved, as only terms with $|\omega| = \Lambda$ give contributions which result in the electron-hole propagator

$$L^{\Lambda}_{\mathrm{ph}}(\boldsymbol{k}\omega, \boldsymbol{u}0) = -\frac{1}{2\pi} \left(\frac{i\Lambda - \varepsilon_{\boldsymbol{k}'}}{(i\Lambda - \varepsilon_{\boldsymbol{k}} - \frac{1}{2}\Sigma^{\Lambda}(\boldsymbol{k}, \Lambda))(i\Lambda - \varepsilon_{\boldsymbol{k}'} - \frac{1}{2}\Sigma^{\Lambda}(\boldsymbol{k}', \Lambda))^2} + \frac{-i\Lambda - \varepsilon_{\boldsymbol{k}'}}{(-i\Lambda - \varepsilon_{\boldsymbol{k}} - \frac{1}{2}\Sigma^{\Lambda}(\boldsymbol{k}, \Lambda))(-i\Lambda - \varepsilon_{\boldsymbol{k}'} - \frac{1}{2}\Sigma^{\Lambda}(\boldsymbol{k}', \Lambda))^2} \right) \quad (4.33)$$

and in the particle-particle propagator

$$L^{\Lambda}_{\mathrm{pp}}(\boldsymbol{k}\omega, \boldsymbol{s}0) = -\frac{1}{2\pi} \left(\frac{-i\Lambda - \varepsilon_{\boldsymbol{k}'}}{(i\Lambda - \varepsilon_{\boldsymbol{k}} - \frac{1}{2}\Sigma^{\Lambda}(\boldsymbol{k}, \Lambda))(-i\Lambda - \varepsilon_{\boldsymbol{k}'} - \frac{1}{2}\Sigma^{\Lambda}(\boldsymbol{k}', \Lambda))^2} + \frac{i\Lambda - \varepsilon_{\boldsymbol{k}'}}{(-i\Lambda - \varepsilon_{\boldsymbol{k}} - \frac{1}{2}\Sigma^{\Lambda}(\boldsymbol{k}, \Lambda))(i\Lambda - \varepsilon_{\boldsymbol{k}'} - \frac{1}{2}\Sigma^{\Lambda}(\boldsymbol{k}', \Lambda))^2} \right). \quad (4.34)$$

In the Katanin scheme (see thm. 3.24) the propagator becomes

$$L^{\Lambda}(\boldsymbol{k}\omega, \boldsymbol{s}\nu) = \frac{\theta(|\omega| - \Lambda)}{i\omega - \varepsilon_{\boldsymbol{k}} - \theta(|\omega| - \Lambda)\Sigma^{\Lambda}(\boldsymbol{k}, \omega)} \cdot \frac{-(i\omega' - \varepsilon_{\boldsymbol{k}})\delta(|\omega'| - \Lambda) + \theta(|\omega'| - \Lambda)\partial_{\Lambda}\Sigma^{\Lambda}(\boldsymbol{k}, \omega')}{[i\omega' - \varepsilon_{\boldsymbol{k}} - \theta(|\omega'| - \Lambda)\Sigma^{\Lambda}(\boldsymbol{k}, \omega')]^2} + (\boldsymbol{k}, \omega) \leftrightarrow (\boldsymbol{k}', \omega'), \quad (4.35)$$

which requires the derivative of the self-energy for a calculation. This derivative can be obtained either by first calculating the corresponding diagram, or by taking the result of the previous step. However, as this is unknown, a further analytical treatment is impossible. By neglecting self-energy effects we are able to further evaluate this term in the static vertex limit, resulting in

$$L^{\Lambda}_{\mathrm{ph}}(\boldsymbol{k}\omega, \boldsymbol{u}0) = \frac{1}{2\pi} \left(\frac{1}{(i\Lambda - \varepsilon_{\boldsymbol{k}})(i\Lambda - \varepsilon_{\boldsymbol{k}+\boldsymbol{u}})} + \frac{1}{(-i\Lambda - \varepsilon_{\boldsymbol{k}})(-i\Lambda - \varepsilon_{\boldsymbol{k}+\boldsymbol{u}})} \right) \quad (4.36)$$

and

$$L^{\Lambda}_{\mathrm{pp}}(\boldsymbol{k}\omega, \boldsymbol{s}0) = \frac{1}{2\pi} \left(\frac{1}{(i\Lambda - \varepsilon_{\boldsymbol{k}})(-i\Lambda - \varepsilon_{-\boldsymbol{k}+\boldsymbol{s}})} + \frac{1}{(-i\Lambda - \varepsilon_{\boldsymbol{k}})(i\Lambda - \varepsilon_{-\boldsymbol{k}+\boldsymbol{s}})} \right) \quad (4.37)$$

for the electron-hole and for the particle-particle propagators, respectively.

[2]The result is easily obtained, for example, by Mathematica and fills half an A4 page.

4.3.2. The ω-Frequency Cut-Off

The cut-off of the form $C^\Lambda = {}^{\omega^2}/_{\omega^2+\Lambda^2}$ has a scale-parameter of the form $\Lambda : \infty \searrow 0$. The derivative of this function is $\mathrm{d}_\Lambda C^\Lambda = -{}^{2\Lambda\omega^2}/_{(\omega^2+\Lambda^2)^2}$, leading to the Green's function

$$G^\Lambda(\boldsymbol{k}\omega n) = \frac{\frac{\omega^2}{\omega^2+\Lambda^2}}{i\omega - \varepsilon_n(\boldsymbol{k}) - \frac{\omega^2}{\omega^2+\Lambda^2}\Sigma_n^\Lambda(\boldsymbol{k}\omega)} \tag{4.38}$$

and to the single-scale propagator

$$S^\Lambda(\boldsymbol{k}\omega n) = -\frac{2\Lambda\frac{\omega^2}{(\omega^2+\Lambda^2)^2}(i\omega - \varepsilon_n(\boldsymbol{k}))}{(i\omega - \varepsilon_n(\boldsymbol{k}) - \frac{\omega^2}{\omega^2+\Lambda^2}\Sigma_n^\Lambda(\boldsymbol{k}\omega))^2}. \tag{4.39}$$

Combining both of them leads to the two-particle propagator

$$L^\Lambda(\boldsymbol{k}\omega, \boldsymbol{s}\nu) = \frac{\frac{\omega^2}{\omega^2+\Lambda^2}}{i\omega - \varepsilon_n(\boldsymbol{k}) - \frac{\omega^2}{\omega^2+\Lambda^2}\Sigma_n^\Lambda(\boldsymbol{k}\omega)} \cdot \frac{-2\Lambda\frac{\omega'^2}{(\omega'^2+\Lambda^2)^2}(i\omega' - \varepsilon_n(\boldsymbol{k}'))}{(i\omega' - \varepsilon_n(\boldsymbol{k}') - \frac{\omega'^2}{\omega'^2+\Lambda^2}\Sigma_n^\Lambda(\boldsymbol{k}'\omega)')^2} + (\boldsymbol{k},\omega) \leftrightarrow (\boldsymbol{k}',\omega'), \tag{4.40}$$

with, again, $\omega' = \omega + \nu$ and $\boldsymbol{k}' = \boldsymbol{k} + \boldsymbol{s}$ for the electron-hole propagator and with $\omega' = -\omega + \nu$ and $\boldsymbol{k}' = -\boldsymbol{k} + \boldsymbol{s}$ for the particle-particle propagator. In the Katanin scheme this becomes

$$L^\Lambda(\boldsymbol{k}\omega, \boldsymbol{s}\nu) = \frac{\frac{\omega^2}{\omega^2+\Lambda^2}}{i\omega - \varepsilon_n(\boldsymbol{k}) - \frac{\omega^2}{\omega^2+\Lambda^2}\Sigma_n^\Lambda(\boldsymbol{k}\omega)} \cdot \frac{-2\Lambda\frac{\omega'^2}{(\omega'^2+\Lambda^2)^2}(i\omega' - \varepsilon_n(\boldsymbol{k}')) + \frac{\omega^2}{\omega^2+\Lambda^2}\delta_\Lambda\Sigma_n^\Lambda(\boldsymbol{k}\omega)}{(i\omega' - \varepsilon_n(\boldsymbol{k}') - \frac{\omega'^2}{\omega'^2+\Lambda^2}\Sigma_n^\Lambda(\boldsymbol{k}'\omega)')^2} + (\boldsymbol{k},\omega) \leftrightarrow (\boldsymbol{k}',\omega'). \tag{4.41}$$

In the static vertex approximation discussed above we have already pointed out that the self-energy will not develop a frequency dependence, so that the Matsubara sums of the single-scale propagator and the two-particle propagators can, in principle, be evaluated in the standard procedure by using the residue theorem. However, the cut-off causes the denominator to be a polynomial of third order whose zeros are very lengthy expressions. Therefore, we skip an analytical evaluation and directly consider the approximation of the vanishing self-energy where the scale-derivative of the full Green's function and the single-scale propagator coincide, that is $S^\Lambda|_{\Sigma=0} = -\mathrm{d}_\Lambda G^\Lambda|_{\Sigma=0} = -\mathrm{d}_\Lambda G_0^\Lambda$ with the derivative of the free Green's function. The evaluation of the Matsubara sum of the single-scale propagator (cf. app. B) then results in

$$\begin{aligned} S^\Lambda(\boldsymbol{k})\big|_{\Sigma=0} = \mathrm{d}_\Lambda G^\Lambda(\boldsymbol{k})\big|_{\Sigma=0} = \mathrm{d}_\Lambda G_0^\Lambda(\boldsymbol{k}) &= \frac{\varepsilon_n(\boldsymbol{k})}{2(\Lambda+\varepsilon_n(\boldsymbol{k}))^2} n_\mathrm{F}(-\Lambda) + \frac{\Lambda}{2(\Lambda+\varepsilon_n(\boldsymbol{k}))} n_\mathrm{F}'(-\Lambda) \\ &- \frac{\varepsilon_n(\boldsymbol{k})}{2(\Lambda-\varepsilon_n(\boldsymbol{k}))^2} n_\mathrm{F}(\Lambda) + \frac{\Lambda}{2(\Lambda-\varepsilon_n(\boldsymbol{k}))} n_\mathrm{F}'(\Lambda) + \frac{2\varepsilon_n^2(\boldsymbol{k})\Lambda}{2(\varepsilon_n^2(\boldsymbol{k})-\Lambda^2)^2} n_\mathrm{F}(\varepsilon_n(\boldsymbol{k})). \end{aligned} \tag{4.42}$$

An analogous calculation can be performed for the particle-particle and for the electron-hole propagator, which leads to lengthy expressions due to the sum of four poles, of which the poles at $\pm\Lambda$ have second order, and the poles at ε_1 and ε_2 may become degenerate, such that two cases have to be treated (for the explicit expressions see appendix B). However, in the zero-temperature limit the Fermi-function, which is used as weighting function, becomes a Heaviside function so that the resulting

expressions can significantly be simplified. In fact, the zero-temperature particle-particle propagator thus becomes

$$L_{\mathrm{pp}}^{\Lambda} = \begin{cases} \frac{1}{4(\varepsilon_1+\varepsilon_2)} \left(\frac{\varepsilon_1(3|\varepsilon_1|+\Lambda)}{(|\varepsilon_1|+\Lambda)^3} + \frac{\varepsilon_2(3|\varepsilon_2|+\Lambda)}{(|\varepsilon_2|+\Lambda)^3} \right) & \text{for } \varepsilon_1 \neq -\varepsilon_2 \\ \frac{-3\varepsilon_1^2-4|\varepsilon_1|\Lambda+\Lambda^2}{4(|\varepsilon_1|-\Lambda)^4} & \text{for } \varepsilon_1 = -\varepsilon_2, \end{cases} \tag{4.43}$$

and the electron-hole propagator is

$$L_{\mathrm{ph}}^{\Lambda} = \begin{cases} -\frac{1}{4(\varepsilon_1-\varepsilon_2)} \left(\frac{\varepsilon_1(3|\varepsilon_1|+\Lambda)}{(|\varepsilon_1|+\Lambda)^3} - \frac{\varepsilon_2(3|\varepsilon_2|+\Lambda)}{(|\varepsilon_2|+\Lambda)^3} \right) & \text{for } \varepsilon_1 \neq \varepsilon_2 \\ \frac{3\varepsilon_1^2+4|\varepsilon_1|\Lambda-\Lambda^2}{4(|\varepsilon_1|-\Lambda)^4} & \text{for } \varepsilon_1 = \varepsilon_2. \end{cases} \tag{4.44}$$

4.3.3. The Interaction Cut-Off

When the interaction cut-off function $C^{\Lambda} = \Lambda$ is applied to the free Green's function, it requires a flow from $\Lambda_0 = 0$ to $\Lambda_f = 1$ to obtain the correct limiting cases. When the fields are rescaled correspondingly, this leads to a continuous scaling of the bare interaction with Λ^2. Hence the interaction is continuously increased from vanishing at $\Lambda_0 = 0t$ to its full form at $\Lambda = 1$. However, it does not lead to a physical regularisation, which is one which regularises divergences. Thus it is only applicable for investigations in which no divergences occur, which is typically achieved by sufficiently large temperatures. But in the approximation of the neglected self-energy this cut-off leaves the dual propagator terms in a simple form, which can be calculated at the beginning and which only requires numerically cheap modifications during the FRG flow. Thus it can be well applied to screen temperature ranges to deduce an estimate for the transition temperature to some ordered phase [125].

With this cut-off the full Green's function and the single-scale propagator become

$$G^{\Lambda}(\boldsymbol{k}\omega n) = \frac{\Lambda}{i\omega - \varepsilon_n(\boldsymbol{k}) - \Lambda\Sigma_n^{\Lambda}(\boldsymbol{k}\omega)} \tag{4.45}$$

and

$$S^{\Lambda}(\boldsymbol{k}\omega n) = \frac{i\omega - \varepsilon_n(\boldsymbol{k})}{(i\omega - \varepsilon_n(\boldsymbol{k}) - \Lambda\Sigma_n^{\Lambda}(\boldsymbol{k}\omega))^2}, \tag{4.46}$$

respectively. The resulting two-particle propagator is then obtained as

$$L^{\Lambda}(\boldsymbol{k}\omega, \boldsymbol{q}\nu) = \frac{\Lambda}{i\omega - \varepsilon_n(\boldsymbol{k}) - \Lambda\Sigma_n^{\Lambda}(\boldsymbol{k}\omega)} \cdot \frac{i\omega' - \varepsilon(\boldsymbol{k}')}{(i\omega' - \varepsilon_{n'}(\boldsymbol{k}') - \Lambda\Sigma_{n'}^{\Lambda}(\boldsymbol{k}'\omega'))^2} + (\boldsymbol{k}, \omega) \leftrightarrow (\boldsymbol{k}', \omega') \tag{4.47}$$

again with $\omega' = \omega + \nu$ and $\boldsymbol{k}' = \boldsymbol{k} + \boldsymbol{s}$ for the electron-hole propagator and with $\omega' = -\omega + \nu$ and $\boldsymbol{k}' = -\boldsymbol{k} + \boldsymbol{s}$ for the particle-particle propagator. In the Katanin scheme this becomes

$$L^{\Lambda}(\boldsymbol{k}\omega, \boldsymbol{q}\nu) = \frac{\Lambda}{i\omega - \varepsilon_n(\boldsymbol{k}) - \Lambda\Sigma_n^{\Lambda}(\boldsymbol{k}\omega)} \cdot \frac{i\omega' - \varepsilon(\boldsymbol{k}') + \Lambda^2\partial_{\Lambda}\Sigma_n^{\Lambda}(\boldsymbol{k}'\omega')}{(i\omega' - \varepsilon_{n'}(\boldsymbol{k}') - \Lambda\Sigma_{n'}^{\Lambda}(\boldsymbol{k}'\omega'))^2} + (\boldsymbol{k}, \omega) \leftrightarrow (\boldsymbol{k}', \omega'). \tag{4.48}$$

Again, in the static vertex approximation, it is possible to evaluate these expressions by the residue theorem, as the self-energy will not develop any frequency dependence. We have, however, not covered this case and, therefore, directly consider the approximation of neglected self-energy and static

vertices. In this case the Λ-derivative can directly be evaluated and be moved out of the Matsubara summation, which now equals the standard two-particle propagator Matsubara sum. Thus the two-particle propagators become

$$L^{\Lambda}_{\mathrm{pp}}(\boldsymbol{k},\boldsymbol{q}) = 2\Lambda \frac{1 - n_{\mathrm{F}}(\varepsilon_n(\boldsymbol{k})) - n_{\mathrm{F}}(\varepsilon_{n'}(\boldsymbol{q}-\boldsymbol{k}))}{\varepsilon_n(k) + \varepsilon_{n'}(\boldsymbol{q}-\boldsymbol{k})} \tag{4.49}$$

for the particle-particle case and

$$L^{\Lambda}_{\mathrm{ph}}(\boldsymbol{k},\boldsymbol{q}) = 2\Lambda \frac{n_{\mathrm{F}}(\varepsilon_n(\boldsymbol{k})) - n_{\mathrm{F}}(\varepsilon_{n'}(\boldsymbol{k}+\boldsymbol{q}))}{\varepsilon_n(k) - \varepsilon_{n'}(\boldsymbol{k}+\boldsymbol{q})} \tag{4.50}$$

for the electron-hole case. The scale-independent part of these expressions can be evaluated at the beginning of the calculation and only has to be multiplied by the actual scaling parameter Λ in the following integration steps to obtain the actual dual propagator. This is already a very simple form, which can be calculated very efficiently. By an additional $T = 0$ limit the Fermi-functions become Heaviside functions, which simplify the calculation in the way that more dual propagator terms become exactly zero and do not contribute.

Beside of these frequently used cut-off schemes other ones are possible, which will be discussed in the following. A special case is the treatment of the temperature as a cut-off parameter.

4.3.4. Further Cut-Off Schemes

The temperature spans the mesh of Matsubara frequencies by $\omega_n = (2n+1)\pi T$ such that each frequency n itself decreases. In this case it is, therefore, useful to keep n instead of ω_n as an argument. In corresponding calculations, however, the energy conservation still connects the entries with the same n, which previously was the frequency number. In order to obtain the temperature as flow parameter, the temperature dependence has to be shifted from the bare interaction to the quadratic part, which is achieved by a rescaling of the Grassmann fields to $\psi'(\boldsymbol{k}n) = T^{3/4}\psi(\boldsymbol{k}\omega_n)$ and $\bar{\psi}'(\boldsymbol{k}n) = T^{3/4}\bar{\psi}(\boldsymbol{k}\omega_n)$. The corresponding bare propagator thus becomes

$$G^{\Lambda}_0(\boldsymbol{k}n) = \frac{T^{\frac{1}{2}}}{i\omega_n - \varepsilon(\boldsymbol{k})}, \tag{4.51}$$

and the flow equations can be derived by the same procedure as given in chapter 3.5. Formally, this corresponds to a cut-off function of $C^{\Lambda=T} = T^{\frac{1}{2}}$. The flow equations for n-particle vertices are analogous to the previous ones up to a factor of $T^{\frac{3n}{2}}$. This cut-off has the advantage that it directly leads to a critical temperature for the phase-transition in one calculation, while other cut-off schemes need several calculations at different temperatures to determine it. Additionally, local symmetries and their Ward identities are fulfilled for the exact flow at every step of the it. Thus it is easier to consider them for truncated schemes.

Momentum cut-off schemes have the advantage that the frequency structure of the propagators and of the vertices are not affected, so that the evaluation of Matsubara frequencies can often be performed analytically. However, when self-energy corrections are present, the Fermi-surface changes during the flow, so that the momentum cut-off has to be adapted to the new surface. Additionally, these cut-offs suppress electron-hole excitations with a small momentum transfer $\boldsymbol{q}$ in the shell $|\varepsilon(\boldsymbol{k}+\boldsymbol{q})| - |\varepsilon(\boldsymbol{k})| < 2\Lambda$. Therefore, the limits $\boldsymbol{q} \to 0$ and $\Lambda \to 0$ do not commute any more, so that the forward scattering

	spinful		SU(2)-symm.	
	indep. elements	share	indep. elements	share
no symmetry	120,472,567	1.00	7,529,536	1.00
complex conj.	60,313,120	0.50	3,783,976	0.50
crossing sym.	30,272,592	0.25	3,765,160	0.50
comp.+cross. sym.	15,174,810	0.13	1,901,788	0.25
C_{4v} sym.	22,127,616	0.18	1,382,976	0.18
all above symmetries	4,131,255	0.03	519,189	0.07

Table 4.3.: The number of independent elements in the two-dimensional Hubbard model, when different symmetries are exploited, and the share to the full calculation. In the spinful case both spin-orbitals are treated separately, while in the SU(2)-symmetric case only one band is present.

for $\boldsymbol{q} \to 0$ can only be investigated at the end of the flow, making stability analyses difficult [104]. Due to these problems, we have not used any momentum shell cut-off in our investigations.

4.4. Symmetries

In order to reduce the numerical demands in terms of memory demand and computation time we exploit the symmetries of the system, which have been presented in theorem 3.17. For this purpose it is sufficient to save only one representative for each of the symmetrically equivalent elements. For each representative another structure holds the full set of indices it belongs to. In order to obtain the other elements again, a pointer to the saved element and two integers of ± 1 are saved, which represent the possible sign change and the complex conjugation in form of a multiplication, so that comparison operations can be avoided which may slow down the code. But the total memory demand is hardly reduced by this approach. However, the number of elements which have to be calculated is significantly reduced for the vertex as well as for the dual propagators. In table 4.3 we show the number of elements which have to be calculated for the two (spin-)orbitals and for the one-band two-dimensional Hubbard model in the static-vertex approximation based on a momentum lattice of 14×14.

For the case that both vertex-inherent symmetries are exploited, this table shows that it is sufficient to calculate only every fourth vertex element in the SU(2)-symmetric case and only every eighth in the spinful case. This should already reduce the calculation time to approximately 25 % and to 13 % compared to the full vertex ones. As these symmetries should always be present, even systems without point group symmetries can gain such speed-ups. However, when the point group symmetry can additionally be exploited, the calculation of only 3 % and of 7 % of the vertex is necessary in the spinful and in the SU(2)-symmetric case, respectively. Thus the calculation can gain a speed-up of up to an order of magnitude by exploiting all symmetries. Additional symmetries may lead to even further gains in performance. However, as the full vertex has to be recovered for the flow step leading to some overhead, these performance gains can only be achieved approximately.

Contrary to these considerations, a phase transition is typically accompanied by a break of symmetry. Hence, when the symmetries are explicitly encoded to obtain the gain in performance, it might become impossible to obtain the phase originating from a break of symmetries. Therefore, in our code all the symmetries have a switch, so that one can either profit from the symmetries of the system or have the possibility of investigating all possible symmetry-breaking phases.

4.5. Performance and Parallelisation

The largest object we are dealing with in our FRG approach is the two-particle interaction $\gamma^{(4,0)\Lambda}$. Now let us consider the case of a momentum mesh spanned by $n_{\boldsymbol{k}}$ momenta, a frequency mesh using n_{ω_F} fermionic and n_{ω_B} bosonic frequencies and a model which requires n_o (spinful) orbitals or bands. Then the size of the full vertex is $n_{\boldsymbol{k}}^3 \cdot n_{\omega_\mathrm{F}}^2 \cdot n_{\omega_\mathrm{B}} \cdot n_o^4$. The calculation of the right hand side of the flow equation in each FRG integration step (cf. eq. (3.28)) requires a momentum space integration and a Matsubara frequency and orbital summations for each vertex element. This results in a numerical complexity of $n_{\boldsymbol{k}}^4 \cdot n_{\omega_\mathrm{F}}^3 \cdot n_{\omega_\mathrm{B}} \cdot n_o^8$. Due to this bad scaling in orbitals, only a few orbitals are feasible within the FRG approach. As pointed out in section 4.1.3 a treatment of the system in band basis, however, reduces the internal summations so that the scaling in bands (which have the same dimension as the orbitals) becomes n_o^6. Alternatively, when SU(2)-symmetry is present, only half the number of orbitals is necessary. Hence, the size of the vertex is reduced by a factor of 16, and the numerical complexity of an FRG step even is reduced by a factor of 196.

Employing the TUFRG with n_FF form-factors only has an effect on the complexity in momentum space, so that we only consider the corresponding part here. The size of the vertex then becomes $n_{\boldsymbol{k}} \cdot n_\mathrm{FF}^2$ instead of $n_{\boldsymbol{k}}^3$ and with equations (3.366)-(3.368) the numerical complexity of one TUFRG integration step becomes $n_{\boldsymbol{k}} \cdot n_\mathrm{FF}^4$ instead of $n_{\boldsymbol{k}}^4$. However, in each integration step a projection between the different channels as provided by equations (3.375)-(3.380) is required. If this projection is performed in momentum space (first line in the corresponding equations), it has a total complexity of $n_{\boldsymbol{k}}^3 \cdot n_\mathrm{FF}^4$ for each element. By shifting the arguments in such a way that the vertex which is projected only depends on one of the integration variables, the other integral can be calculated in advance. Thus, the runtime scaling is reduced to $n_{\boldsymbol{k}}^2 \cdot n_\mathrm{FF}^4$. We implemented this projection as a product of three matrices of which the vertex-independent ones were calculated either once at the beginning of the flow (KS,AM) or for each RG step to save memory (KS,SM). A fit to the corresponding scaling curves of these two versions (cf. top row of fig. 4.3) indeed reveal a scaling of $n_{\boldsymbol{k}}^{2.2} \cdot n_\mathrm{FF}^4$ in good agreement to the assertion.

When the projections are performed in position space (second line of the corresponding equations (3.375)-(3.380)), the sum over position space arguments can be performed in advance, resulting in a numerical complexity of $n_{\boldsymbol{k}} \cdot n_\mathrm{FF}^4$, which is of the same order as the matrix multiplication of the TUFRG step. However, in this approach the vertex itself has to be Fourier transformed to lattice space which has a complexity of $n_{\boldsymbol{k}} \cdot n_\mathrm{bonds}$, with n_bonds referring to the number of bonds required by the combinatorial evaluation of the form-factor and the position space sums. We implemented a corresponding projection (RS,SM) which reveals an impressive scaling (cf. fig. 4.3) of $n_{\boldsymbol{k}}^{0.9} \cdot n_\mathrm{FF}^{2.8}$, which is even better than expected. As the pre-evaluation of the combinatorics allows us to only sum the non-vanishing form-factor combinations, the scaling behaviour can be improved. However, the projection to lattice space can be combined with the combinatorial evaluation providing an $n_{\boldsymbol{k}} \times n_{\boldsymbol{k}}$ matrix for each form-factor projection (RS,AM). As this requires n_FF^4 of those matrices this approach is restricted by the available memory, so that we can not obtain a proper scaling in momentum space. However, this approach reveals a form-factor scaling of n_FF^4, as expected.

A comparison of the four different projection schemes displayed in figure 4.3 shows that the projections in lattice space with a pre-evaluation of the combinatorics with a separate treatment of the Fourier transformation to lattice space of the vertex (RS,SM) is superior to the other approaches, as it is memory efficient, fast and the best in terms of scaling. It even beats the matrix multiplication approach, which usually is advantageous on modern processors.

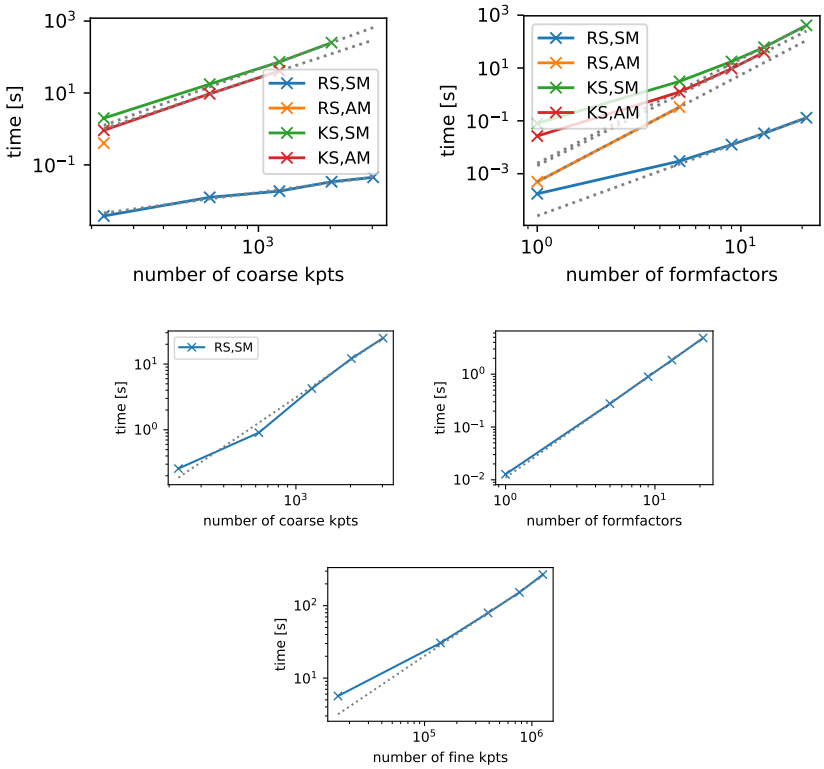

Figure 4.3.: Scaling of different implementations of the projection operation (described in the text) between channels (top row) and the calculation of the dual propagators in form-factor space (bottom row) with respect to momentum resolution and form-factor resolution. The gray dashed lines represent fits to the scaling curves.

The second demanding part in each step is the calculation of the dual propagator in the form-factor basis (cf. eq. (3.364)-(3.365)) which involves a momentum space integral so that its theoretical scaling is $n_{\boldsymbol{k}}^2 \cdot n_{\mathrm{FF}}^2$. Our implementation, as displayed in the lower row of figure 4.3, indeed reveals a scaling of $n_{\boldsymbol{k}}^{1.9} \cdot n_{\mathrm{FF}}^{2.0}$, as expected. As the integral is performed on a mesh where each coarse momentum is refined, this calculation scales linear with the number of refined momenta both, in theory and in the implementation.

The two operations discussed above are in terms of total time the most relevant ones for the calculation of the right hand side of the TUFRG flow equation. Comparing both of them we note that the calculation of the projected dual propagator is always significantly more time demanding than the projection according to the (RS,SM) scheme. However, this only holds for small momentum meshes and for a low number of form-factors in the other projection schemes, due to their disadvantageous scaling behaviour.

Still, with a total scaling of $n_{\boldsymbol{k}}^2 \cdot n_{\mathrm{FF}}^2$ TUFRG calculations are computationally demanding in order to gain results in a desirable precision. Therefore, we aim at using all forms of parallelisation which high-performance computation is offering, that is single-instruction multiple-data (SIMD), shared memory

parallelisation (OpenMP) and distributed data parallelisation (MPI), which will be regarded in more detail in the following subsections.

4.5.1. Single-Instruction Multiple-Data and Memory Access

In order to gain an insight into SIMD parallelisation we regard the CPU as the heart of a computer. Modern CPUs (e.g. Intel Haswell) use registers with a length of 512 bits on which the arithmetic logical unit (ALU) can work. As such registers can typically store eight values of double precision (compiler-dependent), the same operation can simultaneously be performed on all of them by this ALU. As this can be regarded as treating the successive values in the register as a vector, this procedure is also called vectorisation, which is the most prominent implementation of SIMD. When the corresponding CPU architecture-dependent option is provided to the compiler, it tries to optimise the code for those operations. Modern CPUs contain several ALUs which are specialised to perform add, multiply or combined multiply-add operations. The data required for the operations have to be loaded to the processor. This is typically (architecture-dependent) done by passing three levels of cache, which become larger, but also slower to access, the further away they are from the CPU and the closer they are to the main memory. The vertex usually is too large to fit into the cache, so that a permanent data transfer from the main memory to the CPU is required. Such a data stream is possible, when the elements of the vertex are accessed successively, which then is also in perfect alignment for vectorisation.

However, in a straight forward implementation of the flow equations we may move through the elements of the first vertex successively, but the values of the second vertex are distributed in memory, as they are determined by momentum and by frequency conservation. To enable a good data throughput we only treat those parts of the vertices and the bubble which we put in a memory aligned structure. Hence, the corresponding part of the calculation has a perfect memory access and can use vectorisation perfectly, too. Although all values have to be touched twice, this approach significantly improves the performance of the code.

4.5.2. Shared Memory Parallelisation

A compute node of a cluster consists of several CPUs which share their memory. In our code we employ OpenMP, which distributes the loop over the elements whose calculation is assigned to one node, namely to a number of *threads* which run in parallel. In the perfect matching case, the number of threads equals the number of CPUs of a node. When a CPU is assigned to more than one thread, this is called *multi-threading*, which can still result in a gain in performance. This shared memory, however, leads to difficulties, as all processes work on the same memory. While one process has loaded some data into its cache and performs some calculations on it, another thread may have changed the original data. As the loop over elements which have to be calculated is parallelised, each element is only written to by one thread, while unchanged vertex elements are read. In cases in which this can not be verified in such a simple way, every thread obtains its own part of memory in which it saves its results, which are combined with the results of the other threads at the end of the parallel section.

In figure 4.4 we show the shared memory scaling of our SU(2)-symmetric TUFRG implementation on JURECA [1] based on a calculation of the two-dimensional Hubbard model with 35 coarse mesh momenta refined by 15 momenta in each direction and 3 shells of form-factors. We employ one node which contains two Intel Xeon E5-2680 v3 Haswell CPUs with 12 cores each. The implemented code

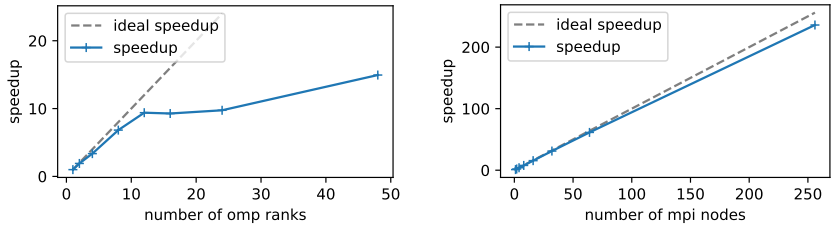

Figure 4.4.: The OMP (left) and MPI (right) scaling behaviour for the calculation of the right hand side for one RG step obtained on JURECA.

scales well up to 12 threads, where the scaling totally breaks down. This probably corresponds to one of the two CPUs blocking the memory access of the other one, so that only 12 of the 24 nodes can work properly. When more than 24 threads are assigned to one node, more than one process is executed on one core, which is called Simultaneous Multi Threading, which provides a slight performance gain in our case.

4.5.3. Distributed Memory Parallelisation

Compute clusters consist of several thousands of nodes, each with its own memory, which are connected to all the others by a high-speed network. To parallelise the calculation for all the nodes we distribute the vertex increment $\mathrm{d}V$, which results from the right hand side of the flow equations (cf. eq. (3.28)), to all the nodes participating in the calculation. Due to the distributed memory each node only knows the part of the increment that was calculated by itself. The results of each part of the vertex are, therefore, sent to all the other processes by a collective communication scheme. For this task we employ the Message Passing Interface (MPI) standard. In fact, for the momentum-grid FRG it is sufficient to have only one communication, after the right hand side of the flow-equation has been calculated, so that the integration step can be performed for all processes in the same way. In the TUFRG case the projection is already distributed over several nodes, so that one communication is required to pass the results of the projection to all processes, and a second one is necessary to distribute the results of the right hand side of the TUFRG flow equation (see eq. (3.366)-(3.371)).

In figure 4.4 we present the scaling behaviour of our code with respect to the MPI parallelisation. The timing is obtained for a calculation of the two-dimensional Hubbard model without the usage of symmetries on a coarse lattice of 55 momenta refined by 25 momenta in each direction and 2 shells of form-factors. For this setting we observe an impressive, almost perfect scaling up to 256 nodes for our implementation of the TUFRG flow equation. Such a scaling allows us to employ a large number of nodes to obtain results from TUFRG calculations within a reasonable amount of time.

Finally, we remark that the systems we have been investigating were sufficiently small, so that each node could save the full vertex. When the system becomes too large, this parallelisation scheme has to be modified such that one node only holds one part of the vertex and obtains the part required for the calculations from the other nodes.

5. Application to the Hubbard Model

As we discussed at the beginning of chapter 3, it is not possible to solve the full solid state Hamiltonian (see eq. (3.1)), neither analytically nor numerically. The numerical limitations of a bad scaling with the number of bands also restrict the application of the (TU)FRG developed in the previous chapter, which formally could be used to calculate the full solid state interaction starting from a free electronic system. It is, therefore, necessary to employ a simplified model, which is sufficient to obtain the relevant interactions.

In the scope of this thesis we aim at developing methods to determine the electronic ground states of materials with correlation effects. As the energy levels close to the Fermi-energy are the most relevant ones for those effects, it is reasonable to use a simple model which describes the bands close to it. One of the simplest ones is the Hubbard model, which contains an approximate kinetic term and an interaction term, as we will derive in the following. So far, this model has been used to describe copper- and iron-based superconductors and basic metals, but it has also served as a toy model for method developments, which is the case for us, too.

The non-interacting part of the solid state Hamiltonian is diagonal in the Bloch-Basis, such that the Hamiltonian can be written as

$$\hat{H} = \int \mathrm{d}\boldsymbol{k} \sum_{n,s} (\varepsilon_{\boldsymbol{k},n,s} - \mu)\, \hat{c}^\dagger_{\boldsymbol{k}ns}\, \hat{c}_{\boldsymbol{k}ns} + \hat{H}_{\mathrm{int}}. \tag{5.1}$$

We remark that this Hamiltonian is not necessarily invariant under point group transformations of the momentum lattice as discussed in section 4.1.3, and a unitary transformation to the natural basis is required to achieve this property. In this discussion, however, the natural basis is not required and we express the Hamiltonian in Wannier states according to equation (2.34) as

$$\begin{aligned}\hat{\mathcal{H}} = \sum_s \sum_{oo',\boldsymbol{R}\boldsymbol{R}'} \left(-t_{\boldsymbol{R}o,\boldsymbol{R}'o'} - \mu\delta_{oo'}\delta_{\boldsymbol{R}\boldsymbol{R}'}\right)\, \hat{c}^\dagger_{\boldsymbol{R}os}\, \hat{c}_{\boldsymbol{R}'o's} \\ + \frac{1}{2}\sum_{ss'} \sum_{\boldsymbol{R}_1\ldots\boldsymbol{R}_4} \sum_{o_1\ldots o_4} U_{\boldsymbol{R}_1o_1,\ldots,\boldsymbol{R}_4o_4}\, \hat{c}^\dagger_{\boldsymbol{R}_1o_1s}\, \hat{c}^\dagger_{\boldsymbol{R}_2o_2s'}\, \hat{c}_{\boldsymbol{R}_3o_3s'}\, \hat{c}_{\boldsymbol{R}_4o_4s}\end{aligned} \tag{5.2}$$

with

$$t_{\boldsymbol{R}o,\boldsymbol{R}'o'} = -\langle \boldsymbol{R}o| \left(-\frac{\boldsymbol{p}^2}{2m} + V(\hat{\boldsymbol{r}})\right) |\boldsymbol{R}'o'\rangle \qquad \text{and} \tag{5.3}$$

$$U_{\boldsymbol{R}_1o_1,\ldots,\boldsymbol{R}_4o_4} = \langle \boldsymbol{R}_1o_1|\, \langle \boldsymbol{R}_2o_2|\, \frac{e^2}{|\boldsymbol{r}-\boldsymbol{r}'|}\, |\boldsymbol{R}_3o_3\rangle\, |\boldsymbol{R}_3o_3\rangle\,. \tag{5.4}$$

Basically the terms $t_{\boldsymbol{R}o,\boldsymbol{R}'o'}$ represent the overlap of orbital o at atom $\boldsymbol{R}$ with the orbital o' at atom $\boldsymbol{R}'$ with respect to the kinetic energy and the atomic potential operators. Figuratively, one speaks of the kinetic energy of an electron which moves from the latter orbital to the former one, and the parameter t is called "hopping" parameter. The terms $U_{\boldsymbol{R}_1o_1,\ldots,\boldsymbol{R}_4o_4}$ stand for the energy of the interaction of two electrons scattered from orbitals o_3 at $\boldsymbol{R}_3$ and o_4 at $\boldsymbol{R}_4$ to orbitals o_2 at $\boldsymbol{R}_2$ and o_1 at $\boldsymbol{R}_1$.

As the Wannier basis states are linear combinations of Bloch states they are, in general, not eigenstates of the non-interacting Hamiltonian. However, in the case of flat bands the dispersion $\varepsilon_{\boldsymbol{k}n}$

becomes $\boldsymbol{k}$-independent, such that there is a one-to-one correspondence between Bloch bands and Wannier basis orbitals. This corresponds to electrons tightly bound to atomic nuclei which are thus localised. This is the case for partially filled d- or f-orbitals in transition metals and rare earths.

The Hamiltonian in equation (5.1) still is the full solid-state Hamiltonian in a different basis and therefore still not computable. Based on the physical significance of the different terms of the Wannier Hamiltonian we can derive reasonable approximations to describe the physics of the system under investigation.

As the ground state phases are mainly driven by low energy excitations, we focus on the one-particle energy bands $\varepsilon_{\boldsymbol{k}n}$ close to the Fermi-energy in the low-temperature limit $T \ll T_F$. We further simplify our model by the assumption that only one band crosses the Fermi-energy and all the other bands are strictly separated from this band. Hence we drop the orbital dependence of the hopping parameter and write $t_{\boldsymbol{R},\boldsymbol{R}'}$ and $U_{\boldsymbol{R}_1,\ldots,\boldsymbol{R}_4}$.

In addition, the materials of interest in this thesis have half-filled d- or f-orbitals which are localised, such that the Wannier basis functions $\phi(\boldsymbol{r}-\boldsymbol{R})$ have their maximum at $\boldsymbol{r}=\boldsymbol{R}$ and decay rapidly with increasing distance $|\boldsymbol{r}-\boldsymbol{R}|$. In the crudest approximation, namely the atomic limit, these functions do not overlap, such that the one-particle energy $\varepsilon_{\boldsymbol{k}n}$ becomes $\boldsymbol{k}$-independent and $t_{\boldsymbol{R},\boldsymbol{R}'} = \varepsilon\delta_{\boldsymbol{R},\boldsymbol{R}'}$. Therefore, in this approximation no inter-atomic transport is possible, such that additional terms have to be taken into account to describe the physics of interest. Hence we allow for nearest and for next-nearest neighbour hoppings and set all other hopping parameters to zero. We simplify our notation by writing $t_{ij} = t_{\boldsymbol{R}_i,\boldsymbol{R}_j}$ and $< i,j >$ for nearest neighbour sites and $\ll i,j \gg$ for second nearest neighbour sites.

For an approximation of the interaction term we assume that the Wannier orbitals are sufficiently strong localised, such that they do not overlap. As the Coulomb interaction decreases by $1/\!/r$ and as the overlap of Wannier orbitals is rapidly decreasing due to their localisation, we only consider the on-site interactions and the nearest neighbour interactions. This is also motivated by the assumption that the strongest interactions dominate the physics at low temperatures. For the local interactions, all Wannier orbitals are located at the same site $\boldsymbol{R}$ which can, due to the Pauli principle, only be occupied by one spin-up and by one spin-down electron. The corresponding term thus becomes

$$\frac{1}{2}\sum_{\boldsymbol{R}_i}\sum_{s,s'} U_{\boldsymbol{R}_i\boldsymbol{R}_i,\boldsymbol{R}_i\boldsymbol{R}_i}\,\hat{c}^\dagger_{\boldsymbol{R}_i s}\hat{c}^\dagger_{\boldsymbol{R}_i s'}\hat{c}_{\boldsymbol{R}_i s'}\hat{c}_{\boldsymbol{R}_i s} = \sum_{\boldsymbol{R}_i} U\,\hat{c}^\dagger_{\boldsymbol{R}_i\uparrow}\hat{c}_{\boldsymbol{R}_i\uparrow}\hat{c}^\dagger_{\boldsymbol{R}_i\downarrow}\hat{c}_{\boldsymbol{R}_i\uparrow} = \sum_{\boldsymbol{R}_i} U\,\hat{n}_{i\uparrow}\hat{n}_{i\downarrow} \tag{5.5}$$

with $U := U_{\boldsymbol{R}_i\boldsymbol{R}_i,\boldsymbol{R}_i\boldsymbol{R}_i}$. The nearest neighbour contributions can be of two different kinds. First, the classical electrostatic Coulomb interaction between two electrons located at neighbouring sites $\boldsymbol{R}_i$ and $\boldsymbol{R}_j$ is described by the direct interaction $U_{\boldsymbol{R}_i\boldsymbol{R}_j,\boldsymbol{R}_j\boldsymbol{R}_i}$. This term can be rewritten as

$$\sum_{<\boldsymbol{R}_i,\boldsymbol{R}_j>}\sum_{s,s'} U_{\boldsymbol{R}_i\boldsymbol{R}_j,\boldsymbol{R}_j\boldsymbol{R}_i}\,\hat{c}^\dagger_{\boldsymbol{R}_i s}\,\hat{c}^\dagger_{\boldsymbol{R}_j s'}\,\hat{c}_{\boldsymbol{R}_j s'}\,\hat{c}_{\boldsymbol{R}_i s} = \sum_{<\boldsymbol{R}_i,\boldsymbol{R}_j>}\sum_{s,s'} V_{ij}\,\hat{n}_{is}\,\hat{n}_{js'}. \tag{5.6}$$

Second, the other term originating from the nearest neighbour contribution is the exchange contribution, in which the creation and the annihilation operators of different spins are at the same site $\boldsymbol{R}_i$ or $\boldsymbol{R}_j$. Using spin and charge operators, this term can equivalently be written as

$$\sum_{<\boldsymbol{R}_i,\boldsymbol{R}_j>}\sum_{s,s'} U_{\boldsymbol{R}_i\boldsymbol{R}_j,\boldsymbol{R}_i\boldsymbol{R}_j}\,\hat{c}^\dagger_{\boldsymbol{R}_i s}\,\hat{c}^\dagger_{\boldsymbol{R}_j s'}\,\hat{c}_{\boldsymbol{R}_i s'}\,\hat{c}_{\boldsymbol{R}_j s} = -2\sum_{<\boldsymbol{R}_i,\boldsymbol{R}_j>} J_{ij}\left(\hat{\boldsymbol{S}}_i\hat{\boldsymbol{S}}_j + \frac{1}{4}\hat{n}_i\hat{n}_j\right) \tag{5.7}$$

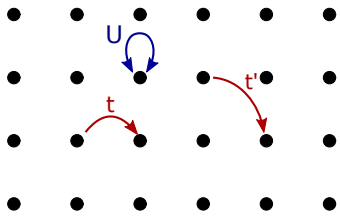

Figure 5.1.: Schematic representation of the effects included in the Hubbard model with onsite-repulsion U (blue), nearest neighbour hopping t and second nearest neighbour hopping t' (red) on an isotropic two-dimensional lattice.

with $J_{ij} := U_{\boldsymbol{R}_i\boldsymbol{R}_j,\boldsymbol{R}_i\boldsymbol{R}_j}$. Considering only this term, a coupling of $J_{ij} > 0$ decreases the energy for a parallel alignment of spins, thus inducing a tendency to a ferromagnetic phase, while a coupling of $J_{ij} < 0$ reduces the energy for an antiparallel alignment of spins, thus inducing a tendency to antiferromagnetism.

Hubbard [32] estimated the strength of the different contributions based on the atomic $3d$-orbital wave-functions as Wannier functions and arrived at $U \approx 20\,\mathrm{eV}$, $V_{ij} \approx 6\,\mathrm{eV}$ and $J_{ij} \approx 0.03\,\mathrm{eV}$ for transition metals. These rather rough estimates, and the assumption of very well localised Wannier functions with little overlap offer the possibility of approximating the interaction by the local interaction term alone.

Combining all the approximations from above, we arrive at the Hubbard model Hamiltonian

$$H = -\sum_{<i,j>,s} t_{i,j}\,\hat{c}^\dagger_{i,s}\,\hat{c}_{i,s} - \sum_{\ll i,j\gg,s} t_{i,j}\,\hat{c}^\dagger_{i,s}\,\hat{c}_{i,s} + U\sum_i \hat{n}_{i\uparrow}\,\hat{n}_{i\downarrow}. \tag{5.8}$$

The different effects are illustrated in figure 5.1: the kinetic energy corresponds to a hopping of electrons between the sites, while the interaction represents the costs of two electrons being located at the same site. Comparing this Hubbard Hamiltonian with the original one, reveals that it has been significantly simplified. Therefore, let us shortly recapitulate the most important approximations.

First, due to the restriction to one band close to the Fermi-energy all the interactions with electronic states in the other bands are neglected. Although these terms are small in comparison to the intra-band interaction, they are not negligible. Hence the Hubbard-interaction U has to be chosen in such a way that it contains the screening effects of the other bands. As these screening effects depend on the form and on the energetic location of the other bands, a general construction of U is not possible. For real materials this can quite accurately be done by constrained RPA calculations. In the scope of this thesis it is, therefore, treated as a phenomenological parameter.

Second, the restriction to the on-site interaction is justified by a comparison of the parameter strengths. While screening effects reduce the values estimated by Hubbard, the exchange contribution J_{ij} is still two to three orders of magnitude smaller than the on-site interaction, and thus its negligence is justified. However, Hubbard [32] estimates that screening reduces the direct interaction V_{ij} only by a factor of 2 and thus remains $10 - 20\,\%$ of the on-site one. While Hubbard estimates these values for $3d$ electrons in transition metals in general, we observe a similar range of values obtained from DFT calculations for electrons in the O p-orbitals and La $3d$-orbitals in La_2CuO_4 which form the conduction band [134] (see table 5.1). Therefore, this direct interaction also has to be considered for

	Schluter [134]	McMahan [135]	Hirayama [136]
U_d	$10 - 12\,\mathrm{eV}$	9.4eV	9.6 eV
U_p	$6 - 8\,\mathrm{eV}$	3.6eV	6.1 eV
V_{pd}	$< 4\,\mathrm{eV}$	0.8eV	2.7 eV

Table 5.1.: Parameters of the extended Hubbard Hamiltonian for La_2CuO_4 taken from ref. [134] and ref. [135]. Here, p refers to O p-orbital electrons and d refers to La $3d$-electrons, so that U_d and U_p are the on-site interactions at the La and the O sites, respectively, and V_{pd} is the interaction between these sites.

an accurate description of those materials, leading to the extended Hubbard model, which is out of scope of this thesis.

Finally, we restrict ourselves to nearest and to second nearest neighbour hoppings, which is justified in the case of strong localised orbitals. If the orbitals become less localised, this limitation can be lifted by including longer ranged hopping terms. In the scope of this thesis we also treat the neighbour hoppings as phenomenological parameters.

Despite its simplicity there exists neither an analytical nor a numerical solution for the Hubbard model. While the hopping terms are diagonal in momentum space, the interaction is diagonal in lattice space. Thus, there does not exist a common basis which prevents an analytical solution. Physically spoken, the kinetic term tends to delocalise the electrons, while the interaction tends to localise them. For a numerical solution, one has to represent the Hamiltonian in one of the bases and one is restricted to a finite lattice of N sites. But as every site has four possible states, the total number of states scales as 4^N. Thus, an exact numerical solution is restricted to small systems in which finite size effects become important and might spoil the physics.

Despite these limitations, the Hubbard model has frequently been used in the solid state theory, as it contains the two most important energy scales, which are the kinetic energy given by the hopping t and the potential energy of the repulsion of two electrons at the same site given by U. In the ground state, the total energy has to be minimised, which leads to a competition between these effects. Considering the half-filled case on a square lattice with nearest neighbour hopping only, the kinetic energy is minimised when every particle can hop to all neighbouring sites. This is the case when every first site is doubly occupied while every second site is empty, or if every first site is occupied by a spin-up and every second one is occupied by a spin-down electron. However, a double occupation of a site goes along with an energetic cost of the Hubbard interaction $U > 0$, making the first state less favourable, while every hopping in the second case leads to a double occupancy of the corresponding site and hence goes along with an energy cost of U. Hence, the ground state phase of the Hubbard model depends on the relation U/t. Thus, by tuning these parameters and those of the extensions to second nearest neighbour hoppings and to nearest neighbour interactions the Hubbard model exhibits a big variety of features like metallic or isolating behaviour, (unconventional) superconductivity, magnetic phases, Mott-insulator transitions and more. Therefore it is frequently used as basis model for correlated electron systems.

However, despite more than 50 years of research on this model, it has only been solved for some special cases like the single site ($t = 0$)-limit, the non-interacting ($U = 0$)-limit [137] or in one-dimension [138] or in infinity-dimensions [139]. In the following sections of this chapter we will first present the computational details of our calculations and then discuss the two-dimensional case, the three-dimensional case and the transition from 2D to 3D.

5.1. Computational Details and Analysis

The calculations of the Hubbard model presented in the upcoming sections were performed based on the FRG code presented in section 4. As the Hubbard model is SU(2)-symmetric, the corresponding SU(2)-symmetric flow equations were employed to obtain the two-particle interactions. The reference, against which the TUFRG is tested, are calculations based on the SU(2)-symmetric full lattice space FRG provided by equation (3.280) in section 5.2. Based on this successful comparison, the two- and three-dimensional Hubbard models are investigated based on the SU(2)-symmetric TUFRG flow equations presented in corollary 3.31 with the lattice-space projections of corollary 3.32.

As we aim at treating large numbers of momentum points, we take the static limit such that the interactions become frequency-independent[1]. As the ground state phase is independent of static self-energies which mainly cause a shift of the chemical potential, we neglect self-energy contributions in our calculations. Employing the Ω-cut-off we can, therefore, analytically solve the Matsubara frequency sum according to section 4.3.2. With these approximations we have an effective one-band model which is only treated in momentum and in form-factor space. To obtain even larger systems we additionally exploit the lattice symmetry to reduce the computational costs as presented in section 4.4. The lattice sizes for the interactions as well as for the propagators which were used for the different calculations are always presented in the corresponding sections.

The initial parameter Λ_0 at which the flow starts should be significantly larger than the band width and is presented separately for each investigation, as it is model-dependent. The initialisation of the vertex as $V = U$ is trivial for the full lattice FRG, while there is an ambiguity in the TUFRG case. In principle, the initial interaction U can equivalently be cast to the different channels or be treated as a flow-independent component, as its projection to any channel is simply U for all on-site form-factor components. For our calculations we take it as this flow-independent component.

As we are interested in the transition to ordered states, the natural choice would be to perform the (TU)FRG flow at finite temperatures. If the metallic state is the ground state, no phase transition appears and $\Lambda = 0$ can be reached. If a phase transition takes place at the investigated temperature, a divergence appears at a finite critical cut-off Λ_c. Therefore, several calculations of the same system parameters for different temperatures are required to obtain a transition temperature. As our calculations typically require 20-30 hours on 14 compute nodes for one parameter set, we want to avoid such a large number of calculations. Therefore the (TU)FRG flow is performed at $T = 0$ so that we will obtain a divergence of the flow at a finite critical cut-off scale Λ_c for all sets of model parameters. This Λ_c defines a window of modes which were not integrated to obtain the interaction at this critical scale. In comparison to this, the band gap results from an integration of all modes except those within the band gap in the BCS theory of superconductivity or in the spin-density wave mean-field theory in the weak coupling limit at a constant density of states. The band gap itself then corresponds to the critical temperature up to a factor of unity. We therefore assume that the critical scale Λ_c is an upper estimate for the critical temperature.

Starting with the initial configuration the (TU)FRG equations are evaluated for decreasing Λ, and the largest element of the two-particle interaction is obtained in each step. If this largest element exceeds a threshold which also depends on the bandwidth, the flow is stopped, and the corresponding cut-off parameter is taken as critical parameter Λ_c. The type of the phase the system turns into can be obtained by the divergence of the corresponding susceptibility (see discussion in section 3.3). To

[1] We also take the $T = 0$-limit, which will be discussed below.

obtain the full description of the system the flow should be continued to $\Lambda = 0$, which requires an accurate treatment of symmetry breaking. This can be done in a purely fermionic way [63] or by the introduction of bosonic fields due to a decoupling by a Hubbard-Stratonovich transformation [140]. However, the current (TU)FRG approach is not suitable for this. Hence the phase has to be deduced from the susceptibility which is obtained either by integrating its flow equations [103, 61] or by a post-processing calculation. It has recently been shown that the post processing susceptibility based on the flow of the two-fermion interaction with the multi-loop extension converges to the susceptibility obtained by its flow equation [66]. The post-processing susceptibility which is based on the two-fermion interaction in the corresponding channel at the critical scale can be compared with the flow-based susceptibility at this scale based on references [103, 61] which display both of them. For the two-dimensional Hubbard model these representations reveal that the two-fermion vertex itself already exhibits the features of all possible arising phases. That is (see sec. 5.2.1 for more details), for example, a strong divergence for a momentum transfer of (π, π) and one of half the intensity for a momentum transfer $(\pi, -\pi)$ if the anti-ferromagnetic susceptibility diverges, or a strong ordering feature with total momentum $\mathbf{0}$ which changes in sign upon a rotation by $\pi/2$, if the d-wave superconducting susceptibility diverges. In this way, the final interaction can be compared to an effective Hamiltonian, which exhibits the corresponding features [104]. This becomes more accurate, when a mean-field decoupling of the two-fermion interaction at the final scale is performed to obtain the phase properties, as described in references [141, 142].

Hence, we did not calculate any susceptibilities, but focused on the effective interaction at the critical scale. Thus, the emerging phase is obtained by a comparison of the final two-fermion interaction of the full lattice space FRG calculation to the effective mean-field Hamiltonians, as we consider a well-known parameter range as a reference. In the TUFRG case the diverging component of the vertex projected to one channel, which leads to the termination of the flow, is directly associated to the emerging phase. Hence we directly obtain the diverging channel (pairing, charge or magnetic), the ordering vector ($\boldsymbol{s}$, $\boldsymbol{u}$ or $\boldsymbol{t}$) and the form-factor symmetry based on the form-factors associated to the corresponding indices. This approach is reasonable, as a post-processing susceptibility based on these two-fermion interactions corresponds to the product of two dual-propagators projected to this channel with the projected vertex. As these dual propagators in general exhibit their largest values at the same momenta as the interaction and as the product of them with the projected interaction is largest for equal form-factors, the post-processing susceptibility will just show the same type of phase as the projected vertex. Although the approach performed in this thesis is less accurate than the FRG+MF one it is sufficient to indicate which ordering tendencies can be expected in different parameter ranges.

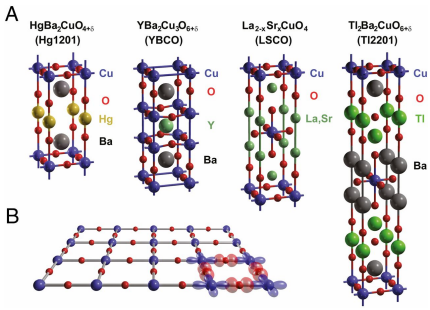

Figure 5.2.: A: Unit cells of the lattice of different copper-oxide superconductors. The characteristic CuO square layers in which the superconductivity takes place can be identified at the top and at the bottom of the unit cells except for YBCO, where it is above and below the Yttrium atom.
B: The relevant CuO-lattice with the Cu $d_{x^2-y^2}$ and O p_σ orbitals forming the valence bonds is displayed. Figure taken from [143].

5.2. The 2D-Hubbard Model

Copper-based high-temperature superconductors consist of active layers of CuO_2, where four copper atoms form a square structure, while they are connected to each other by oxygen atoms (see fig. 5.2). A few of these layers, glued together by Ca- or Y- atoms, form an active block, which is wrapped by charge reservoir blocks. Similarly, iron-based high-temperature superconductors have an active layer of iron-atoms, which are connected by P-, As-, Se- or Te-atoms, which lie above or below the iron-plane and form a tetrahedrical substructure. The holes left by these substructures can be filled with alkali-metal atoms or with a combination of them with an oxygen layer.

Planar superconductivity is observed in these compounds which takes place within the active layers of Cu- or Fe-atoms on a square lattice. The electron hopping between two active layers is small and, therefore, often neglected, so that it suffices to consider the simpler two-dimensional lattice [36]. In this section we will, therefore, also consider the two-dimensional Hubbard model on a square lattice, while the influence of a finite coupling in the perpendicular direction is investigated in section 5.4. In iron-based superconductors typically three bands originating from Fe-d-orbitals cross the Fermi-surface [144], so that a corresponding three-band model is required, as supposed by Eschrig [145]. Focusing on patches around the well localized electron- and hole-pockets which are formed by the three bands, these materials were already treated in the scope of N-patch FRG by Platt [75]. In cuprates, typically only the $d_{x^2-y^2}$ band crosses the Fermi-energy [146], so that the 2D electronic structure can well be reproduced by a one-band Hubbard model [147, 148]. Therefore, we consider the Hubbard Hamiltonian on a square lattice, including nearest neighbour and second nearest neighbour hopping terms as illustrated in figure 5.1. As we assume the lattice to be isotropic, the nearest neighbour hopping is equivalent in x- and in y-direction, and we define this hopping $t := t_x = t_y$ as our energy scale. The second nearest neighbour has the same hopping-distance in every direction, and we denote it as $t' = t_{xy}$. Thus, the Hubbard Hamiltonian of the two dimensional square lattice is

$$H = -t \sum_{\langle i,j\rangle,s} \hat{c}^\dagger_{i,s}\hat{c}_{i,s} - t' \sum_{\langle\langle i,j\rangle\rangle,s} \hat{c}^\dagger_{i,s}\,\hat{c}_{i,s} + U \sum_i \hat{n}_{i\uparrow}\,\hat{n}_{i\downarrow}. \tag{5.9}$$

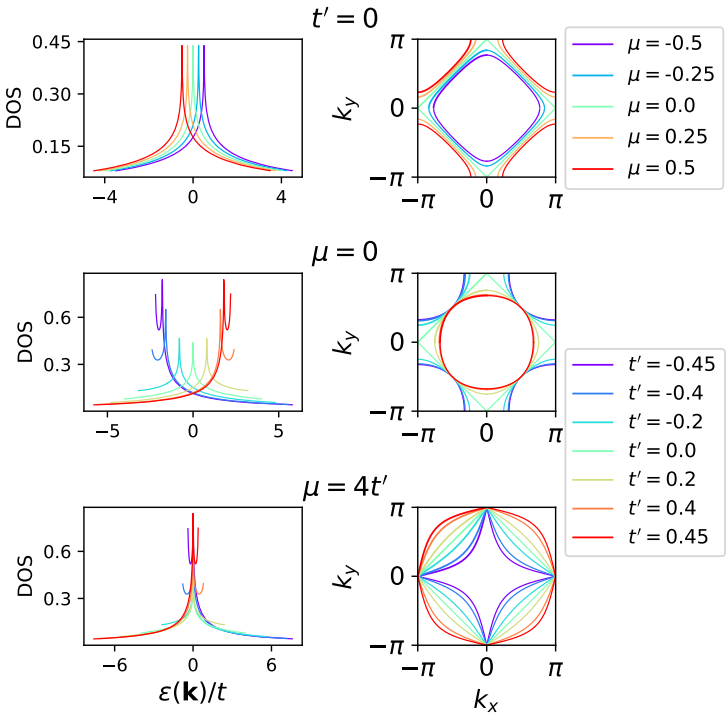

Figure 5.3.: Density of states (DOS) (left) and Fermi-surface (right) of the 2D-Hubbard model. At the top for various values of μ at $t' = 0\,t$. At the centre and bottom for various values of t' at $\mu = 0$ and $\mu = \varepsilon_{\mathrm{vH}}$, respectively.

All in all there are, thus, four parameters t, t', U and μ which can be tuned. However, a simultaneous rescaling of all of them leaves the system invariant, which justifies our *ad hoc* choice of t as energy scale. The non-interacting part of this Hamiltonian can be computed analytically, resulting in the single-particle dispersion

$$\varepsilon(\boldsymbol{k}) = -2t\left(\cos(k_x) + \cos(k_y)\right) - 4t'\cos(k_x)\cos(k_y) - \mu, \tag{5.10}$$

in which we included the chemical potential μ. This dispersion relation exhibits saddle points at $(0, \pm\pi)$ and $(\pm\pi, 0)$ (which are pairwise equivalent due to the 2π-periodicity) leading to logarithmic van-Hove singularities in the non-interacting density of states at the energy $\varepsilon_{\mathrm{vH}} = 4t' - \mu$ as shown in figure 5.3. This figure 5.3 a;so displays Fermi-surfaces for different parameter sets of μ at $t' = 0\,t$. In the half-filled case (i.e. $\mu = 0t$), the Fermi-surface is a perfect square, in which the connection of the points $(\pi, 0)$, $(0, \pi)$, $(-\pi, 0)$ and $(0, -\pi)$ leads to a perfect nesting. This means that the same vectors $\boldsymbol{k} = (\pi, \pi)$ and $\boldsymbol{k} = (\pi, -\pi)$ correspond to a mapping between large segments of the Fermi-surface. Moreover, the four segments of the Fermi-surface touch each other at the van-Hove points, which leads to a large number of free states around these points. When the electron density is reduced, the Fermi-surface moves away from the van-Hove points towards the Γ-point and becomes a smooth curve. The straight lines, which lead to the perfect nesting, slowly fade away, and hardly any remaining contribution can be identified for a filling below one quarter, where the Fermi-surface is almost a circle around the Γ-point. The Fermi-surface behaves similarly, when the electron density is increased above half-filling with the difference that it moves towards the (π, π)-point and forms a circle around this.

If t' is varied and the chemical potential is fixed by $\mu = 4t'$, so that the van-Hove points are always an element of the Fermi-surface, the Fermi-surface bends towards the Γ-point for $t' < 0$ and to the (π, π)-point for $t' > 0$, while it maintains its linear feature close to the van-Hove points (see fig. 5.3). When the two-particle interaction is perturbatively calculated for the van-Hove filling, the particle-particle channel diverges as $\log^2$ at $\boldsymbol{s} = \boldsymbol{0}$ and as log at $\boldsymbol{s} = (\pi, \pi)$, while the particle-hole channel as log diverges at $\boldsymbol{t} = 0$ and as log at $\boldsymbol{t} = (\pi, \pi)$ either for $t' \neq 0$ or as $\log^2$ for $t' = 0$ [61]. As these multiple divergences indicate a competition between different orders, we investigate the case of the van-Hove filling in more detail. As a side effect the only free remaining parameter is the second nearest neighbour hopping t'.

5.2.1. Phase Diagram of the 2D-Hubbard Model

In our calculations we chose $U = 3\,t$, as the calculation of the 2D-Hubbard model aims at comparing our results with previous ones (see [2, 67]), and we vary t' in the range of $[-0.45\,t, 0\,t]$ while maintaining the van-Hove condition for the chemical potential μ. This means that, in the extreme cases, the system is almost empty for $t' = -0.45\,t$ or half filled for $t' = 0\,t$. The calculations were performed for various values of t' within this range for static vertices at $T = 0$ with the full vertex (cf. eq. (3.280)) while exploiting the $\mathrm{C}_{4\mathrm{v}}$-symmetry of the lattice. The initial scale was chosen as $\Lambda_0 = 60\,t$ and the flow continued until the largest vertex entry exceeded a value of $V_{\max}^{\Lambda_c} = 70\,t$, which resulted in the critical scale Λ_c.

The $\Lambda_c - t'$-phase diagram of the two-dimensional Hubbard model which is calculated on a rather coarse 12×12 lattice for the vertex and a 180×180 lattice for the propagator pair (this kind of setup is exemplarily shown in figure 4.2). An analysis of the full momentum vertex structure at this critical scale in the way as described in section 5.1 reveals three different phases: For small values of $-t'$ (i.e.

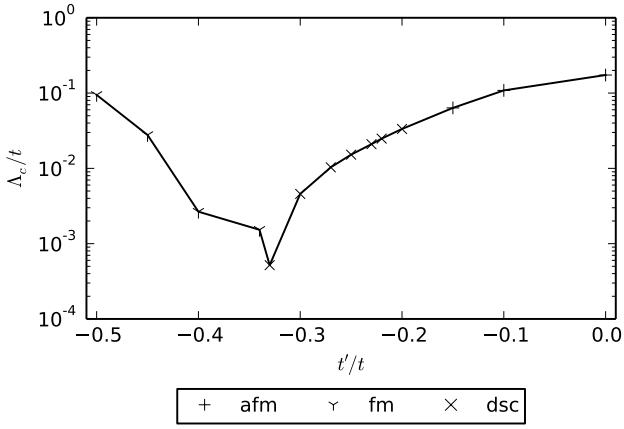

Figure 5.4.: Phase diagram of the 2D-Hubbard model based on the vertex with a full momentum parametrisation.

$-t' < 0.2\,t$) the vertex divergence occurs for an ordering vector of $\boldsymbol{Q} = \boldsymbol{k}_2 - \boldsymbol{k}_3 = (\pi, \pi)$ and at the same time with about half the value for $\boldsymbol{Q} = \boldsymbol{k}_1 - \boldsymbol{k}_3 = (\pi, \pi)$, indicating a divergence in the C- and the D-channel, respectively. In a drastic simplification this feature can be regarded as a broadening of a vertex consisting of delta-functions as $V(\boldsymbol{k}_1, \boldsymbol{k}_2; \boldsymbol{k}_3) = {}^{J}/_{4}(2\delta_{\boldsymbol{k}_2 - \boldsymbol{k}_3, Q} + \delta_{\boldsymbol{k}_1 - \boldsymbol{k}_3, Q})$, which is matched by an effective antiferromagnetic spin-interaction of the form $J \sum_{\langle i,j \rangle} e^{i\boldsymbol{Q}(\boldsymbol{R}_i - \boldsymbol{R}_j)} \boldsymbol{S}_i \boldsymbol{S}_j$ with uniform Heisenberg-interaction J [104]. Thus, we obtain a phase with a long range antiferromagnetic ordering by a vector $\boldsymbol{Q} = (\pi, \pi)$ for small values of $-t'$. This ordering vector is exactly the perfect-nesting vector described above, which connects a large number of states at the Fermi-surface with each other. As the Fermi-surface bends away from the perfect nesting when $-t'$ is increased, the critical scale decreases. However, the antiferromagnetic phase remains intact, although a thorough analysis shows that the ordering vector moves slightly away from the perfect-nesting vector $\boldsymbol{Q}$. This is due to the effect of the Fermi-surface bending, which leads to a set of vectors with a similar length and with a similar direction which map the Fermi-surface to itself.

In an intermediate range of values for $-t'$, i.e. $0.2\,t < -t' < 0.34\,t$, the dominating phase changes. The vertex at the critical scale in this phase has a divergence at $\boldsymbol{k}_1 + \boldsymbol{k}_2 = (0, 0)$, that is in the pairing channel with zero-momentum transfer, which indicates a superconducting ground state. When the incoming wave-vectors and the outgoing ones are close to the same saddle-point $(\pm\pi, 0)$ of the Fermi-surface, the interaction is attractive, while it is repulsive, when the momentum pairs are at different saddle points. As this change of sign is represented by a $d_{x^2-y^2}$-symmetry, this correspondingly indicates a $d_{x^2-y^2}$-wave pairing. This can be described by an effective Hamiltonian of the form $V_{\mathrm{dSC}} = \sum_{\boldsymbol{k}\boldsymbol{k}'} d(\boldsymbol{k}) d(\boldsymbol{k}') \hat{c}^{\dagger}_{\boldsymbol{k}'\uparrow} \hat{c}^{\dagger}_{-\boldsymbol{k}'\downarrow} \hat{c}_{-\boldsymbol{k}\downarrow} \hat{c}_{\boldsymbol{k}\uparrow}$ with $d(\boldsymbol{k}) = d_0(\cos k_x - \cos k_y)$. When $-t'$ is increased within this region, the critical scale indicating the onset of this d-wave superconducting ground state decreases by at least one order of magnitude to $\Lambda_x \approx 10^{-3}\,t$.

Beyond the range of this region another phase appears at $-t' \approx 0.34\,t$. The vertex at this point turns into a state which diverges at $\boldsymbol{k}_3 - \boldsymbol{k}_1 = (0, 0)$. This corresponds to the vertex in the C-channel parametrisation, and thus indicates ferromagnetic order. The critical scale exhibits a drastic decrease between the FM and the dSC phase, which is argued to originate from a competition between these two

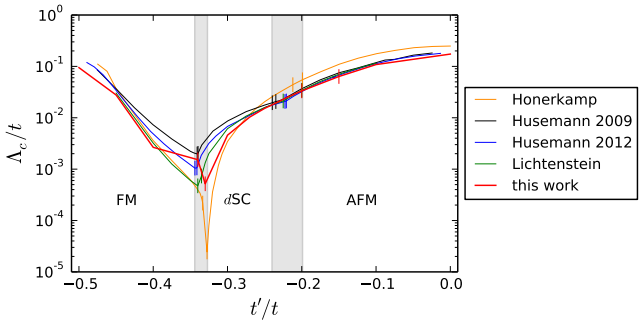

Figure 5.5.: Phase diagram of the 2D-Hubbard model calculated in this work in comparison to results obtained by others, i.e. Honerkamp [150], Husemann ('09) [67], Husemann ('12) [114] and Lichtenstein [2]. The critical temperature obtained by Honerkamp is directly compared to the critical cut-off scales of the other references, revealing the divergence appearing at similar scales, such that a comparison of both properties is reasonable. Further, the critical scales obtained in our calculation are in good agreement with those obtained in the presented works.

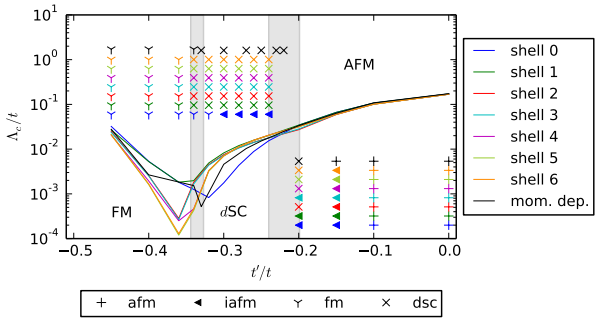

Figure 5.6.: Convergence of the TUFRG approach for the 2D-Hubbard model with an increasing number of shells towards the full momentum space result. According to section 4.2 0, 1, 2, 3, 4, 5, 6 shells correspond to 1, 5, 9, 13, 21, 25, 29 form-factors, respectively.

orders which exclude each other. The van-Hove singularities on the one hand lead to a $\log^2$ divergence of the Cooper pair scattering, while, on the other hand, the logarithmic divergence of the density of states supports ferromagnetic tendencies. As these processes have opposite signs, they suppress each other [104]. While this point is under the debate of being a quantum-critical point [124, 149], our results, in agreement with the observation by others [67, 2], do not support this.

We compare the data obtained by our FRG approach in figure 5.5 with those obtained by other FRG calculations based on the exchange parametrisation [67] or on the N-patch scheme [150], which used the static approximation, too. One can see that the three different approaches reveal good agreements among each other. However, the behaviour of our approach differs in the indicated transition value of t' from the other ones due to a reduced number of investigated t' values. We further attribute differences and especially the discrepancy in the FM region to the coarse momentum resolution.

5.2.2. Convergence of the TUFRG Approach

The TUFRG approach should result in the same phase diagram as the conventional full FRG case, when the basis sets have the same size, that is the number of form-factors are equal to the number of points which discretise the Brillouin zone. As calculations with such a large number of form-factors are not feasible due to the $\mathcal{O}(n_{\mathrm{FF}}^3)$-scaling, we investigated the convergence by increasing the number of form-factor shells taken into consideration, by starting with the on-site one going up to the sixth form-factor shell, which are 29 form-factors according to the C_{4v}-symmetry of the lattice. Hence, the form-factors correspond to those displayed in table 4.2 and to those created for longer ranged bond-vectors in the same way. These calculations were performed on a coarse lattice of 45×45 points for the interactions and a on refined lattice of 1125×1125 points for the dual propagators, while the initial scale and the critical vertex value were chosen as above. In figure 5.6 one can see that the zeroth shell TUFRG is not capable of reproducing the results of the full vertex calculation in the d-wave SC-phase. This is due to the missing d-wave form-factors, which only come into place with the first shell of form-factors. When these first shell form-factors are included, the TUFRG already reproduces the full vertex result of the previous section very well. If even more form-factor shells are taken into consideration, there are hardly any changes of the critical scale in the AFM-phase. In the dSC and FM part of the diagram there are always shell-ranges with almost identical critical scales. Therefore, we only observe a change in the critical scale in the SC-phase when moving from the third to the fourth form-factor shell. However, there is already a change from the first to the second shell in the FM-region and another one from the third to the fourth shell, each of them decreasing the critical scale. This most significant change which appears at the transition between the SC- and the FM-region is expected, as an increased number of shells improves the resolution of both competing orders.

5.3. The Isotropic 3D-Hubbard Model

In this section we consider the isotropic three-dimensional Hubbard model described by the Hamiltonian

$$H = -t \sum_{\langle i,j\rangle,\sigma} \hat{c}^{\dagger}_{i,\sigma}\hat{c}_{j,\sigma} + U \sum_{i} \hat{n}_{i,\uparrow}\hat{n}_{i,\downarrow} \tag{5.11}$$

with the corresponding dispersion relation

$$\varepsilon(\boldsymbol{k}) = -2\,t\,\big(\cos(k_x) + \cos(k_y) + \cos(k_z)\big) - \mu\,. \tag{5.12}$$

The corresponding Fermi-surface at half-filling can be regarded as tubes along the three coordinate axes, which are smoothly connected by a bending Fermi-surface (see fig. 5.7). The density of states (fig. 5.7, right) has a plateau for $[-2\,t, 2\,t]$, while it has a tangent-like increase (decrease) for below (above) this part, revealing a discontinuity at the connecting point $\varepsilon = -2\,t$ ($\varepsilon = 2\,t$). Due to the curved character of the Fermi-surface and the absence of singularities in the density of states, there is no hint towards any perfect nesting. For a TUFRG treatment the form-factors correspond to those generated by the algorithm presented in section 4.2 and displayed in table 5.2, as the corresponding simple-cubic lattice belongs to the $\mathrm{O_h}$-point group. We remark that large parts of the TUFRG analysis of the three-dimensional Hubbard model, which are presented in the following part of this section, are published in reference [151].

5.3.1. Half-Filled Hubbard Model

Using the nearest neighbour form-factors for TUFRG calculations with SU(2)-symmetry and a momentum mesh of 16^3 with a refinement of 35^3 for the propagators we calculated the phase diagram of this 3D-Hubbard model at half-filling for the interactions of $0\,t < U \leq 5\,t$. For the whole range of parameters we observed a transition to an AFM ground state with the ordering-vector (π, π, π), as exemplarily shown for $U = 1\,t$ by a line-scan in figure 5.8. The critical scale tends to $\Lambda_c = 0\,t$ for $U \approx 0\,t$ and increases parabola-like with the interaction strength (see figure 5.9). While other methods obtain a Néel temperature for the phase transition, we treat the critical scale as an effective temperature. A comparison of published results in references [150] and [67] shows that the critical scales have values of the same order of magnitude as the critical temperature, which justifies a direct

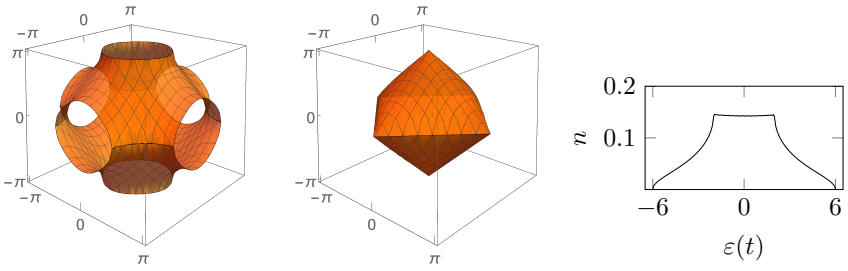

Figure 5.7.: Fermi-surface of the three-dimensional Hubbard model at half-filling (left) and at $\mu = -2\,t$ (centre) and the density of states at half-filling (right).

Name	Shell	Momentum Space Representation
s	0	const
ext. s	1	$\cos(k_x) + \cos(k_y) + \cos(k_z)$
$d_{x^2-y^2}$	1	$\cos(k_x) - \cos(k_y)$
d_{z^2}	1	$-\cos(k_x) - \cos(k_y) + 2\cos(k_z)$
p_x	1	$\sin(k_x)$
p_y	1	$\sin(k_y)$
p_z	1	$\sin(k_z)$
s_3	2	$\cos(k_x)\cos(k_y) + \cos(k_x)\cos(k_z) + \cos(k_y)\cos(k_z)$
d_{xy}	2	$\sin(k_x)\sin(k_y)$
d_{xz}	2	$\sin(k_x)\sin(k_z)$
d_{yz}	2	$\sin(k_y)\sin(k_z)$

Table 5.2.: List of form-factors $f_i(\boldsymbol{k})$ used for the calculations. For the calculations of the Λ_c vs. U-phase diagram at half-filling in section 5.3.1 only the first seven ones were used, which correspond to the on-site and the nearest neighbour form-factors were used, while for the phase diagram of the doped system in section 5.3.2 the full list was used, including some second nearest neighbour form-factors.

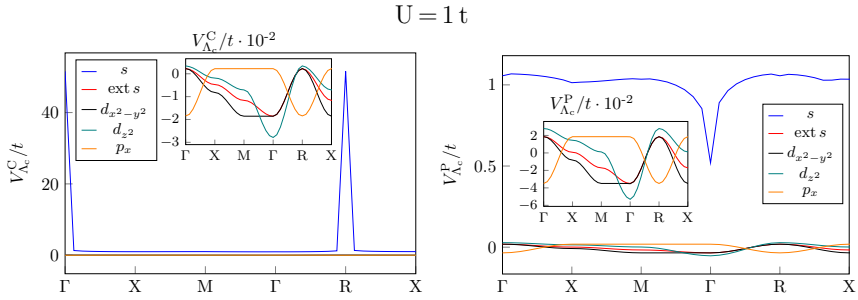

Figure 5.8.: Linescan along the high-symmetry lines connecting $\Gamma = (0,0,0)$, $X = (\pi,0,0)$, $M = (\pi,\pi,0)$ and $R = (\pi,\pi,\pi)$ for the final vertex projected to the form-factor resolved C-channel (left) and the P-channel (right) at half-filling for an initial interaction of $U = 1\,t$.

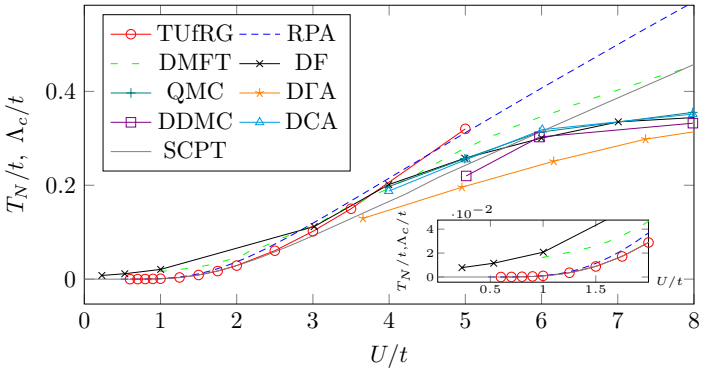

Figure 5.9.: Phase diagram of the half-filled three-dimensional Hubbard model. The critical scale Λ_c obtained in this thesis (TUFRG) indicates a transition to an AFM ground state with (π, π, π) ordering. This result is compared to the Néel temperature indicating a corresponding phase transition obtained by other methods, i.e. spin-fluctuation corrected Random Phase Approximation (RPA) [34, 152, 153], Dynamical Mean Field Theory (DMFT) [154], Dual Fermion (DF) [154], Quantum Monte Carlo (QMC) [155], Dynamical Vertex Approximation (DΓA) [156], Determinantal Diagramatic Monte Carlo (DDMC) [157] and Dynamical Cluster Approximation (DCA) [158].

comparison. However, this is still a hand waving argument so that we rather focus on the shape of the transition curves.

The limit of weak interactions of this model is well described by a perturbative treatment of the relevant charge-pairing channel, which results in a Stoner condition for the corresponding divergence [152]. Freericks *et al.* [153] showed that a division of the critical temperature T_N by 3 can account for local contributions of the pairing channel [34]. The corresponding behaviour is well reproduced by our TUFRG results (see also the inset in fig. 5.9). However, the TUFRG has a slightly larger curvature leading to a transition at smaller critical scales for semi-weak interactions ($1.5\,t \leq U \leq 4\,t$), which is caused by the full inclusion of the other channels. The shape of the TUFRG curve also fits well to the one of the density functional theory (DMFT) [154] and to the one of the dual fermion (DF) approach [154] for semi-weak interactions. In the $U \approx 0\,t$ limit the negligence of non-local correlations in DMFT leads to an overestimation of the critical scale in comparison to RPA. At $U = 4\,t$ the critical scale Λ_c of our method is in good agreement with the critical temperatures obtained by quantum Monte Carlo (QMC) [155] and by the dynamical cluster approximation (DCA) [158]. For stronger interactions $U > 4\,t$ the TUFRG method overshoots all the other results similar to RPA. In order to understand this we first regard the limit of strong interactions, where the three-dimensional Hubbard model becomes the Heisenberg model with $J = {}^{t^2}/_{U}$ and the Néel temperature approaches the Heisenberg limit $T_\mathrm{N} = {}^{3.83\,t}/_{U}$ [159, 160]. While this magnetic ordering temperature decreases, a metal-insulator transition can be observed [155] at a higher transition temperature for $U \approx 12\,t$, leading to an excitation gap for the magnetically disordered phase. Thus, the Néel temperature increases from both sides towards intermediate interactions, where a maximum of it is reached going along with a pseudo-gap like behaviour [161]. These observations reveal that frequencies and especially self-energy effects play a crucial role in the phase diagram of the three-dimensional Hubbard model beginning at intermediate interactions $U \approx 4\,t$. As those effects were neglected by our TUFRG approach and in the RPA, both methods are expected to fail in the corresponding parameter range. Contrary, they

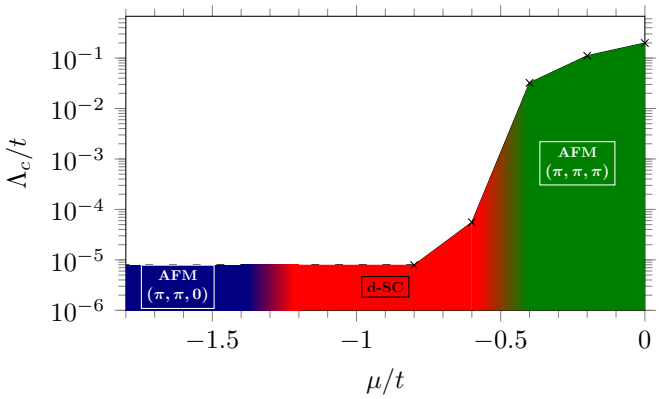

Figure 5.10.: Phase-diagram of the three-dimensional Hubbard model upon doping. For $\mu < 0.8\,t$ the flow did not converge within the precision range provided by our resolution, indicated by a horizontal dashed line. An investigation of the resulting vertex at the final scale and of the increase of the channels during the last steps of the flow lead to the indicated ordering tendencies in this range of parameters.

are explicitly included in the other methods. In addition, RPA and FRG are known to work well only for the weak and for the weak to intermediate interacting regimes, respectively.

Summarising these results yields that the TUFRG without self-energy effects provides good results for a weak interaction strength $U \leq 4\,t$, and the critical scale corresponds well to the Néel temperature of the isotropic Hubbard model.

5.3.2. Doped 3D-Hubbard Model

According to the previous results the TUFRG is capable of a rigorous investigation of the effect of hole-doping on the ground state of the Hubbard model at $U = 4\,t$. Upon corresponding doping the tubes of the Fermi-surface along the axes become smaller until they completely close at $\mu = -2\,t$ (see fig. 5.8). At this value the Fermi-surface has exactly the same square shape in the $x=0$-plane as in the half-filled two-dimensional Hubbard model, thus revealing perfect nesting conditions for vectors of the form $(0, \pm\pi, \pm\pi)$. The same applies for the other planes orthogonal to the axes with corresponding alternative nesting vectors. The density of states for $\mu = -2\,t$ is exactly at the discontinuity which indicates the beginning of the plateau.

For the calculation of the phase diagram we used two shells of form-factors of the O_h point group (see table 5.2) and a momentum mesh of 14^3 points, refined by 35^3 points for the propagators, which was limited by the granted computation time. Based on this we estimated the energy resolution to be of the order of $\mathcal{O}(10^{-5})$ so that the flow is stopped at this scale, if no divergence (i.e. $V^{\mathrm{X}}_{\mathrm{max}} > 30\,t$) has occurred before. Thus we observe a transition for $\mu > -0.7\,t$, while the resolution does not allow to obtain one for smaller values of the chemical potential. Despite the limited resolution we investigated the two-particle interaction in the different channels at the end of the flow for all calculations and, thus, observed three different ground state phases (see fig. 5.10).

At half-filling the system is in an AFM state with the ordering vector (π, π, π), as discussed in the previous section. For a weak hole-doping ($-0.5\,t \lessapprox \mu \lessapprox 0.0\,t$) this AFM order becomes incommensurate, as the main peak moves along the Brillouin-zone surface-planes towards their centre, that is it

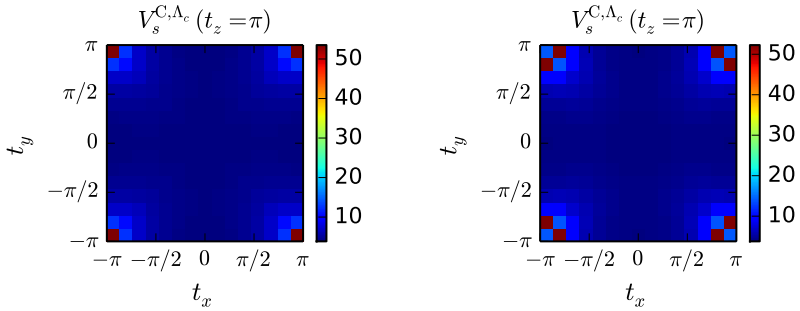

Figure 5.11.: The s-wave form-factor contribution of the full vertex at the final scale Λ_c projected to the C-channel is displayed in the $z=\pi$-plane for $\mu=0.0\,t$ (left) and $\mu=-0.4\,t$ (right). The AFM nesting vector (π,π,π) splits up and becomes incommensurate upon doping, and, thus, moves along the (x,π,π) and along the (π,y,π) lines.

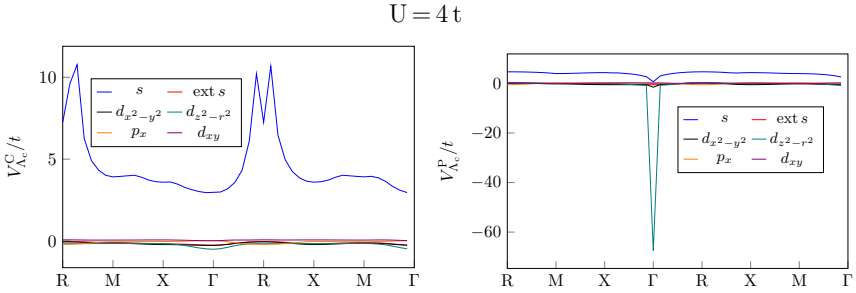

Figure 5.12.: Linescan along the high-symmetry lines connecting $\Gamma=(0,0,0)$, $X=(\pi,0,0)$, $M=(\pi,\pi,0)$ and $R=(\pi,\pi,\pi)$ for the final vertex projected to the form-factor resolved C-channel (left) and to the P-channel (right) with $\mu=-0.6\,t$.

moves along the $x=y=\pi$-axis from $z=\pi$ to $z=0$, as displayed in figure 5.11, and correspondingly for the other axes. At half-filling one can always find a vector of the form (π,π,π) mapping one segment of the Fermi-surface to another one. Upon doping the Fermi-surface changes, so that a mapping is only possible for the corresponding vectors of the form $(\pi,\pi,\pi\pm\epsilon)$, with ϵ being the difference with respect to the perfect nesting. While this phase transition is observed at critical scales ${}^{\Lambda_c}/t\approx 10^{-2}-10^{-1}$, this critical scale drops by three orders of magnitude to 10^{-5}, when the chemical potential is further decreased.

In the doping range of $-0.9\,t\lesssim\mu\lesssim-0.5\,t$ we observe the divergence of the flow in the $d_{z^2-r^2}$-pairing channel for $\boldsymbol{s}=\mathbf{0}$, leading to a corresponding ground state (see fig. 5.12). In the doping range of $-1.3\,t\lesssim\mu\lesssim 0.9\,t$ no divergence was reached, but we observed strong pairing fluctuations in the very same channel. In this region we assume a tendency to this superconducting ground state, as the increase of this contribution is one order of magnitude larger than the AFM one, although the largest coupling at the end of the flow was observed in the AFM channel (see fig. 5.13 and 5.14). As the form-factor of this SC-state belongs to the same irreducible representation as the $d_{x^2-y^2}$ one, a similar behaviour should be observed for the latter one, as their coupling strengths are related by a constant factor. Correspondingly, in figure 5.12 (right) a peak in this form-factor can be observed with a significantly weaker strength. As the relation between these two couplings roughly remains constant throughout the flow, until the divergence is approached, we assume that the numerics can

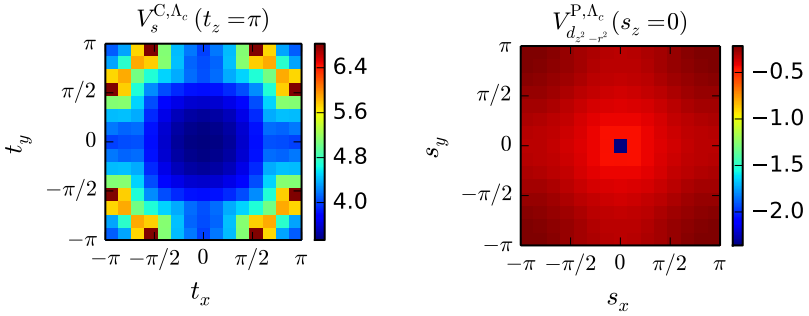

Figure 5.13.: Full vertex at the final scale Λ_c projected to the C-channel (left) and to the P-channel (right) for $\mu = -1.0\,t$. For the C-channel the s-wave contribution is shown in the $z = \pi$-plane, while the $d_{3z^2-r^2}$ form-factor contribution in the $z = 0$-plane is shown for the P-channel.

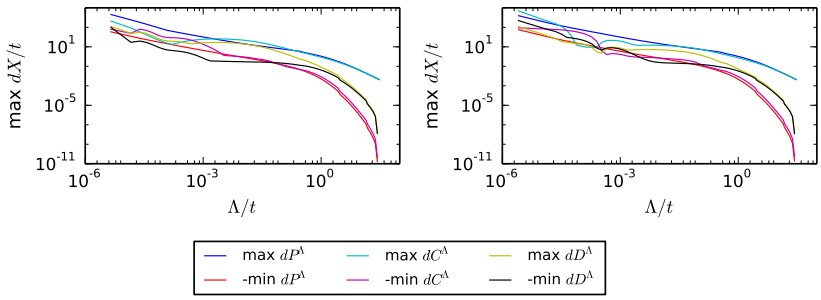

Figure 5.14.: Largest attractive and repulsive increments of the different chantices (i.e. $\max_{i,\boldsymbol{s}}({}^{d}/_{d\Lambda} P^{\Lambda}_{i,i}(\boldsymbol{s}))$, $\max_{i,\boldsymbol{t}}({}^{d}/_{d\Lambda} C^{\Lambda}_{i,i}(\boldsymbol{t}))$, $\max_{i,\boldsymbol{u}}({}^{d}/_{d\Lambda} D^{\Lambda}_{i,i}(\boldsymbol{u}))$ and similarly for $|\min|$) for $\mu = -1.2\,t$ (left) and $\mu = -1.4\,t$ (right), indicating a tendency to SC and AFM order, respectively.

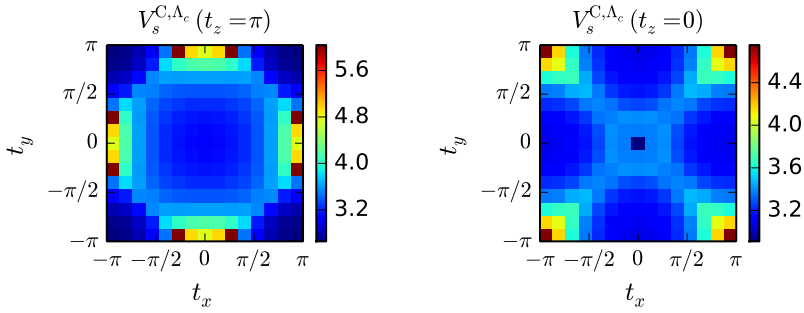

Figure 5.15.: The s-wave form-factor contribution of the full vertex at final scale Λ_c projected to the C-channel for $\mu = -1.8\,t$ in the $z = \pi$-plane (left) and in the $z = 0$-plane (right).

not provide this relation close to a phase transition. If we take a look at the channel corresponding to the AFM instability, the corresponding incommensurate ordering tendency can still be observed (see fig. 5.13, left), while the tendency towards $(\pi, \pi, 0)$ ordering vectors continues. However, the coupling strength of this ordering is smaller than the superconducting one and has a lower increase during the last steps, so that it is suppressed compared to the favoured SC state.

However, for an even stronger hole-doping of $-2\,t < \mu \lesssim -1.3\,t$ this incommensurate AFM-phase dominates over the superconducting one with a set of AFM ordering vectors of the type (π, π, ϵ) in every direction (see fig. 5.15). As the Fermi-surface at $\mu = -2\,t$ corresponds to the perfect nesting two-dimensional one in every plane, the nesting vector becomes $(\pi, \pi, 0)$, exactly as expected. The observed incommensurate AFM order for a filling away from this is, therefore, also in good agreement with this expectation, as the Fermi-surface bends to the outside and thus requires a corresponding adaptation of the ordering vectors.

The results are in good agreement with those of Scalapino and co-workers [162] who investigated the doping of the simple cubic three-dimensional Hubbard model based on the spin-fluctuation theory. Their results revealed a spin-density wave state for the para-magnon propagator for $\mu > 0.8\,t$, which fits to the AFM state we observed. In the region below they observed a $d_{x^2-y^2}$- or a $d_{3z^2-r^2}$-pairing until $\mu \approx -2\,t$, where the system changes to a d_{xy}-pairing. While we observed the same d-wave ordering for $-1.3\,t \lesssim \mu \lesssim -0.8\,t$, we observed a $(\pi, \pi, 0)$-AFM state for $-2\,t < \mu \lesssim -1.3\,t$. On the one hand, our flow did not diverge into a final state in this parameter region. Thus there exists the possibility that we might have missed the appearance of this phase-transition. On the other hand, in the spin-fluctuation theory used by Scalapino *et al.* [162] the interaction is calculated in a diagrammatic RPA-like fashion which only includes singlet and triplet electron-hole diagrams. Moreover, the coupling constants are calculated by Fermi-surface integrals. Our TUFRG approach, however, contains all diagrammatic channels in an unbiased way and their inter-channel couplings. At the same time a fine resolution of the full Brillouin zone is used for the integration, so that no possible contribution may be missed. Hence, the results are assumed to be trustworthy. However, an analysis with an improved resolution would still be of interest to confirm if the phases we extrapolated from the vertex at the end of the flow form the actual ground state phase.

5.4. Non-Isotropic 3D-Hubbard Model

As described in section 5.2, the layers of atoms arranged on a square lattice are the active parts leading to superconductivity in iron- or copper-based SCs. Therefore, approaches considering only these two-dimensional sheets are quite successful in describing the relevant pairing mechanism. However, these layers are embedded in a three-dimensional solid, which influences the tendency to superconductivity. Some previous studies compared the Hubbard model with second nearest neighbour hopping on a two-dimensional square lattice and one on a three-dimensional simple cubic lattice which were either based on a phenomenological spin-fluctuation theory [163] or on the fluctuating exchange approximation [164] or on the mean field theory [165]. In the phenomenological theory it was shown that the critical temperatures in 2D as well as in 3D are similar, when the parameters are scaled by the bandwidth. In the other two studies it was observed that the transition temperature to a d-wave SC state is significantly larger in the two dimensional case than in the three dimensional one. Moreover, these two studies revealed a tendency to a singlet d-wave superconductivity close to the AFM phase, which is stronger than a triplet p-wave SC order in the proximity of FM order.

While these results are consistent the studies only consider an isotropic setting. As the inter-plane-hopping between the active layers of the superconductors will, of course, be smaller than the intra-plane-hopping the investigation of anisotropic 3D-Hubbard models is of interest. Therefore, we model the system by the extended anisotropic Hubbard Hamiltonian

$$H = -\sum_{<i,j>,\sigma} t_{ij}(\hat{c}^\dagger_{i,\sigma}\hat{c}_{j,\sigma} + \hat{c}^\dagger_{j,\sigma}\hat{c}_{i,\sigma}) - \sum_{\ll i,j \gg,\sigma} t'_{ij}(\hat{c}^\dagger_{i,\sigma}\hat{c}_{j,\sigma} + \hat{c}^\dagger_{j,\sigma}\hat{c}_{i,\sigma}) + U\sum_i \hat{n}_{i,\uparrow}\hat{n}_{i,\downarrow}, \tag{5.13}$$

where, again, $<>$ denotes nearest neighbours (NN) and $\ll\gg$ denotes next nearest neighbours (NNN). The hopping parameters are chosen to be

$$t_{ij} = \begin{cases} t & \text{for } i,j \text{ NN in } x\text{-}y\text{-plane} \\ t_z & \text{for } i,j \text{ NN along } z\text{-axis} \end{cases} \qquad t'_{ij} = \begin{cases} t' & \text{for } i,j \text{ NNN in } x\text{-}y\text{-plane} \\ t'_z & \text{for } i,j \text{ NNN in } x\text{-}z\text{- or in } y\text{-}z\text{-plane,} \end{cases} \tag{5.14}$$

thus resulting in the dispersion relation

$$\begin{aligned} \varepsilon(\boldsymbol{k}) = &-2\,t(\cos(k_x) + \cos(k_y)) - 2\,t_z\cos(k_z) \\ &- 4\,t'\cos(k_x)\cos(k_y) - 4\,t'_z(\cos(k_x)\cos(k_z) + \cos(k_y)\cos(k_z)) - \mu \end{aligned} \tag{5.15}$$

which has a bandwidth of $4t + 4t' + 2t_z + 8t'_z$. This set of parameters enables an activation of the third dimension by increasing t_z and t'_z. This means that, on the one hand, the two-dimensional Hubbard model discussed in section 5.2 is again obtained for the choice of $t_z = 0\,t$ and $t'_z = 0\,t$. On the other hand, the extended isotropic 3D-Hubbard model is obtained for $t_z = t$ and $t'_z = t'$, which becomes the model discussed in section 5.3 for a vanishing second nearest-neighbour hopping, that is for $t' = 0\,t$.

This approach of t_z and t'_z as parameters simulating the three-dimensional character is justified, as they represent the overlap of Wannier orbitals[2] of different layers stacked in the z-direction. As a rough estimate, the relation between the xy-lattice parameter a and the distance a_z between two layers in z-direction correspond to the relation between t and t_z. If the planes are close to each other,

[2]The type and orientation of the orbitals is, in general, of importance. As this can be included in the considerations by an additional scaling factor we only, for simplicity, discuss the isotropic orbitals, that is s-orbitals.

that is $a > a_z$, then the orbitals have a large overlap, leading to an enhanced electron mobility in the z-direction $t < t_z$. Therefore, $t_z \gg t$ corresponds to a transition from the three- to the one-dimensional Hubbard model [166]. If the distance of one atom to its neighbours in x-, y- and z-direction is similar, that is $a \approx a_z$, then the orbitals have a similar overlap, resulting in the isotropic case $t \approx t_z$. Finally, if the two layers are further away from each other, that is $a < a_z$, then the orbitals in the z-direction have a small overlap, resulting in a reduced mobility in the z-direction compared to the one within the xy-plane, that is $t > t_z$.

In the case of copper-based superconductors the bonds in the square-plane are formed by oxygen p-orbitals and by copper d-orbitals, which are directed within the planes and therefore only have a small extent in the z-direction. Hence, these materials are described by a parameter setting corresponding to $t > t_z$.

Daré *et. al.* [167] investigated the anisotropic d-dimensional Hubbard model for $t' = t'_z = 0\,t$ at half-filling with a two-particle self-consistent approach based on RPA and derived scaling laws for the transition to the AFM state with the d-dimensional ordering vector $\boldsymbol{Q} = (\pi)^d$. The resulting critical exponents are the same as the $n \to \infty$-limit of the $O(n)$ classical model. However, as the perfect nesting in two dimensions leads to an exponential increase of the correlation length instead of a power law in terms of temperature, the transition from 2D to 3D was only considered for a quasi two-dimensional system with $t_z \ll t$, i.e. $t_z < 0.1\,t$. In this case, the authors observed a regime in which the phase transition occurs, before the movement of single particles between the planes is possible due to thermal fluctuations, as $t_z \ll T_\mathrm{N}$.

In a FLEX based study, Takimoto and Moriya [18] considered the transition of the extended Hubbard model from two dimensions to three dimensions by varying the anisotropic parameter t_z, which is in the range $[0.1\,t,\, 0.8\,t]$, for various electron densities below the half-filled one. The next nearest neighbour hopping in the xy-plane was fixed to $t' = -0.2\,t$, while the anisotropic next nearest neighbour hopping was accordingly scaled as $t'_z = t_z \cdot t'$. In this setting, in good agreement with the differences between the pure 2D- and 3D-phases mentioned above, the d-SC-phase is gradually suppressed, when the hopping in the third direction t_z is increased, while the Néel temperature for the AFM-phase close to half-filling increases. However, the d-SC-phase turns into an incommensurate SDW-phase, which, for small anisotropies of $t_z \approx 0.3\,t$, coexists with the SC order.

With our calculations we aim at extending the parameter range covered for the transition between the 2D- and the 3D-Hubbard model, and we investigate the importance of the features of the Fermi-surface in the xy-plane. For that purpose, we fix the chemical potential to fulfil the two-dimensional van-Hove condition in the $(k_z = 0)$-plane, that is $\mu = 4t' - 2t_z$. At the same time we vary both, t' and t_z, and consider first a vanishing t'_z (cf. sec. 5.4.1), and second a scaled one $t'_z = t_z \cdot t'$ (cf. sec. 5.4.2) in the same way as Takimoto and Moriya did [18]. Thus, only t' and t_z remain as independent parameters which have to be varied, resulting in the the electron densities displayed in table 5.3.

5.4.1. The $t'_z = 0$-Phase Diagram

We investigate the range of $t' \in [-0.5\,t, 0\,t]$ like in section 5.2 and simulate the increasing influence of the next plane by varying t_z over two orders of magnitude, that is ${}^{t_z}/_t \in \{0.01,\, 0.05,\, 0.1,\, 0.5\}$. For some parameter combinations the Fermi-surface of the non-interacting system is displayed in figure 5.16. Upon variation of t' the Fermi-surface changes for all t_z values in the $(k_z = 0)$-plane in the same way as described in section 5.2. For small values of t_z this shape of the Fermi-surface is basically maintained

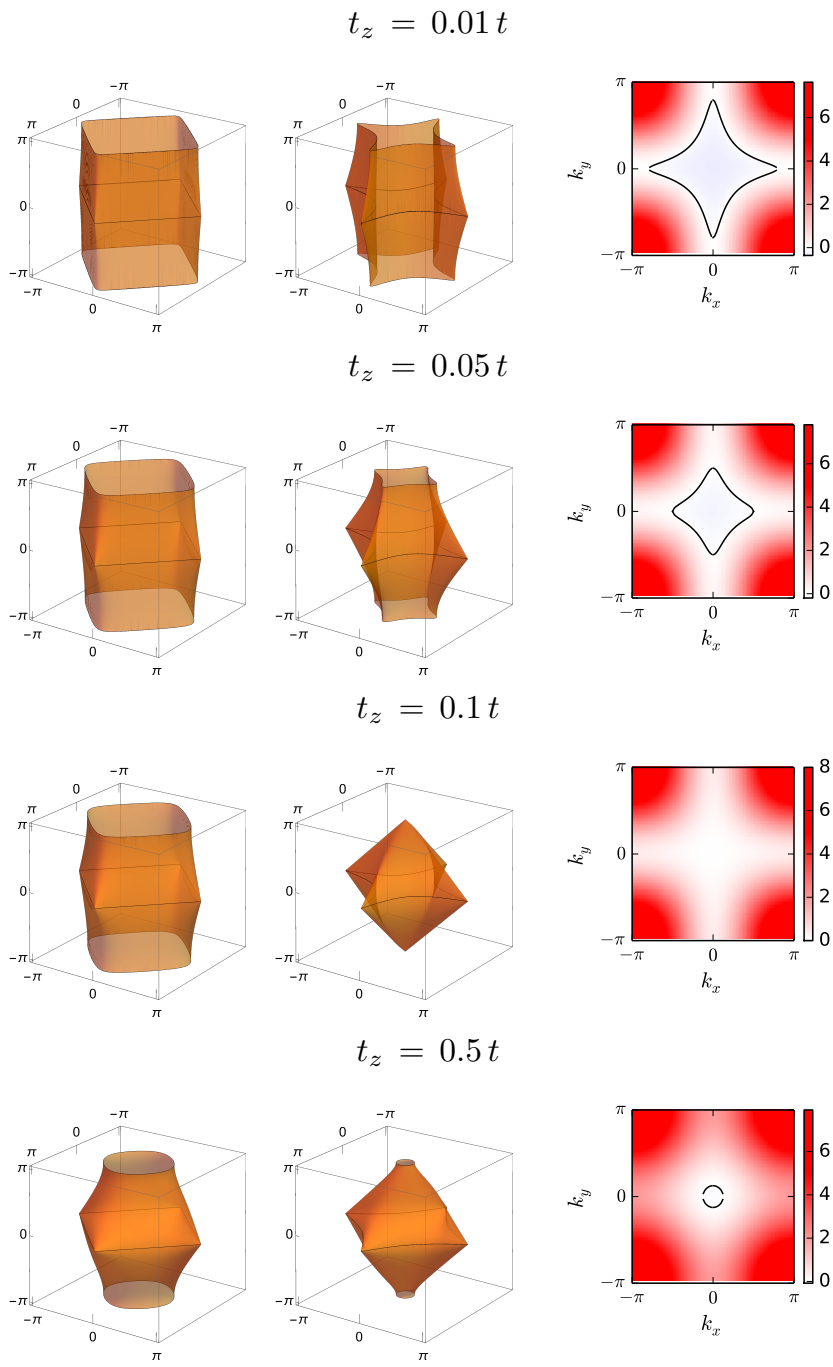

Figure 5.16.: Fermi-surfaces (left and middle column) and energy maps in the ($z = \pi$)-plane (right column) of the non-isotropic Hubbard model. The anisotropy increases from top to bottom corresponding to ${}^{t_z}/_{t} = 0.01, 0.05, 0.1, 0.5$. For $t_z = 0.5$, i.e. in the lowest row, the next-nearest neighbour hopping is $t_z = 0t$ (left) and $t' = -0.24t$ (centre and right) while in the other three cases it is set to $t' = 0t$ (left) and $t' = -0.45\,t$ (centre and right). When $t' = -0.24\,t$ is further increased for $t_z = 0.5\,t$, the Fermi-surface does not reach the ($z = \pi$)-plane any more. Similarly, for $t_z = 0.1\,t$ and $t' = -0.45\,t$ the Fermi-surface only reaches the point $(0, 0, \pi)$.

t'	t_z			
	$0.01\,t$	$0.05\,t$	$0.1\,t$	$0.5\,t$
$0.0\,t$	0.98	0.93	0.90	0.64
$0.01\,t$	0.89	0.86	0.81	0.55
$0.015\,t$	0.85	0.81	0.76	0.49
$0.02\,t$	0.82	0.77	0.71	0.42
$0.024\,t$	0.78	0.72	0.67	0.37
$0.026\,t$	0.76	0.70	0.66	0.34
$0.028\,t$	0.73	0.68	0.62	0.31
$0.030\,t$	0.71	0.66	0.59	0.28
$0.032\,t$	0.68	0.63	0.58	0.26
$0.034\,t$	0.66	0.59	0.53	0.23
$0.036\,t$	0.63	0.56	0.50	0.21
$0.040\,t$	0.56	0.49	0.42	0.16
$0.045\,t$	0.44	0.33	0.23	0.09
$0.050\,t$	0.0			

Table 5.3.: Electron densities for $t'_z = 0\,t$ and the various parameter sets t' and t_z. The electron densities in the case of $t'_z \neq 0$ are almost identical.

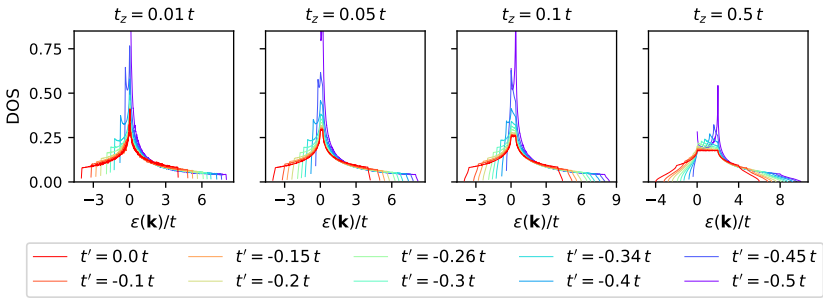

Figure 5.17.: Density of states (DOS) for $t_z/t = 0.01, 0.05, 0.1, 0.5$ from left to right and for various values of t'.

along the k_z-direction, although the edges originating from the van-Hove condition become rounded and slightly move inwards. For increasing values of t_z, the Fermi-surface moves further inwards along the k_z-direction. Thus, the Fermi-surface has a square-shape in the $(k_z = \pi)$-plane for $t_z = 0.1\,t$ over the whole range of values of t', while for $t_z = 0.5\,t$ it is circular for $t' > -0.25\,t$ and closes completely before reaching this plane for $t' < -0.25\,t$.

The density of states (DOS) for $t_z \leq 0.01\,t$ resembles the two-dimensional one (see fig. 5.3), that is a diverging DOS at $\varepsilon = 0\,t$ on top of a small offset resulting from the third dimension. For $t_z = 0.05\,t$ the DOS only features a divergence for all $t' = -0.5\,t$. For small values of $-t'$ it starts to exhibit a plateau between $\varepsilon = 0\,t$ and a small $\varepsilon > 0\,t$ similar to the DOS of the three-dimensional Hubbard model (see fig. 5.7). When $-t'$ is increased, the lowest possible state is moved to higher energies by which the corresponding shoulder evolves into a peak, so that two peaks close to the Fermi-energy are present: One originating from the low-energy shoulder and one at $\varepsilon = 0\,t$ which dominates. For $t_z = 0.1\,t$ the main peak remains at the Fermi-energy, while the peak of the left shoulder and the end of the plateau move to larger energies, so that the left peak and the main peak merge into one for $t' = -0.45\,t$. For $t_z = 0.5\,t$ the onset of the plateau remains at $\varepsilon = 0\,t$, but as the peak of the left

Name	Mom. Space Representation
s	const
-	$\cos(k_x) + \cos(k_y)$
$d_{x^2-y^2}$	$\cos(k_x) - \cos(k_y)$
-	$\cos(k_z)$
p_x	$\sin(k_x)$
p_y	$\sin(k_y)$
p_z	$\sin(k_z)$

Table 5.4.: On-site and first shell form-factors corresponding to the D_{4h}-symmetry group.

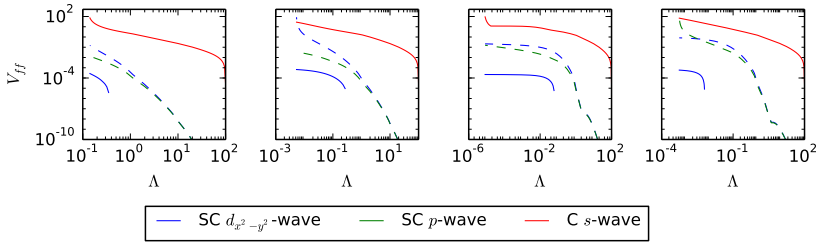

Figure 5.18.: Flow of the charge chantex in the on-site form-factor (C s-wave) and pairing chantex in the p_x (SC p-wave) and the $d_{x^2-y^2}$ (SC $d_{x^2-y^2}$-wave) form-factors towards the critical scales. The sets of parameters correspond, from left to right, to a final antiferromagnetic ($t' = 0\,t$), d-wave superconducting ($t' = -0.24\,t$), ferromagnetic ($t' = -0.4\,t$) and p-wave superconducting ($t' = -0.45\,t$) phase as $t_z = 0.05\,t$.

shoulder moves to positive energies, the main peak remains at the Fermi-energy only for $t' > -0.25\,t$, while it moves to values of higher energy upon increasing $-t'$ in the other cases.

As different ordering vectors are favourable due to the Fermi-surfaces and as a divergence of the DOS indicates a van-Hove singularity, we expect the system to evolve into different ordered states. In order to detect them and to resolve which is the dominant one, calculations employing the TUFRG were performed for these parameters.

As the anisotropy in z-direction breaks some symmetries in comparison to the simple-cubic Hubbard model (see section 5.3), this model has the point group symmetry D_{4h}, which is, as well as the SU(2)-symmetry, exploited to reduce the numerical costs. The form-factors belonging to this point group are displayed in table 5.4, where the similarity to those of the V_{4v} group can clearly be seen. Therefore, we are able to use 21 momenta in each direction for the interactions and resolve the dual propagator integrals on a mesh of $(21 \cdot 11)^3 \approx 12.3 \cdot 10^6$ momenta in a static TUFRG calculation with an Ω-cut-off. The flow is started with an initial interaction of $U = 3\,t$ at $\Lambda_0 = 100\,t$, and it is stopped, when one vertex entry exceeds the value of $V_{\text{crit}} = 70\,t$, signalling a divergence.

During the flow to low scales we keep the maximal values of the chantices for all form-factor combinations under surveillance. As we observed that those with unequal form-factor indices are significantly smaller than those with equal ones, we focus on the latter ones. In figure 5.18 we display the corresponding maximal values of the vertex with equal form factors for four different parameter sets, which represent the four possible orderings we observed in the calculations. During the flow, the on-site C-channel chantex starts to increase right from the beginning of the flow, but reaches a plateau at $\Lambda \approx 1\,t$ with a finite value in the order of $1\,t$. This behaviour displays the emergence of AFM fluctuations and is similarly observed for all investigated parameter sets. Contrary, the behaviour at lower energy scales differs in several ways. In some cases a further increase of the on-site C-channel

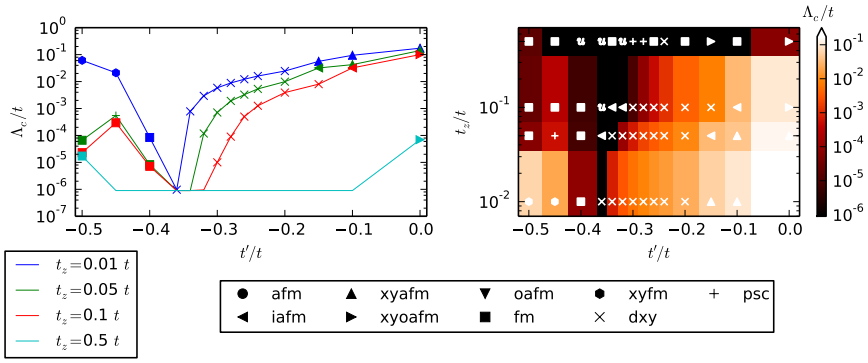

Figure 5.19.: Phase diagram of the anisotropic 3D-Hubbard model with $t'_z = 0\,t$ in two different representations. Due to the limited numerical resolution no divergences for $\Lambda_c < 10^{-6}\,t$ could be observed, so that all the corresponding cases are displayed by a critical scale $\Lambda_c = 9 \cdot 10^{-7}\,t$ without a favourable ordering in the left plot. In the right plot, u as unidentified refers to an appearance of features of different ordering tendencies at the same time, such that even an educated guess is impossible.

chantex is leading to a divergence. In other cases, the P-channel in the $d_{x^2-y^2}$-form-factors or in the p_x- and in the p_y-form-factors rapidly increases, faster than the C-channel, so that its contribution leads to the divergence. As these divergences occur at parameter specific values of Λ and as the assumption of a weak interaction which the TUFRG is based on breaks down, the flow is stopped at this scale which we denote as critical scale Λ_c, as pointed out in section 5.1. While the form-factor resolved behaviour of the chantices during the flow already hints to an emerging phase which will probably occur at the critical scale, an analysis of the vertex at Λ_c projected to the different channels is required to verify this phase and to obtain the ordering vector. In the case of p- or d-wave superconductivity the ordering vector is always $\boldsymbol{s} = (0,0,0)$ in our case, while ordering vectors of the vertex in the C-channel are located at the corner of the Brillouin zone for an AFM ordering (i.e. three-dimensional at $\boldsymbol{t} = (\pi,\pi,\pi)$ or planar e.g. at $\boldsymbol{t} = (\pi,\pi,z)$) and at $\boldsymbol{t} = (0,0,0)$ for an FM ordering. In several cases the vertex at the critical scale not only exhibits the feature of the dominant, but also those of suppressed phases.

The resulting phase diagram based on the parameters introduced above is displayed in figure 5.19. In the figure on the left we observe that the general shape of the $\Lambda_c - t'$-curve is maintained for $t_z < 0.5\,t$ at all the investigated values of t' except for $t' = -0.5\,t$ and that it resembles the one of the two-dimensional Hubbard model (see fig. 5.4). The difference between the curves is a reduction of the critical scale with an increasing importance of the z-direction, which is due to the reduced DOS at the Fermi-energy. Regarding the different phases, we observe a large variety of different AFM orderings for small values of $-t'$ due to the different importance of the z-direction.

First, we fix $t' = 0\,t$ and note that the third dimension is less important for small values of t_z, so that an AFM ordering vector (π,π,z) exists for all values of k_z, which is denoted as the xyafm-phase (see fig. 5.20, first row). This results from the Fermi-surface which basically is a tube with the characteristic square-like shape in the xy-plane enabling perfect nesting. We further note that the critical scales for the onset of the AFM-phase are significantly larger than t_z, as $\Lambda_c \approx 0.18\,t$ for $t_z = 0.01\,t$. These observations for weak interactions are in good agreement with the suppressed hopping in z-direction, as pointed out by Daré [167].

When the z-direction becomes more important ($t_z = 0.1\,t$), the Fermi-surface bends further away from the perfect nesting condition towards the surface of the Brillouin zone, so that the perfect nesting is only possible close to the ($k_z = 0$)-plane. Therefore, we only observe a divergence in this plane (see fig. 5.20, first row) and denote this phase as xy0afm-phase.

Next, we consider small finite values of $-t'$ and note that the xyafm-order which was observed for $t' = 0\,t$ is preserved, before the d-wave pairing becomes dominant when t_z is small. However, for $t_z \geq 0.05\,t$ between the xyafm or the xy0afm order and the d-wave SC order a three-dimensional incommensurate AFM order (iafm) becomes dominant (see fig. 5.20, first row). This results from the fact that, on the one hand, already small finite values of $-t'$ lead to a bending of the Fermi-surface within the xy-plane and that, on the other hand, the values of t' cause an additional bending in the z-direction. Thus, the perfect nesting is no longer fulfilled for (π, π, z) or $(\pi, \pi, 0 + \epsilon)$, but instead a nesting of $(\pi + \epsilon, \pi + \epsilon, \pi)$ becomes favourable, similar to the doped 3D-Hubbard model (see sec. 5.3.2), which agrees well with the observation of reference [18]. The phase diagram (cf. fig. 5.19) suggests that, in comparison to the xy(0)afm-phase the critical scale is enhanced for this phase, so that we assume a three-dimensional AFM ordering with the ordering vector (π, π, π) suppressed by the dominant two-dimensional density of states with a corresponding perfect nesting.

When $-t'$ is further increased, a broad range of d-wave SC appears as a divergence of the P-channel based on $d_{x^2-y^2}$-form-factors (see fig. 5.20, second row), which starts at smaller values of $-t'$ and at lower critical scales Λ_c, when t_z is increased. These smaller values of Λ_c are due to the reduced DOS with increasing values of t_z at the Fermi-surface. As AFM SDW appear at larger scales Λ of the flow, this SC instability is driven by them. At the final scale features of the incommensurate AFM order can still be observed, of which the ordering vector moves further away from (π, π, π) towards $(0, 0, \pi)$ (see fig. 5.20, second row). This can also indicate a coexistence of AFM order and of d-wave SC order in this range, as observed by Takimoto *et al.* [18]. The transition to the $d_x^2 - y^2$ symmetry goes along with a reduction of the $C_{4\mathrm{v}}$ symmetry in the xy-plane to $C_{2\mathrm{v}}$, as a rotation of $\pi/2$ results in a global minus-sign. In the phase diagram we further observe that the d-wave superconductivity tends to very small values of Λ_c for $t' \approx -0.34\,t$, which are beyond our momentum space resolution. At these points we can only take the flow of the chantices in the form-factors in which we expect the divergence and the interaction at the final scale, and then make an educated guess on the final dominant phase. This is done for the non-diverged flow in the right plot of figure 5.19. For some parameter sets the arguments indicating the possible phases are exemplarily shown in table 5.5 and in more detail, including the corresponding figures, in appendix C. When the indications towards two different phases are comparable, we denote this as u in figure 5.19. Although we observe an incommensurate AFM phase in several cases, there might still appear a d-wave SC one, as this phase rapidly evolves during the flow.

At the critical point $t' \approx -0.36\,t$ the FM phase sets in for all investigated values of t_z, indicated by a divergence of V_{C} in the on-site form-factor for an ordering vector of $(0, 0, 0)$. If t' is further reduced, an FM ordering in the xy-plane is observed for $t_z = 0.01\,t$. This results from the Fermi-surface which hardly changes in the z-direction, so that the FM ordering vector is independent of k_z. This xy-plane FM order is denoted as xyfm ordering. For slightly larger hopping strength in z-direction, that is $t_z = 0.05t$, we first also observe an FM order when t' is decreased from the d-wave SC phase, but at $t' = -0.45\,t$ a p-wave SC order appears. As p_x and p_y are equivalent due to the symmetry of the system, this ordering maintains the symmetries within the xy-plane and can be observed in V_{P} corresponding to either form-factors. This p-wave pairing is in strong competition with the AFM ordering which survived throughout the d-wave SC phase and the emerging FM phase (see figure 5.20,

t'	**Possible Phases**	**Observations**
	$t_z = 0.05\,t$	
$-0.34\,t$	iafm $d_{x^2-y^2}$-SC	intermediate *iafm* interaction, weaker $d_{x^2-y^2}$-pairing, $d_{x^2-y^2}$-channel starts to increase
$-0.36\,t$	iafm fm	intermediate *iafm* interaction, slightly weaker *fm* interaction
	$t_z = 0.1\,t$	
$-0.32\,t$	iafm $d_{x^2-y^2}$-SC	intermediate *iafm* interaction, $d_{x^2-y^2}$-channel starts to increase
$-0.34\,t$	iafm fm p-SC, $d_{x^s-y^2}$-SC	intermediate *iafm* interaction, weaker *fm* interaction, C-, p- and $d_{x^2-y^2}$-channel start to increase
$-0.36\,t$	fm iafm p-SC	strong *fm* interaction, slightly weaker *iafm* interaction, p-channel starts to increase

Table 5.5.: Exemplary discussion of possible phases for calculations which did not diverge for $\Lambda > 10^{-7}\,t$. *iafm* corresponds to incommensurate anti-ferromagnetic ordering, p- and d-SC refer to superconducting ordering with the corresponding form-factor shape, *fm* denotes ferromagnetic ordering.

third row). As we did not trace the ordering vector of the chantices during the flow and as both, the anisotropic AFM and the FM order are contained in the on-site form-factor C-channel vertex, we can not distinguish if the p-wave ordering is driven by AFM fluctuations or by FM fluctuations, which is the case for p-type superconductivity in the isotropic 3D-Hubbard model [164, 165]. For $t_z = 0.1\,t$ we observe the same competition between incommensurate AFM, p-wave SC and the FM order which dominates at this point (see fig. 5.20). In all cases with $t_z > 0.01\,t$ we observe a significant drop in the critical scale for $t' = -0.5\,t$. This corresponds to the fact that the system is empty due to the applied van-Hove condition on the chemical potential.

Finally, in the case of $t_z = 0.5\,t$ an AFM ordering in the xy-plane could be resolved for $t' = 0\,t$ at a significantly lower critical scale than in the other cases. This corresponds to the strong influence of t_z on the number of electrons in the system due to the van-Hove nesting condition in the xy-plane (see table 5.3), so that the system already is heavily hole-doped. Both t_z, and the electron density lead to a change of the Fermi-surface, which, therefore, has a circular shape in the xy-plane towards the surface of the Brillouin zone. Thus, it is impossible for the same ordering vector to connect large parts of two Fermi-surfaces, even with the help of a finite z component. As this nesting condition becomes destroyed by increasing $-t'$, the critical scale rapidly drops beyond our resolution. By investigating the chantex resolved flow to the final scale and the interaction at this end point we estimate which phases might result if the flow is continued to even lower scales. For most parameters we obtain an FM phase, but also a d-SC phase for $t' = -0.24\,t$ and a p-wave SC-phase for $t' = -0.28\,t$. However, as the SC phases are driven by spin-density fluctuations, the magnetic phases may still change into a corresponding SC one. For parameters close to $t' = -0.36\,t$ different phases were competing with each other, so that an educated guess was impossible. Only for $t' = -0.5\,t$ we obtained an FM phase with a similar critical scale as observed for $t_z = 0.1\,t$, which is due to the fact that both show a similar behaviour in the DOS at this point.

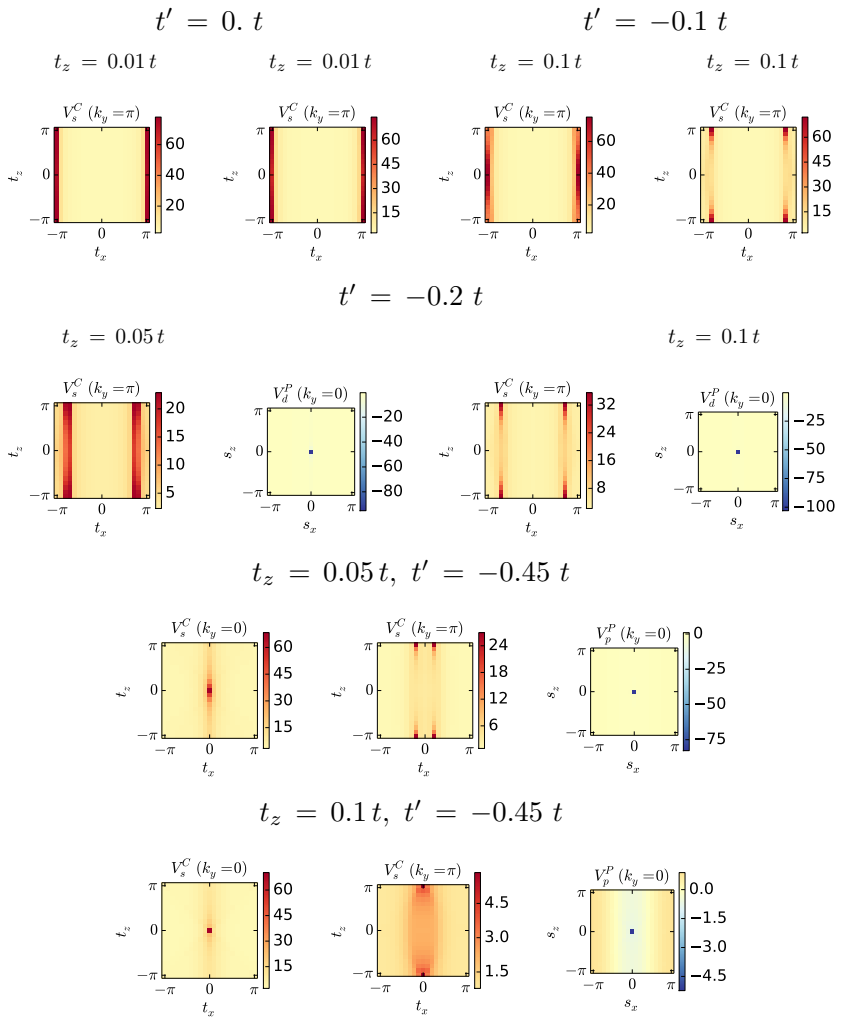

Figure 5.20.: Cuts through the full vertex projected to one channel at the end of the flow.
First row: Visualisation of the different antiferromagnetic ordering vectors based on cuts through the s-wave form-factor contribution of the full vertex projected to the C-channel in the $(k_y = \pi)$-plane for, from left to right, ${}^{t_z}/_{t} = 0.01,\ 0.05,\ 0.1$ at $t' = 0\,t$ and (right) $t_z = 0.1\,t$ at $t' = -0.1t$.
Second row: For parameters $t' = -0.2\,t$ and $t_z = 0.05\,t$ (left pair) and $t_z = 0.1t$ (right pair) the cuts through the on-site form-factor contribution of the full vertex projected to the C-channel in the $(k_y = \pi)$-plane (left in each pair) and through the $d_{x^2-y^2}$ form-factor contribution of the full vertex projected to the P-channel in the $k_y = 0$-plane (right in each pair) show a dominating d-wave superconductivity and a suppressed antiferromagnetic ordering.
Third row: For $t_z = 0.05\,t$ and $t' = -0.45\,t$ a cut through the on-site form-factor contribution of the full vertex projected to the C-channel in the $(k_y = 0)$-plane (left), in the $(k_y = \pi)$-plane (centre) and a cut through the p_x-form-factors contribution of the vertex projected to the P-channel in the $(k_y = 0)$-plane shows the competition between antiferromagnetic, ferromagnetic and the dominating p-wave superconducting order.
Fourth row: same as third row with $t_z = 0.1\,t$ and dominating ferromagnetic ordering.

While we only considered a second-nearest neighbour hopping in the xy-plane and neglected the corresponding one in the z-direction, it is physically reasonable to include it corresponding to the upcoming section.

5.4.2. The $t'_z = t_z \cdot t'$ Phase Diagram

As we initially discussed in this section, the parameter t_z can be regarded as a measure of the proximity of neighbouring layers. As this parameter corresponds to the overlap of orbitals directly positioned above each other, and as t' corresponds to the overlap of orbitals of second nearest neighbours within the xy-plane, it makes sense to include the overlap with second nearest neighbours in the xz- and in the yz-plane by a scaled parameter $t'_z = t_z \cdot t'$. In this way t_z and t' remain the two independent parameters, when we imply the van-Hove condition on the chemical potential, that is $\mu = 4t' - 2t_z$ and investigate the same range of parameters as before, that is $t' \in [-0.5\,t, 0\,t]$ and ${}^{t_z}/_{t} \in \{0.01, 0.05, 0.1, 0.5\}$. As t'_z is at least one magnitude smaller than t_z in our parameter range, it has almost no influence on the Fermi-surface for the quasi two-dimensional case $t_z = 0.01\,t$. In the other cases, the influence on the Fermi-surface is small for small values of $-t'$, that is $-t' < -0.32\,t$ (see fig. 5.21). When this threshold is reached, the t'_z-parameter leads to an increased bending in the z-direction, resulting in a tube with square shape close to the $z = \pi$ surface of the Brillouin zone. At the same time, the inward bend of the Fermi-surface in the $(k_z = 0)$-plane is increased, resulting in a star-like shape, while the opening in the $(k_z = \pi)$-plane is enhanced. In the case of $t_z = 0.5\,t$ this leads to the formation of electron-pockets centred at $(0, 0, \pi)$ (see fig. 5.21). As well as the Fermi-surface, the DOS hardly changes for $-t' < 0.32\,t$ and over the whole t' range for the quasi two-dimensional system. However, in the cases where the Fermi-surface changed, the DOS did so, too. In these cases the peaks of the left shoulder and at the Fermi-surface become more pronounced when t'_z takes larger values (see fig. 5.22). In the case of $t_z = 0.1\,t$ and $t' = -0.45\,t$ both peaks are on top of each other, so that the DOS at the Fermi-surface is significantly increased.

The phase diagram for this set of parameters is obtained in the same way as described in the preceding subsection by an analysis of the form-factor resolved flow of the chantices and the interaction at the final scale projected to the different channels. For $t_z = 0.01\,t$ the phase diagram (see fig. 5.23) equals the one of the previous case with $t'_z = 0\,t$ over the whole range of t'-parameters. Therefore we focus in the following on the cases of $t_z = 0.05\,t$ and $t_z = 0.1\,t$, for which the phase diagram resembles the one resulting from $t'_z = 0\,t$ for values of $t' > -0.3\,t$, both in the critical scale Λ_c, which are numerically almost equal, as well as in the resulting phases. For example, a cut through the vertex at the critical scales results in figures similar to those displayed in figure 5.20, first and second row, for the corresponding parameter sets. This can be expected, as the Fermi-surface is only slightly changed compared to the case of $t'_z = 0\,t$. Therefore, the same AFM fluctuations arise and drive the system into an AFM or d-wave SC phase.

In the region of $t' \approx -0.3\,t$ we observe an increase in the critical scale, at which d-wave pairing appears. On the one hand, the Fermi-surface in the $(k_y = 0)$-plane is linear in the proximity of $k_z = 0$ while, on the other hand, it is less dependent on k_x and k_y close to $k_z = \pi$ compared to the case of $t'_z = 0\,t$, while the Fermi-surfaces in the $(k_z = 0)$- and $(k_z = \pi)$-planes maintain their quadratic form (see fig. 5.24). This setting enhances the incommensurate spin-density waves with a transfer of $k_z = \pi$ which are driving the d-wave pairing. If t' is further increased, the bending of the Fermi-surface in the $(k_z = 0)$-plane is increased to a star-like shape, so that even incommensurate nesting vectors can

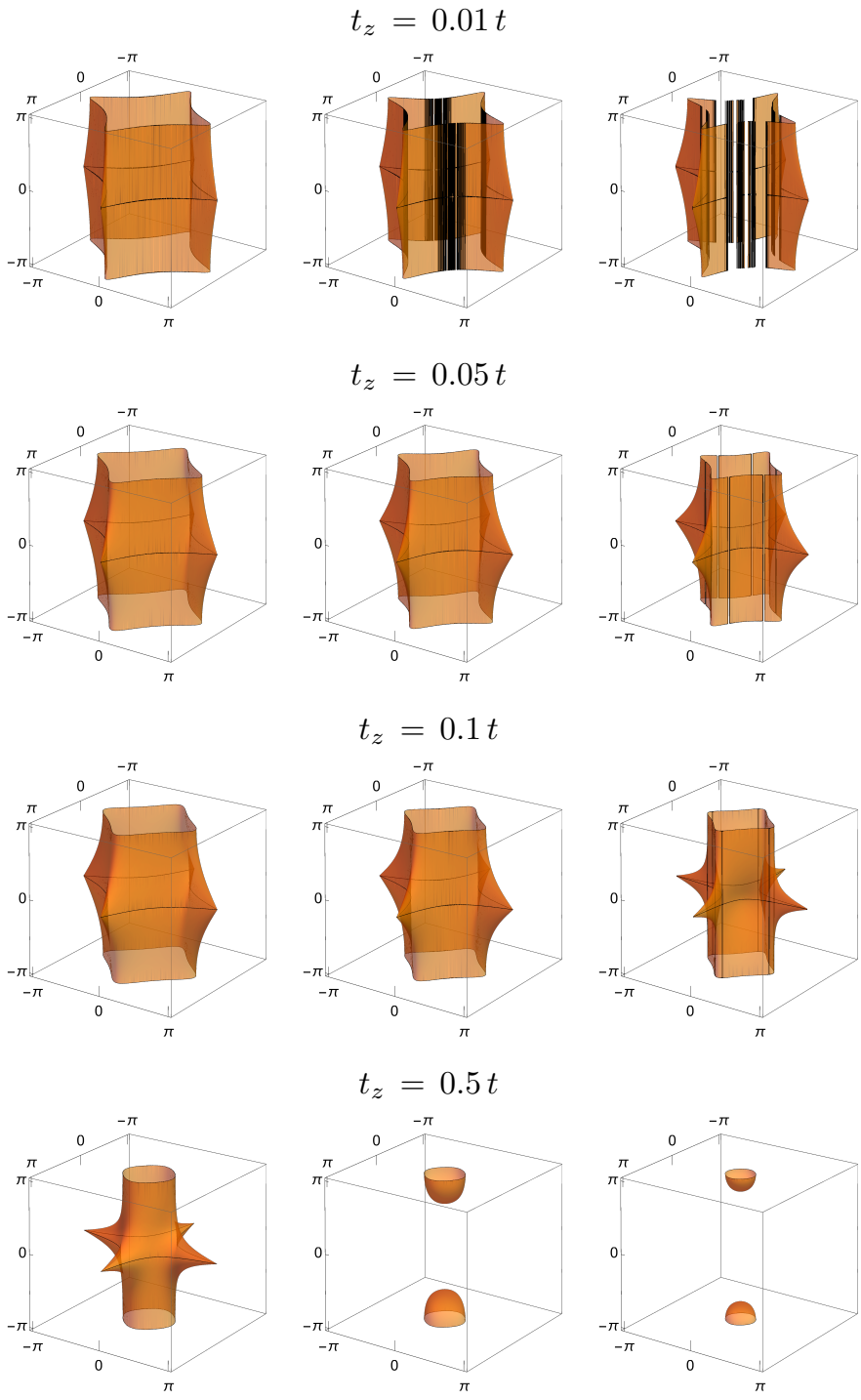

Figure 5.21.: Fermi-surface of the anisotropic Hubbard model with (from top to bottom) $t_z = 0.01\,t,\ 0.05\,t,\ 0.1\,t,\ 0.5\,t$ and (from left to right) $t' = 0.32\,t,\ -0.4\,t,\ -0.45\,t$ while $t'_z = t_z \cdot t'$.

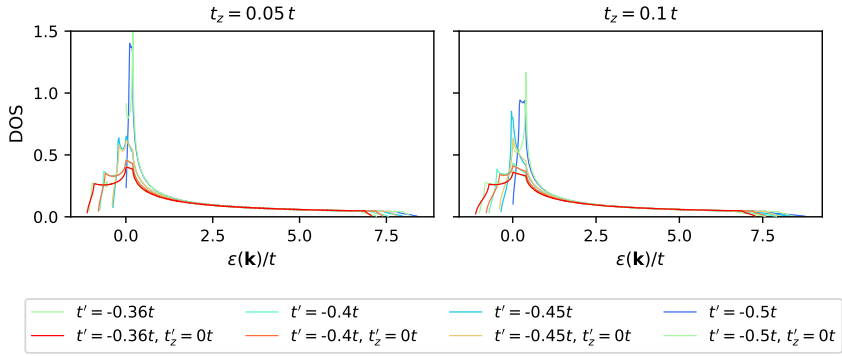

Figure 5.22.: Non-isotropic Hubbard model: Comparison of the density of states (DOS) for $t_z = 0.05\,t$ (left) and $t_z = 0.1\,t$ (right) with $t'_z = 0\,t$ and $t'_z = t_z \cdot t'$.

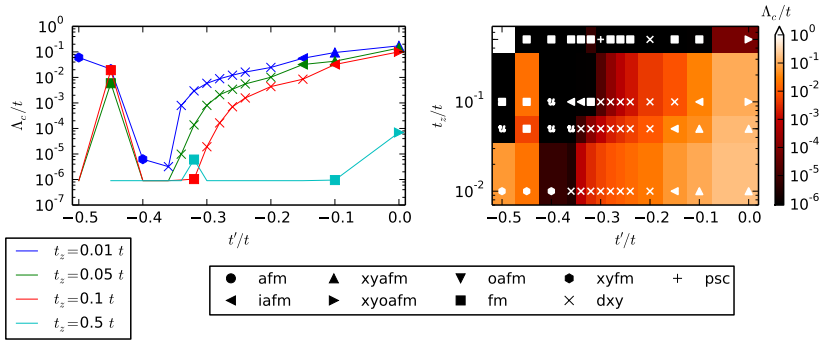

Figure 5.23.: Phase diagram of the anisotropic 3D-Hubbard model with $t'_z \neq 0\,t$ in two different representations. Due to the limited numerical resolution no divergences for $\Lambda_c < 10^{-6}\,t$ could be observed, so that all corresponding cases are displayed as $\Lambda_c = 9 \cdot 10^{-7}\,t$ without a favourable ordering in the left plot. In the right plot, u refers to an appearance of features of different ordering tendencies at the same time, such that even an educated guess is impossible.

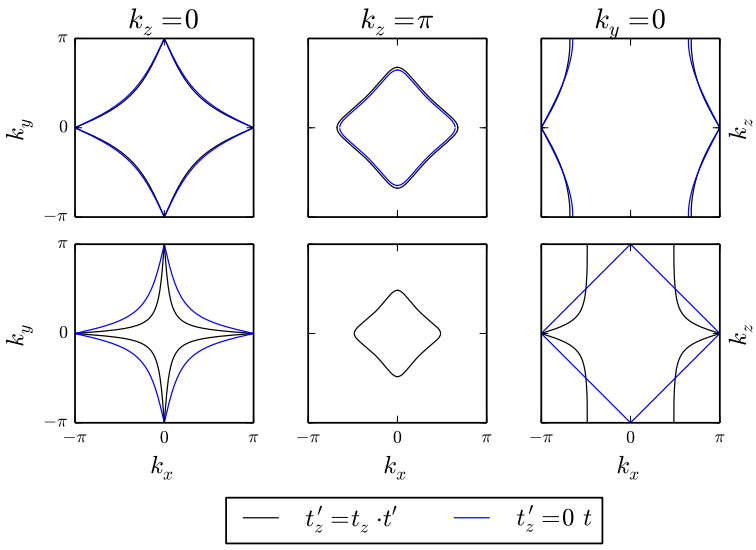

Figure 5.24.: Comparison of the Fermi-surface in the ($k_z = 0$)-, ($k_z = \pi$)- and ($k_y = 0$)-plane (from left to right) resulting from $t'_z = 0\,t$ and $t'_z = t_z \cdot t'$ for $t' = -0.32\,t$ and $t' = -0.45\,t$ in the top and bottom row, respectively, at $t_z = -0.1\,t$.

not connect two larger parts of the Fermi-surface. This heavy distortion of the Fermi-surface leads to the suppression of any order within our resolution.

However, at $t' = -0.45\,t$ a single point of FM ordering within our resolution can be observed. For this parameter the Fermi-surface is a rectangular tube which is only deformed in the ($k_z = 0$)-plane, to fulfil the van-Hove condition (see fig. 5.21 and 5.24). Therefore, large parts of the Fermi-surface can be connected by corresponding nesting vectors which drive the formation of ordering at large critical values. As this setting is easily distorted and we only investigate a coarse set of t' parameters in this region, it appears as a single point. We note at this point, that the p-wave pairing observed in the $t'_z = 0\,t$ case does not appear any more. However, the final interaction still exhibits a corresponding feature.

Such features can also be found when we analyse a the final interaction at the end of the flow when a divergence was not reached. In these cases the p-wave SC order is in a strong competition with incommensurate AFM and FM orderings, which also cause the low critical scales.

Finally, in the case of $t_z = 0.5\,t$ the critical scale is, again, for almost all parameters out of scope of our resolution. Only in the case of $t' = -0.32\,t$ we could resolve a peak, which is due to a favourable nesting condition as the Fermi-surface in the k_z-direction resembles a quadratic tube. In all cases we analysed the final interactions in different planes as well as the form-factor resolved flow of the chantices resulting in the phases displayed in the right phase diagram of figure 5.23. That is, we obtain dominating FM fluctuations for most parameters, only for $t' = -0.2\,t$ a tendency towards d-wave SC and for $t' = 0.28\,t$ a tendency towards p-wave SC.

5.4.3. Discussion of the Anisotropic 3D-Hubbard Model

Although the results of the previous sections are based on the abstract Hubbard model, conclusions for the design of superconductors can be drawn from them. While we treat the system at zero temperature, we assume in our discussion that the critical scale corresponds to a critical temperature at which the observed phase sets in. In two dimensions, however, no transition which breaks any continuous symmetries at finite T can occur according to the Mermin-Wagner theorem [168]. Therefore our results for the two-dimensional Hubbard model in section 5.2 violate the Mermin-Wagner theorem. However, this can be assigned to the approximations in our approach, as Hille *et al.* [169, 170] showed that this theorem seems to be fulfilled if frequency dependence, self-energy contributions and contributions from loops of higher order according to the multiloop FRG scheme are taken into account. Although we neglected those effects, we could show that the different phases observed in the two-dimensional case even exist in the case of three dimensions. Therefore, the general assumption that superconductivity and magnetic order can appear in two-dimensional planes does not violate the Mermin-Wagner theorem as they are embedded either in a three-dimensional solid or are subject to the upper planes of a substrate.

Although the three dimensionality is important to allow long-range ordering at all, the highest critical scales can be reached if the hopping between the superconducting planes is small and the planes are therefore well isolated. This is the case in copper and iron based superconductors, in which the electron mobility between the superconducting planes which we model by t_z is small. This regime is in our case observed for $t_z < 0.1\,t$ where the two-dimensional features dominate the system, as k_z-independent phases appear. This situation of large anisotropy was investigated by Dare *et al.* [167] for half filling, leading to the observation that the anisotropy t_z is in these cases significantly lower than the critical scale. Similarly, we observe $t_z \ll \Lambda_c$ at $t' = 0\,t$ which is close to half filling in the case of large anisotropy (cf. table 5.3). This situation is inverted (i.e. $\Lambda_\mathrm{c} < t_z$) for $t_z = 0.5\,t$, while $t_z = 0.1\,t \approx \Lambda_\mathrm{c}$ holds in the intermediate case. For $t_z = 0.01\,t$ we observe a k_z-independent FM phase at the other end of the t' scale, for which $t_z \ll \Lambda_\mathrm{c}$ also holds, while a three-dimensional FM phase is obtained for $t' = -0.4\,t$ with $\Lambda_\mathrm{c} \ll t_z$. In this way we note that the resulting phase is z-independent, if the for the critical scale $\Lambda_\mathrm{c} \gtrsim t_z$ holds. To explain this, Λ_c is associated with a critical temperature, so that corresponding Matsubara frequencies can be defined of which the first one is even larger than the bandwidth in the z-direction. The motion of the electrons between the planes is therefore still quasi-classical when the transition occurs, which explains the observation of planar phases for $\Lambda_\mathrm{c} \gtrsim t_z$.

All the observations so far indicate the importance of a good separation between the superconducting layers in cuprates. Although the structure is much more complex, we note that a slight increase in T_c was observed for rare-earth 123-HTS materials, when the distance between the CuO layers in the active block was increased [16], which is in a general good agreement with our observations. However, the real structure of these materials is much more complex, as the active blocks of a few CuO planes alternates with charge reservoir blocks, by which we require a different treatment of the hopping between CuO planes within one active layer and from one active block to the next one is required. At the same time the additional charge reservoir blocks induce a doping into the active layers. As this doping can be regulated quite easily, the corresponding dependence was intensively investigated, for example by Takimoto *et al.* [18] for the anisotropic three-dimensional Hubbard model. In our calculations we consider also a substantial hole doping (cf. table 5.3), as we fix the chemical potential to the van-Hove condition within the $(k_z = 0)$-plane.

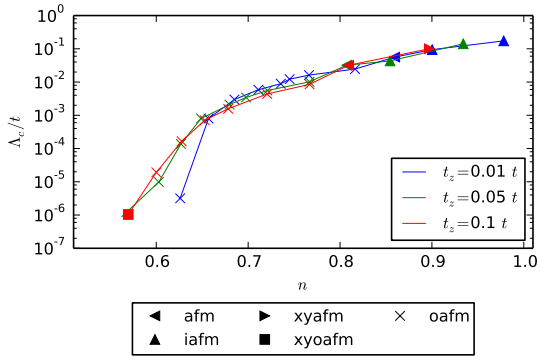

Figure 5.25.: Phase diagram Λ_c versus electron density n for the anisotropic 3D-Hubbard model for $t'_z = t_z \cdot t'$. The symbols are the same as in figures 5.19 and 5.23.

As Takimoto *et al.* fixed $t' = -0.2\,t$ and considered an electron density in the range of $n \in [0.75, 1.0]$ for $t_z \geq 0.1\,t$ the parameters investigated by us were not covered. However, a decrease of the critical scale with a decreasing electron density was observed. Therefore, the resulting d-wave pairing phase with $\Lambda_c = 0.0039\,t$ from our calculations for $t_z = 0.1\,t$ and $n \approx 0.72$ aligns well with their results. Takimoto *et al.* further observed a gradual suppression of the d-wave pairing phase in the T_c–n-phase diagram when t_z is increased. To compare our results with this observation, we compare the resulting phases for different t_z and t' parameters according to the corresponding electron density displayed in table 5.3 (see fig. 5.25). This reveals a slight reduction of the critical scale for d-wave pairing regime when t_z is increased similar to the observations of Takimoto *et al.*. Further, the range of electron densities for which pairing occurs is shifted to larger values for smaller t_z values, but has a similar width. Thus, we assume that the pairing tendency can be stabilised by implying the van-Hove condition in the (k_z=0)-plane or by increasing the anisotropy, that is decreasing t_z.

However, as the parameters describing the mobility of electrons within on sheet of active layers of a HTS (i.e. t and t' in our case) are quantities depending on the materials in the active layer, they can not easily be modified. In contrast, the electron density can easily be varied, such that additional investigations on the doping away from the van-Hove filling are of interest. Moreover, the breakdown of the two-dimensional phase diagram between $t_z = 0.1\,t$ and $t_z = 0.5\,t$ should be in the scope of further investigations.

6. Conclusion and Outlook

6.1. Conclusion

Unconventional and high-temperature superconductivity as observed in copper- and iron-based superconductors and, lately, also in nickelates are among the most important topics in current condensed matter research. The majority of the materials under study are quasi two-dimensional, and therefore the investigations regarding the mechanisms of superconductivity in these materials is often performed in two-dimensional models. As a competition between different spin- and charge-density phases, magnetic orderings and superconductivity was observed in these materials, all the different possible fluctuations have to be treated in an unbiased way. Such an unbiased approach is the Truncated Unity Functional Renormalisation Group (TUFRG), which has already successfully been applied to two-dimensional models. Yet, for a more realistic description and for conceivable other interesting questions, I extended this approach to work in three dimensions. In this way, the influence of the three-dimensionality on the magnetic and on the superconducting phases which was observed in the two-dimensional model was considered by including a weak electron hopping in the direction perpendicular to the two-dimensional planes.

After introducing the required nomenclature and the fundamental theory in chapter 2 and the many-particle Green's functions in section 3.1, I proved some elementary properties of these many-particle Green's functions, which are exploited to simplify the numerical calculations significantly. In section 3.2 the perturbation theory for temperature Green's functions as well as its representation in terms of universal Feynman diagrams were derived, providing the definition of connected Green's functions and of effective actions. Based on the results I provide a short overview on different well established approaches to correlation effects which are based on the perturbation theory: the set of Hedin equations with the GW-approximation and the Parquet approach, which allow the calculation of an effective action. This is the basis for a comparison of perturbation approaches with the functional renormalisation group (FRG) which is derived in a later section of this thesis.

In section 3.3 fermion bilinears were introduced as generalisations of local density- and spin-operators which is barely found in literature. The susceptibilities which result from their expectation values were discussed and related to the Green's functions, so that a simple form for their calculation is obtained based on the effective action.

In section 3.4 generating functionals for full and connected Green's functions were introduced, from which Green's functions, effective interactions and susceptibilities can be derived. These functionals provide an alternative way of deriving perturbation expansions in comparison to section 3.2 for the corresponding objects. The generating functionals for effective interactions and susceptibilities are used in section 3.5 to obtain the hierarchy of flow equations for many fermion-interactions as well as for fermion-boson interactions and susceptibilities (see thm. 3.21) as central result of this section. In contrast to previous derivations based on Nambu fields, I displayed one based on Grassmann variables revealing a more intuitive insight into the structure of the field expansions. In subsection 3.5.3 the FRG equations were compared to the Parquet equations, as the structure of the corresponding equations is similar. Contrary to this similar structure, this analysis reveals that the Parquet equations already contain contributions of interactions of higher order which are typically neglected in FRG calculations. Further, I presented a spin-symmetric version of the flow-equations as well as their Fourier transformed

form in momentum- and in frequency-space. Based on the characteristic momentum structure of these equations I introduced a natural parametrisation of the different contributions to the flow equations. These are the basis of the TUFRG approach introduced in section 3.6, which provides an efficient approximative parametrisation of the effective fermion interactions. As I proved co-working with Eckhardt and Schober in [113], this approach can directly be transferred to the Parquet equations, which therefore and for the sake of brevity is not presented in this thesis.

The central part of this thesis is the development of a high performance implementation of the (TU)FRG equations as described in chapter 4. Here, I presented considerations concerning the simulation of multi-orbital systems, which require the representation in a natural basis to exploit point group symmetries of the system. Using a highly efficient projection routine, I was able to achieve a scaling with respect to the number of form-factors which outperforms the theoretical expectation. Further, the scalability of the final implementation, which exploits all the levels of parallelisation revealed an almost perfect scaling up to 256 nodes. This code was applied to the Hubbard model in two and three dimensions in chapter 5.

First, the two-dimensional Hubbard model was reinvestigated in section 5.2. On the one hand it verifies the correctness of the implementation and on the other hand it shows the convergence of the TUFRG approach to the same results of a calculation treating the full interaction when calculating the t-t'-phase diagram at van-Hove filling. In section 5.3 I investigated the isotropic three-dimensional Hubbard model by applying the TUFRG. This revealed a qualitatively good agreement of the critical scale indicating a phase transition to an antiferromagnetic ground state obtained by our TUFRG calculation with the corresponding Néel temperature obtained by other approaches. Thus the TUFRG is a very efficient tool for the investigation of corresponding systems. When I applied it to the three-dimensional Hubbard model with an increasing hole doping, the antiferromagnetic ground state with a (π, π, π) ordering vector first becomes incommensurate, then turns into a $d_{x^2-y^2}$-superconducting phase and finally transits to a planar antiferromagnetic phase with a $(\pi, \pi, 0)$-ordering vector.

The final and central part of the section on results was devoted to the influence of orbital overlap in the direction perpendicular to the square-plane on the corresponding phase diagram in section 5.4, which can also be regarded as the transition from two to three dimensions. For a comparison of the corresponding phase diagram with the two-dimensional one, the chemical potential was chosen such that the Fermi-surface in the xy-plane resembles the two-dimensional one. For a weak to an intermediate hopping in the z-direction, the shape of the phase diagram and the appearing phases resemble the two-dimensional one, while an increase of the mobility in z-direction reduces the critical scales, in good agreement with the expectations. In addition, strong p-wave pairing fluctuations were found in the ferromagnetic regime, that is for large $-t'$-values. A corresponding superconducting phase may, therefore, be found for a specific choice of parameters.

Although the Hubbard model investigated in this thesis was significantly simplified, it supported the previous approaches which used a two-dimensional model to describe superconductivity in copper- and in iron-based superconductors, as the mobility in the z-direction in those materials is known to be weak. Furthermore, our results support the assumption that the superconducting phase transition is driven by antiferromagnetic fluctuations, which is in good agreement with reference [150].

6.2. Outlook

The implementation presented in this thesis provides the basis for a flexible, modular and therefore easily extendible FRG code which is supposed to be openly accessible and shared by different groups working on FRG methods. The results presented in this thesis are based on the static two-fermion interaction obtained by the TUFRG approach at $T = 0$. A natural extension of the code evidently is the inclusion of the frequency dependence of the interaction and of the self-energy effects. This has previously been done in the scope of the exchange parametrisation [114], which led to a significant increase of the critical scale in the two-dimensional Hubbard model. In the same setting, although it is numerically significantly more demanding, a treatment of the system at finite temperatures is desirable, as this offers a quantitative comparison to critical temperatures obtained by other approaches for correlated systems. Such a finite temperature approach with its own frequency parametrisation [115] has recently been combined with the TUFRG approach and with the multi-loop extension of the FRG equations [66, 169]. This approach appears to fulfil the Mermin-Wagner theorem in two dimensions, but at the same time only provides an mediocre scalability, so that an extension of the code, which is presented within this thesis, to include the mentioned features is of great interest while maintaining the numerical efficiency. A recently suggested alternative parametrisation in terms of frequencies may lead to further computational improvements of the calculations [171]. In this way realistic three-dimensional calculations of correlation effects become possible.

In the approaches mentioned above, the (TU)FRG still comprises the problem, that it runs into a divergence when the critical scale or the transition temperature is reached. In order to obtain the correct ground state and reveal a simultaneous existence of different phases it is, therefore, of interest to overcome this limitation. This can be achieved by including the bosonic terms in the fields which result from the corresponding Hubbard-Stratonovich transformation [140, 172]. However, these extensions are computationally demanding and will, in most cases, provide only additional information on the ground state of the materials.

Besides methodological improvements of the recent code, it provides a powerful tool to be applied to other models of correlated systems. While the Hubbard model in its spin-symmetric form only depends on one band, a calculation of multi-band models and of spinful systems is in reach due to the advantageous scaling, as the truncated unity approach is also applicable in these cases [111]. Therefore, a full TUFRG investigation of the Rashba model with a spin-splitting [173, 174, 175] or a multi-orbital model of cuprate-, iron- or nickel-based superconductors [145, 176] is possible.

Finally, realistic materials like cuprates (e.g. La_2CuO_4), iron chalcogenides (e.g. FeSe) or pnictides and even nickelates (e.g. $Nd_{0.8}Sr_{0.2}NiO]_2$) are in the reach of calculations with the FRG. While the basic mechanisms of superconductivity and of magnetism can well be studied by treating corresponding models, realistic materials are significantly more complex. As density functional theory (DFT) calculations are by now a standard approach to study a condensed matter system starting from *ab initio*, it provides a reasonable starting point for further calculations. However, as the resulting system obtained from DFT is still too large for (TU)FRG calculations, it is reasonable to treat most degrees of freedom with the random phase approximation and the remaining ones of low energy with the presented (TU)FRG. This could also be combined with a preceding GW-calculation or a dynamic mean field theory-calculation [109] which provide a correlated starting point for the FRG approach. In order to obtain the full description of a condensed matter system the (TU)FRG thus takes the efficient interaction of all the other bands with the target bands and with a Green's function which is close to the actual one as starting parameter.

Appendix

A. Details of some Derivations

In this part of the appendix we provide details of some derivations we used in chapter 3.

A.1. Derivation of Propagator Flow Equations

A.1.1. Spinful Case

In the proof of corollary 3.31 only the derivation of the flow equation for the pairing channel in the spinful case was shown. The derivation of the flow equation for the direct channel is based on the definition of $\mathcal{T}_{\mathrm{d}}^{\Lambda}$ according to equation (3.28) in theorem 3.28 and on the corresponding projection operation $\mathbb{P}_{\mathrm{D}}$ defined in definition 44 and exemplified in equation (3.348). This leads to

$$\begin{aligned}\dot{D}_{mn}(\boldsymbol{u}) = \mathbb{P}_{\mathrm{D}}[\mathcal{T}^{\mathrm{d}}]_{mn}(\boldsymbol{u}) = \int \mathrm{d}\boldsymbol{k} \int \mathrm{d}\boldsymbol{k}_u \int \mathrm{d}\boldsymbol{k}'_u \\ \gamma^{(4,0)}(\boldsymbol{k}_u, \boldsymbol{k}-\boldsymbol{u}; \boldsymbol{k}_u-\boldsymbol{u}, \boldsymbol{k})\, L^{\mathrm{ph},\Lambda}(\boldsymbol{k}, \boldsymbol{k}-\boldsymbol{u})\, \gamma^{(4,0)}(\boldsymbol{k}, \boldsymbol{k}'_u-\boldsymbol{u}; \boldsymbol{k}-\boldsymbol{u}, \boldsymbol{k}'_u) f_m(\boldsymbol{k}_u) f_n^*(\boldsymbol{k}'_u)\end{aligned} \tag{A.1}$$

and the insertion of unities leads to the derivation

$$\begin{aligned}\dot{D}_{mn}(\boldsymbol{u}) &= \int \mathrm{d}\boldsymbol{k} \int \mathrm{d}\boldsymbol{k}' \int \mathrm{d}\boldsymbol{k}'' \int \mathrm{d}\boldsymbol{k}_u \int \mathrm{d}\boldsymbol{k}'_u\, \gamma^{(4,0)}(\boldsymbol{k}_u, \boldsymbol{k}-\boldsymbol{u}; \boldsymbol{k}_u-\boldsymbol{u}, \boldsymbol{k}) \\ &\qquad \times \delta(\boldsymbol{k}-\boldsymbol{k}')\, L^{\mathrm{ph},\Lambda}(\boldsymbol{k}', \boldsymbol{k}'-\boldsymbol{u})\, \delta(\boldsymbol{k}'-\boldsymbol{k}'')\, \gamma^{(4,0)}(\boldsymbol{k}'', \boldsymbol{k}'_u-\boldsymbol{u}; \boldsymbol{k}''-\boldsymbol{u}, \boldsymbol{k}'_u)\, f_m(\boldsymbol{k}_u)\, f_n^*(\boldsymbol{k}'_u) \\ &= \int \mathrm{d}\boldsymbol{k} \int \mathrm{d}\boldsymbol{k}' \int \mathrm{d}\boldsymbol{k}'' \int \mathrm{d}\boldsymbol{k}_u \int \mathrm{d}\boldsymbol{k}'_u \sum_{i,j} f_m(\boldsymbol{k}_u) \gamma^{(4,0)}(\boldsymbol{k}_u, \boldsymbol{k}-\boldsymbol{u}; \boldsymbol{k}_u-\boldsymbol{u}, \boldsymbol{k}) f_i^*(\boldsymbol{k}) \\ &\qquad \times f_i(\boldsymbol{k}')\, L^{\mathrm{ph},\Lambda}(\boldsymbol{k}', \boldsymbol{k}'-\boldsymbol{u})\, f_j^*(\boldsymbol{k}')\, f_j(\boldsymbol{k}'')\, \gamma^{(4,0)}(\boldsymbol{k}'', \boldsymbol{k}'_u-\boldsymbol{u}; \boldsymbol{k}''-\boldsymbol{u}, \boldsymbol{k}'_u)\, f_n^*(\boldsymbol{k}'_u) \\ &= \sum_{i,j} \gamma_{mi}^{(4,0)\mathrm{D},\Lambda}(\boldsymbol{u})\, L_{ij}^{\mathrm{ph},\Lambda}(\boldsymbol{u})\, \gamma_{jn}^{(4,0)\mathrm{D},\Lambda}(\boldsymbol{u}),\end{aligned} \tag{A.2}$$

in which we identified the corresponding projected vertex and the dual propagator. For the crossing channel we proceed analogously with $\mathcal{T}_{\mathrm{c}}^{\Lambda}$ and $\mathbb{P}_{\mathrm{C}}$ leading to

$$\begin{aligned}\dot{C}_{mn}(\boldsymbol{t}, o_1o_2, o_3o_4) = \mathbb{P}_{\mathrm{C}}[\mathcal{T}_{\mathrm{c}}]_{mn}(\boldsymbol{t}, o_1o_2, o_3o_4) = -\int \mathrm{d}\boldsymbol{k} \int \mathrm{d}\boldsymbol{k}_t \int \mathrm{d}\boldsymbol{k}'_t \sum_{o'_1o'_2o'_3o'_4} f_m(\boldsymbol{k}_t) \\ \times \gamma_{o_1o'_2, o_4o'_3}^{(4,0)\Lambda}(\boldsymbol{k}_t, \boldsymbol{k}-\boldsymbol{t}; \boldsymbol{k}_t-\boldsymbol{t}, \boldsymbol{k})\, L_{o'_1o'_3, o'_2o'_4}^{\mathrm{ph},\Lambda}(\boldsymbol{k}, \boldsymbol{k}-\boldsymbol{t})\, \gamma_{o'_4o_2, o'_1o_3}^{(4,0)\Lambda}(\boldsymbol{k}, \boldsymbol{k}'_t-\boldsymbol{t}; \boldsymbol{k}-\boldsymbol{t}, \boldsymbol{k}'_t)\, f_n^*(\boldsymbol{k}'_t).\end{aligned} \tag{A.3}$$

When we insert the unities of the form-factor basis into this expression as follows, we get

$$\begin{aligned}\dot{C}_{mn}(\boldsymbol{t}, o_1o_2, o_3o_4) = &-\int \mathrm{d}\boldsymbol{k} \int \mathrm{d}\boldsymbol{k}' \int \mathrm{d}\boldsymbol{k}'' \int \mathrm{d}\boldsymbol{k}_t \int \mathrm{d}\boldsymbol{k}_t' \sum_{o_1'o_2'o_3'o_4'} \\ &f_m(\boldsymbol{k}_t)\, \gamma^{(4,0)\Lambda}_{o_1o_4',o_4o_1'}(\boldsymbol{k}_t, \boldsymbol{k}-\boldsymbol{t}; \boldsymbol{k}_t-\boldsymbol{t}, \boldsymbol{k})\, \delta(\boldsymbol{k}-\boldsymbol{k}')\, L^{\mathrm{ph},\Lambda}_{o_1'o_3',o_2'o_4'}(\boldsymbol{k}', \boldsymbol{k}'-\boldsymbol{t}) \\ &\times \delta(\boldsymbol{k}'-\boldsymbol{k}'')\, \gamma^{(4,0)\Lambda}_{o_2'o_2,o_3'o_3}(\boldsymbol{k}'', \boldsymbol{k}_t'-\boldsymbol{t}; \boldsymbol{k}''-\boldsymbol{t}, \boldsymbol{k}_t')\, f_n^*(\boldsymbol{k}_t') \\ = &-\int \mathrm{d}\boldsymbol{k} \int \mathrm{d}\boldsymbol{k}' \int \mathrm{d}\boldsymbol{k}'' \int \mathrm{d}\boldsymbol{k}_t \int \mathrm{d}\boldsymbol{k}_t' \sum_{o_1'o_2'o_3'o_4'} \sum_{i,j} \\ &f_m(\boldsymbol{k}_t)\, \gamma^{(4,0)\Lambda}_{o_1o_4',o_4o_1'}(\boldsymbol{k}_t, \boldsymbol{k}-\boldsymbol{t}; \boldsymbol{k}_t-\boldsymbol{t}, \boldsymbol{k})\, f_i^*(\boldsymbol{k}) \\ &\times f_i(\boldsymbol{k}')\, L^{\mathrm{ph},\Lambda}_{o_1'o_3',o_2'o_4'}(\boldsymbol{k}', \boldsymbol{k}'-\boldsymbol{t})\, f_j^*(\boldsymbol{k}') \\ &\times f_j(\boldsymbol{k}'')\, \gamma^{(4,0)\Lambda}_{o_2'o_2,o_3'o_3}(\boldsymbol{k}'', \boldsymbol{k}_t'-\boldsymbol{t}; \boldsymbol{k}''-\boldsymbol{t}, \boldsymbol{k}_t')\, f_n^*(\boldsymbol{k}_t'),\end{aligned} \tag{A.4}$$

and we observe that this expression does not explicitly fit the definition of the projection of a vertex to the crossing channel. This problem can, however, be overcome by exploiting the symmetry $\gamma^{(4,0)}(1,2;3,4) = -\gamma^{(4,0)}(1,2;4,3)$ (cf. thm. 3.17.1), which changes the order of the orbital indices, resulting in

$$\begin{aligned}\dot{C}_{mn}(\boldsymbol{t}, o_1o_2, o_3o_4) = &-\int \mathrm{d}\boldsymbol{k} \int \mathrm{d}\boldsymbol{k}' \int \mathrm{d}\boldsymbol{k}'' \int \mathrm{d}\boldsymbol{k}_t \int \mathrm{d}\boldsymbol{k}_t' \sum_{o_1'o_2'o_3'o_4'} \sum_{i,j} \\ &f_m(\boldsymbol{k}_t)\, \gamma^{(4,0)\Lambda}_{o_1o_1',o_1'o_4}(\boldsymbol{k}_t, \boldsymbol{k}-\boldsymbol{t}; \boldsymbol{k}, \boldsymbol{k}_t-\boldsymbol{t})\, f_i^*(\boldsymbol{k}) \\ &\times f_i(\boldsymbol{k}')\, L^{\mathrm{ph},\Lambda}_{o_1'o_3',o_2'o_4'}(\boldsymbol{k}', \boldsymbol{k}'-\boldsymbol{t})\, f_j^*(\boldsymbol{k}') \\ &\times f_j(\boldsymbol{k}'')\, \gamma^{(4,0)\Lambda}_{o_2'o_2,o_3o_3'}(\boldsymbol{k}'', \boldsymbol{k}_t'-\boldsymbol{t}; \boldsymbol{k}_t', \boldsymbol{k}''-\boldsymbol{t})\, f_n^*(\boldsymbol{k}_t') \\ = &-\sum_{i,j} \gamma^{(4,0)\mathrm{C},\Lambda}_{mi}(\boldsymbol{t}; o_1o_4', o_4o_1')\, L^{\mathrm{ph},\Lambda}_{ij}(\boldsymbol{t})\, \gamma^{(4,0)\mathrm{C},\Lambda}_{jn}(\boldsymbol{t}; o_2'o_2, o_3'o_3),\end{aligned} \tag{A.5}$$

which finally equals the corresponding equation in theorem 3.31.

A.1.2. SU(2)-Symmetric Case

For the SU(2)-symmetric case we only showed the derivation of the flow equation for the direct channel (see thm. 3.31). The projection of $\bar{\mathcal{T}}$ (see eq. (3.330) in theorem 3.29) to the pairing channel as defined in definition 44 leads to

$$\begin{aligned}\dot{P}_{mn}(\boldsymbol{s}) = \mathbb{P}[\bar{\mathcal{T}}_{\mathrm{P}}]_{mn}(\boldsymbol{s}) = &\int \mathrm{d}\boldsymbol{k} \int \mathrm{d}\boldsymbol{k}_s \int \mathrm{d}\boldsymbol{k}_s' \\ &V^{\Lambda}(\boldsymbol{k}_s, \boldsymbol{s}-\boldsymbol{k}_s; \boldsymbol{k}, \boldsymbol{s}-\boldsymbol{k})\, L^{\mathrm{pp},\Lambda}(\boldsymbol{k}, \boldsymbol{s}-\boldsymbol{k})\, V^{\Lambda}(\boldsymbol{k}, \boldsymbol{s}-\boldsymbol{k}; \boldsymbol{k}_s', \boldsymbol{s}-\boldsymbol{k}_s')\, f_m(\boldsymbol{k}_s)\, f_n^*(\boldsymbol{k}_s').\end{aligned} \tag{A.6}$$

The insertion of unities then results in

$$\begin{aligned}\dot{P}_{mn}(\boldsymbol{s}) &= \int \mathrm{d}\boldsymbol{k} \int \mathrm{d}\boldsymbol{k}' \int \mathrm{d}\boldsymbol{k}'' \int \mathrm{d}\boldsymbol{k}_s \int \mathrm{d}\boldsymbol{k}'_s \, V^{\Lambda}(\boldsymbol{k}_s, \boldsymbol{s}-\boldsymbol{k}_s; \boldsymbol{k}, \boldsymbol{s}-\boldsymbol{k}) \\ &\qquad \times \delta(\boldsymbol{k}-\boldsymbol{k}') \, L^{\mathrm{pp},\Lambda}(\boldsymbol{k}', \boldsymbol{s}-\boldsymbol{k}') \, \delta(\boldsymbol{k}'-\boldsymbol{k}'') \, V^{\Lambda}(\boldsymbol{k}'', \boldsymbol{s}-\boldsymbol{k}''; \boldsymbol{k}'_s, \boldsymbol{s}-\boldsymbol{k}'_s) \, f_m(\boldsymbol{k}_s) \, f_n^*(\boldsymbol{k}'_s) \\ &= \int \mathrm{d}\boldsymbol{k} \int \mathrm{d}\boldsymbol{k}' \int \mathrm{d}\boldsymbol{k}'' \int \mathrm{d}\boldsymbol{k}_s \int \mathrm{d}\boldsymbol{k}'_s \sum_{i,j} f_m(\boldsymbol{k}_s) \, V^{\Lambda}(\boldsymbol{k}_s, \boldsymbol{s}-\boldsymbol{k}_s; \boldsymbol{k}, \boldsymbol{s}-\boldsymbol{k}) \, f_i^*(\boldsymbol{k}) \\ &\qquad \times f_i(\boldsymbol{k}') \, L^{\mathrm{pp},\Lambda}(\boldsymbol{k}', \boldsymbol{s}-\boldsymbol{k}') \, f_j^*(\boldsymbol{k}') \, f_j(\boldsymbol{k}'') \, V^{\Lambda}(\boldsymbol{k}'', \boldsymbol{s}-\boldsymbol{k}''; \boldsymbol{k}'_s, \boldsymbol{s}-\boldsymbol{k}'_s) \, f_n^*(\boldsymbol{k}'_s) \\ &= \sum_{ij} V_{mi}^{\mathrm{P},\Lambda}(\boldsymbol{s}) L_{ij}^{\mathrm{pp},\Lambda}(\boldsymbol{s}) V_{jn}^{\mathrm{P},\Lambda}(\boldsymbol{s}),\end{aligned} \tag{A.7}$$

which is the flow equation given in equation (3.369). For the crossing channel we proceed analogously, so that the projection of $\bar{\mathcal{T}}^{\mathrm{c}}$ to the form-factors by the operation of $\mathbb{P}_{\mathrm{C}}$ results in

$$\begin{aligned}\dot{C}_{mn}(\boldsymbol{t}) = \mathbb{P}_{\mathrm{C}}[\bar{\mathcal{T}}^{\mathrm{c}}]_{mn}(\boldsymbol{t}) = -\int \mathrm{d}\boldsymbol{k} \int \mathrm{d}\boldsymbol{k}_t \int \mathrm{d}\boldsymbol{k}'_t \, V^{\Lambda}(\boldsymbol{k}_t, \boldsymbol{k}-\boldsymbol{t}; \boldsymbol{k}, \boldsymbol{k}_t-\boldsymbol{t}) \\ L^{\mathrm{ph},\Lambda}(\boldsymbol{k}, \boldsymbol{k}-\boldsymbol{t}) \, V^{\Lambda}(\boldsymbol{k}, \boldsymbol{k}'_t-\boldsymbol{t}; \boldsymbol{k}'_t, \boldsymbol{k}-\boldsymbol{t}) \, f_m(\boldsymbol{k}_t) \, f_n^*(\boldsymbol{k}'_t).\end{aligned} \tag{A.8}$$

The insertion of unities turns this expression to

$$\begin{aligned}\dot{C}_{mn}(\boldsymbol{t}) &= -\int \mathrm{d}\boldsymbol{k} \int \mathrm{d}\boldsymbol{k}' \int \mathrm{d}\boldsymbol{k}'' \int \mathrm{d}\boldsymbol{k}_t \int \mathrm{d}\boldsymbol{k}'_t \, V^{\Lambda}(\boldsymbol{k}_t, \boldsymbol{k}-\boldsymbol{t}; \boldsymbol{k}, \boldsymbol{k}_t-\boldsymbol{t}) \, \delta(\boldsymbol{k}-\boldsymbol{k}') \\ &\qquad \times L^{\mathrm{ph},\Lambda}(\boldsymbol{k}', \boldsymbol{k}'-\boldsymbol{t}) \delta(\boldsymbol{k}'-\boldsymbol{k}'') \, V^{\Lambda}(\boldsymbol{k}, \boldsymbol{k}'_t-\boldsymbol{t}; \boldsymbol{k}'_t, \boldsymbol{k}-\boldsymbol{t}) \, f_m(\boldsymbol{k}_t) \, f_n^*(\boldsymbol{k}'_t) \\ &= -\int \mathrm{d}\boldsymbol{k} \int \mathrm{d}\boldsymbol{k}' \int \mathrm{d}\boldsymbol{k}'' \int \mathrm{d}\boldsymbol{k}_t \int \mathrm{d}\boldsymbol{k}'_t \sum_{i,j} f_m(\boldsymbol{k}_t) \, V^{\Lambda}(\boldsymbol{k}_t, \boldsymbol{k}-\boldsymbol{t}; \boldsymbol{k}, \boldsymbol{k}_t-\boldsymbol{t}) \, f_i^*(\boldsymbol{k}) \\ &\qquad \times f_i(\boldsymbol{k}') \, L^{\mathrm{ph},\Lambda}(\boldsymbol{k}', \boldsymbol{k}'-\boldsymbol{t}) \, f_j^*(\boldsymbol{k}') \, f_j(\boldsymbol{k}'') \, V^{\Lambda}(\boldsymbol{k}, \boldsymbol{k}'_t-\boldsymbol{t}; \boldsymbol{k}'_t, \boldsymbol{k}-\boldsymbol{t}) \, f_n^*(\boldsymbol{k}'_t) \\ &= -\sum_{ij} V_{mi}^{\mathrm{C},\Lambda}(\boldsymbol{t}) \, L_{ij}^{\mathrm{ph},\Lambda}(\boldsymbol{t}) \, V_{jn}^{\mathrm{C},\Lambda}(\boldsymbol{t}),\end{aligned} \tag{A.9}$$

which equals the flow equation given in equation (3.371).

A.2. Channel to Channel Projections

In order to complete the proof of corollary 3.32, in which only the projection from channel D to channel P was explicitly shown, we now consider all the other projections between the channels. We reconsider that these projections (defined in def. 44) are analogous for the SU(2)-symmetric propagators $\bar{P}$, $\bar{D}$ and $\bar{C}$ and for the spinful two-particle propagators P, D and C, as only the momentum dependencies are affected. In the following we, therefore, only show the projections for the latter ones and neglect orbital and frequency indices, as they are not affected by the projections.

The definition of the projection of the full vertex to the P-channel and the one of the back-projection from the C-channel to the full vertex in which the C-channel momenta are expressed by the P-channel ones lead to

$$\mathbb{P}_{\mathrm{P}}[C]_{mn}(\boldsymbol{s}) = \int \mathrm{d}\boldsymbol{k}_s \int \mathrm{d}\boldsymbol{k}'_s \, f_m(\boldsymbol{k}_s) \, f_n^*(\boldsymbol{k}'_s) \sum_{i,j} f_i^*(\boldsymbol{k}_s) \, f_j(\boldsymbol{k}'_s) \, C_{ij}(\boldsymbol{k}_s + \boldsymbol{k}'_s - \boldsymbol{s}), \tag{A.10}$$

which is the first line of the corresponding expression (cf. eq. (3.376)). The second line of equation (3.376) is obtained by Fourier transformations of the form-factors into momentum space as

$$\begin{aligned}
\mathbb{P}_{\mathrm{P}}[C]_{mn}(\boldsymbol{s}) = \int \mathrm{d}\boldsymbol{k}_s \int \mathrm{d}\boldsymbol{k}'_s\, f_m(\boldsymbol{k}_s)\, f_n^*(\boldsymbol{k}'_s) \sum_{i,j} \sum_{\boldsymbol{R}_1,\boldsymbol{R}_2,\boldsymbol{R}_3} \\
e^{i\boldsymbol{k}_s\cdot\boldsymbol{R}_1}\, f_i^*(\boldsymbol{R}_1)\, e^{-i\boldsymbol{k}'_s\cdot\boldsymbol{R}_2}\, f_j(\boldsymbol{R}_2)\, e^{-i(\boldsymbol{k}_s+\boldsymbol{k}'_s-\boldsymbol{s})\cdot\boldsymbol{R}_3}\, C_{ij}(\boldsymbol{R}_3) \\
= \sum_{i,j} \sum_{\boldsymbol{R}_1,\boldsymbol{R}_2,\boldsymbol{R}_3} \int \mathrm{d}\boldsymbol{k}_s \int \mathrm{d}\boldsymbol{k}'_s\, f_m(\boldsymbol{k}_s)\, e^{i\boldsymbol{k}_s\cdot(\boldsymbol{R}_1-\boldsymbol{R}_3)}\, f_n^*(\boldsymbol{k}'_s)\, e^{-i\boldsymbol{k}'_s\cdot(\boldsymbol{R}_2+\boldsymbol{R}_3)} \\
\times f_i^*(\boldsymbol{R}_1)\, f_j(\boldsymbol{R}_2)\, e^{i\boldsymbol{s}\cdot\boldsymbol{R}_3}\, C_{ij}(\boldsymbol{R}_3) \\
= \sum_{i,j} \sum_{\boldsymbol{R}_1,\boldsymbol{R}_2,\boldsymbol{R}_3} f_m(\boldsymbol{R}_1-\boldsymbol{R}_3)\, f_n^*(\boldsymbol{R}_2+\boldsymbol{R}_3)\, f_i^*(\boldsymbol{R}_1)\, f_j(\boldsymbol{R}_2)\, e^{i\boldsymbol{s}\cdot\boldsymbol{R}_3}\, C_{ij}(\boldsymbol{R}_3).
\end{aligned} \tag{A.11}$$

For the projection of the P-channel to the D-channel we proceed analogously with the momentum arguments expressed in the variables of the D-channel. The definitions 44.1 and 44.2 directly lead to

$$\mathbb{P}_{\mathrm{D}}[P]_{mn}(\boldsymbol{u}) = \int \mathrm{d}\boldsymbol{k}_u \int \mathrm{d}\boldsymbol{k}'_u\, f_m(\boldsymbol{k}_u)\, f_n^*(\boldsymbol{k}'_u) \sum_{i,j} f_i^*(\boldsymbol{k}_u)\, f_j(\boldsymbol{k}_u-\boldsymbol{u})\, P_{ij}(\boldsymbol{k}_u+\boldsymbol{k}'_u-\boldsymbol{u}), \tag{A.12}$$

which is the first line in equation (3.377). Again, Fourier transformations lead to

$$\begin{aligned}
\mathbb{P}_{\mathrm{D}}[P]_{mn}(\boldsymbol{u}) = \int \mathrm{d}\boldsymbol{k}_u \int \mathrm{d}\boldsymbol{k}'_u\, f_m(\boldsymbol{k}_u)\, f_n^*(\boldsymbol{k}'_u) \sum_{i,j} \sum_{\boldsymbol{R}_1,\boldsymbol{R}_2,\boldsymbol{R}_3} \\
e^{i\boldsymbol{k}_u\cdot\boldsymbol{R}_1}\, f_i^*(\boldsymbol{R}_1)\, e^{-i(\boldsymbol{k}_u-\boldsymbol{u})\cdot\boldsymbol{R}_2}\, f_j(\boldsymbol{R}_2)\, e^{-i(\boldsymbol{k}_u+\boldsymbol{k}'_u-\boldsymbol{u})\cdot\boldsymbol{R}_3}\, P_{ij}(\boldsymbol{R}_3) \\
= \sum_{i,j} \sum_{\boldsymbol{R}_1,\boldsymbol{R}_2,\boldsymbol{R}_3} \int \mathrm{d}\boldsymbol{k}_u \int \mathrm{d}\boldsymbol{k}'_u\, f_m(\boldsymbol{k}_u)\, e^{i\boldsymbol{k}_u\cdot(\boldsymbol{R}_1-\boldsymbol{R}_2-\boldsymbol{R}_3)}\, f_n^*(\boldsymbol{k}'_u)\, e^{-i\boldsymbol{k}'_u\cdot\boldsymbol{R}_3} \\
\times f_i^*(\boldsymbol{R}_1)\, f_j(\boldsymbol{R}_2)\, e^{i\boldsymbol{u}\cdot(\boldsymbol{R}_2+\boldsymbol{R}_3)}\, P_{ij}(\boldsymbol{R}_3) \\
= \sum_{i,j} \sum_{\boldsymbol{R}_1,\boldsymbol{R}_2,\boldsymbol{R}_3} f_m(\boldsymbol{R}_1-\boldsymbol{R}_2-\boldsymbol{R}_3)\, f_n^*(\boldsymbol{R}_3)\, f_i^*(\boldsymbol{R}_1)\, f_j(\boldsymbol{R}_2)\, e^{i\boldsymbol{u}\cdot(\boldsymbol{R}_2+\boldsymbol{R}_3)}\, P_{ij}(\boldsymbol{R}_3),
\end{aligned} \tag{A.13}$$

which is the second line of equation (3.377).

The projection of the C-channel to the D-channel is treated in the same way, which in the first step results in

$$\mathbb{P}_{\mathrm{D}}[C]_{mn}(\boldsymbol{u}) = \int \mathrm{d}\boldsymbol{k}_u \int \mathrm{d}\boldsymbol{k}'_u\, f_m(\boldsymbol{k}_u)\, f_n^*(\boldsymbol{k}'_u) \sum_{i,j} f_i^*(\boldsymbol{k}_u)\, f_j(\boldsymbol{k}_u-\boldsymbol{u})\, C_{ij}(\boldsymbol{k}_u-\boldsymbol{k}'_u), \tag{A.14}$$

and in the second step, due to Fourier transformations this leads to

$$\begin{aligned}
\mathbb{P}_{\mathrm{D}}[C]_{mn}(\boldsymbol{u}) = \int \mathrm{d}\boldsymbol{k}_u \int \mathrm{d}\boldsymbol{k}'_u\, f_m(\boldsymbol{k}_u)\, f_n^*(\boldsymbol{k}'_u) \sum_{i,j} \sum_{\boldsymbol{R}_1,\boldsymbol{R}_2,\boldsymbol{R}_3} \\
e^{i\boldsymbol{k}_u\cdot\boldsymbol{R}_1}\, f_i^*(\boldsymbol{R}_1)\, e^{-i(\boldsymbol{k}_u-\boldsymbol{u})\cdot\boldsymbol{R}_2}\, f_j(\boldsymbol{R}_2)\, e^{-i(\boldsymbol{k}_u-\boldsymbol{k}'_u)\cdot\boldsymbol{R}_3}\, C_{ij}(\boldsymbol{R}_3) \\
= \sum_{i,j} \sum_{\boldsymbol{R}_1,\boldsymbol{R}_2,\boldsymbol{R}_3} \int \mathrm{d}\boldsymbol{k}_u \int \mathrm{d}\boldsymbol{k}'_u\, f_m(\boldsymbol{k}_u)\, e^{i\boldsymbol{k}_u\cdot(\boldsymbol{R}_1-\boldsymbol{R}_2-\boldsymbol{R}_3)}\, f_n^*(\boldsymbol{k}'_u)\, e^{-i\boldsymbol{k}'_u\cdot(-\boldsymbol{R}_3)} \\
\times f_i^*(\boldsymbol{R}_1)\, f_j(\boldsymbol{R}_2)\, e^{i\boldsymbol{u}\cdot\boldsymbol{R}_2}\, C_{ij}(\boldsymbol{R}_3) \\
= \sum_{i,j} \sum_{\boldsymbol{R}_1,\boldsymbol{R}_2,\boldsymbol{R}_3} f_m(\boldsymbol{R}_1-\boldsymbol{R}_2-\boldsymbol{R}_3)\, f_n^*(-\boldsymbol{R}_3)\, f_i^*(\boldsymbol{R}_1)\, f_j(\boldsymbol{R}_2)\, e^{i\boldsymbol{u}\cdot\boldsymbol{R}_2}\, C_{ij}(\boldsymbol{R}_3),
\end{aligned} \tag{A.15}$$

which are the first and the second line of equation (3.378) in theorem 3.32.

The projections to the C-channel are derived by performing the same steps. The momentum arguments have to be expressed by the arguments of this channel, thus leading to

$$\mathbb{P}_{\mathrm{C}}[P]_{mn}(\boldsymbol{t}) = \int \mathrm{d}\boldsymbol{k}_t \int \mathrm{d}\boldsymbol{k}'_t \, f_m(\boldsymbol{k}_t) \, f_n^*(\boldsymbol{k}'_t) \sum_{i,j} f_i^*(\boldsymbol{k}_t) \, f_j(\boldsymbol{k}'_t) \, P_{ij}(\boldsymbol{k}_t + \boldsymbol{k}'_t - \boldsymbol{t}), \tag{A.16}$$

which is the first line of equation (3.379). The Fourier transformations then lead to

$$\begin{aligned}
\mathbb{P}_{\mathrm{C}}[P]_{mn}(\boldsymbol{t}) &= \int \mathrm{d}\boldsymbol{k}_t \int \mathrm{d}\boldsymbol{k}'_t \, f_m(\boldsymbol{k}_t) \, f_n^*(\boldsymbol{k}'_t) \sum_{i,j} \sum_{\boldsymbol{R}_1,\boldsymbol{R}_2,\boldsymbol{R}_3} \\
&\qquad e^{i\boldsymbol{k}_t\cdot\boldsymbol{R}_1} \, f_i^*(\boldsymbol{R}_1) \, e^{-i\boldsymbol{k}'_t\cdot\boldsymbol{R}_2} \, f_j(\boldsymbol{R}_2) \, e^{-i(\boldsymbol{k}_t+\boldsymbol{k}'_t-\boldsymbol{t})\cdot\boldsymbol{R}_3} \, P_{ij}(\boldsymbol{R}_3) \\
&= \sum_{i,j} \sum_{\boldsymbol{R}_1,\boldsymbol{R}_2,\boldsymbol{R}_3} \int \mathrm{d}\boldsymbol{k}_t \int \mathrm{d}\boldsymbol{k}'_t \, f_m(\boldsymbol{k}_t) \, e^{i\boldsymbol{k}_t\cdot(\boldsymbol{R}_1-\boldsymbol{R}_3)} \, f_n^*(\boldsymbol{k}'_t) \, e^{-i\boldsymbol{k}'_t\cdot(\boldsymbol{R}_2+\boldsymbol{R}_3)} \\
&\qquad \times f_i^*(\boldsymbol{R}_1) \, f_j(\boldsymbol{R}_2) \, e^{i\boldsymbol{t}\cdot\boldsymbol{R}_3} \, P_{ij}(\boldsymbol{R}_3) \\
&= \sum_{i,j} \sum_{\boldsymbol{R}_1,\boldsymbol{R}_2,\boldsymbol{R}_3} f_m(\boldsymbol{R}_1 - \boldsymbol{R}_3) \, f_n^*(\boldsymbol{R}_2 + \boldsymbol{R}_3) \, f_i^*(\boldsymbol{R}_1) \, f_j(\boldsymbol{R}_2) \, e^{i\boldsymbol{t}\cdot\boldsymbol{R}_3} \, P_{ij}(\boldsymbol{R}_3),
\end{aligned} \tag{A.17}$$

which is the second line of equation (3.379).

Finally, the projection from channel D to channel C is obtained by performing the same steps as before, resulting in

$$\mathbb{P}_{\mathrm{C}}[D]_{mn}(\boldsymbol{t}) = \int \mathrm{d}\boldsymbol{k}_t \int \mathrm{d}\boldsymbol{k}'_t \, f_m(\boldsymbol{k}_t) \, f_n^*(\boldsymbol{k}'_t) \sum_{i,j} f_i^*(\boldsymbol{k}_t) \, f_j(\boldsymbol{k}_t - \boldsymbol{t}) \, D_{ij}(\boldsymbol{k}_t - \boldsymbol{k}'_t). \tag{A.18}$$

This expression is the first line of equation (3.380), while the second one is obtained by its Fourier transformation according to

$$\begin{aligned}
\mathbb{P}_{\mathrm{C}}[D]_{mn}(\boldsymbol{t}) &= \int \mathrm{d}\boldsymbol{k}_t \int \mathrm{d}\boldsymbol{k}'_t \, f_m(\boldsymbol{k}_t) \, f_n^*(\boldsymbol{k}'_t) \sum_{i,j} \sum_{\boldsymbol{R}_1,\boldsymbol{R}_2,\boldsymbol{R}_3} \\
&\qquad e^{i\boldsymbol{k}_t\cdot\boldsymbol{R}_1} \, f_i^*(\boldsymbol{R}_1) \, e^{-i(\boldsymbol{k}_t-\boldsymbol{t})\cdot\boldsymbol{R}_2} \, f_j(\boldsymbol{R}_2) \, e^{-i(\boldsymbol{k}_t-\boldsymbol{k}'_t)\cdot\boldsymbol{R}_3} \, D_{ij}(\boldsymbol{R}_3) \\
&= \sum_{i,j} \sum_{\boldsymbol{R}_1,\boldsymbol{R}_2,\boldsymbol{R}_3} \int \mathrm{d}\boldsymbol{k}_t \int \mathrm{d}\boldsymbol{k}'_t \, f_m(\boldsymbol{k}_t) \, e^{i\boldsymbol{k}_t\cdot(\boldsymbol{R}_1-\boldsymbol{R}_2-\boldsymbol{R}_3)} \, f_n^*(\boldsymbol{k}'_t) \, e^{-i\boldsymbol{k}'_t\cdot(-\boldsymbol{R}_3)} \\
&\qquad \times f_i^*(\boldsymbol{R}_1) \, f_j(\boldsymbol{R}_2) \, e^{i\boldsymbol{t}\cdot\boldsymbol{R}_2} \, D_{ij}(\boldsymbol{R}_3) \\
&= \sum_{i,j} \sum_{\boldsymbol{R}_1,\boldsymbol{R}_2,\boldsymbol{R}_3} f_m(\boldsymbol{R}_1 - \boldsymbol{R}_2 - \boldsymbol{R}_3) \, f_n^*(-\boldsymbol{R}_3) \, f_i^*(\boldsymbol{R}_1) \, f_j(\boldsymbol{R}_2) \, e^{i\boldsymbol{t}\cdot\boldsymbol{R}_2} \, D_{ij}(\boldsymbol{R}_3).
\end{aligned} \tag{A.19}$$

These derivations now complete the proof of theorem 3.32.

B. Evaluation of Matsubara Sums

We consider the Matsubara sum over the free Green's function with ω-cut-off

$$\frac{\mathrm{d}}{\mathrm{d}\Lambda}G^{\Lambda} = \frac{1}{\beta}\frac{\mathrm{d}}{\mathrm{d}\Lambda}\sum_{\omega_n}\frac{\omega_n^2}{\omega_n^2+\Lambda^2}\frac{1}{i\omega_n-\varepsilon(\boldsymbol{k})}. \tag{B.1}$$

As the Fermi-function n_F has poles at exactly these ω_n, the sum can be rewritten according to the residue theorem as

$$\frac{\mathrm{d}}{\mathrm{d}\Lambda}G^{\Lambda} = \frac{\mathrm{d}}{\mathrm{d}\Lambda}\frac{1}{2\pi i}\oint \mathrm{d}z\ \underbrace{\frac{-z^2}{-z^2+\Lambda^2}\frac{1}{z-\varepsilon(\boldsymbol{k})}}_{:=g(z)}\, n_\mathrm{F}(z) \tag{B.2}$$

with the substitution $z := i\omega$. The poles of the Fermi-function are entirely located on the imaginary frequency axis, so that the contour is along this line in both directions and closes in the negative and in the positive real part segment. Due to a deformation of the contours, they only enclose the poles of the original function, which, in this case, are $z = \pm\Lambda$ and $z = \varepsilon(\boldsymbol{k})$. Applying the residue theorem again we, therefore, can sum over all these residues instead of calculating the contour integral, so that we get

$$\begin{aligned}
\frac{\mathrm{d}}{\mathrm{d}\Lambda}G^{\Lambda} &= \frac{\mathrm{d}}{\mathrm{d}\Lambda}\sum_{z_0 \text{ poles of } g(z)}\mathrm{Res}_{z_0}\left(\frac{z_0^2}{z_0^2-\Lambda^2}\frac{1}{z_0-\varepsilon(\boldsymbol{k})}\right)n_\mathrm{F}(z_0)\\
&= \frac{\mathrm{d}}{\mathrm{d}\Lambda}\left(\frac{\Lambda}{2(\Lambda-\varepsilon(\boldsymbol{k}))}n_\mathrm{F}(\Lambda)+\frac{\Lambda}{2(\Lambda+\varepsilon(\boldsymbol{k}))}n_\mathrm{F}(-\Lambda)+\frac{\varepsilon(\boldsymbol{k})}{\varepsilon^2(\boldsymbol{k})-\Lambda^2}n_\mathrm{F}(\varepsilon(\boldsymbol{k}))\right)\\
&= \frac{-\varepsilon(\boldsymbol{k})}{2(\Lambda-\varepsilon(\boldsymbol{k}))^2}n_\mathrm{F}(\Lambda)+\frac{\Lambda}{2(\Lambda-\varepsilon(\boldsymbol{k}))}n_\mathrm{F}'(\Lambda)\\
&\quad+\frac{\varepsilon(\boldsymbol{k})}{2(\Lambda+\varepsilon(\boldsymbol{k}))^2}n_\mathrm{F}(-\Lambda)+\frac{\Lambda}{2(\Lambda+\varepsilon(\boldsymbol{k}))}n_\mathrm{F}'(-\Lambda)+\frac{2\varepsilon^2(\boldsymbol{k})\Lambda}{(\varepsilon^2(\boldsymbol{k})-\Lambda^2)^2}n_\mathrm{F}(\varepsilon(\boldsymbol{k})).
\end{aligned} \tag{B.3}$$

This expression is the one given in equation (4.42).

For the electron-hole propagator we proceed with the same steps. In the term

$$L^{\Lambda}(\boldsymbol{k}\boldsymbol{k}') = \frac{1}{\beta}\frac{\mathrm{d}}{\mathrm{d}\Lambda}\sum_{\omega_n}\underbrace{\frac{\omega_n^4}{(\omega_n^2+\Lambda^2)^2}\frac{1}{i\omega_n-\varepsilon(\boldsymbol{k})}\frac{1}{\mp i\omega_n-\varepsilon(\boldsymbol{k}')}}_{:=f} \tag{B.4}$$

the upper sign ("-") stands for the particle-particle and the lower sign ("+") for the electron-hole propagator. This function has poles of second order at $z := i\omega_n = \pm\Lambda$ and poles of first order at $z = \varepsilon(\boldsymbol{k})$ and $z = \mp\varepsilon(\boldsymbol{k}')$, which become poles of second order if $\varepsilon(\boldsymbol{k}) = \pm\varepsilon(\boldsymbol{k}')$. Therefore, we treat these two cases separately. It has to be kept in mind that cases can occur in which one of the energies also equals Λ, which leads to poles of third order. However, in our approach Λ can be chosen such that it does not equal one of the energies present at our grid, so that we can avoid those cases. In the

following we replace $\varepsilon(\boldsymbol{k})$ and $\varepsilon(\boldsymbol{k}')$ by ε_1 and ε_2, respectively, to shorten the notation. In the case of different energies we then obtain the following residues for the particle-particle channel:

$$A := \operatorname*{Res}_{z_0=\Lambda}[f(z)n_{\mathrm{F}}(z)] = \frac{(3\varepsilon_1\varepsilon_2+2\varepsilon_1\Lambda-2\varepsilon_2\Lambda-\Lambda^2)\Lambda}{4(\varepsilon_1-\Lambda)^2(\varepsilon_2+\Lambda)^2}n_{\mathrm{F}}(\Lambda) + \frac{\Lambda^2}{4(\varepsilon_1-\Lambda)(\varepsilon_2+\Lambda)}n'_{\mathrm{F}}(\Lambda) \tag{B.5}$$

$$B := \operatorname*{Res}_{z_0=-\Lambda}[f(z)n_{\mathrm{F}}(z)] = \frac{(-3\varepsilon_1\varepsilon_2+2\varepsilon_1\Lambda-2\varepsilon_2\Lambda+\Lambda^2)\Lambda}{4(\varepsilon_1+\Lambda)^2(\varepsilon_2-\Lambda)^2}n_{\mathrm{F}}(-\Lambda) + \frac{\Lambda^2}{4(\varepsilon_1+\Lambda)(\varepsilon_2-\Lambda)}n'_{\mathrm{F}}(-\Lambda) \tag{B.6}$$

$$C := \operatorname*{Res}_{z_0=\varepsilon_1}[f(z)n_{\mathrm{F}}(z)] = -\frac{\varepsilon_1^4}{(\varepsilon_1+\varepsilon_2)(\varepsilon_1^2-\Lambda^2)^2}n_{\mathrm{F}}(\varepsilon_1) \tag{B.7}$$

$$D := \operatorname*{Res}_{z_0=\varepsilon_2}[f(z)n_{\mathrm{F}}(z)] = \frac{\varepsilon_2^4}{(\varepsilon_1+\varepsilon_2)(\varepsilon_2^2-\Lambda^2)^2}n_{\mathrm{F}}(-\varepsilon_2) \tag{B.8}$$

When we label the first and the second summand of A and B by 1 and 2, respectively, the Λ-derivative leads to

$$\frac{\mathrm{d}}{\mathrm{d}\Lambda}A_1 = \frac{3\varepsilon_1\varepsilon_2+4\varepsilon_1\Lambda-4\varepsilon_2\Lambda-3\Lambda^2}{4(\varepsilon_1-\Lambda)^2(\varepsilon_2+\Lambda)^2}n_{\mathrm{F}}(\Lambda) + \frac{(3\varepsilon_1\varepsilon_2+2\varepsilon_1\Lambda-2\varepsilon_2\Lambda-\Lambda^2)(2\Lambda-\varepsilon_1+\varepsilon_2)\Lambda}{2(\varepsilon_1-\Lambda)^3(\varepsilon_2+\Lambda)^3}n_{\mathrm{F}}(\Lambda) + \frac{(3\varepsilon_1\varepsilon_2+2\varepsilon_1\Lambda-2\varepsilon_2\Lambda-\Lambda^2)\Lambda}{4(\varepsilon_1-\Lambda)^2(\varepsilon_2-\Lambda)^2}n'_{\mathrm{F}}(\Lambda) \tag{B.9}$$

$$\frac{\mathrm{d}}{\mathrm{d}\Lambda}A_2 = \frac{2\Lambda(\varepsilon_1-\Lambda)(\varepsilon_2+\Lambda)+\Lambda^2(2\Lambda-\varepsilon_1+\varepsilon_2)}{4(\varepsilon_1-\Lambda)^2(\varepsilon_2+\Lambda)^2}n'_{\mathrm{F}}(\Lambda) - \frac{\Lambda^2}{4(\Lambda-\varepsilon_1)(\Lambda+\varepsilon_2)}n''_{\mathrm{F}}(\Lambda) \tag{B.10}$$

$$\frac{\mathrm{d}}{\mathrm{d}\Lambda}B_1 = \frac{-3\varepsilon_1\varepsilon_2+4\varepsilon_1\Lambda-4\varepsilon_2\Lambda+3\Lambda^2}{4(\varepsilon_1+\Lambda)^2(\varepsilon_2-\Lambda)^2}n_{\mathrm{F}}(-\Lambda) + \frac{(-3\varepsilon_1\varepsilon_2+2\varepsilon_1\Lambda-2\varepsilon_2\Lambda+\Lambda^2)(2\Lambda+\varepsilon_1-\varepsilon_2)\Lambda}{2(\varepsilon_1+\Lambda)^3(\varepsilon_2-\Lambda)^3}n_{\mathrm{F}}(-\Lambda) - \frac{(-3\varepsilon_1\varepsilon_2+2\varepsilon_1\Lambda-2\varepsilon_2\Lambda+\Lambda^2)\Lambda}{4(\varepsilon_1+\Lambda)^2(\varepsilon_2-\Lambda)^2}n'_{\mathrm{F}}(-\Lambda) \tag{B.11}$$

$$\frac{\mathrm{d}}{\mathrm{d}\Lambda}B_2 = +\frac{2\Lambda(\varepsilon_1+\Lambda)(\varepsilon_2-\Lambda)+\Lambda^2(2\Lambda+\varepsilon_1-\varepsilon_2)}{4(\varepsilon_1+\Lambda)^2(\varepsilon_2-\Lambda)^2}n'_{\mathrm{F}}(-\Lambda) + \frac{\Lambda^2}{4(\Lambda+\varepsilon_1)(\Lambda-\varepsilon_2)}n''_{\mathrm{F}}(-\Lambda) \tag{B.12}$$

$$\frac{\mathrm{d}}{\mathrm{d}\Lambda}C = -\frac{4\Lambda\varepsilon_1^4}{(\varepsilon_1+\varepsilon_2)(\varepsilon_1^2-\Lambda^2)^3}n_{\mathrm{F}}(\varepsilon_1) \tag{B.13}$$

$$\frac{\mathrm{d}}{\mathrm{d}\Lambda}D = \frac{4\Lambda\varepsilon_2^4}{(\varepsilon_1+\varepsilon_2)(\varepsilon_2^2-\Lambda^2)^3}n_{\mathrm{F}}(-\varepsilon_2). \tag{B.14}$$

The corresponding results for the electron-hole channel are obtained by replacing ε_2 by $-\varepsilon_2$.

In the second case mentioned above the energies in equation (B.4) are of equal size, that is $\varepsilon_1 = \mp\varepsilon_2$ (again "$-$" for the particle-particle and "$+$" for the electron-hole case). In this case both channels become equal with the residues

$$E := \operatorname*{Res}_{z_0=\Lambda}[f(z)n_{\mathrm{F}}(z)] = \frac{-3\varepsilon_1\Lambda+\Lambda^2}{4(\varepsilon_1-\Lambda)^3}n_{\mathrm{F}}(\Lambda) - \frac{\Lambda^2}{4(\varepsilon_1-\Lambda)^2}n'_{\mathrm{F}}(\Lambda) \tag{B.15}$$

$$F := \operatorname*{Res}_{z_0=-\Lambda}[f(z)n_{\mathrm{F}}(z)] = \frac{3\varepsilon_1\Lambda+\Lambda^2}{4(\varepsilon_1+\Lambda)^3}n_{\mathrm{F}}(-\Lambda) - \frac{\Lambda^2}{4(\varepsilon_1+\Lambda)^2}n'_{\mathrm{F}}(-\Lambda) \tag{B.16}$$

$$G := \operatorname*{Res}_{z_0=\varepsilon_1}[f(z)n_{\mathrm{F}}(z)] = \frac{4\Lambda^2\varepsilon_1^3}{(\varepsilon_1^2-\Lambda^2)^3}n_{\mathrm{F}}(\varepsilon_1) - \frac{\varepsilon_1^4}{(\varepsilon_1^2-\Lambda^2)^2}n'_{\mathrm{F}}(\varepsilon_1). \tag{B.17}$$

Taking their derivatives with respect to Λ results in

$$\frac{\mathrm{d}}{\mathrm{d}\Lambda}E = \frac{-3\varepsilon_1^2-4\varepsilon_1\Lambda+\Lambda^2}{4(\varepsilon_1-\Lambda)^4}n_\mathrm{F}(\Lambda) - \frac{5\varepsilon_1\Lambda-\Lambda^2}{4(\varepsilon_1-\Lambda)^3}n_\mathrm{F}'(\Lambda) - \frac{\Lambda^2}{4(\varepsilon_1-\Lambda)^2}n_\mathrm{F}''(\Lambda) \tag{B.18}$$

$$\frac{\mathrm{d}}{\mathrm{d}\Lambda}F = -\frac{-3\varepsilon_1^2+4\varepsilon_1\Lambda+\Lambda^2}{4(\varepsilon_1+\Lambda)^4}n_\mathrm{F}(-\Lambda) + \frac{5\varepsilon_1\Lambda+\Lambda^2}{4(\varepsilon_1+\Lambda)^3}n_\mathrm{F}'(-\Lambda) + \frac{\Lambda^2}{4(\varepsilon_1+\Lambda)^2}n_\mathrm{F}''(-\Lambda) \tag{B.19}$$

$$\frac{\mathrm{d}}{\mathrm{d}\Lambda}G = \frac{8\Lambda\varepsilon_1^3(2\Lambda^2+\varepsilon_1^2)}{(\varepsilon_1^2-\Lambda^2)^4}n_\mathrm{F}(\varepsilon_1) - \frac{4\varepsilon_1^4\Lambda}{(\varepsilon_1^2-\Lambda^2)^3}n_\mathrm{F}'(\varepsilon_1) \tag{B.20}$$

For the full dual propagator we, therefore, have to differentiate between both cases and add all the corresponding contributions, that is those in equations (B.9)-(B.14) in the case of $\varepsilon_1 \neq \varepsilon_2$ and those in equations (B.18)-(B.20) in the case of equal energies.

Finally, we proceed to the limit $T = 0$ or $\beta = \infty$. In this limit the Fermi-function n_F becomes a Heaviside function, its first derivative becomes a delta-distribution and the second derivative equals zero. This allows us to simplify the above expression a lot. First, as $\Lambda \searrow 0$ the terms of $n_\mathrm{F}'(\pm\Lambda)$ only contribute at the very end of the flow. The terms of $n_\mathrm{F}(-\Lambda)$ always contribute, while those of $n_\mathrm{F}(\Lambda)$ never contribute, as $\Lambda \geq 0$. For the Heaviside functions of the energies we now have to distinguish between different cases, as the energies ε_1 and ε_2 can be positive or negative. These observations result in the particle-particle propagator of the form

$$L_\mathrm{pp}^\Lambda = \begin{cases} \frac{\varepsilon_1^2\varepsilon_2(3\varepsilon_2-\Lambda)+(3\varepsilon_2-\Lambda)\Lambda^3+\varepsilon_1\Lambda(\varepsilon_2^2+6\varepsilon_2\Lambda-3\Lambda^2)}{4(\varepsilon_1+\Lambda)^3(\varepsilon_2-\Lambda)^3} & \text{for } \varepsilon_1 > 0 \text{ and } \varepsilon_2 < 0, \\ \frac{1}{4(\varepsilon_1+\varepsilon_2)}\left(\frac{\varepsilon_1(3\varepsilon_1+\Lambda)}{(\varepsilon_1+\Lambda)^3} + \frac{\varepsilon_2(3\varepsilon_2+\Lambda)}{(\varepsilon_2+\Lambda)^3}\right) & \text{for } \varepsilon_1 > 0 \text{ and } \varepsilon_2 > 0, \\ \frac{\varepsilon_1^2\varepsilon_2(3\varepsilon_2+\Lambda)-(3\varepsilon_2+\Lambda)\Lambda^3+\varepsilon_1\Lambda(-\varepsilon_2^2+6\varepsilon_2\Lambda+3\Lambda^2)}{4(\varepsilon_1-\Lambda)^3(\varepsilon_2+\Lambda)^3} & \text{for } \varepsilon_1 < 0 \text{ and } \varepsilon_2 > 0, \\ \frac{1}{4(\varepsilon_1+\varepsilon_2)}\left(\frac{\varepsilon_1(3\varepsilon_1-\Lambda)}{(\varepsilon_1-\Lambda)^3} + \frac{\varepsilon_2(3\varepsilon_2-\Lambda)}{(\varepsilon_2-\Lambda)^3}\right) & \text{for } \varepsilon_1 < 0 \text{ and } \varepsilon_2 < 0. \end{cases} . \tag{B.21}$$

An expansion of the first and the third case by $\varepsilon_1 + \varepsilon_2$ and the introduction of absolute values allows us to combine all expressions into the simple form

$$L_\mathrm{pp}^\Lambda = \frac{1}{4(\varepsilon_1+\varepsilon_2)}\left(\frac{\varepsilon_1(3|\varepsilon_1|+\Lambda)}{(|\varepsilon_1|+\Lambda)^3} + \frac{\varepsilon_2(3|\varepsilon_2|+\Lambda)}{(|\varepsilon_2|+\Lambda)^3}\right). \tag{B.22}$$

In the case of equal energies $\varepsilon_1 = -\varepsilon_2$ the zero-temperature limit is obtained analogously, resulting in

$$L_\mathrm{pp}^\Lambda = \frac{3\varepsilon_1^2 - 4|\varepsilon_1|\Lambda - \Lambda^2}{4(|\varepsilon_1|+\Lambda)^4}. \tag{B.23}$$

As mentioned beforehand, the electron-hole propagator is obtained by changing the sign of ε_2 and the global sign. Thus the electron-hole term in the zero-temperature limit becomes

$$L_\mathrm{ph}^\Lambda = \begin{cases} -\frac{1}{4(\varepsilon_1-\varepsilon_2)}\left(\frac{\varepsilon_1(3|\varepsilon_1|+\Lambda)}{(|\varepsilon_1|+\Lambda)^3} - \frac{\varepsilon_2(3|\varepsilon_2|+\Lambda)}{(|\varepsilon_2|+\Lambda)^3}\right) & \text{for } \varepsilon_1 \neq \varepsilon_2, \\ \frac{3\varepsilon_1^2+4|\varepsilon_1|\Lambda-\Lambda^2}{4(|\varepsilon_1|-\Lambda)^4} \text{ for } \varepsilon_1 = \varepsilon_2. \end{cases} \tag{B.24}$$

This equals the equations presented in equation (4.43) and (4.44).

C. Discussion of undiverged flow of the anisotropic 3D-Hubbard model

C.1. $t_z = 0.05\,t$

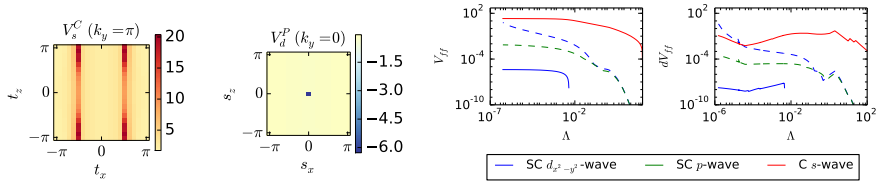

Figure C.1.: From left to right: Cut through the interaction in the C-channel on-site form-factor in the $y = \pi$-plane, in the P-channel d-wave form-factor in the $y = 0$-plane, flow of the largest values of the three main channels and their derivatives for $t' = -0.34\,t$.

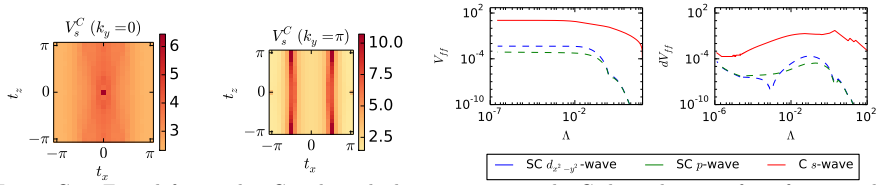

Figure C.2.: From left to right: Cut through the interaction in the C-channel on-site form-factor in the $y = 0$-plane, in the $y = \pi$-plane, flow of the largest values of the three main channels and their derivatives for $t' = -0.36\,t$.

C.2. $t_z = 0.1\,t$

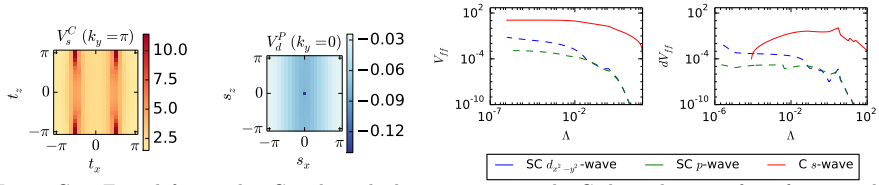

Figure C.3.: From left to right: Cut through the interaction in the C-channel on-site form-factor in the $y = \pi$-plane, in the P-channel d-wave form-factor in the $y = 0$-plane, flow of the largest values of the three main channels and their derivatives for $t' = -0.32\,t$.

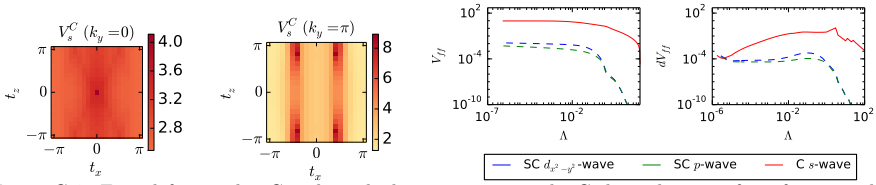

Figure C.4.: From left to right: Cut through the interaction in the C-channel on-site form-factor in the $y = 0$-plane, in the $y = \pi$-plane, flow of the largest values of the three main channels and their derivatives for $t' = -0.34\,t$.

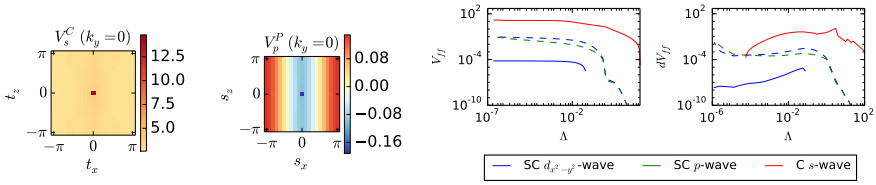

Figure C.5.: From left to right: Cut through the interaction in the C-channel on-site form-factor in the $y = 0$-plane, in the P-channel p-wave form-factor in the $y = 0$-plane, flow of the largest values of the three main channels and their derivatives for $t' = -0.36\,t$.

C.3. $t_z = 0.5\,t$

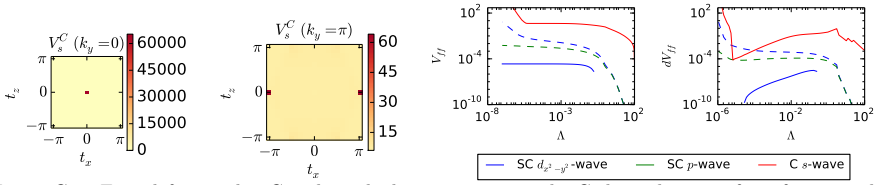

Figure C.6.: From left to right: Cut through the interaction in the C-channel on-site form-factor in the $y = 0$-plane, in the $y = \pi$-plane, flow of the largest values of the three main channels and their derivatives for $t' = -0.1\,t$.

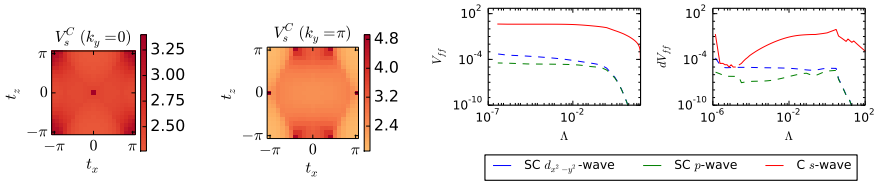

Figure C.7.: From left to right: Cut through the interaction in the C-channel on-site form-factor in the $y = 0$-plane, in the $y = \pi$-plane, flow of the largest values of the three main channels and their derivatives for $t' = -0.15\,t$.

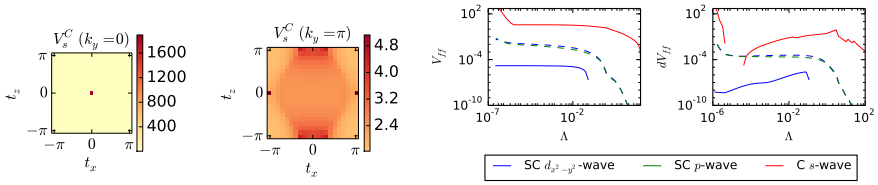

Figure C.8.: From left to right: Cut through the interaction in the C-channel on-site form-factor in the $y = 0$-plane, in the $y = \pi$-plane, flow of the largest values of the three main channels and their derivatives for $t' = -0.2\,t$.

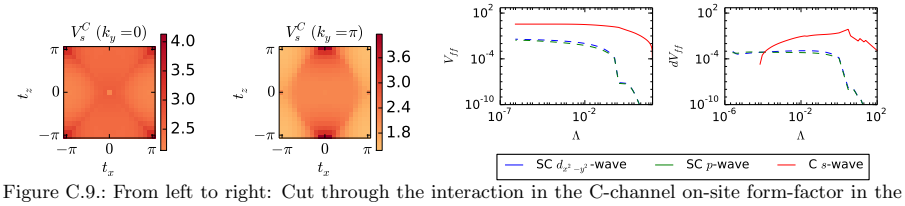

Figure C.9.: From left to right: Cut through the interaction in the C-channel on-site form-factor in the $y = 0$-plane, in the $y = \pi$-plane, flow of the largest values of the three main channels and their derivatives for $t' = -0.24\,t$.

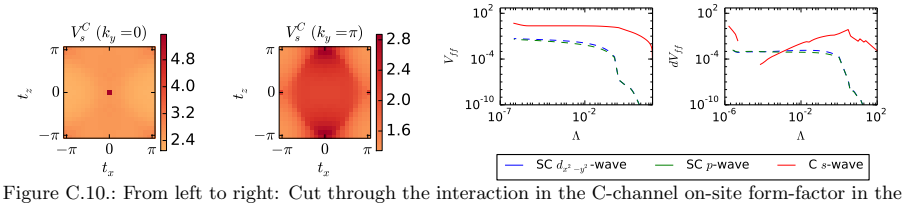

Figure C.10.: From left to right: Cut through the interaction in the C-channel on-site form-factor in the $y = 0$-plane, in the $y = \pi$-plane, flow of the largest values of the three main channels and their derivatives for $t' = -0.26\,t$.

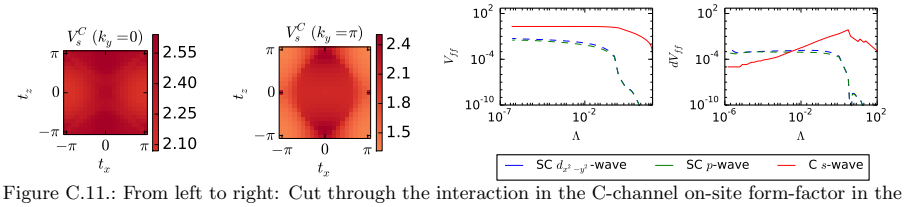

Figure C.11.: From left to right: Cut through the interaction in the C-channel on-site form-factor in the $y = 0$-plane, in the $y = \pi$-plane, flow of the largest values of the three main channels and their derivatives for $t' = -0.28\,t$.

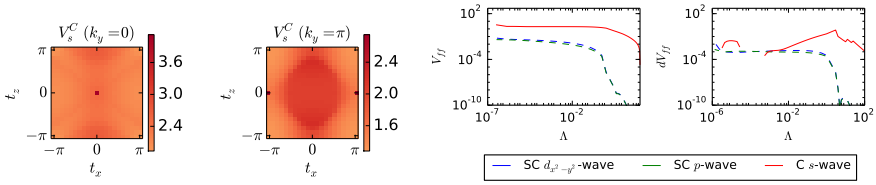

Figure C.12.: From left to right: Cut through the interaction in the C-channel on-site form-factor in the $y = 0$-plane, in the $y = \pi$-plane, flow of the largest values of the three main channels and their derivatives for $t' = -0.32\,t$.

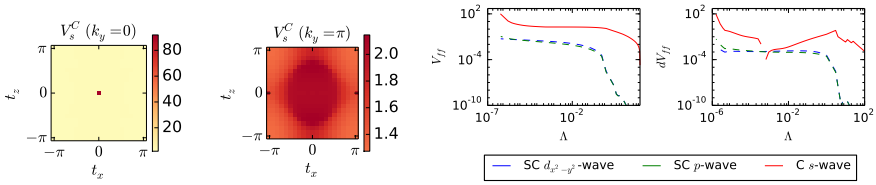

Figure C.13.: From left to right: Cut through the interaction in the C-channel on-site form-factor in the $y = 0$-plane, in the $y = \pi$-plane, flow of the largest values of the three main channels and their derivatives for $t' = -0.34\,t$.

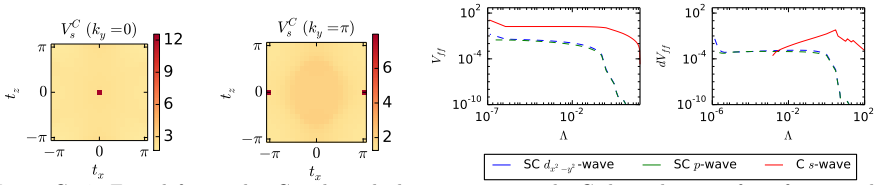

Figure C.14.: From left to right: Cut through the interaction in the C-channel on-site form-factor in the $y = 0$-plane, in the $y = \pi$-plane, flow of the largest values of the three main channels and their derivatives for $t' = -0.36\,t$.

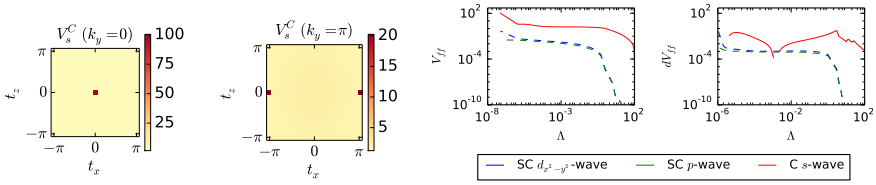

Figure C.15.: From left to right: Cut through the interaction in the C-channel on-site form-factor in the $y = 0$-plane, in the $y = \pi$-plane, flow of the largest values of the three main channels and their derivatives for $t' = -0.4\,t$.

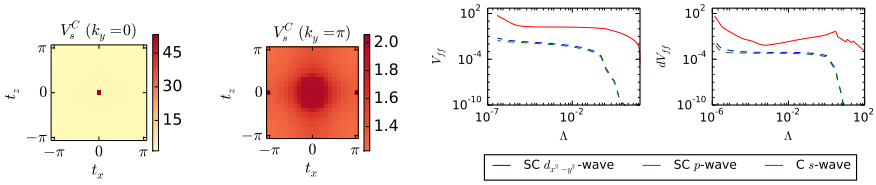

Figure C.16.: From left to right: Cut through the interaction in the C-channel on-site form-factor in the $y = 0$-plane, in the $y = \pi$-plane, flow of the largest values of the three main channels and their derivatives for $t' = -0.45\,t$.

Bibliography

[1] Jülich Supercomputing Centre. JURECA: Modular supercomputer at Jülich Supercomputing Centre. *Journal of large-scale research facilities*, 4(A132), 2018.

[2] J. Lichtenstein, D. Sánchez de la Peña, D. Rohe, E. Di Napoli, C. Honerkamp, and S.A. Maier. High-performance functional renormalization group calculations for interacting fermions. *Computer Physics Communications*, 213:100 – 110, 2017.

[3] H.K. Onnes. The resistance of pure mercury at helium temperatures. *Commun. Phys. Lab. Univ. Leiden*, 12(1), 1911.

[4] S. Anders, M.G. Blamire, F.-Im. Buchholz, D.-G. Crété, R. Cristiano, P. Febvre, L. Fritzsch, A. Herr, E. Il'ichev, J. Kohlmann, J. Kunert, H.-G. Meyer, J. Niemeyer, T. Ortlepp, H. Rogalla, T. Schurig, M. Siegel, R. Stolz, E. Tarte, H.J.M. ter Brake, H. Toepfer, J.-C. Villegier, A.M. Zagoskin, and A.B. Zorin. European roadmap on superconductive electronics – status and perspectives. *Physica C: Superconductivity*, 470(23):2079 – 2126, 2010.

[5] J. Bardeen, L. N. Cooper, and J. R. Schrieffer. Theory of superconductivity. *Phys. Rev.*, 108:1175–1204, Dec 1957.

[6] F. Steglich, J. Aarts, C. D. Bredl, W. Lieke, D. Meschede, W. Franz, and H. Schäfer. Superconductivity in the presence of strong pauli paramagnetism: $Cecu_2si_2$. *Phys. Rev. Lett.*, 43:1892–1896, Dec 1979.

[7] Jérome, D., Mazaud, A., Ribault, M., and Bechgaard, K. Superconductivity in a synthetic organic conductor (tmtsf)2pf 6. *J. Physique Lett.*, 41(4):95–98, 1980.

[8] J.G. Bednorz and K.A. Müller. Possible high t_c superconductivity in the ba-la-cu-o system. *Z. Physik B - Condensed Matter*, 64:189–193, 1986.

[9] Yoichi Kamihara, Hidenori Hiramatsu, Masahiro Hirano, Ryuto Kawamura, Hiroshi Yanagi, and Toshio Kamiya amd Hideo Hosono. Iron-based layered superconductor:/,laofep. *J. Am. Chem. Soc.*, 128:10012–10013, 2006.

[10] Jian-Feng Ge, Zhi-Long Liu, Canhua Liu, Chun-Lei Gao, Dong Qian, Qi-Kun Xue, Ying Liu, and Jin-Feng Jia. Superconductivity above 100 k in single-layer fese films on doped srtio3. *Nature Materials*, 14(3):285–289, Mar 2015.

[11] J. Shiogai, Y. Ito, T. Mitsuhashi, T. Nojima, and A. Tsukazaki. Electric-field-induced superconductivity in electrochemically etched ultrathin fese films on srtio3 and mgo. *Nature Physics*, 12(1):42–46, Jan 2016.

[12] Danfeng Li, Kyuho Lee, Bai Yang Wang, Motoki Osada, Samuel Crossley, Hye Ryoung Lee, Yi Cui, Yasuyuki Hikita, and Harold Y. Hwang. Superconductivity in an infinite-layer nickelate. *Nature*, 572(7771):624–627, Aug 2019.

[13] A. P. Drozdov, M. I. Eremets, I. A. Troyan, V. Ksenofontov, and S. I. Shylin. Conventional superconductivity at 203 kelvin at high pressures in the sulfur hydride system. *Nature*, 525(7567):73–76, Sep 2015.

[14] R. W. Hill, Cyril Proust, Louis Taillefer, P. Fournier, and R. L. Greene. Breakdown of fermi-liquid theory in a copper-oxide superconductor. *Nature*, 414(6865):711–715, Dec 2001.

[15] J. Chang, M. Månsson, S. Pailhès, T. Claesson, O. J. Lipscombe, S. M. Hayden, L. Patthey, O. Tjernberg, and J. Mesot. Anisotropic breakdown of fermi liquid quasiparticle excitations in overdoped la2-xsrxcuo4. *Nature Communications*, 4(1):2559, Oct 2013.

[16] Roland Hott, Reinhold Kleiner, Thomas Wolf, and Gertrud Zwicknagl. Review on superconducting materials, 2013.

[17] B. Keimer, S. A. Kivelson, M. R. Norman, S. Uchida, and J. Zaanen. From quantum matter to high-temperature superconductivity in copper oxides. *Nature*, 518(7538):179–186, Feb 2015.

[18] Tetsuya Takimoto and Tôru Moriya. Superconductivity and antiferromagnetism in the three-dimensional hubbard model. *Phys. Rev. B*, 66:134516, Oct 2002.

[19] Andrey V. Chubukov, M. Khodas, and Rafael M. Fernandes. Magnetism, superconductivity, and spontaneous orbital order in iron-based superconductors: Which comes first and why? *Phys. Rev. X*, 6:041045, Dec 2016.

[20] J. Chang, E. Blackburn, A. T. Holmes, N. B. Christensen, J. Larsen, J. Mesot, Ruixing Liang, D. A. Bonn, W. N. Hardy, A. Watenphul, M. v. Zimmermann, E. M. Forgan, and S. M. Hayden. Direct observation of competition between superconductivity and charge density wave order in yba2cu3o6.67. *Nature Physics*, 8(12):871–876, Dec 2012.

[21] M. Bendele, A. Ichsanow, Yu. Pashkevich, L. Keller, Th. Strässle, A. Gusev, E. Pomjakushina, K. Conder, R. Khasanov, and H. Keller. Coexistence of superconductivity and magnetism in fese_{1-x} under pressure. *Phys. Rev. B*, 85:064517, Feb 2012.

[22] J. P. Sun, K. Matsuura, G. Z. Ye, Y. Mizukami, M. Shimozawa, K. Matsubayashi, M. Yamashita, T. Watashige, S. Kasahara, Y. Matsuda, J.-Q. Yan, B. C. Sales, Y. Uwatoko, J.-G. Cheng, and T. Shibauchi. Dome-shaped magnetic order competing with high-temperature superconductivity at high pressures in fese. *Nature Communications*, 7(1):12146, Jul 2016.

[23] Jun Sung Kim, Seunghyun Khim, Liqin Yan, N Manivannan, Yong Liu, Ingyu Kim, G R Stewart, and Kee Hoon Kim. Evidence for coexistence of superconductivity and magnetism in single crystals of co-doped SrFe2as2. *Journal of Physics: Condensed Matter*, 21(10):102203, Feb 2009.

[24] P. Hohenberg and W. Kohn. Inhomogeneous electron gas. *Phys. Rev.*, 136:B864–B871, Nov 1964.

[25] W. Kohn and L. J. Sham. Self-consistent equations including exchange and correlation effects. *Phys. Rev.*, 140:A1133–A1138, Nov 1965.

[26] Lars Hedin. New method for calculating the one-particle green's function with application to the electron-gas problem. *Phys. Rev.*, 139:A796–A823, Aug 1965.

[27] Christoph Friedrich, Stefan Blügel, and Arno Schindlmayr. Efficient implementation of the *gw* approximation within the all-electron flapw method. *Phys. Rev. B*, 81:125102, Mar 2010.

[28] Richard M. Martin, Lucia Reining, and David M. Ceperley. *Interacting Electrons: Theory and Computational Approaches*. Cambridge University Press, 2016.

[29] Pina Romaniello, Friedhelm Bechstedt, and Lucia Reining. Beyond the *gw* approximation: Combining correlation channels. *Phys. Rev. B*, 85:155131, Apr 2012.

[30] Cyrano De Dominicis and Paul C. Martin. Stationary entropy principle and renormalization in normal and superfluid systems. i. algebraic formulation. *Journal of Mathematical Physics*, 5(1):14–30, 1964.

[31] Cyrano De Dominicis and Paul C. Martin. Stationary entropy principle and renormalization in normal and superfluid systems. ii. diagrammatic formulation. *Journal of Mathematical Physics*, 5(1):31–59, 1964.

[32] J. Hubbard. Electron correlations in narrow energy bands. *Proceedings of the Royal Society of London. Series A, Mathematical and Physical Sciences*, 276:238–257, Nov 1963.

[33] Martin C. Gutzwiller. Effect of correlation on the ferromagnetism of transition metals. *Phys. Rev. Lett.*, 10:159–162, Mar 1963.

[34] Junjiro Kanamori. Electron Correlation and Ferromagnetism of Transition Metals. *Progress of Theoretical Physics*, 30(3):275–289, 09 1963.

[35] P. W. Anderson. The resonating valence bond state in la2cuo4 and superconductivity. *Science*, 235:1196–1198, 1987.

[36] P. W. Anderson, G. Baskaran, Z. Zou, and T. Hsu. Resonating–valence-bond theory of phase transitions and superconductivity in la_2cuo_4-based compounds. *Phys. Rev. Lett.*, 58:2790–2793, Jun 1987.

[37] E. Y. Loh, J. E. Gubernatis, R. T. Scalettar, S. R. White, D. J. Scalapino, and R. L. Sugar. Sign problem in the numerical simulation of many-electron systems. *Phys. Rev. B*, 41:9301–9307, May 1990.

[38] Matthias Troyer and Uwe-Jens Wiese. Computational complexity and fundamental limitations to fermionic quantum monte carlo simulations. *Phys. Rev. Lett.*, 94:170201, May 2005.

[39] Antoine Georges, Gabriel Kotliar, Werner Krauth, and Marcelo J. Rozenberg. Dynamical mean-field theory of strongly correlated fermion systems and the limit of infinite dimensions. *Rev. Mod. Phys.*, 68:13–125, Jan 1996.

[40] G. Kotliar, S. Y. Savrasov, K. Haule, V. S. Oudovenko, O. Parcollet, and C. A. Marianetti. Electronic structure calculations with dynamical mean-field theory. *Rev. Mod. Phys.*, 78:865–951, Aug 2006.

[41] David Bohm and David Pines. A collective description of electron interactions. i. magnetic interactions. *Phys. Rev.*, 82:625–634, Jun 1951.

[42] David Pines and David Bohm. A collective description of electron interactions: Ii. collective vs individual particle aspects of the interactions. *Phys. Rev.*, 85:338–353, Jan 1952.

[43] E. E. Salpeter and H. A. Bethe. A relativistic equation for bound-state problems. *Phys. Rev.*, 84:1232–1242, Dec 1951.

[44] Gang Li, Nils Wentzell, Petra Pudleiner, Patrik Thunström, and Karsten Held. Efficient implementation of the parquet equations: Role of the reducible vertex function and its kernel approximation. *Phys. Rev. B*, 93:165103, Apr 2016.

[45] Gang Li, Anna Kauch, Petra Pudleiner, and Karsten Held. The victory project v1.0: An efficient parquet equations solver. *Computer Physics Communications*, 241:146 – 154, 2019.

[46] Mathias C. T. D. Müller, Stefan Blügel, and Christoph Friedrich. Electron-magnon scattering in elementary ferromagnets from first principles: Lifetime broadening and band anomalies. *Phys. Rev. B*, 100:045130, Jul 2019.

[47] A. Toschi, A. A. Katanin, and K. Held. Dynamical vertex approximation: A step beyond dynamical mean-field theory. *Phys. Rev. B*, 75:045118, Jan 2007.

[48] A. N. Rubtsov, M. I. Katsnelson, and A. I. Lichtenstein. Dual fermion approach to nonlocal correlations in the hubbard model. *Phys. Rev. B*, 77:033101, Jan 2008.

[49] Thomas Ayral and Olivier Parcollet. Mott physics and spin fluctuations: A unified framework. *Phys. Rev. B*, 92:115109, Sep 2015.

[50] Thomas Ayral and Olivier Parcollet. Mott physics and collective modes: An atomic approximation of the four-particle irreducible functional. *Phys. Rev. B*, 94:075159, Aug 2016.

[51] Grigory V. Astretsov, Georg Rohringer, and Alexey N. Rubtsov. Dual parquet scheme for the two-dimensional hubbard model: Modeling low-energy physics of high-T_c cuprates with high momentum resolution. *Phys. Rev. B*, 101:075109, Feb 2020.

[52] Kenneth G. Wilson. Renormalization group and critical phenomena. i. renormalization group and the kadanoff scaling picture. *Phys. Rev. B*, 4:3174–3183, Nov 1971.

[53] Kenneth G. Wilson. Renormalization group and critical phenomena. ii. phase-space cell analysis of critical behavior. *Phys. Rev. B*, 4:3184–3205, Nov 1971.

[54] Joseph Polchinski. Renormalization and effective lagrangians. *Nuclear Physics B*, 231(2):269 – 295, 1984.

[55] H. J Schulz. Superconductivity and antiferromagnetism in the two-dimensional hubbard model: Scaling theory. *Europhysics Letters (EPL)*, 4(5):609–615, Sep 1987.

[56] D. Zanchi and H. J. Schulz. Superconducting instabilities of the non-half-filled hubbard model in two dimensions. *Phys. Rev. B*, 54:9509–9519, Oct 1996.

[57] D. Zanchi and H. J. Schulz. Weakly correlated electrons on a square lattice: Renormalization-group theory. *Phys. Rev. B*, 61:13609–13632, May 2000.

[58] Christof Wetterich. Exact evolution equation for the effective potential. *Physics Letters B*, 301(1):90 – 94, 1993.

[59] Peter Kopietz and Tom Busche. Exact renormalization group flow equations for nonrelativistic fermions: Scaling toward the fermi surface. *Phys. Rev. B*, 64:155101, Sep 2001.

[60] Manfred Salmhofer and Carsten Honerkamp. Fermionic renormalization group flows: Technique and theory. *Progress of Theoretical Physics*, 105(1):1–35, 2001.

[61] Christoph J. Halboth and Walter Metzner. Renormalization-group analysis of the two-dimensional hubbard model. *Phys. Rev. B*, 61:7364–7377, Mar 2000.

[62] A. A. Katanin. Fulfillment of ward identities in the functional renormalization group approach. *Phys. Rev. B*, 70:115109, Sep 2004.

[63] Manfred Salmhofer, Carsten Honerkamp, Walter Metzner, and Oliver Lauscher. Renormalization group flows into phases with broken symmetry. *Progress of Theoretical Physics*, 112(6):943–970, 12 2004.

[64] Fabian B. Kugler and Jan von Delft. Multiloop functional renormalization group that sums up all parquet diagrams. *Phys. Rev. Lett.*, 120:057403, Jan 2018.

[65] Fabian B. Kugler and Jan von Delft. Multiloop functional renormalization group for general models. *Phys. Rev. B*, 97:035162, Jan 2018.

[66] Agnese Tagliavini, Cornelia Hille, Fabian B. Kugler, Sabine Andergassen, Alessandro Toschi, and Carsten Honerkamp. Multiloop functional renormalization group for the two-dimensional Hubbard model: Loop convergence of the response functions. *SciPost Phys.*, 6:9, 2019.

[67] C. Husemann and M. Salmhofer. Efficient parametrization of the vertex function, Ω scheme, and the $t, t^{'}$ hubbard model at van hove filling. *Phys. Rev. B*, 79:195125, May 2009.

[68] Wan-Sheng Wang, Yuan-Yuan Xiang, Qiang-Hua Wang, Fa Wang, Fan Yang, and Dung-Hai Lee. Functional renormalization group and variational monte carlo studies of the electronic instabilities in graphene near $\frac{1}{4}$ doping. *Phys. Rev. B*, 85:035414, Jan 2012.

[69] Michael Golor, Timo Reckling, Laura Classen, Michael M. Scherer, and Stefan Wessel. Ground-state phase diagram of the half-filled bilayer hubbard model. *Phys. Rev. B*, 90:195131, Nov 2014.

[70] Carsten Honerkamp. Density waves and cooper pairing on the honeycomb lattice. *Phys. Rev. Lett.*, 100:146404, Apr 2008.

[71] Daniel D. Scherer, Michael M. Scherer, and Carsten Honerkamp. Correlated spinless fermions on the honeycomb lattice revisited. *Phys. Rev. B*, 92:155137, Oct 2015.

[72] D. Sánchez de la Peña, J. Lichtenstein, and C. Honerkamp. Competing electronic instabilities of extended hubbard models on the honeycomb lattice: A functional renormalization group calculation with high-wave-vector resolution. *Phys. Rev. B*, 95:085143, Feb 2017.

[73] Stefan A. Maier, Jutta Ortloff, and Carsten Honerkamp. Multiorbital effects in the functional renormalization group: A weak-coupling study of the emery model. *Phys. Rev. B*, 88:235112, Dec 2013.

[74] M. M. Scherer, C. Honerkamp, A. N. Rudenko, E. A. Stepanov, A. I. Lichtenstein, and M. I. Katsnelson. Excitonic instability and unconventional pairing in the nodal-line materials zrsis and zrsise. *Phys. Rev. B*, 98:241112, Dec 2018.

[75] C. Platt, W. Hanke, and R. Thomale. Functional renormalization group for multi-orbital fermi surface instabilities. *Advances in Physics*, 62(4-6):453–562, 2013.

[76] Yuan-Chun Liu, Fu-Chun Zhang, Thomas Maurice Rice, and Qiang-Hua Wang. Theory of the evolution of superconductivity in sr2ruo4 under anisotropic strain. *npj Quantum Materials*, 2(1):12, Mar 2017.

[77] Wan-Sheng Wang, Cong-Cong Zhang, Fu-Chun Zhang, and Qiang-Hua Wang. Theory of chiral p-wave superconductivity with near nodes for sr_2ruo_4. *Phys. Rev. Lett.*, 122:027002, Jan 2019.

[78] J.W. Negele. *Quantum Many-particle Systems*. CRC Press, 2018.

[79] M.S. Dresselhaus, G. Dresselhaus, and A. Jorio. *Group Theory: Application to the Physics of Condensed Matter*. Springer Berlin Heidelberg, 2007.

[80] A. L. Fetter and J. D. Walecka. *Quantum Theory of Many-Particle Systems*. McGraw-Hill, Boston, 1971.

[81] Giolio Albert Heinrich Schober. *Quantum Field Theory of Material Properties: Its Application to Models of Rashba Spin Splitting*. PhD thesis, Ruperto-Carola Universität zu Heidelberg, 2016.

[82] Georg Rohringer. *New routes towards a theoretical treatment of nonlocal electronic correlations*. PhD thesis, Technische Universität Wien, 2013.

[83] Paul C. Martin and Julian Schwinger. Theory of many-particle systems. i. *Phys. Rev.*, 115:1342–1373, Sep 1959.

[84] Murray Gell-Mann and Francis Low. Bound states in quantum field theory. *Phys. Rev.*, 84:350–354, Oct 1951.

[85] D. R. Hartree. The wave mechanics of an atom with a non-coulomb central field. part ii. some results and discussion. *Mathematical Proceedings of the Cambridge Philosophical Society*, 24(1):111–132, 1928.

[86] V. Fock. Näherungsmethode zur lösung des quantenmechanischen mehrkörperproblems. *Zeitschrift für Physik*, 61(1):126–148, Jan 1930.

[87] A. A. Abrikosov. Electron scattering on magnetic impurities in metals and anomalous resistivity effects. *Physics Physique Fizika*, 2:5–20, Sep 1965.

[88] V. Janiš. Stability of self-consistent solutions for the hubbard model at intermediate and strong coupling. *Phys. Rev. B*, 60:11345–11360, Oct 1999.

[89] V. Yu. Irkhin, A. A. Katanin, and M. I. Katsnelson. Effects of van hove singularities on magnetism and superconductivity in the $t - t^{'}$ hubbard model: A parquet approach. *Phys. Rev. B*, 64:165107, Oct 2001.

[90] S. X. Yang, H. Fotso, J. Liu, T. A. Maier, K. Tomko, E. F. D'Azevedo, R. T. Scalettar, T. Pruschke, and M. Jarrell. Parquet approximation for the 4×4 hubbard cluster. *Phys. Rev. E*, 80:046706, Oct 2009.

[91] G. Rohringer, A. Toschi, H. Hafermann, K. Held, V. I. Anisimov, and A. A. Katanin. One-particle irreducible functional approach: A route to diagrammatic extensions of the dynamical mean-field theory. *Phys. Rev. B*, 88:115112, Sep 2013.

[92] N.E Bickers and D.J Scalapino. Conserving approximations for strongly fluctuating electron systems. i. formalism and calculational approach. *Annals of Physics*, 193(1):206 – 251, 1989.

[93] N. E. Bickers and S. R. White. Conserving approximations for strongly fluctuating electron systems. ii. numerical results and parquet extension. *Phys. Rev. B*, 43:8044–8064, Apr 1991.

[94] N. E. Bickers. *Self-Consistent Many-Body Theory for Condensed Matter Systems*, pages 237–296. Springer New York, New York, NY, 2004.

[95] Christoph Friedrich and Arno Schindlmayr. Many-body perturbation theory: The *gw* approximation. In *Lecture Notes of the 45th IFF Spring School "Computing Solids-Models, ab initio methods and supercomputing"*. Forschungszentrum Jüelich, 2014.

[96] Christoph Friedrich, Arno Schindlmayr, and Stefan Blügel. Efficient calculation of the coulomb matrix and its expansion around within the {FLAPW} method. *Computer Physics Communications*, 180(3):347 – 359, 2009.

[97] Andris Gulans, Stefan Kontur, Christian Meisenbichler, Dmitrii Nabok, Pasquale Pavone, Santiago Rigamonti, Stephan Sagmeister, Ute Werner, and Claudia Draxl. exciting: a full-potential all-electron package implementing density-functional theory and many-body perturbation theory. *Journal of Physics: Condensed Matter*, 26(36):363202, Aug 2014.

[98] Arno Schindlmayr and R. W. Godby. Systematic vertex corrections through iterative solution of hedin's equations beyond the *GW* approximation. *Phys. Rev. Lett.*, 80:1702–1705, Feb 1998.

[99] Mathias Christian Thomas David Müller. *Spin-wave excitations and electron-magnon scattering in elementary ferromagnets from ab initio many-body perturbation theory.* Dissertation, RWTH Aachen University, Jülich, 2017. Auch veröffentlicht auf dem Publikationsserver der RWTH Aachen University; Dissertation, RWTH Aachen University, 2017.

[100] Mathias C. T. D. Müller, Stefan Blügel, and Christoph Friedrich. Electron-magnon scattering in elementary ferromagnets from first principles: Lifetime broadening and band anomalies. *Phys. Rev. B*, 100:045130, Jul 2019.

[101] Humphrey J. Maris and Leo P. Kadanoff. Teaching the renormalization group. *American Journal of Physics*, 46(6):652–657, 1978.

[102] U. Ellwanger and C. Wetterich. Evolution equations for the quark-meson transition. *Nuclear Physics B*, 423(1):137 – 167, 1994.

[103] C. Honerkamp, M. Salmhofer, N. Furukawa, and T. M. Rice. Breakdown of the landau-fermi liquid in two dimensions due to umklapp scattering. *Phys. Rev. B*, 63:035109, Jan 2001.

[104] Walter Metzner, Manfred Salmhofer, Carsten Honerkamp, Volker Meden, and Kurt Schönhammer. Functional renormalization group approach to correlated fermion systems. *Rev. Mod. Phys.*, 84:299–352, Mar 2012.

[105] J F Rentrop, S G Jakobs, and V Meden. Two-particle irreducible functional renormalization group schemes—a comparative study. *Journal of Physics A: Mathematical and Theoretical*, 48(14):145002, Mar 2015.

[106] Daniel F. Litim. Optimized renormalization group flows. *Phys. Rev. D*, 64:105007, Oct 2001.

[107] Simplikios and Heraklit. "Panta Rhei: Everything Flows", this philosophical statement is assigned to Heraklit although, indeed it first appeared in works of Simplikios.

[108] Severin Georg Jakobs. *Functional renormalization group studies of quantum transport through mesoscopic systems.* Phd thesis, RWTH Aachen, 2009.

[109] C. Taranto, S. Andergassen, J. Bauer, K. Held, A. Katanin, W. Metzner, G. Rohringer, and A. Toschi. From infinite to two dimensions through the functional renormalization group. *Phys. Rev. Lett.*, 112:196402, May 2014.

[110] Fabian B Kugler and Jan von Delft. Derivation of exact flow equations from the self-consistent parquet relations. *New Journal of Physics*, 20(12):123029, Dec 2018.

[111] Giulio A. H. Schober, Jannis Ehrlich, Timo Reckling, and Carsten Honerkamp. Truncated-unity functional renormalization group for multiband systems with spin-orbit coupling. *Frontiers in Physics*, 6:32, May 2018.

[112] David Sánchez de la Peña, Julian Lichtenstein, Carsten Honerkamp, and Michael M. Scherer. Antiferromagnetism and competing charge instabilities of electrons in strained graphene from coulomb interactions. *Phys. Rev. B*, 96:205155, Nov 2017.

[113] C. J. Eckhardt, G. A. H. Schober, J. Ehrlich, and C. Honerkamp. Truncated-unity parquet equations: Application to the repulsive hubbard model. *Phys. Rev. B*, 98:075143, Aug 2018.

[114] C. Husemann, K.-U. Giering, and M. Salmhofer. Frequency-dependent vertex functions of the (t, t') hubbard model at weak coupling. *Phys. Rev. B*, 85:075121, Feb 2012.

[115] Nils Wentzell, Gang Li, Agnese Tagliavini, Ciro Taranto, Georg Rohringer, Karsten Held, Alessandro Toschi, and Sabine Andergassen. High-frequency asymptotics of the vertex function: Diagrammatic parametrization and algorithmic implementation. *Phys. Rev. B*, 102:085106, Aug 2020.

[116] Demetrio Vilardi, Ciro Taranto, and Walter Metzner. Nonseparable frequency dependence of the two-particle vertex in interacting fermion systems. *Phys. Rev. B*, 96:235110, Dec 2017.

[117] L. Markhof, B. Sbierski, V. Meden, and C. Karrasch. Detecting phases in one-dimensional many-fermion systems with the functional renormalization group. *Phys. Rev. B*, 97:235126, Jun 2018.

[118] Timo Reckling and Carsten Honerkamp. Approximating the frequency dependence of the effective interaction in the functional renormalization group for many-fermion systems. *Phys. Rev. B*, 98:085114, Aug 2018.

[119] Wan-Sheng Wang, Zheng-Zhao Li, Yuan-Yuan Xiang, and Qiang-Hua Wang. Competing electronic orders on kagome lattices at van hove filling. *Phys. Rev. B*, 87:115135, Mar 2013.

[120] Yuan-Yuan Xiang, Fa Wang, Da Wang, Qiang-Hua Wang, and Dung-Hai Lee. High-temperature superconductivity at the fese/srtio$_3$ interface. *Phys. Rev. B*, 86:134508, Oct 2012.

[121] Yuan-Yuan Xiang, Yang Yang, Wan-Sheng Wang, Zheng-Zao Li, and Qiang-Hua Wang. Functional renormalization group study of pairing symmetry and pairing mechanism in iron-selenide superconductors. *Phys. Rev. B*, 88:104516, Sep 2013.

[122] Wan-Sheng Wang, Miao Gao, Yang Yang, Yuan-Yuan Xiang, and Qiang-Hua Wang. Possible superconductivity in the electron-doped chromium pnictide laocras. *Phys. Rev. B*, 95:144507, Apr 2017.

[123] Karsten Ahnert and Mario Mulansky. Odeint – solving ordinary differential equations in c++. *AIP Conference Proceedings*, 1389(1):1586–1589, 2011.

[124] Carsten Honerkamp and Manfred Salmhofer. Temperature-flow renormalization group and the competition between superconductivity and ferromagnetism. *Phys. Rev. B*, 64:184516, Oct 2001.

[125] Carsten Honerkamp, Daniel Rohe, Sabine Andergassen, and Tilman Enss. Interaction flow method for many-fermion systems. *Phys. Rev. B*, 70:235115, Dec 2004.

[126] Julian Lichtenstein, Jan Winkelmann, David Sánchez de la Peña, Toni Vidović, and Edoardo Di Napoli. Parallel adaptive integration in high-performance functional renormalization group computations, 2016.

[127] Gaël Guennebaud, Benoît Jacob, et al. Eigen v3. http://eigen.tuxfamily.org, 2010.

[128] Nicola Marzari and David Vanderbilt. Maximally localized generalized wannier functions for composite energy bands. *Phys. Rev. B*, 56:12847–12865, Nov 1997.

[129] Nicola Marzari, Arash A. Mostofi, Jonathan R. Yates, Ivo Souza, and David Vanderbilt. Maximally localized wannier functions: Theory and applications. *Rev. Mod. Phys.*, 84:1419–1475, Oct 2012.

[130] Nicola Marzari et al. Wannier90(v3.0.0). http://http://www.wannier.org/, 2019.

[131] Stefan Maier. *Functional renormalization-group approaches to multiband models and antiferromagnetically ordered phases*. PhD thesis, RWTH Aachen University, 2014.

[132] S.A. Maier, C. Honerkamp, and Q.-H. Wang. Interplay between point-group symmetries and the choice of the bloch basis in multiband models. *Symmetry*, pages 313–343, 2013.

[133] Tim R. Morris. The exact renormalization group and approximate solutions. *International Journal of Modern Physics A*, 09(14):2411–2449, 1994.

[134] Michael Schluter, Mark S. Hybertsen, and Niels E. Christensen. Calculation of the many body interaction parameters in the hightc compound la2cuo4. *Physica C: Superconductivity*, 153-155:1217 – 1218, 1988. Proceedings of the International Conference on High Temperature Superconductors and Materials and Mechanisms of Superconductivity Part II.

[135] A. K. McMahan, James F. Annett, and Richard M. Martin. Cuprate parameters from numerical wannier functions. *Phys. Rev. B*, 42:6268–6282, Oct 1990.

[136] Motoaki Hirayama, Takahiro Misawa, Takahiro Ohgoe, Youhei Yamaji, and Masatoshi Imada. Effective hamiltonian for cuprate superconductors derived from multiscale ab initio scheme with level renormalization. *Phys. Rev. B*, 99:245155, Jun 2019.

[137] R. T. Scalettar. *Quantum Materials: Experiments and Theory*, volume 6 of *Modeling and Simulation*, chapter An Introduction to the Hubbard Hamiltonian, page Sec. 4. Verlag des Forschungszentrum Jülich, 2016.

[138] Elliott H. Lieb and F. Y. Wu. Absence of mott transition in an exact solution of the short-range, one-band model in one dimension. *Phys. Rev. Lett.*, 20:1445–1448, Jun 1968.

[139] Antoine Georges and Gabriel Kotliar. Hubbard model in infinite dimensions. *Phys. Rev. B*, 45:6479–6483, Mar 1992.

[140] Tobias Baier, Eike Bick, and Christof Wetterich. Temperature dependence of antiferromagnetic order in the hubbard model. *Phys. Rev. B*, 70:125111, Sep 2004.

[141] J. Reiss, D. Rohe, and W. Metzner. Renormalized mean-field analysis of antiferromagnetism and d-wave superconductivity in the two-dimensional hubbard model. *Phys. Rev. B*, 75:075110, Feb 2007.

[142] Jing Wang, Andreas Eberlein, and Walter Metzner. Competing order in correlated electron systems made simple: Consistent fusion of functional renormalization and mean-field theory. *Phys. Rev. B*, 89:121116, Mar 2014.

[143] Neven Barišić, Mun K. Chan, Yuan Li, Guichuan Yu, Xudong Zhao, Martin Dressel, Ana Smontara, and Martin Greven. Universal sheet resistance and revised phase diagram of the cuprate high-temperature superconductors. *Proceedings of the National Academy of Sciences*, 110(30):12235–12240, 2013.

[144] Youichi Yamakawa, Seiichiro Onari, and Hiroshi Kontani. Nematicity and magnetism in fese and other families of fe-based superconductors. *Phys. Rev. X*, 6:021032, Jun 2016.

[145] Helmut Eschrig and Klaus Koepernik. Tight-binding models for the iron-based superconductors. *Phys. Rev. B*, 80:104503, Sep 2009.

[146] Seung Woo Jang, Takao Kotani, Hiori Kino, Kazuhiko Kuroki, and Myung Joon Han. Quasiparticle self-consistent gw study of cuprates: electronic structure, model parameters and the two-band theory for tc. *Scientific Reports*, 5(1):12050, Jul 2015.

[147] L. F. Mattheiss. Electronic band properties and superconductivity in $la_{2-y}x_ycuo_4$. *Phys. Rev. Lett.*, 58:1028–1030, Mar 1987.

[148] Warren E. Pickett. Electronic structure of the high-temperature oxide superconductors. *Rev. Mod. Phys.*, 61:433–512, Apr 1989.

[149] Kay-Uwe Giering and Manfred Salmhofer. Self-energy flows in the two-dimensional repulsive hubbard model. *Phys. Rev. B*, 86:245122, Dec 2012.

[150] Carsten Honerkamp and Manfred Salmhofer. Magnetic and superconducting instabilities of the hubbard model at the van hove filling. *Phys. Rev. Lett.*, 87:187004, Oct 2001.

[151] J. Ehrlich and C. Honerkamp. Functional renormalization group for fermion lattice models in three dimensions: Application to the hubbard model on the cubic lattice. *Phys. Rev. B*, 102:195108, Nov 2020.

[152] R. T. Scalettar, D. J. Scalapino, R. L. Sugar, and D. Toussaint. Phase diagram of the half-filled 3d hubbard model. *Phys. Rev. B*, 39:4711–4714, Mar 1989.

[153] J. K. Freericks and Mark Jarrell. Magnetic phase diagram of the hubbard model. *Phys. Rev. Lett.*, 74:186–189, Jan 1995.

[154] Daniel Hirschmeier, Hartmut Hafermann, Emanuel Gull, Alexander I. Lichtenstein, and Andrey E. Antipov. Mechanisms of finite-temperature magnetism in the three-dimensional hubbard model. *Phys. Rev. B*, 92:144409, Oct 2015.

[155] Staudt, R., Dzierzawa, M., and Muramatsu, A. Phase diagram of the three-dimensional hubbard model at half filling. *Eur. Phys. J. B*, 17(3):411–415, 2000.

[156] G. Rohringer, A. Toschi, A. Katanin, and K. Held. Critical properties of the half-filled hubbard model in three dimensions. *Phys. Rev. Lett.*, 107:256402, Dec 2011.

[157] E. Kozik, E. Burovski, V. W. Scarola, and M. Troyer. Néel temperature and thermodynamics of the half-filled three-dimensional hubbard model by diagrammatic determinant monte carlo. *Phys. Rev. B*, 87:205102, May 2013.

[158] P. R. C. Kent, M. Jarrell, T. A. Maier, and Th. Pruschke. Efficient calculation of the antiferromagnetic phase diagram of the three-dimensional hubbard model. *Phys. Rev. B*, 72:060411, Aug 2005.

[159] Anders W. Sandvik. Critical temperature and the transition from quantum to classical order parameter fluctuations in the three-dimensional heisenberg antiferromagnet. *Phys. Rev. Lett.*, 80:5196–5199, Jun 1998.

[160] Ian Affleck, Z. Zou, T. Hsu, and P. W. Anderson. Su(2) gauge symmetry of the large-u limit of the hubbard model. *Phys. Rev. B*, 38:745–747, Jul 1988.

[161] Sebastian Fuchs, Emanuel Gull, Matthias Troyer, Mark Jarrell, and Thomas Pruschke. Spectral properties of the three-dimensional hubbard model. *Phys. Rev. B*, 83:235113, Jun 2011.

[162] D. J. Scalapino, E. Loh, and J. E. Hirsch. Fermi-surface instabilities and superconducting d-wave pairing. *Phys. Rev. B*, 35:6694–6698, May 1987.

[163] Satoshi Nakamura, Tôru Moriya, and Kazuo Ueda. Spin fluctuation-induced superconductivity in two and three dimensional systems. *Journal of the Physical Society of Japan*, 65(12):4026–4033, 1996.

[164] Ryotaro Arita, Kazuhiko Kuroki, and Hideo Aoki. Spin-fluctuation exchange study of superconductivity in two- and three-dimensional single-band hubbard models. *Phys. Rev. B*, 60:14585–14588, Dec 1999.

[165] P. Monthoux and G. G. Lonzarich. Magnetically mediated superconductivity in quasi-two and three dimensions. *Phys. Rev. B*, 63:054529, Jan 2001.

[166] Jakub Imriška, Mauro Iazzi, Lei Wang, Emanuel Gull, Daniel Greif, Thomas Uehlinger, Gregor Jotzu, Leticia Tarruell, Tilman Esslinger, and Matthias Troyer. Thermodynamics and magnetic properties of the anisotropic 3d hubbard model. *Phys. Rev. Lett.*, 112:115301, Mar 2014.

[167] Anne-Marie Daré, Y. M. Vilk, and A. M. S. Tremblay. Crossover from two- to three-dimensional critical behavior for nearly antiferromagnetic itinerant electrons. *Phys. Rev. B*, 53:14236–14251, Jun 1996.

[168] N. D. Mermin and H. Wagner. Absence of ferromagnetism or antiferromagnetism in one- or two-dimensional isotropic heisenberg models. *Phys. Rev. Lett.*, 17:1133–1136, Nov 1966.

[169] Cornelia Hille, Daniel Rohe, Carsten Honerkamp, and Sabine Andergassen. Pseudogap opening in the two-dimensional hubbard model: A functional renormalization group analysis. *Phys. Rev. Research*, 2:033068, Jul 2020.

[170] Cornelia Hille, Fabian B. Kugler, Christian J. Eckhardt, Yuan-Yao He, Anna Kauch, Carsten Honerkamp, Alessandro Toschi, and Sabine Andergassen. Quantitative functional renormalization group description of the two-dimensional hubbard model. *Phys. Rev. Research*, 2:033372, Sep 2020.

[171] Nahom K. Yirga and David K. Campbell. Frequency dependent functional renormalization group for interacting fermionic systems, 2020.

[172] P. Strack, R. Gersch, and W. Metzner. Renormalization group flow for fermionic superfluids at zero temperature. *Phys. Rev. B*, 78:014522, Jul 2008.

[173] Jay D. Sau, Roman M. Lutchyn, Sumanta Tewari, and S. Das Sarma. Generic new platform for topological quantum computation using semiconductor heterostructures. *Phys. Rev. Lett.*, 104:040502, Jan 2010.

[174] Florian Loder, Arno P Kampf, and Thilo Kopp. Superconductivity with rashba spin–orbit coupling and magnetic field. *Journal of Physics: Condensed Matter*, 25(36):362201, Aug 2013.

[175] Henning G. Hugdal and Asle Sudbø. p-wave superconductivity in weakly repulsive 2d hubbard model with zeeman splitting and weak rashba spin-orbit coupling. *Phys. Rev. B*, 97:024515, Jan 2018.

[176] Takashi Miyake, Kazuma Nakamura, Ryotaro Arita, and Masatoshi Imada. Comparison of ab initio low-energy models for lafepo, lafeaso, bafe2as2, lifeas, fese, and fete: Electron correlation and covalency. *Journal of the Physical Society of Japan*, 79(4):044705, 2010.

List of Publications

Hereby I declare that this thesis was compiled solely by myself. However, parts of it have already been published in previous articles in collaboration with the authors listed below, which I am sincerely grateful for. Especially parts of chapters 3.5 and 5.3 are contained in these publications, which are indicated in the abstracts at the beginning of each of these chapters. Following are the corresponding publications:

- J. Ehrlich and C. Honerkamp. Functional renormalization group for fermion lattice models in three dimensions: Application to the hubbard model on the cubic lattice. *Phys. Rev. B*, 102:195108, Nov 2020
- Giulio A. H. Schober, Jannis Ehrlich, Timo Reckling, and Carsten Honerkamp. Truncated-unity functional renormalization group for multiband systems with spin-orbit coupling. *Frontiers in Physics*, 6:32, May 2018
- C. J. Eckhardt, G. A. H. Schober, J. Ehrlich, and C. Honerkamp. Truncated-unity parquet equations: Application to the repulsive hubbard model. *Phys. Rev. B*, 98:075143, Aug 2018

Band / Volume 234
Towards Magneto-Elastomeric Nanocomposites with Supramolecular Activity
L. S. Fruhner (2021), XVI, 213 pp
ISBN: 978-3-95806-538-3

Band / Volume 235
Geometric and Electronic Properties of Heteromolecular Organic Monolayers on Noble Metal Substrates Studied by Photoemission Spectroscopy and X-ray Standing Waves
G. van Straaten (2021), vii, 115 pp
ISBN: 978-3-95806-539-0

Band / Volume 236
Nanoparticle assemblies: Order by self-organization and collective magnetism
A. Qdemat (2021), xix, 282 pp
ISBN: 978-3-95806-542-0

Band / Volume 237
γ-Aminobutyrate as carbon and nitrogen source for *Corynebacterium glutamicum* and regulation of the catabolic genes by GabR
L. Zhu (2021), 111 pp
ISBN: 978-3-95806-543-7

Band / Volume 238
Single-Trap Phenomena in Nanowire Biosensors
Y. Kutovyi (2021), 171 pp
ISBN: 978-3-95806-544-4

Band / Volume 239
Single crystal growth and neutron scattering studies of novel quantum materials
X. Wang (2021), VI, 145 pp
ISBN: 978-3-95806-546-8

Band / Volume 240
Structure and Dynamics of Magnetocaloric Materials
N. A. Maraytta (2021), vii, 146 pp
ISBN: 978-3-95806-557-4

Band / Volume 241
Novel insights into the transcriptional regulation of cell division in *Corynebacterium glutamicum*
K. J. Kraxner (2021), V, 83 pp
ISBN: 978-3-95806-560-4

Band / Volume 242
Interplay of proximity effects in superconductor/ferromagnet heterostructures
A. Stellhorn (2021), ix, 219 pp
ISBN: 978-3-95806-562-8

Band / Volume 243
Silencing and counter-silencing of the Lsr2-like protein CgpS in *Corynebacterium glutamicum*
J. Wiechert (2021), IV, 265 pp
ISBN: 978-3-95806-569-7

Band / Volume 244
Molecular Layer Functionalized Neuroelectronic Interfaces:
From Sub-Nanometer Molecular Surface Functionalization to Improved Mechanical and Electronic Cell-Chip Coupling
N. R. Wolf (2021), IV, 101, xx pp
ISBN: 978-3-95806-570-3

Band / Volume 245
Surface Acoustic Waves in Strain-Engineered Thin (K,Na)NbO_3 Films:
From Basic Research to Application in Molecular Sensing
S. Liang (2021), VI, 125 pp
ISBN: 978-3-95806-571-0

Band / Volume 246
Tailoring neuroelectronic interfaces via combinations of oxides and molecular layers
X. Yuan (2021), 113 pp
ISBN: 978-3-95806-572-7

Band / Volume 247
Stoichiometric control and magnetoelectric coupling in artificial multiferroic heterostructures
P. Schöffmann (2021), vii, 176 pp
ISBN: 978-3-95806-575-8

Band / Volume 248
A Unified Framework for Functional Renormalisation Group Calculations and its Application to Three Dimensional Hubbard Models
J. Ehrlich (2021), xvi, 213 pp
ISBN: 978-3-95806-582-6

Schlüsseltechnologien / Key Technologies
Band / Volume 248
ISBN 978-3-95806-582-6

Mitglied der Helmholtz-Gemeinschaft

JÜLICH
Forschungszentrum